Proceedings of the 32nd International Cosmic Ray Conference

Aug. 11-18, 2011

Beijing, China

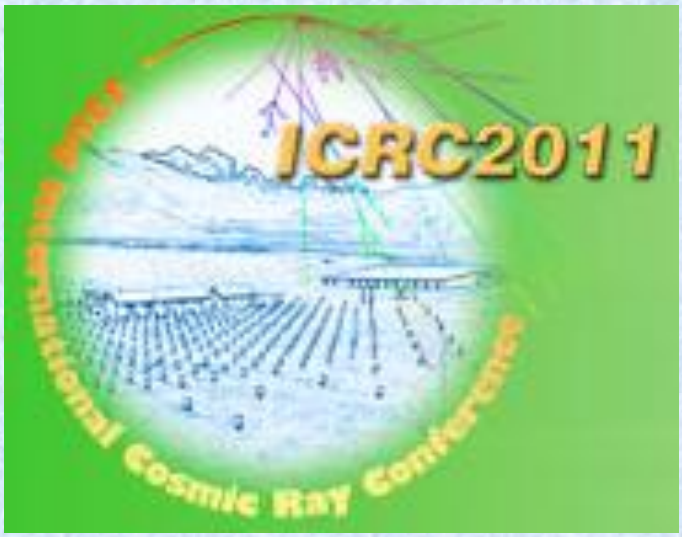

Volume: 4/12

HE Sessions: 2.1-2.6

Under the auspices of the International Union of Pure and Applied Physics (IUPAP)

32nd International Cosmic Ray Conference

August 11-18, 2011, Beijing, China

Organized by the

Institute of High Energy Physics

19B YuquanLu, Shijingshan District Beijing, 100049, P.R.China

Under the auspices of the

International Union of Pure and Applied Physics (IUPAP)

Co-sponsors of the ICRC2011

Chinese Academy of Sciences (CAS)

National Natural Science Foundation of China (NSFC)

China Center of Advanced Science and Technology(CCAST)

Institute of High Energy Physics (IHEP)

Committees

International Advisory Committee (IAC)

Chairman: Suresh Tonwar

Wlodzimierz Bednarek	Evgeny Berezhko	Daniel Bertrand
Hesheng Chen	Kwong Sang Cheng	Bruce Dawson
Cheng Fang	Erwin Flueckiger	Sunil Gupta
Hongbo Hu	Karl-Heinz Kampert	Johannes Knapp
Frank Krennrich	Tipei Li	Paolo Lipari
Tan Lu	Yuqian Ma	Juan Carlos Sanabria
Ronald Shellard	Yoichiro Suzuki	Michael Walter
Jingxiu Wang		

National Advisory Committee (NAC)

Chairman: Youheng Tan

Changjiang Dai	Chongshou Gao	Xiaoyu Gao
Mao He	Zuoxiu He	Anxiang Huo
Haohuai Kuang	Jun Mu	Chengrui Qing
Jingru Ren	Luorui Sun	Minghan Ye
Naijian Zhang	Qingqi Zhu	

National Organizing Committee (NOC)

Chairman: Hesheng Chen

Xiaojun Bi	Zhen Cao	Jin Chang
Guoming Chen	Shaomin Chen	Yao Chen
Zigao Dai	Weiqun Gan	Hongbo Hu (Secretary)
Jing Huang	Minghuey A Huang	Xiangdong Ji
Guiming Le	Zuotang Liang	Jun Lin
Siming Liu	Huanyu Wang	Jianmin Wang
Yifang Wang	Yihua Yan	Changgen Yang
Qian Yue	Jun Zhang	Li Zhang
Shuangnan Zhang	Xinmin Zhang	Pengfei Zhuang

Local Organizing Committee (LOC)

Chairman: Huanyu Wang

Gang Chen	Luobu Danzeng	Tiejun Deng
Lijun Guo	Huihai He	Hongbo Hu (co-chairman)
Huanyu Jia	Shumei Jia	Hong Lu
Xinhua Ma	Xianru Meng	Yue Sun
Ruiguang Wang	Tongzhou Xu (co-chairman)	Zhiguo Yao
Min Zha	Huimin Zhang	Xueyao Zhang

Contents

HE.2: Muons and Neutrinos

HE2.1 Muon experiments

Muon induced electromagnetic shower reconstruction in ANTARES neutrino telescope

SALVATORE MANGANO[1], FOR THE ANTARES COLLABORATION
[1]*IFIC - Instituto de Física Corpuscular, Edificio Institutos de Investigatión, Apartado de Correos 22085, 46071 Valencia, Spain*
manganos@ific.uv.es

DOI: 10.7529/ICRC2011/V04/0158

Abstract: The primary goal of the ANTARES telescope is the detection of high energy cosmic muon neutrinos. The neutrinos are identified by the upward going muons that are produced in charged current neutrino interactions in the vicinity of the detector. The Cherenkov light produced by the muons in the detection volume is measured accurately by an array of photosensors. Muons that are going downward are background for neutrino searches. These muons are the decay products of cosmic-ray collisions in the Earth's atmosphere. The energy loss in water of a muon with an energy above a TeV is characterized by discrete bursts of Cherenkov light originating mostly from pair production and bremsstrahlung (electromagnetic showers). This paper presents a method to identify and count electromagnetic showers produced by the muons. The method can be used to select a sample of highest energy muons with the ANTARES detector.

Keywords: Neutrino telescope, Electromagnetic shower reconstruction, High energy muons.

1 Introduction

The ANTARES neutrino telescope is located on the bottom of the Mediterranean Sea, roughly 40 km off the French coast. The main objective is the observation of extraterrestrial neutrinos. Relativistic charged leptons produced by neutrino interactions in and around the detector produce Cherenkov light in the sea water. This light is detected by an array of photomultiplier tubes (PMTs), allowing the muon direction to be reconstructed. The muon energy loss can be estimated from the sum of the measured number of photoelectrons.

The detector is installed at a depth of 2475 m and consists of twelve vertical lines approximately 450 m long equipped with a total of 885 PMTs. The lines are separated from each other by about 65 m, anchored to the sea bed by a dead weight and held taut by a buoy located at the top. The instrumented part of the line starts 100 m above the sea bed, with 25 storeys every 14.5 m along the line. A storey consists of three PMTs pointing downward at an angle of 45° with respect to the vertical direction, in order to maximise the detection efficiency of upward going tracks.

ANTARES is operated in the so called all-data-to-shore mode: all pulses above a threshold (typically 0.3 photoelectrons) are digitized off-shore and sent to shore to be processed in a computer farm. This computer farm applies a set of trigger criteria in order to separate muon-induced Cherenkov light from background light. The main sources of the background light are the decay of ^{40}K nuclei and the bioluminescence of organisms in the sea water. A detailed description of the ANTARES detector is given in [1].

Although ANTARES is optimised for upward going particle detection, the most abundant signal is due to the atmospheric downward going muons produced by the interaction of primary cosmic-rays in the atmosphere. Being the most penetrating particles in such air showers, muons with enough energy can reach the detector and are reconstructed by the detection of the Cherenkov light they emit when propagating through water. The ANTARES detector has the capability to follow highly energetic muons over a few hundred metres.

The processes contributing to the energy loss of a muon in water include ionisation, e^+e^- pair production, bremsstrahlung, and photonuclear interactions. Below 1 TeV, the muon energy loss is dominated by the continuous ionisation process. Above 1 TeV, the muon energy loss is dominated by pair production and bremsstrahlung [2], which are radiative processes classified as electromagnetic showers. They are characterized by large energy fluctuations and discrete bursts along the muon track. The average muon energy loss per unit track length due to these electromagnetic showers increases linearly with the energy of the muon allowing its energy to be determined. Counting electromagnetic showers along muon tracks gives an estimate of the muon energy [3] and can help in designing a better energy reconstruction algorithm. A similar measurement technique as the one presented in this article has been published recently by the Super-Kamiokande experiment [4].

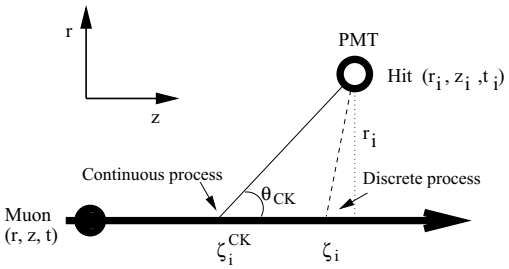

Figure 1: *Schematic view of the Cherenkov light detection. The thick line represents the muon trajectory, the thin line the path of the Cherenkov light and the thin dashed line the path of the shower light. The muon goes through a reference point* (r, z, t)*. The Cherenkov light is emitted at an angle* $\theta_{\rm CK}$ *with respect to the muon track at point* $\zeta_i^{\rm CK}$ *and is detected by a PMT as a hit at point* (r_i, z_i, t_i)*. The shower light is emitted at point* ζ_i *and is detected by the same PMT at different time.*

2 Algorithm for shower identification

The purpose of the electromagnetic shower identification is to distinguish Cherenkov photons emitted continuously along the muon track, from the Cherenkov photons induced by electromagnetic showers. Because of the radiation length in water ($X_0 = 35$ cm), these showers never extend more than a few metres and can be considered point-like light sources in the ANTARES detector. The showers can be identified from a localised increase of the number of emitted photons above the continuous baseline of Cherenkov photons emitted by a minimum ionizing muon.

In what follows, a hit is a photomultiplier signal exceeding a threshold of 0.3 photoelectrons. The shower algorithm consists of two steps. The first step is to identify and reconstruct downward going muon track candidates. In the second step, a distinct shower candidate is identified by looking for an accumulation of hits on a point along the muon path. The criteria to isolate the accumulation are defined from a simulation code based on Corsika [5].

2.1 Simulation

Cosmic-ray interactions in the atmosphere including shower development were simulated for primary energies between 1 TeV and 10^5 TeV, and incident angles between zero (vertical) and 85 degrees with Corsika. The primary cosmic-ray composition and flux model considered was a simplified version[1] of the Hörandel model [6]. The hadronic interaction model chosen was QGSJET [7]. The result of the Corsika simulation consists of muons with their positions and times and kinematic vectors on the surface of the sea. The muon propagation through water, the discrete energy losses at high energies, the Cherenkov light production and propagation, including scattering, and the response of the detector was simulated using the ANTARES KM3 code [8]. KM3 uses tables generated from a simulation with GEANT 3 which parametrise the arrival time and the amount of light detected by individual PMTs. These tables take into account the angular dependence of the acceptance of the PMT as well as the measured properties of the water at the ANTARES site. The muon propagation uses the MUSIC code [9] and is done in short steps (1 m). If the energy loss of the muon over the step exceeds a threshold (1 GeV), an electromagnetic shower is initiated and shower photons are emitted, otherwise if the energy loss of the muon over the step is below the threshold muon Cherenkov photons are emitted. The optical background was assumed flat at a rate of 60 kHz on each photomultiplier.

2.2 Algorithm

Muon events are reconstructed by using an existing algorithm [10, 11] which provides an estimate of the direction and position of the muon at a given time. Measured hit times are compared to the expected arrival time of direct Cherenkov photons. The expected Cherenkov photon arrival time $t_i^{\rm CK}$ for each hit i is calculated as (see Figure 1):

$$t_i^{\rm CK} = t + \frac{1}{c}\Big(z_i - z - \frac{r_i}{\tan\theta_{\rm CK}}\Big) + \frac{n}{c}\frac{r_i}{\sin\theta_{\rm CK}}, \quad (1)$$

where t is the time where the muon passes point (r, z), c is the speed of light in vacuum, n is the refraction index of water (n is about 1.38), $\theta_{\rm CK}$ is the Cherenkov angle for a relativistic muon in water ($\theta_{\rm CK} = 42^o$) and r_i is the perpendicular distance between the muon trajectory and the PMT. Equation (1) separates the direction along the track and the direction perpendicular to the track. The direction along the track (z-coordinate) is given by the muon momentum vector. The direction perpendicular to the track (r-coordinate) is given by the photon momentum vector in water. Hits too far in time from the expected muon hit time $-t_{min} < t_i - t_i^{\rm CK} < t_{max}$, are assumed to be background hits and are rejected, whereas direct hits have a roughly Gaussian distribution at zero with a width of 20 ns. The value for $t_{min} = 20$ ns is given by mainly the dispersion of light in water and the timing resolution of the PMT, whereas $t_{max} = 200$ ns is defined by the value where the number of signal hits approaches the level of background hits. Furthermore, the above defined time interval is subdivided into two intervals. The early interval contains mostly muon Cherenkov photons and is given by $|t_i - t_i^{\rm CK}| < t_{min}$. The Cherenkov photon emission position ($\zeta_i^{\rm CK}$) along the muon trajectory is given by:

$$\zeta_i^{\rm CK} = z_i - z - \frac{r_i}{\tan\theta_{\rm CK}}. \quad (2)$$

The late interval is defined by $t_{min} < t_i - t_i^{\rm CK} < t_{max}$ and contains mostly electromagnetic shower photons. These shower photons may not necessarily be emitted at the Cherenkov angle from the muon track. The emission angle is left as a free parameter and, with the photon emission

1. The primary composition of the flux is subdivided into only five mass groups, namely proton, helium, nitrogen, magnesium and iron.

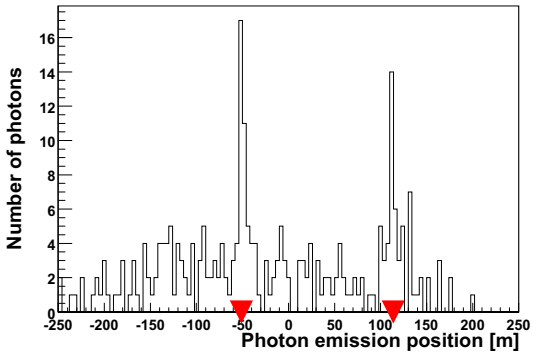

Figure 2: *The number of detected photons projected along the muon trajectory for an atmospheric muon event with two electromagnetic showers. The peaks indicate the shower positions on the muon trajectory, with the reconstructed shower positions indicated by the triangles.*

taking place at ζ_i (see Figure 1), the hit time is given by

$$t_i = t + \frac{\zeta_i - z}{c} + \frac{n}{c}\sqrt{r_i^2 + (z_i - \zeta_i)^2}. \quad (3)$$

Equation (3) can be solved for $\zeta_i^{\pm}$, yielding:

$$\zeta_i^{\pm} = \frac{-B_i \pm \sqrt{B_i^2 - 4AC_i}}{2A},$$

where

$$\begin{aligned} A &= 1 - n^2, \\ B_i &= 2(n^2 z_i - z - c(t_i - t)), \\ C_i &= c^2(t_i - t)^2 + 2cz(t_i - t) + z^2 - n^2(r_i^2 + z_i^2). \end{aligned}$$

All calculated ζ_i^{CK}, ζ_i^{+} and ζ_i^{-} positions along the muon track are collected in a one-dimensional histogram. As an example of such a histogram, Figure 2 shows all the calculated photon emission positions along the muon trajectory. The electromagnetic showers are identified by an excess of photons above the continuous baseline of photons emitted by a minimum ionizing muon. Two excesses are visible that can be attributed to the two reconstructed showers.

3 Selection and results

The selection and performance of the shower identification algorithm has been studied and validated with a sample of simulated atmospheric multi-muons with constant background light as described in section 2.1.

3.1 Selection

The shower algorithm makes use of tracks fitted with the muon reconstruction algorithm described in [10] with two additional criteria. These criteria require the tracks to be traced for at least 125 m and to have a minimum of twelve hits used in the track reconstruction. These selected tracks account for around 65% of all reconstructed tracks. The advantage of the selected tracks is not only that the direction of the tracks is better reconstructed, but also that the tracks are long enough to have a high probability to emit showers.

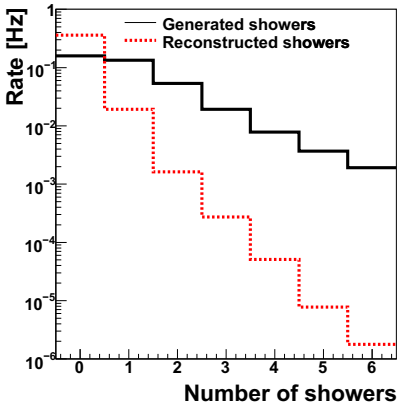

Figure 3: *Muon event rate as a function of the shower multiplicity for reconstructed showers and for generated showers which have shower photons detected on at least five different storeys for the Corsika simulation.*

The parameters in the shower reconstruction algorithm are the width and the height of the peak. The analysis has been tuned to select showers with a high level of purity, possibly at the expense of efficiency. For each selected peak, the number of hits is integrated in a ± 5 m interval around the peak center. Only peaks having at least 10 hits over the muon-track Cherenkov photon baseline in this interval of 10 m are selected. The number of baseline hits is defined as the average density of hits along the track times the interval width of 10 m. In addition, in order to suppress fake identified showers, hits from at least five different storeys are required in each peak.

3.2 Results

The main result of the shower reconstruction algorithm is the shower multiplicity per atmospheric muon event. The atmospheric muon events are usually muons in a bundle with an average multiplicity of around 3.3. Figure 3 shows the event rate as a function of the number of generated showers with shower photons detected on at least five different storeys. Also shown is the number of reconstructed showers selected with the cuts mentioned in section 3.1. The average shower reconstruction efficiency over all shower energies is around 4%. The reconstruction algorithm starts to be efficient for shower energies above 300 GeV.

Figure 4 shows the number of generated showers with shower photons detected on at least five different storeys per atmospheric muon event as a function of the muon energy. The muon energy refers to the muon with the largest energy in the bundle. The number of generated shower and reconstructed shower increases as a function of the muon

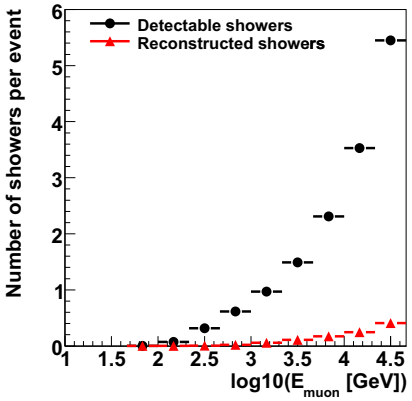

Figure 4: *Average number of detectable showers which have shower photons detected on at least five different storeys per atmospheric muon event as a function of the muon energy. Also shown is the average number of reconstructed showers.*

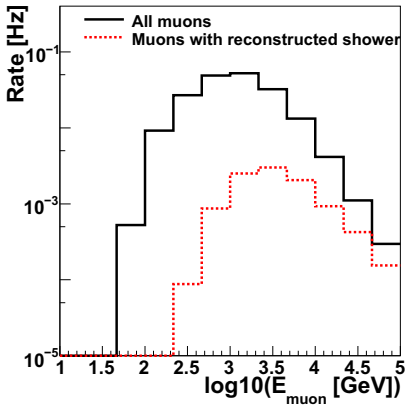

Figure 5: *The solid line shows the energy distribution of all reconstructed atmospheric muons. The dotted lines represent the muon energy distribution for the muons with at least one reconstructed shower.*

energy. Figure 5 shows the energy distribution of all muons as well as the one with at least one reconstructed shower. The muons have an average energy of 1.2 TeV, whereas muons with at least one identified shower have on average 2.5 times higher energy.

4 Conclusion

A method to identify showers emitted by atmospheric muons has been applied to simulated data of the ANTARES detector. The main differences between the shower light and the muon Cherenkov light are that the shower light is produced on a point along the muon path. The essential element of the algorithm is that the selection of shower photons is reduced to a one-dimensional problem. The performance of the identification algorithm has been validated using a sample of simulated atmospheric muon events.

The aim of this proceeding has been more to demonstrate the capability to detect electromagnetic showers than to make precise measurements. A more elaborated analysis is needed, in order to use the number of electromagnetic showers as a robust estimate of the muon energy. Moreover, the method discussed here for selecting showers emitted by downward going muons could be used also for upward going muons with the main purpose of selecting the highest energy upward going muons.

Acknowledgments

I gratefully acknowledge the support of the JAE-Doc postdoctoral programme of CSIC. This work has also been supported by the following Spanish projects: FPA2009-13983-C02-01, MultiDark Consolider CSD2009-00064, ACI2009-1020 of MICINN and Prometeo/2009/026 of Generalitat Valenciana.

References

[1] M. Ageron et al, 2011, "ANTARES: the first undersea neutrino telescope", arXiv:1104.1607v1.

[2] K. Nakamura et al, 2010, "The review of particle physics",J. Phys., G 37.

[3] R. Gandhi and S. Panda, 2006, "Probing the cosmic ray 'knee' and very high energy prompt muon and neutrino fluxes via underground muons", JCAP, 0607.

[4] S. Desai, 2008, "Study of TeV Neutrinos with Upward Showering Muons in Super-Kamiokande", Astropart. Phys., 29 p. 42-54.

[5] D. Heck, D. and Schatz, G. and Thouw, T. and Knapp, J. and Capdevielle, J. N., 1998, "CORSIKA: A Monte Carlo code to simulate extensive air showers", Report, Forschungszentrum Karlsruhe, FZKA-6019.

[6] J. R. Hoerandel, 2003, "On the knee in the energy spectrum of cosmic rays", Astropart. Phys. 19, p.193-220.

[7] S. Ostapchenko, 2007, "Status of QGSJET", AIP Conf. Proc., 928, p. 118-125.

[8] D. J. L. Bailey, 2002, "Ph.D. Thesis, Oxford University, Monte Carlo tools and analysis methods for understanding the ANTARES experiment and predicting its sensitivity to Dark Matter", see also http://antares.in2p3.fr/Publications/index.html#thesis.

[9] P. Antonioli and C. Ghetti and E. V. Korolkova and V. A. Kudryavtsev and G. Sartorelli, 1997, Astropart. Phys. 7, p. 357-368.

[10] M. Ageron et al., 2009, 'Performance of the First ANTARES Detector Line", Astropart. Phys. 31, 277-283.

[11] B. Ronald, 2008, "Ph.D. Thesis, Amsterdam University, The ANTARES Neutrino Telescope: Performance studies and analysis of first data", see also http://antares.in2p3.fr/Publications/index.html#thesis.

The relation between the deposit energies of the muons and their primary energies, and the relation between the deposit energies and their Cherenkov light yields in KM3 detector

NOBUSUKE TAKAHASHI[1], YOSHIHIDE OKUMURA[1], AKEO MISAKI[2]
[1]*Graduate School of Science and Technology, Hirosaki University, Hirosaki, 036-8561 Japan*
[2]*Innovative Research Organization, Saitama University, Saitama, 338-8570 Japan*
amisaki@sand.ocn.ne.jp
DOI: 10.7529/ICRC2011/V04/0198

Abstract: In the KM3 detector or pre-KM3 detector like AMANDA, one may recognize that [1] the deposit energies of the muon produced in the detector by neutrino interaction are proportional to their primary muon energies and [2] these deposit energies are equivalent to Cherenkov light yield produced by the deposit energies. In these detectors in which high energy muons are detected via Cherenkov light, one may recognize that the primary energies of the muons are uniquely determined by measuring Cherenkov yields in the detector under the prepositions of [1] and [2]. We have carried out extensive numerical compute experiments for the examination on the validities of the prepositions [1] and [2]. In our present paper, we discuss these validities quantitatively in detail.

Keywords: High energy muon, Muon propagation, Energy determination of the muon, KM3 detector

1 Introduction

In the KM3 detector or pre-KM3 detector, one estimates the energies of (extremely) high energy muons resulted in the neutrino interactions through Cherenkov light yields. Then, one assumes implicitly that the energy loss of the muon may be proportional to the primary energy of the muon and the Cherenkov light yields may be equivalent to the energy loss of the muon. In our paper, we examine whether this validity is really guaranteed or not by our extensive and rigorous computer numerical experiment.

2 A hypothetical detector for measuring Cherenkov light yields

In Figure 1, we schematically show a hypothetical detector in our computer numerical experiment. We make muons with given primary energies to inject into the hypothetical detector and pursue the behaviors of the muons concerned, taking into account of the stochastic characters in all physical processes concerned exactly. In the passage of the muons concerned in the detector, we exactly simulate the behaviors of the muons, namely, where, what kind of the interactions (bremsstrahlung, direct electron pair or photonuclear interaction) and what the dissipated energy. The detail of the stochastic treatment on the behaviors of the muon is explained in another paper by the same authors [1].

The Cherenkov light yields are produced by both the muon themselves and by the electromagnetic cascade showers initiated by muons which are generated by bremsstrahlung, direct electron pair production or photonuclear interaction. In Figure 2, we give the ratios of the Cherenkov light yields due to the accompanied electromagnetic cascade showers to those due to [these accompanied showers plus muons themselves]. It is clear from the figures that above the energies of 10^{15}eV, the most of the Cherenkov light are occupied by those from the electromagnetic cascade showers and those from muons themselves can be neglected.

Fluctuation of the Cherenkov light yields produced in the accompanied electromagnetic cascade showers are consist of two parts. The first part is the fluctuation of the dissipated energies due to different physical processes (bremsstrahlung, direct electron pair production and photo nuclear interactions) and the second part is the fluctuation in the accompanied electromagnetic cascade showers. Due to these different natures of the fluctuations, the developments of Cherenkov light yields show the complexity.

3 The correlation between the total Cherenkov light yields and the corresponding energy loss

The total Cherenkov light yield denotes the sum of those due to the muons themselves and those from the accompanied cascade showers by the muons and the dissipated energy losses denote the total energy losses due to physi-

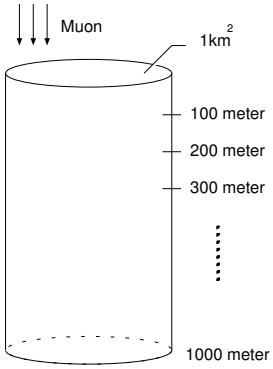

Figure 1: Observation points for measuring the energy losses due to muons and the Cherenkov light yields due to the energy losses.

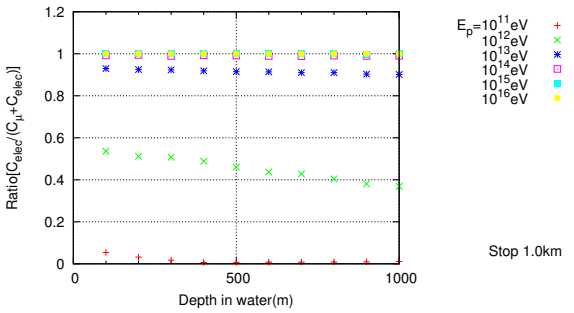

Figure 2: The Ratios of the Cherenkov light yields due to the accompanied electromagnetic cascade showers due to muon to those due the muons themselves as the function of the length traversed for different primary energies.

cal processes of the bremsstrahlung and others. In Figures 3 to 7, we give the correlation diagram between the total Cherenkov light yields and the dissipated energies (energy deposits) muons up to 200, 500 and 1000 meters for 10^{14}, 10^{15}, 10^{16}eV, respectively. The sampling number is 500.

In Figures 3 and 4, we give the correlation diagram between the total Cherenkov light yields and the energy losses at 200 meters, 500 meters and 1000 meters from the injection point for 10^{14}eV and 10^{15}eV muons, respectively. It is clear from the correlations at different observation points overlap partially, which fluctuations in both the total Cherenkov light yields and the energy losses are complicate and large. At the observation point of 200 meter(shallower depth), The correlation, namely, the fluctuation of the total Cherenkov lights yields (the energy losses) for given the total energy losses (Cherenkov light yields) become larger, compared with those at larger 1000 meters (deeper depth).

In Figures 5 to 7, we give the similar correlations at 200 meter, 500 meter and 1000 meters for 10^{16}eV where the Cherenkov light yields due to muon themselves are completely neglected. At 100 meter observation point, the uncertainty in the energy loss spreads over two decades and the uncertainty in the total Cherenkov light yields spread over two decades or more.

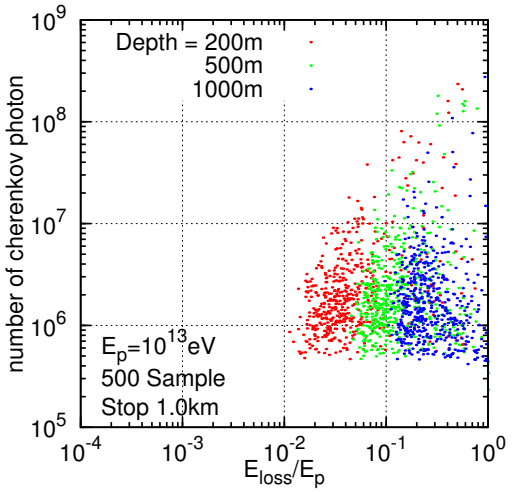

Figure 3: The correlation between the energy losses of muons and the Cherenkov light yields at 200, 500, 1000 meters for 10^{13} eV.

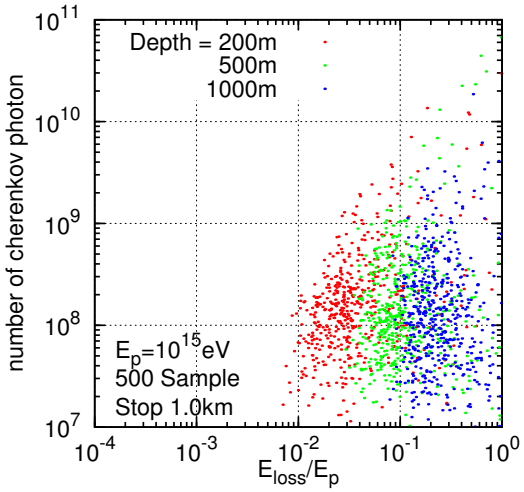

Figure 4: The similar graph to Figure 3 for 10^{15} eV.

At the observation point of 1000 meters, the uncertainty of the energy losses spread over one decade, while the Cherenkov light yields spread over two decades. Here, notice roughly speaking, that $\sim$ 10 % of the primary energy is dissipated at most.

From the comparison among the Figures 3 to 7, we cannot claim that the energy loss may be proportional to the primary energy and, furthermore, total Cherenkov light yields may be proportional to the energy loss.

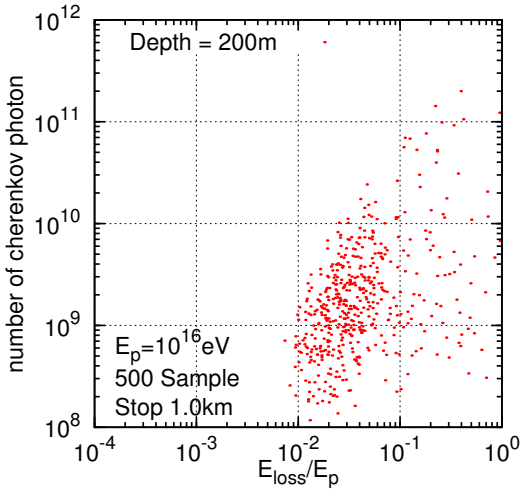

Figure 5: The similar graph to Figure 3 at 200 meters for 10^{16} eV.

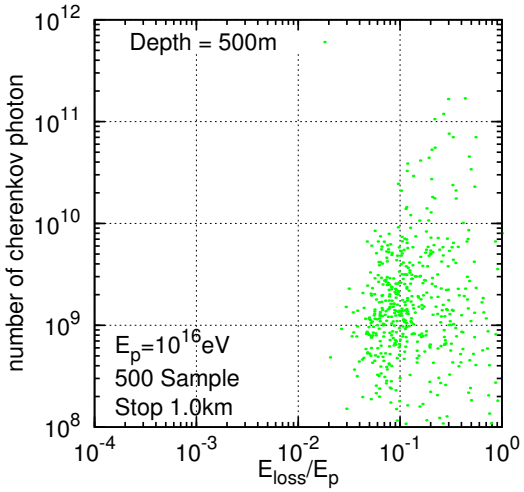

Figure 6: The similar graph to Figure 5 at 500 meters..

In Figures 8 and 9, we give the transition curves of the total Cherenkov light yields as the function of the depths for 10^{13}, 10^{15}eV, respectively. Here, the total Cherenkov light yield for given depth denotes total quantity of Cherenkov light at given depth. The sampling number is 500 per each primary energy. The uncertainty bars attached to each curve denote show the ranges within which 68 % of the total number of the events are included which correspond to one sigma in the normal distribution. The distributions of the event numbers around their average values are far from the normal distributions. Also, it is clear from the figures that we cannot estimate the energy loss from the total Cherenkov light yields, taking large deviation from the average values.

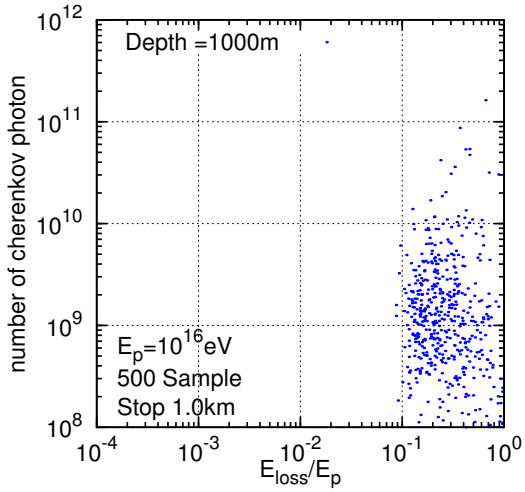

Figure 7: The similar graph to Figure 5 at 1000 meters..

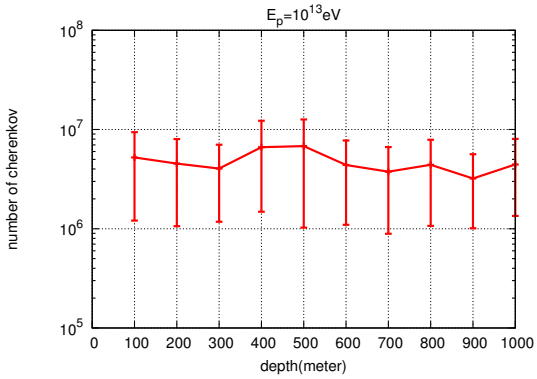

Figure 8: The transition curve of the Cherenkov light yields as the function of the depth for 10^{13} eV. The sampling number is 500.

In Figures 10 and 11, we give the individual transition curve initiated by a muon. We overplot three different curves for the same primary energies. [Shortest] denotes the real transition initiated by a muon with shortest range among 500 sampled events. [Longest] denote the transition curve initiated by a muon with the longest ranger among the same sampled. [Average-like] denotes the transition curve by a muon with range of which is nearest to the average range among the same sampled. The transition curves with shortest in Figure 10 die within 100 meters from the starting point. The muon with shortest range for primary energy of 10^{13} eV terminates, owing to the catastrophic energy loss of the bremsstrahlung. Correspondingly, the catastrophic energy loss due to the bremsstrahlung causes an electromagnetic cascade shower with extremely high primary gamma ray (bremsstrahlung) and the cascade shower produce Cherenkov light yield. We

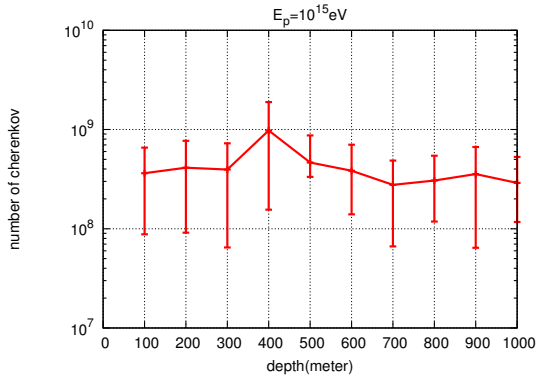

Figure 9: The similar graph to Figure 8 for 10^{15} eV. The sampling number is 100.

simulate the cascade shower exactly under the framework of one dimensional and Approximation B. [2]. and then, considering the effect of the absorption in the Cherenkov light yields which electrons in the cascade showers generate. The reason why there are no significant differences in the general picture between the average-like and the longest comes from that the length of 1000 meter is pretty short for total absorption of the Cherenkov light yields 10^{13}eV muons. Notice that the saw-like character of individual transition curve in the figure which is quite different from the smoother curves in Figure 8.

Similarly, we show the corresponding ones initiated by the primary muon of 10^{15}eV in Figure 11. It is clear from the Figure 11 that fluctuations become violent, compared with the case of 10^{13}eV. Here, even the transition curve with shortest range does not lie within 1000 meters. The saw-like character of individual transition curve become more violent compared with 10^{13}eV.

Also, it is clear from Figures 8 and 11 that we cannot the individual energy loss from the corresponding energy loss which cannot directly connect with primary muon energy. Furthermore, it is necessary to know the information on the neutrino energy spectrum which finally produces the muons concerned as for the estimation of primary muon energies. Thus, it is easily concluded for the moment that we can estimate neither the primary energy of muons from their energy losses, nor their energy losses from their total Cherenkov light yields. This is the real problem which KM3 projects face for the present.

References

[1] Y.Okumura, N.Takahashi and A.Misaki, the contributed paper to this conference.

[2] B.Rossi:1956, High-Energy Particles, Prentice-Hall, Inc.

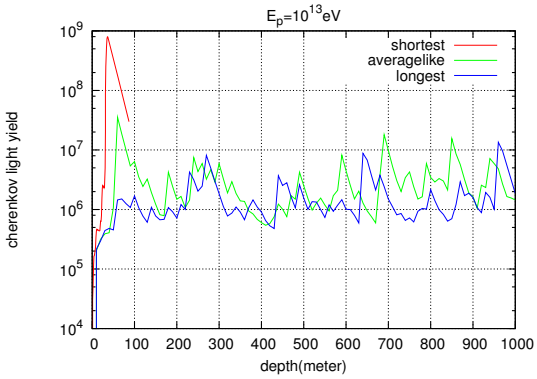

Figure 10: Individual transition curve of the Cherenkov light yields as the function of the depth with shortest, average-like and the longest range for 10^{13} eV.

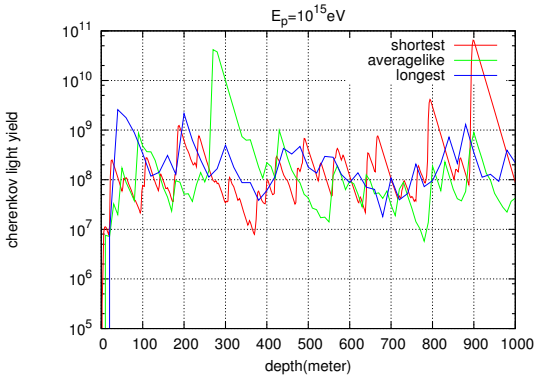

Figure 11: The similar graph to Figure 10 for 10^{15} eV.

Fluctuation of high energy muons and induced Cherenkov photons in water

YOSHIHIDE OKUMURA[1], NOBUSUKE TAKAHASHI[1], AKEO MISAKI[2]
[1]*Graduate School of Science and Technology, Hirosaki University, Hirosaki, 036-8561 Japan*
[2]*Innovative Research Organization, Saitama University, Saitama, 338-8570 Japan*
taka@cc.hirosaki-u.ac.jp
DOI: 10.7529/ICRC2011/V04/0251

Abstract: The range fluctuation on high energy muon is exactly treated in the sense of computer numerical experiment. The survival probabilities obtained by our *simple time sequential method* are compared with those obtained by the traditional method (v_{cut} *procedure method*). The agreement between them is well. We examine the typical behaviors of individual muons, with the shortest range, with average like range and with the longest range and clarify their characteristics. Further more, we notice that the agreement between them is well as far as the muons' behaviors are concerned, but we expect that the behavior of the Cherenkov light yields become different between them.

Keywords: Fluctuation, High energy muon, Deposit energy of muon, Cherenkov transition

1 Introduction

In the KM3 detectors deployed in the Antarctic, the ocean and lake, [2,3,4,5] what is the most important is to decide the energies of high energy muons due to neutrino interactions from the experimental and technical point of view. In the energy determination of high energy muons, there are two indispensable problems to be carefully examined, the first is the examination on the fluctuation of the traversed lengths of the muons and the second is the fluctuation on the Cherenkov light yields initiated by both the muons themselves and their daughters' electromagnetic cascade showers. In the present paper, we study the range fluctuation of high energy muons and in an another contribute paper[1], we study the fluctuation in the Cherenkov light from the electromagnetic cascade showers[1].

2 *The* v_{cut} *procedure method* and *the simple time sequential method* in the treatment of high energy muons

The Monte Carlo method is the one of the most powerful means to study fluctuation of the problems concerned. As far as the treatment of the range fluctuation of high energy muons by the Monte Carlo method is concerned, there exist two independent approaches. The one is the procedure of splitting the radiative energy loss in two terms, a continuous "soft" term for $v < v_{cut}$ and a stochastic "hard" term for ($v_{cut} < v < 1$) in the fundamental equation for the muons' energy losses which we name tentatively v_{cut} *procedure method* [6,7,8]. The other is *the simple time sequential method* developed by us in which the interaction points of the muons and their dissipated energies are directly determined [9,10] and, here, all possible physical processes are treated in stochastic manner without the introduction if cut. In the present paper, we take the minimum energy of the muon as 1GeV.

3 The validity of *the simple time sequential method* and comparison of our calculations with those obtained by v_{cut} *procedure method*

Our *simple time sequential method* had been confirmed by the results obtained by the analytical theory[11]. Now our results are compared with that by Lipari and Stanev[6] in Figure 1 and that of Klimushin et al.[8] in Figure 2. The agreement between our results and those by *the* v_{cut} *procedure method* are well, taking into account of the some differences in the cross sections concerned.

4 Individual behavior of the muon for 1 EeV

In our method, we exactly simulate the whole history of individual muon, namely, we know where the muon interact with matter, know what kind of the interaction (bremmstrahlung or direct electron pair or photonuclear interaction) occur and know how much energy is dissipated for the muons concerned. In Figures 3 to 5, we give the muon

1. As for the induced photons in water, it will be discussed in an another contributed paper[1].

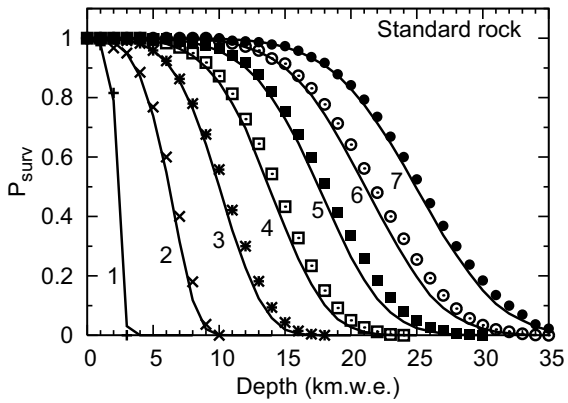

Figure 1: The comparison of our survival probabilities with those by Lipari and Stanev [6]. Curves labels correspond to following set of primary energies: (1)1TeV, (2)10TeV, (3)10^2TeV, (4)10^3TeV, (5)10^4TeV, (6)10^5TeV, (7)10^6TeV. The continuous lines show our results and symbols are read out from the graph by Lipari and Stanev.

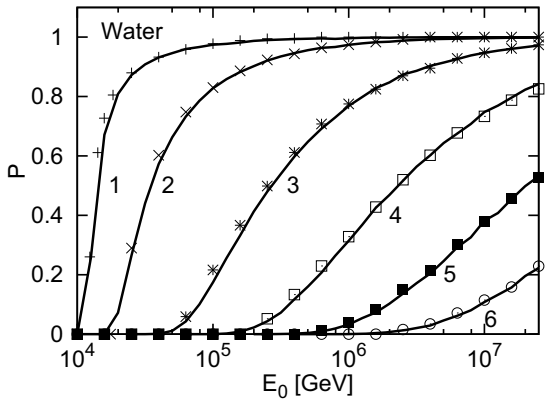

Figure 2: The comparison of our survival probabilities with those by Klimushin et al [7] The continuous lines are obtained by us, while symbols are readout from those by Klimushin et al for primary energies from 10^{13} eV to 3×10^{16} eV. The numerical figures attached each curve denote the threshold energy is 10 TeV. Curves labels correspond to following set of depths: (1)1.15km, (2)3.45km, (3)8.05km, (4)12.65km, (5)17.25km, (6)21.39km.

with shortest range, one with the average like range and one with the longest range. Here, the average like range denotes the most nearest range among the total sampling the muon. In this case, the shortest range is 8.27 kilo meters, while the longest range 54.8 kilo meters. We should say there is big fluctuation in the range distribution for 10^{18} eV muon.

In these figures, the abscissa denotes the depth from the starting point, and the ordinate denote the ratio of the

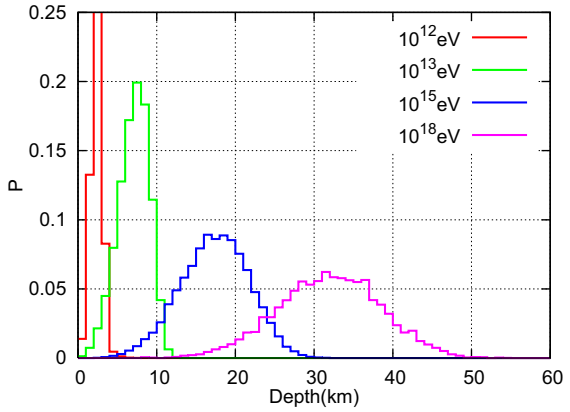

Figure 6: The range distributions for different primary energies from 10^{12} eV to 10^{18} eV.

muon's energy at the given depth to primary energy. The colors of "needles" denote the kinds of the interactions (bremsstrahlung (red), direct pair production (green), and photo nuclear interaction (blue) and the lengths of the needles denote the ratio of the dissipated energies due to the specified interaction to primary energy, the line graphs in the figure denote the ratio of the muon's energy to primary energy at the depths. In v_{cut} *procedure method*, usually they adopt v_{cut} = 10^{-3} to 10^{-5}. Consequently, they cannot consider discrete energy dissipation as shown in the figures whose v is smaller than v_{cut}.

In Table1, we give more detailed information around the number of the specified interactions and the corresponding energy losses in the case of shortest ranges, ones with the average like ranges and ones with the longest ranges. In Tablel 2, we give the ratios of the dissipated energies due the specified interactions to the primary energies in the cases of the shortest ranges, average-like ranges and the longest ranges. <average> denote the arithmetic average among total sampling of the event (500 sampling), while [average-like] are not <average>, but muons whose real range (individual) in the nearest to their average values.

It is clear from these tables that the muons with the shortest ranges are turned to lose their energy by the bremsstrahlung (the so called "catastrophic" energy loss, while the muon with the longest loses their energies by repeating a large number of interactions of direct electron pair production with rather small energies (rather "continuous"). In Table 3, we give the range distributions for 10^{12} eV to 10^{18} eV. These range distributions above 10^{14} eV may be well approximated by the Gaussian distribution whose the average and the standard deviation is given in Table 3.

5 Conclusion

As far as the dissipated energies due to muons are concerned , the results obtained by *the simple time sequential*

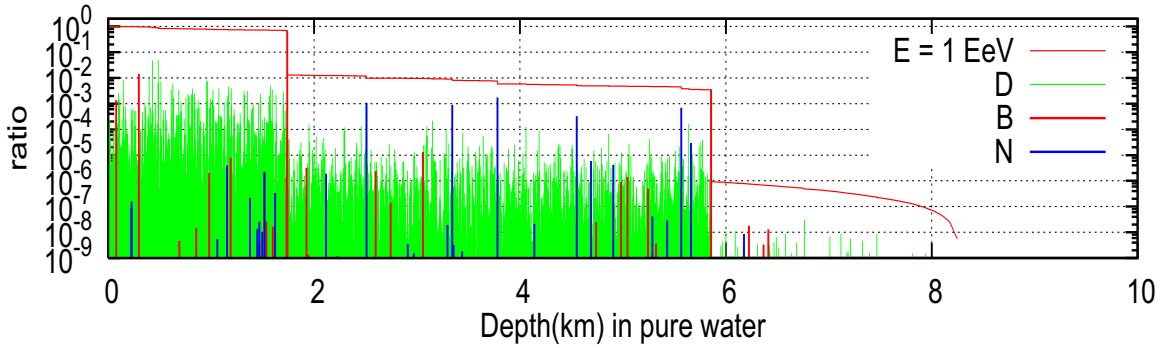

Figure 3: The transition for energy loss due to specified interactions as the function of the depth for the 10^{18} eV muon with shortest range.

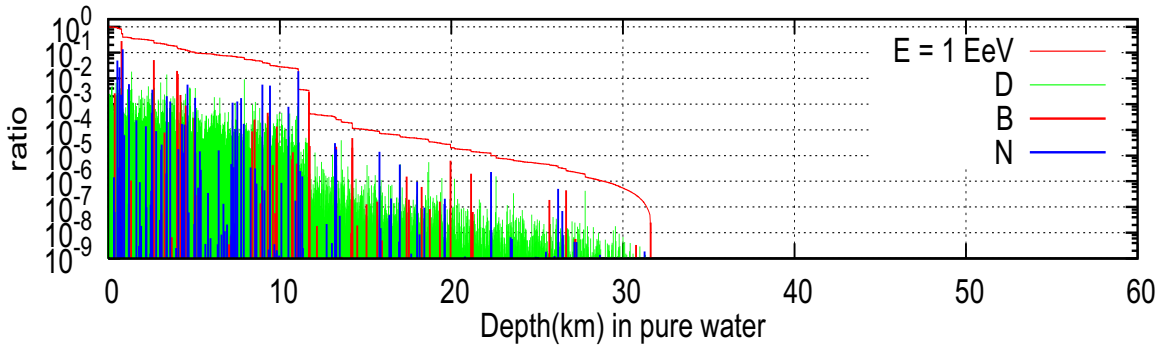

Figure 4: The similar graph to Figure 3 for 10^{18} eV with the average-like range.

Table 1: The details of the characteristics on the muons with the shortest range, the average like range, the longest range and the average range.

$E_p = 10^{12}eV$	Range [km]	Energy loss by brems	Number of interaction	Energy loss by direct pair	Number of interaction	Energy loss by nuclear	Number of interaction
<Average>	2.39×10^{0}	1.09×10^{11}	4.67×10^{0}	1.70×10^{11}	2.39×10^{2}	4.43×10^{10}	3.37×10^{0}
Shortest	6.23×10^{-2}	9.81×10^{11}	2	4.73×10^{8}	4	3.99×10^{8}	1
Average-like	2.51×10^{0}	1.17×10^{11}	3	1.44×10^{11}	232	1.37×10^{11}	4
Longest	9.29×10^{0}	6.09×10^{10}	8	1.44×10^{11}	288	1.66×10^{9}	2
$E_p = 10^{15}eV$							
<Average>	1.72×10^{1}	3.38×10^{14}	4.64×10^{1}	4.96×10^{14}	6.56×10^{3}	1.61×10^{14}	5.31×10^{1}
Shortest	1.68×10^{0}	8.59×10^{14}	5	8.87×10^{13}	628	5.20×10^{13}	4
Average-like	1.73×10^{1}	4.23×10^{14}	35	4.75×10^{14}	6363	9.67×10^{13}	56
Longest	3.16×10^{1}	1.82×10^{14}	70	7.50×10^{14}	10981	5.84×10^{13}	91
$E_p = 10^{18}eV$							
<Average>	3.17×10^{1}	3.24×10^{17}	1.04×10^{2}	4.59×10^{17}	2.48×10^{4}	2.17×10^{17}	1.66×10^{2}
Shortest	8.27×10^{0}	7.04×10^{17}	33	2.91×10^{17}	7285	4.77×10^{15}	40
Average-like	3.19×10^{1}	3.76×10^{17}	95	3.51×10^{17}	22395	1.64×10^{17}	173
Longest	5.48×10^{1}	7.52×10^{16}	190	7.61×10^{17}	45367	2.73×10^{17}	299

method is the same value as those obtained by *the v_{cut} procedure method* shown as in Figures 1 and 2, because the introduction of v_{cut} into the fundamental equation never change the total quantity of the dissipated energy.

However, when we treat the Cherenkov light yields due to muons concerned, the discrepancy on the Cherenkov light yields between two method is expected to become clear.

The first, how to dissipate energies into the Cherenkov part are quite different in both method and consequently, the transition curves for Cherenkov light yields by our method

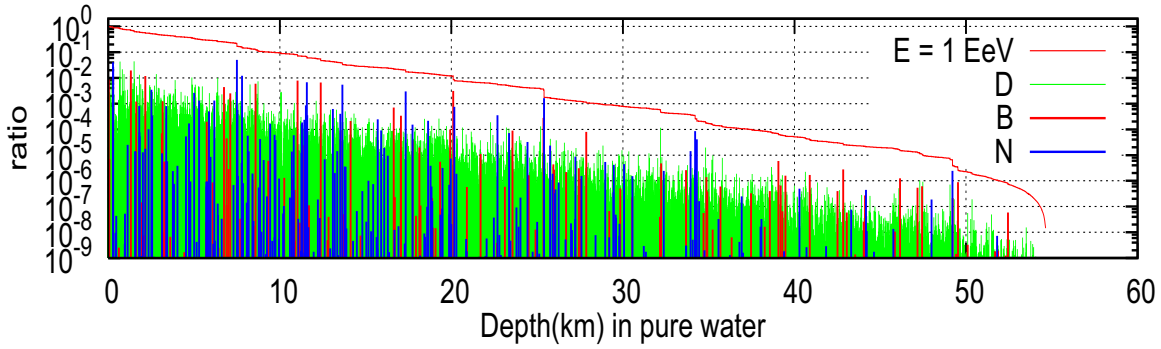

Figure 5: The similar graph to Figure 3 for 10^{18} eV with the longest range.

Table 2: The ratios of dissipated energies from bremsstrahlung, direct electron pair production and photo nuclear interaction to the total energy loss.

$E_p = 10^{12} eV$	Brems	Direct Pair	Nuclear
<Average>	3.37×10^{-1}	5.26×10^{-1}	1.37×10^{-1}
Shortest	9.99×10^{-1}	4.81×10^{-4}	4.06×10^{-4}
Average-like	2.94×10^{-1}	3.62×10^{-1}	3.44×10^{-1}
Longest	2.95×10^{-1}	6.97×10^{-1}	8.04×10^{-3}
$E_p = 10^{15} eV$			
<Average>	3.40×10^{-1}	4.98×10^{-1}	1.62×10^{-1}
Shortest	8.59×10^{-1}	8.87×10^{-2}	5.20×10^{-2}
Average-like	4.25×10^{-1}	4.78×10^{-1}	9.72×10^{-2}
Longest	1.84×10^{-1}	7.57×10^{-1}	5.90×10^{-2}
$E_p = 10^{18} eV$			
<Average>	3.24×10^{-1}	4.59×10^{-1}	2.17×10^{-1}
Shortest	7.04×10^{-1}	2.91×10^{-1}	4.77×10^{-3}
Average-like	4.22×10^{-1}	3.94×10^{-1}	1.84×10^{-1}
Longest	6.78×10^{-2}	6.86×10^{-1}	2.46×10^{-1}

Table 3: The average values, the standard deviations and the relative variance of the range distributions of muons with 10^{11} eV to 10^{18} eV.

E_p [eV]	$< R >$ [km]	σ [km]	$\sigma / < R >$
10^{11}	4.75×10^{-1}	2.39×10^{-1}	5.03×10^{-1}
10^{12}	2.51	5.32×10^{-1}	2.12×10^{-1}
10^{13}	7.18	1.97	2.74×10^{-1}
10^{14}	1.23×10^{1}	3.35	2.72×10^{-1}
10^{15}	1.73×10^{1}	4.35	2.51×10^{-1}
10^{16}	2.22×10^{1}	5.16	2.32×10^{-1}
10^{17}	2.70×10^{1}	5.86	2.17×10^{-1}
10^{18}	3.19×10^{1}	6.52	2.04×10^{-1}

may give different values from those by *the v_{cut} procedure method*.

The second, the muons may be produced by neutrino interaction, with different energies. Different energy muons are treated inconsistent manner, because of the constant of v_{cut}. Namely, how to produce the Cherenkov light yield have inconsistency in it.

The third, neutrinos, parents of the muons, have spectrum. This spectrum greatly increases the uncertainty in the Cherenkov light yields.

In conclusion, the Cherenkov light yields obtained by *the simple time sequential method* may give considerable different results from those by *the v_{cut} procedure method*.

References

[1] Y.Okumura, N.Takahashi and A.Misaki, a contributed paper to this conference
[2] F.Halzen and S.R.Klein, Rev.Sci.Instrum. 2010, **81**: 081101
[3] ANTARES Collb., 2010, arXiv:10007v1 [astro-ph.HE]11 Juli
[4] NEMO Collb., Astropart.Phys., 2010, **33**, 263
[5] Baikal.Coll., Astropart.Phys., 1997, **7**, 263
[6] P.Lipari, T.Stanev, Phys.Rev., 1991, **D44**, 3543
[7] S.Iyer Dutta, M.H.Reno, O.Sarcevic and D.Sekel, Phys. Rev., 2001, **63**, 094020
[8] S.I.Klimushin, E.V.Bugaev, I.A.Sokalski, Phys. Rev., 2001, 64, 014016
[9] N.Takahashi, A.Misaki, A.Adachi, N.Ogita, Y.Okamoto, K.Mitsui, H.Kujirai, S.Miono, O.Saavedra, Proc.18th ICRC, bangalore, India, 1983, **11**, 443-446
[10] N.Takahashi, H.Kujirai, A.Adachi, N.Ogita, A.Misaki, Uchusen-Kenkyuu, 1984, **28**, 120
[11] A.Misaki and J.Nishimura, Uchusen Kenkyuu, 1976, **21**,250
(ICR-Report-4577-4, University of Tokyo, 1977)

32ND INTERNATIONAL COSMIC RAY CONFERENCE, BEIJING 2011

Observation of Anisotropy in the Arrival Direction Distribution of Cosmic Rays at TeV Energies with IceCube

THE ICECUBE COLLABORATION[1]
[1]*See special section in these proceedings*

Abstract: The IceCube neutrino detector at the South Pole is sensitive to atmospheric muons produced by primary cosmic rays in the TeV energy range. The high rate of events (about 2 kHz in the full 86-string detector) allows for searches of anisotropy in the arrival direction distribution of cosmic rays at the level of a few parts per mille. Using the muon data recorded with IceCube between 2007 and 2010, we show that the cosmic ray flux in the southern hemisphere is not isotropic, but exhibits significant structure on multiple angular scales. In addition to large-scale features in the form of strong dipole and quadrupole moments, the data include several localized regions of excess and deficit on scales between 10° and 30°. These features are statistically significant. The origin of the features is currently unknown.

Corresponding Authors: Segev BenZvi[2] (*sybenzvi@icecube.wisc.edu*), Marcos Santander[2] (*santander@icecube.wisc.edu*), Simona Toscano[2] (*toscano@icecube.wisc.edu*), Stefan Westerhoff[2] (*swesterhoff@icecube.wisc.edu*)
[2]*Dept. of Physics, University of Wisconsin-Madison, Madison, WI 53703, USA*

DOI: 10.7529/ICRC2011/V04/0306

Keywords: Cosmic Rays – TeV; Anisotropy; Muons; Neutrinos

1 Introduction

The IceCube detector, deployed between 1450 m to 2450 m below the surface of the South Polar ice sheet, is designed to detect upward-going neutrinos from astrophysical sources. However, it is also sensitive to downward-going muons from cosmic-ray air showers. To penetrate the ice and trigger the detector, the muons must be produced by cosmic rays with energies of at least several TeV. The arrival direction of a cosmic muon is typically within 0.2° of the direction of the primary particle, so the arrival direction distribution of muons is also a map of cosmic ray arrival directions between about 1 and several hundred TeV.

At energies of a few TeV, it is believed that galactic magnetic fields should randomize the arrival directions of charged cosmic rays. However, in recent years an anisotropy in the arrival direction distribution has been reported on both large and small angular scales. The anisotropy is observed in the northern sky between several TeV and several hundred TeV by the Tibet ASγ array [1], Super-Kamiokande [2], Milagro [3, 4], ARGO-YBJ [5], and EAS-TOP [6]. In 2010, an analysis of muons recorded by the IceCube detector also revealed a large-scale anisotropy in the southern sky [7]. In these proceedings, we present the results of a search of the southern sky for anisotropy on all angular scales using data recorded between May 2009 and May 2010.

2 The IceCube Detector and Data

IceCube is a km^3-size neutrino detector frozen into the glacial ice sheet at the geographic South Pole. High-energy charged particles passing through the detector emit Cherenkov radiation, and their tracks are recorded by an array of Digital Optical Modules (DOMs) embedded in the ice. The DOMs are attached to 86 vertical cables, or strings (with 60 DOMs per string), which are used to transmit data to the surface. Construction of IceCube was completed in December 2010. The detector has been operating in various configurations since construction began. Between 2007 and 2008, it was operated with 22 strings deployed (IC22), between 2008 and 2009 with 40 strings (IC40), and between 2009 and 2010 with 59 strings.

Muons are identified using a simple majority trigger, which requires 8 or more DOMs in local coincidence within a 5 μs window. The trigger rate of downgoing muons is 0.5 kHz in IC22, 1.2 kHz in IC40, and 1.4 kHz in IC59, about a factor of 10^6 larger than the neutrino rate. The rate is too large to transfer complete waveforms for all events via satellite, so the muon data are reconstructed on-line and compressed using a Data Storage and Transfer (DST) format. Muon tracks are identified using a maximum-likelihood reconstruction, and the event arrival direction and energy estimators are stored in DST files and sent north by satellite. Digitized waveforms are discarded due to limited bandwidth.

The analysis presented in this paper uses the DST data collected during IC59 operations between May 20, 2009 and May 30, 2010. The data set contains nearly 3.4×10^{10} muon events recorded during a live time of 335.5 days. A cut in zenith angle at 65° removes less well-reconstructed tracks near the horizon, reducing the final analysis sample to 3.2×10^{10} events. The median angular resolution of events in the sample is 3°; unlike the neutrino analysis, the cuts have not been optimized for point source identification. Using simulated data, we estimate the median energy of the events to be 20 TeV. The energy resolution of the cosmic ray primaries is about $\Delta \log (E/\mathrm{eV}) = 0.5$.

3 Analysis

3.1 Calculation of the Reference Level

The arrival direction distribution of cosmic rays in IceCube exhibits anisotropy caused by non-physical effects such as gaps in the detector uptime. These effects must be removed before any physical anisotropy can be identified. Therefore, the first step in the analysis is the creation of a "reference map," a sky map that describes what the arrival direction distribution would be if the cosmic ray flux were isotropic. The reference map must be subtracted from the arrival direction distribution in the data to find regions where the cosmic ray flux deviates from the isotropic expectation.

We estimate a reference map for IC59 data using the time-scrambling method of Alexandreas et al. [8]. The sky is binned into an equal-area grid in equatorial coordinates with 0.9° resolution using the publicly-available HEALPix library [9]. From this sample two sky maps are produced. The data map $N(\alpha, \delta)$ stores the arrival directions of all events. For each detected event in the data map, "fake" events are generated by keeping the local zenith and azimuth angles (θ, ϕ) fixed but reassigning the time to that of another event recorded within a pre-defined time window Δt. The event times within the window are resampled 20 times and used to generate 20 fake celestial coordinate pairs (α, δ) which are used to fill a reference sky map $\langle N(\alpha, \delta) \rangle$ with a weight of 1/20.

A known disadvantage of the method is that it can be biased by a strong anisotropy, leading to artificial deficits or excesses next to regions of true excess or deficit [3]. However, the procedure does preserve the local arrival direction distribution of the data and naturally compensates for variations in the event rate which are difficult to model, such as changes in atmospheric conditions which affect the production of muons in air showers. The only critical requirement for time scrambling is to choose the buffer length Δt such that detector conditions remain stable during this period. Using χ^2 tests to compare the distribution of arrival directions in local coordinates across measurement periods, we have verified that the IceCube detector is stable over periods of at least one full day. In this analysis we choose $\Delta t = 24$ hr.

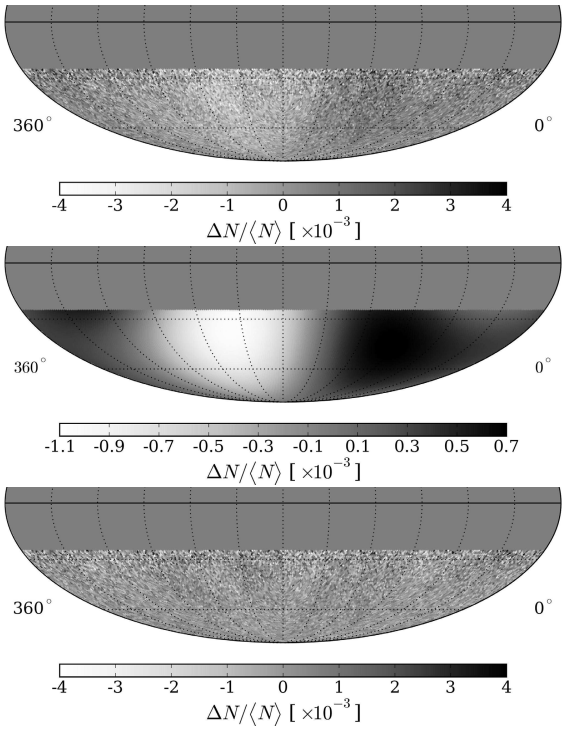

Figure 1: *Top*: Relative intensity of the IC59 data produced with $\Delta t = 24$ hr. *Middle*: Fit of dipole and quadrupole moments to the relative intensity. *Bottom*: Residual map after removal of the dipole and quadrupole.

3.2 Relative Intensity

Once the data and reference maps are calculated, deviations from isotropy can be analyzed by computing the relative intensity

$$\frac{\Delta N_i}{\langle N \rangle_i} = \frac{N_i(\alpha, \delta) - \langle N_i(\alpha, \delta) \rangle}{\langle N_i(\alpha, \delta) \rangle}. \quad (1)$$

which gives the amplitude of deviations from the isotropic expectation in each angular bin i. The significance of the deviation in bin i can be calculated using the method of Li and Ma [10].

A map of relative intensity of the IC59 data, binned with 0.9° resolution, is shown at the top of Fig. 1. The map exhibits obvious correlations between bins, such as a broad excess in the relative counts near $\alpha = 105^\circ$ and a broad deficit near $\alpha = 225^\circ$. The relative intensity in these regions is of order 10^{-3}. This structure is the large-scale anisotropy reported in the IC22 data by Abbasi et al. [7]. Since the IC59 data set is larger than that of IC22 by an order of magnitude, it is possible to see the large-scale structure in the data without further rebinning.

3.3 Removal of Large-Scale Structure

The relative intensity shown at the top of Fig. 1 is dominated by large-scale structures, but there are additional

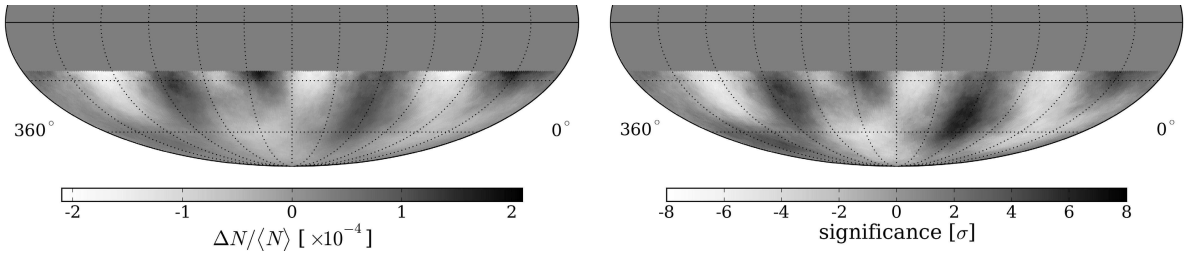

Figure 2: IC59 residual maps after subtraction of dipole and quadrupole moments, showing relative intensity (left) and significance before trial factors are applied (right). The maps have been smoothed with a circular window of 20°.

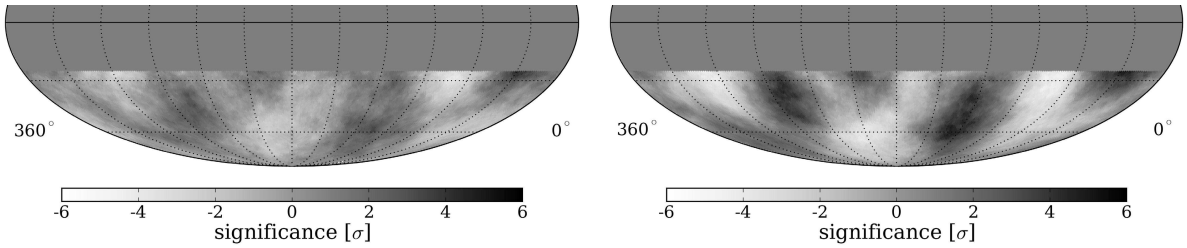

Figure 3: Residual maps from IC22 (left) and IC40 (right) showing the significance of deficit and excess regions with 20° smoothing.

small-scale features in the map. This can be demonstrated by calculating the angular power spectrum of the data, which exhibits significant power not only at the largest angular scales, but also down to scales of about 10° (see detailed discussion in Abbasi et al. [11]).

We can also demonstrate the presence of small-scale structure by explicitly removing the largest angular correlations in the data. This is accomplished by fitting dipole and quadrupole terms to the relative intensity map and then subtracting the fit to obtain a map of residual counts. In the middle panel of Fig. 1, we show the result of the fit of dipole and quadrupole moments to the intensity map. By themselves, these two terms account for much of the amplitude of the per-mille anisotropy observed in the data. However, the fit $\chi^2/\text{ndf} = 14743/14187$ corresponds to a χ^2-probability of approximately 0.05%, suggesting that the dipole and quadrupole are not sufficient to explain all of the structures observed in the angular distribution of $\Delta N/\langle N\rangle$.

Subtraction of the dipole and quadrupole fit from the data gives the bottom panel in Fig. 1. The fit residuals are relatively featureless at first glance, but the bin size is not optimized for a study of significant anisotropy at angular scales larger than the angular resolution of the detector. To increase the sensitivity to the small-scale structure in the data, we apply a smoothing procedure which takes the reference level and residual data counts in each bin and adds the counts from pixels within some angular radius of the bin. This procedure results in a map with Poisson uncertainties, though the bins are no longer statistically independent.

Smoothed residual maps of relative intensity and significance are shown in Fig. 2. To make this figure, a smoothing radius of 20° was chosen. Strong regions of excess and deficit are visible in the data. Note that the actual size of any given excess or deficit region (and thus the optimal smoothing scale) is not known *a priori*. Therefore, we study the sky map on all smoothing scales from 3° (the angular resolution of the data) to 45° in steps of 1° and search for regions of high significance at any location.

Applying this procedure, the two most significant features on the sky are a region with a peak significance of 5.3σ at a smoothing radius of 22° ($\alpha = 122.4^\circ, \delta = -47.4^\circ$) and a region of peak significance 4.9σ at a smoothing radius of 13° ($\alpha = 263.0^\circ, -44.1^\circ$). The significance values account for statistical trials due to the scan over smoothing radii and the location of the most significant pixels. The trial factors were estimated using a Monte Carlo simulation of an isotropic flux recorded by the IceCube detector.

4 Systematic Checks

Several tests have been performed on the data to ensure the stability of the observed anisotropy and to rule out possible sources of systematic bias. Among the influences that might cause spurious non-physical anisotropies are the detector geometry, the detector livetime, non-uniform exposure of the detector to different regions of the sky, and diurnal and seasonal variations in atmospheric conditions. Due to its unique location at the South Pole, many of these effects play a lesser role for IceCube than for detectors at the middle latitudes. We check the validity of this assumption by searching the data for a signal expected in solar coordinates, and by examining the data from previous configurations of the detector.

4.1 Solar Dipole Analysis

The cosmic rays at TeV energies do not co-rotate with the Earth about the Sun, and so it is expected that the flux of cosmic rays should exhibit a dipole modulation in solar coordinates. The expected change in relative intensity is given by

$$\frac{\Delta I}{I} = (\gamma + 2)\frac{v}{c}\cos\theta, \quad (2)$$

where I is the cosmic ray intensity, $\gamma = 2.7$ is the power law index of the energy spectrum at several TeV, v/c is the ratio of the orbital velocity of the Earth with respect to the speed of light, and θ is the angle between the cosmic ray arrival direction and the direction of motion of the Earth. Given $v = 30$ km s^{-1}, we expect an amplitude of 4.7×10^{-4}.

The solar dipole provides a convenient measurement with which to check the analysis technique. The reference and data maps were computed in solar coordinates, and the relative intensity map has been fit with a dipole function. A single dipole describes the data quite well: the fit $\chi^2/\text{ndf} = 14206.8/14192$ corresponds to a χ^2-probability of 41.6%. The dipole is aligned at a longitude of 270° in solar coordinates, following the expectation for a relative-motion anisotropy in this coordinate frame. Its amplitude is $(3.66 \pm 0.14 \pm 0.99) \times 10^{-4}$, in agreement with the expectation within the large systematic uncertainty. A more detailed study of the solar dipole anisotropy is presented in Abbasi and Desiati [12].

4.2 Anti-Sidereal Time Analysis

Seasonal variations in the solar dipole anisotropy can create spurious signals in equatorial coordinates, and vice-versa. We study this effect using an artificial time scale called anti-sidereal time, which is calculated by reversing the sign of the transformation between universal time and sidereal time. No physical anisotropy is expected in this reference frame, but it can be used to identify systematic distortions due to seasonal effects.

We have produced sky maps using anti-sidereal coordinates and performed the same analysis presented in Section 3. No regions of significant excess or deficit are observed in the anti-sidereal maps for any smoothing scale. A detailed discussion is provided in [11].

4.3 Comparison to IC22 and IC40 Data

An important cross-check of the IC59 analysis can be made by applying the same method to data recorded in the two data periods prior to IC59. The IC22 data set contains 4×10^9 events recorded between July 2007 and April 2008, and the IC40 data set contains 1.9×10^{10} events recorded between April 2008 and April 2009. While the samples are smaller than IC59, we expect to observe the most prominent structures in these data, albeit with reduced significance. The IC22 and IC40 data can be used to verify that the structures observed in the arrival direction distribution do not depend on the geometry of the detector or the data-taking period. For example, the shape of IC22 was highly asymmetrical, with a long and a short axis.

In Fig. 3, we show the residual maps from IC22 and IC40 after the subtraction of dipole and quadrupole terms and smoothing by 20°. While none of the features in IC22 and IC40 have a pre-trial significance above 5σ, they align with the regions of deficit and excess observed with IC59 data (cf. Fig 2). The main features on both large and small scales appear to be persistent in all data sets.

5 Conclusions

Using 3.2×10^{10} events recorded with the partially-deployed IceCube detector between May 2009 and May 2010, we have found that the arrival direction distribution of cosmic rays at several TeV exhibits significant anisotropy on several angular scales. The data are dominated by dipole and quadrupole moments, but there is also significant structure on angular scales down to about 10°. These structures become visible in the sky map when the dominant terms are subtracted.

There is currently no explanation for these local enhancements in the cosmic ray flux, and so the study of cosmic ray arrival directions in the TeV region will continue to be a major ongoing effort in IceCube. We are currently studying the anisotropy in the 79-string configuration of the detector (IC79). During the next several years, with the IceCube detector operating in its complete 86-string configuration, the data will increase by 4.5×10^{10} events per year. With these high statistics we will be able to study possible time dependencies in the anisotropy and compare to similar studies in the northern hemisphere [4, 13]

References

[1] M. Amenomori et al., Astrophys. J., 2005, **626**: L29
[2] G. Guillian et al., Phys. Rev., 2007, **D75**: 062003
[3] A.A. Abdo et al. Phys. Rev. Lett., 2008, **101**: 221101
[4] A.A. Abdo et al. Astrophys. J., 2009, **698**: 2121
[5] S. Vernetto et al. Proc. 31st ICRC, 2009, Łódź, Poland
[6] M. Aglietta et al. Astrophys. J., 2009, **692**: L130
[7] R. Abbasi et al., Astrophys. J., 2010, **718**: L194
[8] D.E. Alexandreas et al., NIM A, 1993, **328**: 570
[9] K.M. Gorski et al., Astrophys. J., 2005, **622**: 759
[10] T.-P. Li and Y.-Q. Ma, Astrophys. J., (1983), **272**: 317
[11] R. Abbasi et al., arXiv:1105.2326 [astro-ph], submitted to Astrophys. J., 2011
[12] R. Abbasi and P. Desiati, these proceedings.
[13] M. Amenomori et al., Astrophys. J., 2010, **711**: 119

Study of High p_T Muons in IceCube

THE ICECUBE COLLABORATION[1]
[1]*See special section in these proceedings*

Abstract: Muons with a high transverse momentum (p_T) are produced in cosmic ray air showers mostly via semileptonic decay of heavy quarks and the decay of high p_T kaons and pions in jets. These high p_T muons have a large lateral separation from the shower core and accompanying muon bundle. IceCube, a kilometer-scale neutrino telescope consisting of an array of photodetectors buried in the ice of the South Pole and a surface air shower array, is well suited for the detection of high p_T muons. The surface shower array can determine the energy, core location and direction of the cosmic ray air shower while the in-ice array can do the same for the high p_T muon. This makes it possible to measure the cosmic ray muon lateral separation distribution at distances greater than 200 meters. The preliminary results from analysis of data from 25% of the full IceCube detector will be presented.

Corresponding authors: L. Gerhardt[2,3] (*lgerhardt@lbl.gov*), S. R. Klein[2,3] (*SRKlein@lbl.gov*)
[2]*Lawrence Berkeley National Laboratory, Berkeley, California 94720*
[3]*University of California, Berkeley, Berkeley, California 94720*
DOI: 10.7529/ICRC2011/V04/0323

Keywords: cosmic rays, muons, icecube

1 Introduction

IceCube, a kilometer-scale neutrino telescope, is well suited for measuring the lateral separation of muons in cosmic ray air showers. Completed in December 2010, it consists of a 1 km^3 array of optical sensors (digital optical modules, or DOMs) buried deep in the ice of the South Pole and a 1 km^2 surface air shower array called IceTop. IceTop has an energy threshold of 300 TeV and can reconstruct the direction of showers with energies above 1 PeV within $\sim$1.5° and locate the shower core with an accuracy of $\sim$10 m [1]. The in-ice DOMs (here referred to as IceCube) are buried in the ice 1450 m under IceTop on kilometer-long strings of 60 DOMs with an intra-DOM spacing of 17 m. IceCube can reconstruct high quality tracks of high energy muons with $< 1^\circ$ accuracy. IceTop and IceCube can be used together to select cosmic ray events with a muon with a minimum lateral separation of $\sim$200 m. The measurement of the lateral separation distribution of muons in air showers provides a valuable check on air shower simulation models and can be used as an independent method for determining the cosmic ray composition [2].

The most common source of muons with a large lateral separation is muons with a high transverse momentum (p_T) primarialy from charm and bottom mesons and jets of high p_T partons [2]. The transverse separation is given by:

$$d_T = \frac{p_T h c}{E_\mu} \quad (1)$$

where E_μ is the energy of the high p_T muon, and h is the interaction height of the shower, here taken as an average value of 25 km. The interaction height loosely depends on the composition and a full treatment of this is planned in the future. Using a separation of 200 m (75 meters more than the string separation) as a rough threshold for the two-track resolution distance of the high p_T muon from the shower core gives a minimum resolvable p_T of 8 GeV/c for a 1 TeV muon. Rough calculations predict on the order of tens of high p_T muon events in the studied data sample [2].

The combined acceptance for cosmic ray air showers that pass through both IceTop and IceCube is 0.3 km^{2}sr for the full 86-string IceCube array [3]. By the end of the austral summer of 2006/2007, 22 IceCube strings and 26 IceTop tanks had been deployed. The combined acceptance for showers that trigger both IceTop-26 and IceCube-22 is 0.09 km^{2}sr. In 2007 the discriminator threshold settings for IceTop were changed partway through the year to sub-optimal values, so this analysis discards the data taken during this period leaving 114 days of livetime. A search has been conducted in this data for cosmic ray events with a muon with a large lateral separation.

The underground muon detector MACRO has previously measured the separation between muons in air showers for shower energies ranging roughly from 10^4 GeV to 10^6 GeV [4]. MACRO measured muon pair separations out to a distance of about 65 meters. They verified the linear relationship between p_T and separation shown in Eq. 1 (with a

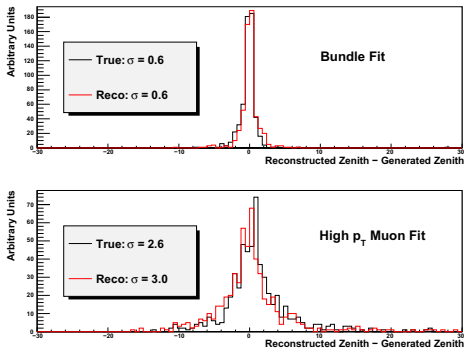

Figure 1: Zenith angle resolution of the high p_T reconstruction algorithm. The sigma are the results of Gaussian fits to the distributions.

small offset due to multiple scattering of the muons) out to momenta up to 1.2 GeV/c.

2 Reconstruction Methods

High p_T muons appear as a separate track coincident in time and parallel with the track from the central core of low p_T muons. Generally the bundle of low p_T muons leaves more light in the detector than the high p_T muon.

Current reconstruction algorithms in IceCube are designed to reconstruct single tracks. In order to reconstruct high p_T double-track events the hit DOMs (i.e. DOMs that detect at least one photon) are attributed to either the muon bundle or high p_T muon based on their timing and position. The muon bundle is reconstructed first by the IceTop surface array. This reconstruction serves as a seed for a likelihood-based reconstruction using the IceCube DOMs. Only IceCube DOMs within 90 m of the seed track are used for bundle reconstruction. The high p_T muon hits are selected relative to the reconstructed bundle track. The high p_T muon arrives at the same time but laterally separated from the bundle, so its hits will have a negative time residual relative to the bundle reconstruction. Additionally, high p_T muon hits are required to be at least 90 m from the reconstructed muon bundle track. The high p_T muon hit track is reconstructed using a likelihood reconstruction with a downgoing hypothesis.

Figure 1 shows the performance of this procedure after reconstruction quality selection criteria have been applied. The zenith angle resolution for groups determined using the true simulation information (black, solid lines) is compared to the resolution for groups determined using the splitting algorithm (red, dashed lines) for the muon bundle (top) and high p_T muon (bottom). Roughly 50% of the events fail to reconstruct because there are not enough DOMs in one of the groups.

These reconstruction algorithms achieve a zenith angle (space angle) resolution of 0.6° (1.3°) for the muon bundle and 2.6° (8.2°) for a high p_T muon separated by 200 m. The resolution is worse for the high p_T muon because fewer DOMs are hit. While high p_T muons with a greater separation are much easier to resolve with the two track algorithm, they also tend to be lower energy (see Eq. 1) and hit fewer DOMs. The average number of DOMs hit by the high p_T muon is 15, compared to 90 for the muon bundle. Additionally, because high p_T muons have fewer hit DOMs, a DOM hit by the muon bundle that is incorrectly placed in the high p_T group has a much larger effect on the reconstruction of the high p_T track (it can also degrade the bundle resolution, but to a lesser extent). These factors degrade the resolution of the high p_T track direction and timing. The spatial resolution of the high p_T muon track (as measured by the difference between the reconstructed track and the true track at the point of closest approach to the detector) is 40 m in x, y, and z.

3 Signal and Background Separation

Since high p_T muons occur in only a fraction of simulated showers, a toy model based on CORSIKA [5] proton showers was used to model the signal. A single muon is inserted into an existing CORSIKA event containing a muon bundle from an air shower. This modified shower is then run through the standard IceCube propagation, detector simulation, and reconstruction routines. Simulations insert a muon with energy of 1 TeV separated 100, 150, 200, and 400 m from the shower core.

Cosmic ray air showers that do not generate a high p_T muon (called 'single muon bundles') are a background to this search. Since they generate only one track in the array, these events are mostly eliminated by requiring there be two well-reconstructed tracks in the IceCube detector.

The IceCube 22-string configuration is large enough that the rate of simultaneous events from cosmic rays is significant. Muon bundles from two (or more) air showers can strike the array within the 10 μs event window, producing two separated tracks. These so-called double-coincident events are another background for air showers with high p_T muons. Since these double-coincident events are uncorrelated in direction and time, requiring that both reconstructed tracks be parallel (within 15° of each other) and occur within $\pm$600 ns can eliminate most of these events. However, an irreducible background remains from double-coincident events that happen to come from roughly the same direction and time. The rate of double-coincident events can be estimated by looking at the off-time rate of events (i.e. events with tracks that occur more than 600 ns apart) in the data that pass all other selection criteria.

A number of selection criteria are applied to separate events with high p_T muons. The events are required to trigger at least 6 DOMs in IceTop and at least 8 DOMs in IceCube. The events are also required to have high quality two-track reconstructions. This includes requiring that the tracks have at least one hit DOM with a time residual of less than 15 ns (a 'direct hit') and that tracks pass within the

detector fiducial volume. Further reduction of single muon bundles is done based on the differences in event topologies and timing. For instance, single muon bundles are well-reconstructed by a single track hypothesis, while the high p_T muon events are not. Figure 2 shows the negative log of the reduced likelihood of a single track reconstruction for single muon bundles, and showers with an inserted 8 and 16 GeV/c p_T, 1 TeV muon (separation of 200 m and 400 m from the shower core, assuming an average interaction height of 25 km). Well-reconstructed events have a lower likelihood value on this plot. For large separations, this variable separates single muon bundles from showers which contain a high p_T muon. This analysis retains events with a likelihood greater than 7.5. Next we require that the high p_T muon track be a robust track in the detector with at least 6 direct hits. Finally, the remaining background single muon bundle events are removed by requiring the perpendicular separation between tracks to be at least 160 m. The number of events passing each type of selection criteria for data and simulated background and signal are shown in Table 1.

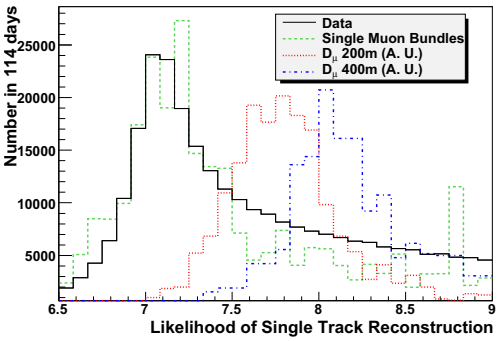

Figure 2: Negative log of the reduced likelihood for the single track reconstruction

4 Results

After applying all selection criteria 53 events remain in 114 days of data. No events remain in the simulated background. One event that passes all the selection criteria is shown in Fig. 3. The reconstructed high p_T muon and bundle track have a perpendicular separation of 207 m at the center of the detector. The two tracks arrive within 470 ns and 3.3° of each other.

4.1 Purity of Final Sample

Simulation of single muon bundle background events is too computationally intensive to accumulate large statistics. Although no simulated single muon bundle event passed all the selection criteria, the possibility exists that some single muon bundle background events could survive in the final data sample. In order to estimate the purity of

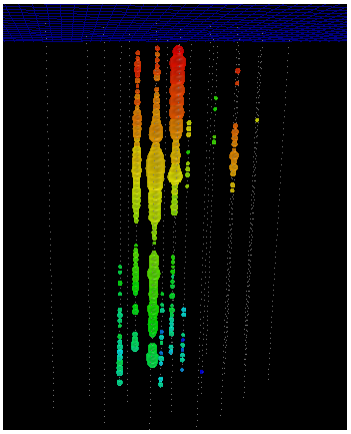

Figure 3: Candidate shower with a high p_T muon. The cosmic ray bundle is on the left and the high p_T muon is on the right.

the final sample a study has been conducted of simulated events which pass the reconstruction quality and double-coincident selection criteria (without applying the criteria designed to remove single track events). At this cut level, the only events left in the single muon bundle background are events which are incorrectly split into two tracks by the splitting algorithm. Two previously unused variables were developed that focused on studying how well the bundle fit described the high p_T muon hits and vice versa.

The first variable is the standard deviation of the time residual relative to the reconstructed bundle track (σ_{bundle}). Only hits belonging to the high p_T muon reconstructed track (time residual $<$ 100 ns and distance from the bundle $>$ 90 m) were used to calculate σ_{bundle}. In the single muon bundle background σ_{bundle} is small because the bundle reconstruction is equally good at describing both sets of hits. Conversely, events with high p_T muons have a laterally separated track that is causally disconnected from the bundle track. This leads to larger values of σ_{bundle}.

The second variable is the mean of the time residuals relative to the reconstructed high p_T muon track. Only hits within 90 m of the bundle track are used for this calculation. This variable uses the fact that the parallel but laterally separated high p_T muon track have a negative time residual relative to the bundle track. Single muon bundles incorrectly split into two groups tends to have time residuals that are closer to zero because both groups are causally consistent with the bundle hypothesis.

These two variables are shown in Fig. 4. The background single muon bundles and high p_T muon simulation are at a relaxed cut level with only reconstruction quality and double-coincidence selection criteria applied, while the data points are after all selection criteria have been applied. The dashed grey line is a fit to the mean of the background single muon bundle points. To estimate the purity of the data sample, this line has been moved upwards until every simulated single muon bundle event is below it. Thirty-one

Cut	Data	Simulation	Simulated Signal (%)
IceTop and IceCube Trigger	1.35 x 10^7	1.47 x 10^7	100%
Bundle and High p_T Reconstructions Successful	4.59 x 10^5	3.04 x 10^5	49%
Double-Coincidence Cuts	1.16 x 10^5	1.35 x 10^5	25%
Reconstruction Quality Cuts	2.57 x 10^4	1.64 x 10^4	13%
Single Track Cuts	53	0	8%

Table 1: Number of events in 114 days for data and simulated background. The percentage passing rates for simulated high p_T muons with a lateral separation of 200 m (8 GeV/c) are shown as well.

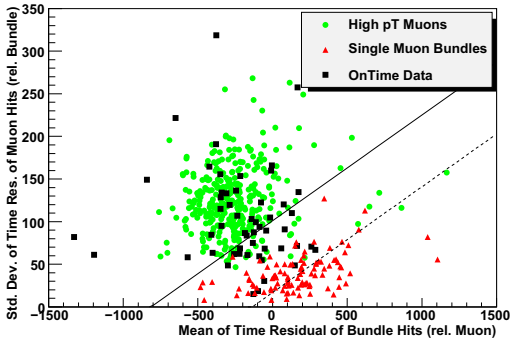

Figure 4: Standard deviation versus mean of time residuals. Note that the selection criteria have been relaxed for the simulated events.

of the fifty-three data events lie above the line, giving a preliminary estimation for the purity of the final event sample of at least 58%.

4.2 Estimation of Double-Coincident Rates

As mentioned in Section 3, an irreducible background remains from double-coincident cosmic rays. The number of these events in the on-time window ($\pm$600 ns) can be estimated by counting the number of events with tracks that occur with a time difference greater than 600 ns after applying all other selection criteria. In the final data sample, eight events were found in this off-time window. To be conservative, two events with a time difference greater than 20,000 ns are discarded. The remaining six events were spread over a time range of 2260 ns, giving an expectation that 3 of the 53 events in the $\pm$600 ns on-time window are due to double-coincident cosmic rays.

4.3 Lateral Distribution of Muons

Figure 5 shows the preliminary perpendicular separation between the bundle and high p_T muon reconstructions at the center of the detector. The black solid lines are the 53 data events that passed all selection criteria. Preliminary estimations indicate that this sample is 58% pure. The dashed red lines are the data events that passed all selection criteria, but had time differences greater than $\pm$600 ns. These events have been scaled down to the rate of 3 events in the on-time window.

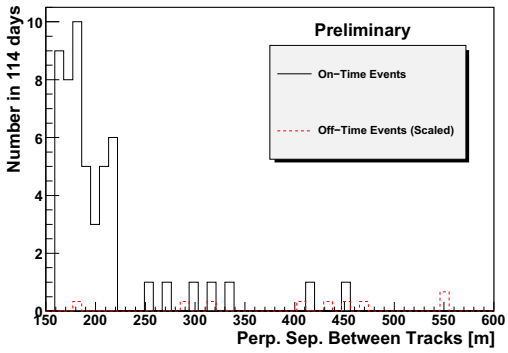

Figure 5: Preliminary perpendicular separation between bundle and high p_T muon reconstructions at the center of the detector.

5 Conclusions

A search for cosmic ray events with laterally separated muons has been conducted in 114 days with 25% of the full IceCube detector. The fraction of single muon bundle events remaining in the final sample has been conservatively estimated to be 42% and the number of background double-coincident events has been shown to be very small. Further searches with IceCube data with larger instrumented volume will have important implications for cosmic ray composition and air shower simulation.

References

[1] S. Klepser, 21st European Cosmic Ray Symposium (2008), arXiv:0811.1671.
[2] L. Gerhardt and S. Klein, 31st ICRC (2009), in arXiv:0909.0055.
[3] X. Bai and T.K. Gaisser, Proceedings of the TeV Particle Astrophysics II Workshop, J. Phys.: Conf. Ser. **60**:74 (2007).
[4] M. Ambrosio *et al.* , Phys. Rev. D **60**:032001 (1999).
[5] D. Heck, Forschungszentrum Karlsruhe Report FZKA 6019 (1998).

WILLI-EAS, a detector for observing atmospheric and EAS muons

ILIANA BRANCUS[1], BOGDAN MITRICA[1], ALEXANDRA SAFTOIU[1], MIREL PETCU[1], HEINIGERD REBEL[2], ANDREAS HAUNGS[2], OCTAVIAN SIMA[3], DENIS STANCA[1], GABRIEL TOMA[1], MARIN DUMA[1]
[1]*National Institute of Physics and Nuclear Engineering, Bucharest, Romania*
[2]*Karlsruhe Institute of Technology, Campus North, Institut fur Kernphysik, Karlsruhe, Germany*
[3]*Department of Physics, University of Bucharest, Bucharest, Romania*
mitrica@nipne.ro
DOI: 10.7529/ICRC2011/V04/0400

Abstract: The central part of WILLI - EAS is a compact calorimeter type detector set up for measuring the inclusive flux and the charge ratio of atmospheric muons in various directions of muon incidence. A mini array EAS is added and going to be operated for registering extensive air showers in order to study the muon charge ratio in EAS as affected by the geomagnetic field. The observed muon charge ratio measured for incident muons with energy < 1 GeV exhibits a pronounced azimuthal asymmetry (East-West effect) due to the different influence of the geomagnetic field on the trajectories of positive and negative muons in air. The flux measurements performed with the WILLI detector, taking into account muon events with energies > 0.4 GeV, show a diurnal modulation of the muon flux. The analysis of the muon events for energies < 0.6 GeV reveals an aperiodic variation of the muon flux. The WILLI detector has been extended to WILLI-EAS with 12 detector stations arranged as an rray. Simulations studies of the muon charge ratio for the correlated EAS, (initiated by H and Fe primaries, with energies in a range 10^{13} eV - 10^{15} eV), show detailed effects of the direction of EAS incidence relative to the geomagnetic field, depending, in particular, of the primary mass.

Keywords: Atmospheric muons, EAS, simulation

1 Introduction

The muons are a prominent EAS component, important as muons are deeply penetrating long living particles and have features informing about energy and nature of the parent primary cosmic rays. In IFIN-HH Bucharest a WILLI -EAS detection system has been set up [1] in IFIN-HH Bucharest, ($44°26'$ N latitude, $26°04'$ E longitude and sea level), in collaboration with KIT, Germany, to measure and to study the muon flux and the charge ratio (the ratio of the positive to negative muons) in EAS, following the suggestions and theoretical studies in Refs. [2, 3].

Figure 1 displays a geometrical layout of the WILLI-EAS array, with a figure of the WILLI detector for measuring the muon charge ratio (in the upper left corner) [4] and with a description of the unit of the mini-array for detecting the shower event (in the lower right corner) [5].

The simulations of the muon flux have been performed using CORSIKA [6] and GEANT [7] codes.

2 The WILLI detector

The WILLI detector [4] is a modular system consisting of 16 scintillator layers for recording the energy and the time signature of the muon, and 4 scintillator modules, on each side of the stack, acting as anticounters. A module is made of 1 cm Al plate and a plastic scintillator (NE 114) of $90 \times 90 \times 3$ cm^3.

We use a method to determine the muon charge ratio by measuring the lifetime of the muons stopped in the matter, overcoming the uncertainties appearing in the measurements using magnetic spectrometers, which are affected by systematic effects at muon energies less than 1 GeV, due to problems in the particle and trajectory identification (under the influence of the Earth's magnetic field).

2.1 Vertical measurements of muon charge ratio

In the beginning, the measurements have been performed with vertical acceptance of the WILLI detector. Results are shown in Figure 2 [8], in comparison with other data. Different from the CAPRICE measurements [9] at different geomagnetic cutoff, using a magnetic spectrometer, our data show reduced systematic errors due to a very good muon identification.

Figure 3 presents a comparison of the muon charge ratio measured for vertical muons and for muons measured with the WILLI detector inclined at $45°$, separately in the East and West directions, displaying a good agreement with simulation predictions [10].

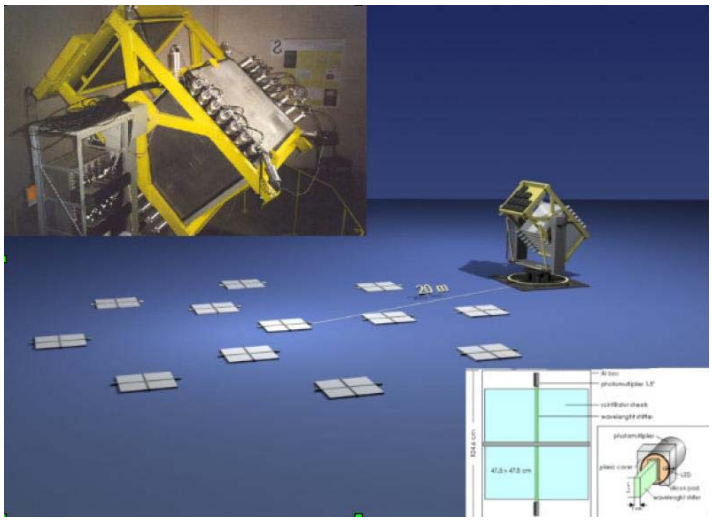

Figure 1: The WILLI-EAS detector system [1], composed by the WILLI detector (in the upper left corner) and a mini array of 12 stations with plastic scintillators (detail of one detection station in the lower right corner).

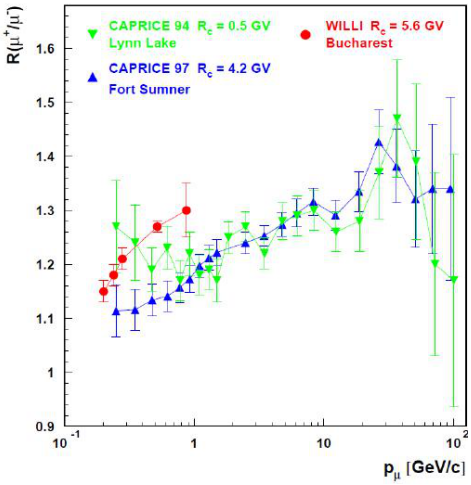

Figure 2: Muon charge ratio at the sea level for near-vertical direction of incidence [8].

Figure 4 displays the azimuthal dependence of the muon charge ratio for muons with inclined incidence of mean value of 35°, and a mean momentum 0.5 GeV/c [11]. The measurements show a pronounced East-West effect (see Figure 4), in good agreement with simulations based on the DPMJET model [12] and as expected from the East-West effect found in neutrino measurements. The Okayama group reported about observations of a less pronounced azimuthal dependence [13], explained by the higher energies (> 1 GeV) of the observed muons.

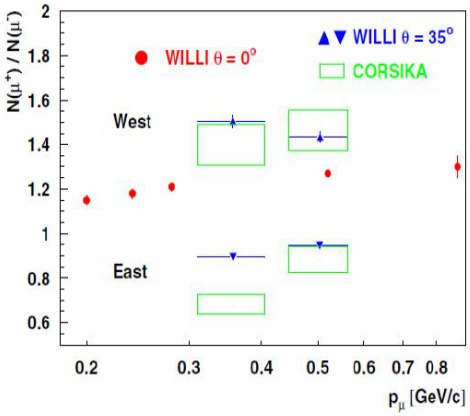

Figure 3: The energy dependence of the muon charge ratio, displaying also the East-West effect [10].

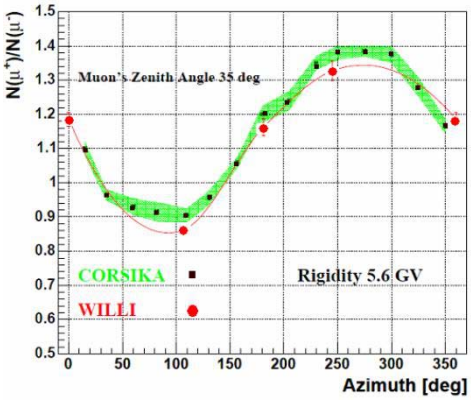

Figure 4: The azimuth dependence of the muon charge ratio compared with the CORSIKA simulations [11].

2.2 Correlation of the atmospheric muon flux with solar activity

The primary flux of cosmic rays is influenced by the solar activity, and this is reflected in the muon flux by a modulation observed at the ground level. Aperiodic variations, linked to the solar activity, can also happen. Due to the configuration of WILLI detector, we can select all muons passing through the detector with energies > 0.4 GeV, or only muons with a small energy range, $(0.4 - 0.6)$ GeV. Measuring the atmospheric muon flux in this way, we have observed periodic and aperiodic effects.

The Figure 5 displays the flux of muons, for the period of (03.08 - 17.09), 2010, with a diurnal modulation of the flux in the upper plot and unexpected drops in the lower part. Previous measurements exhibit a similar behaviour for the period (17.02 - 20.02), 2009 [14]. An explanation of these findings is in preparation.

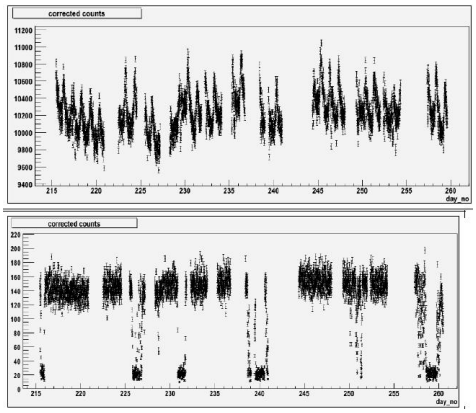

Figure 5: Muon count rate vs. time (expressed in day number of the year). Each point represents a 10 min data acquisition time. In the upper panel the flux of muons with energies $E > 0.4$ GeV is displayed, while in the lower one the flux of muons with 0.4 GeV$< E < 0.6$ GeV is given.

3 The WILLI-EAS detection system

The detector is extended to WILLI-EAS detection system by scintillation detectors (see Figure 1) for performing measurements of the muon charge ratio with WILLI in correlation with a small particle detector array - EAS. Each unit of the array is a scintillator plate of 1 m^2 area, 3 cm thickness, measuring the arrival times of the shower front and the energy deposit in the detectors [5].

The features of the charge ratio for the EAS muon component have been extensively studied on basis of Monte Carlo simulations [2] revealing that the radial and azimuthal muon density distributions of EAS observed by surface detector are strongly influenced by the magnetic field of the Earth, (see Figure 6). The features depend on the direction of EAS incidence (zenith and azimuth) relative to the geomagnetic field and on the energy of the registered muons.

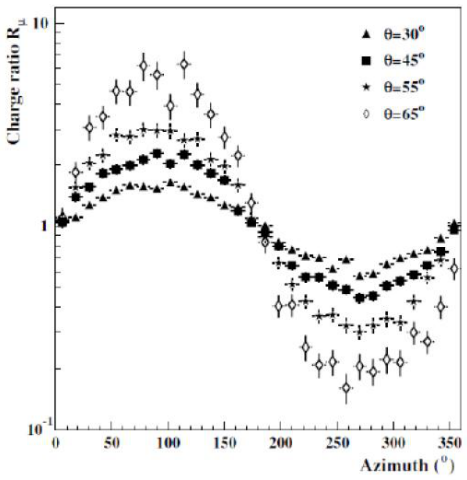

Figure 6: Azimuthal variation of the charge ratio of the muon density of proton-induced EAS incident with different zenith angles Θ from the North with the primary energy of 10^{15} eV, observed at a radial distance of 45-50 m and for a muon energy threshold of 0.1 GeV [2].

Using the modified version of SHOWREC [15] program, simulation studies have been performed for H and Fe generated showers ($10^{13} - 10^{15}$ eV) in order to study the reconstruction quality for the real configuration of the mini-array.

In Figure 7 the quality of reconstruction for the real configuration of the mini-array, for a zenithal angle of 30° of 250 showers, incident in the center of the array, is plotted.

Taking into account the acceptance of WILLI detector [16]] for muon energy < 1 GeV, the simulations of showers produced by H and Fe cosmic primaries, show a different variation of the muon charge ratio on the azimuthal position of WILLI. This effect could provide some indications of the mass composition of cosmic rays (see Figure 8).

The first tests of WILLI-EAS operation have started in 2011. This experimental device is presently the only one to measure efficiently the muon charge ratio of the lateral muon density distribution of EAS. For achieving a sufficient statistical accuracy the measurements are expected to run for a minimum of 5 years. The measurements and corresponding analyses should provide information about the influence of the geomagnetic field on the propagation of muons in air, eventually also on the hadronic interaction features and about the primary mass composition of cosmic rays with energies between in the range of $(10^{13} - 10^{15})$ eV.

4 Concluding remarks

- At muon energies < 1 GeV, the muon flux seems to depend not only on the particular observation site but also on the direction of muon incidence, significantly influenced by geomagnetic field and at low muon energies modulated by solar events.

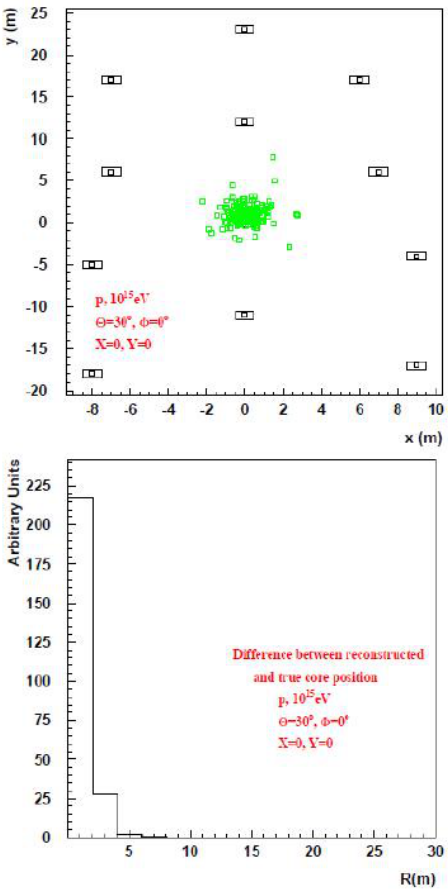

Figure 7: The reconstructed shower cores for 250 H incident showers placed in the same position (0,0) for 30° - up and the quality of the reconstruction for the showers - down.

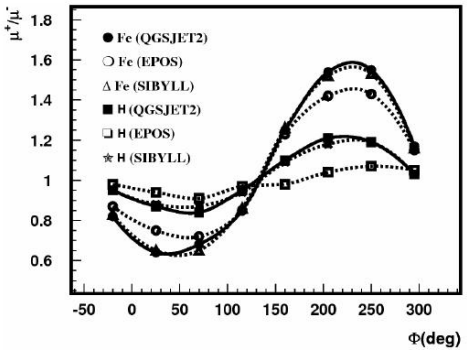

Figure 8: Dependence of the charge ratio on the azimuth position of WILLI for proton and iron induced showers, at 15-20 m [15].

- Our method to measure the muon charge ratio with a small compact detector minimizing the systematic errors of magnetic spectrometers for low energy muons, reaches accuracies in order of few percents.
- The actual WILLI detector set up allows directional measurements for muons, enabling to observe the East-West effect in the muon charge ratio, which is due to the geomagnetic field.
- The WILLI-EAS detection system investigating the muon charge ratio in EAS is expected to provide information about the muon propagation of low energy muons. Comparing the simulations of Fe and H induced showers with energies in the range of $(10^{13} - 10^{15})$ eV is indicating features of mass discrimination.

5 Acknowledgement

This work was (partially) supported by the Romanian Authority for Scientific Research, grant IDEI 1442/2008 and PN 09 37 01 05. We thank the KASCADE Grande experiment, which has ceded for use the scintillators of the mini array.

References

[1] I. M. Brancus et al., 2008, Proc. ISVHECRI 2006, Nucl. Phys. B (Proc. Suppl.), 175, 370
[2] H. Rebel et al., 2008, J. Phys. G: Nucl. Part. Phys., 35, 085203
[3] I. M. Brancus et al., 2009, Proc. ISVHECRI 2008, Nucl. Phys. B (Proc. Suppl.), 196, 227
[4] B. Vulpescu et al., 1998, Nucl. Instr. & Meth. Phys. Res., A414, 205
[5] H. Bozdog et al., 2001, Nucl. Instr. & Meth. Phys. Res., A465, 455
[6] D. Heck et al., 1998, Report FZKA 6019 Forschungszentrum Karlsruhe
[7] GEANT Detector Description and Simulation Tool, Cern (1993), Program Library Long Writeup W5013
[8] I. M. Brancus et al., 2007, Proc. 6th NWAP, Univ. of Algrave, Faro, Portugal
[9] J. Kremer et al., 1999, Phys. Rev. Lett., 83, 4241
[10] B. Mitrica et al., 2006, Nucl. Phys. B (Proc. Suppl), 151, 295
[11] B. Mitrica et al., Proc. of ICRC 2007, Merida, Mexico, Vol. 5 (HE part 2), 1569
[12] J. Ranft, 1995, Phys. Rev. D, 51, 64
[13] S. Tsuji et al., Proc. of ICRC 2007, Vol. 8, 233-236
[14] A. Saftoiu et al., 2011, Rom. J. Phys., in press
[15] O. Sima et al., 2004, Report FZKA 6985 Forschungszentrum Karlsruhe
[16] B. Mitrica, 2010, PhD thesis, University of Bucharest

Seasonal modulation in the Borexino cosmic muon signal

DAVIDE D'ANGELO[1] FOR THE BOREXINO COLLABORATION
[1] *Università degli Studi di Milano and I.N.F.N. sez. Milano, via Celoria 16 - Milano (Italy)*
davide.dangelo@mi.infn.it
DOI: 10.7529/ICRC2011/V04/0510

Abstract: Borexino is an organic liquid scintillator detector located in the underground Gran Sasso National Laboratory (Italy). It is devoted mainly to the real time spectroscopy of low energy solar neutrinos via the elastic scattering on electrons in the target mass. The data taking campaign started in 2007 and led to key measurements of ^{7}Be and ^{8}B solar neutrinos as well as antineutrinos from the earth (geo-neutrinos) and from nuclear power reactors. Borexino is also a powerful tool for the study of cosmic muons that penetrate the Gran Sasso rock coverage and thereby induced signals such as neutrons and radioactive isotopes which are today of critical importance for upcoming dark matter and neutrino physics experiments. Having reached 4y of continuous data taking we analyze here the muon signal and its possible modulation. The muon flux is measured to be $(3.41 \pm 0.01) \cdot 10^{-4}\mathrm{m}^{-2}\mathrm{s}^{-1}$. A modulation of this signal with a yearly period is observed with an amplitude of (1.29±0.07)% and a phase of (179±6) d, corresponding to June 28^{th}. Muon rate fluctuations are compared to fluctuations in the atmospheric temperature on a daily base, exploiting the most complete atmospheric data and models available. The distributions are shown to be positively correlated and the effective temperature coefficient is measured to be $\alpha_T = 0.93 \pm 0.04$. This result is in good agreement with the expectations of the kaon-inclusive model at the laboratory site and represents an improvement over previous measurements performed at the same depth.

Keywords: Borexino, Muon, Cosmic, Seasonal, Modulation

I. Introduction. The flux of cosmic muons detected deep underground shows variations which are in first approximation seasonal. The effect is known and studied since many decades [1]. At Gran Sasso National Laboratory in central Italy the rock coverage is about 3800 m w.e. and the expected amplitude of the modulation is ∼1.5%. Borexino is a scintillator detector with an active mass for muon detection of 1.33 kt and, being spherical, its acceptance is independent of the angle of the incoming muons. It therefore plays a key role in measuring the cosmic muon flux and its modulation with reduced systematics. Moreover as air temperature data is available from weather forecast web services, the correlation with the muon flux can be investigated and the effective temperature coefficient can be determined. Such temperature coefficient, with a larger exposure, can in future be used to determine indirectly the K/π ratio in the interaction of primary cosmic rays in the atmosphere, probing a complementary energy region compared with existing accelerator experiments.

II. Borexino Detector. The Borexino detector was designed to have very low intrinsic background. The central scintillation volume, 278 t of ultra-pure PC (pseudocumene) doped with 1.5 g/l of the fluor PPO (2,5-diphenyloxazole), is contained in a spherical Inner Vessel (IV), 8.5 m in diameter, made of 125 µ m thick nylon. It is shielded by two buffer layers consisting of PC and a small amount of the light quencher DMP (dimethylphthalate). The surrounding Stainless Steel Sphere (SSS) of 13.7 m diameter holds 2212 inward-facing 8" photomultiplier tubes (PMT) that detect scintillation light from the central region. All these components form the Inner Detector (ID) [2].

Though Borexino is located deeply underground, in Hall C of the Gran Sasso Laboratory (LNGS), the residual muon flux is $\sim 1.2\,\mu/\mathrm{m}^2/\mathrm{h}$, still too large for neutrino measurement, so the muons must be individually tagged. To accomplish this task the ID is surrounded by a powerful muon detector [3]. It is composed by a high domed steel tank of 18 m diameter and 16.9 m height filled with 2 100 t of ultra-pure water and instrumented with 208 PMTs which detect the muon Čerenkov emission. The Water Tank also serves as additional passive shielding against external radiation. This system is called the Outer Detector (OD).

III. Cosmic Muon Flux. This analysis is based on the first 4 years of Borexino data, taken between May 16^{th} 2007 and May 15^{th} 2011, with the exclusion of calibration data, data not passing the validation procedure and data for which the OD was not functioning properly. Events in coincidence with the spills of the Cern-to-GranSasso neutrino beam are discarded (details in [3]). The remaining data set shows no prolonged or unevenly distributed off time. This analysis is based only on muon events that triggered both

ID and OD. The total resulting exposure is $\sim 1.41 \cdot 10^6$ t·d and includes a sample of $\sim 4.6 \cdot 10^6$ muons.

We have measured the muon rate through the ID using different strategies at our disposal and achieved identical results. The overall detector's efficiency is 99.992%. In [3] are reported details on the muon tagging methods and on how the efficiencies have been evaluated. The average muon rate is (4310±10) counts per day, where the statistical error is negligible and the systematic error reflects the uncertainty in the efficiency and possible threshold effects. The rate corresponds to a cosmic muon flux of $(3.41 \pm 0.01) \cdot 10^{-4}\mathrm{m}^{-2}\mathrm{s}^{-1}$, taking into account also the uncertainty in the SSS radius.

This is the first measurement available for Hall C so far and the first obtained with a spherical detector at LNGS: existing measurements were obtained with detectors whose acceptance strongly depended on the muon incidence angle and are therefore affected by larger systematics. They have been performed by LVD in Hall A ([4]) and by MACRO in Hall B ([5]) and are respectively $(3.31 \pm 0.03) \cdot 10^{-4}\mathrm{m}^{-2}\mathrm{s}^{-1}$ and $(3.22 \pm 0.08) \cdot 10^{-4}\mathrm{m}^{-2}\mathrm{s}^{-1}$.

IV. Flux Modulation. Muons observed in underground sites arise mostly from the decay of pions and kaons produced by primary cosmic ray particles interacting with nuclei in the atmosphere[6]. Only mesons decaying before further interaction produce muons energetic enough to traverse the rock coverage of an underground site. Air temperature increases during summer, leading to an expansion of the traversed medium, which in turn increases the fraction of such mesons. The following formula is generally used to relate the muon intensity variations to the atmospheric temperature fluctuations:

$$\frac{\Delta I_\mu}{I_\mu^0} = \int_0^\infty dX \alpha(X) \frac{\Delta T(X)}{T^0(X)} \tag{1}$$

where $I_\mu^0 = I_\mu(T_0, E > E_{thr})$ is the differential muon intensity integrated from the energy threshold ($E_{thr} \sim 1.8$ TeV)[7] to infinity, assuming the atmosphere is isothermal at temperature T^0, and ΔI_μ are fluctuations about I_μ^0; $\alpha(X)$ is the temperature coefficient that relates fluctuations in the atmospheric temperature at depth X, $\Delta T(X)/T^0(X)$, to the fluctuations in the integral muon intensity; the integral extends over atmospheric depth from the altitude of muon production to the ground.

Other underground experiments have studied these effects, at the Gran Sasso site (MACRO [8], LVD [4]) and at different underground locations([9], [10] and refs. therein).

The muon intensity measured day by day is shown in fig. 1 (lower panel) for the 1329 days for which valid data was available. A modulation is clearly visible; fitting the distribution with the following function:

$$I_\mu = I_\mu^0 + \delta I_\mu cos\left(\frac{2\pi}{T}(t - t_0)\right) \tag{2}$$

we obtain an average intensity $I_\mu^0 = (3.414 \pm 0.002) \cdot 10^{-4}\mathrm{m}^{-2}\mathrm{s}^{-1}$, a period $T = (366 \pm 3)$d, a modulation amplitude $\delta I_\mu = (4.4 \pm 0.2) \cdot 10^{-6}\mathrm{m}^{-2}\mathrm{s}^{-1}$ corresponding to $(1.29 \pm 0.07)\%$ and a phase $t_0 = (179 \pm 6)$d; the χ^2/NDF is 1558/1325. A Lomb-Scargle analysis of the data identifies the same period. It should be noted that due to the limited size of the detector, a day with 100% duty cycle features a statistical error of ∼1.5% (1σ), comparable to the expected modulation. Therefore in spite of the fair value of reduced χ^2, we regard this fitting exercise only as a first order approximation; in the hypothesis, explored here, that the modulation is related to the air temperature fluctuations, the main maxima and minima can occur at different dates in successive years and short term effects are well expected to perturb the overall seasonal behavior.

V. Atmospheric Model. The atmosphere consists of many layers that vary continuously in temperature and pressure. A possible parametrization ([10] and with more details[7]) considers the atmosphere as an isothermal body with an effective temperature, T_{eff}, obtained from a weighted average over atmospheric depth:

$$T_{\text{eff}} = \frac{\int_0^\infty dX T(X) W(X)}{\int_0^\infty dX W(X)} \tag{3}$$

where the weight $W(X)$ reflects the temperature dependence of the production of mesons in the atmosphere and their decay into muons that can be observed at depth.

Eq. 1 can now be written in term of the "effective temperature coefficient" α_T:

$$\frac{\Delta I_\mu}{I_\mu^0} = \alpha_T \frac{\Delta T_{\text{eff}}}{T_{\text{eff}}} \tag{4}$$

The weight $W(X)$ can be written as the sum $W_\pi + W_K$, representing the contribution of pions and kaons to the overall variation in muon intensity.

$$W^{\pi,K}(X) \simeq \frac{(1 - X/\Lambda'_{\pi,K})^2 e^{-X/\Lambda_{\pi,K}} A^1_{\pi,K}}{\gamma + (\gamma+1) B^1_{\pi,K} K(X) (\langle E_{th} \cos\theta \rangle / \epsilon_{\pi,K})^2} \tag{5}$$

where:

$$K(X) \equiv \frac{(1 - X/\Lambda'_{\pi,K})^2}{(1 - e^{-X/\Lambda'_{\pi,K}})\Lambda'_{\pi,K}/X} \tag{6}$$

The parameters $A^1_{\pi,K}$ include the amount of inclusive meson production in the forward fragmentation region, masses of mesons and muons, and muon spectral index; the input values are $A^1_\pi = 1$ and $A^1_K = 0.38 \cdot r_{K/\pi}$, where $r_{K/\pi}$ is the K/π ratio. The parameters $B^1_{\pi,K}$ reflect the relative atmospheric attenuation of mesons; the threshold energy, E_{th}, is the energy required for a muon to survive to a particular depth; the attenuation lengths for the cosmic ray primaries, pions and kaons are Λ_N, Λ_π and Λ_K respectively with $1/\Lambda'_{\pi,K} = 1/\Lambda_N - 1/\Lambda_{\pi,K}$. The muon spectral index is given by γ. The meson critical energy, $\epsilon_{\pi,K}$, is the meson energy for which decay and interaction have an equal probability. The value of $\langle E_{th} \cos\theta \rangle$ used here is the median of the distribution. The values for these parameters can be

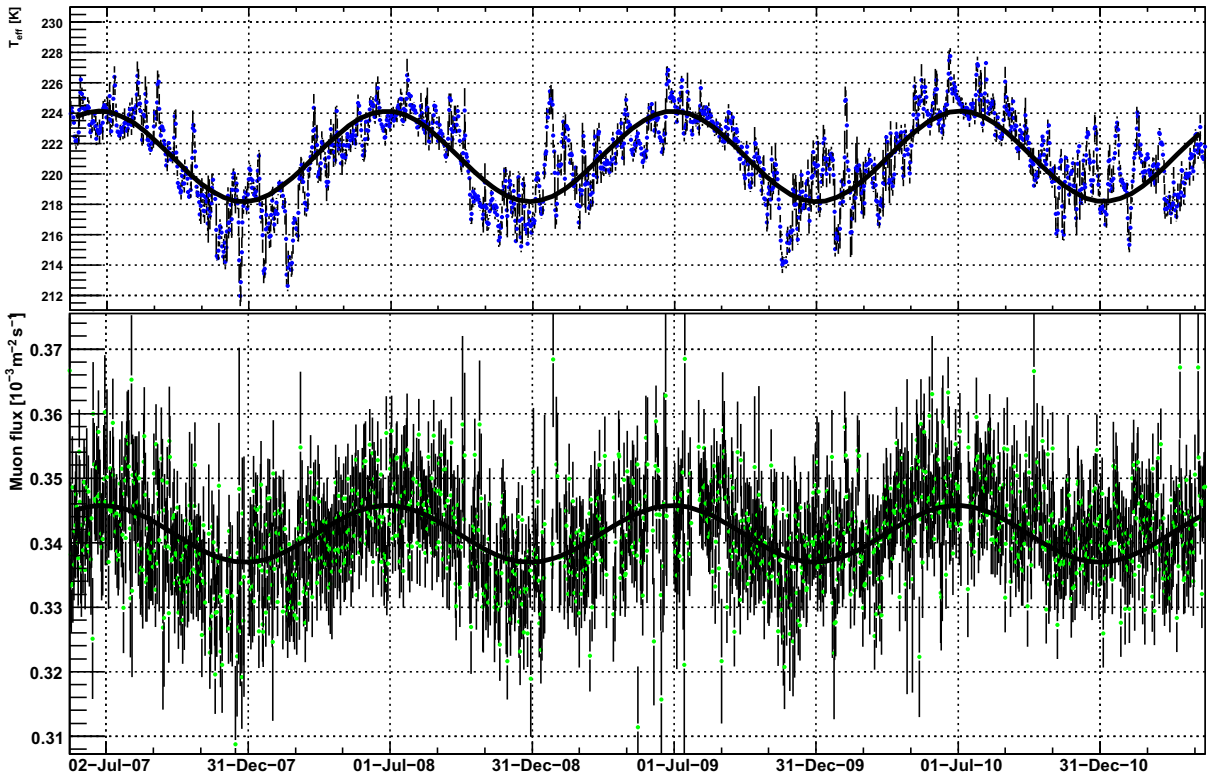

Figure 1: Upper panel: effective temperature $T_{\rm eff}$ computed day by day using eq. 7 and averaging over the 4 daily measurements available. Lower panel: Cosmic Muon Signal. The seasonal modulation is evident. Daily binning.

found in tab. 1 of [10], with the exception of $\langle E_{th}\cos\theta\rangle$ which is site dependent and is found by MC simulations. At LNGS $\langle E_{th}\cos\theta\rangle$ = 1.833 TeV according to [7]. The dependency of $W(X)$ on $T_{\rm eff}$ is however moderate.

Since the temperature is measured at discrete atmospheric levels X_n, eq. 3 becomes:

$$T_{\rm eff} \simeq \frac{\sum_{n=0}^{N} \Delta X_n T(X_n)(W_n^{\pi} + W_n^{K})}{\sum_{n=0}^{N} \Delta X_n (W_n^{\pi} + W_n^{K})} \qquad (7)$$

where $W_n^{\pi,K} \equiv W^{\pi,K}(X_n)$.

Fig. 2 shows the temperature in the atmosphere for the LNGS site and the weights used in eq. 7 as functions of the pressure levels. As it can be seen the higher layers of atmosphere are given a higher weight. Here are produced most of the muons which are energetic enough to cross the rock coverage of an underground site. Muons produced in lower level will be in average less energetic and a larger fraction of them lies below threshold.

VI. Temperature Modulation. The temperature data was obtained from the European Center for Medium-range Weather Forecasts (ECMWF)[11] which exploits different types of observations (e.g. surface, satellite and upper air sounding) at many locations around the planet, and uses a global atmospheric model to interpolate to a particular location. In our case, the exact LNGS coordinates have been used: 13.578E, 42.454N. Atmospheric temperature is provided by the model at 37 discrete pressure levels in the [1-1000]hPa range (1 hPa = 1.019 g/cm^2), four times a day at 00.00 h, 06.00 h, 12.00 h and 18.00 h. Based on this data set, the effective temperature $T_{\rm eff}$ was calculated using eq. 7 four times a day[1]

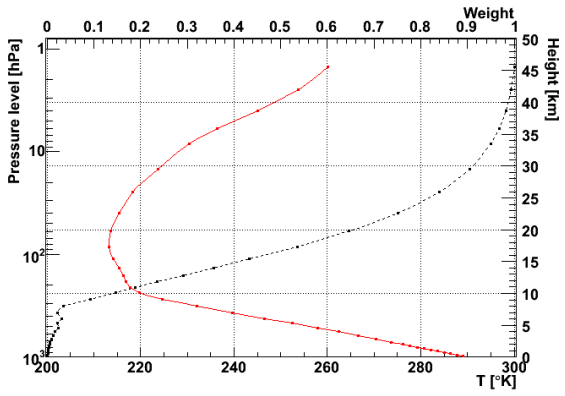

Figure 2: Average temperature (solid red line) and normalized weight $W(X)$ (black dashed line) as a function of pressure levels computed at the LNGS site.

1. The analysis in [8] and [4] instead used data from the air soundings performed by the Areonautica Militare Italiana (AM)[12] ∼130km from the lab. This data set is significantly

For the 4y period $\langle T_{\rm eff}\rangle$ = 220.99K. Fig. 1 (upper panel) shows $\langle T_{\rm eff}\rangle$ for each day obtained averaging the 4 available measurement and estimating the error from their variance. The fit with a function analogous to eq. 2 returns $T_{\rm eff}^{fit} = (221.153 \pm 0.007)$K, amplitude (2.98 ± 0.01)K corresponding to 1.35%, period $T = (369.2 \pm 0.2)$d and phase (174.0 ± 0.4)d. However here the error bars are much smaller and the χ^2/NDF is very poor confirming that the sinusoidal behavior is only a first order approximation. Aside from small scale fluctuations, additional winter maxima can be observed which can be ascribed to the known meteorological phenomenon of the Sudden Stratospheric Warmings (SSW [13]) and whose effect is sometimes comparable in amplitude with the underlying seasonal modulation.

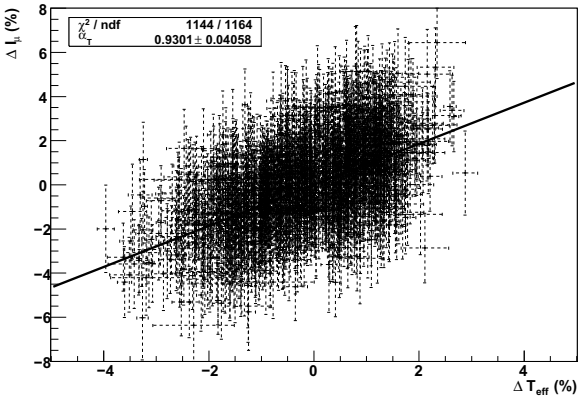

Figure 3: $\Delta I_\mu/\langle I_\mu\rangle$ vs. $\Delta T_{\rm eff}/\langle T_{\rm eff}\rangle$. Each point is a day.

VII. Correlation. Observing fig. 1 the correlation between fluctuations in atmospheric temperature and cosmic muon flux is evident. To quantify such correlation we plotted for every day $\Delta I_\mu/\langle I_\mu\rangle$ vs $\Delta T_{\rm eff}/\langle T_{\rm eff}\rangle$ in fig. 3. Only days with duty cycle $\geq 50\%$ have been included for a total of 1165 days. The correlation coefficient (R-value) between these two distributions is 0.60 indicating indeed a positive correlation. To determine α_T, a linear regression was performed accounting for error bars on both axes using a numerical minimization method. As a result we obtain $\alpha_T = 0.93 \pm 0.04$ with χ^2/NDF = 1144/1164. We have evaluated the systematic error by varying the assumptions adopted in computing the average flux and temperature with respect to the available data set and we have found that it is small compared to the statistical error. This result is consistent and features smaller errors when compared to $\alpha_T = 0.91 \pm 0.07$, the previous measurement by MACRO at Gran Sasso [14].

The predicted value for α_T tends asymptotically to unity with increasing depth of the site, as a deeper rock coverage samples a higher portion of the muon energy spectrum. Fig. 4 shows this behavior along with existing measurements. The method to compute predicted values as a function of site depth is detailed in [10], and for LNGS is $\alpha_T = 0.92 \pm 0.02$ considering muon production from both

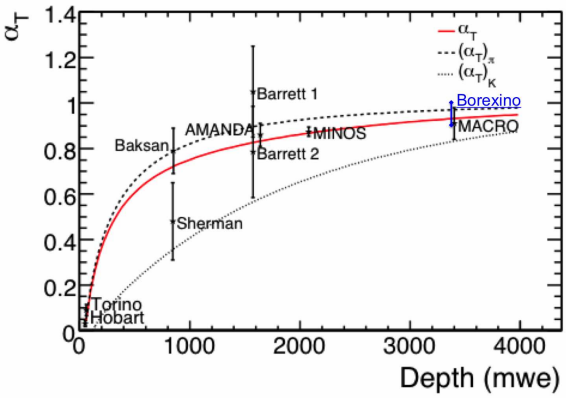

Figure 4: Predicted values of α_T as a function of detector depth and the existing measurements at various depths [10].

pions and kaons. The systematic uncertainty was found by modifying the input parameters according to their uncertainties and recalculating.

With a longer exposure we foresee to measure α_T with better precision and open way to indirect determination of the K/π ratio in the interaction of primary cosmic rays in the atmosphere with the method detailed in [10, 7] and probing a complementary energy region compared with existing accelerator experiments.

Acknowledgments

We thank E.W. Grashorn of CCAPP, Ohio State University for insightful discussions and S.M. Osprey of NCAS, University of Oxford (UK) for promptly providing ECMWF air temperature data interpolated on the LNGS coordinates.

References

[1] Barrett et al., Rev. Mod. Phys., 1952, **24**: 133.
[2] G. Alimonti et al., NIM, 2009, **A600**: 568-593.
[3] G. Bellini et al., JINST, 2011, **6**: 05005
[4] M.Selvi for the LVD coll., talk at 31^{st} ICRC, 2009.
[5] M. Ambrosio et al., Phys. Rev., 1995, **D 52**: 3793.
[6] T.K. Gaisser, 1990, Cosmic rays and particle physics, Cambridge Univ. Press
[7] E.W. Grashorn et al., Astr. Phys., 2010, **33**: 140-145.
[8] M. Ambrosio et al., Astropart. Phys., 1997, **7**: 109-124.
[9] A. Bouchta, in Proc. 26^{th} ICRC, 1999.
[10] P. Adamson et al., Phys. Rev. D, 2010, **81**: 012001.
[11] ECMWF ERA-Interim data obtained courtesy of the BADC http://badc.nerc.ac.uk/ṽiew/ badc.nerc.ac.uk_ATOM_dataent_12458543158227759
[12] available from Univ. of Wyoming: http://weather.uwyo.edu/upperair/sounding.html
[13] S. Osprey et al., Geoph. Res. Lett., 2009, **36**, L05809.
[14] M.Ambrosio et al. Phys. Rev., 2003, **D67**, 042002.

incomplete if compared to ECMWF, although it provided us a useful cross-check.

Measurement of the Atmospheric Muon Charge Ratio by Using a Cosmic Ray Telescope

S. ABDOLLAHI[1,2], M. BAHMANABADI[1], D. PURMOHAMMAD[2], S. MORTAZAVI MOGHADDAM[1]
[1]*Department of Physics, Sharif University of Technology, P.O.Box 11155-9161, Tehran, Iran*
[2]*Science Faculty, Imam Khomeini International University, Qazvin, Iran*
abdollahi.soheila@gmail.com
DOI: 10.7529/ICRC2011/V04/0749

Abstract: The charge ratio of cosmic muons has important information in both "the atmospheric neutrinos anomaly" and "the hadronic interactions". We measured the muon charge ratio ($R_\mu = N_{\mu^+}/N_{\mu^-}$) in the cosmic rays flux at the momenta range 0.76-1.60 GeV/c at Sharif University of Technology in Tehran ($35^\circ 43' N$, $51^\circ 20' E$) and 1200 m above sea level (890 gcm^{-2}) by using a cosmic ray telescope. We used the delayed coincidence method based on reduced mean life time of negative muon due to nuclear capture in matter. By finding R_μ in different time intervals, we indicated 3 week time interval is proper to obtain R_μ and in this time interval, $R_\mu = 1.18 \pm 0.03$. So we compared the experimental data to predictions of CORSIKA simulations using high energy interaction model (QGSJET-II) and two low energy interaction models (URQMD and GHEISHA) in the energy range from 10^{12} eV to 10^{16} eV for primary particles. We obtained R_μ=1.04 with QGSJET-URQMD models and R_μ=1.06 with QGSJET-GHEISHA models. From the measurement of muons flux in different zenithal and azimuthal angles, the muon angular distribution is obtained as $I(\theta) = I(0)\cos^n\theta$. So the influence of the geomagnetic field leads to a dependence of the muon flux on the azimuth angle (East-West effect), in particular for low energy muons.

Keywords: Muon Charge Ratio, Extensive Air Shower, Cosmic Rays

1 Introduction

The primary cosmic rays are mainly protons and heavier ionized nuclei impinging earth's atmosphere and induce a cascade of secondary particles which is called extensive air shower (EAS). Generally the first secondary particles are unstable subatomic particles that decay into muons [1].

$$\pi^\pm \to \mu^\pm + \nu_\mu(\overline{\nu}_\mu)$$
$$\kappa^\pm \to \mu^\pm + \nu_\mu(\overline{\nu}_\mu)$$

Muons due to relativistic time dilation are present near sea level and decay via the weak interaction according to

$$\mu^\pm \to e^\pm + \nu_e(\overline{\nu}_e) + \overline{\nu}_\mu(\nu_\mu).$$

Study of muon flux in different azimuthal angles shows an asymmetry in muon angular distribution from east and west directions that can be traced by the earth's magnetic field effect which deflects trajectories of charged secondary particles (East-West effect). Zenithal distribution of muon flux is also as a power function of $\cos\theta$.
The muon charge ratio is a significant quantity which reflects important features of the hadronic meson production in cosmic ray collisions and it provides useful information for neutrino physics [2]. To study the muon angular distribution and determining of muon charge ratio, we carried out series of experiments by cosmic ray telescope at Sharif University of Technology in Tehran and simulated extensive air showers with CORSIKA code to compare the experimental results and predictions of CORSIKA simulations.

2 Coincidence experiment arrangement and data analysis

The cosmic ray telescope consists of 2 plastic scintillators ($30 \times 10 \times 1 cm^3$) with spacing 1m from each other. This telescope is a rotatable device around its vertical axis in different zenithal and azimuthal angles and is placed in the 4^{th} floor of Physics Department of Sharif University of Technology, under 80 cm concrete. To study the muon angular distribution, we measured muons flux in azimuthal angles of 0° (north), 90° (west), 180° (south) and 270° (east) and in zenithal angles of $20^\circ \pm 17^\circ$, $40^\circ \pm 17^\circ$ and $60^\circ \pm 17^\circ$. The measurements were done in 24-h time intervals. The operation of coincidence electronic circuit (Fig.1) is initiated when an incident muon passes through the top scintillator. In these experiments, the muons which pass through both scintillators are considered. Thus the generated signal of top PMT is sent to the 8-channel fast discriminator (CAEN N413A), with threshold of 23mV, after amplifying by the fast amplifier ($\times 10$, CAEN N412). Then the output of discriminator is connected to the 'start' input of a Time to Amplitude Converter (TAC, ORTEC 566) with a time

Azimuth angle \ Zenith angle	$\theta = 0°$	$\theta = 20°$	$\theta = 40°$	$\theta = 60°$
$\phi = 0°$	219.28 ± 1.64	196.11 ± 1.56	128.32 ± 1.26	61.58 ± 0.87
$\phi = 90°$	219.28 ± 1.64	195.27 ± 1.55	128.05 ± 1.26	61.24 ± 0.87
$\phi = 180°$	219.28 ± 1.64	195.72 ± 1.55	128.47 ± 1.26	61.12 ± 0.87
$\phi = 270°$	219.28 ± 1.64	186.09 ± 1.52	125.51 ± 1.24	60.65 ± 0.86

Table 1: Muon flux obtained in different directions.

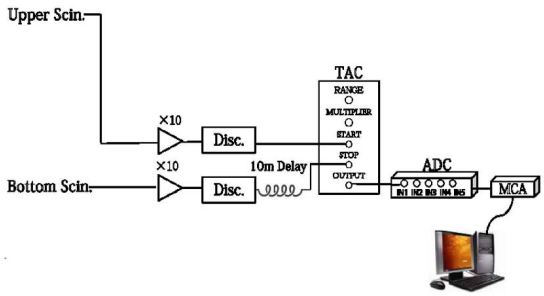

Figure 1: Setup of coincidence experiment electronic circuit.

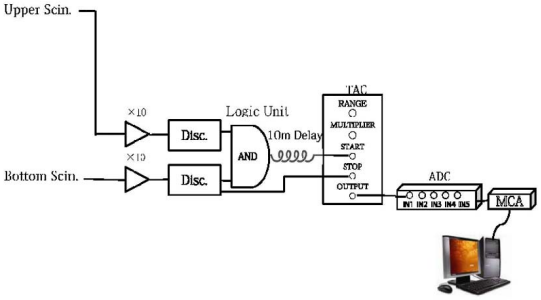

Figure 2: Setup of muon decay experiment electronic circuit.

range 200 ns. In a similar way, generated signal of bottom PMT is directed to 'stop' input of TAC by a 10m delay cable. Finally output of TAC is sent to a Multi-Channel Analyzer (MCA) via an Analog to Digital Converter unit (ADC). Table 1 shows the muon flux in different angles.
Since dependence of muon flux on zenith angle is as $I(\theta) = I(0)\cos^n\theta$, we estimated '$n$' by fitting this function to experimental data. The values of 'n' were obtained $n = 1.90 \pm 0.16$, $n = 1.91 \pm 0.15$, $n = 1.90 \pm 0.14$ and $n = 1.92 \pm 0.27$ for directions north, west, south and east respectively.

3 Muon decay arrangement and data analysis

To determine the muon charge ratio, we used delayed coincidence method based on different interaction of positive and negative muons with matter. Positive muons can only decay, while negative muons trapped in atomic orbit, are decayed or absorbed by atomic nuclei that cause to reduce mean life time of negative muon. Probability of negative muon capture by atomic nuclei is proportional to Z^4 that Z is atomic number of host atoms. Thus the life time of negative muon decreases significantly according to host material. Table 2 shows average life time and decay probability of negative muon in some media [3]. Thus we recorded muons decay with an arrangement like as Fig.2. To ensure a muon which decays in the bottom scintillator is the same muon that has passed through the top scintillator, we used a logic unit of AND (CAEN N405). Time range of TAC was set to 10 μs.
Decay experiments were done 7 times and each of them was operated in 1 week time interval. In all decay experiments, telescope was located vertically. Total muons decay distribution function in scintillator is including superposition of several decays as follows [4]:

$$\frac{dN}{dt} = \frac{N_{\mu^+}}{\tau_{\mu^+}} e^{(\frac{-(t+\tau_{delay})}{\tau_+})}$$

$$+\frac{N_{\mu^-}}{\tau_{\mu^-}} P_{decay} e^{(\frac{-(t+\tau_{delay})}{\tau_-})}$$

$$+C_{bg} e^{(\frac{-(t+\tau_{delay})}{\tau_{bg}})} + \epsilon_{bg}. \quad (1)$$

Where first and second sentences are related to positive and negative muons decay and third and fourth sentences are related to background radiation. In eq.1, P_{decay} indicates probability of muon decay in scintillator, τ_{delay} presents delayed time in experiment circuit and τ_{bg} stands for time constant of background radiation.
Before determining muon charge ratio, we should estimate τ_{bg}. Although using the logic unit of AND in muon decay experiments make us sure that a significant fraction of the recorded events are related to the single-particle decay, but there are recorded events that aren't related to single particle. These events are recorded as a decay background radiation in eq.1. To determine time constant of

Medium	Mean life time (ns)	Decay probability (%)
Vacuum	2197.03 ± 0.04	100
Carbon	2026.3 ± 1.5	92.15
Oxygen	1795.4 ± 2	81.57
Aluminium	864.0 ± 1	39.05
Lead	75.4 ± 1	2.75

Table 2: Average life time and decay probability of negative muon in some media.

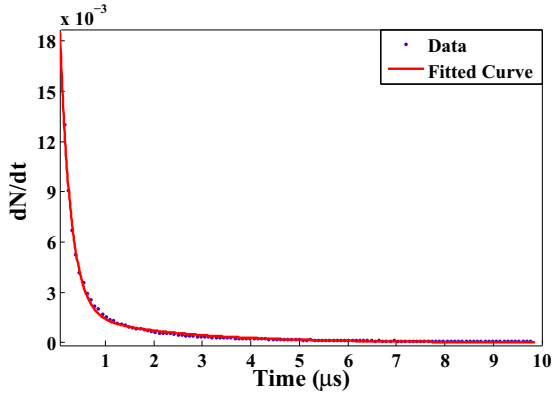

Figure 3: A sample of fitting eq.1 to muon decay spectrum.

background radiation (τ_{bg}), we carried out series of experiments with one scintillator to records muon decays in all zenithal angles. We determined τ_{bg} by fitting eq.1 to these data. Average time constant (τ_{bg}) was calculated 284.8 ns. Then by fitting eq.1 to muon decay experiments data in one week time intervals, we determine muon charge ratio. Fig.3 shows an example of fitting eq.1 on muon decay data. Finally the average muon charge ratio was obtained 1.15±0.03 in one week time intervals. To evaluate muon charge ratio in different time intervals, we added decay experiments data together and made data in 2 to 6-week time intervals. The values of muon charge ratio in different time intervals (Fig.4) show the fluctuations are very small and for three-week time interval and more, the values of $\overline{R}_\mu$ tend to a fixed amount 1.18±0.03.

4 Simulating of EAS to find muon charge ratio

In order to study the muon component, some detailed Monte Carlo simulations of the EAS development have been performed. We have simulated EAS events by CORSIKA (COsmic Ray Simulations for KAscade) code [5] for proton and alpha particles as primary particles. Energy range for primary particles was selected from 1 TeV to 10 PeV. The values of geomagnetic field components for Tehran ($B_x = 27.99\mu T$, $B_Z = 38.49\mu T$) were obtained from U.S. Geomagnetic Data Center.
Zenith and azimuth angles of primary particles in the simulations are 0°-60° and −180°-180° respectively. About 1600 showers have been simulated. We selected secondary muons with momentum values between 0.76-1.60 GeV/c and zenith angles values $\theta \leq 17°$ which are close to energy range and zenith angle range of the telescope. The muon charge ratio was obtained 1.06 in QGSJET-GHEISHA models and 1.04 in QGSJET-URQMD models.

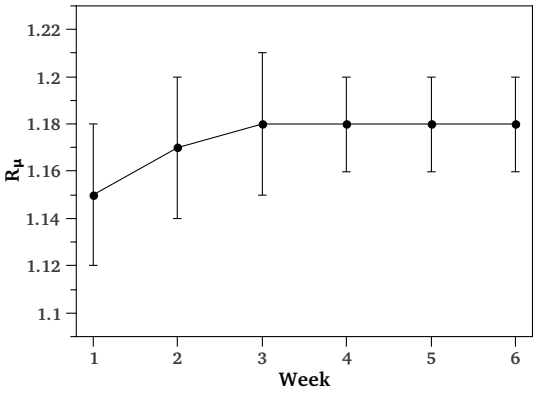

Figure 4: Muon charge ratio in different time intervals.

5 Concluding remarks

To determine the muon charge ratio in the cosmic rays flux at the momenta range 0.76-1.60 GeV/c, we carried out experiments at Sharif University of Technology in Tehran ($35°43'N$, $51°20'E$) and 1200 m above sea level ($890 gcm^{-2}$) by using a cosmic ray telescope. Because of background radiation as a noise in decay experiments, we ran a series of experiments to record background radiation and determine τ_{bg} in eq.1. Finally we estimated background radiation time constant, 284.8 ns and determined $\overline{R}_\mu = 1.15 \pm 0.03$ in one week time interval. Obtained values for muon charge ratio in different time intervals show that the fluctuations are very small and for three-week time interval and more, $\overline{R}_\mu$ tend to a fixed amount 1.18±0.03. Meanwhile we simulated EASs with CORSIKA code and obtained $R_\mu = 1.06$ in QGSJET-GHEISHA models and 1.04 in QGSJET-URQMD models. The muons angular distribution shows the received flux in west is higher than east direction and the muon flux is as $I(\theta) = I(0)\cos^n\theta$ in zenith angle θ, with $n = 1.90 \pm 0.16$, $n = 1.91 \pm 0.15$, $n = 1.90 \pm 0.14$ and $n = 1.92 \pm 0.27$ for directions north, west, south and east respectively.

References

[1] Thomas K. Gaisser: 1990, cosmic Rays and Particle Physics, Cambridge University Press

[2] Brancus, I.M. et. al., 26th International Cosmic Ray Conference, 1999
[3] T. Suzuki, D. F. Measday, J. P. Roalsvig, Phys. Rev. C, 1987, **35**(6): 2212-2224
[4] M. Bahmanabadi, F. Sheidaei, M. Khakian, J. Samimi, Phys. Rev. D, 2006, **74**(8)
[5] D. Heck et. al., Report FZKA6019 (Forschungszentrum Karlsruhe), 1998

Performance of EMMA Tracking Stations

T. RÄIHÄ[1], L. BEZRUKOV[2], T. ENQVIST[1], H. FYNBO[3], L. INZHECHIK[2], J. JOUTSENVAARA[1], T. KALLIOKOSKI[4], J. KARJALAINEN[1], P. KUUSINIEMI[1], K. LOO[4], B. LUBSANDORZHIEV[2], T. MONTO[4], V. PETKOV[2], J. SARKAMO[1], M. SLUPECKI[4], W.H. TRZASKA[4], AND A. VIRKAJÄRVI[1]
[1]*Oulu Southern Institute and Department of Physics, University of Oulu, Finland*
[2]*Institute of Nuclear Research, Russian Academy of Sciences, Moscow, Russia*
[3]*Department of Physics and Astronomy, University of Aarhus, Denmark*
[4]*Department of Physics, University of Jyväskylä, Finland*
tomi.raiha@oulu.fi
DOI: 10.7529/ICRC2011/V04/0873

Abstract: EMMA is an underground cosmic-ray experiment being constructed at the depth of 75 metres in the caverns of Pyhäsalmi mine in Finland. By June 2011 six of the nine detector stations have been constructed and two are already fully equipped with detectors and taking data. In the present paper the first results on the performance of EMMA tracking stations are presented.

Keywords: EMMA experiment, underground muon measurements, knee composition

1 Introduction

Despite numerous efforts to measure and explain the composition of cosmic rays in the knee region the results are inconclusive and the models inadequate. Most experiments indicate that at the knee energies the composition changes from light to heavier particles but its magnitude tends to depend on the detection technique and analysis method used in the experiment. The EMMA experiment (Experiment with MultiMuon Array [1]) is designed to study the composition in a new way by measuring the lateral density distribution of high-energy muons event by event. The experiment is being built at the depth of 75 metres in the Pyhäsalmi mine. The rock overburden sets an average energy threshold of 50 GeV for vertical muons filtering out also all other components of the extensive air shower (EAS).

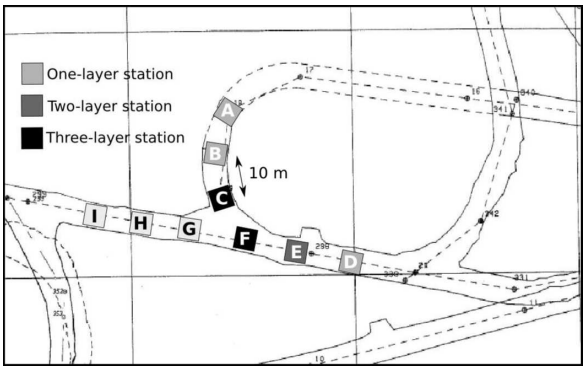

Figure 1: The layout of EMMA as viewed from the top. Stations A-F have been constructed. Stations C and F are three-layer tracking stations. The average distance between the centres of neighbouring stations is 10 m.

2 Description of the Experiment

EMMA will consist of nine detector stations arranged in the patterns shown in Fig. 1. The layout is imposed by the outline of the existing caverns. Each station is 15 m^2 and the distance between the centres of neighboring stations is 10 m. Currently (June 2011) six stations (marked A-F) have been constructed and two of them (stations B and C) are fully equipped with detectors and are taking data since April 2011.

The bulk of EMMA detectors consists of MUB drift chambers ($20 \times 365 \times 2$ cm^3) obtained from the decommissioned LEP-DELPHI [2] experiment at CERN. The drift chambers are operated with Ar:CO_2 (92%:8%) gas mixture that is mixed on ground and delivered through a 100 m pipeline to the EMMA level. The flow rate is slow so the used gas is simply vented to the cavern and dispersed by the mine's ventilation system.

The drift chambers are glued together into groups of seven (3+4 overlapping chambers), called planks. They have a

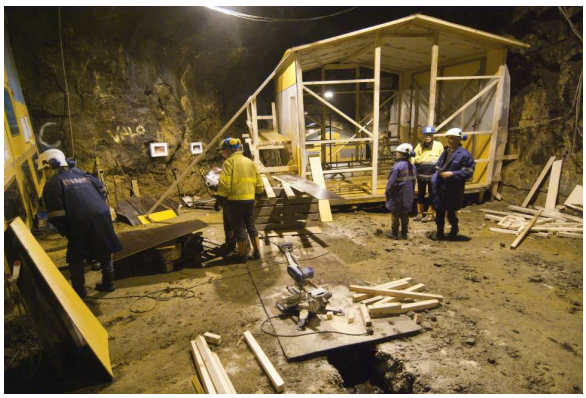

Figure 2: EMMA construction phase in Spring 2011. The three-layer tracking station F is under construction, two-layer station E locating behind it. The three-layer station C is partly visible on the left. One-layer stations A, B and D are behind other stations.

size of $85 \times 365 \times 6$ cm^3 each, and they are placed in the stations either in one, two or three layers. The vertical distance between plank layers is 112.5 cm. In total, 79 planks are used covering the effective area of 135 m^2.

EMMA will also include 96 plastic scintillation detectors (SC16s [3, 4]), each having a size of $50 \times 50 \times 3$ cm^3 and covering the total area of 24 m^2. One SC16 consists of 16 small-size plastic scintillation units ($12 \times 12 \times 3$ cm^3), which use avalance photodiodes (APDs) to register collected light enabling their compact design. All scintillation detectors have been delivered to Pyhäsalmi and will be mounted in EMMA stations after their testing is completed.

A view of the contruction of EMMA is shown in Fig. 2. Two- and three-layer stations can be used to reconstruct the tracks of muons and the shower arrival direction. Three-layer stations C and F were built in the centre of EMMA where the muon density is the highest and reliable tracking is crucial. The third three-layer station will be added later. The scintillation detectors will form the fourth layer in the central stations. Our simulations indicate that the fast, high-granularity layer improves the accuracy of shower reconstruction and especially the reconstruction of high-density muon events.

EMMA aims to measure the composition of cosmic rays around the knee region by studying the lateral distribution of high-energy muons ($E > 50$ GeV) event by event. The high-energy muons are produced at high altitudes close to the primary interaction carrying more direct information about the primary particle than low-energy particles produced closer to the ground level. The position of shower core and, similarly, the muon density in the core can be reconstructed by fitting a two-dimensional muon density function to the measured muon multiplicities in the detector stations providing nearly a model-independent estimate for the primary energy as described in [1]. Correspondingly, the shape parametre of the fitted muon density function tells the type of the primary particle.

In addition to composition analysis, EMMA is prepared to catch very high-density muon bundles detected in some CERN experiments [6, 7, 8]. By so far, none of the high-energy interaction models was able to explain such bundles. EMMA may give a new insight to this phenomenon as it is designed to reconstruct the number of muons up to high densities and reconstruct their lateral shape.

3 Event Reconstruction

Before delivery underground each drift chamber is position calibrated in the surface laboratory. To be accepted for installation the detector must reach the hit position resolution of better than 1 cm^2 and the muon detection efficiency at the level of 90-95%.

The 75 m thick rock layer above EMMA filters out most of the particles of EAS letting only high-energy muons to reach the EMMA level. The effect of rock overburden on muon trajectories was studied in detail with Geant4 [9] simulations. The results indicate that muons traversing the rock preserve their line of flight to better than one degree making the reconstruction of the shower direction possible.

Based on the parallelism of tracks the shower arrival direction and the tracks of muons can be reconstructed with data from the multi-layer stations. The track reconstruction is done with a two-step procedure: to approximate the shower direction in order to find the most optimal tracks and to give the final shower arrival direction from these tracks.

To find the first estimate for the shower arrival direction a 'check-all-possibilities' technique is used in which all such directions are studied that lead to tracks with hits in all three detector layers. The direction giving the largest number of parallel tracks is selected as the estimate for the shower arrival direction. After that the most optimal tracks are searched with respect of the reconstructed shower arrival direction. The tracks are selected on the basis of χ^2 test after which the final shower arrival direction is calculated from these tracks. Performing independent track reconstruction for each multi-layer station before combining the results yields a reliable reconstruction of the shower arrival direction. Furthermore, time and hit information of scintillation detectors will improve the reconstruction of the tracks of muons and exclude miss-interpreted shower arrival directions as sometimes may happen for highly inclined showers.

4 Performance of Track Reconstruction

EMMA track reconstruction program was optimised and tested with realistic simulations. The track reconstruction procedure is identical for all three-layer stations and, therefore, only the results for station C (three layers of planks) are presented.

4.1 Numerical Analysis Setup

Proton- and iron-initiated showers simulated by CORSIKA [5] (QGSJET01 + FLUKA) at the energy range of 0.1 – 31.6 PeV with zenith angles of 0 – 60 ° were used as an input to Geant4 simulations in which high-energy muons were transported through the rock close to the EMMA level and then simulated in detail through the last few metres in rock and through station C. The position uncertainty, detector efficiency, detector noise and afterpulses were taken into account in simulations. The simulated events were reconstructed with the track reconstruction program and the reconstruction results were analysed by comparing them with corresponding simulation parametres. The results are preliminary because the parametres of the track reconstruction software need more fine-tuning.

4.2 Test Results

Before a reconstructed event is qualified for the analysis it has to pass event qualification checks. An event could be rejected, e.g., if it contained a localised cluster of tracks such as those originating from muon-induced electromagnetic showers produced in the rock close to the cavern ceiling. The local track cluster can be found by calculating the local track density around each track and comparing it to the average track density in the station.

Efficiencies for events at different muon sizes to pass qualification checks are shown in Fig. 3. As can be seen, the efficiencies are $> 90\%$ up to simulated shower zenith angle 30 ° after which they start to decrease strongly. This is because the event must include at least one three-layer track to get rid of events with wrongly reconstructed shower arrival direction.

Figure 3 also shows probabilities that the error in extracted shower direction is larger than 10 ° (dashed lines close to the horizontal axis). A very inclined shower may sometimes be interpreted as a vertical shower but can be recognised when the shower arrival direction is obtained independently by scintillation detectors.

Some muons in the bundle may pass through the station the way that they are not reconstructable. This realises if the muon produces hits only in one plank layer or no hits at all. Some hits may be lost due to low detector efficiencies or due to muons passing through the gaps between chambers or planks. Therefore, in order to obtain the muon multiplicity in the station, the number of reconstructed tracks has to be corrected slightly upwards to compensate the number of lost tracks.

For the simulated events, the reconstructed muon multiplicity as a function of true simulated muon multiplicity set in corresponding simulations for showers with reconstructed zenith angle < 10 ° is presented in Fig. 4. Black horizontal lines represent 15% uncertainty to give a reference for the spread of data points. As visible, muon multiplicity reconstruction accuracy is moderate at least up to multiplicity 100. Further study is needed to extend primary energy range towards higher energies, gather more statistics at high multiplicities and find out the saturation limit of the station.

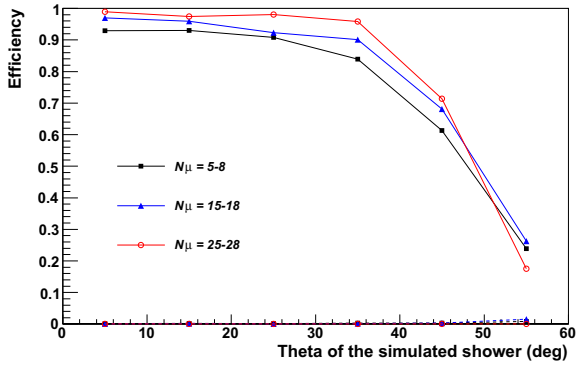

Figure 3: Data points represent the efficiency to reconstruct an event at different muon multiplicity ranges with the simulated shower zenith angle. The lines connecting the data points are only to guide the eye. Points connected by dashed lines (close to the horizontal axis) show probability that the error of reconstructed shower direction was > 10 °. The results are preliminary.

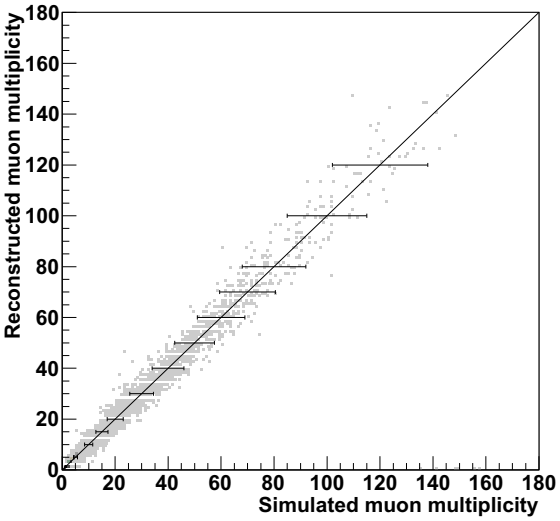

Figure 4: First estimate of the reconstructed vs. simulated muon multiplicity for simulated events in station C shown as grey symbols. Black horizontal lines indicate 15% uncertainty range. The diagonal is represented by a solid line.

5 Track Distribution Analysis

First preliminary analysis of the track multiplicity distribution measured in Spring 2011 (33 days of data) with station C was performed by comparing measured track multiplicity distribution with predictions from simulations. In the analysis, the cosmic rays were assumed to contain only protons. CORSIKA program (QGSJET01 + GHEISHA) was used to simulate proton-initiated showers at discrete energies in the energy range $10^{12} - 6.3 \times 10^{16}$ eV, zenith angles ranging up to $35\,^{\circ}$. The index of primary energy spectrum was set to -2.7 below 3 PeV and to -3.1 above it. The effect of rock overburden to muon parametres was estimated by applying 45 GeV $\times \sec\theta$ energy cutoff in the analysis.

The measured track distribution was cleaned from events which included local cluster of tracks of electromagnetic showers produced by single muons (the method is described in detail in [1]). Although the electromagnetic shower following a muon to the cavern is a relatively rare process they play an important role because the number of events decreases rapidly with multiplicity. As a consequence, single muons with electromagnetic showers may contribute to the track distribution over a wide multiplicity range. Such events can be, however, filtered out, with the method described in [1].

As the first approximation, the effect of detector response to the simulated track multiplicities was neglected and the simulated track distribution was simply normalised to experimental data. The reconstructed track distribution measured with station C is shown in Fig. 5 as white circles. Respectively, the simulated track distribution, assuming that all cosmic rays are pure protons, is shown with a solid line as normalised to the measured track multiplicity 5.

The results show that the similarity between the measured and simulated track multiplicity distributions is good although some details are not included in the analysis yet. In addition, mixed composition scenario will be implemented in further analysis.

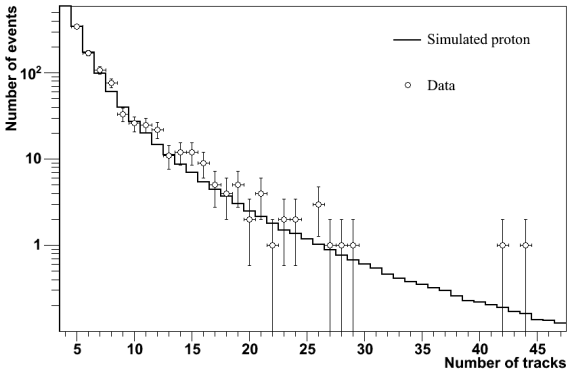

Figure 5: Preliminary track multiplicity distribution extracted from a 33 days data sample collected by station C. The solid line represents the simulated distribution normalised to the measured value at multiplicity equal 5.The normalisation was necessary because the detector response was not yet included. The simulation was calculated assuming that all primary cosmic-ray particles are protons. The comparison is shown for multiplicities > 4.

6 Conclusions

Six out of nine detector stations of the EMMA experiment have been constructed. Two of them (stations B and C) are already fully equipped and taking data. The first version of the newly developed software for event reconstruction works well. The positions of hits can be reconstructed with good accuracy and the uncertainties in reconstruction of the shower arrival direction and muon multiplicities with the tracking stations are at a good level. The addition of the high-granularity, fast scintillation detectors will considerably improve the event reconstruction. Data analysis of the first measured tracks has started. The obtained multiplicity spectrum matches well the simulations.

Acknowledgements

The support from the Magnus Ehrnrooth Foundation, the Vilho, Yrjö and Kalle Väisälä Foundation, the Finnish Cultural Foundation, and the Jenny and Antti Wihuri Foundation is gratefully acknowledged. The work is funded by the European Union Regional Development Fund and it has also been supported by the Academy of Finland.

References

[1] P. Kuusiniemi *et al.* , Astrophysics and Space Sciences Transactions, 2011, **7**: 93-96

[2] DELPHI Collaboration, Nuclear Instruments and Methods, 1991, **A**(303): 233

[3] V. Volchenko *et al.* , Central European Journal of Physics, 2010, **8**(3): 445-447

[4] E.V. Akhrameev *et al.* , Nuclear Instruments and Methods in Physics Research, 2009, **A**(610): 419-422

[5] D. Heck *et al.* , 1998, Report Forschungzentrum Karlsruhe FZKA **6019**

[6] Petr Travnicek, 2003, PhD. Thesis, Charles University, Prague

[7] V. Avati *et al.* , Astroparticle Physics, 2003, **19**: 513-523

[8] H.G.S. Wilkens, 2003, PhD. Thesis, University of Nijmegen.

[9] S. Agostinelli *et al.* , Nuclear Instruments and Methods in Physics Research, 2003, **A**(506): 250-303

32ND INTERNATIONAL COSMIC RAY CONFERENCE, BEIJING 2011

Quantifying uncertainties in the high energy neutrino cross-section

AMANDA COOPER-SARKAR[1], PHILIPP MERTSCH[2], SUBIR SARKAR[2]
[1]*Particle Physics, University of Oxford, Keble Road, Oxford OX1 3RQ, UK*
[2]*Rudolf Peierls Centre for Theoretical Physics, University of Oxford, 1 Keble Road, Oxford OX1 3NP, UK*

p.mertsch1@physics.ox.ac.uk

DOI: 10.7529/ICRC2011/V04/0890

Abstract: We compare predictions for high energy neutrino and anti-neutrino deep inelastic scattering cross-sections within the conventional DGLAP formalism of next-to-leading order QCD, using the latest parton distribution functions such as CT10, HERAPDF1.5 and MSTW08 and taking account of PDF uncertainties. From this we derive a benchmark cross-section and uncertainty which is consistent with the results obtained earlier using the ZEUS-S PDFs. We advocate the use of this for analysing data from neutrino telescopes, in order to facilitate comparison between their results.

Keywords: Deep Inelastic Scattering, Neutrino Physics, High Energy Cosmic Rays.

1 Introduction

Searches for high-energy cosmic neutrinos rely on predictions for the neutrino cross-section at high energies. These have however sizeable uncertainties deriving from the uncertainties on the parton distribution functions (PDFs) of the nucleon. Conventional PDF fits use the next-to-leading-order (NLO) DGLAP formalism [1, 2, 3, 4] of QCD to make predictions for DIS cross-sections of leptons on hadrons. At low x it may be necessary to go beyond the DGLAP formalism in order to sum $\ln(1/x)$ diagrams, as in the BFKL formalism [5, 6, 7] (for recent work see Refs. [8, 9]), or to even consider non-linear terms as in the colour glass condensate model [10, 11]. While the exact theoretical framework at low x is still contested it has been suggested [13, 12, 14, 15, 16] that observations of ultra high-energy neutrinos could itself be used to measure the cross-section thereby constraining the models. It is therefore important to not only consider the prediction for the cross-section but also to estimate their uncertainties in the conventional NLO DGLAP formalism.

In the framework of the quark-parton model, high energy neutrino deep inelastic scattering (DIS) accesses large values of Q^2, the invariant mass of the exchanged vector boson, and small values of Bjorken x, the fraction of the momentum of the incoming nucleon taken by the struck quark. Thus in evaluating uncertainties on high energy neutrino DIS cross-sections it is important to use the most up-to-date information from the experiments at HERA, which have accessed the lowest x and highest Q^2 scales to date. H1 and ZEUS have now combined the data collected in the years 1994–2000 to give very accurate inclusive cross-sections in the range $6 \times 10^{-7} < x < 0.65$ and $0.045 < Q^2 < 30000$ GeV^2 [17]. These data have not been available (or not been used) in previous predictions [18, 19, 20]. It is the purpose of the present paper to re-evaluate the high energy cross-sections using the most up-to-date PDF sets, with particular emphasis on those which do use these precise, combined HERA data. The calculation is made using PDFs which were evaluated in NLO DGLAP fits, and our calculation of the neutrino structure functions and cross-sections is also made consistently at NLO. For further details, we refer the interested reader to Ref. [21].

2 Formalism

The kinematics of lepton hadron scattering is described in terms of the variables Q^2, Bjorken x, and y which measures the energy transfer between the lepton and hadron systems. The double differential charged current (CC) cross-section for neutrino and anti-neutrino production on isoscalar nucleon targets is given by [22]

$$\frac{\mathrm{d}^2\sigma}{\mathrm{d}x\,\mathrm{d}Q^2} = \frac{G_\mathrm{F}^2 M_W^4}{4\pi(Q^2+M_W^2)^2 x}\sigma_\mathrm{r},$$

where the reduced cross-section $\sigma_\mathrm{r}(\nu(\bar{\nu})N)$ is

$$\sigma_\mathrm{r} = \left[Y_+ F_2^\nu(x,Q^2) - y^2 F_\mathrm{L}^\nu(x,Q^2) + Y_- x F_3^\nu(x,Q^2)\right],$$

and F_2, xF_3 and F_L are related directly to quark momentum distributions, with $Y_\pm = 1 \pm (1-y)^2$.

The QCD predictions for these structure functions are obtained by solving the DGLAP evolution equations at NLO

in the $\overline{\rm MS}$ scheme with the renormalisation and factorization scales both chosen to be Q^2. These equations yield the PDFs at all values of Q^2 provided these distributions have been input as functions of x at some input scale Q_0^2.

In QCD at leading order, the structure function $F_{\rm L}$ is identically zero, and the structure functions F_2 and xF_3 for charged current neutrino interactions on isoscalar targets can be identified with quark distributions. At NLO these expressions must be convoluted with appropriate coefficient functions in order to obtain the structure functions (and $F_{\rm L}$ is no longer zero) but these expressions still give us a good idea of the dominant contributions. Cross-sections for neutral current (NC) and anti-neutrino interactions are calculated in a similar way.

3 Parton Density Functions

Uncertainties on PDFs derive from two sources: experimental errors and parametrisation uncertainties. To allow for the estimation of the error induced in the predicted observable, i.e. cross-sections in the present case, modern PDF sets provide not only the best-fit PDF but also variants that reflect these different uncertainties. For experimental errors a set of variant PDFs, so-called eigenvectors, is obtained after diagonalisation of the error matrix. The eigenvectors are linearly independent such that the individual experimental errors can be added in quadrature. The variants for the parametrisation uncertainties are obtained from fits by varying certain parameter values (e.g. the starting scale Q_0^2 for evolution and the value of $\alpha_{\rm s}(M_Z)$) or the parametrisation for the input PDF parametrisation at Q_0^2.

The PDF4LHC group has recently benchmarked modern parton density functions [23]. Since our concern is with high energy neutrino cross-sections, rather than with LHC physics, we focus on PDF sets which make use of the newly combined accurate HERA data [17]. Of all the PDFs considered by the PDF4LHC only HERAPDF1.0 [17]) and NNPDF2.0 [24] used these data. However there has been a subsequent update of the CTEQ6.6 [25] PDFs to CT10 [26] which does use these data, while HERAPDF1.0 has recently updated to HERAPDF1.5 [27] using an preliminary combination of HERA data from 2003–2007 as well as the published combined data. We will utilise the CT10 and HERAPDF1.5 PDFs for the present study; we also consider the MSTW2008 PDFs in order to compare with other recent calculations of high energy neutrino cross-sections [20], although we caution that these have *not* included the most accurate HERA low x data relevant to the present study.

4 Results

The calculation of the CC and NC cross-sections in NLO has been performed using `DISPred` [28]. The PDFs have been implemented through the LHAPDF interface [29]. Particular care has been exercised to perform a self-consistent calculation. For example the PDFs from LHAPDF are mostly defined for a limited range in Q^2 and x and "freeze" beyond this range, which would result in underestimation of the cross-section at high energies; therefore we have used other implementations [30, 31]. Naturally, the cross sections have been calculated at a consistent order with respect to the PDFs.

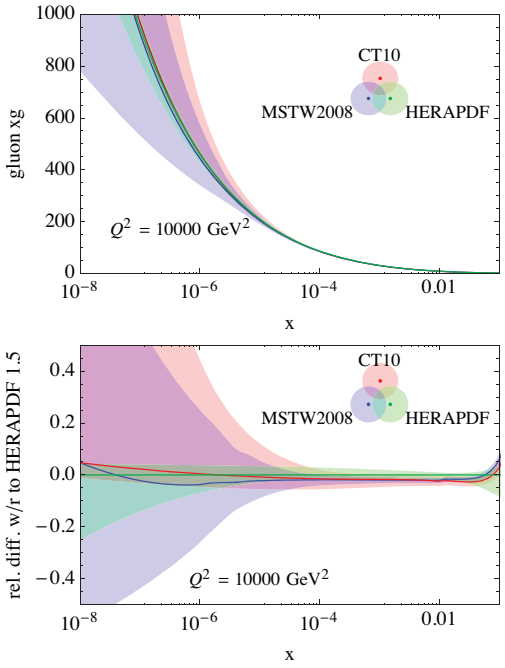

Figure 1: **Top panel:** Gluon structure function at $Q^2 = 10^4$ GeV^2 for the three PDF sets used. **Bottom panel:** The relative deviations and uncertainties (at 68% c.l.) with respect to the central value of HERAPDF1.5. The uncertainty bands are shown *with* member 9 for HERAPDF1.5 and member 52 for CT10.

Figure 1 compares the gluon PDF and its uncertainty at $Q^2 = 10000$ GeV^2 for the three PDFs which we consider. This value of Q^2 is in the middle of the range which contributes significantly to the neutrino cross-sections. We see that the central values of the gluon PDFs are all very similar, whereas the uncertainty estimates differ. The CT10 and HERAPDF1.5 uncertainties are actually very similar if we leave out member 52 from the CT10 error set. This error set was introduced into the CT10 analysis to allow for a larger uncertainty at low x [32]. Previous CTEQ analyses such as CTEQ6.6 [25] do not have such an extreme error set. The problem with such an *ad hoc* introduction of a steeply increasing gluon PDF is that at low x it leads to a very strong rise of the unphysical.

The larger error band of MSTW2008 is partly due to the fact that it does not include the most up to date HERA data, which have significantly reduced errors at low x. However the more striking difference between MSTW2008 and both

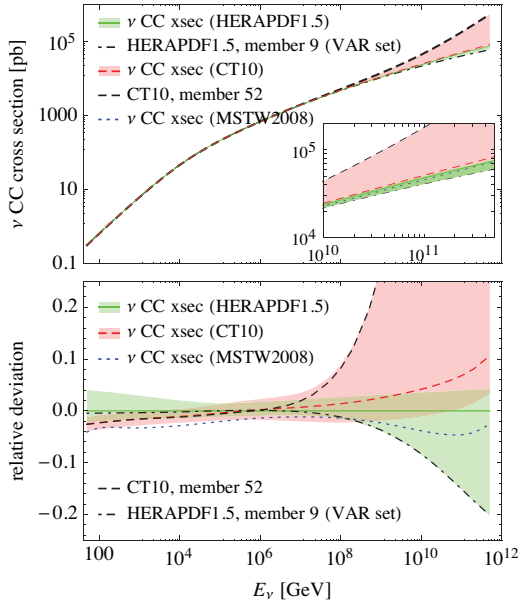

Figure 2: Comparison of the total cross-section (top panels) and uncertainties (bottom panels) for CC scattering as predicted by the HERAPDF1.5, CT10 and MSTW2008 (central member only) PDF sets. The cross-sections and deviations for member 9 of HERAPDF1.5 and member 52 of CT10 are indicated by the dashed and dot-dashed lines, respectively.

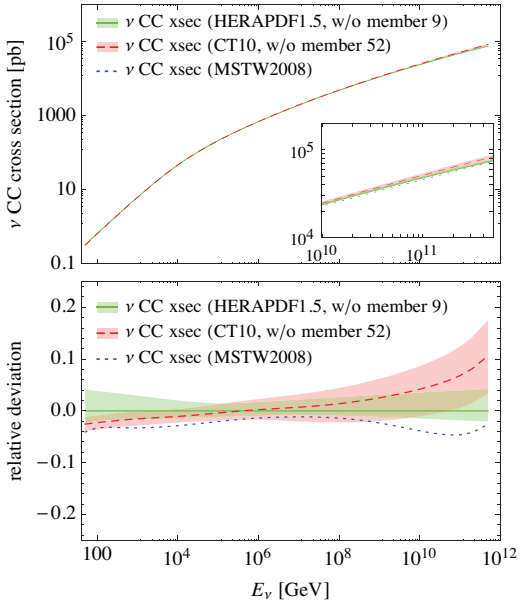

Figure 3: Same as Fig. 2, but excluding member 9 of the HERAPDF1.5 set and member 52 of the CT10 set.

HERAPDF1.5 and CT10 is the downward divergence of its error band which is due to the gluon becoming negative at low x, Q^2. At NLO the gluon PDF does not have to be positive, although one might consider that it going negative signals a breakdown of the DGLAP formalism. However measurable quantities such as the longitudinal structure function F_L, which is closely related to the gluon at small x, *must* be positive. The CT(EQ) analyses do not allow such negative gluon variants. We have checked for HERAPDF1.5 that the (moderately) negative gluon does not lead to negative F_L. The MSTW2008 set however includes member PDF sets with negative gluons that do lead to negative F_L and are thus unphysical.

In Fig 2 (top panel) we compare the CC cross-sections, along with their total uncertainties (including that coming from the variation of $\alpha_s(M_Z)$), as predicted by HERAPDF1.5 and CT10. The MSTW2008 central prediction is also included for comparison. In Fig 2 (bottom panel) we emphasize the small differences in the central values of the PDFs and their relative uncertainties. In order to highlight the effect of the extreme members of HERAPDF1.5 and CT10 in Figs 3, we show these plots without member 9 of the HERAPDF15 variations (which allows for the gluon to become negative at low x and Q^2) and without member 52 for CT10 (the cross-section for which rises $\propto E_\nu^{0.7}$ whereas for the central member it rises $\propto E_\nu^{0.3}$). However *any* power-law rise in the cross-section will eventually violate the Froissart bound, which requires the rise to be no faster than $\log^2 s$ [33]. This should result in a reduction of the cross-section at high energies, by a factor of ~ 2 at $E_\nu = 10^{12}$ GeV [34] and perhaps even more [35].

5 Conclusions

We find that the predictions of high energy neutrino DIS cross-sections from the central values of HERAPDF1.5, CT10 and MSTW2008 PDFs are very similar. However the predictions for the uncertainties (deriving from the uncertainties on the input PDFs) differ quite strongly. If we exclude error sets which either lead to too steep a rise in the cross-section, or allow the low x gluon to be negative at low Q^2, then we find that the uncertainty estimates of HERAPDF1.5 and CT10 — both of which use the most up-to-date, accurate HERA data — are remarkably consistent. In particular, we find the uncertainties to be much smaller than claimed recently [20].

Our results for the high energy neutrino and anti-neutrino CC and NC DIS cross-sections and their uncertainties using HERAPDF1.5 at NLO are shown in Fig. 4. The general trend of the uncertainties can be understood by noting that as one moves to higher neutrino energy one also moves to lower x where the PDF uncertainties are increasing. The PDF uncertainties are smallest at $10^{-2} \lesssim x \lesssim 10^{-1}$, corresponding to $s \sim 10^5$ GeV^2. When the high x region becomes important the neutrino and anti-neutrino cross-sections are different because the valence contribution to xF_3 is now significant. This is seen in Fig. 4, as is the onset

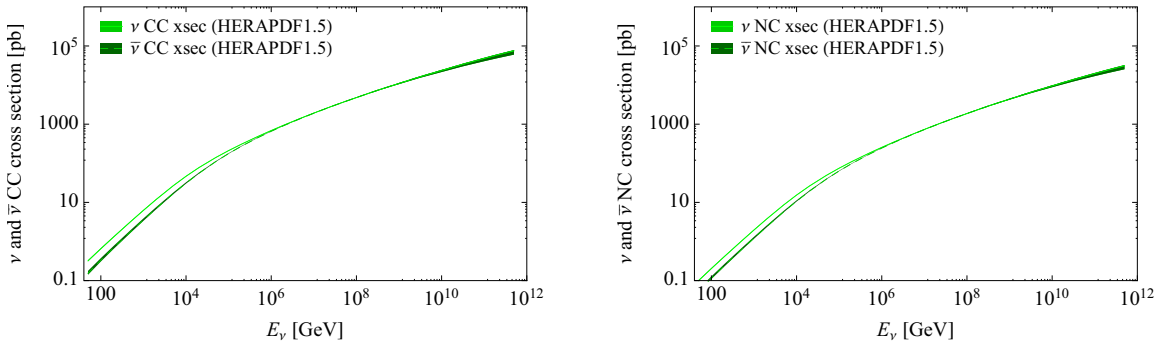

Figure 4: Neutrino and anti-neutrino cross-sections on isoscalar targets for CC and NC scattering for HERAPDF1.5.

of the linear dependence of the cross-sections for $s < M_W^2$. Note that our predictions are made for $Q^2 > 1$ GeV^2 since perturbative QCD cannot sensibly be used at lower values. For higher energies, we intend to upgrade ANIS [36] to use the HERAPDF1.5 (differential) cross-sections. Meanwhile, the tabulated cross sections for protons, neutrons and isoscalar targets are available from a webpage [37]; differential cross sections are available upon request. Any measured deviation from these values would signal the need for new physics beyond the DGLAP formalism.

References

[1] G. Altarelli, G. Parisi, Nucl. Phys. B **126** (1977) 298.
[2] V. N. Gribov, L. N. Lipatov, Sov. J. Nucl. Phys. **15** (1972) 438.
[3] L. N. Lipatov, Sov. J. Nucl. Phys. **20** (1975) 94.
[4] Y. L. Dokshitzer, Sov. Phys. JETP **46** (1977) 641.
[5] E. A. Kuraev, L. N. Lipatov, V. S. Fadin, Sov. Phys. JETP **45** (1977) 199.
[6] I. I. Balitsky, L. N. Lipatov, Sov. J. Nucl. Phys. **28** (1978) 822.
[7] L. N. Lipatov, Sov. Phys. JETP **63** (1986) 904.
[8] J. Rojo, G. Altarelli, R. D. Ball, S. Forte, [arXiv:0907.0443 [hep-ph]].
[9] F. Caola, S. Forte, J. Rojo, Phys. Lett. **B686** (2010) 127; Nucl. Phys. **A854** (2011) 32.
[10] F. Gelis, E. Iancu, J. Jalilian-Marian, R. Venugopalan, Ann. Rev. Nucl. Part. Sci. **60** (2010) 463.
[11] V. P. Goncalves, P. Hepp, Phys. Rev. D **83** (2011) 014014
[12] A. Kusenko, T. J. Weiler, Phys. Rev. Lett. **88** (2002) 161101.
[13] L. A. Anchordoqui, A. M. Cooper-Sarkar, D. Hooper, S. Sarkar, Phys. Rev. D **74** (2006) 043008.
[14] L. Anchordoqui, T. Han, D. Hooper, S. Sarkar, Astropart. Phys. **25** (2006) 14.
[15] S. Palomares-Ruiz, A. Irimia, T. J. Weiler, Phys. Rev. D **73** (2006) 083003.
[16] L. A. Anchordoqui, H. Goldberg, D. Gora, T. Paul, M. Roth, S. Sarkar, L. L. Winders, Phys. Rev. D **82** (2010) 043001.
[17] F. D. Aaron *et al.* [H1 & ZEUS Collaboration], JHEP **1001** (2010) 109.
[18] R. Gandhi, C. Quigg, M. H. Reno, I. Sarcevic, Phys. Rev. D **58** (1998) 093009.
[19] A. Cooper-Sarkar, S. Sarkar, JHEP **0801** (2008) 075.
[20] A. Connolly, R. S. Thorne, D. Waters, arXiv:1102.0691 [hep-ph].
[21] A. Cooper-Sarkar, P. Mertsch and S. Sarkar, arXiv:1106.3723 [hep-ph]; to appear in JHEP.
[22] R. Devenish, A. Cooper-Sarkar, "Deep inelastic scattering", Oxford University Press (2004).
[23] S. Alekhin *et al.*, arXiv:1101.0536 [hep-ph].
[24] R. D. Ball, L. Del Debbio, S. Forte, A. Guffanti, J. I. Latorre, J. Rojo, M. Ubiali, Nucl. Phys. **B838** (2010) 136-206. [arXiv:1002.4407 [hep-ph]].
[25] W. K. Tung, H. L. Lai, A. Belyaev, J. Pumplin, D. Stump, C. P. Yuan, JHEP **0702** (2007) 053.
[26] H. -L. Lai, M. Guzzi, J. Huston, Z. Li, P. M. Nadolsky, J. Pumplin, C. -P. Yuan, Phys. Rev. **D82** (2010) 074024.
[27] A. Cooper-Sarkar [on behalf of the H1 & ZEUS Collaborations], arXiv:1012.1438 [hep-ph].
[28] J. Ferrando, [arXiv:1007.5489 [hep-ph]]; J. Ferrando, P. Mertsch, in preparation.
[29] `http://projects.hepforge.org/lhapdf/pdfsets`
[30] `http://www.phys.psu.edu/~cteq/#PDFs`
[31] `http://projects.hepforge.org/mstwpdf/`
[32] P. Nadolsky, private communication.
[33] R. Fiore, L. L. Jenkovszky, A. V. Kotikov, F. Paccanoni, A. Papa, Phys. Rev. D **73** (2006) 053012.
[34] M. M. Block, P. Ha, D. W. McKay, Phys. Rev. **D82** (2010) 077302.
[35] A. Y. Illarionov, B. A. Kniehl, A. V. Kotikov, [arXiv:1105.2829 [hep-ph]].
[36] A. Gazizov, M. P. Kowalski, Comput. Phys. Commun. **172** (2005) 203.
[37] `http://www-pnp.physics.ox.ac.uk/~cooper/neutrino/`

Studies of multi-pixel Geiger-mode MRS APDs for muon veto scintillator detectors of cryogenic experiments

R. FALKENSTEIN[1], V.M. GOLOVIN[3], P. GRABMAYR[1], J. JOCHUM[1], B.K. LUBSANDORZHIEV[1,2], N.B. LUBSANDORZHIEV[2], R.V. POLESHUK[2], F. RITTER[1], CH. SAILER[1], B.A. SHAIBONOV (JR)[2], K. VON STURM[1].
[1]*Kepler Centre for Astro and Particle Physics, University of Tuebingen, Tuebingen, Germany*
[2]*Institute for Nuclear Research of the Russian academy of Sciences, Moscow, Russia*
[3]*Centre of Perspective Technology and Apparatus (CPTA), Moscow Russia*
lubsand@rambler.ru
DOI: 10.7529/ICRC2011/V04/1054

Abstract: In this paper, we present results of extensive studies of multi-pixel Geiger-mode avalanche photodiodes (MRS APDs) used in plastic scintilltor muon veto detectors of cryogenic experiments.

Keywords: Multi-pixel Geiger-mode avalanche photodiodes, MRS APD, plastic scintillators, WLS fibres.

1 Introduction

Two astroparticle physics low background experiments are located in the underground laboratory of the University of Tübingen. In order to shield them against cosmic ray muons, active muon veto detectors will be installed. Both of the muon veto systems will be constructed using plastic scintillator panels. Each panel contains a wavelength shifting fibre (WLS) which is embedded in a U-shaped groove. Both ends of the fibre are read out by multi-pixel Geiger-mode avalanche photodiodes (MRS APDs). Extensive studies of the main parameters of MRS APDs, e.g. breakdown voltages, gain and parameters temperature dependencies have been carried out.

2 Multi-pixel Geiger-mode avalanche photodiodes (MRS APDs)

Multi-pixel avalanche photodiodes working in a restricted Geiger mode have been getting intense development for the last two decades [1-5]. They consist of many micro-cells on the common silicon substrate, which are connected in parallel. Each micro-cell is connected in series with a quenching resistor. The device has a metal-resistor semiconductor layer structure and is operated in the limited Geiger-mode. The multi-pixel Geiger-mode APD used for our experiments are produced by CPTA, Moscow. For further details on MRS APDs the reader is referred to [6,7].

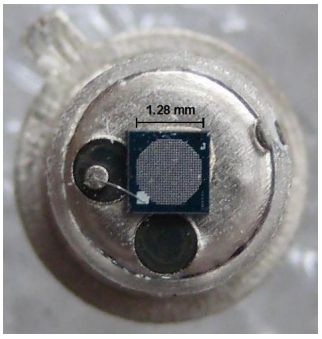

Figure 1: Photograph of a MRS APD.

The sensitive area of the MRS APD has an octagonal shape with 1.28 mm between opposed sides and is protected by an epoxy layer (see figure 1). The device consists of 796 pixels and it is packaged in a common metal TO-18 enclosure. The sensitive micro-cells of 40x40 μm^2 size are divided by grooves, filled with an optical nontransparent material in order to suppress optical crosstalk between the pixels [7]. The MRS APD is based on a n+pp+ doping layer structure as can be seen in figure 2. This structure leads to a high electric field gradient in the zone around the thin (~1 μm) n+p junction. This is the region where the avalanche multiplication of the photoelectrons occurs, however the generation of the photoelectrons mainly occurs in the p but also in the n+ regions. The structure of the MRS APD used in this work is optimized for the detection of light in the green and red part of the optical spectrum.

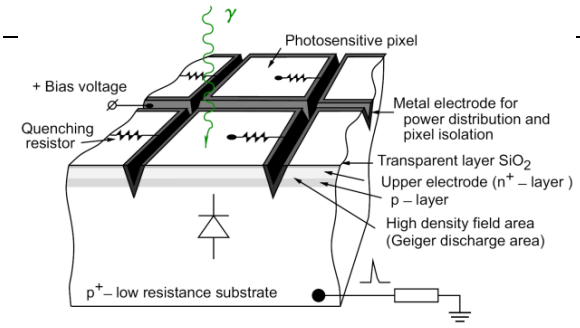

Figure 2: Simplified topology of the MRS APD [6,7].

MRS APDs have a high internal gain, which is almost comparable to that of vacuum photomultipliers. Each micro-cell of a MRS APD can be represented by a microcapacitor C_{pixel}. If now a breakdown occurs in one of the cells, it promptly discharges until such time as the voltage across it has decreased below the breakdown voltage. From this it follows that the total amount of charge flowing out of the microcapacitor during the breakdown is given by:

$$Q_{pixel} = C_{pixel} \cdot (V_{bias} - V_{bd})$$

where C_{pixel} is the capacitance of a single pixel and V_{bd} the breakdown voltage. The internal gain is thus given by:

$$G = Q_{pixel}/e$$

where e is the electron charge.
The photon detection efficiency (PDE) of a MRS APD is the ratio of the detected number of photons to the number of incident photons. It is the product of three parameters:

$$PDE = QE \cdot \varepsilon_{geom} \cdot \varepsilon_{Geiger}$$

where QE is the quantum efficiency, ε_{geom} the geometric factor and ε_{Geiger} the overvoltage-dependent probability that a photoelectron or hole triggers a Geiger discharge in silicon. The geometric factor is entirely defined by the topology of the MRS APD. It is given by the ratio of the sensitive area of all pixels combined, to the total surface of the element and has a value of $\varepsilon_{geom} \sim 0.6\text{-}0.7$ [6,7]. The PDE of the MRS APDs is about 25-30% at 515 nm in average [7].

3 I-V measurements

All of the MRS APDs (~ 300) were first characterized by measuring their reverse current-voltage characteristics (I-V curves) [8]. First of all, these curves can be used to determine the breakdown voltages (V_{bd}) of the MRS APDs, which is an important parameter, since it defines the working point of the particular MRS APD, which is about 10-20 % above the breakdown voltage. In addition, the I-V measurement is also useful to identify damaged MRS APDs and to get an estimate for the quality of the particular MRS APD. During the measurements the temperature was stabilized to 20 °C using a Peltier cooling system. For each voltage step 20 readings of the current were done with a delay of 200 ms.

Figure 3. Different bunches of MRS APD with similar breakdown voltages.

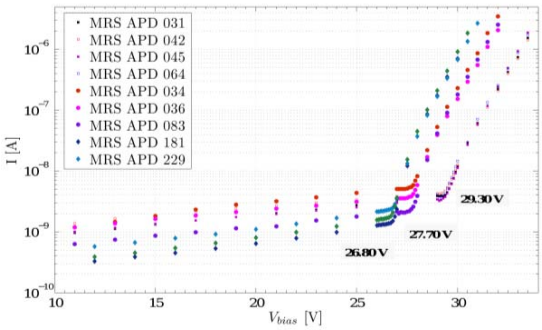

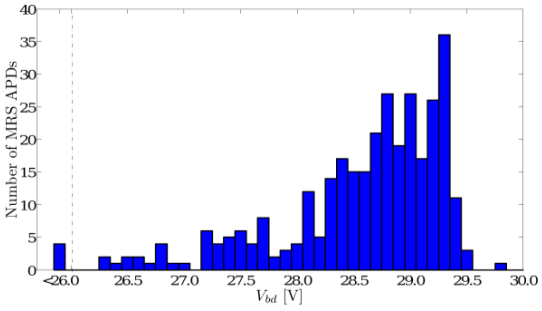

Figure 4: Frequency distribution of the breakdown voltages of 326 tested MRS APDs [8].

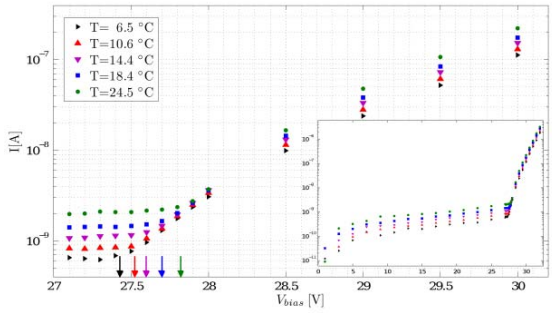

Figure 5: The reverse I-V characteristic of MRS APD #092 at different temperatures (the arrows indicate the breakdown voltages). The small embedded illustration shows the whole I-V curve.

The breakdown voltages and the corresponding leakage currents for each MRS APD were extracted from the I-V curves. Figure 3 shows the reverse I-V curves of different MRS APDs. All characterized MRS APDs are divided into subgroups with similar breakdown voltages. The frequency distribution of the breakdown voltages is shown in figure 4. More than 80 % of the tested MRS

APDs have breakdown voltages in the range of 28.7 ± 0.7 V [8].
For several MRS APDs, the I-V measurements were also carried out for different temperatures. As can be seen in figure 5, the breakdown voltage increases with the temperature.

4 Gain measurements

MRS APDs have an outstanding single photoelectron resolution. As a consequence the peaks corresponding to 0-, 1-, 2-, … photoelectron (p.e.) signals are clearly separated in the charge distribution as shown in figure 6. By means of these spectra, the gain of the MRS APD can be determined. The intrinsic gain of a MRS APD can be calculated by using the distance between two neighboring peaks in the pulse height spectrum.

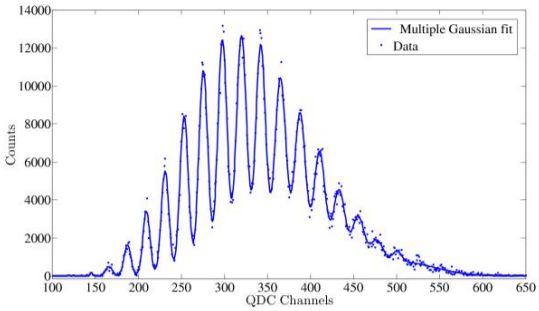

Figure 6: A typical multi p.e. charge spectrum of a MRS APD.

The gain as a function of the overvoltage $\Delta V = V_{bias} - V_{bd}$ for six different MRS APDs is diagrammed in figure 7. As expected, the gain depends linearly on the overvoltage.

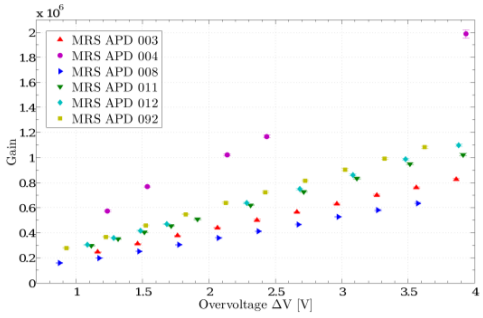

Figure 7: The gain of six different samples of MRS APDs as a function of the overvoltage measured at the temperature of 5.0 °C.

As can be seen in figure 8, the gain increases with lower temperatures at a fixed bias voltage.

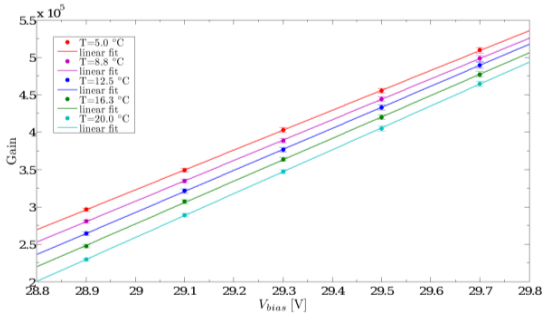

Figure 8: The gain as a function of the bias voltage for different temperatures.

This is due to the fact, that the breakdown voltage decreases with lower temperatures, resulting in a higher overvoltage, and therefore a higher gain. The breakdown voltages for the different temperatures are extracted by linear extrapolation of these curves to zero gain and are plotted as a function of the temperature in figure 9. These data in turn are fitted to linear functions in order to get the temperature gradient dV_{bd}/dT. This temperature gradient is ~ 0.02 V/°C for the measured MRS APDs.

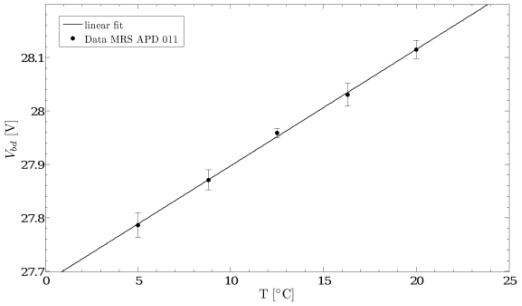

Figure 9: The breakdown voltage as a function of the temperature.

5 Measurements with scintillators

Plastic scintillator tiles will be used to build up two different muon veto systems in the Tuebingen underground laboratory [8].
The scintillator tiles are manufactured by the UNIPLAST company located in Vladimir, Russia. The panels are based on extruded polystyrene with 1.5% PTP (paraterphenyl, primary scintillator) and 0.01% POPOP (WLS, secondary scintillator) incorporation. They are etched by a chemical agent, resulting in the formation of a thin white layer (70-100 μ m) over the tile surface [6,7]. This deposit acts as a diffuse reflector layer. The panels are 126 cm long, 20 cm wide and have a thickness of 0.7 cm. The top face contains a U-shaped groove with an embedded wavelength shifting (WLS) fibre from Kuraray[1]. The WLS fibre is glued into the groove with a Bicron BC-600

[1] Y11(250)M s-type, Ø = 1 mm

epoxy optical cement. Both ends of the fibre are coupled with MRS APDs via an optical connector. This configuration should allow a homogeneous light collection over the whole panel area. The panel is wrapped in a diffuse reflecting Tyvek foil in order to enhance the light yield. In addition it is wrapped in pond liner in order to achieve light-tightness. In our measurements the light yield is measured as a function of the position where a minimum ionizing particle (MIP) strikes the scintillator panel.
The light yield of the plastic scintillator panel was tested with cosmic ray muons (i.e. MIPs). A PMT-scintillator based trigger setup which can be moved along the scintillator panel is used in order to define an area of impact. The trigger setup consists of two small scintillator tiles with a size of 20 x 10 cm^2 and each tile is coupled to PMTs[2] via light guides on both narrow sides. One of these scintillator trigger tiles is placed above, and the other below the scintillator panel. The distance between these two tiles is ~ 80 cm. An incident cosmic ray muon crossing both trigger tiles then defines a muon event if the coincidence condition is true. Due to the coincidence condition, the electromagnetic background is reduced. In order to determine the light yield, muon spectra were taken using a QDC. The low charge part of the spectrum due to radioactivity background was fitted to Gaussians and the muon peak was fitted to Moyal-functions [9] in order to get the most probable value for the energy loss (in units of QDC channels) for a MIP event. The Moyal-function is an analytical approximation of the Landau-Vavilov distribution [10] which describes the energy loss distribution in thin absorbers and is given by:

$$M = a \cdot exp(-(\lambda+exp(-\lambda))/2)$$

where $\lambda = (\mu-\mu_{mp})/b$, μ_{mp} is the most probable value and b is a constant depending on the absorber [11].

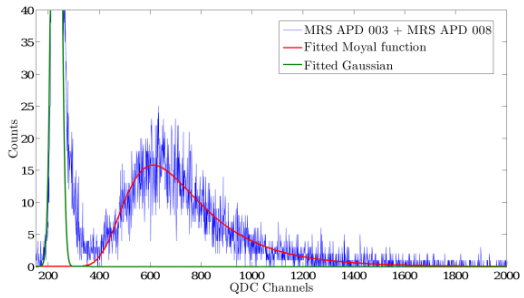

Figure 10: Cosmic ray muon spectrum. The peak due to muon corresponds to a light output of ~ 25 p.e.

A typical charge spectrum of the scintillator panels due to cosmic muons is shown in figure 10. The peak due to muon corresponds to a light output of ~ 25 p.e. It can be seen, that the muon peak is clearly separated from the low energy part due to radioactivity background with a peak-to-valley ratio of ~ 4. Measurements have shown that the light yield at the far end of the tile is reduced by about 20 % [8].

6 Conclusion

Extensive studies of MRS APDs parameters demonstrated their good performance, robustness and suitability for use in plastic scintillator panels readout for muon veto detectors of underground cryogenic experiments.

7 Acknowledgements

The work has been supported by project SFB #TR27 by DFG.

8 References

[1] Z. Sadygov, 1998, Russian Agency for Patents and Trademarks, Patent No. RU 2102820.
[2] V. Golovin, 1999, Russian Agency for Patents and Trademarks, Patent No. RU 2142175.
[3] D. McNally, V. Golovin, Nuclear Instruments and Methods A, 2009, 610: 150-153.
[4] Z. Sadygov et al., Nuclear Instruments and Methods A, 2006, **567**: 70.
[5] D. Renker, E. Lorenz, Journal of Instrumentation, 2009, **4**, P04004.
[6] A. Akindinov et al., Nuclear Instruments and Methods A, 2005, **539**: 172.
[7] Yu. Musienko et al., Instruments and Experimental Techniques, 2008, **51**(1), 101-107.
[8] R. Falkenstein, Diploma Thesis, University of Tuebingen, 2011.
[9] J.E. Moyal, Phil. Mag. 1955, **46**: 263.
[10] L.D. Landau, J.Phys.(USSR) **8**: 201.
[11] T. Davidek, R. Leitner, Atlas note, 1997, ATL-TILECAL-97-114.

[2] Hamamatsu R6427, Ø = 28 mm

32ND INTERNATIONAL COSMIC RAY CONFERENCE, BEIJING 2011

Observations of Large Scale Sidereal Anisotropy in 1 and 11 TeV cosmic rays from the MINOS experiment.

J. K. DE JONG[1] FOR THE MINOS COLLABORATION
[1] *Department of Physics, Oxford University, Oxford, United Kingdom OX1 3RH*
jeffrey.dejong@physics.ox.ac.uk
DOI: 10.7529/ICRC2011/V04/1185

Abstract: The MINOS Near and Far Detectors are two large, functionally-identical, steel-scintillating sampling calorimeters located at depths of 220 mwe and 2100 mwe respectively. The detectors observe the muon component of hadronic showers produced from cosmic ray interactions with nuclei in the earth's atmosphere. From the arrival direction of these muons, the anisotropy in arrival direction of the cosmic ray primaries can be determined. The MINOS Near and Far Detector have observed anisotropy on the order of 0.1% at 1 and 11 TeV respectively. The amplitude and phase of the first harmonic at 1 TeV are $8.2\pm1.7(\text{stat.})\times10^{-4}$ and $(8.9\pm12.1(\text{stat.}))^\circ$, and at 11 TeV are $3.8\pm0.5(\text{stat.})\times10^{-4}$ and $(27.2\pm7.2(\text{stat.}))^\circ$.

Keywords: MINOS, Atmospheric muons, Seasonal Variations, Sidereal Anisotropy

1 Introduction

Cosmic ray primaries in the 1 TeV to 100 TeV energy regime are thought to originate within our galaxy [1]. Curvature in the galactic magnetic field (GMF) and multiple interactions with local scattering objects are expected to eliminate point-of-origin information and cause the observed arrival direction of cosmic ray primaries to be highly isotropic. However, large scale anisotropies at these energies have been observed by Milagro [2], the Tibet Air Shower Array [3], ARGO-YBJ [16], IceCube [4] and Super-Kamiokande [5].

Anisotropy can be introduced through multiple different mechanisms. Compton and Getting [6] predicted a dipole effect could arise due to the rotation of the solar system around the galactic center with the excess appearing in the direction of motion. Diffusion of cosmic rays out of the galactic-disk into the galactic-halo could introduce an anisotropy perpendicular to the disk [1]. At TeV energies the heliosphere could produce a cosmic-ray excess in the direction of the heliotail; this excess should diminish with energy and is expected to be negligible above 10 TeV [7]. Discrete sources have been shown capable of creating anisotropy at higher energies [10, 11].

MINOS is a two detector long baseline neutrino beam oscillation experiment[9]. The 0.98 kton Near Detector, located at the Fermi National Accelerator Laboratory in Batavia, IL., is situated 94 m underground, below a flat overburden of 225 meters of water equivalent (mwe). The vertical muon threshold is 0.05 TeV. The raw atmospheric muon trigger rate is 27.29 ± 0.01 Hz. The 5.4 kton Far Detector is located in the Soudan Underground Mine State Park in Soudan, MN., 720 m below the surface. The vertical overburden is 2100 mwe and the muon threshold is 0.73 TeV. The trigger rate at the Far Detector is 0.5364 ± 0.0001 Hz. The MINOS detectors are two large, functionally-identical, steel-scintillating sampling calorimeters. The steel-scintillator planes are oriented vertically for optimal detection of horizontal beam neutrinos. As a consequence the detector has negligible acceptance for vertical muons increasing to near unity for horizontal muons.

The MINOS detectors do not measure the arrival direction or energy of the cosmic ray primary. These quantities are inferred from the muons produced in the air shower. These muons are highly boosted objects and travel nearly parallel to the direction of the original primary. The mean surface energy for muons observed at the Near(Far) Detector is 0.1 TeV(1.1 TeV). The mean cosmic ray primary energy is ten times larger [8] than the mean muon surface energy. The Near and Far Detectors therefore measure the anisotropy of 1.0 TeV and 11 TeV primaries respectively.

The expected level of cosmic ray anisotropy at TeV energies is 0.1 %. Spurious sidereal anistropies can be created by the detectors' non-uniform sky exposure. The diurnal and seasonal variation in the muon flux due to variation in the atmospheric temperature can interfere to produce a anisotropy with a sidereal component. Both of these

effects must be removed to obtain a reliable measurement of the true cosmic ray anisotropy. The former has be mitigated by accurately measuring the detector livetime; the latter by first measuring and then subtracting out the seasonal variation component.

2 Event Selection

The goal of this analysis is to identify large scale anisotropies in the arrival direction of atmospheric muons in the MINOS data set. The size of the data-set limits the search to anisotropies larger than 10°. These muons travel near parallel to the direction of the original cosmic ray primary; the large underground momentum of the muons limits the amount of multiple scattering in the overburden to be no more than 2°. The selection criteria have been chosen to obtain a detector pointing accuracy that, when combined with the scattering in the overburden and the initial scatter of the muon, gives an angular resolution on the direction of the primary cosmic-ray of 5°. Moon shadow searches performed using the MINOS Far Detector data have demonstrated that the detectors have a negligible pointing bias [12].

The same selections are applied to the data collected at the Near and Far Detectors. The candidate event must contain one and only one track. This track must be longer than 2 m and possess a vertex which is no further than 50 cm from the detector edge. The χ^2/ndf of the track-fit must be less than 1, and the residual of the track to a straight line must be less than 0.04 m. Finally, it is required that the data be collected during a period of good detector run conditions. In summary the Far (Near) Detector had an effective live-time of 93.4 % (76.0 %), and a selection efficiency of 63.8 % (32.4 %). The Near Detector selection efficiency is much lower than that in the Far Detector as events in the down-stream end of the detector trigger the readout but are not reconstructed. After all selections we retain 67.7×10^6 events in the Far Detector and 0.989×10^9 events in the Near Detector.

3 Seasonal Variations

When cosmic ray primaries interact with nuclei in the upper atmosphere the subsequent showers contains kaons and pions. These mesons can either interact or decay producing the muons which we observe underground. The probability that a meson will decay is proportional to its energy and the density of the atmosphere through which it travels. Increasing the temperature of the atmosphere decreases the density reducing the probability that a meson will interact thereby increasing the observed muon rate underground. The relationship between atmospheric temperature and muon rate

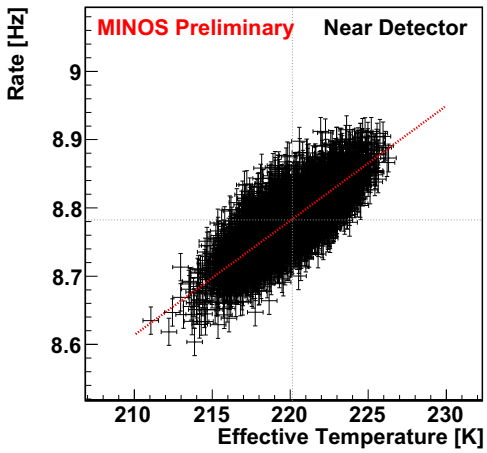

Figure 1: The observed muon rate at the MINOS Near Detector versus effective atmospheric temperature. The data is binned in 6 hr intervals centered around the ECMWF data points. The errors on the muon rate are statistical. The temperature errors are set to $\pm$0.5K. The red line is the best-fit of the data to equation 1.

underground can be written as

$$\frac{\Delta R_\mu}{\langle R_\mu \rangle} = \alpha_T \frac{\Delta T_{\rm eff}}{\langle T_{\rm eff} \rangle} \qquad (1)$$

where ΔR_μ is the deviation from the overall average muon rate. $\langle R_\mu \rangle$ is the muon intensity evaluated at a temperature $\langle T_{\rm eff} \rangle$. α_T is the coefficient of correlation between rate and temperature. The temperature $T_{\rm eff}$ is an effective temperature of the atmosphere which weights the temperature of the atmosphere at different depths by the probability of a muon being produced at that elevation [13]. The temperature as a function of depth has been determined using the European center for Medium-Range Weather Forecasts(ECMWF) atmospheric model [15]. The model provides atmospheric temperatures at 37 different pressure levels between 1 and 1000 hPa at four different times (0000 h, 0600 h, 1200 h,1800 h) throughout the day.

The average muon rate and temperature at the MINOS Near (Far) Detectors is 8.7820$\pm$0.003 Hz (0.32566$\pm$0.00004 Hz) and 220.1$\pm$0.5K (222.2$\pm$0.5K) respectively. Figure 1 plots the observed muon rate at the Near Detectors versus the effective atmospheric temperatures. To determine the value of α_T a linear regression was performed on the data using ROOT's MINUIT fitting package. The best fit values for α_T are 0.421$\pm$0.004(stat.) for the Near Detector, and 0.886$\pm$0.009(stat.) for the Far Detector [1]. The value of α_T is larger at the deeper Far

1. This measure of α_T at the Far Detector is in agreement with our previous publication [13]

Detector as it samples from higher energy mesons which have an increased probability of interacting.

4 Sidereal Anisotropy

Detector acceptance effects dominate the number of events observed in declination making a true two-dimensional map, accurate to 0.1%, impossible. The rotation of the earth washes out these effects in right ascension. If no anisotropy exists, and provided we account for differing exposure as a function of detector right ascension[2], we would expect the number of observed events to be flat as a function of right ascension.

The rate-weighted number of muons as a function of right-ascension (α) and declination (δ) are determined in each 1° detector right ascension bin k

$$n(\alpha,\delta)_k = \sum_{m=1}^{N_\mu} 1(\alpha^m,\delta^m)\frac{< R >}{R(T^m_{\rm eff})} \qquad (2)$$

where $< R >$ is the average muon rate and R is the expected muon rate at the current effective temperature T^m_{eff}. The two-dimensional sky-map is determined by summing over all detector right ascension bins and correcting for the different live times t_K in each bin.

$$N(\alpha,\delta) = \sum_{k=1}^{360} n(\alpha,\delta)_k \frac{< t >}{t_K} \qquad (3)$$

where $\langle t \rangle$ is the average detector live time per detector right ascension bin. The level of anisotropy A in the right-ascension bin α_i for a given declination bin δ_j is

$$A(\alpha_i,\delta_j) = \frac{N(\alpha_i,\delta_j) - < N(\delta_j) >}{< N(\delta_j) >} \qquad (4)$$

where $< N(\delta_j) >$ is the average number of events per right ascension bin for that declination bin. The one-dimensional sky-map is obtained by integrating the data over all declination bins.

A second order harmonic is typically used to describe the one-dimensional anisotropy

$$A(\alpha) = 1 + \sum_{n=1}^{2} A_n cos\left[\frac{n\pi}{180}(\alpha - \phi_n)\right]. \qquad (5)$$

Figure 2 plots the one-dimensional cosmic-ray sidereal anisotropy as observed by the atmospheric muons observed in the MINOS detectors. The data in figure 2 was fit to equation 5. The amplitude and phase of the primary harmonic are $3.8\pm0.5(\text{stat.})\times10^{-4}$ and $27.2\pm7.2(\text{stat})^\circ$ for the Far Detector data (11 TeV primary) and $8.2\pm1.7(\text{stat.})\times10^{-4}$ and a phase of $8.9\pm12.1(\text{stat})^\circ$ for the Near Detector data (1 TeV primary). A $5.3\,\sigma$ deficit is observed in the Far detector data between 150° and 245°, the chance probability of this deficit occurring randomly is 0.001%. An $11.1\,\sigma$ deficit is observed in the Near Detector data between 155° and 225° with a chance probability much less than 0.0001%. The Near detector also sees a $7.8\,\sigma$ excess between 50° and 140° also with a chance probability much less than 0.0001%.

The large statistics collected using the Near Detector are sufficient to allow an exploration of the two-dimensional anisotropy sky-map. Figure 3 plots the two-dimensional significance, defined as

$$\sigma(\alpha_i,\delta_j) = \frac{N(\alpha_i,\delta_j) - < N(\delta_j) >}{\sqrt{< N(\delta_j) >}} \qquad (6)$$

for 1 TeV CR primaries, where $< N(\delta_j) >$ is the total number of events in the 5° smoothed data sample. A significant deficit is observed Near the north galactic pole (192° ra, +27° dec), and an excess is observed around the heliotail. The energy of our Near Detector data sample is equivalent to that collected by ARGO-YBJ experiment [16]; and the two-dimensional sky-maps look similar.

5 Conclusion

The MINOS Near and Far Detector have been used to measure the anisotropy in the arrival direction of cosmic rays at energies of 1 TeV and 11 TeV. The amplitude of the first-harmonic has been observed to decrease with increasing energy from $8.2\pm1.7(\text{stat.})\times10^{-4}$ at 1 TeV to $3.8\pm0.5(\text{stat.})\times10^{-4}$ at 11 TeV. The two-dimensional sky-map at 1 TeV is consistent with previous publications. The MINOS experiment continues to take data and a more detailed analysis of the data will be forthcoming.

6 Acknowledgments

This work was supported by the US DOE, the UK STFC, the US NSF, the State and University of Minnesota, the University of Athens, Greece and Brazil's FAPESP and CNPq. We are grateful to the Minnesota Department of Natural Resources, the crew of Soudan Underground Laboratory, and the staff of Fermilab for their contributions to this effort.

References

[1] V.S. Berezinksii, S.V. Bulanov, V.A. Dogiel & V.S. Ptuskin (1990) Astrophysics of Cosmic Rays (Amsterdam; North Holland)

[2] A.A. Abdo *et al*. The Astrophysical Journal, **698** 2121 (2009)

2. Detector right ascension is the location to which the vertical axis of the detector is pointing

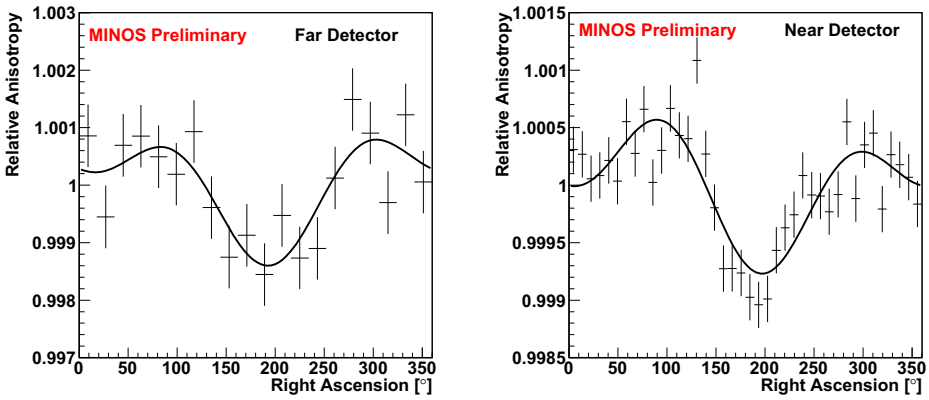

Figure 2: The one-dimensional projection of the Near and Far Detector sky-maps. The level of anisotropy in both data samples is 0.1%. The mean primary energy for the Far Detector is 11 TeV, and for the Near Detector is 1 TeV.

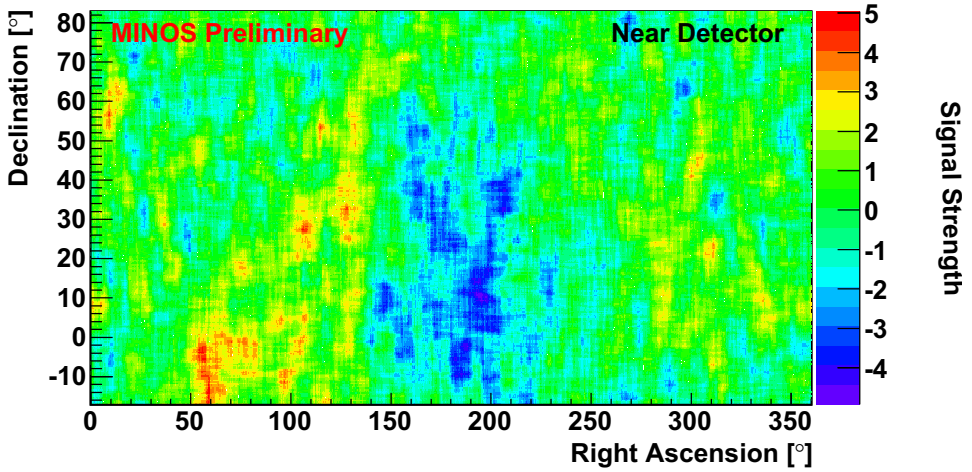

Figure 3: The two-dimensional significance sky-map for 1 TeV cosmic rays as determined using the MINOS Near Detector. A 5 ° smoothing has been applied.

[3] M. Amenomori *et al*. The Astrophysical Journal Letters, **626** L29, (2005)

[4] R. Abbasi *et al*. The Astrophysical Journal Letters, **718** L194 (2010)

[5] G. Guillian *et al*. Physical Review **D75** 062003, (2007)

[6] A.H. Compton, & I.A. Getting, Phys. Rev. **47**, 817

[7] K. Nagashima, K. Fujimoto,& R.M. Jacklyn, J.Geophys.Res. **103** 17429 (1998)

[8] M. Murakami *et al*., Nuovo Cimento **C2**, 635 (1979)

[9] D.G. Michael *et al*. (MINOS), Nucl. Instr. & Methods **A596**, 190 (2008)

[10] V.S. Ptuskin, F.C. Jones, E.S. Seo, & R. Sina. Adv. Space Res. **37** 1909 (2006)

[11] A. Strong, I. Moskalenko & V. Ptuskin. Annu. Rev.Nucl. Part. Syst. **57** 285 (2007)

[12] P. Adamson *et al*. (MINOS), Astropart.Phys.**34** 457 (2011)

[13] P. Adamson *et al*, (MINOS), Phys. Rev. **D81** 012001 (2010)

[14] J.K. de Jong and E.W.Grashorn for the MINOS collaboration, *Seasonal variation in the MINOS Detectors* Proceedings of the 31^{st} ICRC, Łódź 2009

[15] S. Osprey *et* al. Geophysical Research Letters **36** L05809, doi:10.1029/2008GL036359 (2009)

[16] J.L. Zhang, S.W. Cui for the ARGO-YBJ collaboration, *Observation of TeV cosmic ray anisotropy by the ARGO-YBJ experiment* Proceedings of the 31^{st} ICRC, Łódź 2009

Status Report on Project GRAND

POIRIER, J. [1], D'ANDREA, C. [1], BALL, M. [1], BARRY, C. [1], CATANACH, T. [1], CHENG, L. [1], WILSON, T., SWARTZENDRUBER, C.[2]
[1]*University of Notre Dame, Notre Dame, IN 46556 USA*
[2]*Bethany Christian Schools, Goshen, IN 46526 USA*

poirier@nd.edu

DOI: 10.7529/ICRC2011/V04/1292

Abstract: GRAND is an array of position sensitive proportional wire chambers (PWCs) located at 86.2 deg W, 41.7 deg N at an elevation of 220 m located near the University of Notre Dame. The 64 detector stations have a total of 82 sq-m of muon detector area. The geometry of the PWC detector stations (four stacked pairs of x and y planes) allows the measurement of charged particle tracks in two orthogonal planes to within less than 0.5 degrees, on average. Muons are 99% differentiated from electrons by means of a 51 mm thick steel plate above the last pair of x and y planes. An overview of the operation of Project GRAND is given.

Keywords: muons, detector, array

1 Introduction

Project GRAND is a muon array of 64 detector stations near the University of Notre Dame and is located at 86.2 deg W and 41.7 deg N 220 m above sea level [1-4]. The detectors consist of proportional wire chambers (PWCs) manufactured with a winding machine and glass frames making them cost effective and provide precision results. Each gas detector enclosure has an x and a y plane of 80 cells. Four of these boxes are arranged vertically above each other with a 5 cm thick steel plate above the bottom pair which allows muon/electron differentiation to 96% efficiency; given the 4:1 muon:electron ratio at ground level, the muon candidates are therefore 99% pure. The measurement of each incident angle is determined with good resolution (less than 0.5 deg in each of the two perpendicular planes). If needed, the arrival time of the muon is recorded to an absolute precision within milliseconds. The data, initially recorded on internal disk storage, are backed up to an external disk each hour and to a second remote backup disk with a two-hour delay. Data have been collected and archived since 2005 on disk storage and from 1990 on 8 mm magnetic tapes. There is a plan to transcribe these early data on tapes to disk for easier subsequent analyses. The muon array has a second trigger which selects extensive air shower events of muons and electrons; the two types of data are collected at the same time and stored separately. This paper updates a previous status report: Poirier et al. (2007) and references therein. A website contains additional information: www.nd.edu/~grand.

2 Experimental array

Project GRAND is an array of 64 proportional wire chamber stations dispersed in an area of 100 m x 100 m in an 8 x 8 grid pattern. The 200 mm of vertical separation between the planes with a PWC cell width of 14 mm gives good angular resolution for each track in two orthogonal planes (x=east-up, y=north-up). The effective muon detector area of a station is 1.29 sq-m for a total muon collection area of 82 sq-m. The array records about 1700 muons/sec (a single-track trigger). The single-track muon data are compacted in real time by recording only the wire numbers of complete tracks (a single x and y hit in every plane). In 1990 this compaction required eight 'fast' computers working in parallel; now it is easily performed with but a single computer. Each muon's time is determined to within a few milliseconds, absolute, by means of a WWVB radio receiver. A quartz crystal clock is used as a backup clock in cases of poor radio reception from WWVB; it can be calibrated absolutely using the concurrent radio data before and after the outage. The experiment also runs with a trigger for extensive air showers (a multiple-track trigger) at a rate of about one Hz.

3 Geographical location

For cosmic ray physics associated with solar effects it is important to have muon detectors located at different longitude so that, as the earth rotates, the effect of the sun is visible to at least one detector at any time since solar activity occurs randomly. Figure 1 shows the locations of cosmic ray muon detectors which are now active. The locations of the circles give the longitude and latitude of the muon detector; the area of the circle is proportional to the area of the detector and hence its counting rate.

4 Upgrades

Uptime has been enhanced by going from tape to disk data storage, backing up data, using uninterruptable power supplies, and a new software program which enables a replacement external disk to be installed without stopping the data acquisition. A better operating efficiency for the detectors can be achieved by: A) addressing gas leaks in the system that transports the Ar/CO_2 gas mixture to the detectors and in the detectors themselves. This includes >300 m of underground tubing and their compression fittings. The low flow rate of the gas mixture and the extended distances for the leaks to occur make finding the leaks difficult. Several new leak-finding techniques will be utilized. B) Humidity in the hut (a 3.4 m x 3.4 m structure housing the PWC detectors) impregnates the Styrofoam insulator between ground and high voltage causing added HV current in the hut's isolation resistor producing a voltage drop to the detector thus lowering its efficiency. If the dehumidifier in the hut has to work too hard in the summer, it raises the temperature in the hut and trips off the dehumidifier so the hut does not overheat. Different methods to seal the Styrofoam against the absorption of water are being examined which would then eliminate the need for the dehumidifier thus solving two problems at once.

The Center for Research Computing (CRC, at Notre Dame) has engineered and provided an archival data storage device capable of storing up to 7 TB of data. Currently it stores data from 2005 to the present (with a two-hour delay). Prior data from 1990 to 2005 are archived on 8 mm magnetic tape. Copying these data on tape to disk storage will begin soon so all of GRAND's archived data, from 1990 to the present, will be online and hence available for presentation on its website for easy viewing and digital transference on request.

5 Education and outreach

GRAND's muon array is ideal for student participation and collaborative work. Since ~1989, there have been one to three REU (Research Experiences for Undergraduates) students working on Project GRAND for 10 weeks during the summer months; for the past eight years, two REHS (Research Experiences for High School students), and one to two RET (Research Experiences for Teachers); these "RE" programs are sponsored by the National Science Foundation [8]. For the past four years there have been two to three Notre Dame undergraduate students working on GRAND during the two semesters of the academic school year. It takes the REU students about two hours each week at the experiment changing gas tanks and recording various operating parameters to determine if everything is working properly. These students then spend most of their time analyzing data to extract physics, utilizing and writing the programs to do this work. Conversely the REHS students spend most of their time at the experiment locating and addressing various problems while spending one day a week on campus looking at and analyzing the data.

There have been three undergraduate theses, one master's thesis in Electrical Engineering, and two doctoral theses in Physics utilizing GRAND. Two high school teachers have worked on the experiment's physical structures. There has been a one-hour luncheon lecture on GRAND each summer to all the REU and RET students. At the beginning of each summer session, Calvin Swartzendruber, who has worked as an RET teacher for eight years, gives the entire incoming Notre-Dame class of REHS students an introductory talk on-site at GRAND to explain the detector and its capabilities.

An REU student, Rachel Bergen, wrote the first version of Project GRAND's website. This website presents data and pictures on the project (introduction, the detector array, detector modules, trailer, data acquisition system, in-depth description, publications, vital statistics, recent progress). The website can be found online at http://www.nd.edu/~grand. Calvin Swartzendruber has instituted a valuable addition to this website, "Live Data and Statistics" showing the operation of GRAND for various periods of time: 15 months, 5 weeks, 9 days, or 1.5 days (the latter showing up to the last 10 minutes of real time, invaluable for diagnostic work). Prof. Doug Thain from Notre Dame's Department of Electrical Engineering and two of his graduate students instituted another website; with the help of CRC it has now been converted to: https://grandbackup.phys.nd.edu. By logging on to this website and clicking "Dayfiles", one can select the total muon rate for selected periods of time from late 2005 until the present, with or without corrections for air pressure. In addition, a single hut's data can be displayed or all 64 huts at once, individually displayed. The data are displayed visually, making it easy to analyze from a remote site; these data can also be obtained digitally from the website. GRAND's cosmic ray data of muon rates, are easy to visualize and analyze, thus making it a natural vehicle for an outreach program.

6 Ground level enhancement January 2005

GRAND has previously published data on the 20 January 2005 GLE [5] which has been used in analyzing the multiple-component structure of this solar event [6]. Since the timing is important in this analysis, these data was reanalyzed in smaller time bins. Each muon is tagged with a time referenced to WWVB, the radio time standard of the U.S. In Figure 2 these data are displayed

in 15-second wide bins; smaller time bins become more dominated by statistical errors. The FWHM width of these data for this GLE is three minutes. These data have been statistically enhanced by selecting angles near vertical [5]. This enhancement is possibly due to the lower than average energy of the solar protons and/or their preferred direction.

7 Forbush decrease of October 2003

The decrease in total muon counting rate at GRAND for October 29 and 30, 2003 is shown in Figure 3 [7] which shows ~8% rapid decrease in counting rate with the beginning of the more leisurely subsequent rise. The figure below this shows the mean *angle* of the muons during this same time frame. The upper, diamond points are the mean muon angle (in degrees) projected to the north-up plane; the lower, square points are the same for angles projected to the east-up plane. Although the angular change is very small (0.5 degree for the upper, north-up plane, points and somewhat smaller for the lower, east-up, points), it is obtained by averaging the angles of ~0.5 million muon angles making even this tiny effect statistically significant. It is also correlated with the rapid decrease in the counting rate of the muons; the time position of the mid-down point in muon rate is closely associated with the mid-up point in the muon angle. This is possibly the first direct proof that the decrease in cosmic rays is due to the charged cosmic rays being deflected in angle by the magnetic fields contained in a coronal mass ejection as it nears the earth.

8 Acknowledgments

Grand was built with assistance from the National Science Foundation and is operated by gifts from the University of Notre Dame and individuals. Thanks to the Center for Research Computing for providing the on-campus data backup system that contributes to the 24/7 continuous operation and security of the data. Thanks to Brian Knorr, Freddy Martinez, Tom Scrace, James Tucci, Jr. and Meghan Mahoney for their work on the data analyses. Thanks to the National Science Foundation for programs assisting students and teachers in participating in basic research.

9 References

[1] Fasso, A. and Poirier, J. Phys Rev D, 2001, **63**, 036002.
[2] Fields, B. et al., in Proceedings of the 25th International Cosmic Ray Conference, 1997, **6**, 365-368.
[3] Poirier, J. and D'Andrea, C. in Proceedings of the 27th International Cosmic Ray Conference, 2001, 3923-2926.
[4] Poirier, J. et al., in Proceedings of the 26th International Cosmic Ray Conference, 1999, **2**, 64-67.
[5] D'Andrea, C. and Poirier, J., Geophysical Research Letters, 2005, **32**, L14102.
[6] Moraal, H., McCracken, K.G., Stoker, P. H., Journal of Geophysical Research, 2008, **13**, A12101.
[7] D'Andrea, C., Poirier, J., and Balsara, D. S., Advances in Space Research, 2009, **44**, 1247.
[8] National Science Foundation programs.

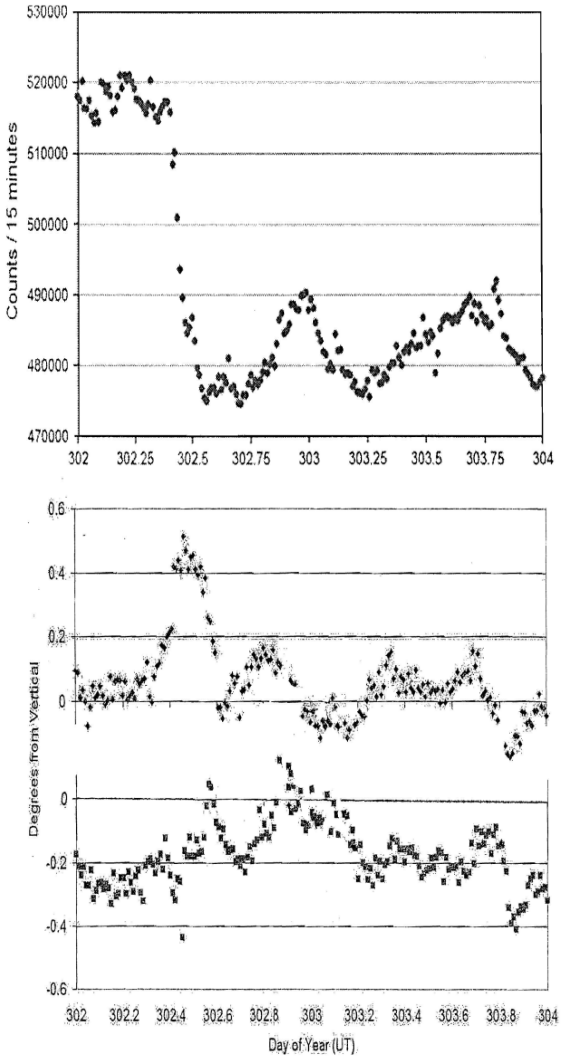

Figure 3.
Upper figure: shows GRAND's counting rate for the October 29, 2003 Forbush decrease from day-of-year 302 to 304. GRAND's total counting rate dropped by 8%. *Lower two figures:* show the mean angle of muons for the same period of time. Diamonds (upper points) show the mean angle in the north-up projected plane with vertical muons = 0 degrees. There is a 0.5 deg change in the mean direction in the north-up plane during the time of the Forbush decrease, indicative of a deficiency in the south caused by the deflection of the cosmic rays by the coronal mass ejection's magnetic field. Squares (lower points) show the mean angle of muons in the east-up projected plane.

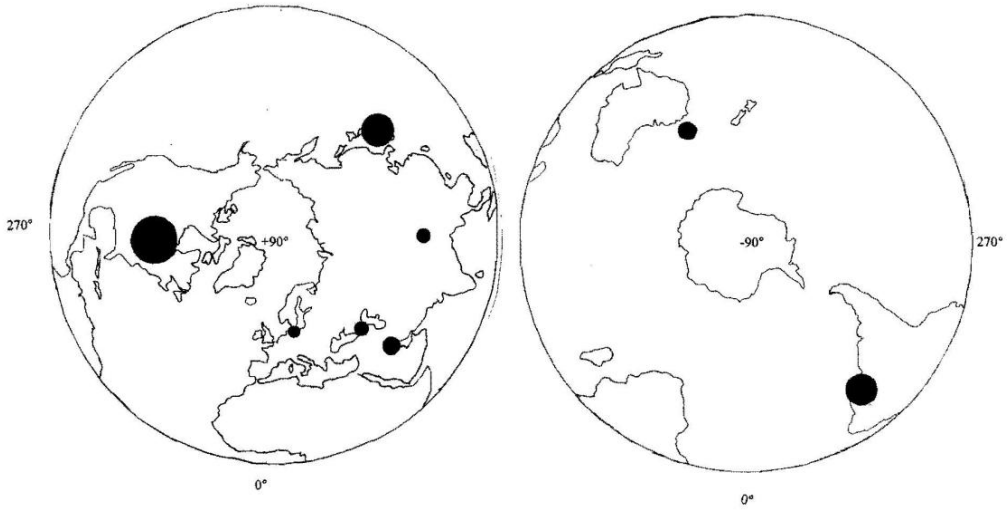

Northern Hemisphere Southern Hemisphere

Figure 1: Map of cosmic ray muon detector locations around the world. Circles indicate geographical positions within the earth's equator); angular position from 0-deg (bottom) represents the detector's longitude; latitude is represented by the linear distance from the equator toward the center which is the North Pole at +90 deg (Northern Hemisphere), or the South Pole at -90 deg (Southern Hemisphere). The area of the muon detector is represented by the area of the circle and is proportional to their counting rates. Northern hemisphere detectors are in order of longitude: Germany (Europe), Kuwait (Persian Gulf), Armenia (Middle East), Beijing (China), Nagoya (Japan), and GRAND (North America); Southern hemisphere, right figure: Hobart (Tasmania) and San Martinho (South America). Uniform worldwide coverage allows the sun to be seen 24 hours a day.

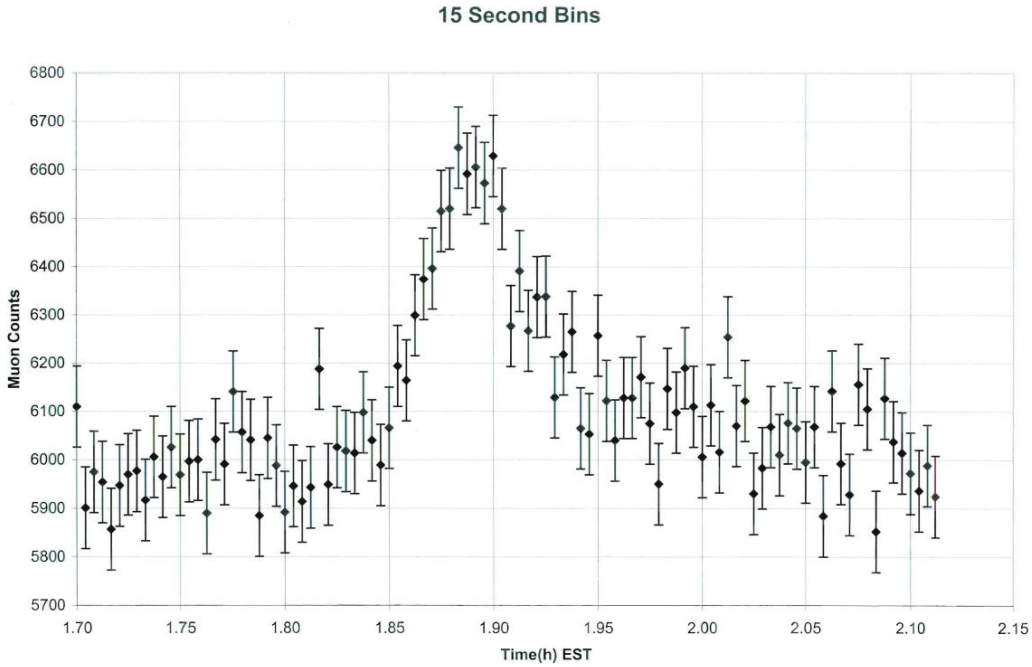

Figure 2. GRAND's muon data in EST (UT-5) showing the time details of the GLE of 20 January 2005 in 15-second wide time bins. The data are for muon angles near vertical [see 5] which yield a better signal/background ratio.

HE.2.2: Solar, atmospheric and related neutrino experiments

Is It Possible to Extract the Evidence for Neutrino Oscillation Definitely in the Cosmic Ray Experiments?
—Re-Analysis of *L/E* Distribution Performed by Super-Kamiokande in the Computer Numerical Experiment—

E.KONISHI[1], Y.MINORIKAWA[2], V.I.GALKIN[3], M.ISHIWATA[4], I.NAKAMURA[5], N.TAKAHASHI[1], M.KATO[6], A.MISAKI[7]
[1]*Graduate School of Science and Technology, Hirosaki University, Hirosaki 036-8561, Japan*
[2]*School of Science and Engineering, Kinki University, Higashi-Osaka 577-8502, Japan*
[3]*Department of Physics, Moscow State University, Moscow 119992, Russia*
[4]*Faculty of Science and Technology, Meisei University, Tokyo 191-8506, Japan*
[5]*Comprehensive Analysis Center for Science, Saitama University, Saitama 338-8570, Japan*
[6]*Kyowa Interface Science Co.Ltd., Saitama 351-0033, Japan*
[7]*Innovative Research Organization, Saitama University, Saitama 338-8570, Japan*
amisaki@sand.ocn.ne.jp
DOI: 10.7529/ICRC2011/V04/0191

Abstract: On the examination on *L/E* analysis performed by Super-Kamiokande Collaboration, we have concluded that the study on neutrino oscillation with the use of cosmic ray beams cannot specify neutrino oscillation parameters reliably, because the cosmic ray experiments cannot determine the direction of the incident neutrino, while the accelerator experiment can do, if neutrino oscillation really exists. We examine the fundamental assumption postulated by Super-Kamiokande Collaboration that the direction of the incident neutrino is approximately the same as that of the emitted lepton does not hold even if approximately and their L_μ/E_ν (L_μ/E_μ) distribution does not show any maximum oscillations which is the logical consequence of the survival probability for a given flavor such as ν_μ.

Keywords: neutrino oscillation, quasi-elastic scattering, cosmic rays

1 Introduction

The detection of the neutrino oscillation is constructed entirely upon the survival probability for a given flavor such as ν_μ:

$$P(\nu_\mu \to \nu_\mu) = 1 - sin^2 2\theta \cdot sin^2\left(1.27\Delta m^2 L_\nu/E_\nu\right), \quad (1)$$

where L_ν and E_ν denote, the flight length of the incident neutrino from the generation point to the interaction point and its energy, respectively.
Then, for maximum oscillations under SK neutrino oscillation parameters, we have

$$1.27\Delta m^2 L_\nu/E_\nu = (2n+1)\times\frac{\pi}{2}, \quad (2)$$

where $sin^2 2\theta = 1.0$ and $\Delta m^2 = 2.4\times10^{-3}$ eV^2 [1].
From Eq.(1), we should have the following values of L_ν/E_ν for maximum oscillations.

$$L_\nu/E_\nu = \begin{cases} 515\ \text{km/GeV} & \textit{for } n=0 \quad (3-1) \\ 1540\ \text{km/GeV} & \textit{for } n=1 \quad (3-2) \\ 2575\ \text{km/GeV} & \textit{for } n=2 \quad (3-3) \end{cases}$$

and so on.

However, generally speaking, it is pretty difficult to decide oscillation parameters, $sin^2 2\theta$ and Δm^2 definitely from the cosmic ray experiments, because in principle, one cannot observe the directions of the incident neutrinos due to the nature of cosmic ray beams, while one can decide the directions of the incident neutrinos in the accelerator experiments, because we know the exit of the neutrino beams from the accelerator.

2 Why Do We Emphasize the Importance of QEL Events as Fully Contained Events?

In spite of the difficulty inherent in the cosmic ray experiments exclusively, but not inherent in the accelerator experiments, if one tries to "accurate" experiments in the cosmic ray experiments, one should try to exclude other uncertainties as much as possible, keeping aside uncertainty for the directions of the incident neutrinos. Consequently, one must choose the most reliable events with the highest quality among all possible detectable events. The events which satisfy such severe conditions are single ring lepton (electron or muon) events due to quasi elastic scattering (QEL) which are generated in the detector and terminated in it (*Fully Contained Event*). In this case, one may know the kinds of the neutrinos, the directions of the emitted leptons and their energies.
The single ring lepton events due to QEL are expressed in the followings:

$$\left.\begin{aligned} &\nu_e + n \to p + e^- \\ &\nu_\mu + n \to p + \mu^- \\ &\bar{\nu}_e + n \to n + e^+ \\ &\bar{\nu}_\mu + n \to n + \mu^+ \end{aligned}\right\} \quad (4)$$

The differential cross section for QEL is given as follows[2]:

$$\frac{\mathrm{d}\sigma_{\ell(\bar{\ell})}(E_{\nu(\bar{\nu})})}{\mathrm{d}Q^2} = \frac{G_F^2 \cos^2\theta_C}{8\pi E^2_{\nu(\bar{\nu})}} \times \\ \times\left\{ A(Q^2) \pm B(Q^2)\left[\frac{s-u}{M^2}\right] + C(Q^2)\left[\frac{s-u}{M^2}\right]^2 \right\}, \quad (5)$$

where

$$A(Q^2) = \frac{Q^2}{4}\left[f_1^2\left(\frac{Q^2}{M^2} - 4\right) + f_1 f_2 \frac{4Q^2}{M^2} + \right. \\ \left. + f_2^2\left(\frac{Q^2}{M^2} - \frac{Q^4}{4M^4}\right) + g_1^2\left(4 + \frac{Q^2}{M^2}\right)\right],$$

$$B(Q^2) = (f_1 + f_2) g_1 Q^2,$$

$$C(Q^2) = \frac{M^2}{4}\left(f_1^2 + f_2^2 \frac{Q^2}{4M^2} + g_1^2 \right).$$

The signs + and – refer to $\nu_{\mu(e)}$ and $\bar{\nu}_{\mu(e)}$ for charged current (c.c.) interactions, respectively. The Q^2 denotes the four momentum transfer between the incident neutrino and the charged lepton. Details of other symbols are given in [2].
In Figure 1, we give the relation between the scattering angles and the ratio of the emitted muons' energy to the parent muon due to QEL for different primary neutrino energies. It is clear from the figure that we cannot neglect the effect of large angle scattering including the backscattering in QEL, if we consider larger flux of the neutrinos with smaller energies.

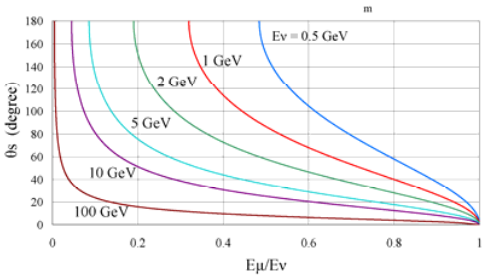

Figure 1. The relation between E_μ / E_ν and the scattering angle θ_s due to QEL for different primary energies.

In Figure 2, we give the schematic view of the muons for different typical zenith angles, focusing on their azimuthal angles in QEL. It is clear from the figure that the effect of the azimuthal angle in QEL on the directions of the emitted muons cannot be neglected, particularly in the horizontal like neutrinos.

It is easily surmised from Figures 1 and 2 that for neutrinos with given directions (downward or upward), there are two directions (downward or upward) of the emitted muons. Namely, downward (upward) vertical like neutrinos produce downward (upward) muons with smaller scattering or produce upward (downward) muons with backscattering. Downward (upward) horizontal-like neutrinos produce either downward (upward) muons or upward (downward) ones which may depend on the accidental combinations of scattering angles and the azimuthal angles in QEL. The situation around the directions of muons is too complicated and it is impossible to understand the situation without careful and exact simulation, considering the neutrino flux and the geometry of the detector.

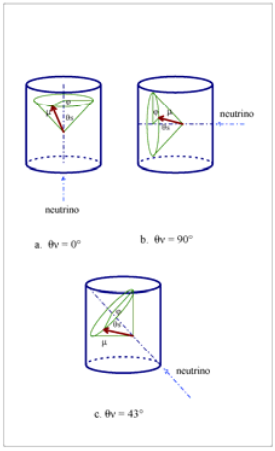

Figure 2. Schematic view for the effect of the azimuthal angle on the direction of the muon for the typical directions of the neutrinos.

3 SK *Assumption on the Direction* and the Transform of Energy

We carry out the extensive computer numerical experiments in which all possible factors are taken into account, considering the stochastic characters of the physical processes concerned as exactly as possible.

In Figure 3, we give the correlation between L_ν and L_μ with oscillation. Super-Kamiokande Collaboration postulate the fundamental assumption (*SK Assumption on the direction*) that the direction of the incident neutrino is approximately the same as that of the emitted muon[3,4,5][1]. It is clear from the figure that *SK Assumption on the direction* does not hold even if approximately, which is the cornerstone for their analysis on neutrino oscillation.

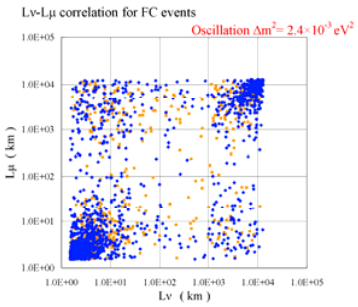

Figure 3. The correlation between L_ν and L_μ for the neutrinos and muons (blue points) and anti-neutrinos and anti-muons (red points) for one SK live day.

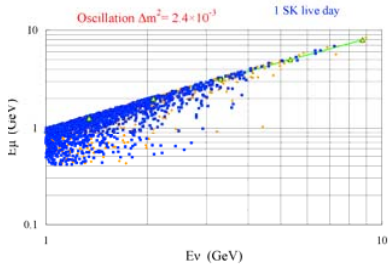

Figure 4. The correlation between E_ν and E_μ for the neutrino and muons (blue points) and the anti-neutrino and anti-muons (red point) for one SK live day. The line shows the relation between them obtained by Super-Kamiokande Collaboration.

Also, Super-Kamiokande Collaboration give the approximated formula from which they derive the energy of the incident neutrinos (Eq.(9) in [3]). The idea of making the approximated formula denotes implicitly that the relation between E_ν and E_μ is unique, but not stochastic. However, it is not true. The relation between E_ν and E_μ is quite stochastic, the nature of which depends on the combination of QEL and the neutrino spectrum. In Figure 4, we give the correlation between E_ν and E_μ together with their polynomial approximation (the line in the figure)[2]. It is clear from the figure that the correlation cannot be neglected.

[1] Here L_μ denotes the corresponding flight length of the emitted muon.

4 *L/E* Distributions by our Computer Numerical Experiments

4.1 L_ν/E_ν distribution

Super-Kamiokande Collaboration had obtained the data for neutrino oscillation for 1489.2 live days[1]. We have carried out 25 SK live days in the unit of 1489.2 live days (one SK live day). In Figure5, we give L_ν/E_ν distribution, adopting neutrino oscillation parameters obtained by Super-Kamiokande Collaboration. Our L_ν/E_ν distribution indicates well the existence of the first maximum oscillation (A), the second maximum oscillation (B) and the third maximum oscillation (C). This is the evidence that our computer numerical experiments are carried out in a correct manner. To make the existence of the maximum oscillation clearer, we plot our L_ν/E_ν

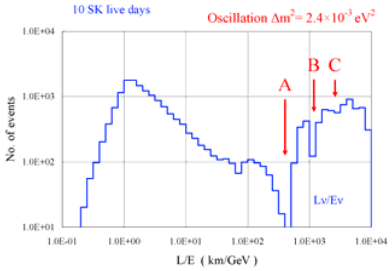

Figure 5. L_ν/E_ν distribution obtained by us for 10 SK live days. The arrows A, B and C indicate the locations of the first, the second and the third maximum oscillations, respectively.

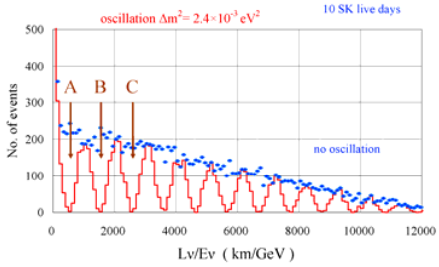

Figure 6. L_ν/E_ν distributions with and without oscillation in linear scale for 10 SK live days.

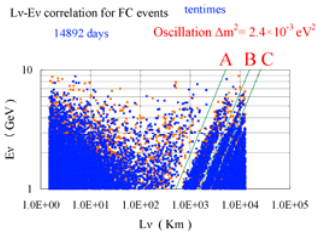

Figure 7. Correlation between L_ν and E_ν for 10 SK live days. A, B and C indicate the locations of the first, the second and the third maximum oscillations.

[2] Here E_μ is the energy of the emitted muon due to QEL.

distribution together with the corresponding one without oscillation in a linear scale in Figure 6. The maximum oscillations after the fourth one are surely found.

The alternative expression of the existence of the maximum oscillations is given in the correlation diagram between L_ν and E_ν in Figure 7. The vacant regions in the figure indicated by A, B and C show the first, the second and third maximum oscillations.

4.2 L_μ/E_μ distribution

On the other hand, we examine L_μ/E_μ distribution. Notice that Super-Kamiokande Collaboration really did not measure L_ν and E_ν but L_μ and E_μ, because they cannot measure L_ν and E_ν due to of their neutrality. We give L_μ/E_μ distribution with oscillation together with the corresponding one without oscillation in a linear scale in Figure 8. From the comparison of Figures 8 with 6, it is clear that there are no maximum oscillations in L_μ/E_μ distribution. In Figure 9, we give the correlation diagram between L_μ and E_μ. Here, we cannot find any vacant regions which correspond to the locations of the maximum oscillations. In conclusion, we cannot find any indication on the maximum oscillations through L_μ/E_μ distribution. This fact tells us that we cannot specify the neutrino oscillation parameters in L_μ/E_μ analysis.

Super-Kamiokande Collaboration approximate L_ν with L_μ based on *SK assumption on the direction* and replace E_ν by the approximate formula of E_μ. Namely, they claim that they measure L_ν/E_ν through this procedure. However, this claim have lost the ground, because *SK assumption on the direction* does not hold even if approximately.

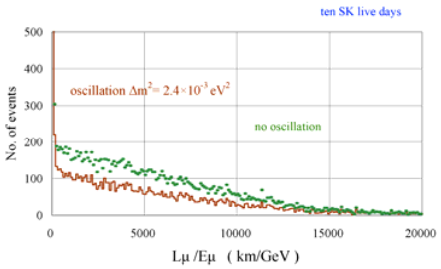

Figure 8. L_μ/E_μ distributions with and without SK neutrino oscillation in linear scale for 10 SK live days.

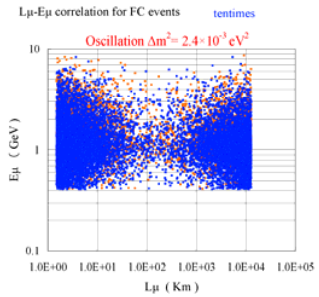

Figure 9. Correlation between L_μ and E_μ for 10 SK live days.

Finally, we compare our *L/E* distribution with that obtained by Super-Kamiokande Collaboration in Figure 10. There are two remarkable differences between our *L/E* distribution and theirs. The first one is that we have the sharp maximum oscillation near 515km/GeV, while they have far broader range for the first maximum oscillation. The second one is that we have the maximum frequency for the events at $\sim$ 1 km/GeV, while they have the corresponding one at $\sim$ 20 km/GeV, by an order of magnitude larger than ours. As for the position of the maximum oscillation, it is unnatural for them to have far wider vacant region for the events, considering the nature of the maximum oscillations. As for the maximum frequency for the events, Super-Kamiokande Collaboration should have the horizontal like events there, which contradict with real ones, because the horizontal like events cannot be expected to be more frequent due to smaller solid angles.

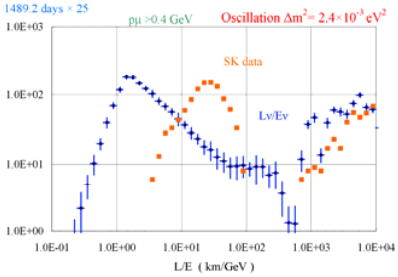

Figure 10. The comparison of our L_ν/E_ν distribution with the corresponding distribution obtained by Super-Kamiokande Collaboration. The experimental data obtained by Super-Kamiokande collaboration are read out from their data[3].

5 Conclusion

We have concluded that Super-Kamiokande Collaboration may not measure the real direction of incident neutrinos in their *L/E* analysis who are based on *SK assumption on the direction*. Consequently, we suggest them to re-analysis the zenith angle distribution of the neutrino events, abandoning *SK assumption on the direction.*

References

[1]Ashie,Y. et. al., Phys. Rev. **D**, 2005, **71** : 112005-
[2]Renton,P.: 1990, Electro-weak Interaction, Cambridge University Press. See p. 405.
[3] Ishitsuka,M., Ph.D Thesis:2004, University of Tokyo. See p.138
[4]Kajita, T., Y.Totsuka, Y., Rev.Mod.Phys., 2001, **73**: 85-. See p.101
[5]Jung,CK et. al., Annual Rev.Mod.Sci.,2005,**15**:431-. See p. 453
[6] Ashie,Y. et. al., Phys. Rev. Lett. 2004, **93**:10180-1.

Analysis of nuclear de-excitation γ-rays using T2K data

KOH UENO[1] FOR THE T2K COLLABORATION
[1]*Kamioka Observatory, ICRR, University of Tokyo, Higashi-Mozumi, Kamioka, Hida, Gifu 506-1205, Japan*
ueno@suketto.icrr.u-tokyo.ac.jp
DOI: 10.7529/ICRC2011/V04/0253

Abstract: In searches for supernova relic neutrinos (SRN) or GUT monopoles in Super-Kamiokande (SK), nuclear de-excitation γ-rays induced by neutral-current (NC) interactions of atmospheric neutrinos with ^{16}O are one of the major background sources. However, until recently their kinematic properties and absolute yield were largely unknown. The T2K experiment started in January 2010, and its beam energy is typical of atmospheric neutrinos which induce NC de-excitation γ-rays. We have selected low energy (4 - 30 MeV) NC events in the T2K data, and comparing these events with MC we'll estimate the amount of NC background relevant for low energy analyses in SK. Preliminary results and future prospects for this analysis are presented.

Keywords: neutrino interaction, water Cherenkov detector, neutral current, nuclear de-excitation, supernova relic neutrino, GUT monopole

1 Introduction

In searches for supernova relic neutrinos (SRN) or GUT monopoles in Super-Kamiokanede (SK) [1, 2], nuclear de-excitation induced by neutral-current (NC) interactions of atmospheric neutrinos with ^{16}O is one of the major background sources. When the excited nucleus from a neutrino interaction decays to its ground state, γ-rays, nucleons, and heavy particles are emitted. When the emitted nucleons (especially neutrons) interact with other ^{16}O nuclei in water, they may also become excited and emit γ-rays. Even if the energy of each γ-ray is below 10 MeV, the total number of Cherenkov photons from a cascade of all the γ-rays (or their Compton electrons) in a single event is often reconstructed above the thresholds of low energy analyses at SK. However, their kinematic properties and absolute yield have large uncertainties, and data is needed for calibration.

2 T2K experiment

The Tokai-to-Kamioka (T2K) [3] is a long baseline neutrino oscillation experiment that started in January 2010, which uses a high intensity muon neutrino beam produced at J-PARC and directed toward SK, 295 km away. The main purpose of the experiment is to determine the last unknown mixing angle, θ_{13}, by observing the oscillation of $\nu_\mu \rightarrow \nu_e$. However, since its beam energy is similar to that of atmospheric neutrinos it is also useful to study various phenomena at SK related to atmospheric neutrinos interactions, including the emission of de-excitation γ-rays from NC interactions in the water.

Figure 1 shows the result of the T2K Monte Carlo (MC) simulation for interactions with reconstructed energy[1] between 4 - 30 MeV. In this energy range, more than 95 % of events come from NC interactions, of which about 80% are elastic (NCE) events. T2K beam NC neutrino events are expected to peak around 6 MeV due to the 6.18 MeV and 6.32 MeV de-excitation γ-rays from ^{15}O* and ^{15}N* decays, respectively. However, in this energy range the many γ-ray background events from radioactivity in the PMT case and glass usually make it impossible to exclusively tag neutrino-induced events. However, the GPS-based T2K beam timing is accurate to 200 ns, and cuts on this time profile dramatically enhance our ability to reject these backgrounds.

3 Event selection

3.1 Data set and reduction

We have performed a low energy (4 - 30 MeV) NCE event search on the T2K data. Table 1 shows a summary of each T2K RUN used in this analysis. After a total charge cut and an outer detector trigger cut, the data are subjected to a fiducial volume (FV) cut. As mentioned above, the main source of background for this search is produced by γ-rays emitted from the materials of the detector structure and therefore a higher background rate is expected near the inner detector (ID) walls. To reduce this background, we

1. We assume all Cherenkov photons in an event come from a single electron, and reconstruct the total energy (not the kinetic energy) of the electron.

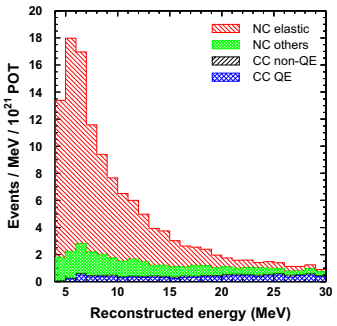

Figure 1: Expected energy distribution assuming 1×10^{21} POT and its breakdown by neutrino interaction mode.

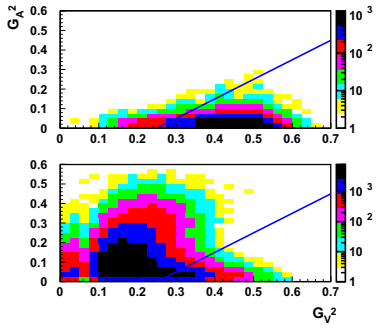

Figure 2: Correlation between the vertex goodness ($\mathrm{G_V}^2$) and the angular goodness ($\mathrm{G_A}^2$). The top figure shows the T2K MC and the bottom the background, and in both figures only events above 4.5 MeV in the FV are used. Each cut line corresponds to the threshold of ovaQ $\equiv \mathrm{G_V}^2 - \mathrm{G_A}^2 = 0.25$.

first reject events whose dwall, the distance to the nearest ID wall, is less than 2 meters. This cut defines the FV. However, some events originating from outside of the FV have the possibility of being reconstructed within the FV. To remove these events, we cut on the event's distance to the nearest ID wall projected backwards from its vertex position along its reconstructed direction ("effwall"). Events whose effwall is very short are highly likely to be γ-rays from the ID walls and are removed.

	RUN-I	RUN-II
Run start	Jan. 2010	Nov. 2010
Run end	Jun. 2010	Mar. 2011
POT (protons on target)	3.23×10^{19}	1.11×10^{20}
#spill	9.99×10^{5}	1.48×10^{6}
#bunch	6	8
GPS accuracy	$\pm$200 ns	$\pm$200 ns

Table 1: Summary of each T2K RUN.

To further reject the remaining backgrounds, especially mis-reconstructed events, we check the quality of the reconstructed vertex (vertex goodness) and direction (angular goodness). The vertex goodness is evaluated by a fit of the PMT timing distribution, where a sharp timing distribution defines a large goodness. The angular goodness is evaluated using the uniformity of the spatial distribution of hit PMTs around the reconstructed direction: the more uniform the distribution is the smaller the goodness. The correlation between the vertex goodness ($\mathrm{G_V}$) and the angular goodness ($\mathrm{G_A}$) is shown in Figure 2. The top figure shows the T2K MC signal[2] and the bottom shows the background. In both figures only events above 4.5 MeV in the FV are used. We can efficiently separate signal from background events if we use the following variable: ovaQ $\equiv \mathrm{G_V}^2 - \mathrm{G_A}^2$.

Comparing the MC prediction and expected background, the signal-to-noise ratio is found to be strongly dependent on the reconstructed energy. Thus, we optimized the cut criteria of effwall and ovaQ simultaneously in each energy bin so as to maximize the following figure-of-merit (FM),

$$\mathrm{FM} \equiv \frac{\mathrm{N_{signal}}}{\sqrt{\mathrm{N_{signal}} + \mathrm{N_{background}}}}, \qquad (1)$$

where $\mathrm{N_{signal}}$ and $\mathrm{N_{background}}$ are the numbers of signal and background, respectively, in each energy bin. After the criteria are tuned for all bins, we fit the discrete values to a line and use it as the reduction criteria. Strictly speaking, because the T2K experiment has had different beam intensities and beam bunch structures during its runs, the relative background level has always been changing. Therefore, we prepared cut criteria for various beam intensities and bunch structures. Figure 3 shows the signal-to-noise ratios before and after all cuts assuming a constant beam intensity of 20 kW and six bunches per beam spill with a GPS timing accuracy of 200ns. We can see a great improvement in the background rejection ability by introducing the cuts explained above, particularly in the energy region below $\sim$ 6 MeV, where backgrounds are expected to be large.

3.2 Further cuts to select NC elastic events

In this analysis' energy region, there are fewer NC non-elastic events expected relative to NCE events as shown above (Figure 1), which makes it difficult to discern non-elastic events from CC events. We therefore opt to select only NCE events for this study. To enrich the sample in NCE interactions, we apply additional cuts: a multi-peak cut on the event's timing structure to reject decay electron events and a cut on the Cherenkov opening angle to remove muon-like events.

2. The range this term indicates will be narrowed to only NC elastic events later.

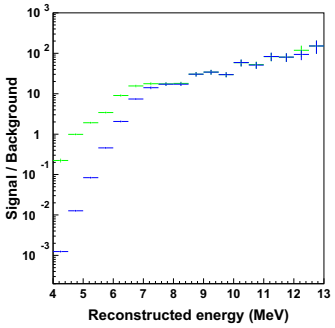

Figure 3: Signal-to-noise ratios before (dark) and after (light) all cuts assuming a beam intensity of 20 kW and six bunches and a GPS timing accuracy of 200 ns.

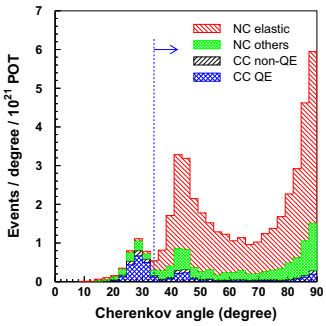

Figure 4: Expected Cherenkov angle distribution assuming 1×10^{21} POT and its breakdown by neutrino interaction mode. The dashed line shows the threshold below which events are rejected.

The multi-peak cut rejects events which have a subevent occurring 1 to 20 μs before the candidate event. More technically, the event's hit PMTs are ordered in time after applying a time-of-flight correction and the maximum number of hit PMTs within a sliding 30 ns time window (N30) is calculated. If N30 is above 25, the candidate event is rejected since the timing peak is likely to be a parent muon of the candidate event. That is, the candidate event is likely a decay electron from that muon.

A Cherenkov opening angle cut is applied as follows: the opening angle is estimated by histogramming the angles defined by all possible combinations of three hit PMTs. The histogram is then divided into 100 angle bins and peaks are located by finding successive seven bins combinations with the largest number of entries. The middle of the seven bins is taken to be the Cherenkov angle of the event. Figure 4 shows the expected Cherenkov angle distribution and its breakdown by neutrino interaction mode. The leftmost peak with $\theta_C < 34^\circ$ is mostly muons that come from CC and NC non-elastic interactions that remain in the signal energy region due to their low momenta. Since the NCE component (white) is low in the region $\theta_C < 34^\circ$, all events with $\theta_C < 34^\circ$ are removed from the data (the threshold is shown by the dotted line and arrow). Electrons from a single γ-ray have a Cherenkov angle of $\theta_C \sim 42^\circ$ while in the rightmost peak around 90° most events lack on a clear Cherenkov ring pattern and are likely multi-ring events, where each ring corresponds to a secondary γ-ray emitted from an excited ^{16}O in a random direction.

3.2.1 Calculation of the relative neutrino event timing to the bunch timing

The relative timing of the neutrino interaction to a spill's leading edge (ΔT_0) is roughly calculated combining the neutrino time-of-flight from J-PARC to SK and the hardware timing offsets in the both places. Then ΔT_0 is corrected projecting the reconstructed vertex onto the T2K beam direction so that we can compare all events timing at the center of the SK coordinate. Furthermore, ΔT_0 is again corrected for photon propagation in the SK tank. With knowledge of the GPS timing of the spill leading edge, the timing of hit PMTs, and the time of flight difference between hit PMTs and the reconstructed vertex, we can acquire the GPS time when the neutrino passes through the plane containing the SK origin perpendicular to the beam direction. A similar estimation of the timing of neutrino interaction is also done in a separate analysis, the fully-contained (FC) analysis, which uses several hundred MeV neutrino events. Here we use only the 200 ns (the GPS accuracy) before and after the 581 ns interval bunch center positions fitted by the FC analysis to select the final sample.

3.3 Reduction results

After all cuts, 21 events remain in the RUN-I/II data sample. In Figure 5, the energy distributions of the final sample is overlaid with the POT-normalized MC expectation. In the distribution the data and MC are in good agreement within statistical fluctuations.

The comparison of the event timing distributions between the final sample in this analysis and the bunch center positions fitted by those of the fully contained analysis events is shown in Figure 6. All ΔT_0 agree with the bunch center positions within the precision of the GPS timing.

We have also performed a Kolmogorov-Smirnov (KS) test for the event rates in RUN-I and II. The maximum vertical difference D between the observation and the ideal cumulative event distribution was 0.484 for RUN-I and 0.173 for RUN-II after normalization by each final data sample. This corresponds to KS probabilities of 30.6 % and 68.6 %, respectively. These probabilities are acceptable as statistical fluctuations.

In Table 2 we summarize the number of remaining events and the expectation from the T2K MC. Since the systematic

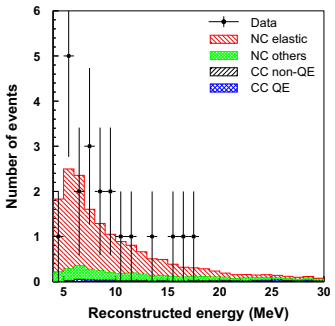

Figure 5: Comparison of energy distribution of the final data sample and the POT-normalized MC.

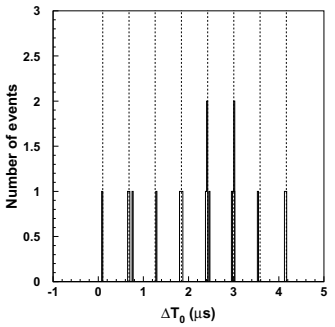

Figure 6: ΔT_0 distribution of all events in the RUN-I/II final sample during compared to the bunch center positions as fitted by the fully contained events analysis (eight dashed vertical lines).

errors are currently under estimation, only the statistical errors are shown. Data are consistent with the MC.

4 Summary

We searched for nuclear de-excitation γ-rays induced by neutrino-nucleon NCE interactions at SK in the T2K data. In RUN I/II (amounting to 1.43×10^{20}POT), 21 events remain and their ΔT_0 distribution is consistent with the bunch timing fitted by the FC analysis. The number of final candidate events is also consistent with the MC expectation. After systematic errors are estimated accurately, the present result will be used to estimate the extent of low energy backgrounds in searches for SRN and GUT monopoles at SK.

NC elastic	13.9 ± 0.1 (stat)
NC others	3.15 ± 0.05 (stat)
$\nu_\mu + \bar{\nu}_\mu$ CC QE	0.63 ± 0.02 (stat)
$\nu_\mu + \bar{\nu}_\mu$ CC non-QE	0.24 ± 0.01 (stat)
$\nu_e + \bar{\nu}_e$ CC	< 0.01
Beam unrelated events	3.3 ± 0.1 (stat)
Expectation (Total)	21.2 ± 0.2 (stat)
Observation	21 ± 5 (stat)

Table 2: Comparison of the final event sample for the observation and expectation. Since the systematic errors are under estimation, only the statistical error is shown.

References

[1] "Supernova Relic Neutrino Studies at Super-Kamiokande", K. Bays et al., Proc. ICRC **31**, 0822, 2009

[2] "Search for GUT monopoles at Super-Kamiokande", K. Ueno et al., Proc. ICRC **31**, 0670, 2009

[3] "The T2K experiment", K. Abe et al. (T2K Collaboration), (2011), accepted for publication in Nucl. Instrum. Methods, article in press, doi: 10.1016/j.nima.2011.06.067, arXiv:1106.1238 [physics.ins-det].

Observation of Atmospheric Neutrino-induced Cascades in IceCube-DeepCore

THE ICECUBE COLLABORATION[1]
[1]*See special section of these proceedings*

Abstract: Atmospheric neutrino-induced cascades are observed in the 79-string IceCube detector with the DeepCore extension. Using 23 days of data, a high statistics sample shows an excess of cascades at 8.2 sigma, and with tighter cuts 74 events are observed of which 62 % are predicted to be cascades. A full-year analysis is underway and a significant detection of atmospheric electron neutrinos is expected.

Corresponding authors: Chang Hyon Ha[2] (*cuh136@phys.psu.edu*), D. Jason Koskinen[2] (*koskinen@psu.edu*)
[2]*Dept. of Physics, Pennsylvania State University, University Park, PA 16802, USA* DOI: 10.7529/ICRC2011/V04/0324

Keywords: DeepCore; IceCube; neutrino

1 Introduction

The main mission of the DeepCore extension to IceCube is to observe neutrinos at energies as low as 10 GeV [1]. At these energies there are valuable science topics such as neutrino oscillations [2] and neutrinos from low mass WIMP dark matter annihilation [3]. In order to detect these neutrinos, DeepCore uses denser module spacing, upgraded photomultiplier tubes (PMTs), and deployment in the clearest ice along with a lower trigger threshold than the surrounding IceCube detector. Full information about the DeepCore infill can be found here [4]. Figure 1 shows a schematic of IceCube with DeepCore.

In this paper, we discuss the performance of the first year DeepCore with 79 strings of IceCube installed (IC-79). In this configuration the DeepCore sub-array includes 6 densely instrumented strings optimized for low energies plus the 7 adjacent standard strings. Finally, we present preliminary results on the first observation of atmospheric neutrino-induced cascades in IceCube. A test set (7 % of full data) using 23 days is used in this work, and prospects for a full year are shown in Section 3.3.

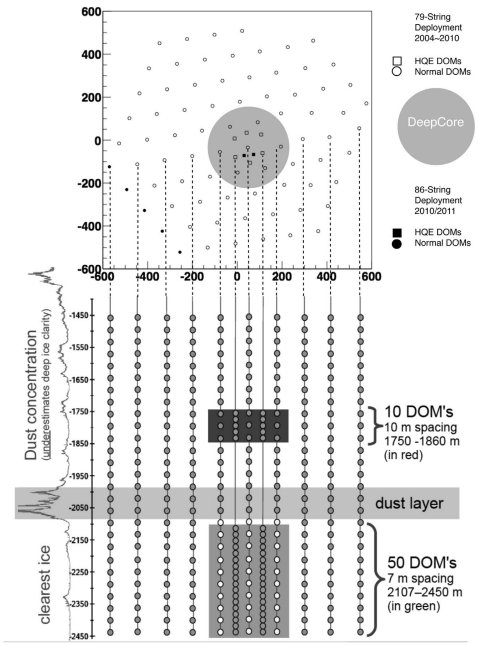

Figure 1: Schematic top and side views of IceCube in its 79-string configuration. The DeepCore infill array and the relative dust concentration are also shown.

2 Performance

The IC-79 detector finished a year-long data-taking cycle in May 2011 and these data have been processed and reconstructed.

Full PMT waveforms are read out from digital optical modules (DOMs) in hard local coincidence (HLC) which requires hits in a DOM and at least one nearest neighbor or next nearest-neighbor DOM must register a hit in a time span of $\pm$1000 ns. IceCube also records soft local coincidence hits (SLC), for which no neighboring hits are re-

quired [5]. Although the DOM noise rate is a factor of 50 higher in SLC mode than in HLC mode, with current software cleaning algorithms, SLC hits from physics interactions can be identified with over 90 % purity. This provides an advantage at low energies where the fraction of SLC hits is significant, because including the SLC hits improves reconstruction, background rejection, and particle identification.

A low trigger threshold (SMT3) is applied to all DOMs in the fiducial region (shaded area below the dust layer in Figure 1) by requiring 3 or more HLC hits within a 2500 ns time window. Additionally, the high quantum efficiency PMTs, with a 35 % increase in light collection with respect to regular IceCube PMTs, help trigger on neutrinos with energies as low as 10 GeV.

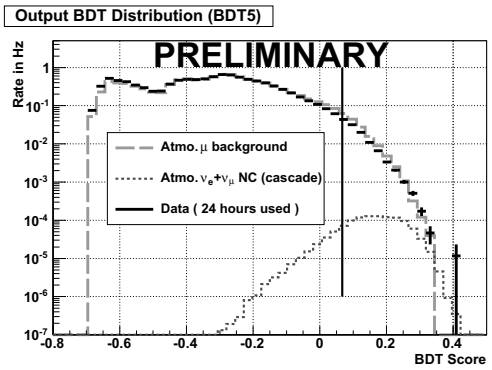

Figure 2: Output BDT5 Distribution based on the five variables. Cut on BDT5 >0.067 is indicated with vertical line.

3 Observation of Atmospheric Cascades

Atmospheric neutrinos are the products of the interaction or decay of pions and kaons produced when cosmic ray primaries interact with nucleons in the upper atmosphere. Charged-current (CC) electron and tau neutrino interactions, and neutral-current (NC) neutrino interactions of any flavor, produce cascades that are approximately spherical. However, IceCube can not distinguish between a CC cascade and an NC cascade at considered energies. While atmospheric muon neutrinos have been observed in large quantities by IceCube [6] atmospheric cascades have a substantially lower flux and have not been identified in previous IceCube analyses. For current cascade searches above 1 TeV, there are on-going analyses with the 40 string IceCube detector [7, 8].

3.1 Background

Before seeing neutrinos in DeepCore, one must remove the cosmic ray muon background. Furthermore, the poor directionality in cascades as compared to tracks makes it difficult to use the Earth as a shield from the cosmic ray muon background as is done in conventional ν_μ^{CC} detection [6]. The signal is therefore required to be contained in DeepCore, and veto techniques are applied to remove about six orders of magnitude of background events while retaining reasonable signal efficiency for atmospheric neutrino-induced cascades in the fiducial volume.

3.2 Event Selection

IC-79 was operational from June 2010 to May 2011 with over 90 % up-time for physics analysis. The DeepCore SMT3 trigger fired at a rate of 180 Hz, which was reduced to 17 Hz using an on-line filter run at the South Pole. In the DeepCore on-line filter, an estimate of a neutrino interaction vertex and its time is obtained by calculating the center of gravity (COG) of all HLC hits in the fiducial region. An event is rejected when hits in the veto region have times consistent with an incoming muon. A 90 % cosmic ray muon background rejection is achieved with respect to the trigger while keeping $>$ 99 % atmospheric neutrinos that interact in the fiducial volume. Noise cleaning algorithms remove noise hits which are not correlated in space and time with other hits. Then, events with at least 8 total remaining hits and at least 4 hits in the fiducial region are selected.

In order to attain a manageable data volume for time-consuming reconstructions, the first background rejection is achieved by an initial selection with a Boosted Decision Tree (BDT) [9]. The "BDT5" has 5 simple observables which quantify the event topology in the detector. These are constructed from the position and shape of the hits in the detector, and their time and charges. Figure 2 shows the output distribution and the reduction cut is made at 0.067. After the BDT5, the data rate is reduced to 0.1 Hz and atmospheric ν_e rate is predicted as 6.3×10^{-4} Hz, corresponding to 63 % retention with respect to the trigger.

This reduced data set was then processed with iterative likelihood reconstructions taking into account detailed Cherenkov light propagation in the ice [10]. Hits falling outside a time window [-3000 ns, +2000 ns] with respect to the trigger, or outside of 150 m radius of a neighboring hit within a 750 ns time window are removed. Then, with the cleaned hits, after demanding 8 or more hits in the fiducial region within a 1000 ns sliding window, another BDT is formed with 7 input parameters (BDT7). The first two variables measure the locations of the earliest hits in terms of radial and vertical coordinates to select contained events. The next three variables separate cascade-like events from muon-like events; an event is split in half then charge deposition, COG, and particle speed are compared between the two separate halves. The final two compare a likelihood of a cascade hypothesis to that of a muon hypothesis. The top left plot of Figure 3 shows the output BDT7 distribution. A cut at $\mathrm{BDT7} > 0.22$ reduces the atmospheric muon background to 5.0×10^{-4} Hz by rejecting a factor of 200 more (3.6×10^5 cumulatively) background while retaining

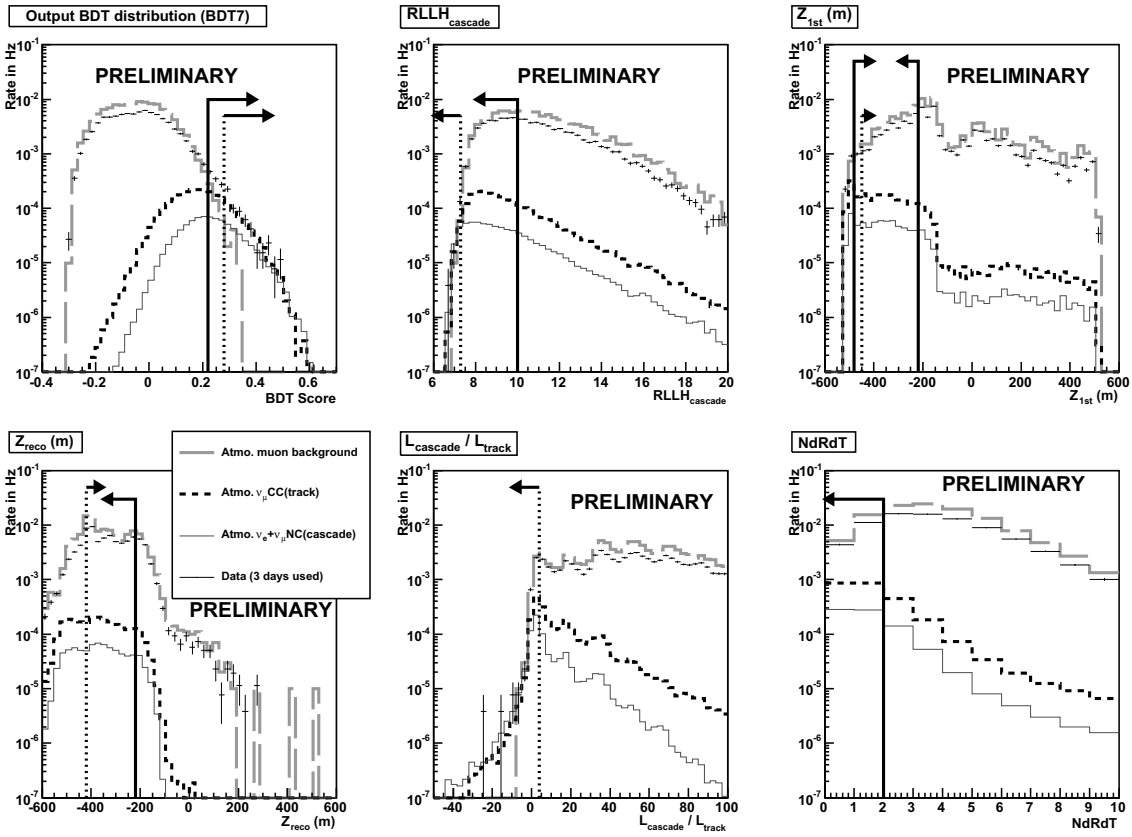

Figure 3: The output distribution of BDT7 in shown upper left corner and extra cuts to select two neutrino samples are listed as well. These plots are after BDT5 cut. Solid vertical lines indicate the final loose cut sample while the dotted vertical lines are for final hard cut sample. Arrows indicate events kept.

~ 40 % of the ν_e signal (2.6×10^{-4} Hz) compared to the previous BDT5 cut.

3.3 Results

Two sets of cuts on input variables to BDT7 were used for the final selection of neutrino-rich samples. The first aims for a high efficiency (Loose Cut) while the second aims for a higher purity (Hard Cut). Figure 3 shows two combinations of these cut options. The Loose Cut option is indicated in solid vertical lines. Two containment cuts $\mathrm{Z_{1st}}$ (upper right) and $\mathrm{Z_{reco}}$(lower left) based on the vertex depth measurements ensure that most signal events are well contained inside the DeepCore fiducial volume. The NdRdT (lower right) extends the on-line veto method by adding a travel speed window to catch only muon-produced light in the veto region and therefore removes residual muon background events. Finally, the cut $\mathrm{RLLH_{cascade}}$ (upper middle) selects events that fit a cascade hypothesis well, as measured by the log likelihood from a fit. With the Loose Cut options, the events observed are consistent with ν_μ^{CC}, ν_μ^{NC}, and ν_e interactions with only two cosmic ray muon events expected in 28 hours of simulation. 824 events are observed in 23 days of a test data with 590 total background event expectation (ν_μ^{CC} + μ) corresponding to a cascade excess of 8.2 sigma. Systematic errors are not included.

Signal simulation of atmospheric neutrinos predicted approximately 5,000 cascades and 9,400 ν_μ^{CC} events per year (three flavor oscillations included based on the parameters in [11]) as shown in Figure 4 with an estimated mean energy of 40 GeV. Unfortunately, events below 10 GeV are not accurately simulated in current neutrino generation and are not included in this work [12]. When considering oscillations of atmospheric neutrinos the data rate of ν_μ^{CC} events is reduced by 20 % with the Loose Cut selection. The effect of oscillations on ν_e and ν_x^{NC} ($x = \mu, e, \tau$) is marginal compared to the data rate indicated as a dotted line in Figure 4. The ν_τ oscillation from ν_x in these energies is not yet included and under active development with a new simulation package, GENIE [13]. Since there is no distinction among ν_e, ν_τ, and ν_x^{NC} in the IceCube detector at these energies, a small amount of the 20 % disappeared ν_μ events may be re-introduced as cascades if they oscillate to ν_τ.

The Hard Cut selection for higher purity is shown with dotted vertical lines on the plots in Figure 3. Compared to the Loose Cut option, these cuts are stronger and mainly focused on rejecting ν_μ^{CC} events. The containment cuts are

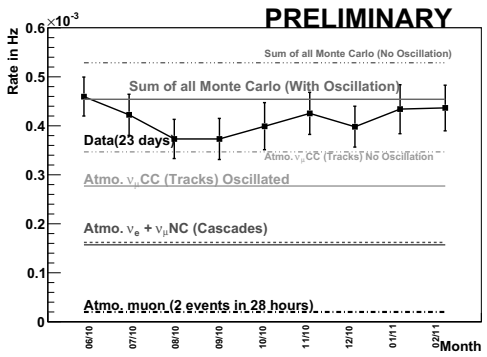

Figure 4: Loose Cut result. The event rate in hertz as function of months is shown. The squares are 23 days of test data while simulations are indicated with the various lines. Dotted lines are the rates without ν_μ oscillations and horizontal solid lines are with oscillation. The data rate shows an excess over the ν_μ prediction and can be explained with two contributions; oscillation and cascades. Here, the signal predictions are based on Barr *et al.* [14]

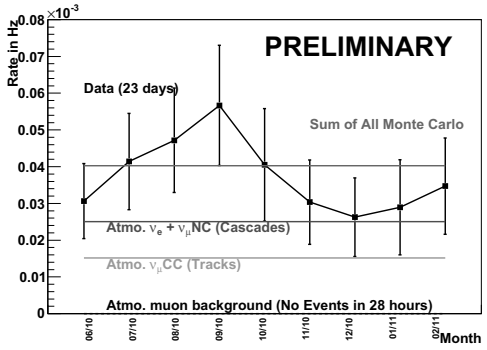

Figure 5: Hard Cut result. The sum of all Monte Carlo is consistent with 23 days of data rate. The cascades are expected to contribute 62 % and the tracks are expected to be 38 %. No atmospheric muon background event remain in 28 hours. The oscillation effect is less than 3 % due to higher energies of cascades and not included here.

enforced to a volume smaller than the fiducial region to identify an outgoing track from a $\nu_\mu^{\rm CC}$ interaction. With 23 days of test data, we observe 74 total events (50 cascades and 30 tracks are expected from simulation), showing a 5 sigma excess of cascades. A sample of about 790 cascades per year with a background of about 480 $\nu_\mu^{\rm CC}$ events are expected from Figure 5. The remaining $\nu_\mu^{\rm CC}$ events have short muons with a median track length of 80 m where the muon tracks are not easily visible due to detector granularity. Half of the cascades are predicted to be ν_e events and the other half are $\nu_\mu^{\rm NC}$ events. This selection favors higher energy cascades and the mean cascade energy increases to

	Loose Cut			
	$\rm N^{obs}$	$\rm C^{sig}$ ($\rm C^{bg}$)	σ	$\rm N^{sig}$ ($\rm N^{bg}$)
23 days	824	312 (590)	8.2	208 (694)
1 year	-	4951 (9364)	-	3285 (11030)
	Hard Cut			
	$\rm N^{obs}$	$\rm C^{sig}$ ($\rm C^{bg}$)		$\rm N^{sig}$ ($\rm N^{bg}$)
23 days	74	50 (30)	5.0	25 (55)
1 year	-	791 (479)	-	404 (866)

Table 1: The number of events are shown with two final selections. $\rm N^{obs}$ means observed events in real data. $\rm C^{sig}$ and $\rm C^{bg}$ refer predictions of the cascade signal and its background respectively. $\rm N^{sig}$ and $\rm N^{bg}$ refer predictions of the electron neutrino signal and its background respectively.

200 GeV, so that oscillation of $\nu_\mu \rightarrow \nu_x$ has a small (< 3 %) effect. The atmospheric muon simulation predicts zero events in 28 hours. A seasonal effect in rates will be studied more carefully with the full data.

3.4 Conclusion

In conclusion, we observe atmospheric neutrino-induced cascade events with 23 days of test data for the first time with IceCube 79 string detector and a highly significant detection of atmospheric electron neutrinos is expected with forthcoming full-year analysis. The preliminary numbers are summarized in Table 1. Possible sources of systematic errors include ice modeling, detection efficiency of DOMs, neutrino-nucleon cross-sections, and atmospheric neutrino flux normalizations. Those uncertainties are under evaluation.

References

[1] IceCube Collaboration R. Abbasi *et al.* , arXiv:0907.2263
[2] IceCube Collaboration, paper 0329, these proceedings
[3] IceCube Collaboration, paper 0292, these proceedings
[4] IceCube Collaboration D. J. Koskinen, WSPC-Proceedings WIN11, 2011
[5] IceCube Collaboration R. Abbasi *et al.* , Nucl. Instrum. Meth Phys. Res. A 601, 294 (2009)
[6] IceCube Collaboration R. Abbasi *et al.* , Physical Review D83, 2011
[7] IceCube Collaboration, paper 1097, these proceedings
[8] IceCube Collaboration, paper 0759, these proceedings
[9] H. Voss *et al.* Proc. Sci. ACAT (2007) 040
[10] AMANDA Collaboration J.Ahrens *et al.* NIM A524 (2004), 169-194
[11] M.C. Gonzalez-Garcia *et al.* JHEP 04 (2010) 056
[12] IceCube Collaboration R. Abbasi *et al.* , in progress
[13] C. Andreopoulos *et al.* , NIM A614 (2010)
[14] G. D. Barr *et al.* , Phys. Rev. D 70, 023006 (2004)

32ND INTERNATIONAL COSMIC RAY CONFERENCE, BEIJING 2011

Atmospheric neutrino oscillations with DeepCore

THE ICECUBE COLLABORATION[1]
[1]*See special section in these proceedings*

Abstract: IceCube DeepCore can study atmospheric neutrino oscillations through a combination of its low energy reach, as low as about 10 GeV, and its unprecedented statistical sample, of about 150,000 triggered atmospheric muon neutrinos per year. With the diameter of the earth as a baseline, the muon neutrino disappearance minimum and tau neutrino appearance maximum are expected at about 25 GeV, which is considerably lower energy than typical IceCube neutrino events, but higher than the energies at which accelerator-based experiments have detected oscillations. We present here the status of the newly developed low energy reconstruction algorithms, the expected experimental signatures, and the proposed approach for such neutrino oscillation measurements.

Corresponding authors: Sebastian Euler[2] (seuler@icecube.wisc.edu), Laura Gladstone[3](gladstone@icecube.wisc.edu), Jason Koskinen[4](koskinen@psu.edu), Donglian Xu[5](dxu@crimson.ua.edu) DOI: 10.7529/ICRC2011/V04/0329

[2]*III. Physikalisches Institut, RWTH Aachen University, D-52056 Aachen, Germany*
[3]*Dept. of Physics, University of Wisconsin, Madison, WI 53706, USA*
[4]*Dept. of Physics, Pennsylvania State University, University Park, PA 16802, USA*
[5]*Dept. of Physics and Astronomy, University of Alabama, Tuscaloosa, AL 35487, USA*

Keywords: IceCube DeepCore, ν_μ disappearance, ν_τ appearance

1 IceCube DeepCore

IceCube is a cubic-kilometer neutrino observatory located at the geographic South Pole. IceCube construction began in 2004 and was completed in December 2010. The complete detector consists of 86 strings deployed into the glacial ice, each of which consists of 60 Digital Optical Modules (DOMs) located between depths of 1450 m and 2450 m. Seventy-eight strings are arranged on a hexagonal grid with an average 125 m horizontal spacing and 17 m vertical DOM spacing. The remaining 8 strings are more closely spaced in the center of the detector, with horizontal distances of 40 - 70 m and vertical DOM spacing of 7 m. The 8 inner densely instrumented strings, optimized for low energies, together with the surrounding 12 IceCube standard strings, form the DeepCore inner detector (Fig. 1). These 8 inner strings have 10 DOMs located between 1750 m and 1850 m in depth and 50 DOMs located between 2100 m and 2450 m. The ice at depths between 1970 m and 2100 m, formed about 65,000 years ago [1], has a relatively short absorption length, and is known as the "dust layer". The 10 DOMs on each DeepCore string deployed above the dust layer help reject cosmic ray muons which are the major background to atmospheric neutrino studies. The ice below 2100 m has a scattering length about twice that of the ice in the upper part of the IceCube detector [2]. The lower 50 DeepCore DOMs are deployed in this very clear ice. DeepCore DOMs contain high quantum efficiency photomultipliers (HQE PMTs [3]) which add $\sim$ 35% increase in efficiency compared to the standard IceCube DOMs. With denser string and DOM spacing, clearer ice, as well as higher efficiency PMTs, DeepCore is optimized for low energy neutrino physics [4]. Fig. 2 shows the predicted ν_μ and ν_e effective areas at both trigger and online veto levels. Below 100 GeV the addition of DeepCore increases the effective area of IceCube by more than an order of magnitude.

2 Neutrino Oscillation Physics in DeepCore

The IceCube DeepCore sub-array has opened a new window on atmospheric neutrino oscillation physics with its low energy reach to about 10 GeV. The oscillation measurement is also made feasible by DeepCore's location at the bottom center of IceCube, which allows the surrounding IceCube strings to act as an active veto against cosmic ray muons, the primary background to atmospheric neutrino measurements. A muon background rejection of 8×10^{-3} for the overall IceCube trigger ($\sim$ 2000 Hz) is achieved by applying a veto algorithm which rejects events with particle speed (defined as the speed of a particle trav-

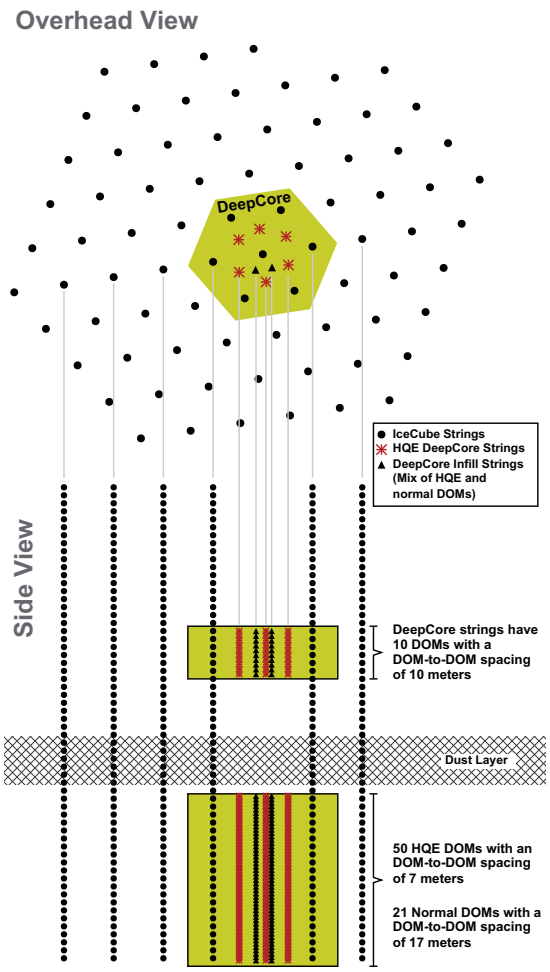

Figure 1: Overhead and side views of the IceCube DeepCore detector. The shaded hexagon in the overhead view shows the area covered by the DeepCore sub-array. On the side view, the hatched region shows the dust layer, and shaded boxes indicate the location of the DeepCore DOMs, 10 in each string above the dust layer, and 50 in each string below the dust layer.

eling from the hit in the surrounding region to the center of gravity (COG) in DeepCore) between 0.25 m/ns and 0.4 m/ns. The scheme of this veto algorithm is demonstrated in Fig. 3. With further expected improvements in the veto and event reconstruction algorithms, DeepCore expects to achieve a cosmic-ray muon rejection factor of 10^6 or better [6]. Specific methods to investigate the oscillation phenomenon will be discussed in detail in the following subsections.

2.1 ν_μ Disappearance

The earliest atmospheric neutrino oscillation evidence can be traced back to the zenith angle dependence of the double ratio measurement at few GeV energies in Super-Kamiokande [7]. IceCube DeepCore, with its approximately 13 MT fiducial volume, is capable of making atmospheric neutrino oscillation measurements above 10 GeV, an energy region that has not been well explored by previous atmospheric neutrino oscillation experiments. From Fig. 4, a significant deficit in the neutrino flux at 25 GeV is expected from the $\nu_\mu \rightarrow \nu_\mu$ survival probability. In Fig. 5 this disappearance signature is shown for one year of simulated DeepCore data. The disappearance signal assumes that the path length is the diameter of the Earth, and therefore the ideal neutrino sample should contain only up-going neutrino-induced muons. An intrinsic difficulty for all experiments in identifying perfectly up-going neutrino-induced muon tracks is that the average opening angle, defined as the angle between the final state lepton direction and the incoming neutrino direction, increases with decreasing energy. The uncertainty in the opening angle can be approximated as $\Delta\Phi \simeq 30^\circ \times \sqrt{(1GeV)/E_{\nu_\mu}}$. This effect will smear the oscillation signature in the neutrino flux at lower energies. However, as shown in Fig. 5, DeepCore simulations indicate the potential to measure oscillations even if "up-going" tracks are defined to include measured directions over the wide range of values, $-1.0 < \cos(\theta) < -0.6$ [4].

2.2 ν_τ Appearance

The OPERA neutrino detector, located at the underground Gran Sasso Laboratory (LNGS), was designed for direct observation of $\nu_\mu \rightarrow \nu_\tau$ appearance. OPERA announced a first tau lepton candidate from ν_μ oscillation, and continues operation to achieve a statistically significant observation [8, 9]. DeepCore is currently acquiring data and will collect the world's largest inclusive sample of ν_τ. From Fig. 4, the region where ν_μ flux reaches its minimum is the same region where ν_τ flux shows its corresponding maximum from $\nu_\mu \rightarrow \nu_\tau$ oscillation. ν_τ that interact in DeepCore will produce an electromagnetic or hadronic shower, or "cascade". Events with short tracks which are beyond DeepCore's ability to separate from cascades, are an irreducible background to cascade-like events. Therefore, cascade-like events include: 1) neutral current (NC) events from all three neutrino flavors (e, μ, τ), 2) ν_μ charged current (CC) events with short tracks ($< \sim$ O (10) m), 3) ν_τ charged current events with τ-leptons decaying into electrons or hadrons, 4) ν_τ charged current events with τ-leptons decaying into muons whose track length is less than O (10) m. DeepCore should detect an excess of cascade-like events due to oscillation compared to the number of cascade events expected without oscillation. DeepCore may also be able to detect a distortion in the energy spectrum of cascade events due to ν_τ appearance. The simulated excess of cascade-like events above $\sim$ 25 GeV in DeepCore is shown in Fig. 6. The deficit of oscillated cascade-like events compared to unoscillated below $\sim$ 25 GeV is due to the rapid oscillation in the ν_μ and ν_τ survival probabilities shown in Fig. 4. Within the rapid oscillation regime,

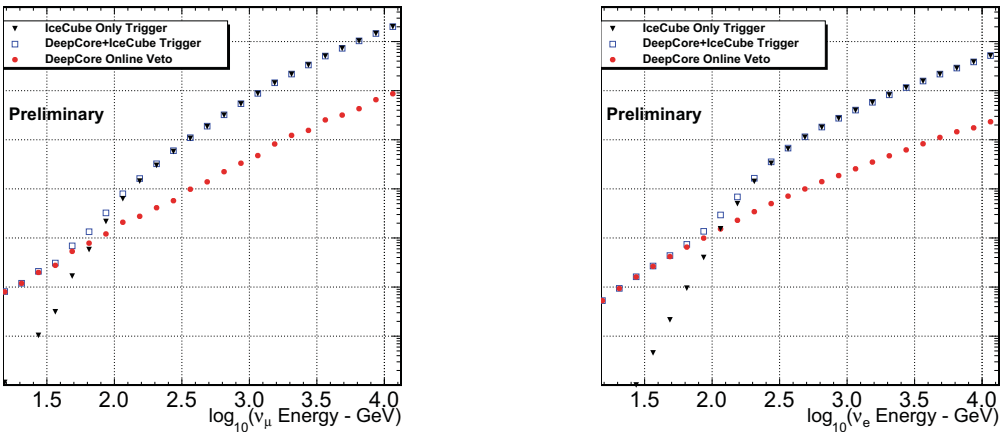

Figure 2: Effective areas for muon neutrinos (left) and electron neutrinos (right). Triangles: IceCube standard strings only, trigger level. Squares: IceCube including DeepCore strings, trigger level. Circles: IceCube DeepCore after applying the online veto.

a large fraction of ν_μ charged current (CC) events oscillate into ν_τ events. The produced tau lepton from those ν_τ CC events always decay to at least one neutrino, reducing the visible energy and possibly resulting in an event below the detector energy threshold. However, without oscillation, these low energy ν_μ CC events would be classified as cascade-like due to their short tracks. This significant deficit between the oscillated and unoscillated cascade-like event rates near the detector threshold may offer an opportunity to measure ν_μ disappearance in the cascade channel. The feasibility of measuring the excess of cascade-like events above 25 GeV, as well as systematic effects due to the ice properties, DOM efficiency and other factors, are under study.

2.3 Reconstruction Algorithms

Several reconstruction algorithms are being developed specifically for low-energy analysis in DeepCore. With shorter muon track lengths, low-energy events include a higher proportion of "starting" and fully contained muon events as opposed to through-going muons. The oscillation analysis also depends on separating track-like ν_μ charged current events from cascade-like all-flavor neutral current and ν_e and ν_τ charged current events. Fully-contained-muon reconstruction algorithms calculate the length of the track from the reconstructed beginning and end points of the track. Fig. 7 shows the difference between reconstructed and true track length from simulated data reconstructed with one such algorithm. The starting muon event signature consists of a cascade associated with the charged-current muon neutrino interaction and a track associated with the resulting muon. Reconstructions of such events therefore include the contributions of the cascade and the track. An algorithm under development for seeding these reconstruc-

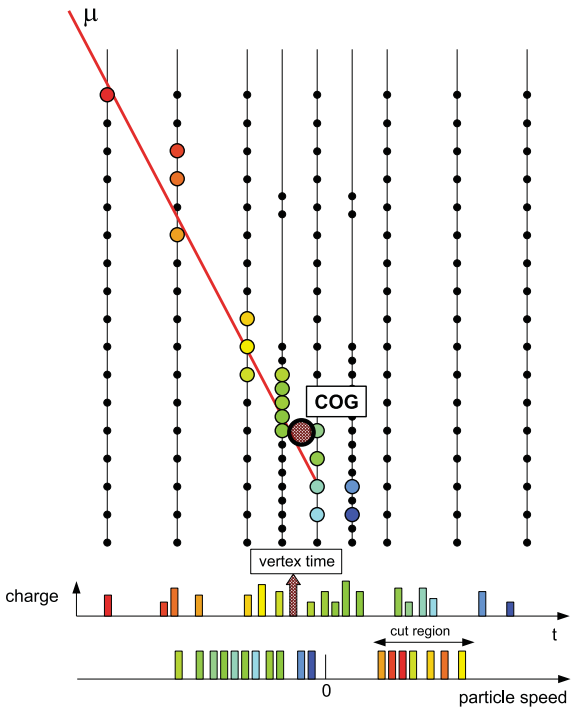

Figure 3: Scheme of veto algorithm based on simulation. Upper part demonstrates a down-going muon hitting the DOMs with hit sequence varying from earliest in red to latest in blue. The big black circle exhibits the COG of the hits in DeepCore. Bottom part includes the vertex time and particle speed per hit. The "cut region" illustrates a cut based on the particle speeds which are consistent with down-going muons.

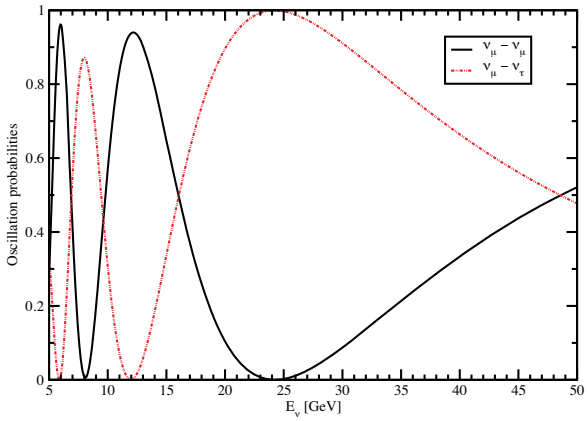

Figure 4: Oscillation probabilities for ν_μ with $sin^2 2\theta_{13} = 0.1$, $\Delta m^2_{31} = 2.5 \times 10^{-3} eV^2$, $L = 12757$ km [5].

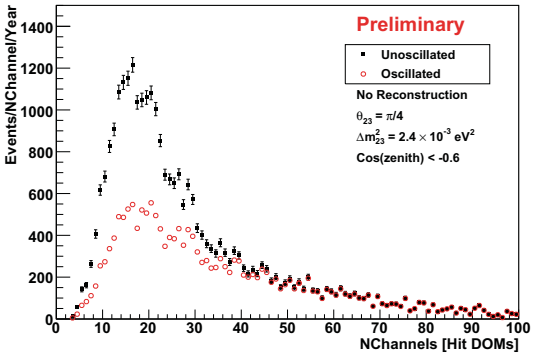

Figure 5: Simulated ν_μ disappearance with one year DeepCore data. Filled squares: Distribution of number of hit DOMs (NChannel) assuming no oscillation. Empty circles: Distribution of number of hit DOMs (NChannel) with oscillation.

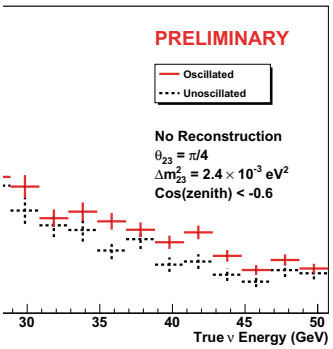

Figure 6: Simulated ν_τ appearance with one year DeepCore data. Dotted lines: Distribution of true neutrino energy assuming no oscillation. Solid lines: Distribution of true neutrino energy with oscillation.

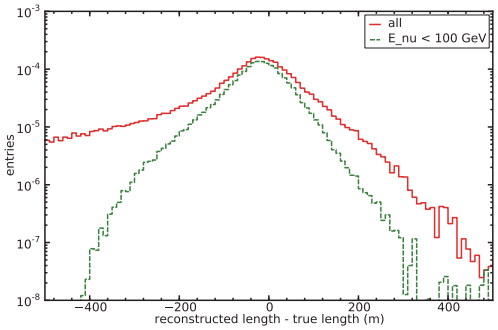

Figure 7: Difference between reconstructed track length and Monte Carlo simulation true track length.

tions and thereby separating tracks from pure cascades is based on a Fermat Surface [10].

3 Conclusions

Simulations suggest that IceCube DeepCore may have the capability to measure atmospheric neutrino oscillations in an energy range which complements existing accelerator measurements. DeepCore construction is complete and the detector is already collecting data. New reconstruction algorithms suited to low energy measurements will enable IceCube to fully exploit the physics capabilities of DeepCore.

References

[1] P. B. Price, K. Woschnagg, and D. Chirkin, Geophys. Res. Lett. **27**, 2129-2132 (2000)

[2] A. Achterberg et al. [IceCube Collaboration], Astroparticle Physics, **Volume 26**, Issue 3, October 2006, Pages 155-173

[3] R. Abbasi et al., Nuclear Instruments and Methods **A618** (2010) 139-152, 1-21 June 2010

[4] Darren Grant, D. Jason Koskinen, and Carsten Rott [IceCube Collaboration], Proceedings of the 31^{st} ICRC, LODZ, POLAND, 2009

[5] O. Mena, I. Mocioiu and S. Razzaque, Phys. Rev. D **78**, 093003 (2008)

[6] Olaf Schulz, Sebastian Euler, and Darren Grant [IceCube Collaboration], Proceedings of the 31^{st} ICRC, LODZ, POLAND, 2009

[7] Y. Fukuda et al. [Super-Kamiokande Collaboration], Phys. Rev. Lett. **81**, 1562 (1998)

[8] R. Acquafredda et al. [OPERA Collaboration], New J. Phys. **8**, 303 (2006)

[9] N. Agafonova et al. [OPERA Collaboration], Phys. Lett. **B691** 138-145 (2010)

[10] J. G. Learned, [arXiv 0902.4009 (2009)]

32ND INTERNATIONAL COSMIC RAY CONFERENCE, BEIJING 2011

Neutron tagging and its physics application in Super-Kamiokande-IV

HAIBING ZHANG[1] FOR THE SUPER-KAMIOKANDE COLLABORATION
Department of engineering physics, Tsinghua University, Beijing, China
zhanghb02@mails.tsinghua.edu.cn
DOI: 10.7529/ICRC2011/V04/0353

Abstract: With the electronics upgrade in 2008, the fourth phase of Super-Kamiokande (SK) is now capable of detecting thermal neutrons from neutrino interactions with $\sim$ 20% efficiency. Observation of neutrons produced in atmospheric neutrino interactions is presented. Preliminary results of a background study for the supernova relic neutrino (SRN) detection are shown. Prospects of future SRN searches and possible improvement of background rejection for proton decay searches with neutron tagging in SK-IV and beyond are also discussed.

Keywords: Neutron tagging, water Cherenkov detector, supernova relic neutrino, proton decay

1 Introduction

Tagging neutrons produced in neutrino interactions with water can extend the physics scope of water Cherenkov detectors (WCD). For example, a delayed-coincidence detection of positron and neutron capture offers a powerful way to identify low energy anti-neutrino via the inverse beta decay reaction (IBD) $\bar{\nu}_e + p \rightarrow e^+ + n$. This is of crucial importance to allow the detection of SRN. Neutron tagging could also improve proton decay search sensitivity by rejecting potential atmospheric neutrino backgrounds accompanied by neutrons.

Two independent methods were proposed to add neutron tagging capability for WCD's. The first approach [1] involves doping water with water soluble compound of gadolinium, neutron capture on which yields gamma cascades with total energy $\sim$8 MeV. These relatively high energy γ-rays should be readily seen by a WCD such as SK whose trigger threshold is typically $\sim$5 MeV. In the second approach [2], a new trigger logic is introduced to force the DAQ system to take 500 μs data without threshold after each primary event (e.g. e^+ in IBD) above the so-called super-high-energy (SHE) trigger ($\sim$10 MeV). A search of 2.2 MeV γ emitted from neutron capture on free proton is then performed off-line exploiting the spatial and temporal correlation between neutron capture and the primary event. After the successful demonstration of detecting neutron capture in SK-III [3], the forced trigger scheme has been incorporated into the new SK DAQ system which was upgraded in 2008.

2 Neutron tagging in pure water

The 2.2 MeV γ generates only $\sim$7 PMT hits on average in SK and in general can not be precisely reconstructed on its own due to PMT noise interference. But the neutron produced in inverse beta decay is typically of low energy, which is quickly thermalized and captured with a free mean path $\sim$50 cm. So to a good approximation, the 2.2 MeV γ shares a common vertex with the primary event, which is used to do a time-of-flight (TOF) correction. A 10 ns sliding window is then applied to search candidate timing peaks above PMT noise. Backgrounds include PMT noise, radioactivity from surrounding rock and radon contamination in water, etc. In this study, the 2.2 MeV γ detection efficiency is evaluated using Monte Carlo (MC), while the background probability is estimated using SK-IV real data.

2.1 Selection criteria for neutron capture events

To identify the 2.2 MeV γ from candidate timing peaks, the following criteria are used first:(1) Number of hits in the 10 ns window (N10) is greater than 7; (2) No major cluster hits (Ncluster), N10 $-$ Ncluster $>$ 5; (3) Less backward going hits (Nback), N10 $-$ Nback $>$ 6; (4) Less hits that have low hit probability (Nlow), N10 $-$ Nlow $>$ 4. After this stage of pre-selection, the signal efficiency and background probability are 20.8% and 3.9%, respectively.

A further reduction utilizes the likelihood ratio constructed from four discriminating variables: number of PMT hits around N10 peak in 300 ns widow (N300 - N10), root mean square (RMS) of PMT hit timings (T_{rms}), RMS of azimuth angle of hit vectors along the estimated direction (ϕ_{rms}), and mean angle between hit vectors and estimated direction (θ_{mean}), as shown in Fig. 1. Requiring the likelihood

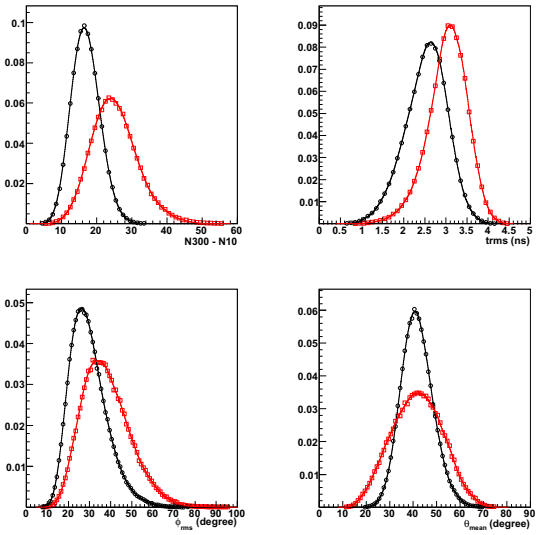

Figure 1: Normalized distributions of N300 − N10 (a), T_{rms} (b), ϕ_{rms} (c) and θ_{mean} (d). The points represent signal (circle) and background (square) histograms and the lines indicate corresponding PDF's.

ratio to be greater than 0.35, the background probability is brought down to 1%, while the signal efficiency is 19.3%.

2.2 Verifying neutron tagging efficiency using an Am/Be source

To verify neutron tagging efficiency given above, experimental tests were conducted with an Am/Be source embedded in a bismuth germanite (BGO) scintillator. The prompt and delayed event-pair is generated via: $\alpha + {}^{9}\mathrm{Be} \rightarrow {}^{12}\mathrm{C}^{*} + n$; ${}^{12}\mathrm{C}^{*} \rightarrow {}^{12}\mathrm{C} + \gamma$(prompt); $n + p \rightarrow d + \gamma$(delayed). The scintillation light induced by 4.43 MeV deexcitation γ serves as the primary event. Note that the reaction to the ground state of ^{12}C also exists, where no 4.43 MeV deexcitation γ is emitted. The experimental apparatus was deployed at the center of the tank, during which the trigger gate to catch 2.2 MeV γ was temporarily enlarged to 800 μs in order to obtain a complete neutron capture time spectrum. To estimate source related background (e.g. ground transition neutron), 10 Hz 800μs random trigger data was also taken.

The final N10 distribution after all cuts applied is shown in Fig. 2, where for Am/Be data all backgrounds are subtracted according to random trigger data. Signal efficiencies for MC and data are (19.2±0.1)% and (19.0±0.2)%, respectively. Data is in good agreement with MC. Fig. 3 shows the distribution of time difference (ΔT) between delayed neutron signal and prompt event. The neutron lifetime in pure water is measured to be $(201.8 \pm 4.7)\mu$s using a unbinned maximum likelihood fitting as shown in Fig. 3.

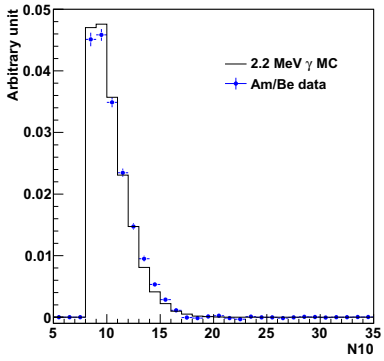

Figure 2: Comparision of N10 between Am/Be data and MC after all cuts applied.

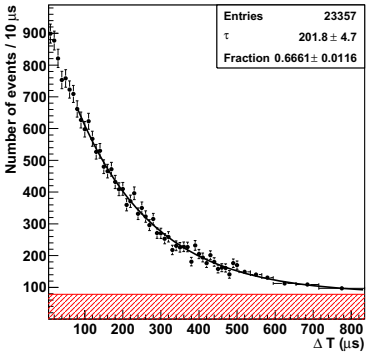

Figure 3: Distribution of ΔT. Shaded histogram indicates background.

3 Observation of neutrons in atmospheric neutrino data

In atmospheric neutrino events, neutrons can be produced in neutrino interactions (e.g. inverse beta decay) as well as secondary interactions from daughter products. A search of neutrons in fully-contained (FC) neutrino events is conducted using 740.2 live days of SK-IV atmospheric neutrino data. The final N10 after likelihood cut is shown in Fig. 4, where the fraction of accidental background is estimated from the known background probability (1%) and the rest are assumed to be neutron capture signal. The expected spectrum is reproduced by data fairly well. Fig. 5 shows the ΔT distribution together with the fitted neutron lifetime, which is consistent with the measurement using an Am/Be source. Both figures demonstrate, for the first time, a clear observation of neutrons produced in neutrino interactions in a water Cherenkov detector.

Fig. 6 shows neutron yield (number of neutrons in one event) as a function of visible energy of atmospheric neutrino events. It can be seen that above 100 MeV (visible energy), on average more than one neutron is produced per

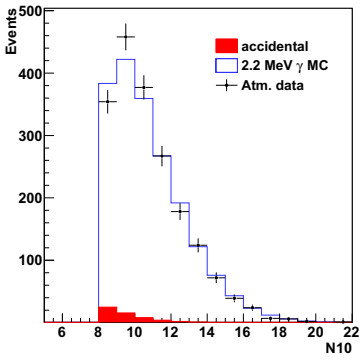

Figure 4: Final N10 of neutron candidates in atmospheric FC data.

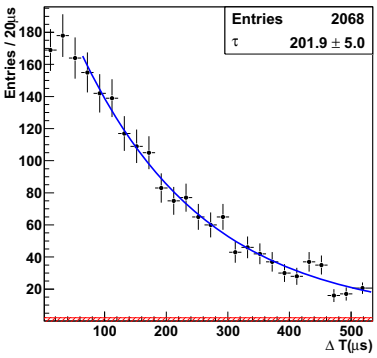

Figure 5: Distribution of ΔT of neutron candidates in atmospheric FC events. Shaded histogram show expected accidental background.

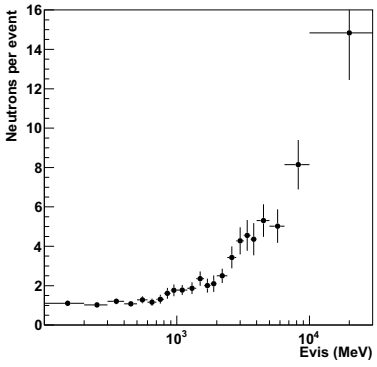

Figure 6: Efficiency corrected neutron yield as function of visible energy.

event. And in general the higher visible energy, the more neutrons are produced. The neutron multiplicity is shown in Fig. 7.

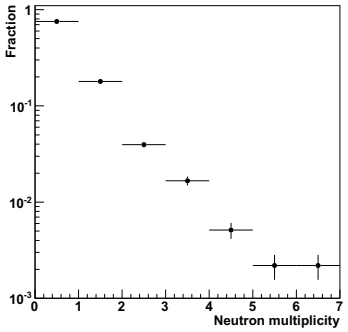

Figure 7: Neutron multiplicity per event.

4 Background study for SRN detection

SRN is most likely to be detected in SK via the inverse beta decay reaction $\bar{\nu}_e + p \rightarrow e^+ + n$. Current SK sensitivity is limited by cosmic-ray muon induced spallation products (below 16 MeV) and decay electrons from sub-Cherenkov muons produced by atmospheric neutrinos (above 16 MeV). Tagging the neutron in inverse beta decay will improve SK's sensitivity by rejecting most decay electrons, as well as opening up lower energy window. Study of SK-IV data can provide valuable insights into neutron correlated backgrounds to the SRN search, estimation of which is still largely uncertain.

Currently four major backgrounds remain for the SRN search: $\nu_\mu/\bar{\nu}_\mu$ CC decay electrons, $\nu_e/\bar{\nu}_e$ CC, NC elastic and heavy particle (μ/π) leakage. Events without a delayed neutron capture signal can be rejected. SK-IV data reveals that neutrons can also be produced in neutrino interactions (other than anti-neutrino interactions) at relevant energies, e.g. the out going proton in $\nu_\mu + n \rightarrow \mu^- + p$ can induce neutrons while propagating in water.

Fig. 8 shows the energy spectrum (line) and observed number of neutrons in each energy bin (points) in SRN search side bands:(1) events with two Cherenkov rings, (2) events with decay electron(s) or having a preceding nuclear gamma, (3) mu-like events, (4) isotropic events from NC processes and (5) pion events. Neutrons are seen in all the side bands. Taking into account the efficiency, the observed average yield is close to 1 neutron per event. It is clear that not all neutrons are induced by anti-neutrino interactions. Neutrons from neutrino interactions must also have a significant contribution. Below 30 MeV where SRN events are most likely to occur, NC background stands out to be the most important one, not only because has it the similar rising spectrum but also it's often accompanied by neutrons. However, multiple neutrons are possible, as shown in Fig. 9. Especially for NC events, a MC study shows that more than one neutron is produced most of the time, which is supported by SK-IV data, as shown in Fig. 8 (4) and Fig. 9 (4). These NC events can be rejected if multiple neutrons are detected. Hence higher neutron tagging

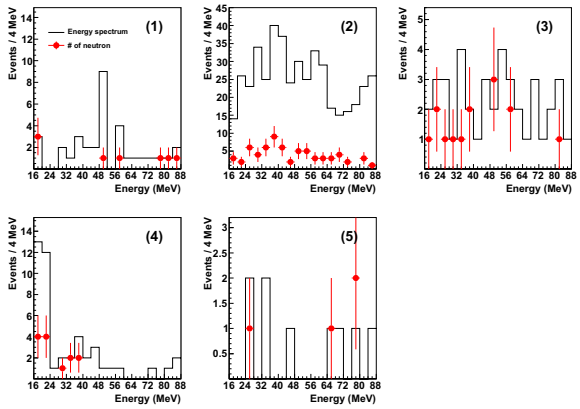

Figure 8: Energy spectrum and observed number of neutrons in SRN search side bands. Solid line represents the reconstructed energy assuming an electron and points indicate the number of neutrons observed in each enrgy bin.

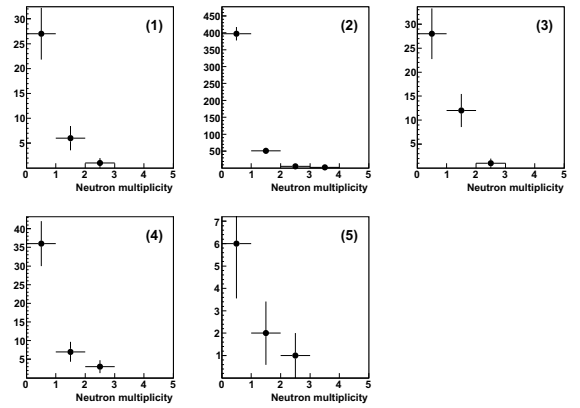

Figure 9: Observed neutron multiplicity in SRN side band events.

efficiency is desirable, which can be achived by the other neutron tagging method, i.e. loading SK with gadolinium (GADZOOKS![5]).

5 Prospects and outlook

Neutron tagging can also play an important role in proton decay searches. Taking $p \to e^+\pi^0$ as an example, the estimated background rate is $2.1 \pm 0.3 \pm 0.8$ events/megaton·year[4], which arise mainly from atmospheric neutrino interactions. Some background process are: (a) $\nu_e + p \to e^- + p + \pi^+$; (b) $\nu_e + n \to e^- + p + \pi^0$; (c) $\nu_e + n \to e^- + n + \pi^+$; (d) $\nu_e + n \to e^- + p + \pi^0$. The outgoing proton in (d) induces neutrons through hadronic interaction in ^{16}O. Process (a) and (b) do not have neutrons in the final state and remains irreducible. Process (c) and (d) can be rejected if neutron in the final state can be identified. Table 1 shows neutron yield in $p \to e^+\pi^0$ search

# of neutrons in one event	Fraction (%)
0	31.5
1	30.1
2	18.2
3	9.2
4	5.2
>=5	5.8

Table 1: Neutron production in proton decay background.

side band (total momentum $<$ 500 MeV/c, 700 MeV/c^2 $<$ total invariant mass $<$ 1200 MeV/c^2), from which one can estimate how many backgrounds can be reduced by tagging neutrons. For example, $\sim$23% backgrounds can be rejected by tagging neutrons in pure water. In case of a Gd-loaded detector, $\sim$56% backgrounds can be rejected assuming neutron tagging efficiency is 67.7% [3]. Note that this is a conservative estimation since the simulation of neutron production is incomplete in current MC.

In sum, a new trigger logic has been implemented in SK-IV to tag thermal neutron captures in pure water. Neutron tagging efficiency and background probability are found to be, respectively, 19.3% and 1%. Signal efficiency and neutron capture time in pure water is well verified using an Am/Be source. Clear neutron capture signal is observed in atmospheric neutrino data, which demonstrates the potential to reject backgrounds for future proton decay searches. Precise estimation of NC contribution and neutron production in NC events are of high priority for future SRN search programs.

Intense R&D is currently underway towarding a gadolinium-enhanced SK. Higher efficiency and lowered energy threshold are expected to greatly improve SK's sensitivity to the SRN search in future.

Acknowledgements: This work is supported by the National Natural Science Foundation of China (grants 10875062 and 10911140109).

References

[1] J. F. Beacom and M. R. Vagins, Phys. Rev. Lett., 2004, **93**: 171101.
[2] S. Chen and Z. Deng, Nucl. Phys. B Proc. Suppl., 2007, **166**: 252.
[3] H. Watanabe *et al.*, Astrop. Phys., 2009, **31**: 320.
[4] H. Nishino *et al.*, Phys. Rev. Lett., 2009, **102**: 141801.
[5] L. Marti, these proceedings.

32ND INTERNATIONAL COSMIC RAY CONFERENCE, BEIJING 2011

A wide-band solar neutrino trigger for Super-Kamiokande

GIADA CARMINATI[1] FOR THE SUPER-KAMIOKANDE COLLABORATION
[1]*Department of Physics and Astronomy, University of California, Irvine, Irvine CA 92697 USA*
g.carminati@uci.edu
DOI: 10.7529/ICRC2011/V04/0723

Abstract: Super-Kamiokande observes the elastic scattering of ^{8}B solar neutrinos on electrons. At present the recoil electron energy analysis threshold is 5 MeV. The first step to data analysis below 5 MeV is a lower trigger threshold. An observation of a solar neutrino signal at 4 MeV would open up the transition region between vacuum and matter oscillation. The new DAQ electronics installed in September 2008 enables the readout of every single hit using a software trigger rather than a hardware trigger. However, the trigger threshold is currently not significantly reduced. A new trigger system, the Wideband Intelligent Trigger (WIT), simultaneously triggers and reconstructs very low energy electrons. The current WIT system comprises 8 quad-core CPUs and is specifically designed to trigger with close to 100% efficiency on electrons above 4 MeV. Plans for a more powerful WIT system that can reach Super-Kamiokande's event reconstruction limit of 3 MeV are also presented.

Keywords: Super-Kamiokande, ^{8}B solar neutrinos, WIT

1 Introduction

Super-Kamiokande (SK) [1] is a water Cherenkov detector for neutrino physics and proton-decay search and is located underground at a depth of 1000 m in Kamioka Township, Japan. The detector consists of a stainless steel tank containing 50000 tons of pure water that houses an inward-facing array of about 11000 20" photomultipliers (PMTs) and an outward-facing array of about 2000 8" PMTs. The fraction of surface area covered by the 20" PMT photo-cathode is 40%. About six photo-electrons from Cherenkov light per MeV are observed.

Below about 100 MeV most PMT signals are due to single photon 'hits', i.e. PMT's struck by one Cherenkov photon. For such hits, the resolution of the hit arrival time is about 3 ns. Due to the large size of SK, it takes Cherenkov photons up to 220 ns to traverse the detector, and the relative PMT hit times can be used to reconstruct the point of origin (event vertex) of the light. The signal is due to Cherenkov photon hits that are coincident within roughly 5 ns, while the dark noise hits are random. Once the vertex is reconstructed the time-of-flight subtracted hit times improves the signal to noise ratio. The electron's or positron's direction is reconstructed from the direction of the characteristic 42° opening angle Cherenkov cone. The energy of the event is determined using the observed Cherenkov light intensity.

Above about 10 MeV, this event reconstruction works very well since there are many more Cherenkov light hits (about 60) than hits due to dark noise (about 12 within 220 ns). Near and below 5 MeV sophisticated vertex reconstruction programs are needed, since there are only about 25 to 30 collected photo-electrons from Cherenkov light. Events from radioactive background increase exponentially with decreasing energy. Most of this background comes from the PMTs themselves: the PMT glass and the fiberglass backing the PMT enclosures.

A new electronics and online system replaced the whole data acquisition (DAQ) system [2] in September 2008, starting the SK-IV phase. In the new DAQ scheme, the hardware event trigger for the data reduction is replaced by processing all the hits in the online farm. This enables the lowering of the solar neutrino detection threshold. Using the improved vertex fit program that has been introduced since SK-II [3], a new trigger system, the Wideband Intelligent Trigger (WIT), simultaneously triggers and reconstructs very low energy (above 4 MeV) electrons.

2 New DAQ System

With the former DAQ system, the detector triggered if the analog sum of the received signals exceeded a certain threshold. That reduced the data transfer rate. However, it limited the decrease of the trigger event threshold.

The new front-end electronics is based on a charge-to-time converter and a multi-hit Time-to-Digital converter (TDC) [4]. TCP/IP based readout channels permit obtaining input pulse rates of 85 kHz/ch. In the former system this rate was 1.4 kHz/ch [2]. The new online system is capable of processing large data flow up to 470 MB/s. To handle this flow of data, Gigabit and 10-Gigabit Ethernet technologies

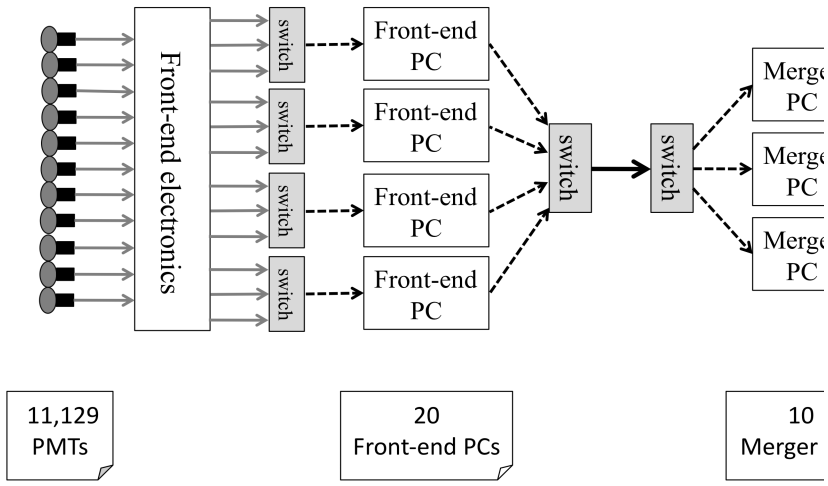

Figure 1: Schematic view of the data acquisition system and the WIT system. The data are transferred to the WIT PCs via Gigabit Ethernet (dashed line) or 10-Gigabit Ethernet lines (bold solid line).

are used and the load is distributed over Linux based PCs with 2GB RAM and Intel Dual Core CPU (Xeon 5160) operating at 3GHz frequency. In this way, the new DAQ system sends all the data to the online PCs and the event selections is done by software instead of a hardware trigger module.

The online data system consists of 20 front-end PCs which receive all the hit data from the front-end electronics. Data processed in the front-end PCs are then sent to 10 Merger PCs for event building. In the Merger PCs, as suggested by their name, the data are merged and different software triggers are applied to select candidates for various physics analyses. From the Merger PCs, the triggered events are sent to an Organizer PC where the data are merged and sorted in time order and then written onto the disk for offline analyses. The disk writing speed of the Organizer PC is the bottleneck of the new DAQ system. The maximum value of writing on the disk is about 50 MB/s.

Taking advantage of a cut on the fiducial volume, the Wide-band Intelligent Trigger (WIT) reduces the final data size and the energy threshold can be lowered down to 4 MeV.

3 Event Reconstruction

Electrons below 20 MeV can travel only a few centimeters in water, therefore their Cherenkov light is approximately a point source. The reconstruction of this vertex relies solely on the relative timing of the hits.

WIT uses two different vertex reconstruction algorithms. A fast online fit (Clusfit) pre-filters low energy events, eliminating isolated hits to reduce the effects of dark noise and reflected or scattered light. More details on the fast fit are given in [5]. If the vertex of the fast online fit is farther than 2 m from any PMT, the event is later reconstructed by a second fit. This procedure reduces both the processing time and the final data size, and it also improves the rejection of the background, in particular the radioactive background originating in the PMT glass and the fiberglass backings of the PMT enclosures.

The second reconstruction algorithm is based on a precise fitter, BONSAI (Branch Optimization Navigating Successive Annealing Iterations), which uses all hits from an event to form the timing residuals to determine the vertex positions.

BONSAI performs a maximum likelihood fit to the timing residuals of the Cherenkov signal as well as the background for each vertex hypothesis. The hypothesis with the largest likelihood is chosen as the reconstructed vertex. This procedure has some technical difficulties due to the accidental coincidence of background hits after the time-of-flight subtraction that can produce local likelihood maxima at several position far away from the global maximum, i.e. the true vertex. Due to the large size of SK, the search for the true global maximum can be tricky and time consuming. To improve speed performances as well as to reduce the number of mis-reconstructions, a pre-reconstruction algorithm (STORE) searches for a good starting position based on a list of vertex candidates calculated from PMT hit combinations of four hits. The time residuals of all four hits in each combination must be zero at its associated point. Any event with four hits or more is reconstructed.

4 The WIT System

The WIT system comprises 2 16-core modules and will work in parallel to the Organizer PC. It will receive the merged data from the Merger PCs before any software trigger is applied, since WIT performs its own trigger.

Each module comprises a HP ProCurve Switch 2900-24G which receives the data flow through 1-Gigabit Ethernet

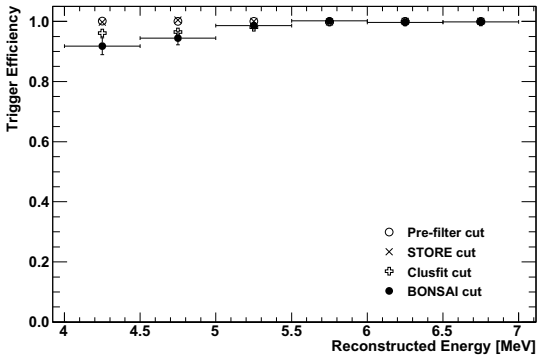

Figure 2: Efficiencies of the trigger criteria as a function of the reconstructed energy. For easier reading, the error bars are drawn only for the last cut.

lines. The switch sends then the data to 2 PCs through 10-Gigabit Ethernet lines. Each Linux based PC comprises 2 Intel Quad Core CPU (Xeon Harpertown 5462) operating at 2.8 GHz frequency and with 16 GB RAM. The block diagram of the WIT system is shown in Fig. 1.

5 Trigger Efficiency

The efficiency of the trigger is evaluated using data from the Ni–Cf light source. A detailed description of this light source is given in [6]. In this study, the Ni source was positioned at (35.3, -70.7, 0) cm with respect to the center of the detector. To subtract the background, data without the Ni source were used.

The efficiency ε is defined as the fraction of events in the source data (N^s) minus the events in the no-source data (N^b) which passes a selection criterion:

$$\varepsilon = \frac{N^s_{cut} - f N^b_{cut}}{N^s - f N^b}$$

The factor $f = t^s/t^b$ takes into account the renormalization according to the different livetimes of the source and the background samples.

Fig. 2 shows the efficiencies of each subsequent trigger criterion as a function of the reconstructed event energy. For easier reading, the error bars are drawn only for the last cut. The pre-filter cut selects the events with at least 11 hits above the dark noise level in the 220 ns window. If the goodness of the pre-reconstruction algorithm STORE is larger than 6.6, i.e. 60% of the 11 hits above the dark noise, then the events survive the STORE cut. When the vertex of the fast online fit (Clusfit) is farther than 2 m from any PMT, the events pass the Clusfit cut. If the reconstructed vertex of BONSAI is also farther than 2 m from any PMT, the events pass the BONSAI cut. Between 4 and 4.5 MeV, the WIT efficiency after the BONSAI cut is 92% $\pm$ 3%.

6 Time Performance

The current WIT system has been tested for time performance. Using 1 of the 4 WIT PCs, Fig. 3 shows that the average computing time to process one second of data decreases with the total number of processes run parallel on the same PC. Since each PC has 8 cores, if 9 processes run at the same time, no computing time improvement is observed.

The average computing time can be reduced by roughly 7.8 per PC, i.e. a factor of 31 for the complete system, running parallel the all cores. New commercially available PCs are 4 times faster than the current WIT PCs. Thus, 1 new 16-core PC in addition to the current WIT system will trigger and reconstruct the total Super-Kamiokande data flow at energies as low as 4 MeV.

7 Capabilities of WIT

The motivation for a lower energy threshold is the study of solar (via elastic electron-neutrino scattering) and anti-electron neutrino (via inverse-β reactions) oscillations.

The direction of recoiling electrons from ^{8}B solar neutrino interactions provides a good signature, so a signal to background ratio (after cuts) as low as 5% is possible. Since solar neutrinos are single events, the analysis threshold is defined by the background rate after all cuts are applied. An observation of a solar neutrino signal at 4 MeV would open up the transition region between vacuum and matter oscillation.

A measurement of anti-electron neutrinos requires tagging the produced neutron in (delayed) coincidence with the prompt positron. Such tagging might be done with captures on dissolved Gd ions [7]. SK is able to reconstruct such positrons, with an event reconstruction limit at 3 MeV [8]. Low energy electrons have the same vertex resolution, since the annihilation photons do not produce Cherenkov

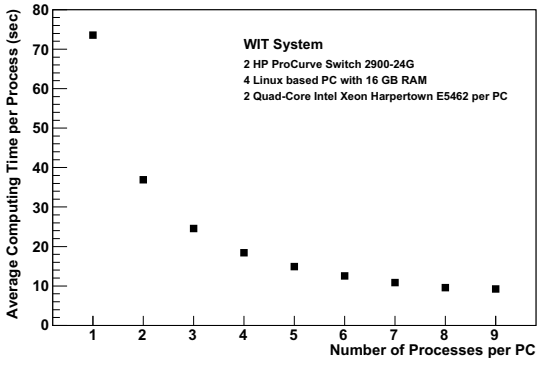

Figure 3: Average computing time to process one second of data as a function of the number of processes per PC. The errors are smaller than the size of the marker.

light. Since the energy threshold of neutrinos (if a neutron capture tag is available) are only limited by the event reconstruction, a 3 MeV threshold should be possible.

In this scenario with neutron tagging, SK should be able to observe few diffuse supernova neutrino background events per year. In addition, the anti-neutrino spectrum from Japan's nuclear power reactors will be collected at a rate of several thousands events per year, allowing the most stringent limits to be placed on solar neutrino oscillation parameters [9].

8 Conclusion

With the introduction of the new DAQ electronics, SK can read out every single hit using a software trigger rather than a hardware trigger. The new trigger system, the Wideband Intelligent Trigger (WIT), simultaneously triggers and reconstructs very low energy electrons. It is specifically designed to trigger with close to 100% efficiency on electrons above 4 MeV and it reconstructs event vertices further than 2 m from any PMT, in order to reduce the computing time and the final data size as well as the radioactive background originating in the PMT glass and the fiberglass backings of the PMT enclosures.

These new tools should enable SK to measure the spectral distortions of the recoil electron energy spectrum from ^{8}B solar neutrino-electron scattering from the transition between matter and vacuum solar neutrino oscillations. Furthermore, if a neutron capture tag is available, SK can do a precise determination of the solar neutrino oscillation parameters with a high statistics neutrino spectrum as well as an observation of the diffuse supernova neutrino background.

References

[1] S. Fukuda *et al.* [Super-Kamiokande Coll.], Nucl. Instr. Meth. A, 2003, **501**, 418-462.
[2] S. Yamada *et al.* , IEEE Trans. Nucl. Sci., 2010, **57**, 428-432.
[3] M. Smy, Proc. of the 30th ICRC, 2007, **5**, 1279-1282.
[4] H. Nishino *et al.* , Nucl. Instr. Meth. A, 2007, **610**, 710-717.
[5] J. Hosaka *et al.* [Super-Kamiokande Coll.], Phys. Rev. D, 2006, **73**, 112001.
[6] T. Iida, Ph.D. Thesis, University of Tokyo, 2009.
[7] J.F. Beacom and M.R. Vagins, Phys. Rev. Lett., 2004, **93**, 171101.
[8] H. Watanabe *et al.* [Super-Kamiokande Coll.], Astrop. Phys., 2009, **31**, 320-328.
[9] S. Choubey and S.T. Petcov, Phys. Lett. B, 2004, **594**, 333-346.

32ND INTERNATIONAL COSMIC RAY CONFERENCE, BEIJING 2011

On neutrino oscillations searches with ANTARES

GOULVEN GUILLARD[1†], JÜRGEN BRUNNER[2], ON BEHALF OF THE ANTARES COLLABORATION
[1]*Laboratoire de Physique Corpusculaire (CNRS/IN2P3) & Université Blaise Pascal, Clermont-Ferrand, France*
[2]*Centre de Physique des Particules de Marseille (CNRS/IN2P3) & Université de la Méditerranée, Marseille, France*
[†]*guillard@in2p3.fr*
DOI: 10.7529/ICRC2011/V04/0819

Abstract: Although the first evidence for neutrino oscillations came from measurements on atmospheric neutrinos in underground experiments, neutrino oscillations have yet to be demonstrated in high energy neutrino telescopes, whose energy threshold is significantly higher. Recent studies have shown that a clean sample of atmospheric neutrinos with energies as low as 20 GeV can be isolated in the ANTARES neutrino telescope. Such a threshold is low enough to allow the observation of neutrino oscillation features. A robust analysis method is presented which allows the extraction of atmospheric neutrino oscillation parameters.

Keywords: neutrino oscillations, ANTARES, neutrino telescope

1 Introduction

It is now well established that neutrinos can switch from a flavour to another, neutrino flavour eigenstates for the weak interaction being different from neutrino mass eigenstates. This phenomenon, hypothesized in 1957 by Pontecorvo and described more precisely in the early sixties [1], is known as neutrino oscillations, and has been measured by a number of experiments [2].

Although part of the scientific program of the ANTARES neutrino telescope, oscillations studies have been delayed because of the difficulty to reliably reconstruct muons at a sufficiently low energy. Indeed, the granularity of ANTARES is rather coarse compared with the range of GeV muons in water : its 885 photomultiplier tubes are distributed by triplets placed 14.5 m apart along the detector lines, themselves spaced by about 60 m [3]. As a consequence, the energy range where the effect of the atmospheric neutrino oscillations should be visible is situated at the very edge of the detector sensitivity, which makes the neutrino oscillations measurement very challenging.

The topic experienced a regain of interest since the completion of the detector in 2008. As progress was steadily made in the detailed understanding of the detector and of its environment, it became clear that it should be possible to extract a clean sample of atmospheric neutrinos with energies around the first minimum in the survival probability of muon neutrinos propagating through the Earth.

Even though dedicated experiments are more sensitive for the measurements of neutrino oscillations, such an analysis is an important check for ANTARES. The analysis being very sensitive not only to the telescope efficiency but also to the quality of the angular and energy reconstruction, it becomes a benchmark for the understanding of the detector.

2 Purpose

Neutrinos oscillations are commonly described in terms of E/L dependence, where E is the neutrino energy and L its oscillation path length [2]. For a neutrino telescope such as ANTARES, detecting neutrinos crossing the Earth, L can be translated as $2R\sin\theta$, R being the Earth radius and θ the anti-elevation (that is, the angle between the neutrino direction and the horizontal axis : $\theta = \pi/2$ for a vertical upgoing neutrino). Within the two-flavour approximation, the ν_μ survival probability can then be written

$$P(\nu_\mu \to \nu_\mu) \simeq 1 - \sin^2 2\theta_{23} \sin^2 \left(2.54 R \Delta m^2_{32} \frac{\sin\theta}{E} \right),$$

θ_{23} and Δm^2_{32} being respectively the mixing angle and the squared mass difference of the involved mass eigenstates (with R in km, E in GeV and Δm^2_{32} in eV^2).

According to recent results from the MINOS experiment [4], the first minimum in the muon neutrino survival probability $E/\sin\theta$ spectrum occurs at about 24 GeV (figure 1). This interesting region is in principle accessible for ANTARES. Indeed, Monte-Carlo simulations have shown that it is possible to extract clean samples of atmospheric neutrinos with energies in this range, which should enable the observation of the first minimum.

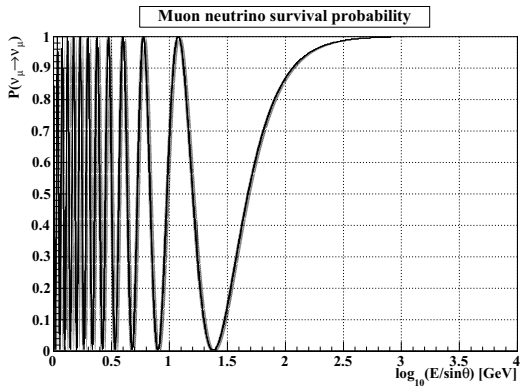

Figure 1: Survival probability of muon neutrinos as a function of $E/\sin\theta$ in the two-flavour approximation, with $\sin^2 2\theta_{23} = 1$ and $\Delta m^2_{32} = 2.32 \times 10^{-3}\,\mathrm{eV}^2$ (the line width corresponds to MINOS $1\,\sigma$ uncertainty on this parameter [4]), neglecting matter effects.

3 Method

A simple and robust method to measure neutrino oscillations in ANTARES consists in taking advantage of the different granularity of the detector along and across the detection lines. Indeed the range of muons below about 20 GeV makes them unlikely to give signal on different lines. They can be well reconstructed however using only one line, especially if they are close to the vertical. These low energy vertical tracks should be suppressed in the current oscillation scenarios compared to the more energetic and less vertical ones. Consequently, the observed ratio between the number of tracks giving signal on a single detector line (1D tracks) and the number of tracks giving signal on several detector lines (3D tracks) should differ from the expected ratio in the case of no oscillations. Many systematic effects such as the global flux normalisation or absolute detection efficiencies should cancel in this ratio, leading to a small residual systematic effect. The observed ratio can be expressed in terms of Monte-Carlo events as

$$R = \frac{N_{\mathrm{1D}}^{no\ osc} - \sin^2 2\theta_{23} \cdot f_{\mathrm{1D}}}{N_{\mathrm{3D}}^{no\ osc} - \sin^2 2\theta_{23} \cdot f_{\mathrm{3D}}}, \qquad (1)$$

where $N_{\mathrm{1D|3D}}^{no\ osc}$ is the number of expected 1D (3D) tracks without neutrino oscillations and

$$f_{\mathrm{1D|3D}} = \sum_i \sin^2\left(2.54 R \Delta m^2_{23} \frac{\sin\theta_i}{E_i}\right)$$

is summed over each event i.

For each value of Δm^2_{23} the mixing angle can be calculated analytically from the measurement of R according to equation 1. The statistical and systematic errors from R propagate directly into an error on the mixing angle, which leads to a band in the $(\theta_{23}, \Delta m^2_{32})$ plane.

Tracks are reconstructed using a fast reconstruction algorithm [5], which has the advantage of being more efficient at lower energies than other existing reconstruction strategies. A cut on the estimated quality of the fitted track and on the reconstructed angle is performed, in order to select well-defined events and to increase the upgoing neutrinos purity. The 1D tracks are required to be reconstructed using hits from at least 8 detector storeys. Lowering this cut would considerably enhance the number of 1D events and thus the sensitivity to oscillations, but would also increase dramatically the contamination from misreconstructed atmospheric muons. Such a hard cut ensures a very low contamination and leads to a minimal track length of about 100 m. The energy threshold is thus roughly 20 GeV, which is below the first oscillation minimum in the $E/\sin\theta$ spectrum.

This method is robust as it does not depend on many assumptions, nor does it rely on an energy estimator. Furthermore the reconstruction algorithm is used only to assert the quality of the selected events. Finally, assuming they affect similarly 1D and 3D events, the ratio should cancel most systematics, and in particular the large uncertainties on the atmospheric neutrino flux normalization and the uncertainties on the detector simulation. The strict hit selection criteria and the strong cut on the number of hit storeys minimize the sensitivity of the ratio to potential biases in the optical background simulation. Remaining systematic uncertainties are expected to be within a few percents, smaller than the current statistical errors.

4 Expected sensitivity

Table 1 shows, according to MINOS results [4], the number of expected events for a 170 days Monte-Carlo sample (this corresponds to 2008 active time). The atmospheric neutrino flux is weighted to match Bartol parametrization [6]. The contamination of misreconstructed downgoing atmospheric muons is negligible. The number of 1D events is suppressed by 16 % in the case of oscillations while the number of 3D events is suppressed only by 3.6 %. The effect to be observed is however small : the suppression of 1D tracks concerns only 26 events for this sample. It is clear that the $E/\sin\theta$ spectrum cannot be reliably extracted under such conditions : a larger statistics is needed.

	no osc.	osc.	contamination
1D tracks	186	160	4.7
3D tracks	522	504	1.2

Table 1: Number of expected $\nu_\mu/\bar{\nu}_\mu$ charged current events, after 170 days of lifetime, with and without oscillations, for 1D and 3D tracks, and number of misreconstructed atmospheric muons surviving the cuts.

The sensitivity after 1000 days, which may be achieved after 4 or 5 years of real data taking depending on various external conditions, is presented in figure 2, extrapolating

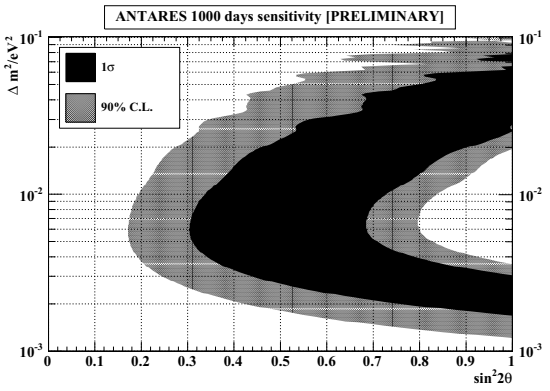

Figure 2: ANTARES expected sensitivity to atmospheric neutrino oscillations after 1000 days.

from the numbers given in table 1. The number of expected 1D events is roughly one per day, which leads for 1000 days to a statistical error of about 3 % (∼30 events). Studies where PMT and water parameters have been varied within their tolerance have shown that a 3 % systematic error on R is realistic. Consequently, a total standard deviation of about 5 % on R has been used to draw the measurement contours of figure 2.

According to these results, although not competitive with dedicated experiments, ANTARES should be sensitive to neutrino oscillation parameters through disappearance of atmospheric muon neutrinos with the simple and robust analysis presented here. Current preliminary results using a restricted data sample are compatible with world oscillation data. Processing of the whole ANTARES data set is foreseen.

5 Prospects

Several directions are currently being investigated to improve ANTARES sensitivity to neutrino oscillations. In a near future, it should be possible to increase significantly the number of low energy reconstructed muons thanks to a dedicated reconstruction algorithm coupled to an optimized hit selection, which would reduce statistical uncertainties using the same amount of data. Furthermore the use of a different reconstruction algorithm would be an important cross-check of such an analysis. Additionally, the proportion of low energy events can be improved by selecting events contained in the detector.

Such improvements should enhance ANTARES sensitivity to neutrino oscillation parameters. They might also allow the extraction of the $E/\sin\theta$ spectrum, which would be a great opportunity to cross-check the understanding of the detector.

6 Conclusions

A robust method to extract atmospheric muon neutrino oscillation parameters from ANTARES data has been presented. Although not competitive with dedicated experiments, ANTARES should be able to reach some sensitivity to these parameters, which would be a demonstration of the understanding of the ANTARES detector. Preliminary analysis of a restricted data sample is compatible with existing constraints on neutrino oscillation parameters. The complete analysis of ANTARES data is ongoing.

References

[1] B. Pontecorvo, JETP **33** (1957) 549 ; B. Pontecorvo, JETP **34** (1958) 247 ; Z. Maki, M. Nakagawa and S. Sakata, Progr. Theoret. Phys. **28** (1962) 1579.

[2] See e.g. U. Dore and D. Orestano, Rep. Prog. Phys. **71** (2008) 106201 [arXiv:0811.1194] for a review.

[3] M. Ageron *et al.*, accepted by Nucl. Instr. and Meth. **A**, April 2011 [arXiv:1104.1607] and references therein.

[4] P. Adamson *et al.*, Phys. Rev. Lett. **106** (2011) 181801 [arXiv:1103.0340].

[5] J.A. Aguilar *et al.*, Astropart. Phys. **34** (2011) 652 [arXiv:1105.4116].

[6] G.D. Barr *et al.*, Phys. Rev. D **70** (2004) 023006 [arXiv:astro-ph/0403630].

Studies on the unfolding of the atmospheric neutrino spectrum with IceCube 59 using the TRUEE algorithm

THE ICECUBE COLLABORATION[1]
[1]*See special section in these proceedings*

Abstract: The measurement of the atmospheric neutrino energy spectrum provides information about the diffuse neutrino flux from extragalactic sources. A relative increase of the spectrum toward higher energies could be evidence for neutrino producing hadronic processes in the cosmic high energy accelerators, such as active galactic nuclei or gamma ray bursts. IceCube is currently the largest neutrino detector on Earth and is placed in the antarctic ice at the geographic South Pole. IceCube permits the detection of neutrinos with energies beyond 10^6 GeV. Since the acceptance and the resolution of neutrino telescopes suffer from the finite resolution and limited acceptance, a regularized unfolding method is used to extract the energy distribution of neutrinos from the measured observables. For AMANDA, the unfolding was done with the $\mathcal{RUN}$ algorithm. Based on the basic concept of this program and for data analyses in the ROOT frame, a new deconvolution algorithm (TRUEE) has been written and tested. With this new algorithm, studies on the analysis of the atmospheric neutrino spectrum measured with the IceCube 59 string configuration are presented.

Corresponding authors: Natalie Milke[2] (*natalie.milke@udo.edu*), Wolfgang Rhode[2] (*wolfgang.rhode@udo.edu*), Tim Ruhe[2] (*tim.ruhe@udo.edu*)
DOI: 10.7529/ICRC2011/V04/0833
[2]*Department of physics, TU Dortmund University, D-44221 Dortmund, Germany*

Keywords: IceCube; TRUEE; RUN; regularized unfolding; atmospheric neutrino; energy spectrum

1 Introduction

IceCube is the largest neutrino detector ever built and is located at the geographic South Pole. It consists of 5160 digital optical modules (DOM) arranged along 86 strings forming a three-dimensional grid covering a cubic kilometer in the glacial ice [1]. While traveling through the ice the high energy neutrino-induced muons produce Cherenkov light which can be detected by the DOMs providing directional and energy information of the muon track. One of the main goals of IceCube is the detection of extragalactic neutrinos for understanding of cosmic ray production in cosmic accelerators. Neutrinos from interactions of cosmic rays with the Earth's atmosphere represent a background for the extragalactic neutrinos. Thus, a precise measurement of the atmospheric neutrino flux is important for understanding this background. Since the spectral index of the flux distribution depending on neutrino energy is lower for extragalactic neutrinos (following the spectral behavior of Fermi accelerated cosmic rays $\gamma \sim 2$ [2]) than for atmospheric neutrinos ($\gamma \sim 3.7$) [3], a contribution of extragalactic neutrinos would cause an enhancement of the flux in the high energy region of the spectrum.

The energy of the primary particles is convoluted with the interaction probability and the detector finite resolution and limited acceptance. Therefore the neutrino energy has to be estimated from energy-correlated, measured observables. For this purpose a regularized unfolding algorithm is developed and applied.

In this paper the atmospheric neutrino sample from the measurement with the IceCube 59 (IC 59) string configuration is used. The energy spectrum is unfolded with the new deconvolution algorithm TRUEE.

2 Regularized unfolding

The convolution of the neutrino energy with the interaction probability and detector response gives us the measured observables in the detector and this relation can be expressed as a Fredholm integral equation of the first kind if neglecting background. From discretization a linear matrix equation can be obtained where the measured distribution is a product of the detector response matrix and the neutrino energy distribution. The response matrix is obtained from Monte Carlo (MC) simulation. Thus, an unfolding algorithm needs as input MC-simulated assumed energy distribution with the resulting distributions of measured observables to determine the detector response and the measured observables distributions from data to estimate the neutrino energy flux.

Every unfolding requires an a-priori assumption about some properties of the result realized in a regularization to reduce strong negative correlations between unfolded data points. Here the Tikhonov regularization [5] is used achieving a smooth distribution by minimizing the curvature of the result during the unfolding fit.

3 Unfolding algorithm TRUEE

In AMANDA, the precursor of IceCube, the **R**egularized **UN**folding ($\mathcal{RUN}$) algorithm [6] was used to unfold lepton energy spectra [7]. $\mathcal{RUN}$ was developed in 1984 using the programming language FORTRAN 77. Therefore $\mathcal{RUN}$ is not easy to install and use in combination with modern software. TRUEE - **T**ime-dependent **R**egularized **U**nfolding for **E**conomics and **E**ngineering problems or just **TRUE E**nergy is a new software including the $\mathcal{RUN}$-based unfolding algorithm.

One special property of the $\mathcal{RUN}$ algorithm is the parametrization of unfolded distribution using a superposition of cubic basis splines. The spline coefficients are determined from the unfolding and the superposed function is transformed to the final histogram. At the spline overlaping points (knots) the function is continuously differentiable up to the second derivative, so that a Tikhonov regularization with the second derivatives in the smoothing operator can be performed. The user determines the number of splines by defining the number of knots. Regularization is controlled by the number of degrees of freedom, which can be given by the user but can also be suggested by the software. A small number leads to strong regularization.

TRUEE has been developed within the Collaborative Research Centre SFB 823 in Dortmund. Besides the core regularized unfolding from $\mathcal{RUN}$ the new software contains user friendly functions, which make the procedure of an unfolding analysis more comfortable. The functions used in this analysis are explained in the next section using the IC 59 neutrino sample.

4 Unfolding analysis

For this analysis 10 % of the measured data were used. After event selection a sample of 3160 neutrino events measured within the zenith angle range of 88° to 180° with IC 59 is obtained. Thus, most of the events in the sample were caused by neutrinos having traveled through the Earth before undergoing an interaction inside or in the vicinity of IceCube. For 100 % of the data we expect more than 30000 neutrino-induced events and thus higher statistics in the high energy region. Based on a Monte Carlo study the purity of the sample is estimated to be higher than 95 %, therefore the background formed by atmospheric muons is neglected. The sample is obtained using straight precuts followed by an event selection using the multivariate method Random Forest [8] within the framework Rapid Miner [9].

4.1 Selection of observables

As a first step the selection of energy-dependent observables is made. TRUEE automatically produces scatter plots of the sought-after variable and observables and the related profile histograms to check if a correlation is present. The inspection of scatter plots with different observables showed the correlation between primary neutrino energy and the following observables:

- Number of DOMs having a signal
- Number of strings with at least one hit-DOM
- Track length in a certain time window (MPEFit_LDirC)

Figure 1 shows the correlation between neutrino energy and number of DOMs.

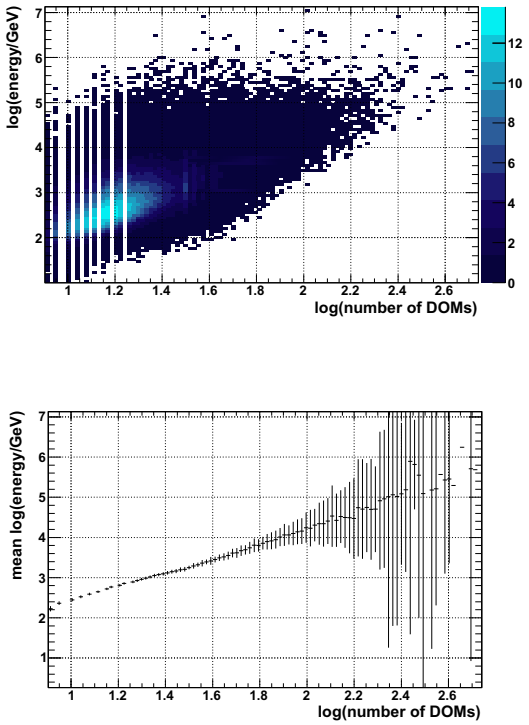

Figure 1: An example of scatter plot and related profile histogram to check the correlation between the energy and the observable (here number of DOMs). An optimal correlation is present in a monotonically changing profile function with small uncertainties.

Since TRUEE is able to use up to three observables at the same time for unfolding, different binnings of the selected observables for the response matrix have been checked. The most suitable binnings could be chosen by inspecting results after running unfolding in the test mode (see Sec. 4.2).

4.2 Test mode

An unfolding algorithm expects input from the user concerning some parameters such as the number of bins for histograms or the degree of regularization. To check which user-defined parameter settings give the optimal unfolding result a test mode is included in TRUEE. In this mode only simulations are used. Since we neglect the atmospheric muon background, the MC sample contains only neutrino events after application of event selection techniques. The energy distribution of simulated neutrino events has been reweighted, so that the generated flux follows the atmospheric neutrino flux predicted by Honda [3] containing a prompt component from Naumov Recombination Quark Parton Model (Naumov RQPM) [4]. The prompt component consists of neutrinos from decays of short-lived mesons containing charm quarks.

An MC sample that is statistically equivalent to the expected experimental data sample is used as a pseudo real data sample for unfolding. Since the real sought-after distribution is known in this case, it can be compared to the unfolded distribution. The optimal parameter settings are chosen with an L-curve approach [10] by examining the tradeoff between regularization strength and fit to the true distribution. For the IC 59 sample the following parameter settings are used for the final unfolding:

- Number of DOMs with 20 bins
- Number of strings with 10 bins
- Track length with 10 bins
- Number of knots 16
- Number of degrees of freedom 5

The unfolded test spectrum is shown in Fig. 2.

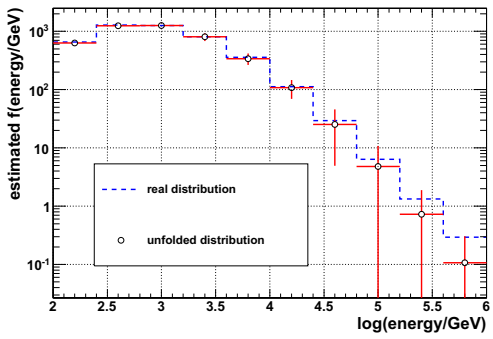

Figure 2: Unfolding of pseudo data compared to the real distribution using test mode. The unfolding does not consider the interaction probability, acceptance or systematic uncertainties.

4.3 Unfolding result

The unfolding procedure with the parameter settings determined in Sec. 4.2 can now be applied to the IC 59 neutrino sample. The generated MC neutrino sample for determination of the detector response contains only simulated events that undergo an interaction within or close to the detector. This procedure is necessary to reduce simulation time and memory. After passing all event selection steps the final sample contains only a fraction of neutrino events. Thus, the unfolded distribution represents only neutrinos which interacted, triggered the detector and passed the event selection (Fig. 3).

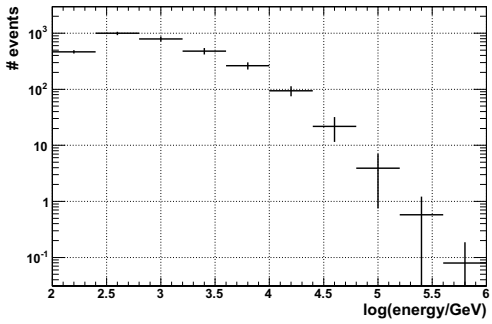

Figure 3: Unfolding of IC 59 data gives the distribution of selected neutrino events depending on energy. The unfolding does not consider the interaction probability, acceptance or systematic uncertainties, yet. Furthermore with the full data sample the number of events per bin will increase by a factor of ten.

To calculate the neutrino flux for all neutrinos within the zenith angle range, the unfolded spectrum has to be divided by the effective area. The effective area is the ratio of observed event rate and incoming flux and depends on the properties of the selected event sample. It includes the muon neutrino cross section, the probability for the muon to be detected and the detector efficiency for muon detection and event reconstruction. The effective area for the current sample is shown in Fig. 4.

The effective area is rising at higher energies due to the increasing cross section of neutrinos and to the higher length of the muon tracks. Therefore the probability to detect and reconstruct such a long track is rising. For the events with vertical upgoing tracks the effective area is decreasing because of the rising probability for absorption of neutrinos by the Earth.

We demonstrate the performance of the unfolding technique by showing an example in Fig. 5 of how an unfolded energy distribution (Fig. 3) can be translated into a neutrino flux spectrum when the effective area (Fig. 4) is known. Additional spectra have been unfolded with the same parameter settings but with different assumptions of the neutrino flux in MC to check the possible bias introduced by the assumption. Shown are results trained with

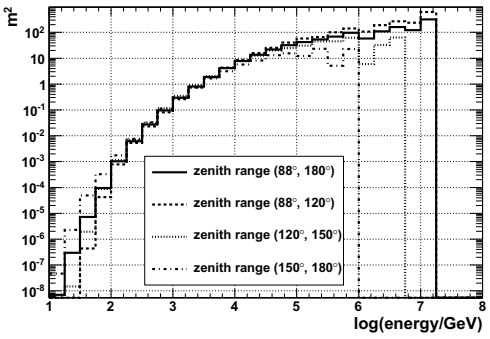

Figure 4: Effective area for the current neutrino sample dependent on neutrino energy. Illustrated are areas for different zenith angle ranges and for the average of the whole zenith range considered in the analysis.

MC weighted to atmospheric (Honda), to atmospheric with prompt (Honda-Naumov) and to atmospheric with prompt and $1.6 \cdot 10^{-8} E^{-2}$ neutrino flux. All three results have only small deviation in the low statistics region, thus the introduced bias is negligible.

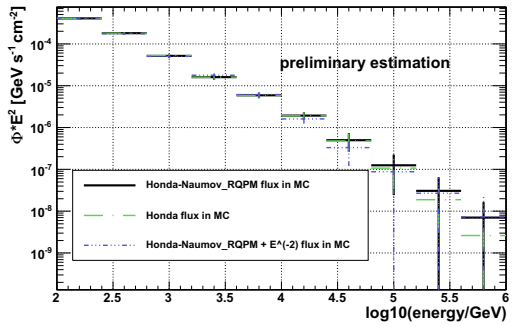

Figure 5: An example of the atmospheric neutrino energy spectrum from 10 % of IC 59 data unfolded with TRUEE. Shown are three unfolding results, using different MC distributions to determine the detector response. The uncertainties take into account statistics and bin-to-bin correlation, determined by the unfolding software. The spectrum is weighted by squared energy for a better illustration.

Since a continuous function is unfolded taking into account event migration between bins, the last bin is estimated to be non-zero even though the statistics of current sample is low.

4.4 Verification of simulation

A function to verify the result was developed in $\mathcal{RUN}$ and was transferred to TRUEE. The user has the possibility to check whether the simulation of all observables agrees with the experimental data and thus verify the unfolding result. After the unfolding, the MC events are reweighted by the unfolded distribution. The MC sample describes the real data now. In this case all observables, not only those which have been used for the unfolding, should match in their distribution the measured data. The observables whose distributions do not match are not correctly simulated. If none of the distributions match, probably the unfolding did not work properly. In this case the user should check if the simulation of the detector response was correct. For the unfolding example shown in this paper the verification showed an agreement between the experimental data and reweighted simulations.

5 Conclusion and outlook

The new unfolding algorithm TRUEE shows a good performance in estimation of an atmospheric neutrino spectrum. The algorithm is able to estimate a steep distribution covering several orders of magnitude and thus is a dedicated tool for astroparticle physics. The analysis is facilitated by additional functions and an easy installation and ease of use of the software.

A new energy region of the atmospheric neutrino flux can be explored with IC 59. The simulation predicts an extension to energies up to 10^6 GeV. The estimation of the neutrino energy spectrum with 10 % of the IC 59 data will be done by unfolding with TRUEE. The subsequent unfolding of the 100 % IC 59 data sample is expected to determine the energy spectrum with more precision in the high energy region due to higher statistics.

6 Acknowledgements

This work is supported by the German Research Foundation DFG (SFB 823/C4 and SFB 876/C3).

References

[1] F. Halzen, S. R. Klein, Rev. Sci. Instrum., 2010, **81**(081101)
[2] E. Fermi, Phys. Rev., 1949, **75**(8): 1169-1174
[3] M. Honda et. al., Phys. Rev. D, 2007, **75**(4): 043006
[4] E. V. Bugaev et. al., Il Nuovo Cimento C, 1989, **12**(1): 41-73
[5] A. N. Tikhonov: 1963, On the solution of improperly posed problems and the method of regularization, Sov. Math. 5
[6] V. Blobel: 1996, The RUN Manual - Regularized Unfolding for High-Energy Physics Experiments, Technical Note TN 361, OPAL
[7] R. Abbasi et. al., Astroparticle Physics, 2010, **34**: 48-58
[8] L. Breiman, Machine Learning, 2001, **45**(1): 5-32
[9] S. Fischer et. al., 2002, Technical Report, Collaborative Research Center 531, University of Dortmund
[10] C. L. Lawson, R. J. Hanson: 1974, Solving Least Squares Problems, Prentice-Hall, Englewood Cliffs, NJ

Search for Neutrinos from Far Supernovae with Super-Kamiokande

MICHAEL SMY[1,2] FOR THE SUPER-KAMIOKANDE COLLABORATION
[1]*University of California, Irvine*
[2]*Institute of the Physics and Mathematics of the Universe*

smy@michael.ps.uci.edu

DOI: 10.7529/ICRC2011/V04/0855

Abstract: Supernovae release more than 99% of their energy in the form of neutrinos, so neutrino measurements are the most direct tool to study them. However, present detectors detect bursts from an individual supernova only if it happens in our own galaxy, a fairly rare event. The alternative is the detection of the constant neutrino flux due to supernovae anywhere which measures the typical neutrino emission characteristics folded with the rate of core-collapse supernovae. A search for this important signal is presented.

Keywords: Neutrino, Supernova

1 Core Collapse Supernovae

Massive stars end their life as a supernova, an explosion typically brighter than the host galaxy of the star. Several types of supernovae have been identified; core collapse supernovae happen when the iron core of a sufficiently massive dying star (which cannot produce energy via nuclear fusion) acquires enough mass to collapse gravitationally and force neutronization of protons and electrons into neutrons and neutrinos. If the collapse is halted by the Fermi pressure of the neutrons, a neutron star results, and more than 99% of the binding energy is released in form of neutrinos. The observation of these supernova neutrinos is the unique and only chance to peek into the inside of the dying star. Unfortunately, the small neutrino cross section and present detector masses allow detection of these "neutrino bursts" only if the supernova happens in our own galaxy. An alternative is the continuous measurement of the sum of all core collapse supernovae throughout the universe: a diffuse, isotropic flux of neutrinos. The energy of this signal is somewhat lessened due to red shift. The flux is also quite low because of the large average distance.

2 Obsevation in Super-Kamiokande

Super-Kamiokande [1] is a ~50,000 ton water Cherenkov detector optically divided into an inner ~32,000 ton detector viewed by ~11,100 20" photomultiplier tubes and an outer veto region viewed by ~1,800 8" photomultiplier tubes located 2,700m water equivalent underground. The signal event rate is dominated by inverse β decay of electron-type anti-neutrinos. Radioactive decays of cosmic muon-induced nuclear spallation products define the lower energy bound of sensitivity: the lifetime of these products can be many seconds, so not all can be tagged by their preceding muons. The upper energy bound is due to atmospheric neutrino background. In particular, charged-current interactions of atmospheric muon neutrinos can produce muons near or below Cherenkov threshold. Those muons remain invisible and their decay electrons are a serious background. Other backgrounds are electronic noise, outside radioactivity (e.g. PMT glass) and solar neutrinos.

3 Calculation of Positron Spectrum

The positron spectrum seen by a terrestrial detector depends on the average neutrino emission spectrum, the history of core-collapse supernova, their red-shifts and the inverse β cross section. Even though the supernova neutrino emission spectrum has a rich structure (i.e. due to neutrino – neutrino interactions), the resulting terrestrial positron spectrum is likely to be somewhat insensitive to it since it is an average of many supernovae at different red shifts. Horiuchi, Beacom and Dwek [2] provided a method using an effective two-parameter description of the neutrino emission spectrum which is able to match most calculations. The spectrum is assumed to be Fermi-Dirac and the parameters are the neutrino temperature and neutrino luminosity. Figure 1

shows the resulting positron spectra for an anti-electron neutrino luminosity of $6x10^{52}$ erg.

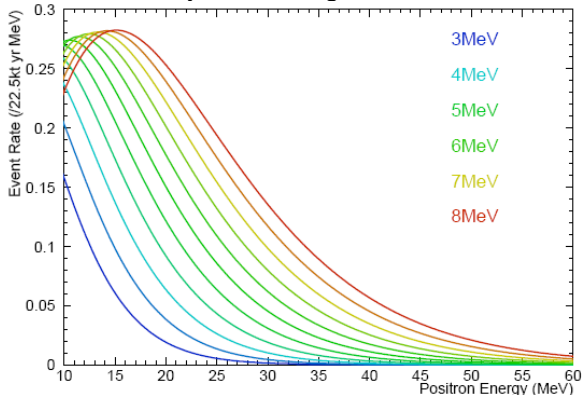

Figure 1. Positron Spectra Resulting from a Fermi-Dirac Effective Eupernova Neutrino Emission Spectrum. The anti-electron neutrino luminosity is $6x10^{52}$ erg.

4 Comparison to a Previous Search

In 2003, Super-Kamiokande published an upper flux limit of 1.2/cm^2/s [3] above 19.3 MeV of neutrino energy (18 MeV total positron energy) based on 1496 days of data collected during the first phase of the experiment (1996-2001). For this search, we greatly increased the efficiency of the analysis, updated the cross section, considered (and removed when possible) additional background sources, improved the statistical analysis and almost doubled the exposure to 2853 days of livetime, 794 days of which (the second phase of the experiment; 2002-2005) were accumulated with reduced inner detector photo-cathode coverage (~5,200 20" photomultiplier tubes). The reduced coverage is due to an accident destroying ~60% of the inner detector photomultiplier tubes. The third phase (2006-2008) of the experiment has the same coverage as the first phase.

In particular, the tagging of spallation products from preceding muons was improved. Previously, a likelihood was formed based on the time difference between muon and candidate, the distance of closest approach, and the "residual charge" (difference between the observed light yield of the muon and the expected light yield of a minimum ionizing track of the observed length). We now reconstruct the dE/dx of these tracks based on the measured times of arrival of Cherenkov photons at the photomultiplier tubes. The peak of the dE/dx profiles of spallation-causing muons correlates with the position of the spallation product. Also, an improved muon fitter categorizes muons into (i) through-going single muons, (ii) stopping muons, (iii) short-track muons ("corner clippers"), and (iv) muon bundles. The likelihood is tuned for each category. As a consequence, the signal efficiency of the spallation cut was improved from 73% to about 90%. The spallation removal efficiency was also improved: after a tighter cut on the likelihood there is no evidence of remaining spallation between 16 MeV and 18 MeV of positron energy. Figure 1 contrasts the correlation of spallation data perpendicular to (top panel) and along the muon track (bottom panel) with the expected random coincidence (a sample formed from subsequent rather than preceding μ's). Table 1 lists the efficiencies.

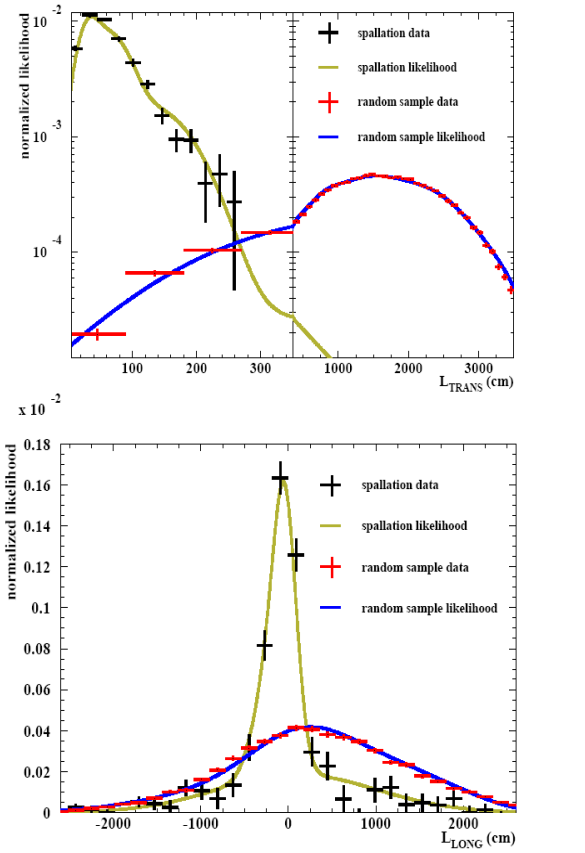

Figure 2. The top (bottom) panel shows the distance of closest approach L_{trans} (longitudinal distance L_{long}) of spallation products to preceding muon tracks in comparison to random coincidence.

Solar neutrinos at 16 MeV form a much larger background than at 18 MeV. Solar neutrino events are due to elastic electron-neutrino scattering, a very forward-peaked process. The removal critically depends on the angular resolution of the recoil electron which is dominated by multiple Coulomb scattering. Reconstructing the amount of multiple Coulomb scattering event-by-event we tuned the position of a cut placed on the angle between reconstructed recoil electron and solar direction by minimizing the expected signal over the square root of the expected background as a function of energy and the reconstructed amount of multiple Coulomb scattering. The solar cut efficiencies are given in Table 1.

Compared to the previously published analysis, several additional cuts remove (atmospheric neutrino) background: candidates with preceding gammas ("pre-activity") or following events ("post-activity") are removed with greater efficiency, charged pions in the sample are identified and rejected by the "sharpness" of their Cherenkov cones, and candidates with correlated outer detector activity are removed (in addition to the normal outer detector veto of events).

Cut	SK-I/III	SK-II
Electronic Noise	99%	99%
Spallation (Low Energy)	81.8% (16-18 MeV)	76.2% (17.5-20 MeV)
Spallation (High Energy)	90.8% (18-24 MeV)	89.2% (20-26 MeV)
Solar ν's (Low Energy)	73.8% (16-17 MeV)	74% (17.5-18 MeV)
Solar ν's (Mid Energy)	82.1% (17-18 MeV)	82% (18-19MeV)
Solar ν's (High Energy)	87.8% (18-19 MeV)	88% (19-20MeV)
Solar ν's (Highest E)	93% (19-20 MeV)	93% (20-21MeV)
π's from atmospheric ν's	98%	97%
Cherenkov angle	95% / 94%	88%
Incoming Event	98%	98%
Combined efficiency	78.5%/76.7%	69.2%

Table 1. Cut Efficiencies of the analysis.

The published result is based on binned χ^2 test to the energy spectrum of the candidate sample after all cuts were applied. Now we perform an unbinned maximum likelihood fit to three samples: in addition to the signal sample we also fit to a sample which has a large reconstructed Cherenkov angle and to another sample which has a small reconstructed Cherenkov angle. The signal sample contains also decay electrons from atmospheric muon-neutrino charged-current interactions producing invisible muons, atmospheric electron-neutrino charged-current interactions, and atmospheric neutrino neutral-current interactions. To constrain the amount of atmospheric neutral-current background, the large angle sample was added since these interactions often produce several gammas leading to fairly isotropic events. That large angle sample also contains some charged pions and muons from atmospheric neutrino interactions. Many of these however reconstruct at small Cherenkov angles as well, so a fit to all three samples disentangles all three kinds of backgrounds.

5 Results

Figure 2 (3) shows the data with ~11,100 (~5,200) inner detector photomultiplier tubes. Supernova neutrinos would appear in the central panel which shows events with reconstructed Cherenkov cone angles between 38 and 50 degrees. The decay electrons from invisible muons and electrons/positrons from atmospheric ν_e's will of course also appear in the central panel. Atmospheric neutral-current background mostly reconstruct as isotropic events (right panel; angle above 78 degrees) and below ~20MeV in the central panel. Remaining pions and muons from atmospheric neutrinos show up in the left panel (angle between 20 and 38 degrees) or above ~40MeV in the right panel.

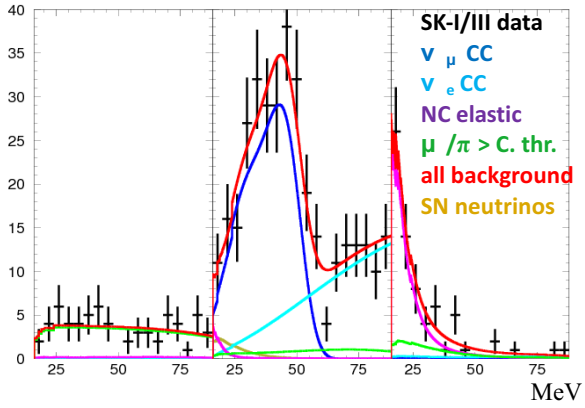

Figure 2. Fit to SK-I and SK-III Data. The top line shows all backgrounds combined. In the low angle region, all background is due to charged pion and muon production from atmospheric neutrinos. The high angle region is dominated by atmospheric neutrino neutral current interactions with a small pion/muon component. The central region is dominated by invisible muon production from atmospheric neutrinos. Above ~60 MeV, atmospheric electron-neutrinos dominate. Below 18MeV, neutral current interactions start to become important. The central plot also shows the best fit relic contribution.

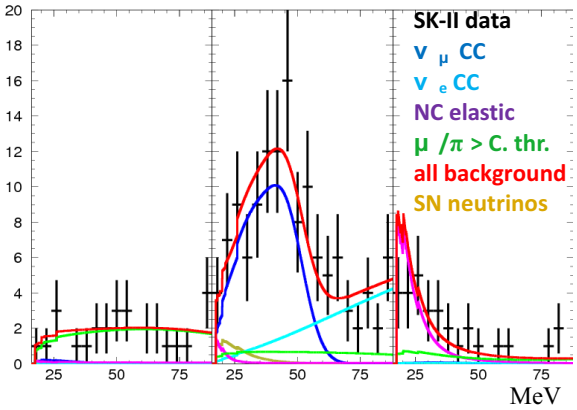

Figure 3. Same as Figure 1 but for SK-II Data.

The data in both Figure 2 and Figure 3 is well described by just atmospheric neutrino background, so no significant excess due to supernova neutrinos was found. The likelihood of the fit is used to place a 90% upper limit on the supernova neutrino flux. To obtain this limit, the likelihood was marginalized over all background rate parameters to obtain the likelihood as a function of only the supernova event rate. The 90% limit is defined as the rate below which 90% of the area underneath that likelihood is contained. Typical likelihoods of the first, second, and third phase of the experiment as well as the combined likelihood is shown in Figure 4. In this case, the 90% C.L. limit is about <5events/year for positron energies above 16 MeV which corresponds to a flux of about 2.7/cm^2/s above 17.3 MeV. Figure 5 shows the 90% C.L. event rate limit as a function of temperature (dashed line) and the 90% C.L. excluded area of event rate versus neutrino temperature. Table 2 lists the typical supernova anti-electron neutrino luminosity limit for each temperature assuming a Fermi-Dirac emission spectrum.

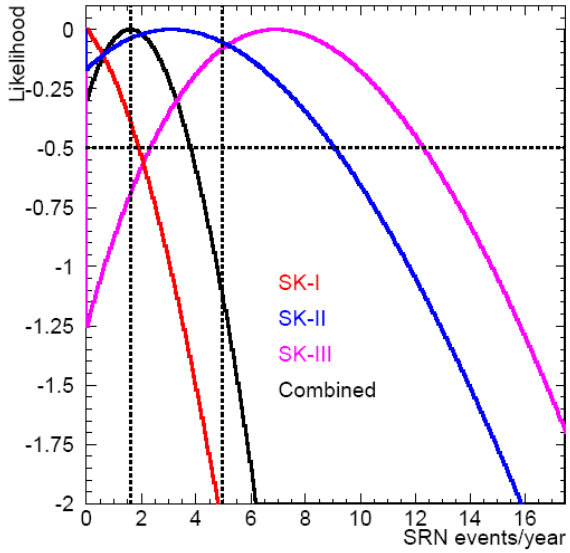

Figure 4. Example of Likelihood (T=6MeV) as a Function of Supernova ν Event Rate. The intersection with the dotted horizontal line illustrates the 1σ range of the fit. The right (left) dotted vertical line shows the 90% C.L. upper limit (best fit) of the supernova event rate.

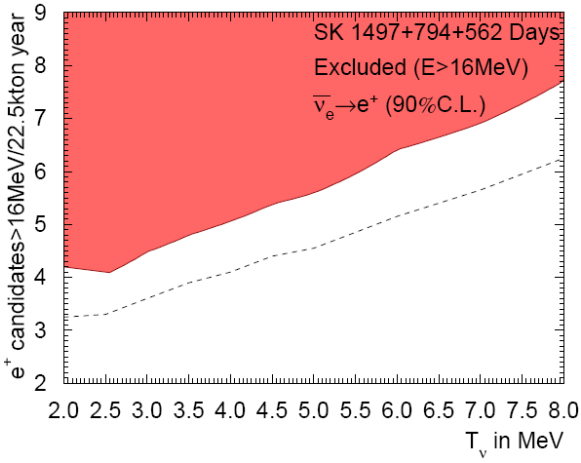

Figure 5. 90% C.L. Excluded Area of Supernova Event rate Versus Neutrino Temperature. The dashed line gives the event rate limit given a particular neutrino temperature.

T [MeV]	3	3.5	4	4.5	5.0	5.5
L [10^{53} erg]	9.0	4.8	2.9	2.1	1.5	1.3
T [MeV]	6.0	6.5	7.0	7.5	8.0	
L [10^{53} erg]	1.1	0.92	0.82	0.75	0.70	

Table 2. 90% C.L. Upper Luminosity Limit for a Given Anti-electron Neutrino Temperature T.

6 Conclusion

We have largely improved the diffuse distant supernova neutrino search, reduced the lower energy threshold, and doubled the exposure. There is no evidence of a signal. We present a new upper 90% C.L. limit of about 2.7/cm^2/s above 17.3 MeV neutrino energy.

References

[1] Fukuda et. al., Nucl. Instr. Meth. **A501** (2003): 418
[2] Yüksel, Ando, Beacom, Phys. Rev. **C74**(2006): 015803; Horiuchi, Beacom, Dwek, Phys. Rev. **D79**(2009): 083013
[3] Malek et. al., Phys. Rev. Lett. **90** (2003): 061101

Data acquisition system for nearby supernova bursts at Super-Kamiokande

TAKAAKI YOKOZAWA[1], YOSHINARI HAYATO[1], MASAHIRO IKENO[2], MASAYUKI NAKAHATA[1], SHOEI NAKAYAMA[1], YOSHIHISA OBAYASHI[1], KIMIHIRO OKUMURA[3], MASATO SHIOZAWA[1], TOMONOBU TOMURA[1], TOMOHISA UCHIDA[1], SATORU YAMADA[4],

[1]*Kamioka Observatory, Institute for Cosmic Ray Research, University of Tokyo, 456 Higashi-Mozumi, Hida, Gifu, 5061205 Japan*

[2]*KEK, High Energy Accelerator Research Organization, 1-1 Oho, Tsukuba, Ibaraki, 3050801 Japan*

[3] *Institute for Cosmic Ray Research, University of Tokyo, 5-1-5 Kashiwanoha, Kashiwa, Chiba, 2770882 Japan*

[4]*Research Center for Neutrino Science, Tohoku University, 6-3 Aramakiazaaoba, Aoba, Sendai, Miyagi, 9808578 Japan*

yokozawa@suketto.icrr.u-tokyo.ac.jp

DOI: 10.7529/ICRC2011/V04/1081

Abstract: Super-Kamiokande (SK) is a ring imaging water Cherenkov detector that consists of 50 ktons of pure water and about 13000 photomultiplier tubes (PMT). If a supernova burst happens near our solar system (for example Betelgeuse or Antares), the neutrino event rate at SK is expected to be greater than 30 MHz and the current data acquisition system(DAQ) will only be able to record about 20% of the events. Therefore, we are developing an independent DAQ system for such nearby supernova bursts. This system records the total number of hit PMTs since the energy distribution of supernova neutrinos is rather narrow, it is possible to estimate the number of neutrino events using only the total number of hits. We have developed a new set of modules which collect the number of hit PMTs from the existing front-end electronics. Using this new module it will be possible to record the full time profile of the energy sum of supernova burst neutrino events in the detector during the burst. We have made a prototype of this module and checked its performance using the Super-Kamiokande detector. We report on the results of this prototype test.

Keywords: Super-Kamiokande, Cherenkov detector, supernova, neutrino, DAQ, FPGA

1 Introduction

SK is a ring imaging water Cherenkov detector that consists of 50 ktons of pure water located underground at a depth of 1,000 m. The outer most 2 m of the detector is called the Outer Detector (OD, 1,885 PMTs) and the inside is called the Inner Detector (ID, 11,129 PMTs). SK observes atmospheric neutrinos [1], solar neutrinos [2], supernova burst neutrinos [3] and artificial neutrinos from an accelerator [4]. In September 2008, we installed new front-end electronics, called QBEE, and started data taking as SK-IV phase.

The observation of supernova burst neutrinos is one of the main goals of SK. Supernova explosions (SN) are induced by the core collapse of massive stars, which release about $3*10^{53}$ erg of energy per burst. In 1987, neutrinos from a supernova burst in the Large Magellanic Cloud, called SN1987A, were detected by the Kamiokande II [3], IMB [5] and Baksan [6] detectors. Based on these observations SK is expected to observe around 10,000 neutrinos if a supernova burst happens at the center of our galaxy.

On June 2009, it was reported that Betelgeuse's luminosity has decreased by 15 percent over the past 15 years. Betelgeuse and Antares are among the nearest supernova candidate stars around 500 light years distant. Though surface phenomena do not have a direct connection to the activity of the core, it is worthwhile to prepare for possible nearby supernova. If a supernova burst occurs in Betelgeuse or Antares, tens of millions of neutrinos are expected to interact in the SK detector and the maximum event rate is estimated to be more than 30MHz over 10 seconds. Since the current SK DAQ system is not designed to record such a huge amount of continuous data. Therefore, another independent data acquisition system is being prepared to record neutrino events from such bursts.

In this paper we will describe the current SK DAQ system and the concept of the new DAQ system in section 2. Development of a prototype and performance are presented in section 3. A summary and plan appear in section 4.

2 The concept of new DAQ system

In the current SK DAQ system, PMT signal are fed to custom front-end electronics called the QTC (charge timing converter) Based Electronics with Ethernet

(QBEE) [7]. The QTC developed for QBEE digitizes the timing and the charge information from PMTs [8]. The digitized data are sent to the front-end PCs via Gigabit Ethernet by SiTCP[9] and merged. Then, combined data are sent to the other set of PCs for event building and software triggering to select events. Finally, the selected events are written to the disk.

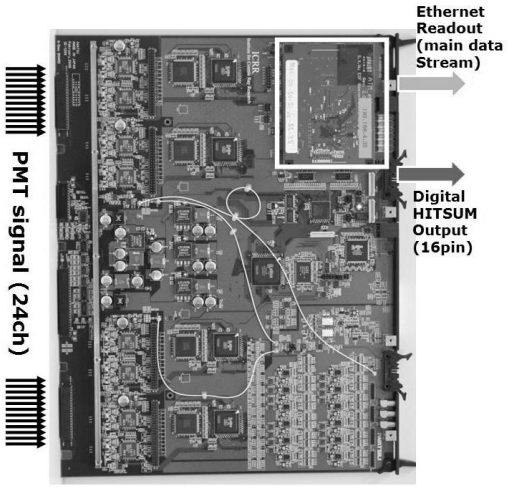

Fig. 1. The QBEE. At left side 24 PMT signals are input and at right the main data stream, including timing and charge information, Digital HITSUM, the number of hit PMT and a 60MHz source clock are output.

If a high rate burst happens, the data flow may become slow due to disk I/O limitation. Each QBEE has a DRAM buffer to store the data and it is possible to store 6 million events in 10 seconds. However, in case of a supernova in Betelgeuse or Antares, about a few tens of millions neutrinos are expected to interact and the maximum event rate is expected to exceed 30 MHz. Even such a high event rate case, first 3 seconds of data can be written to disk. However, some fraction of events will be lost after the first 3 seconds due to the overflow of the DRAM buffer on QBEE.

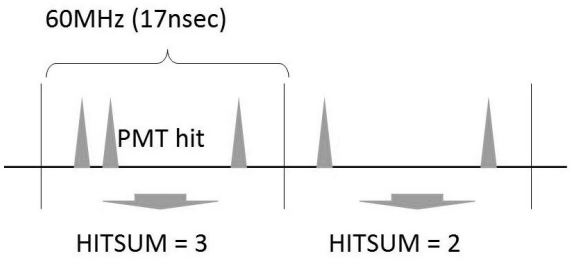

Fig. 2. The diagram of the Digital HITSUM. If 3 PMT hits occur in 17 nanoseconds at 1 QBEE board, the Digital HITSUM is 3. One QBEE processes 24 PMT channels, so the maximum Digital HITSUM is 24 and therefore requires a 5- bit port.

It is important to save the neutrino event rate continuously during the burst to understand the mechanism of the SN burst, even if event by event information is not available. Therefore a new independent DAQ system is being developed. This new DAQ system, called the Nearby SN DAQ System, is required to save necessary data stably and constantly, independent from the number of events happening in the detector.

The Nearby SN DAQ System records the time profile of the total number of hit PMTs in the detector. This system cannot record individual time and charge information of each PMT, but it is able to record calorimetric information of the neutrino burst. Since most of the PMT hits from supernova neutrino events are at the one photoelectron level and the number of hit PMTs is essentially proportional to the energy deposited in the detector.

The number of hit PMTs from each QBEE is provided as a digital signal as shown in Fig. 1. In addition to sending the charge and the timing information via Ethernet, QBEE also outputs the total number of hits with 17 nanosecond timing resolution. This is called Digital HITSUM. The QBEE counting scheme is shown in Fig. 2. The Digital HITSUM uses Low Voltage Differential Signaling (LVDS) and contains 5 bits of digital information for the number of hits and a 60 MHz source clock. The Digital HITSUM is continuously output even if data flow is suspended by disk writing limitations.

In order to collect and record the sum of Digital HITSUM, a new module called the Digital HITSUM collector is developed. This module is designed to reduce the data size by averaging in time, because the sampling rate of original Digital HITSUM is still too high to record all the data at 60MHz. The data rate is about 500 TB/day if we try to store the data at 60MHz. To reduce the data size, an FGPA based circuit is used to lower the sampling frequency is used. A block diagram of the Nearby SN DAQ System is shown in Fig. 3.

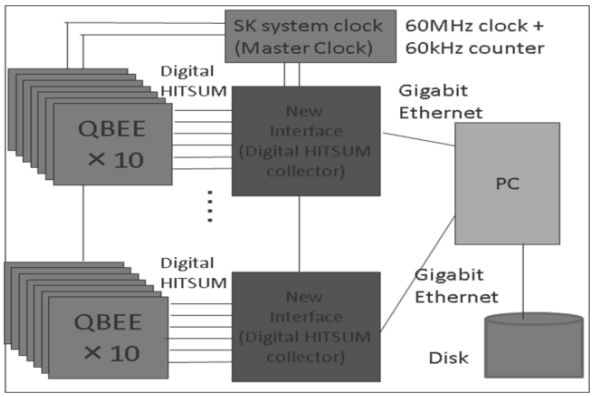

Fig. 3 Block diagram of the Nearby SN DAQ System. Digital HITSUMs generated by the QBEEs are collected by the Digital HITSUM collector. The SK Master Clock is used for the system clock. Ten Digital HITSUMs are summed at 60 kHz, sent to PC, and saved to disk.

The sampling frequency is chose to be 0.06 MHz based on optimizing the quality of data against its size. The

main background of this system is the 4,500 Hz PMT dark noises, roughly 0.83 hits/17ns. If the sampling frequency is too low, it becomes difficult to distinguish SN neutrino events from fluctuations of the PMT dark noise. The typical number from hit PMT of SN neutrino events are ~120 hits/event (6 hits/MeV*20 MeV/event). The relationship between timing resolution and PMT dark noise fluctuation is summarized in Table 1.

By comparing the number of hits PMT of SN neutrino fluctuation and the dark noise hits, it turns out that it is not possible to reduce the sampling frequency less than 0.01 MHz. Otherwise, it becomes difficult to distinguish signal from noise. On the other hand, it is difficult to store data faster than 0.1 MHz. Considering these limitations, the sampling frequency is determined as 0.06 MHz.

Sampling frequency [MHz]	Number of dark noise in one signal [hits/bin]	Dark noise fluctuation
60	0.83	+/- 0.9
10	5	+/- 2.2
1	50	+/- 7.1
0.1	500	+/- 22
0.06	830	+/- 26
0.01	5000	+/- 71

Table 1. Sampling frequency and dark noise fluctuation

In addition to the usual 0.06 MHz summed HITSUM, the module is able to save the original 60 MHz HITSUM information for up to 60 second if a SN-like burst is detected. For this purpose, a NIM input/output port is used to notify the SN-like events internally and externally. The 4GB of memory is equipped to buffer the 60 MHz sampling data over another Gigabit Ethernet port.

The system clock source of the Nearby SN DAQ system is the 60 MHz Master Clock, which is also used in the main SK DAQ system. It also provides event number, so it is possible to correlate the main SK DAQ events with this system data.

3 Development of prototype

A prototype of the module is shown in Fig. 4. Its input/output functionality and stability have been checked. At the front of this module, there are NIM input/output ports (2 ports each), summed 60 MHz HITSUM output port with LVDS, Master Clock, Digital HITSUM input port from QBEE(10 ports), and Gigabit Ethernet port for summed 60 kHz HITSUM to output the data saved in a 4 GB memory space.

In order to test the Ethernet interface and the event number readout, a test bench is prepared as shown in Fig. 5. The VME trg32 module generates an event number. The Master Clock module encodes the event number and generates a 60 MHz clock pulse. The Linux PC is used to receive the Ethernet output. The data from Ethernet output was successfully readout by the PC and the event number in the data is found to be correct.

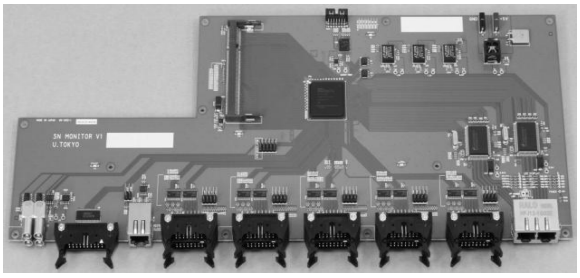

Fig.4. Picture of the interface board. From the left side of front panel, NIM input/output, 60 MHz LVDS output, Master Clock input, Digital HITSUM input, and Gigabit Ethernet output port.

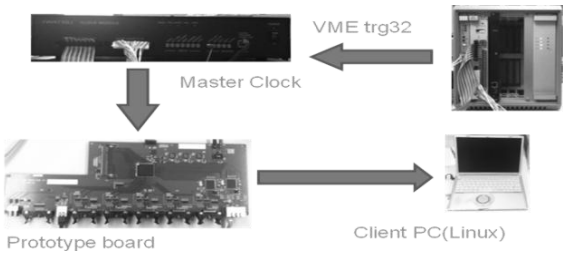

Fig. 5. 60MHz clock and event number which are provided by the Master Clock are sent to the prototype board. The event number is generated by a VME trg32 module. The decoded event numbers are sent to a Linux PC via Gigabit Ethernet and checked.

In order to test the Digital HITSUM readout stability, a Digital HITSUM from a QBEE is sent to the prototype board and summed 60 kHz HITSUM is read out via Ethernet. The input to the QBEE was a 10 kHz NIM signal. As a result of this test, the Digital HITSUM readout system and its Ethernet interface were confirmed to work properly. Also, the memory system is found to be functioning.

In summary, all the input/output ports and the memory systems are tested and confirmed to work. As a next step, we are planning to test the prototype board in the SK detector.

4 Summary and plan

We are now developing a new data acquisition system for nearby supernova explosion at SK. This system will record the total number of hit PMTs at 60 kHz, and recode 60 MHz data for 60s if SN burst-like phenomena are detected. For this purpose, a prototype board with an FPGA based module to collect the number of hits from

the SK front-end boards has been developed and tested. Basic functionality of this board is checked and seems to work as expected. As the next step, we are planning to install the prototype board in SK detector this summer for the further tests.

[1] Y. Fukuda *et al.* (Super-Kamiokande), **"**Evidence for Oscillation of Atmospheric Neutrinos**"**, *Phys. Rev. Lett.,* vol. 81, 1998, pp. 1562-1567.

[2] M. B. Smy *et al.* (Super-Kamiokande), "Precise measurement of the solar neutrino day-night and seasonal variation in Super-Kamiokande-I", *Phys. Rev. D,* vol. 69, 2004, 011104.

[3] K. Hirata *et al.*, **"**Observation of a neutrino burst from the supernova SN1987A**"**, *Phys. Rev. Lett.* vol. 58, 1987, pp. 1490 – 1493.

[4] E. Aliu *et al.* (K2K), "Evidence for Muon Neutrino Oscillation in an Accelerator-Based Experiment", *Phys. Rev. Lett.,* vol. 94, 2005, 081802.

[5] Alekseev, E. N., et al. (IMB collaboration), "Observation of a neutrino burst in coincidence with supernova SN1987A in the Large Magellanic Cloud", *Phys. Rev. Lett.*, vol. 58, 1987, 1494.

[6] Bionta, R. M., et al., "possible detection of a neutrino signal on 23 february 1987 at the baksan underground scintillation telescope of the institute of nuclear research", *J. Exp. Theor. Phys. Lett.* vol. 45, 1987, 589

[7] S. Yamada, et. al., "Commissioning of the New Electronics and Online System for the Super-Kamiokande Experiment", *IEEE Transactions on Nuclear Science*, vol. 57, 2010, pp. 428-432

[8] H. Nishino et al., "High-Speed Charge-to-Time Converter (QTC) ASIC for the Super-Kamiokande Experiment", *Nuclear Instruments and Methods in Physics Research Section A*, vol. 610, 2009, pp. 710-717.

[9] T. Uchida, "Hardware-Based TCP Processor for Gigabit Ethernet" *IEEE Transactions on Nuclear Science*, vol. 55, 2008, pp. 1631-1637.

32ND INTERNATIONAL COSMIC RAY CONFERENCE, BEIJING 2011

The ICARUS Experiment at Gran Sasso Underground Laboratory

ALFREDO G. COCCO[1,2]
[1]*On Behalf of the ICARUS Collaboration*
[2]*Istituto Nazionale di Fisica Nucleare*
Sezione di Napoli (Italy)
alfredo.cocco@na.infn.it

DOI: 10.7529/ICRC2011/V04/1340

Abstract: The ICARUS Experiment is the first example in a novel detector generation, able to provide on a large mass scale the imaging capabilities of the old famous "bubble chamber" together with ionization energy measurement. The T600 detector operates at GranSasso Underground Laboratory, studying cosmic rays, neutrino oscillation, proton decay and supernova neutrino. Potentialities of this novel electronic imaging telescope are presented through preliminary data analysis results on events reconstructed with unprecedented details.

Keywords: Liquid Argon TPC, Neutrino oscillation, Supernova neutrino, Proton decay.

1 Introduction

The ICARUS T600 cryogenic detector is the biggest Liquid Argon TPC realized ever, with the cryostat containing 600 tons of Liquid Argon. The ICARUS Experiment represents the result of a many year effort in R&D studies along a path of increasing mass and complexity laboratory and industrial prototypes. At the same time, the ICARUS detector marks a major milestone towards the realization of a multi kiloton LAr detector.

The ICARUS T600 addresses a wide physical program operating as a continuously sensitive general-purpose observation instrument. It is collecting a wide variety of events from the Universe, namely cosmic rays (atmospheric and solar neutrino interactions), but also neutrinos from the CNGS beam, produced at CERN and reaching Gran Sasso after a flight of about 730 km under the Earth surface. Neutrinos still play a key role in fundamental physics since clarifying the neutrinos nature and the pattern of the mixing between different flavors could unveil possible extensions of the present Standard Model of particle interactions and could also shed light on fundamental questions like Dark Matter and baryon asymmetry in the Universe. ICARUS T600 could also provide interesting results on supernova explosion mechanism in case of a galactic supernova event. ICARUS opens a completely new way to explore the unknown too. In particular it will be searching for rare unobserved up to now events like the long sought for proton decay (in particular into exotic channels), with zero background in one of its 3^{32} nucleons. Relying on the LAr-TPC three-dimensional, high granularity imaging and calorimetric capabilities, few proton decay events may be enough to discover matter instability.

2 The ICARUS detector

The ICARUS detector is the first large scale realization of the Liquid Argon Time Projection Chamber (LAr-TPC) technique. It can be considered the large scale modern version of the old-famous bubble chambers because of its high granularity the 3D imaging capabilities and the excellent calorimetric properties. The LAr-TPC concept was proposed by C. Rubbia in 1977 [1] and is based on the possibility to drift in high purity Liquid Argon free electrons over long distances in an electric field. The LAr-TPC thus successfully reproduces the extraordinary imaging features of the bubble chamber with the further achievement of being a fully electronic detector, continuous sensitive, self triggering and potentially scalable to huge masses. The ICARUS T600 is now installed in the Hall B of the Gran Sasso underground National Laboratory (LNGS) of Istituto Nazionale di Fisica Nucleare (INFN), shielded against cosmic rays by about 1400 meters of rock. Smoothly running under stable conditions since months, the detector is demonstrating high-level technical performances, as will be shown in the following.

The ICARUS T600 detector consists of a large cryostat split into two identical, adjacent half-modules with internal dimensions $3.6 \times 3.9 \times 19.6$ m^3 and filled with about 760 tons of ultra-pure liquid Argon. An uniform electric field ($E_{\rm drift}$ = 500 V/cm) is applied to the LAr bulk: each half-module houses two TPCs separated by a common cath-

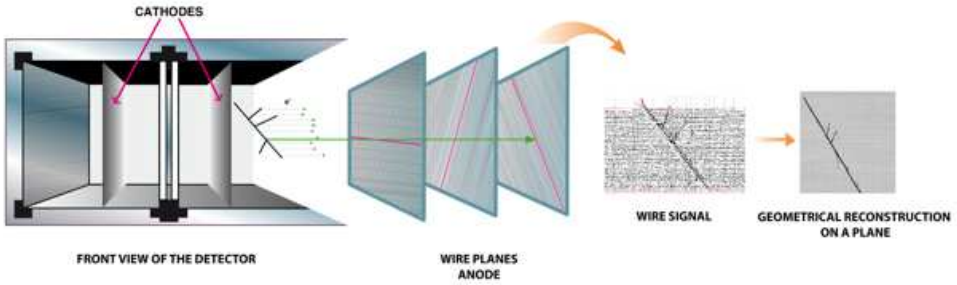

Figure 1: Icarus Liquid Argon TPC working principle: ionization electrons are drifted in the active volume and collected by the anode wire plane.

ode. Charged particles crossing the medium produce ionization and scintillation light along their path. Scintillation light has a wavelength of about 128 nm (UV) with a yield of about 5000 γ/mm for a mip particle; this provides a prompt signal that can be used for triggering purposes by means of Photo Multiplier Tubes (PMTs), suitable to detect VUV scintillation light and operating at the LAr cryogenic temperature. Ionization on the other hand has a yield of about 5000 electrons per mm; these electrons are drifted by the uniform electric field towards three wire planes where the signal is recorded, ensuring a redundant tridimensional track reconstruction. Thanks to the low transverse diffusion of charge in LAr, the electron images of ionization tracks are preserved along the 1.5 m maximum drift distance, as shown in figure 1. Wires are spaced by 3 mm and wire planes are oriented at a different angles (0^o, $+60^o$, -60^o) with respect to the horizontal direction. Therefore, combining the wire coordinates on each plane at a given drift time, a three-dimensional image of the ionizing event can be reconstructed. A remarkable resolution of about 1 mm^3 is uniformly achieved over the whole detector active volume (about 170 m^3).

Globally, 53248 wires with length up to 9 m are installed in the detector and individually readout by the data acquisition electronics; the DAQ design allow to continuously read-out and digitize independent waveforms of signals from each wire of the TPCs. The data are stored in multi-event circular buffers which are frozen and readout when a trigger signal occurs, minimizing the dead time. The average electronic noise achieved with the custom designed low noise front-end is of about 1500 electrons r.m.s. to be compared with about 15000 free electrons produced by a minimum ionizing particle in 3 mm (S/N about 10).

3 Detector operation and performances

A fundamental requirement for the performance of a LAr-TPC is the high purity of the Liquid Argon with respect to electronegative impurities (mainly O_2, H_2O and CO_2); a very low concentration level, less than 0.1 ppb, is required in order to safely operate the drift chamber. To this aim, each half-module is equipped with two gas argon and one liquid argon recirculation/purification systems. Argon gas is continuously drawn from the cryostat ceiling and, once re-condensed, drops into Oxysorb^{TM} filters to finally get back into the LAr containers. LAr instead is recirculated by mean of an immersed, cryogenic pump and is purified through standard Hydrosorb/Oxysorb^{TM} filters before being re-injected into the cryostats. Electron lifetimes exceeding 6 ms are reached after few months of operation.

During summer 2010 the first events from the CNGS neutrino beam and cosmic rays were detected. The trigger system relies on both, the scintillation light signals provided by the internal PMTs and the CNGS proton beam extraction time. As a starting layout, for each of the four chambers, the analog sum of signal from PMTs is exploited with a discrimination threshold set at around 100 photoelectrons, guaranteeing an almost full efficiency for the interactions induced by CNGS neutrinos. The trigger for the CNGS neutrino interactions is based on the presence of the PMT signal within a CNGS related gate.

The CNGS run started in stable conditions on October 1st and continued till the beam shutdown, on November 22^{nd}; in this period 5.8×10^{18} pot were collected out of the 8.0×10^{18} delivered by CERN, with a detector lifetime up to 90% since November 1^{st}. The 78% of the whole collected sample of events, corresponding to 4.54×10^{18}, has been preliminarily analyzed: 94 ν_μCC and 32 NC events have been identified by means of visual scanning into a 434 ton fiducial volume, while 6 events need for further analysis to be classified (being at edges the muon track is too short do be visually recognized); this result is in full agreement with the number of interactions predicted in the whole energy range up to 100 GeV (2.6 ν_μ CC and 0.86 ν NC for each 10^{-17}/pot), accounting for fiducial volume and DAQ dead-time. Examples of CNGS beam neutrino interaction is shown in figure 2.

Identification of the nature of particles is obtained by studying the event topology and the energy deposition per track length unit as a function of the particle range (dE/dx versus range) for muons/pions, kaons and protons [2, 3, 4, 5]. A dedicated reconstruction program based on the polygonal line algorithm [6] for 3D reconstruction, and on neural network for particle identification has been recently developed by the ICARUS Collaboration to this purpose.

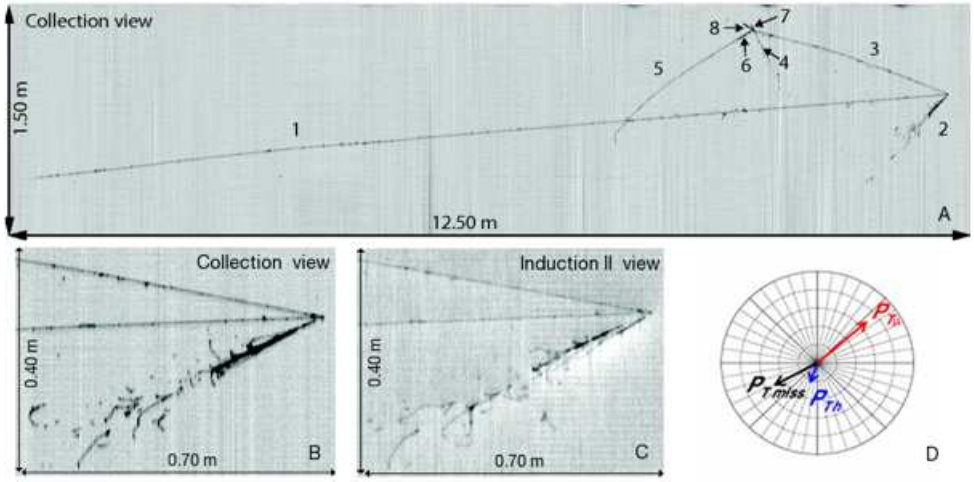

Figure 2: Example of ν_μCC interaction from the CNGS beam.

Electrons are fully identified by the characteristic electromagnetic showering, well separated from π^0 via γ reconstruction, dE/dx signal comparison and π^0 invariant mass measurement at the level of 10^{-3}. This feature guarantees a powerful identification of the CC electron neutrino interactions, while rejecting NC interactions to a negligible level. The electromagnetic energy resolution $\sigma(E)/E = 0.03/\sqrt{E(\mathrm{GeV})} \oplus 0.01$ is estimated in agreement with the $\pi^0 \rightarrow \gamma\gamma$ invariant mass measurements in the sub-GeV energy range [7]. The measurement of the Michel electron spectrum from muon decays, where bremsstrahlung photons emission is taken into account [8], provided the energy resolution below critical energy (E_c 30 MeV), $\sigma(E)/E = 0.11/\sqrt{E(\mathrm{MeV})} \oplus 0.02$. At higher energies the estimated resolution for hadronic showers is $\sigma(E)/E = 0.3/\sqrt{E(\mathrm{GeV})}$. However the LAr-TPC detector allows to identify and measure, track by track, each hadron produced in interactions, through ionization and range, leading to a much better energy resolution. For long muon track escaping the detector, momentum is determined exploiting the multiple scattering along the track, studying its displacements with respect to a straight line. The procedure, implemented as a Kalman filter technique and validated on cosmic rays stopping muons, allows a resolution $\Delta p/p$ that can be as good as 10%, depending mainly on the track length [9].

4 Future developments: the sterile neutrino puzzle

Recently an increasing number of experimental anomalies together with indication from cosmology on the role of a fourth family of neutrino raised the interest on the existence of a sterile neutrino. In-fact, the 3.8σ $\bar{\nu}_e$ excess signal in a $\bar{\nu}_\mu$ beam observed by LSND for the first time has been confirmed by the MiniBooNE experiment, suggesting a possible $\bar{\nu}_\mu \rightarrow \bar{\nu}_e$ oscillation ($0.2 < \Delta m^2 < 2.0$ eV^2, $\sin^2(2\theta) < 10^{-3}$) beyond the three neutrino flavour oscillation scheme as observed in solar/atmospheric neutrino experiments [10]. At the same time a recent re-evaluation of the $\bar{\nu}_e$ reactor spectra (about 3% of flux increase) brought out a $\bar{\nu}_e$ deficit at many short-baseline reactor experiments [11] and revived the SAGE/GALLEX ν_e deficit from the MegaCurie radioactive source [12], hinting at a fast disappearance rate ($\Delta m^2 > 1.5$ eV^2, $0.02 < \sin^2(2\theta) < 0.23$ at 99.7% C.L.). Furthermore, the latest WMAP data seem not to exclude, or even to prefer, a scenario with more than three neutrinos since recent analysis of the CMB lineshape performed by the WMAP Collaboration [13] gives the number of effective neutrino as $N_{\mathrm{eff}} = 4.34 + 0.86 - 0.88$; although only a one sigma effect, this estimate suggests the number of degrees of freedom at radiation-matter decoupling time could be larger than expected, leaving room for an extra light particle. At the same time recent results on ^{4}He abundance bring Big Bang Nucleosynthesis to favor more than the three known neutrino species [14], being the number of relativistic degrees of freedom directly related to the expansion rate of the Universe in the radiation dominated expansion phase.

In such a situation the use of two identical LAr-TPC detectors on a short baseline refurbished neutrino beam at the CERN-PS could represent a way to solve the puzzle [15]. The neutrino beam would be a low energy ν_μ beam produced by 19.2 GeV protons of at least $1.25 \times 10^{20} pot/yr$ intensity. The far detector, located at about 850 m from the target, could be ICARUS-T600 itself, while the near detector, at 127 m, would be a 150 ton active mass LAr-TPC (possibly a clone of one ICARUS-T600 semi-module having the length reduced by a factor of two). The LAr-TPC technique appears the ideal detector for the study of low energy neutrino events thanks to its very high ν_e detection efficiency combined with an extremely high-level rejection of associated NC background events. Moreover the usage of two identical detectors together with the very similar intrinsic ν_e spectra in the two positions, ensure that

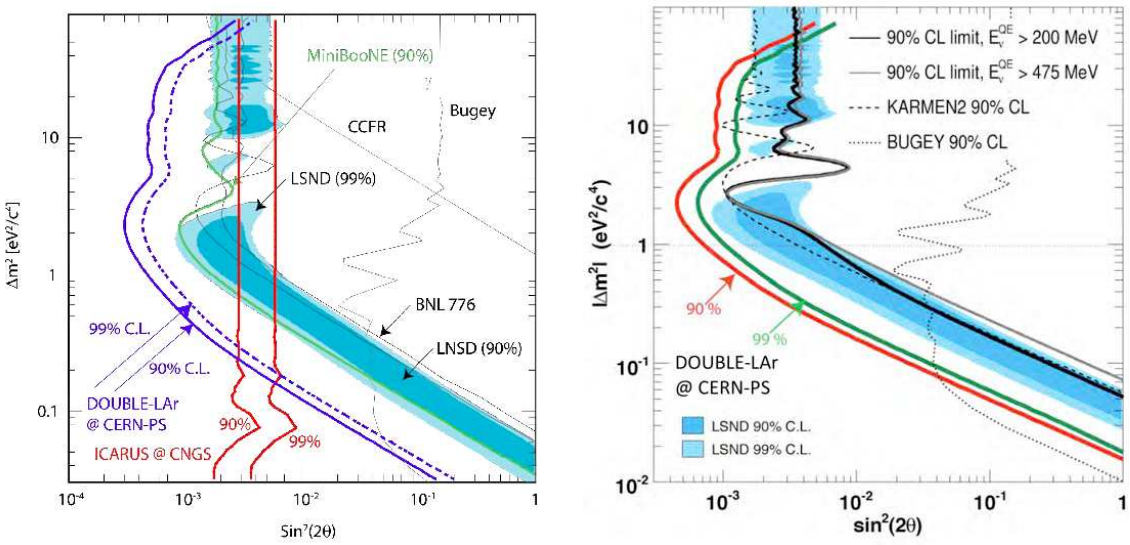

Figure 3: Expected sensitivity for the proposed experiment exposed at the CERN-PS neutrino beam (left) and anti-neutrino (right) for 2.5×10^{20} pot. The LSND allowed region is fully explored both for neutrinos. In the neutrino case, the expectations from CNGS2/ICARUS T600 at LNGS are also shown.

experimental and cross-section biases cancels out. It would thus be possible to perform the search for both $\nu_\mu \rightarrow \nu_e$ LSND appearance signal and $\nu_\mu \rightarrow \nu_x$ reactor disappearance anomaly, with promising sensitivity in only 2(4) years data taking in neutrino (antineutrino) mode, as shown in figure 3.

5 Conclusions

The ICARUS-T600 detector, installed underground at the LNGS laboratory, has started data taking during 2010 after a long R&D and installation phase. The successful assembly and operation of this LAr-TPC is the experimental proof that this technique is mature. It has demonstrated to have unique imaging capability, spatial and calorimetric resolutions and the possibility to efficiently distinguish electron from π^0 signals, thus allowing to reconstruct and identify events in a new way with respect to the other neutrino experiments. After a short commissioning phase this experiment is ready for the 2011-2012 run, addressing a wide physics programme. The main goal is to collect events from the CNGS neutrinos beam from CERN-SPS to search for the $\nu_\mu \rightarrow \nu_\tau$ oscillation, but also to study solar and atmospheric neutrino and explore in a new way the nucleon stability in particular channels beyond the present limits. Furthermore ICARUS-T600 is so far the major milestone towards the realization of a much more massive LAr detector. Actually the employment of this technique at a refurbished CERN-PS ν beam has been proposed after the ICARUS-T600 exploitation at LNGS to definitely solve the sterile neutrino puzzle.

References

[1] C.Rubbia, *"The Liquid-Argon Time Projection Chamber: A new Concept for Neutrino Detector"*, CERN-EP/77-08 (1977).
[2] P.Benetti et al., Nucl. Instr. and Meth. **A332** (1993) 395
[3] P.Cennini et al., Nucl. Instr. and Meth. **A345** (1994) 230
[4] F.Arneodo et al., Nucl. Instr. and Meth. **A449** (2000) 36
[5] F.Arneodo et al., Nucl. Instr. and Meth. **A498** (2003) 292
[6] B.Kegl et al., IEEE Trans. Patt. An. and Mach. Intell. **22** (2000) 381
[7] A.Ankowski et al., Acta Phys. Pol. **B41** (2010) 103
[8] S.Amoruso et al., Eur. Phys. J. **C33** (2004) 233
[9] A.Ankowski et al., Eur. Phys. J. **C48** (2006) 667
[10] A.A.Aguilar-Arevalo et al., Phys. Rev. Lett. **105** (2010) 181801
[11] G.Mention et al., Phys. Rev. **D83** (2011) 073006
[12] J.N.Abdurashitov et al., Phys. Rev. **C73** (2006) 045805
[13] E.Komatsu et al., Astrophys. J. Suppl. **192** (2010) 18
[14] Y.I.Izotov and T.X. Thuan, Astrophys. J. **710** (2010) L67
[15] B.Baibussionov et al., arXiv:0909.0355
C.Rubbia CERN-SPSC-2011-012
C.Rubbia SPSC-M-773 (2011)

HE.2.3: Neutrino telescopes and neutrino astronomy

32ND INTERNATIONAL COSMIC RAY CONFERENCE, BEIJING 2011

Magnetic Field and Flavor Effects in Gamma-Ray Burst Neutrino Fluxes

PHILIPP BAERWALD[1,*], SVENJA HÜMMER[1], WALTER WINTER[1]
[1] *Institut für Theoretische Physik und Astrophysik, Universität Würzburg, 97074 Würzburg, Germany*
[*] *Speaker*
philipp.baerwald@physik.uni-wuerzburg.de
DOI: 10.7529/ICRC2011/V04/0036

Abstract: We reanalyze the prompt neutrino flux from gamma-ray bursts (GRBs) on the basis of the particle physics involved. Using the example of the often used reference Waxman-Bahcall GRB flux, we show how a specific flux shape is changed to a "double peak"-structure by considering a more detailed treatment of the photohadronic interactions, the dominant loss mechanisms, and flavor mixing. We also discuss the robustness of this prediction in diffuse or stacked fluxes, which depends on the distribution of the burst parameters. For example, we show that the redshift distribution is dominated by $z \approx 1$.

Keywords: high energy neutrinos, gamma-ray bursts, multi-messenger physics

1 Introduction

In recent years, neutrino telescopes, such as IceCube [1], have led to significant progress in the field of astrophysical neutrinos and its possible contribution to multi-messenger physics. The connection of neutrinos to highly energetic events such as gamma-ray bursts (GRBs) could help to determine if GRBs are a source of the ultra high energy cosmic rays (UHECR). The different GRB models, such as the fireball model [2] or the cannonball model [3], predict the production of high energy protons. However, so far, the non-detection of high energy astrophysical neutrinos has only led to tighter contraints on the different astrophysical source models. Most prominently, it was recently announced in Ref. [4] that the most general form of the GRB fireball model is already under pressure by the IceCube-40 diffuse flux limit. As a consequence, it might be time to take a closer look at the original calculations and what the systematics of the input assumtions are.

2 Revising the GRB Neutrino Flux

The generally accepted concept for gamma-ray bursts (GRBs) is based on charged particles, *i.e.* electrons and protons, being ejected with highly relativistic velocities from a compact central object. The ejection of these particles leads to the formation of relativistic shocks at which the particles can be accelerated even further. The accelerated electrons transfer their energy to photons leading to the characteristic high energy emission detected at the Earth. The exact mechanism used to describe this transfer depends on the GRB model. The measured photon spectrum of a GRB is commonly described by a Band function [5]. The spectrum of the emitted protons of a GRB can not be directly probed with today's methods. However, it is assumed that these GRB protons are connected to the extra-galactic component of the cosmic ray spectrum, and therefore a E^{-2} spectrum is assumed for the GRB protons. A possible way to verify this assumption and GRB being a source of UHECR would be a detection in neutrinos. This should be possible as the accelerated protons could interact with the emitted photons inside the GRB. Photohadronic interactions can lead to the production of charged pions. Hence, the decay (chain) of the charged pions produces neutrinos. For most calculations of the neutrino flux from GRB, such as the one by Waxman and Bahcall (WB) [6], these $p\gamma$-interactions are approximated with the Δ-resonance[1],

$$p + \gamma \to \Delta^+ \to \pi + p' \quad . \tag{1}$$

Here π can be a charged or a neutral pion while p' is either a neutron or a proton. The resulting prompt GRB neutrino emission is generally considered to have the so-called WB flux shape, taken from Ref. [6], for the aforementioned in-

1. Technically there are several of these approximations which parameterize the interaction cross section slightly different, but all are dubbed "Δ-resonance approximation". Even the one used by Waxman and Bahcall in Ref. [6] implies additional production modes.

put spectra,

$$E_\nu^2 \phi \propto \begin{cases} \left(\frac{E_\nu}{E_{\nu,\mathrm{b}}}\right)^{\alpha_\nu} & \text{for } E_\nu < E_{\nu,\mathrm{b}} \\ \left(\frac{E_\nu}{E_{\nu,\mathrm{b}}}\right)^{\beta_\nu} & \text{for } E_{\nu,\mathrm{b}} \leq E_\nu < E_{\nu,\pi} \\ \left(\frac{E_\nu}{E_{\nu,\mathrm{b}}}\right)^{\beta_\nu} \left(\frac{E_\nu}{E_{\nu,\pi}}\right)^{-2} & \text{for } E_\nu \geq E_{\nu,\pi} \end{cases} \tag{2}$$

with $\alpha_\nu \simeq +1$ and $\beta_\nu \simeq 0$, where this form applies to the muon neutrinos from pion decays. The values for the break energies used in Ref. [6] are $E_{\nu,\mathrm{b}} \simeq 10^5\,\mathrm{GeV}$ and $E_{\nu,\pi} \simeq 10^7\,\mathrm{GeV}$. However, as discussed in Refs. [7, 8], a more detailed treatment of the particle interactions should be applied. In a multi-step process it was first shown that by only inserting the aforementionend photon and proton spectra it is possible to reproduce the WB flux shape numerically from the Δ-resonance approximation used in Ref. [6]. On the other hand, it is possible to simulate photohadronic interactions with Monte Carlo codes such as the SOPHIA algorithm [9]. The results from SOPHIA show that apart from the $\Delta(1232)$-resonance the full photohadronic cross section includes contributions from higher resonances, direct (t-channel) processes, and high energy processes which can lead to the production of multiple charged pions (of both signs). Hence, a analytic parameterization of the SOPHIA result, taken from Ref. [10], was used in the next steps. Moreover, it is essential for the correct simulation of the particle interactions and decays not to integrate out intermediate particles and treat the losses for each particle species individually. Especially synchrotron losses due to the magnetic fields present in the interaction region lead to a separation of the different particle species, in case of $p\gamma$ interactions in GRBs mainly $\pi^\pm$, $\mu^\pm$, and K^+, when looking at the energy spectrum, see Ref. [11]. The break energy due to synchrotron losses E_c strongly depends on particle properties as described by the formula

$$E_c = \sqrt{\frac{9\pi\epsilon_0 m^5 c^5}{\tau_0 e^4 B^2}}\,, \tag{3}$$

where B is the magnetic field, and m and τ_0 are the rest frame mass and life time of the type of particle, respectively. Another phenomenom which needs to be accounted for when discussing neutrinos in general is neutrino flavor mixing. As GRBs are considered to be events at cosmologic distances, it is sufficient to include flavor mixing as averaged neutrino oscillations. Thus, the full photohadronic interaction cross section together with the effect of synchrotron losses of intermediate particles and flavor mixing alter the neutrino flux, resulting in a characteristic neutrino flux shape at the observer, see figure 1. In figure 1 the muon neutrino (and muon anti-neutrino) flux at the observer is depicted (thick solid curve), including the contributions from additional particle decays such as n or K^+, for details see Ref. [8]. The contributions from ν_e (dashed curve) and ν_μ (dotted curve) are also depicted. The gray band represent the uncertainty on the flux due to the current precision on the neutrino mixing angles. The thin dashed line represents the classical WB flux shape. Still, as one can see a "double peak" from the neutrinos from pion and muon decay replaces the plateau of the WB spectrum. Moreover, a high energy contribution from kaon decays gives a visible bump. Thus, it may be possible to determine the value of the magnetic field of a GRB from the neutrino data, since the magnetic field can be calculated from the (synchrotron cooling) breaks in the neutrino spectrum. Figure 1 also includes an alternative normalization of the muon neutrino spectrum (thin solid curve) by scaling the flux depending on the total energy in muon neutrinos compared to the WB spectrum.

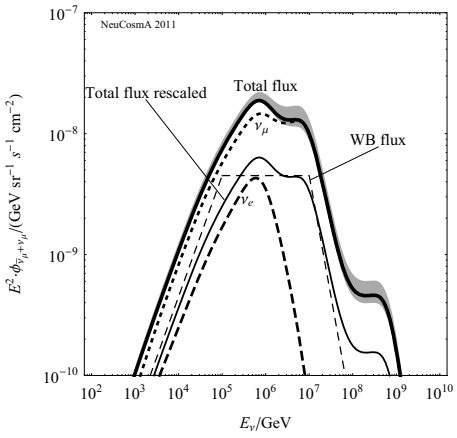

Figure 1: This figure shows the resulting muon neutrino (and anti-neutrino) flux on earth after considering the full photohadronic cross section, magnetic field effects on the intermediate particles and flavor mixing of the produced neutrinos (thick solid curve). Also depicted are the relative contributions from ν_e (dashed curve) and ν_μ (dotted curve). The shaded area represents the uncertainty range originating from the current bounds of the neutrino mixing angles. The thin dashed line represents the well-known WB spectrum. The thin solid line is a rescaled version of the thick solid line, however with the total energy in muon neutrinos normalized to the WB spectrum. The figure is adapted from Ref. [8].

3 Systematics in Aggregated Fluxes

The detailed analysis of GRB in recent years has shown that the measured parameters of GRB are distributed over a wide range. Therefore, it is important to understand the individual effect of each parameter on the spectrum. Here, simulations are a plausible tool to deconvolute the effect of the parameters, as real spectra are affected from all of them. Hence, the effect of the separate parameters, namely the magnetic field B, the Lorentz factor Γ, the photon spectrum and the redshift z, was examined. In the next section the effect of this distribution will be illustrated at

the example of z.

A parameter that recently was discussed as an essential part of GRB flux calculations is the redshift z. Even though measurements of z have only been possible after the discovery of the optical afterglows, it was already possible to measure the redshift of a significant fraction of GRBs. Furthermore, afterglow measurements led to the identification of the connection of long ($T_{90} > 2\,\mathrm{s}$) GRBs to core-collapse supernovae. It is therefore a reasonable assumption that the (long) GRB rate follows the star formation rate (SFR). However, how justified is this assumption and how does the redshift affect the diffuse flux from GRBs? One should remember that for a diffuse flux computation all sources have to be considered, *e.g.* by numerical integration. Unfortunately, the known number of GRBs is still limited for a diffuse flux. A commonly used approach for other astrophysical sources is a stacking analysis of the brightest known sources. This approach only has limited accuracy. Still, since it is possible to simulate identical bursts at different redshifts, a viable method to quantify the effect of the distribution of z is by combining both approaches. By generating a larger number of bursts at different redshifts using Monte Carlo sampling and aggregating the single burst spectra, it is possible to obtain an (quasi-)diffuse "aggregated flux". A sample size of 10000 bursts seems realistic for this method, assuming a time window of 10 years of data taking and 1000 bursts per year. The probability to pick a z is derived from the SFR by Hopkins and Beacom [12] including the correction factor for the evolution of the GRB rate with z introduced by Kistler *et al.* [13]. As each burst has the same properties at the source, the contribution to diffuse flux is determined by the scaling of the flux ϕ_ν with redshift, $E_\nu^2\phi_\nu \propto d_L^{-2}(z)$. Here, $d_L(z)$ is the luminosity distance which can be written as a function of z in the standard Λ-CDM cosmology. In the left plot of figure 2 the distribution of the 10000 bursts with randomly distributed redshifts following the aforementioned star formation rate is depicted (histogram). The figure also includes the analytic function for the number of bursts $\mathrm{d}N/\mathrm{d}z$ (dashed curve) and the relative contribution of bursts at z to the total diffuse flux, $\mathrm{d}N/\mathrm{d}z \cdot d_L^{-2}(z)$ (solid curve). As can be seen from the histogram in figure 2 the largest number of bursts is found at $z \approx 2-3$. However, the main contribution comes from bursts at $z \approx 1$. Therefore, nearly all neutrinos of the diffuse flux should come from bursts with $z \leq 2$, assuming every burst is intrinsically identical apart from the redshift. Moreover, as one can see from the depicted aggregated flux in the right plot of figure 2 there should also be a shift to higher energies compared to the "standard burst" (dashed curve) from the previous section, due to $E \propto (1+z)^{-1}$. Hence, the z value of the peak of $\mathrm{d}N/\mathrm{d}z$ may not be an ideal choice, as the main contribution to the diffuse neutrino flux should come from bursts with $z \approx 1$. Also, when calculating back from the observed flux, assuming $z = 2$ leads to an overestimation the flux from the GRB. Moreover, by comparing the histogram to the peak of the relative contribution function at $z \approx 1$ it is possible to conclude that rare, but quite close bursts still yield a significant flux. In case of a stacking analysis this can have an significant impact on extrapolated bounds, especially if only few bursts are stacked.

When analyzing the flux bounds from astrophysical sources one also has to consider the effect of the low statistics. Thus, using only a very limited number of GRB for the extrapolation of a flux limit only gives limited precision. For a set of 50 burst the probability to be within $\pm 20\%$ of the actual diffuse flux is only 30%, which rises to 51% for 300 bursts and 94% for 10000 bursts.

Moreover, the effect of the other parameters also alters the result for the diffuse GRB neutrino flux. The distribution of the magnetic field, the Lorentz factor and the parameters of the photon spectrum, *i.e.* the spectral indices and the photon break energy, changes the flux shape and/or the normalization. First of all, the magnetic field distribution can lead to an obscuration of the single burst features of the flux shape when the distribution is too wide. Second, again depending on the actual source model, the Lorentz factor can either solely changes the normalization and not affect the shape apart from a shift in energy, or it can also totally obscure the single flux shape. However, compared to z the distribution of Γ is poorly known as this parameter can so far only be obtained for very few bursts, and not even a conclusive approach for the distribution is currently available. This result therefore is rather speculative. Third, the photon spectrum changes details such as the first slope of the spectrum is steeper compared to the considered single burst, the low energy break of the neutrino spectrum is shifted to higher energies (due to a lower energy photon break), and the peaks from pion decays gets enhanced compared to the peak from muon decays, but the basic shape is unaffected.

4 Summary and Conclusions

It has been shown that it is possible to numerically reproduce the well-known WB flux shape of GRB neutrinos from the classic Band function photons and a E^{-2} proton spectrum using the Δ-resonance approximation of $p\gamma$ interactions. Then the effect of the full photohadronic cross section was probed using an analytic parameterization of the full photohadronic interaction cross section. In this approach intermediate particles are not integrated out and losses such as synchrotron losses can be treated for each particle species individually. Moreover, with respect flavor mixing the muon neutrino flux shape at the observer was altered to a characteristic "double peak" shape plus a high energy contribution from kaon decays. Especially the breaks in the neutrino flux spectrum from synchrotron cooling of secondaries could be used to probe the magnetic field, if ever a high enough detection rate of

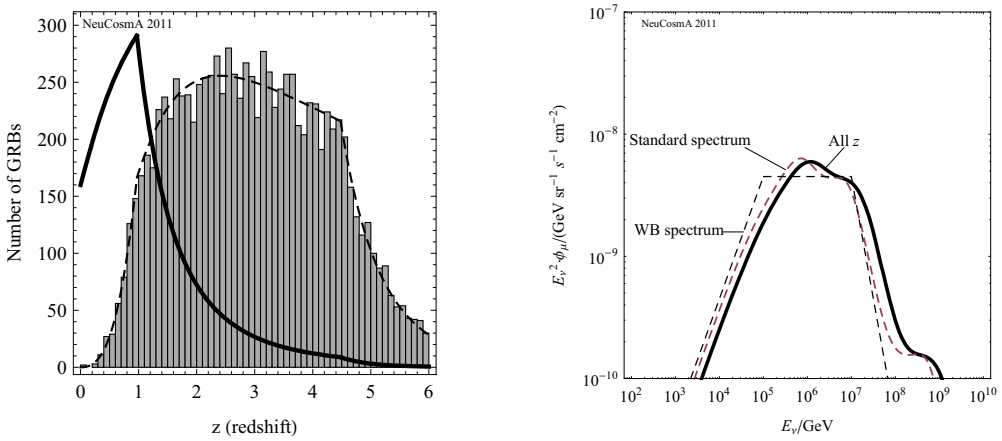

Figure 2: In the left plot the distribution of 10000 bursts with random z values is depicted (histogram), the dashed curve represents the analytic GRB rate depending on redshift derived from the SFR by Hopkins and Beacom [12] including a correction for evolution with redshift, taken from Ref. [13]. The thick solid curve represents the relative contribution of bursts at a redshift z to the total diffuse flux which is calculated by multiplying $d_L^{-2}(z)$ to the GRB rate. The right plot depicts the aggregated flux (thick solid curve), compared to the single burst flux (dashed curve). The normalization of the total flux is done by matching the energy in muon neutrinos to the one in the WB spectrum (thin dashed curve). Both plots are adapted from Ref. [14].

these neutrinos would be achieved. In a next step the effect of the distribution of individual parameters was probed. It is shown at the example of the redshift z how the GRB rate, based on the star formation rate, may peak at redshifts $z \approx 2-3$, but the neutrino flux is dominated by bursts with $z \approx 1$. This can lead to a difference in flux up to a factor of 5. Similar effects of the most common burst not leading to the main contribution were also found for the magnetic field, the Lorentz factor, and the target photon field defined by the spectral indices and the photon break energy. In case of the magnetic field this can lead to a smearing out of the single burst features for a wide distribution as the peak of the flux shape strongly depends on B. Due to the lack of data the effect of Γ is more speculative and dependent on the source model. The photon spectrum variation leads to a steeper first slope, a shift of the first break of the neutrino spectrum to higher energies, and an enhancement of the peak from pions and the kaon contribution. In a final step the effect of (low) statistics effects on stacking analysis was discussed again using the redshift as the example of choice. It was concluded that 10000 bursts are needed to probe the diffuse flux with low uncertainty.

In the future, it may be possible to use this framework for the analysis of measured photon spectra of GRB. However, the parameters such as the Lorentz factor and the magnetic field, which are needed for the simulation, are in general hard to measure.

Acknowledgements: P.B. is supported by the DFG Graduiertenkolleg GRK1147 Theoretische Astrophysik und Teilchenphysik.

References

[1] J. Ahrens et al. (IceCube collaboration), Astropart. Phys., 2004, **20**(5): 507-532
[2] P. Meszaros, M.J. Rees, Astrophys. J., 1993, **405**(1): 278-284
[3] A. Dar, A. De Rujula, Phys. Rept., 2004, **405**(4): 203-278
[4] M. Ahlers, M.C. Gonzalez-Garcia, F. Halzen, **arXiv:1103.3421v1** [astro-ph.HE]
[5] D. Band et al., Astrophys. J., 1993, **413**(1): 281-292
[6] E. Waxman, J.N. Bahcall, Phys. Rev. Lett., 1997, **78**(12): 2292-2295
[7] P. Lipari, M. Lusignoli, D. Meloni, Phys. Rev., 2007, **D75**(12): 123005
[8] P. Baerwald, S. Hümmer, W. Winter, Phys. Rev., 2011, **D83**(6), 067303
[9] A. Mücke et al., Comput.Phys.Commun., 2000, **124**(2-3): 290-314
[10] S.R. Kelner, F.A. Aharonian, Phys. Rev., 2008, **D78**(3): 034013
[11] T. Kashti, E. Waxman, Phys. Rev. Lett., 2005, **95**(18): 181101
[12] A.M. Hopkins, J.F. Beacom, Astrophys. J., 2006, **651**(1): 142-154
[13] M.D. Kistler et al., Astrophys. J., 2009, **705**(2): L104-L108
[14] P. Baerwald, S. Hümmer, W. Winter, *to appear*

32ND INTERNATIONAL COSMIC RAY CONFERENCE, BEIJING 2011

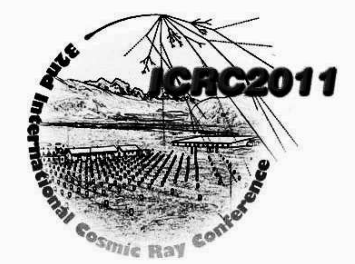

Atmospheric Muon Spectrum from Catastrophic Energy Losses in IceCube

THE ICECUBE COLLABORATION[1]
[1]*See special section in these proceedings*

Abstract: While the primary purpose of IceCube is the search for high-energy astrophysical neutrinos, the overwhelming majority of events is caused by downgoing cosmic-ray induced muons. This provides a high-statistics data set which can be used for both detector calibration and supplemental physics investigations. In this work, we present a method to identify TeV-scale catastrophic energy losses along muon tracks and its application to the separation of single high-energy muons from large-multiplicity bundles which dominate the event sample above the horizon at high energies. The information can be used to derive the single-muon energy spectrum at all zenith angles up to energies of hundreds of TeV. We demonstrate that our measurement is sensitive to a cutoff of the proton spectrum at the cosmic ray knee and potentially to the prompt lepton flux caused predominantly by decay of charmed hadrons in atmospheric CR interactions.

Corresponding authors: Patrick Berghaus[2] *(berghaus@icecube.wisc.edu)*, Chen Xu[2] *(chen@udel.edu)*
[2]Bartol Research Institute, University of Delaware, USA

DOI: 10.7529/ICRC2011/V04/0085

Keywords: Muon Spectrum, Stochastic Losses, Knee

1 Introduction

In recent work on high-energy atmospheric muon fluxes, it was pointed out that second-generation astrophysical neutrino detectors such as IceCube should be able to substantially extend the energy range of muon energy spectrum measurements and hence address various important open problems in cosmic-ray physics. These include verification of hadronic interaction models, primary composition at PeV energies and prompt contributions to the lepton flux [1].

From an experimental perspective, the main challenge in the measurement of the muon energy spectrum is limited spatial resolution due to the sparse instrumentation of the detector. With a minimum separation of 17 meters between Digital Optical Modules (DOMs) in IceCube, resolution of individual muons within a shower is usually impossible. Previous measurements [2, 3] took advantage of the shorter range of large-multiplicity muon bundles compared to individual high-energy muons during passage through matter to measure the muon spectrum at large slant depths near the horizon. The limited angular resolution of the detector and background from up-going atmospheric neutrinos mean that the range of this technique is limited to values up to approximately 100 TeV. Furthermore, the muon spectrum can in this way only be measured in an angular region where the relative contribution from prompt interactions is lowest, excluding investigation of this flux component for practical purposes.

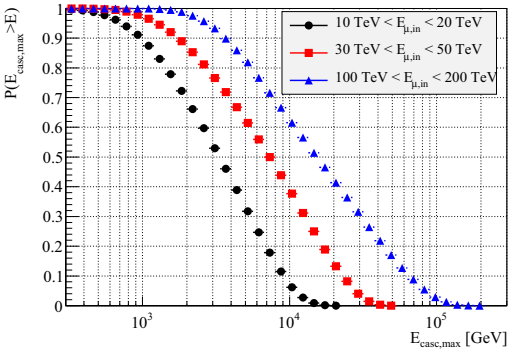

Figure 1: Probability for a stochastic loss above a given energy to occur within the detector volume, for three typical muon energy ranges. The simulation was performed using MMC [5].

In order to take advantage of the full potential of a large-volume detector, it is therefore necessary to develop a method that allows separation of showers with exceptionally highly energetic muons from the dominant background of bundles containing low-energy muons of higher multiplicity. It has long been proposed to make use of the fact that the stochasticity of energy deposition along muon tracks increases with energy [4]. In this analysis, by identifying muon track segments with unusually strong photon

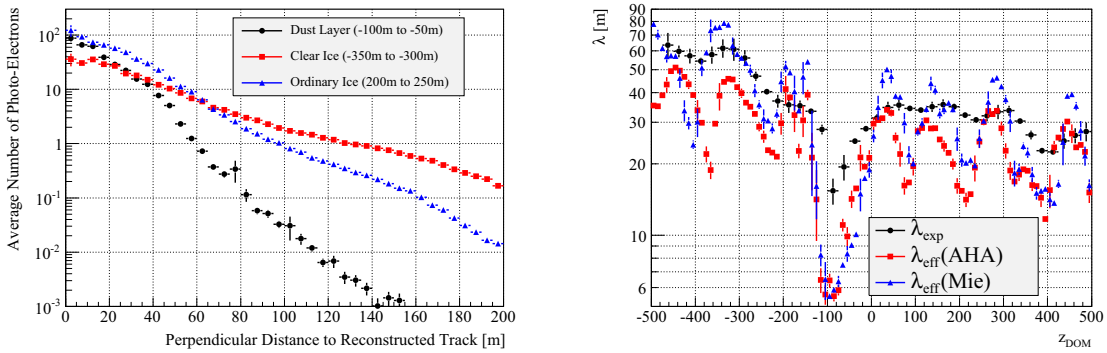

Figure 2: Left: Average number of photo-electrons registered in IceCube DOMs as a function of perpendicular distance from reconstructed muon tracks for three different depth bins. Values are averaged over events with a total charge $Q_{tot} > 1000$ p.e. Right: Value of scattering parameter λ_{exp} from fitting distributions on the left to Eq. 1 in dependence of vertical depth. The value of $z_{DOM} = 0$ corresponds to the center of the IceCube array, located 1950 meters below the surface of the ice. The effective scattering length in two different ice models [6] is included for comparison. It is important to note that the physical meaning of λ_{eff} and λ_{exp} is not identical. Fine structures in the depth dependence are inherently smeared out in the experimentally derived parameter.

emission, the amplitude of individual stochastic losses can be used to infer the most likely energy of the parent muon, as illustrated in Figure 1.

2 Energy Estimation Method

The IceCube detector array records Cherenkov photons emitted by relativistic particles during passage through ice. The amount of charge in the optical modules provides calorimetric information that can be used to calculate the energy released in the event.

Previous energy reconstructions relied on prior assumptions about ice properties whose accuracy was necessarily limited. The method described here is based exclusively on experimental observations. Its is based on two simple assumptions:

- Down-going tracks in IceCube consist mainly of muon bundles dominated by minimum-ionizing muons which lose their energy smoothly and continuously.
- The total number of emitted Cherenkov photons is in good approximation proportional to the deposited energy.

As illustrated in Figure 2, the total amount of light registered in the DOMs can then be approximated by the empirical function

$$\frac{dE(x=x_0)}{dx} \propto Q(x_0) \cdot d(x_0) \cdot \exp\left(\frac{d(x_0)-25}{\lambda_{exp}(x_0)}\right) \quad (1)$$

where $\frac{dE(x)}{dx}$ is the energy loss at vertical depth x, Q is the total charge in each DOM and d is the perpendicular distance between a DOM and the reconstructed muon track.

This data-derived model only relies on a single scattering parameter λ_{exp}, which varies in dependence of the local ice properties. From the charge in each DOM, it is possible to calculate a value that is approximately proportional to the energy deposited in its vicinity. Monte-Carlo simulated data are only required to determine the proportionality factor in Eq. 1 and for verification. Assuming point-like isotropic emitters on the track, clusters of exceptionally high values can be used to identify energetic stochastic energy losses. An example can be seen in Figure 3.

There are two important additional benefits that arise naturally from this technique. The first is the reduction of biases resulting from uncertainties about exact ice properties, allowing for detailed investigation of simulation biases. The other is the availability of information about differential energy deposition, permitting the construction of more accurate event energy estimators.

3 Analysis Procedure

This analysis was based on data from IceCube in its 59-string configuration (IC59). Only events with a total of more than one thousand photo-electrons registered in the detector were considered. This selection provides a sample of events at all zenith angles which is not biased by the quality criteria used to select physics filter streams.

The analysis procedure itself mainly consists of two relatively simple steps. First, a sample of muon tracks with strong stochastic losses inside the detector volume were identified. Then, the energy of the strongest single energy deposition was reconstructed and its spectrum compared to various benchmark models.

The principal conditions that were imposed in the selection are:

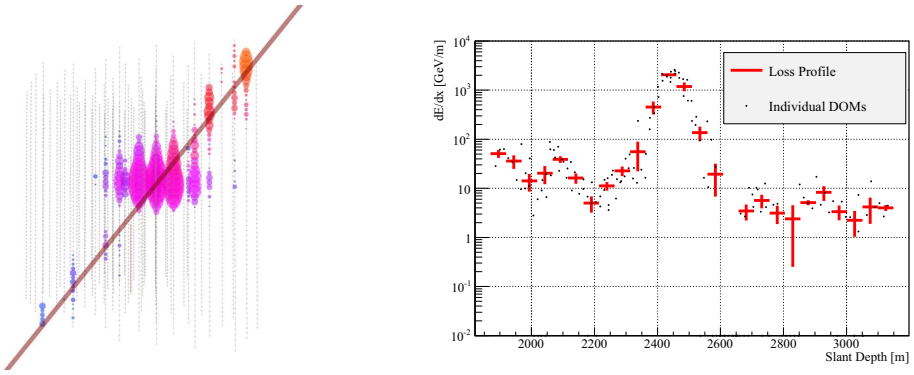

Figure 3: Example for massive stochastic loss event found in IC59 data. The energy deposition estimate shown on the right hand side is consistent with an 80 TeV cascade. The x-axis corresponds to the distance along the track, measured from the surface of the ice.

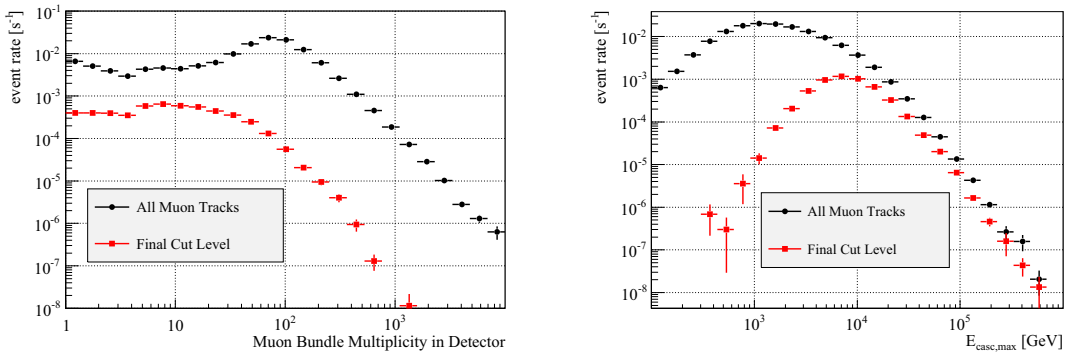

Figure 4: Left: Muon multiplicity in cosmic-ray showers at entry into detector volume before and after selection cuts, simulated using CORSIKA/SIBYLL. The analysis favors muon bundles of moderate multiplicities while reducing both high-multiplicity bundles and low-energy tracks with high recorded DOM charges due to unusual topologies. Right: Effect of selection cuts in dependence of true maximum stochastic loss energy. The effective threshold energy lies around 10 TeV.

- Presence of a well-reconstructed muon track with a length of at least 600 meters inside the detector volume.
- A peak energy loss value in a 50-meter bin along the track which exceeds the median differential energy loss in the event by a factor of 10.
- Location of peak energy loss within 150 meters from at least 50 DOMs, assuring containment within the main detector volume.

Figure 4 shows the cumulative effect of the cuts.

So far, the effective threshold energy for stochastic losses lies around 10 TeV. It is in principle possible to reduce this threshold further by relaxing the requirement on the total recorded DOM charge.

4 Result

To estimate the sensitivity of the method, the measured energy spectrum of stochastic losses was compared to simulations based on various primary composition models [7]:

- **Constant Composition**: The spectrum of each primary nucleus type changes by the same amount at an energy corresponding to the cosmic-ray knee.
- **Rigidity-Dependent Cutoff**: Each component of the cosmic ray flux is subject to a cutoff at an energy that is proportional to the charge of the nucleus.
- **Mass-Dependent Cutoff**: Similar to the previous model, but assuming a cutoff dependent on the nuclear mass. The main distinction here is a sharper transition, resulting in a stronger cutoff signature.
- **No Knee**: This additional model was included for purposes of illustration only, assuming unbroken spectra for each component and therefore completely

eliminating the knee. It should be noted that this assumption is strongly disfavored by previous experimental results.

Figure 5 shows the preliminary result, based on a subsample of 10 percent of the data taken with IC59. For models incorporating a cutoff in the individual primary spectra, a corresponding effect can clearly be discerned in the simulated muon-induced stochastic losses. The limited experimental statistics do not yet allow any definite statement about preferred models, even while neglecting systematic uncertainties.

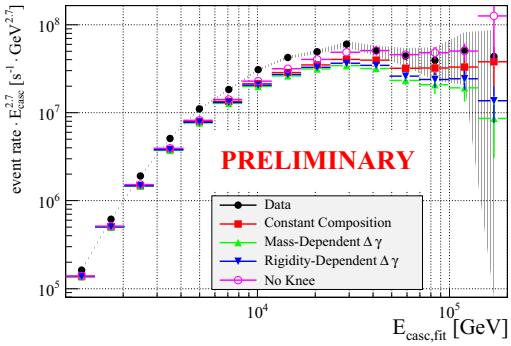

Figure 5: Comparison of reconstructed maximum stochastic loss energy for simulated and experimental data summed over all zenith angles. All simulated curves were obtained by reweighting the same data set generated with CORSIKA. Experimental data correspond to a subset of ten percent of IC59 events. The error band is purely statistical.

5 Conclusion and Outlook

As can be seen from comparing Figures 5 and 6, the highest muon energy found in the analyzed sample is most likely located around 500 TeV, with slight variations depending on the exact primary spectrum. This means that despite the fact that the spectrum falls off almost as the fourth power of the particle energy, the range of the measurement can be extended by roughly an order of magnitude compared to earlier experiments. The method presented here furthermore allows the measurement of cosmic-ray induced muon spectra independently of the zenith angle, introducing an entirely new degree of freedom.

Consequently, it will be possible to address a variety of new physics issues that were previously inaccessible. It has already been demonstrated that the behavior of cosmic rays around the knee can now be probed directly. A separate but equally important question is the contribution of prompt production processes to lepton fluxes at high energies. In optimistic models, the charm-induced component becomes dominant around 300 TeV at near-vertical angles [8] and would therefore be directly measurable. If on the other

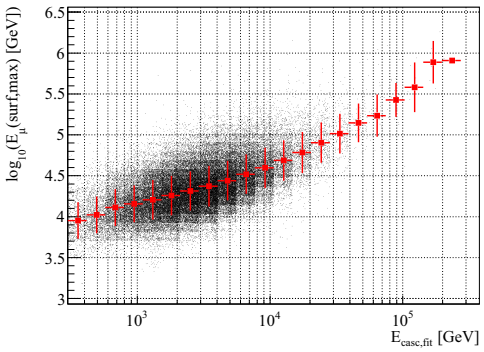

Figure 6: Relation between reconstructed cascade and muon surface energy obtained from Monte-Carlo simulation, assuming a poly-gonato primary spectrum and neglectic prompt muons. The change in slope around 10 TeV can be attributed to threshold effects.

hand the prompt muon flux were low enough to be dominated by decays of unflavored light mesons [9], it should be possible to set a stringent limit that would strongly constrain the atmospheric neutrino background in searches for astrophysical sources.

It should also be emphasized that the method to distinguish unusually energetic muons from large-multiplicity background events is readily adaptable for analyses targeting neutrino fluxes at energies in the PeV range.

References

[1] S. I. Sinegovsky, A. A. Kochanov, T. S. Sinegovskaya, A. Misaki and N. Takahashi, Int. J. Mod. Phys. A **25** (2010) 3733, [arXiv:0906.3791].

[2] P. Desiati [AMANDA Collaboration], *Proc. of ICRC 2003*.

[3] P. Berghaus [IceCube Collaboration], *Proc. of ICRC 2009*, [arXiv:1004.2093].

[4] R. P. Kokoulin and A. A. Petrukhin, Nucl. Instrum. Meth. A **263** (1988) 468.

[5] D. Chirkin and W. Rhode, [arXiv:hep-ph/0407075].

[6] See the contribution by D. Chirkin in these proceedings.

[7] J. R. Hörandel, Astropart. Phys. **19**, 193 (2003), [arXiv:astro-ph/0210453].

[8] T. K. Gaisser, Nucl. Phys. Proc. Suppl. **118** (2003) 109, [arXiv:astro-ph/0502380].

[9] J. I. Illana, P. Lipari, M. Masip and D. Meloni, Astropart. Phys. **34** (2011) 663, [arXiv:1010.5084].

32ND INTERNATIONAL COSMIC RAY CONFERENCE, BEIJING 2011

Search for neutrinos from transient sources with the ANTARES telescope and optical follow-up observations

AGERON M.[1], AKERLOF C.[2], AL SAMARAI I.[1], BASA S.[3], BERTIN V.[1], BOER M.[4], BRUNNER J.[1], BUSTO J.[1], DORNIC D.[5], KLOTZ A.[4,6], SCHÜSSLER F.[7], VALLAGE B.[7], VECCHI M.[1] AND ZHENG W.[2] ON BEHALF THE ANTARES, TAROT AND ROTSE COLLABORATIONS

[1] *CPPM, CNRS/IN2P3 - Université de Méditerranée, 163 avenue de Luminy, 13288 Marseille Cedex 09, France* [2] *Randall Laboratory of Physics, Univ. of Michigan, 450 Church Street, Ann Arbor, MI, 48109-1040, USA* [3] *LAM, BP8, Traverse du siphon, 13376 Marseille Cedex 12, France* [4] *OHP, 04870 Saint Michel de l'Observatoire, France* [5] *IFIC - Instituto de F0̆131sica Corpuscular, Edificios Investigacion de Paterna, CSIC - Universitat de Val'encia, Apdo. de Correos 22085, 46071 Valencia, Spain* [6] *IRAP, 9, avenue du Colonel Roche, BP44346, 31028 Toulouse Cedex 4, France* [7] *CEA-IRFU, centre de Saclay, 91191 Gif-sur-Yvette, France*

dornic@ific.uv.es

DOI: 10.7529/ICRC2011/V04/0090

Abstract: The ANTARES telescope is well suited to detect neutrinos produced in astrophysical transient sources as it can observe a full hemisphere of the sky at all the times with a duty cycle close to unity and an angular resolution better than 0.5 degrees. Potential sources include gamma-ray bursts (GRBs), core collapse supernovae (SNe), and flaring active galactid nuclei (AGNs). To enhance the sensitivity of ANTARES to such sources, a new detection method based on coincident observations of neutrinos and optical signals has been developed. A fast online muon track reconstruction is used to trigger a network of small automatic optical telescopes. Such alerts are generated one or two times per month for special events such as two or more neutrinos coincident in time and direction or single neutrinos of very high energy. Since February 2009, ANTARES has sent 37 alert triggers to the TAROT and ROTSE telescope networks, 27 of them have been followed. First results on the optical images analysis to search for GRB and core-collapse SNe will be presented.

Keywords: high energy neutrino, GRB, optical follow-up.

1 Introduction

The detection of high energy cosmic neutrino from a source would be a direct evidence of the presence of hadronic acceleration within the source and provide important information on the origin of the high energy cosmic rays. Powerful sources of transient nature, such as gamma ray bursts or core collapse supernovae, offer one of the most promising perspectives for the detection of cosmic neutrinos as, due to their short duration, the background from atmospheric neutrinos and muons is strongly reduced. For example, several authors predict the emission of neutrinos in correlation with multi-wavelength signals, e.g. the Fireball model of GRBs [1]. As neutrino telescopes observe a full hemisphere of the sky (even the whole sky if downgoing events are considered) at all times, they are particularly well suited for the detection of transient phenomena.

The ANTARES neutrino telescope [2] is located in the Mediterranean sea, 40 km South of the french coast of Toulon, at a depth of about 2500 m below sea level. The detector is an array of photomultipliers tubes (PMTs) arranged on 12 slender vertical detection lines. Each string comprises up to 25 floors, i.e. triplets of optical modules (OMs) housing one PMT each. Data taking started in 2006 with the operation of the first line of the detector. The construction of the 12 line detector was completed in 2008. The main goal of the experiment is to search for neutrinos of astrophysical origin by detecting high energy muons ($\geq$100 GeV) induced by their neutrino charged current interaction in the vicinity of the detector. Due to the large background from downgoing cosmic ray induced muons, the detector is optimised for the detection of upgoing neutrino induced muon tracks.

In this paper, the implementation and the first results of a strategy for the detection of transient sources is presented. This method, earlier proposed in [3], is based on the optical follow-up of selected neutrino events very shortly after their detection by the ANTARES neutrino telescope. The alert system is known as "TAToO" (Telescopes and ANTARES Target of Opportunity) [4],

2 ANTARES neutrino alerts

The criteria for the TAToO trigger are based on the features of the neutrino signal produced by the expected sources.

Several models predict the production of high energy neutrinos greater than 1 TeV from GRBs [5] and from Core Collapse Supernovae [6]. Under certain conditions, multiplet of neutrinos can be expected [7].

Two online neutrino trigger criteria are currently implemented in the TAToO alert system:

- the detection of at least two neutrino induced muons coming from similar directions within a predefined time window;
- the detection of a single high energy neutrino induced muon.

A basic requirement for the coincident observation of a neutrino and an optical counterpart is that the pointing accuracy of the neutrino telescope should be at least comparable to the field of view of the TAROT [8] and ROTSE [9] telescopes ($\approx 2^\circ \times 2^\circ$).

To select the events which might trigger an alert, a fast and robust algorithm is used to reconstruct the calibrated data. This algorithm uses an idealized detector geometry and is independent of the dynamical positioning calibration. As a result, the hits of the three OMs of a storey are grouped and their location assigned to the barycenter of the storey. The storey orientations as well as the line-shape deviations from straight lines are not considered in the online reconstruction. A detailed description of this algorithm and its performances can be found in [10]. The principle is to minimize a χ^2 which compares the times of selected hits with the expectation from a Cherenkov signal of a muon track. The resulting direction of the reconstructed muon track is available within about $10\ \mathrm{ms}$ and the obtained minimal χ^2 is used as fit quality parameter to remove miss-reconstructed tracks.

Atmospheric muons, whose abundance at the ANTARES detector [11] is roughly six orders of magnitude larger than the one of muons induced by atmospheric neutrinos, are the main background for the alerts and have to be efficiently suppressed. Among the surviving events, neutrino candidates with an increased probability to be of cosmic origin are selected [12].

In order to establish the criteria used for our neutrino selection, we have analysed a subsample of data taken by ANTARES after the completion of the 12-line detector, corresponding to a livetime of 70.3 days. During this period, around 350 upgoing neutrino candidates were reconstructed and have been compared to a Monte Carlo (MC) simulation of atmospheric muons and neutrinos using the same lifetime.

Figure 1 shows the angular resolution of the online algorithm as a function of the neutrino energy. This resolution is defined as the median of the space angular difference between the direction of the incoming neutrino and the reconstructed neutrino-induced muon. For neutrinos with an energy higher than a few tens of TeV, an angular resolution of 0.4 degree is achieved, despite of the approximations related to the detector geometry. For example, the inclination of the ANTARES line for a typical sea current of 5 cm/s induces a systematic angular deviation of less than 0.2 degree.

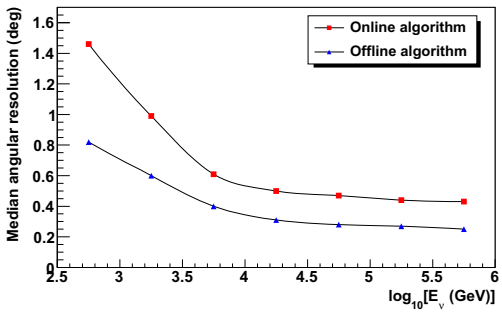

Figure 1: Angular resolution obtained for both online and offline reconstructions as a function of the neutrino energy.

2.1 Multi-neutrino trigger

The typical signature of the transient emission of high energy neutrinos is a neutrino burst, i.e. a multiplet of neutrino events originating from the source in a short time window. A trigger for this event type is implemented as the detection of two upgoing events reconstructed with at least two lines in a 15 minutes time window with a maximum angular difference of 3°. The time window was optimized to include most predictions of the neutrino emission by various models for transient sources. The 3° angular window was selected to match the convolution of the track reconstruction angular resolution and the field of view of the robotic optical telescopes ($\approx 2^\circ \times 2^\circ$). The accidental coincidence rate due to background events, from two uncorrelated upgoing atmospheric neutrinos, is estimated to be 7×10^{-3} coincidences per year with the full ANTARES detector. With such a small background, the detection of a doublet (triplet) in ANTARES would have a significance of about 3 (5) sigma.

2.2 High energy event trigger

Since the neutrino energy spectrum for signal events is expected to be harder than for atmospheric neutrinos, a cut on the reconstructed energy efficiently reduces the atmospheric neutrino background while most of the signal events are kept. The selection of the alert candidates is based on two simple energy estimators: the number of storeys used in the track fit and the total amplitude (in photoelectrons) of the hits in the storeys.

The event selection for the high energy trigger has been tuned on atmospheric neutrinos in order to obtain a false alarm rate of about 25 alerts per year. This rate was agreed between ANTARES and the optical telescope collaborations. A requirement of at least 20 storeys on at least three lines and an amplitude greater than 180 photoelec-

trons will select around 25 high energy events per year with the full 12 line configuration of the ANTARES detector. The TAToO alert criteria select neutrinos of energies above 10 TeV for the single high energy trigger (calculated with a neutrino Monte Carlo generated with an E^{-2} energy spectrum).

Figure 2 shows the estimation of the point spread function for a typical high energy neutrino alert. Around 70% of the events are contained in the field of view of a typical robotical telescope ($\approx 2^\circ \times 2^\circ$). With a larger delay (few tens of minutes after the time of the burst), we are able to run the standard reconstruction tool which provides a much better angular resolution using the dynamical positioning of the detector lines [13]. Simulations indicate that, with this algorithm, ANTARES reaches an angular resolution smaller than about 0.3-0.4° for neutrino energies above 10 TeV (curve labeled 'offline algorithm' in Figure 1).

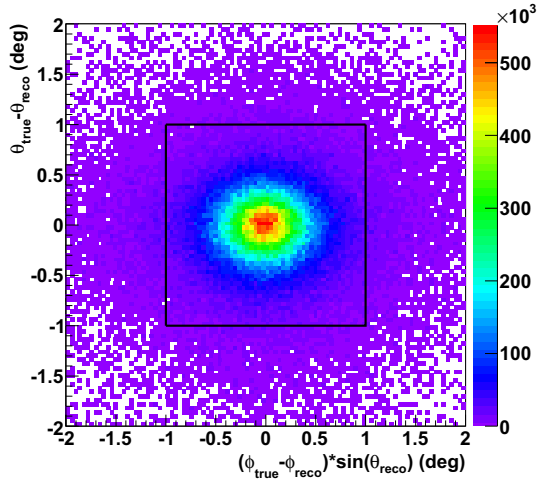

Figure 2: Bi-dimensional angular resolution. The black square corresponds to the TAROT telescope field of view ($\approx 2^\circ \times 2^\circ$).

3 Observation strategy of the robotical telescopes

ANTARES is organizing a follow-up program in collaboration with the TAROT and ROTSE telescopes The TAROT [8] network is composed of two 25 cm optical robotic telescopes located at Calern (France) and La Silla (Chile). The ROTSE [9] network is composed of four 45 cm optical robotic telescopes located at Coonabarabran (Australia), Fort Davis (USA), Windhoek (Namibia) and Antalya (Turkey). The main advantages of these instruments are the large field of view of about 2 x 2 square degrees and their very fast positioning time (less than 10s). These telescopes are perfectly tailored for such a program. Thanks to the location of the ANTARES telescope in the Northern hemisphere (42.79 degrees latitude), all the six telescopes are used for the optical follow-up program. Depending on the neutrino trigger settings, the alert are sent at a rate of abour one or two times per month. With the current settings, the connected telescopes can start taking images with a latency of the order of one minute with respect to the neutrino event (T0).

As it was said before, the rolling search method is sensitive to all transient sources producing high energy neutrinos. For example, a GRB afterglow requires a very fast observation strategy in contrary to a core collapse supernovae for which the optical signal will appear several days after the neutrino signal. To be sensitive to all these astrophysical sources, the observational strategy is composed of a real time observation followed by few observations during the following month. For the prompt observation, 6 images with an exposure of 3 minutes and 30 images with an exposure of 1 min are taken respectively by the first available TAROT and ROTSE telescopes. The integrated time has been defined in order to reach an average magnitude of about 19. For each delayed observation, six images are taken at T0+1,+2, +3, +4, +5, +6, +7, +9, +15, +27 days after the trigger for TAROT (8 images for ROTSE the same days plus T0+16 and T0+28 days).

4 Optical image analysis

Once the images are taken, they are automatically dark subtracted and flat-fielded at the telescope site. Once the data are copied from the telescopes, an offline analysis is performed combining the images from all sites. This off-line program is composed by three main steps: astrometric and photometric calibration, subtraction between each image and a reference one and light curve determination for each variable candidates.

Curently, two offline analysis pipelines are used: the ROTSE automated pipeline and one specially adapted to the TAROT and ROTSE image quality based on a program originally developed for the supernova search in the Super-Nova Legacy Survey (SNLS) project. Cases like variable PSF due to the atmospheric conditions or the lower quality images on the CCD edges have to be optimized in order not to loose any optical information. The choice of the reference is based on quality criteria such as the limiting magnitude and the seeing. For the GRB search, the reference is picked among the follow-up observations (few days after the alert) where no GRB signal is expected anymore while for SN search, either we consider the first night observation or we order it few months later to have a better quality reference in absence of a SN signal. It is also planned that the image analysis step will be included at the end of the automatic detection chain.

The ROTSE pipeline has been applied to five alerts from which optical images have been recorded during the first 24 hours after the neutrino alert sending. The minimum delay between the neutrino detection and the first image is

around 70 s. No object has been found for which the light curve is compatible with a fast time decreasing signal.

5 Conclusion

The method used by the ANTARES collaboration to implement the search for coincidence between high energy neutrinos and transient sources followed by small robotic telescopes has been presented. Of particular importance for this alert system are the ability to reconstruct online the neutrino direction and to reject efficiently the background. With the described ANTARES alert sending capability, the connected optical telescopes can start taking images with a latency of the order of one minute, which will be reduced to about 15 s in the near future. The precision of the direction of the alert is much better than one degree. The quasi-online availability of a refined direction obtained using the measured geometry of the ANTARES detector further improves the quality and efficiency of the alert system.

The alert system is operational since February 2009, and as of May 2011, 37 alerts have been sent, all of them triggered by the high energy selection criterium. No doublet trigger has been recorded yet. After a commissioning phase in 2009, almost all alerts had an optical follow-up in 2010, and the live time of the system over this year is strictly equal to the one of the ANTARES telescope, namely 87%. These numbers are consistent with the expected trigger rate, after accounting for the duty cycle of the neutrino telescope. The image analysis of the 'prompt' images has not permitted to discover a GRB afterglow associated to the high energy neutrino. The analysis of the rest of the images to look for the light curve of a core collapse SN is still on-going.

The optical follow-up of neutrino events significantly improves the perspective for the detection of transient sources. A confirmation by an optical telescope of a neutrino alert will not only provide information on the nature of the source but also improve the precision of the source direction determination in order to trigger other observatories (for example very large telescopes for redshift measurement). The program for the follow-up of ANTARES neutrino events is already operational with the TAROT and ROTSE telescopes and results based on analysis of the optical images will be presented in a forthcoming paper. This technique could be extended to observations in other wavelength regimes such as X-ray or radio.

6 Acknowledgments

This work has been financially supported by the GdR PCHE in France. I greatfully acknowledge the financial support of MICINN (FPA2009-13983-C02-01 and MultiDark CSD2009-00064) and of Generalitat Valenciana (Prometeo/2009/026).

References

[1] T. Piran, Phys. Rept. **314** (1999) 575.
[2] E. Aslanides *et al.*, ANTARES Collaboration, astro-ph/9907432. P. Coyle *et al.*, Proc. 31^{st} ICRC, Lódź 2009, arXiv:1002.0701v1.
[3] M. Kowalski, A. Mohr, Astropart. Phys. **27** (2007) 533.
[4] D. Dornic *et al.*, Nucl. Instrum. Meth. A **626-627** (2011) S183. S. Basa *et al.*, Nucl. Instrum. Meth. A **602** (2009) 275.
[5] E. Waxman, J. Bahcall, Phys. Rev. Lett. 78 (1997) 2292; P. Meszaros, E. Waxman, Phys. Rev. Lett. **87** (2001) 171102; C. Dermer, A. Atoyan, Phys. Rev. Lett. **91** (2003) 071102; S. Razzaque, P. Meszaros, E. Waxman, Phys. Rev. Lett. **90** (2003) 241103.
[6] S. Ando, J. Beacom, Phys. Rev. Lett. **95** (2005) 061103.
[7] S. Razzaque, P. Meszaros, E. Waxman, Phys. Rev. Lett. **94** (2005) 109903.
[8] M. Boer *et al.*, Astron. Astrophys. Suppl. Ser. **138** (1999) 579.
[9] C.W. Akerlof *et al.*, Public. Astron. Soc. Pac. **115** (2003) 132.
[10] J.A. Aguilar *et al.*, ANTARES Collaboration, Astropart. Phys. **34** (2011) 652.
[11] J.A. Aguilar *et al.*, ANTARES Collaboration, Astropart. Phys. **34** (2010) 179.
[12] J.A. Aguilar *et al.*, ANTARES Collaboration, Phys. Lett. B**696** (2011) 16.
[13] A. Heijboer, http://antares.in2p3.fr/Publications/thesis/2004/Aart-Heijboer-phd.pdf, PhD thesis, Universiteit van Amsterdam, Amsterdam, The Netherlands.

32ND INTERNATIONAL COSMIC RAY CONFERENCE, BEIJING 2011

Search for neutrino emission of gamma-ray flaring blazars with the ANTARES telescope

DORNIC D.[1] ANTARES COLLABORATION
[1] *IFIC - Instituto de Fisica Corpuscular, Edificios Investigacion de Paterna, CSIC - Universitat de Valencia, Apdo. de Correos 22085, 46071 Valencia, Spain*
dornic@ific.uv.es
DOI: 10.7529/ICRC2011/V04/0091

Abstract: The ANTARES telescope is well suited to detect neutrinos produced in astrophysical transient sources as it can observe a full hemisphere of the sky at all the times with a duty cycle close to unity. The background and point source sensitivity can be drastically reduced by selecting a narrow time window around the assumed neutrino production period. Radio-loud active galactic nuclei with their jets pointing almost directly towards the observer, the so-called blazars, are particularly attractive potential neutrino point sources, since they are among the most likely sources of the observed ultra high energy cosmic rays and therefore, neutrinos and gamma-rays may be produced in hadronic interactions with the surrounding medium. The gamma-ray light curves of blazars measured by the LAT instrument on-board the Fermi satellite reveal important time variability information. A strong correlation between the gamma-ray and the neutrino fluxes is expected in this scenario.

An unbinned method based on the minimization of a likelihood ratio was applied to a subsample data collected in 2008 (61 days live time). By looking for neutrinos detected in the high state periods of the AGN light curve, the sensitivity to these sources has been improved by about a factor 2 with respect to a standard time-integrated point source search. First results on the search for ten bright and variable Fermi sources are presented.

Keywords: ANTARES, Neutrino astronomy, Fermi transient sources, time-dependant search, blazars

1 Introduction

The production of high-energy neutrinos has been proposed for several kinds of astrophysical sources, such as active galactic nuclei, gamma-ray bursters, supernova remnants and microquasars, in which the acceleration of hadrons may occur. Neutrinos are unique messengers to study the high-energy universe as there are neutral and stable, interact weakly and travel directly from their point of creation in the source without absorption. Neutrinos could play an important role in understanding the mechanisms of cosmic ray acceleration and their detection from a source would be a direct evidence of the presence of hadronic acceleration in that source.

Radio-loud active galactic nuclei with their jets pointing almost directly towards the observer, the so-called blazars, are particularly attractive potential neutrino point sources, since they are among the most likely sources of the observed ultra high energy cosmic rays and therefore, neutrinos and gamma-rays may be produced in hadronic interactions with the surrounding medium [1]. The gamma-ray light curves of blazars measured by the LAT instrument onboard the Fermi satellite reveal important time variability information on timescale of hours to several weeks, with intensities always several times larger than the typical flux of the source in its quiescent state [2]. A strong correlation between the gamma-ray and the neutrino fluxes is expected in this scenario.

In this paper, the results of the first time-dependent search for cosmic neutrino sources in the sky visible to the ANTARES telescope are presented. The data sample used in this analysis is described in Section 2, together with a discussion on the systematic uncertainties. The point source search algorithm used in this time-dependent analysis is explained in Section 3. The results are presented in Section 4 for a search on a list of ten selected candidate sources.

2 ANTARES

The ANTARES collaboration has completed the construction of a neutrino telescope in the Mediterranean Sea with the connection of its twelfth detector line in 2008 [3]. The telescope is located 40 km on the southern coast of France (42^o48'N, 6^o10'E) at a depth of 2475 m. It comprises a three-dimensional array of photomultipliers housed in glass spheres (optical modules), distributed along twelve slender lines anchored at the sea bottom and kept taut by a buoy at the top. Each line comprises up to 25 storeys of triplets of optical modules (OMs), each housing a single 10" PMT. Since lines are subject to the sea current and can change

shape and orientation, a positioning system comprising hydrophones and compass-tiltmeters is used to monitor the detector geometry. The main goal of the experiment is to search for neutrinos of astrophysical origin by detecting high energy muons (>100 GeV) induced by their neutrino charged current interaction in the vicinity of the detector.

The arrival time and intensity of the Cherenkov light on the OMs are digitized into hits and transmitted to shore, where events containing muons are separated from the optical backgrounds due to natural radioactive decays and bioluminescence, and stored on disk. A detailed description of the detector and the data acquisition is given in [3] [4]. The arrival times of the hits are calibrated as described in reference [5]. The online event selection identifies triplets of OMs that detect multiple photons. At least 5 of these are required throughout the detector, with the relative photon arrival times being compatible with the light coming from a relativistic particle. Independently, events were also selected which exhibit multiple photons on two sets of adjacent, or next to adjacent floors.

The data used in this analysis corresponds to the period from September 6th to December 31st, 2008 (54720-54831 modified Julian day), taken with the full detector. Some filtering has been applied in order to exclude periods in which the bioluminescence-induced optical background was high. The resulting effective life time is 60.8 days. Atmospheric neutrinos are the main source of background in the search for astrophysical neutrinos. These neutrinos are produced from the interaction of cosmic rays in the Earth's atmosphere.Only charged current interactions of neutrinos and antineutrinos were considered. An additional source of background is due to the mis-reconstructed atmospheric muons. The track reconstruction algorithm derives the muon track parameters that maximize a likelihood function built from the difference between the expected and the measured arrival time of the hits from the Cherenkov photons emitted along the muon track. This maximization takes into account the Cherenkov photons that scatter in the water and the additional photons that are generated by secondary particles (e.g. electromagnetic showers created along the muon trajectory). The algorithm used is outlined in [6]. The value of the log-likelihood per degree of freedom (Λ) from the track reconstruction fit is a measure of the track fit quality and is used to reject badly reconstructed events, such as atmospheric muons that are mis-reconstructed as upgoing tracks. Neutrino events are selected by requiring that tracks are reconstructed as upgoing and have a good reconstruction quality. In addition, the error estimate on the reconstructed muon track direction obtained from the fit is required to be less than 1^o.

The angular resolution can not be determined directly in the data and has to be estimated from simulation. However, the comparison of the data and MonteCarlo simulations from which the time accuracy of the hits has been degraded has yielded a constrain on the uncertainty of the angular resolution of the order of 0.1^o [8]. Figure 1 shows the cumulative distribution of the angular difference between the reconstructed muon direction and the neutrino direction with an assumed spectrum proportional to E_ν^{-2}, where E_ν is the neutrino energy. For this period, the median resolution is estimated to be 0.4 +/- 0.1 degree.

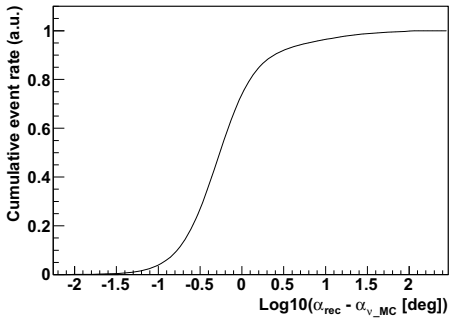

Figure 1: Cumulative plot of the distribution of the angle between the true Monte Carlo neutrino direction and the reconstructed muon direction for E^{-2} upgoing neutrino events selected for this analysis.

3 Time-dependent search algorithm

This time dependant point source analysis is done using an unbinned method based on a likelihood ratio maximization. The data is parameterized as a two components mixture of signal and background. The goal is to determine, at a given point in the sky and at a given time, the relative contribution of each component and to calculate the probability to have a signal above a given background model. The likelihood ratio λ is the ratio of the probability density for the hypothesis of background and signal ($H_{sig+bkg}$) over the probability density of only background (H_{bkg}):

$$\lambda = \sum_{i=1}^{N} log \frac{P(x_i|H_{sig+bkg})}{P(x_i|H_{bkg})} \quad (1)$$

$$\lambda = \sum_{i=1}^{N} log \frac{\frac{n_{sig}}{N}.P_{sig}(\alpha_i,t_i) + (1-\frac{n_{sig}}{N}).P_{bkg}(\alpha_i,t_i)}{P_{bkg}(\alpha_i,t_i)} \quad (2)$$

where n_{sig} and N are respectively the unknown number of signal events and the total number of events in the considered data sample. $P_{sig}(\alpha_i,t_i)$ and $P_{bkg}(\alpha_i,t_i)$ are the probability density function (PDF) for signal and background respectively. For a given event i, t_i and α_i represent the time of the event and the angular difference between the coordinate of this event and the studied source.

The probability densities P_{sig} and P_{bkg} are described by the product of two components: one for the direction and one for the timing. The shape of the time PDF for the signal event is extracted directly from the gamma-ray light curve assuming the proportionality between the gamma-ray and the neutrino fluxes. For the signal event, this directional

PDF is described by the one dimension point spread function, which is the probability density of reconstructing an event at an angular distance from the true source position. The directional and time PDF for the background are derived from the data using respectively the observed declination distribution of selected events in the sample and the observed time distribution of all the reconstructed muons. Figure 2 shows the time distribution of all the reconstructed events and the selected upgoing events for this analysis. Once normalized to an integral equal to 1, the distribution for all reconstructed events is used directly as the time PDF for the background. When data is at 0, it means that there are no data taken during these periods (ie detector in maintenance) or data with a very poor quality (high bioluminescence or bad calibration).

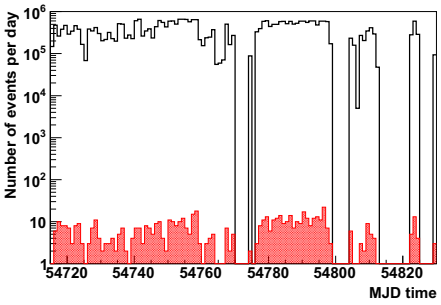

Figure 2: Time distribution of the reconstructed events. Black: distribution for all reconstructed events. Red filled: distribution of selected upgoing events ($\Lambda > -5.4$ and $\beta < 1^o$).

The null hypothesis is given with $n_{sig} = 0$. The obtained value of λ_{data} on the data is then compared to the distribution of λ given the null hypothesis. Large values of λ_{data} compared to the distribution of λ for the background only reject the null hypothesis with a confident level equal to the fraction of the scrambled trials above λ_{data}. This fraction of trials above λ_{data} is referred as the p-value. The discovery potential is then defined as the average number of signal events required to achieve a p-value lower than 5σ in 50 % of trials. Figure 3 shows the average number of events required for a 5σ discovery (50 % C.L.) produced in one source located at a declination of -40^o as a function of the total width of the flare periods. These numbers are compared to the one obtained without using the timing information. Using the timing information yields to an improvement of the discovery potential by about a factor 2-3 with respect to a standard time-integrated point source search [8].

4 Search for neutrino emission from gamma-ray flare

This time-dependent analysis has been applied to bright and variable Fermi blazar sources reported in the first year

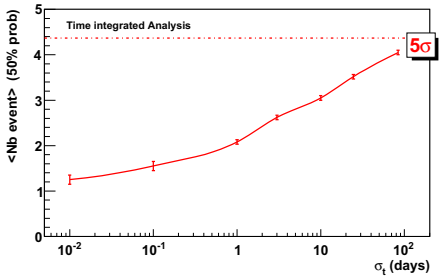

Figure 3: Average number of events required for a 5σ discovery (50 % C.L.) produced in one source located at a declination of -40^o as a function of the width of the flare period. These numbers are compared to the one obtained without using the timing information.

Fermi LAT catalogue [9] and in the LBAS catalogue (LAT Bright AGN sample [10]). The sources located in the visible part of the sky by Antares from which the averaged 1 day-binned flux in the high state is greater than 20 10^{-8} photons.cm^{-2}.s^{-1} above 300 MeV in the studied time period and with a significant time variability are selected. This list includes six flat spectrum radio quasars (FSRQ) and four BLlacs. Table 1 lists the characteristics of the ten selected sources.

Name	OFGL name	Class	redshift	F_{300}
PKS0208-512	J0210.8-5100	FSRQ	1.003	4.43
AO0235+164	J0238.6+1636	BLLac	0.940	13.19
PKS0454-234	J457.1-2325	FSRQ	1.003	13.56
OJ287	J0855.4+2009	BLLac	0.306	2.48
WComae	J1221.7+28.14	BLLAc	0.102	2.58
3C273	J1229.1+0202	FSRQ	0.158	8.68
3C279	J1256.1-0548	FSRQ	0.536	15.69
PKS1510-089	J1512.7-0905	FSRQ	0.36	28.67
3c454.3	J2254.0+1609	FSRQ	0.859	24.58
PKS2155-304	J2158.8-3014	BLLac	0.116	7.89

Table 1: List of bright variable Fermi blazars selected for this analysis. F_{300} is the gamma-ray flux above 300 MeV (10^{-8} photons.cm^{-2}.s^{-1}).

The light curves published in Fermi web page for the monitored sources [11] are used for this analysis. These light curves correspond to the one-day binned time evolution of the average gamma-ray flux above a threshold of 100 MeV from August 2008 to August 2010. The high state periods are defined using a simple and robust method based on three main steps. First, the baseline is determined with an iterative linear fit. After each fit, the points where the flux is above a given threshold are suppressed. When the baseline is computed, all the points (green dots) where the flux minus its error are above the baseline plus two times its fluctuation and the flux is above the baseline plus three times its fluctuation are used as priors from which the flares are defined. The last step consists on, for each selected point, adding the adjacent points for which the emission is com-

patible with the flare. Finally, an additional delay of 0.5 day is added before and after the flare in order to take into account that the precise time of the flare is not known (1-day binned LC). With this definition, a flare has a width of at least two days. Figure 4 shows the time distribution of the Fermi LAT gamma-ray light curve of 3C454 for almost 2 years of data and the determined high state periods (blue histogram). With the hypothesis that the neutrino emission follows the gamma-ray emission, the signal time PDF is simply the normalized de-noise light curve.

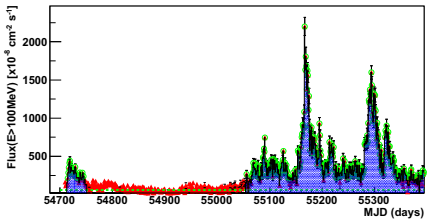

Figure 4: Gamma-ray light curve (red dots) of the blazar 3C454.3 measured by the LAT instrument onboard the Fermi satellite above 100 MeV for almost 2 years of data. Blue histogram: high state periods. Green line and dots: baseline and significant dots above this baseline used for the determination of the flare periods.

The most significant source is 3C279, which has a pre-trial p-value of 1.03 %. The unbinned method finds one high-energy neutrino event located at 0.56^o from the source location during a large flare in November 2008. Figure 5 shows the time distribution of the Fermi gamma-ray light curve of 3C279 and the time of the coincident neutrino event. This event has been reconstructed with 89 hits spread on 10 lines with a track fit quality $\Lambda = -4.4$ and an error estimate $\beta = 0.3^o$. The post-trial probability is computed taking into account the ten searches. The final probability, 10 % is compatible with background fluctuations.

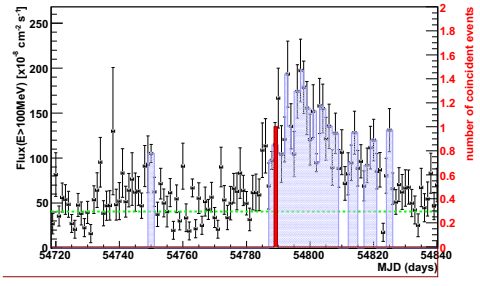

Figure 5: Gamma-ray light curve (black dots) of the blazar 3C279 measured by the LAT instrument onboard the Fermi satellite above 100 MeV. Blue histogram: high state periods. Green dashed line: fit of a baseline. Red histogram: time of the ANTARES neutrino event in coincidence with 3C279.

5 Summary

This paper discusses the first time-dependent search for cosmic neutrinos using the data taken with the full 12 lines ANTARES detector during the last four months of 2008. Time-dependent searches are significantly more sensitive than standard point-source search to variable sources thanks to the large reduction of the background of atmospheric muons and neutrinos over short time scales. This search has been applied to ten very bright and variable Fermi LAT blazars. The most significant observation of a flare is 3C279 with a p-value of about 10 % after trials for which one neutrino event has been detected in time/space coincidence with the gamma-ray emission. Limits have been obtained on the neutrino fluence for the ten selected sources. The most recent measurements of Fermi in 2009-11 show very large flares yielding a more promising search of neutrinos [12].

6 Acknowledgments

I greatfully acknowledge the financial support of MICINN (FPA2009-13983-C02-01 and MultiDark CSD2009-00064) and of Generalitat Valenciana (Prometeo/2009/026).

References

[1] Gaisser T.K., Halzen F., Stanev T., Phys. Rep. 258 (1995) 173; Learned J.G., Mannheim K., Ann. Rev. Nucl. Part. Sci. 50 (2000) 679; Halzen F., Hooper D., Rep. Prog. Phys. 65 (2002) 1025.
[2] Abdo A. A. *et al*. 2010, ApJ, 722, 520
[3] Ageron M. *et al.*, ANTARES Collaboration, NIMA-D-10-00948R2, astro-ph.IM/1104.1607v1.
[4] Aguilar J.A. *et al.*, ANTARES Collaboration, Nucl. Instrum. Meth. A **570** (2007) 107.
[5] Aguilar J.A. *et al.*, ANTARES Collaboration, Astropart. Phys. **34** (2011) 539.
[6] Heijboer A., http://antares.in2p3.fr/Publications/thesis/2004/Aart-Heijboer-phd.pdf, PhD thesis, Universiteit van Amsterdam, Amsterdam, The Netherlands.
[7] Neyman, J. 1937, Phil. Trans. Royal Soc. London, Series A, 236, 333
[8] Bogazzi C., this conference
[9] Abdo, A. A. *et al.* 2010, ApJS, 188, 405
[10] Abdo, A. A. *et al.* 2010, ApJ, 715, 429
[11] http://fermi.gsfc.nasa.gov/ssc/data/access/lat/
[12] Abdo, A. A. *et al.* 2011, ApJL, 733, L26; Ackermann, M. *et al.* 2010, ApJ, 721, 721; Abdo, A. A. *et al.* 2010, ApJ, 721, 1425; Abdo, A. A. *et al.* 2010, ApJL, 714, L73;

32ND INTERNATIONAL COSMIC RAY CONFERENCE, BEIJING 2011

Moon shadow observation with the ANTARES neutrino telescope

COLAS RIVIÈRE[1], CARLA DISTEFANO[2], FOR THE ANTARES COLLABORATION
[1]*CPPM, Aix-Marseille Université, CNRS/IN2P3, Marseille, France*
[2]*INFN - Laboratori Nazionali del Sud (LNS), Catania, Italy*
riviere@in2p3.fr
DOI: 10.7529/ICRC2011/V04/0098

Abstract: The ANTARES neutrino telescope is operating in the Mediterranean sea in its full configuration since May 2008. While designed to observe up-going neutrinos, it also records many signals of down-going muons produced by the interaction of high energy cosmic rays in the atmosphere. The shadowing of cosmic rays by the Moon produces a deficit of muons coming from this direction at the ANTARES level. The observation of this deficit of events can be used to check the correct pointing of the detector with respect to a known object.

The strategies to observe this Moon shadow are discussed ant the current results are presented.

Keywords: high energy neutrino, ANTARES, Moon shadow

1 Introduction

The ANTARES neutrino telescope is operating in the Mediterranean Sea in full 12 lines configuration since May 2008 [1]. Thanks to the good optical properties of the water of the deep sea, the median angular resolution obtained with the current reconstruction algorithm is estimated to be 0.4° for cosmic neutrinos with an E^{-2} flux [2].

The pointing performance of the detector relies on the knowledge of parameters, such as the relative delays of the optical sensors within each detector line as well as between the lines, the instantaneous shape of the detector lines which is influenced by the sea current or the absolute orientation of the detector.

The values of these parameters have been calibrated before immersion of the detector lines and are regularly measured in situ during operation. The relative time delays are measured using a laser beacon and LED beacons, and also with physical quantities such as the ^{40}K decay or the atmospheric muon tracks [3]. The alignment measurements are performed continuously with acoustic emitters and transceivers, tiltmetres and compasses [4]. The absolute orientation of the telescope is obtained by the triangulation of acoustic signals between anchors of the lines and the deployment vessel at the sea surface, positioned by GPS [5]. The uncertainties on these values are small enough to ensure the optimal performances of the telescope, but it remains very important to verify the correct operation of the detector using a calibration source. While no such source exists, some possibilities remain:

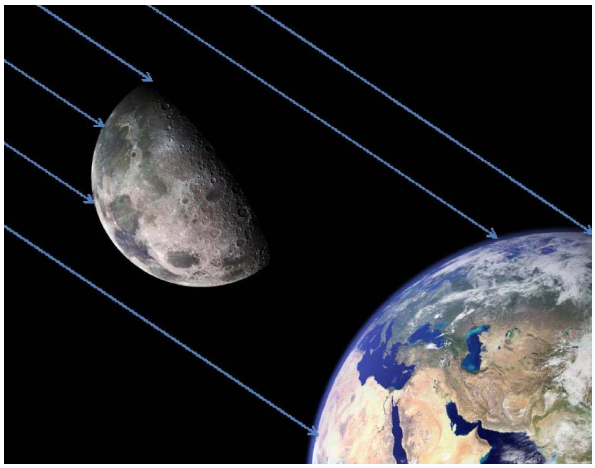

Figure 1: Illustration of the Moon blocking the cosmic rays, thus producing a deficit of muons originating from this direction.

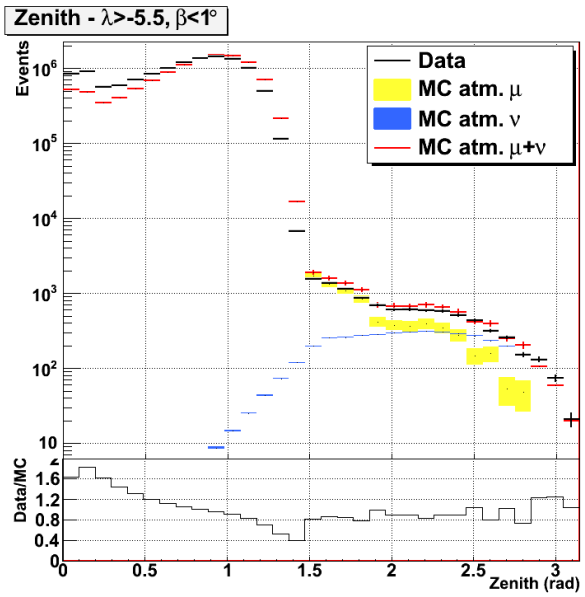

Figure 2: Top: Distribution of the reconstructed zenith of the events of the data set used in this analysis: data (black), Monte Carlo (red=yellow+blue). Bottom: Data/MC ratio.

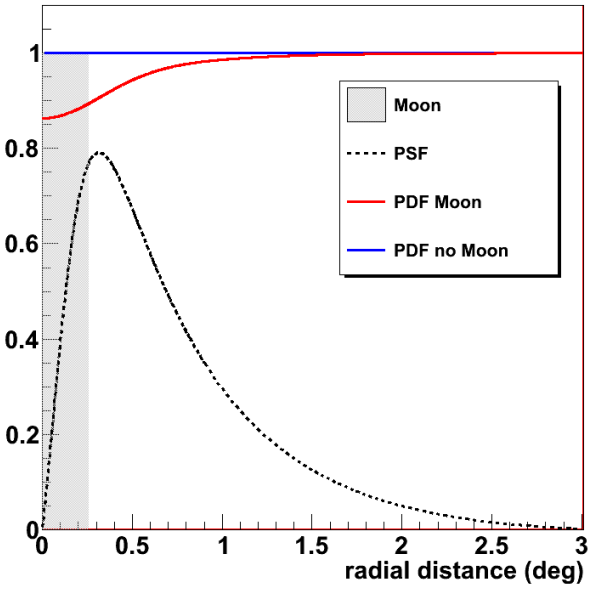

Figure 3: Black: Parametrization of the PSF of the events at less than 10° from the Moon position. Blue: Constant PDF in the H_0 hypothesis. Red: PDF in the H_1 hypothesis.

- The observation of a coincidence between an air shower at sea level with a surface array and the resulting muons at ANTARES level [6].
- The observation of the Moon shadow. This technique, first proposed in 1957 [8], relies on the absorption of cosmic rays by the Moon, as illustrated on figure 1. As the cosmic rays are the source of the down-going muons at the telescope level, this absorption induces a deficit of the number of observed muons in the Moon direction.

2 Data and Monte Carlo

2.1 Data set and reconstruction

The apparent Moon radius is on average $R_{Moon} = 0.259^\circ$, which is smaller than the resolution of ANTARES, in particular for down-going atmospheric muons; thus the observation of the Moon shadow requires large statistics. For the work reported here, 884 days of data taken between 2007 and 2010 (including periods with 5, 10 and 12 lines configurations) have been analysed.

These data have been processed using the standard track reconstruction algorithm of ANTARES. As this algorithm is optimised for up-going tracks of cosmic origin, an algorithm dedicated to the reconstruction of down-going atmospheric muons would improve the results presented in this paper.

The event selection criteria used here are the same as presented in [7], i.e. an error estimate $\beta < 1^\circ$ and a quality of reconstruction of the track $\lambda > -5.5$.

2.2 Monde Carlo

The point spread function (PSF) used to generate pseudo experiments and to compute our search strategy is obtained from Monte Carlo simulation (MC). Each data run is simulated as close as possible to the experimental condition (same detector condition, bioluminescence rate, etc.), generating both atmospheric muons and atmospheric neutrinos. An example of data/MC comparison is represented in figure 2.

The PSF is extracted from this MC using all the events reconstructed in a region of 10° around the Moon position (figure 3). With the chosen selection criteria, the median angular resolution is 0.75°.

Concerning the shape of the event density in the Moon region, we assume the event probability density function (PDF) is uniform in the abscence of Moon[1], we call this hypothesis H_0. The PSF in the Moon hypothesis (H_1) is obtained by computing the 2D convolution product of the

1. If we consider a 10° radius region around the Moon direction, there is actually a counting rate modulation of $\pm 20\%$, but this is a dipolar modulation which cancels out during the likelihood computation, so it is neglected for simplicity. Only second or higher order modulations could change the likelihood.

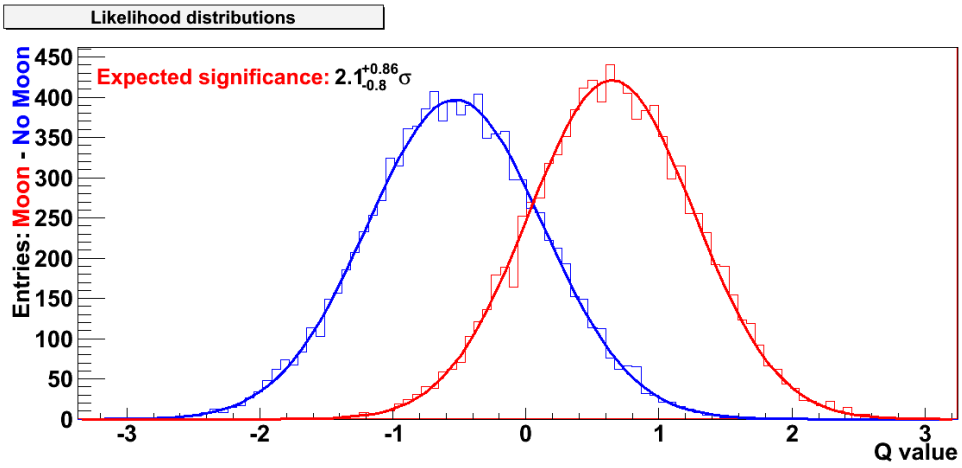

Figure 4: Distributions of the likelihood test function values, for the H_0 hypothesis in blue and for H_1 in red.

PSF with the Moon shape:

$$PDF(x|H_0) \propto 1$$
$$PDF(x|H_1) \propto (1 - PSF \otimes \delta_{Moon})(x)$$

3 Search strategy

Different search strategies have been studied, a simple on/off search, a χ^2 test of histograms [7] and the one presented here, a likelihood search. The results of these different approaches are compatible.

3.1 Likelihood method

For the likelihood search we build a test function based on the likelihood ratio using the expected distributions corresponding to the Moon hypothesis H_1 and no Moon hypothesis H_0. The test function used is the logarithm of the likelihood ratio:

$$t = \sum_{events\ i} \log \frac{PDF(r_i|H_1)}{PDF(r_i|H_0)}$$

3.2 Pseudo-experiments

In order to test the search method, to estimate its power and to compute the significance, pseudo-experiments are performed. After generating uniform event distributions in an area around the Moon position, a smearing is applied using the PSF, followed by a shadowing which is or is not applied for the events originating from the Moon direction. The pseudo experiments presented here are generated with the same event statistics as available in the 2007-2010 data sample.

The distributions of the values of the test function obtained with the pseudo experiments are presented in figure 4. For a given value of the test function, its p-value (probability to obtain a value at least as important from a background fluctuation) is computed using the H_0 distribution (blue). The significance of this p-value can then equivalently be expressed in term of sigma.

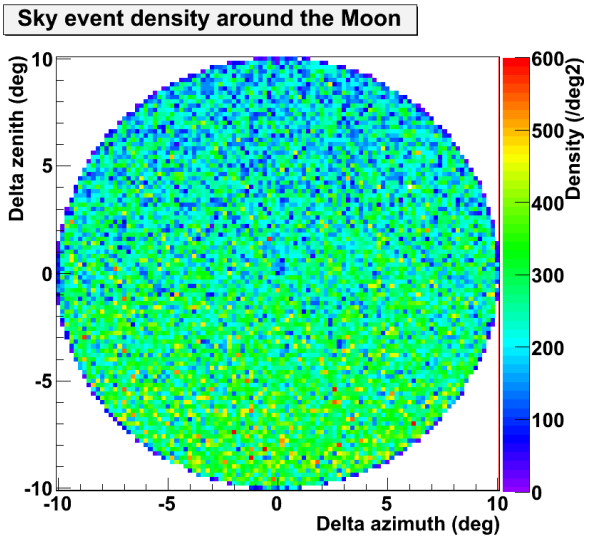

Figure 5: Event density around the Moon location $(0, 0)$.

The H_1 distribution (red) is used to estimate the power of the test. With the current event statistics, we could expect $2.1^{+0.9}_{-0.8}\sigma$. With 2, 5 and 10 times this statistics, we obtain respectively 2.8 ± 0.9, 4.2 ± 0.9 and $5.9 \pm 0.9\sigma$.

4 Preliminary results

The experimental event density in the Moon region is represented in figure 5 and the density as a function of the distance to the Moon position is shown on figure 6.

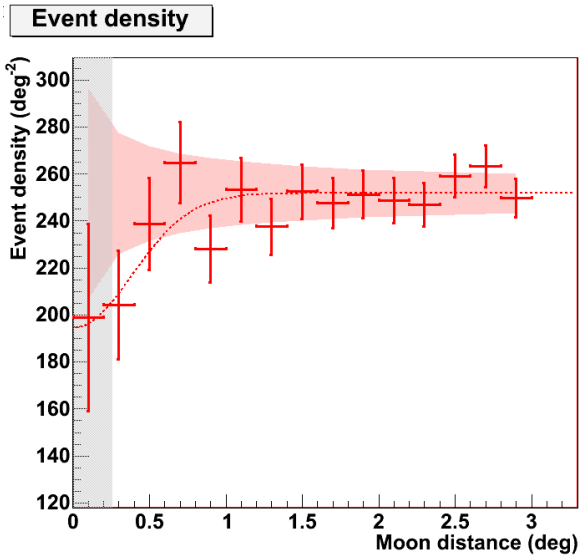

Figure 6: Event density as a function of the distance to the Moon.

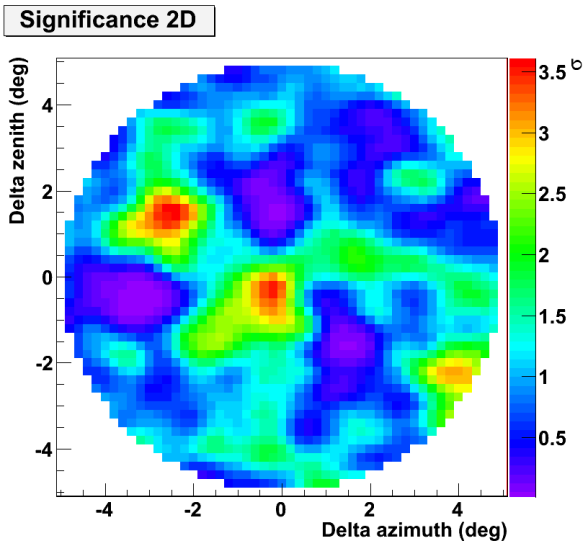

Figure 7: Significance of the search around the Moon location $(0, 0)$.

The value of the test function obtained experimentally for the Moon position is $Q = 1.17$, which has a p-value of 0.007. This corresponds to 2.7σ, which is within the expected range. This is however not significant enough to unambiguously reject the H_0 assumption.

Scanning over directions around the Moon position (see figure 7), we find similar hot spots; which are compatible with statistical fluctuations.

5 Conclusion and outlook

A search for the observation of the Moon shadow with the ANTARES neutrino telescope has been performed on a dataset corresponding to 884 days of livetime. The resulting Moon shadow significance, 2.7σ, is within the expected range and compatible with other analysis [7]. At this point, this result is not strong enough to put interesting constrains on ANTARES pointing capabilities.

The increase of statistics or the development of a track reconstruction algorithm optimized for down-going atmospheric muons should improve this results.

ANTARES will also perform campaigns of measurement of atmospheric showers by mean of a surface array installed on a boat above the detector, allowing to compare the direction of muons in coincidence with ANTARES. This will provide an additional check of the ANTARES pointing performance.

References

[1] J.A. Aguilar *et al.*, Submitted to Nucl. Instr. and Meth., April 2011 [arXiv:1104.1607]

[2] S. Adrián-Martínez *et al.*, Submitted to Astropart. Phys, August 2011 [arXiv:1108.0292]

[3] J.A. Aguilar *et al.*, Astropart. Phys. 34, 2011, **34**: 539-549 [arXiv:1012.2204]

[4] M. Ardid *et al.*, Nucl. Inst. and Meth., 2009, **A602**: 174-176

[5] G. Halladjian, Ph.D. report, Université Aix Marseille, 2010

[6] J.-P. Ernenwein, A. Tsirigotisb, S. Tzamarias, Nucl. Inst. and Meth., 2009, **A602**: 88-90

[7] C. Distefano for the ANTARES Collaboration, HEP 2011

[8] G.W. Clark, Phys. Rev., 1957, **108**: 450-457

[9] T.-P. Li, Y.-Q. Ma, Astrophys. Journal, 1983, **272**: 317-324

[10] M. Bazzotti, G. Carminatia, A. Margiotta, M. Spurio, Computer Physics Communications, 2010, **181-4**: 835-836

32ND INTERNATIONAL COSMIC RAY CONFERENCE, BEIJING 2011

Optical properties in deep sea water at the site of the ANTARES detector

SALVATORE MANGANO[1], FOR THE ANTARES COLLABORATION
[1]*IFIC - Instituto de Física Corpuscular, Edificio Institutos de Investigatión, Apartado de Correos 22085, 46071 Valencia, Spain*
manganos@ific.uv.es
DOI: 10.7529/ICRC2011/V04/0100

Abstract: The ANTARES neutrino telescope is located at a depth of 2475 m in the Mediterranean Sea. Its main objective is the observation of extraterrestrial neutrinos. Relativistic charged leptons produced by neutrino interactions in and around the detector produce Cherenkov light in the sea water detected by a three dimensional grid of photomultiplier tubes. The propagation of Cherenkov light depends on the optical properties of the sea water and their understanding is crucial to reach the optimal performance of the detector. This paper presents the measurements made between 2008 and 2010 of the light velocity and attenuation length at the ANTARES site with a system of light sources (LEDs and laser) at different wavelengths (between 400 nm and 532 nm). The time variability of the optical properties are presented and the derived values are compared with theoretical predictions.

Keywords: Neutrino telescope, Optical Beacon system, Optical properties, Refractive index.

1 Introduction

The ANTARES neutrino telescope [1] is located at the bottom of the Mediterranean Sea at a depth of 2475 m, roughly 40 km offshore from Toulon in France. Sea water is used as the detection medium for the Cherenkov light emitted by relativistic charged particles resulting from interaction of neutrinos around or inside the detector. The particle direction is reconstructed from the arrival time of detected photons through the array of photomultiplier tubes (PMTs).

The measurement of the refractive index is performed with a pulsed light source shining through water and the time of light distributions of photons detected by PMTs at different distances from the source. The attenuation length is measured by the amount of light detected by these PMTs. The optical properties are measured at wavelengths between 400 nm and 532 nm and are compared with theoretical predictions.

A precise measurement of the optical properties minimizes the uncertainty on many physical results as seen in [2]. Moreover, the optical properties may change in time due to sea current. Several measurements of those presented in this paper have been performed in the past [3, 4, 5].

2 Experimental setup

The ANTARES detector consists of a three dimensional array of 885 PMTs arranged in twelve vertical approximately 450 m long lines. Along each line with a vertical separation of 14.5 m, PMTs are grouped in triplets and oriented with their axis pointing downward at an angle of 45^o with respect to the the vertical line direction. The horizontal separation between lines is about 70 m.

The PMTs are sensitive to single photons in the wavelength range between 350 nm and 600 nm. They have a peak quantum efficiency of about 25% between 350 nm and 450 nm. The PMT measures the arrival time and charge amplitude of the detected photons.

The Optical Beacon system consists of a series of pulsed light sources distributed through the detector. The primary aim of the Optical Beacon system is the time calibration between the PMTs to reach the best angular resolution of the detector. In addition the Optical Beacon system can be also used to determine the optical properties of water.

There are four LED Beacons per line and one laser Beacon at the bottom of the central line. One LED Beacon contains 36 individual LEDs distributed over six vertical faces shaping an hexagonal cylinder. On each face, five LEDs point radially and one upwards. All the LEDs emit light at a nominal wavelength of 470 nm except two LEDs located on the lowest Beacon of line 12 which emit light at nominal wavelength of 400 nm.

The LEDs emit light with a maximum intensity of $\sim$160 pJ and a pulse width of $\sim$4 ns (FWHM). The laser is a more powerful device and emits shorter pulses than the LEDs. The laser emits pulses of light with a maximum intensity of ($\sim$1 μJ) and pulse width of $\sim$0.8 ns (FWHM) at a nominal wavelength of 532 nm. The LEDs and laser flash at

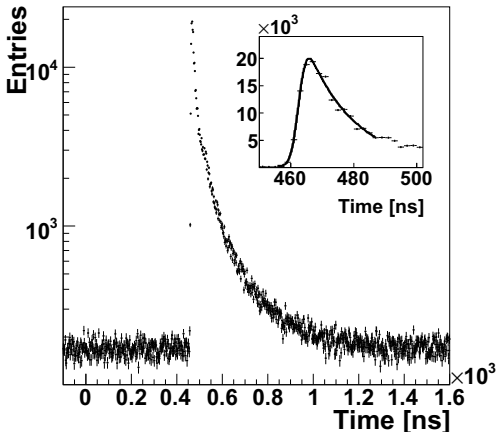

Figure 1: Arrival time distribution of LED light detected by a PMT at around 100 m. The inset shows a zoom around the signal region. Superimposed is the result of the fit to the convolution of a gaussian distribution and an exponential distribution (see text).

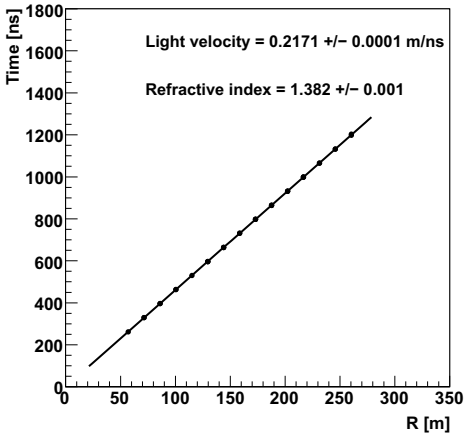

Figure 2: The figure shows the arrival time as a function of the distance between the LED and the different PMTs. The slope of a linear fit to the arrival time versus distance gives the inverse of the light velocity.

a frequency of 330 Hz. Further details about the Optical Beacon system can be found elsewhere [6, 7, 8].

The light spectrum of the three sources (two LEDs with nominal wavelengths of 470 nm and 400 nm and one laser with nominal wavelength of 532 nm) were measured using a high resolution calibrated spectrometer from Ocean Optics HR4000CG-UV-NIR. The spectrometer was cross-checked with the Green Nd-YAG laser (532 nm). The measured peak wavelengths of the LEDs in pulsed mode operation are 468.5 $\pm$ 14.4 nm and 403.1 $\pm$ 6.9 nm respectively.

3 Data acquisition and data analysis

In the special calibration data taken with Optical Beacon system, the emission time and the position of the isotropic light flash, as well as the arrival time and the position when the light reaches the PMTs are known. From the time and position difference between the PMTs the refractive index is measured, whereas the amount of light collected by these PMTs gives an information about the attenuation length.

3.1 Data acquisition

The various measurements of the water optical properties were taken from May 2008. Only data with stable background rates and below 100 kHz have been analyzed. The special calibration data duration takes only few minutes. One single upward looking LED of the lowest Optical Beacon in the line emits more than 10^5 light flashes towards the PMTs above. The photons are collected by the PMTs in the line. Figure 1 shows the arrival time distribution of photons for a LED Beacon illuminating a PMT located at 100 m. The small tail of delayed photons is due to the light scattering between LED and PMT. The zero time is defined by the illumination time of the LED. The flat distribution before and after the peak shows the detected optical background.

3.2 Data analysis

Since the light path used in the analysis (few 100 m) has the same order as the scattering length the scattering has in some way to be taken in account. The arrival time distributions are fitted to a function which is the convolution of a gaussian distribution and an exponential distribution [9, 10]. The gaussian distribution models the transit time spread of the PMTs, the time width of the optical sources and the effect of the chromatic dispersion in water, while the exponential distribution models the scattering of photons in water. The fit function is given by

$$f(t) = b + h \cdot e^{-\frac{t-\mu}{\tau}} \cdot \mathrm{Erfc}\left(\frac{1}{\sqrt{2}}\left(\frac{\sigma}{\tau} - \frac{t-\mu}{\sigma}\right)\right), \quad (1)$$

where t is the arrival time of the photons and the fit parameters are the background (b), the height of the fit function (h), the mean and width of the gaussian distribution (μ, σ) and the exponential constant (τ). The Erfc(t) is the complementary error function distribution $\mathrm{Erfc}(t) = \frac{2}{\sqrt{\pi}} \int_t^\infty e^{t'^2} dt'$. An example of such a fit is shown in the zoom of Figure 1. The fit is made in the range from -100 ns to the time of the most populated bin plus 20 ns. The arrival time at each PMT is given by the fitted mean value of the gaussian distribution. The fit is stable with respect to changes in the fit range and histogram binning.

The distances between Optical Beacon and PMT versus the measured arrival times are shown in Figure 2 (note there

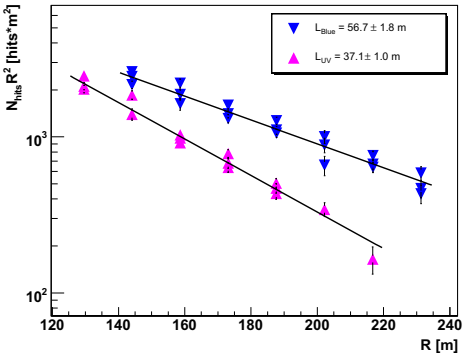

Figure 3: Amount of light collected by the PMTs as a function of the distance. The fit result of an exponential function is shown.

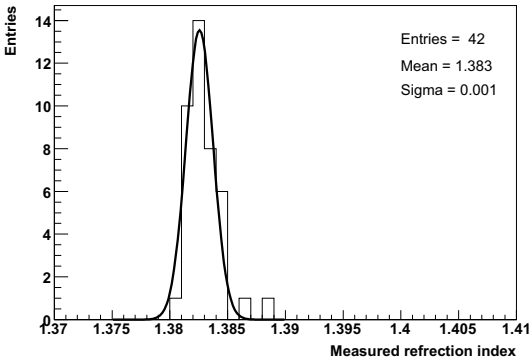

Figure 4: The measured refractive index for a total of 42 runs with an emission wavelength of 470 nm. The result to a fit to a gaussian distribution is shown.

can be up to three PMTs at each distance). Due to the small wavelength range of the individual LEDs the light dispersion is minimized. By selecting only the PMTs of the same line as the emission of light the uncertainty on the PMT angular acceptance and the PMT positions are reduced. In this analysis, no correction of the PMT positions due to line movements have been applied. The minimal distance is set to eliminate the PMT which receives too much light and have an erroneous time estimation caused through the early photon effect (for explanation see [8]) . The minimal distance for the fit range is defined as the distance where the average collected charge per hit (usually referred to as the amplitude) in the signal region is below 1.5 photo-electrons. The maximum distance is introduced due to avoid noise fluctuations. The signal has to be significantly larger than the average background (above seven sigmas). The slope of a linear fit through the measured points gives the inverse of the measured velocity of light in water (v_m). The measured refractive index is defined as

$$n = c/v_m \tag{2}$$

with $c = 3 \cdot 10^8 m/s$. The error of the refractive index given in Figure 2 is the error estimated by the linear fit.

As seen in Figure 1 the PMTs perform a time resolved measurement of the collected light. The amount of light detected depends on the attenuation length, whereas the shape of the arrival time distribution of the detected light is related to the photon path length distribution of the scattered photons. For the attenuation length measurement a similar selection criteria as in the refraction index measurement is used. An exponential fit to the collected charge as a function of the distance is shown in Figure 3 for two runs with sources with wavelength of 470 nm (tagged as Blue) and wavelength of 400 nm (tagged as UV). The attenuation length L is obtained by

$$I \cdot R^2 \sim I_0 \cdot e^{\frac{-R}{L}}, \tag{3}$$

where I_0 is the intensity at the source and I the intensity detected by a PMT at a distance R.

4 Monte Carlo measurement

The Monte Carlo simulation takes into account the geometry of the detector and the optical properties of the water (refraction index, scattering length and absorption length). Monte Carlo generated time distributions with a large variety of optical properties has been used to analyze the time distributions and calculate the refraction index and also to check the stability of the analysis method. The analysis method was first validated with a Monte Carlo sample without scattering at three different refractive index. The variation of the absorption length between 30 m and 120 m has nearly no influence on the refraction index, with variation of the refraction index of less than 0.1%. A variation in the scattering length between 20 m and 50 m produces an uncertainty of 0.3% in the measurement of the refractive index.

5 Data measurement

Between May 2008 and March 2010 a total of 42 runs were taken with a nominal wavelength of 470 nm, 14 runs with a nominal wavelength of 400 nm and 13 runs with a nominal wavelength of 532 nm and have been analyzed according to the methods explained in section 3.2. The measured refraction of the 42 runs are shown in the Figure 4 and the mean value is evaluated by fitting the distribution with a gaussian. The fitted attenuation lengths for some of these runs as function of the data period are shown in Figure 5. The fitted values are reasonably stable with time.

Since November 2010 runs with a modified Optical Beacon have been collected with light emission at six additional wavelengths with nominal peak values of 385, 400, 440, 460, 505 and 518 nm. First results are expected soon.

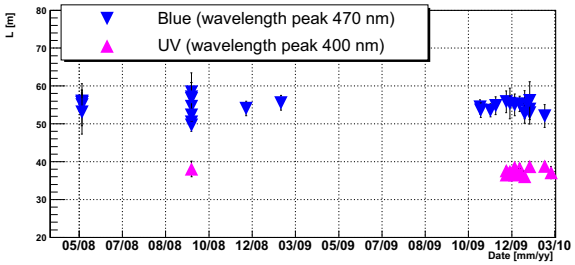

Figure 5: Time evolution of the attenuation length parameter for one and a half year of data taking for two different wavelengths.

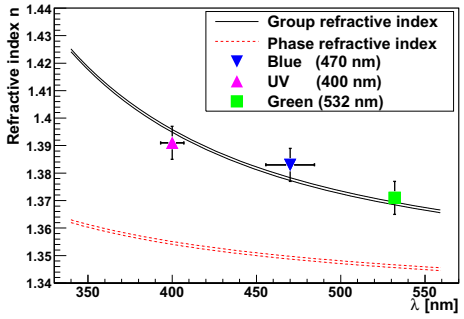

Figure 6: Group and phase refractive index as a function of the wavelength for a given temperature and salinity with measured data points and its systematical error bars. The upper curves (solid) show the group refractive index, the lower curves (dotted) give the phase refractive index.

These measured refractive index with their systematic errors estimated in section 4 are shown in Figure 6. Also shown is the parametric formula of the refractive index. The refractive index at the ANTARES site depends on the wavelength, on the temperature, on the salinity of the water and the pressure at the depth of the detector. The parametric formula for the phase refractive index of Quan and Fry [11], based on data from Austin and Halikas [12], is modified with appropriate pressure corrections as suggested in [3]. The phase refractive index for sea water as a function of wavelength, temperature (T), salinity (S) and pressure (p) is given by

$$n_p(340 < \lambda(nm) < 560, S(\%) = 3.844, \\ T(^oC) = 13.2, 200 < p(atm) < 240) = \\ 1.32292 + (1.32394 - 1.32292) \cdot \frac{p - 200}{240 - 200} + \\ \frac{16.2561}{\lambda} - \frac{4382}{\lambda^2} + \frac{1.1455 \cdot 10^6}{\lambda^3}, \quad (4)$$

where λ is the wavelength of light.

The group refractive index (n) [4] is related to its phase refractive index (n_p) through

$$n = \frac{n_p}{1 + \frac{\lambda}{n_p}\frac{dn_p}{d\lambda}}. \quad (5)$$

The parametrization of the refractive indexes n and n_p is shown in Figure 6 for the given values of temperature, salinity and for a pressure between 200 atm and 240 atm. The measurements are in agreement with the parametrization of the group refractive index.

6 Conclusion

Pulsed light sources with wavelengths between 400 nm and 532 nm shining through sea water and the time of light distribution detected by the PMTs at distances between few tens and few hundred meters from the source have been used to measure the refraction index. Dedicated Monte Carlo simulation has been used to validate the analysis method and to evaluate the systematics. The data results are compatible with the parametrization of the group refractive index.

Acknowledgments

I gratefully acknowledge the support of the JAE-Doc postdoctoral programme of CSIC. This work has also been supported by the following Spanish projects: FPA2009-13983-C02-01, MultiDark Consolider CSD2009-00064, ACI2009-1020 of MICINN and Prometeo/2009/026 of Generalitat Valenciana.

References

[1] M. Ageron et al, 2011, "ANTARES: the first undersea neutrino telescope", arXiv:1104.1607v1.
[2] J.A.Aguilar et al., 2010, "Zenith distribution and flux of atmospheric muons measured with the 5-line ANTARES detector", Astropart. Phys. 34.
[3] J.A.Aguilar et al., 2005, "Transmission of light in deep sea water at the site of the Antares neutrino telescope", Astropart. Phys 23.
[4] I.A.Danilchenko, '2003, 'The dispersion formula and the light group velocity in a water", arXiv:physics/0306020.
[5] Lubsandorzhiev, Bayarto K. and Pokhil, P. G. and Vasiliev, R. V. and Vyatchin, Y. E., 2003, "Measurements of group velocity of light in the Lake Baikal water", Nucl. Instrum. Meth. A502.
[6] M. Ageron et al, 2007, "The ANTARES optical beacon system", Nucl. Instrum. Meth. A578.
[7] J.A.Aguilar, "Analysis of the Optical Beacon system and search for point-like sources in the Antares neutrino telescope", PhD thesis, University of Valencia, 2008.
[8] J.A.Aguilar et al., 2011, "Time calibration of the ANTARES neutrino telescope", Astropart. Phys. 34.
[9] S. Brandt, "Data Analysis", Text book.

[10] A.G.Frodesen at al., "Probability and statistics in particle physics", Text book.
[11] X. Quan & Fry: "Empirical equation for the index of refraction of seawater", E. Appl. Opt.30:18 (1995).
[12] Austin, R.W. and G. Halikas, 1976, "The index of refraction of seawater", Scrip. Inst. Ocean. SIO Ref.76-1.

32ND INTERNATIONAL COSMIC RAY CONFERENCE, BEIJING 2011

Characterizing the search for UHE neutrinos with the ARIANNA detector

K. DOOKAYKA[1], FOR THE ARIANNA COLLABORATION
[1] *Dept. of Physics & Astronomy, University of California, Irvine CA 92697*
dookayka@uci.edu
DOI: 10.7529/ICRC2011/V04/0144

Abstract: The ARIANNA experiment exploits unique properties of the Ross Ice Shelf, namely its radio transparency and radio reflectivity at the ice-water boundary beneath the shelf, to search for UHE neutrinos. Simulation studies show that, with the full array, we can expect to detect ~ 40 GZK events/year using the ESS model. The excellent sensitivity results from the low energy threshold ($> 3 \times 10^{17}$ eV), large volume (513 km^3), and viewing slightly more than half the sky. We have developed simulation tools to estimate the sensitivity to all neutrino flavors. In this paper, we will also present the angular coverage and energy dependent sensitivity of the detector.

Keywords: ARIANNA, Antarctica, neutrino, EHE, UHE, GZK, astronomy, detector, sensitivity, performance, simulation

1 Introduction

The ARIANNA experiment is being developed [1, 2] to study ultra-high energy (UHE) neutrinos (a) from the by-products of interactions of energetic cosmic-rays with the cosmic microwave background (the Greisen-Zatsepin-Kuzmin process leading to GZK ν's [3]), or (b) originating from GRBs and other point, possibly exotic, sources. It will consist of an array of autonomous stations, each equipped with 4 to 8 linearly polarized radio antennas, operating just under the surface of the Ross Ice Shelf (RIS) and listening for Askaryan pulses [4], i.e. radio Cherenkov radiation from interactions between UHE ν's and the nuclei in the ice.

At EeV energies, the low neutrino flux, compounded by the tiny neutrino-nucleon cross-section, requires a detector with a large effective volume. ARIANNA takes advantage of the radio transparency, quietness and reflectivity of the ice shelf to achieve a large enough aperture to search for such neutrino signals. A full array with stations spanning 30 km$\times$30 km, with a 570 m shelf thickness, equates to a detector volume of 513 km^3 (or $\sim$ a half a teraton of ice).

Early simulation work (see [5]) was carried out to understand the detecting capabilities of densely packed arrays: stations separated by 0.3 km. Here, our goal is to better understand the sensitivity and characteristics of the individual station. Specifically, we seek to understand the station sensitivity with E_ν for all ν flavors, its energy resolution and angular coverage. Compared to previous studies, new features have been added. For instance, we account for the angular dependence of the antennas, ν_τ regeneration and shadowing effects in the simulation. For reconstruction, we now use time domain information of waveforms.

2 Simulation work

We select the energy spectrum of ESS [6] to benchmark the sensitivity over the energy range of 10^{17}-$10^{21.5}$ eV, which assumes (1) pure proton composition, (2) injection spectra proportional to E^{-2} and with an exponential cutoff at $10^{21.5}$ eV, (3) sources of cosmic ray evolution as a function of redshift in the same way as AGN, and (4) the concordance cosmological model; we call is the ESS(standard) flux. The electron and muon neutrino fluxes are summed, and redistributed by oscillations into a 1:1:1 flavor ratio.

Neutrino interactions create showers that generate Askaryan pulses. As Table 1 shows, hadronic showers are initiated by neutral current (NC) and charged current (CC) events. The outgoing lepton in CC ν_e events initiates a co-located electromagnetic shower that is modified by the LPM effect. For ν_τ interactions, due to the double-bang mechanism, typically two hadronic showers are generated: one at the interaction vertex and another by the τ-decay. The simulation assumes (incorrectly) that both hadronic showers occur at the same position, selecting only the shower with the greatest energy, which is a somewhat conservative approximation of the ν_τ rates. In the work reported here, the outgoing muon in CC ν_μ is ignored.

The distribution of the inelasticity, y ($= (E_\nu - E_l)/E_\nu$), where E_l is the energy of the outgoing lepton) is chosen according to [7]. Considering the relative cross-sections between NC and CC interactions over the relevant energy interval, about two-thirds of the interactions are CC.

The diffuse flux of GZK ν's will arrive isotropically, so neutrino directions are picked randomly, and interaction vertices are selected at random within a fiducial volume of 4 km $\times$ 4 km $\times$ 0.57 km (deep). The ARIANNA station is

current	flavor	f_{em}	f_{had}
charged	ν_e	$1-y$	y
	ν_μ	-	y
	ν_τ	-	y (>0.5)
neutral	all	-	y

Table 1: Fractional distribution of electromagnetic and hadronic components of shower

frequency	beamwidth (BW)		gain
(MHz)	E-plane	H-plane	(dBi)
<300	74°	144°	5.9
300-600	70°	128°	6.6
600-900	74°	134°	6.2
900-1200	78°	132°	6.0

Table 2: LPDA antenna parameters

centered in the middle on the upper surface, antennas facing down. Once the neutrino direction is selected, the simulation evaluates the radiated power that reaches a particular receiver antenna by considering the profile of the width of the Cherenkov cone, absorption, polarization, reflection and other factors. In addition, the neutrino events are assigned a weight to account for absorption by the Earth. The weight for ν_τ is adjusted to accommodate regeneration effects, whereby τ leptons decay to lower energy ν_τ's [8]. At this point, ν_τ interactions must begin within the fiducial volume, which underestimates the interaction rate for horizontal directions.

The radio emission from the interactions is parametrized by theoretical models [9] that have been validated by accelerator measurements [10]. For electromagnetic showers, the LPM effect is approximately included by reducing the width of cone (i.e. the $\Delta\theta_{em}$ in the electromagnetic counterpart of Eq. 2 below) but maintaining the magnitude of the electric field at the Cherenkov angle, θ_c [11].

The temperature gradient in the RIS, ranging from $-28°$C at the surface to $\sim -1°$C at the water-ice boundary, impacts the attenuation length of signal propagation. A simple linear model of the temperature gradient is used to compute a depth-dependent average attenuation length that integrates over the path between the interaction point and the surface station for direct and reflected rays. At present, although the frequency dependence of the attenuation length can be explicitly treated, the results reported here use a simple average that is integrated between 100 MHz and 1 GHz. Since the details of the frequency dependence attenuation will affect the shape of the waveforms, we plan to include a detailed study of frequency-dependent attenuation in the near future to help with energy and angular reconstruction.

The density of the upper 100 m of the RIS increases with depth, varying exponentially between 0.36 gcm^{-3} to 0.92 gcm^{-3} [12]. The variation creates a depth-dependent variation in the index of refraction ranging between 1.3 at the surface to 1.8, which is modeled to begin at a depth of 100 m and remains 1.8 down to the water-ice interface. The graded index causes signal paths to curve away from the surface, giving rise to shadow regions surrounding the the ARIANNA station. The shadow regions reduce the sensitivity for direct events but has relatively little impact on reflected events which dominate the event rates.

Signals that reflect from the water-ice surface are conservatively assumed to reflect with 50% power, although recent measurements [13] show that the ice-water boundary may reflect more power. We also assume that polarization of the signal is preserved at the boundary, again, compatible with recent measurements.

The baseline design of the ARIANNA station includes 4-8 log periodic antennas (LPDAs) arranged in a geometrically symmetric pattern, facing downward, and with the top of the antenna buried $\sim$1 m below the surface of the snow. In this paper, we assume 8 antennas per station, with a nominal majority logic criteria of 3/8, but similar sensitivities are obtained with a majority logic of 4/8 or even 2/4 due to the symmetry (essentially, both of the parallel antennas surrounding the ARIANNA station typically see the same signal amplitudes). We use the manufacturer's specification to obtain the frequency dependent gain and angular response, and confirm the basic properties with a simulation package from [14]. The properties are summarized in Table 2.

To take advantage of the new capabilities of the waveform digitizer, designed by Kleinfelder [15], we model two trigger methods. The first is the more traditional method of triggering on a signal amplitude exceeding a specified level compared to the root mean square voltage fluctuations of the signal chain (due to the antenna, amplifier, and digitizer). The voltage threshold is nominally set to $5{\cdot}V_{rms}$, but studies show that varying it from $3{\cdot}V_{rms}$ to $8{\cdot}V_{rms}$ causes the sensitivity to decrease by a factor 2 only. So while the threshold value has modest impact on the station sensitivity, it has a dramatic impact on the rate of triggers due to random thermal fluctuations. The second method investigates noise suppression in each antenna channel due to a specific pattern of trigger conditions (eg. we may require that a signal contain a large positive value followed by a large negative value, or vice-versa). The pattern trigger selects on general features of the expected Askaryan pulse from a neutrino interaction, while greatly reducing the rate of triggers due to thermal noise.

3 Results and discussion

One advantage of ARIANNA is its large field of view. As seen in Fig. 1, the station views more than half sky. The solid angle coverage, Ω, is 2.8π. The plot also shows the higher detection rate of reflected events: they systematically account for at least 90%. The direct events occur exclusively around the horizon, and inclusion of the ν_τ regeneration effects significantly enhances their rate.

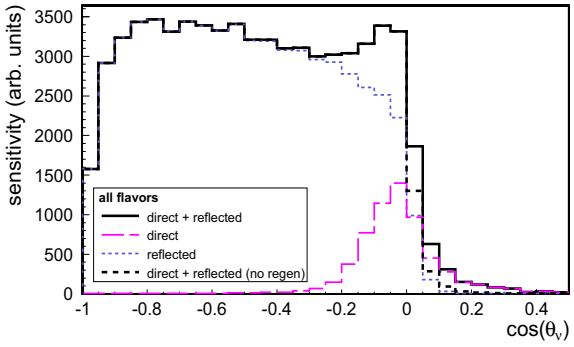

Figure 1: Preliminary angular sensitivity. On the horizontal axis, 0 is the horizon, and negative values are downgoing neutrinos. The solid black line shows an enhancement of events around the horizon due to ν_τ regeneration effects. The dotted black line is the same simulation without the effect.

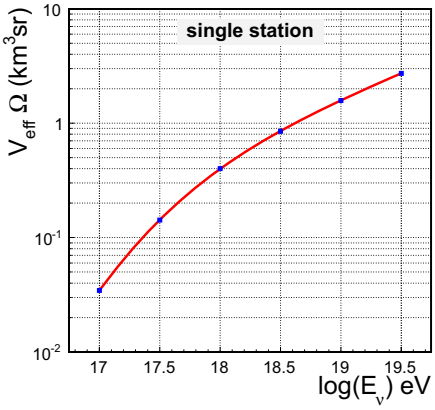

Figure 2: Effective aperture for a single station.

Projection maps of interaction vertices indicate that direct events are clustered closer to the station, while a small fraction of reflected events extend up to 1000-1500 m. Therefore, locating stations at least 1 km apart means that they essentially behave as independent detectors.

Fig. 2 gives the effective volume as a function of energy for a single station, averaged over neutrino flavor. For an array of independent stations, the total effective volume essentially scales linearly with the number of stations. Simulation shows that a 31 $\times$ 31 station array has the potential to observe $\sim$40 GZK ν's/year from the ESS [6] model predictions.

The sensitivity to different flavor neutrino for a ESS (standard) flux is given in Fig. 3. ARIANNA will detect neutrinos in the range $10^{17.5}$ to 10^{20} eV, with a peak response in the "sweet spot" of GZK spectrum and a low energy threshold.

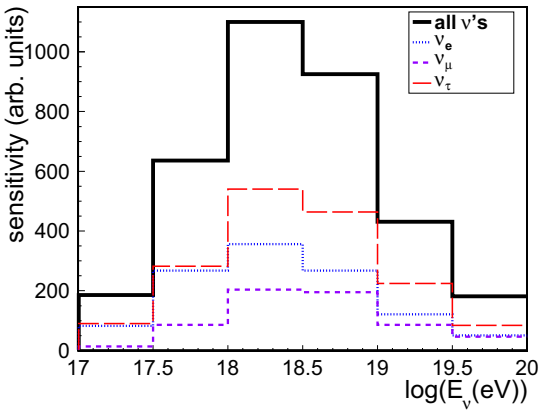

Figure 3: Flavor sensitivity based on ESS (std) GZK flux.

Energy resolution For a single station, the spatial location of the vertex can only be determined for nearby interactions. For the majority of events, the direction to the shower constrains the maximum distance to the vertex, and simulations are used to determine a mean distance, averaged over all events, for a given measured propagation direction of the Askaryan pulse, $\langle d(\theta) \rangle$. Waveform information such as maximum amplitude, relative timing between receivers, polarization, and details of the time profiles are used to reconstruct event parameters such as direction and energy.

The neutrino energy is calculated by sequence of steps: (1) use waveform information to compute the amplitude of the Askaryan signal at a reference distance of 1 m from the vertex, which is related to shower energy by standard parameterization [9], and (2) the neutrino energy is computed by dividing the shower energy by the inelasticity, averaged over neutrino energy and neutrino flavor. The averaging is required at this point because the inelasticity for a given event is unknown. In addition, there is no attempt to identify neutrino flavor in the reconstructions presented here.

The signal observed by the ARIANNA antenna, V_{obs}, is computed from the electric field, $\mathcal{E}_s$ at the antenna convolved with the antenna response. In the frequency domain, we have:

$$V_{obs} = \mathcal{E}_s \otimes [\mathcal{K} \cdot \langle \mathrm{f_E} \rangle \cdot \mathrm{e}^{(-2\ln 2(\frac{\theta_{\mathrm{inc}}}{\langle \theta_{\mathrm{BW}} \rangle})^2)}] \qquad (1)$$

where $\mathrm{f_E}$ is the component of the signal within the E-plane of the LPDA. The exponential term is responsible for the angular dependence in the gain of the antenna averaged over E and H plane response; θ_{BW} are taken from Table 2, and θ_{inc} to the angular components in the E and H antenna planes of incoming ray. In this analysis, $\mathrm{f_E}$ is averaged over angle and θ_{BW} is averaged over frequency. The constant term, $\mathcal{K}$, contains effective height term as a function of frequency and the gain of the antenna.

The surface field is related to the benchmark field at 1 m from the interaction, $\mathcal{E}_0$, by including attenuation and re-

flection losses, propagation, and geometrical effects associated with the propagation direction of the detected pulse with respect to the Cherenkov cone:

$$\mathcal{E}_s \approx \mathcal{E}_0 \cdot \langle f_{had} \rangle \cdot \frac{e^{-\langle d(\theta) \rangle / \langle L \rangle}}{\langle d(\theta) \rangle} \cdot e^{(-\ln 2(\frac{\theta_v - \theta_c}{\langle \Delta\theta_{had} \rangle})^2)} \cdot \sqrt{R} \quad (2)$$

For ν_e interactions, a similar term involving f_{em} must be added to the expression, but in the absence of flavor ID, it is ignored. Simulations were used to obtain the hadronic fraction $\langle f_{had} \rangle = 0.8$, averaged over flavor and energy spectrum. The reflectivity factor, R, which accounts for reflective losses for events that reflect from the water-ice boundary, is set to 0.5, despite a small admixture of direct events. Since the vertex position is not reconstructed, the depth dependent attenuation length must be averaged over the ice thickness, $\langle L \rangle$. The second exponential term accounts for the finite width of the Cherenkov cone. Time profile information can be used to obtain $(\theta_v - \theta_c)$ [16] and it is assumed that the resolution is within 1°. Finally, $\Delta\theta_{had}$ describes the frequency dependent width of the cone, and averaged over frequency in the event analysis. No distinction is made between hadronic and electromagnetic showers in the reconstructions.

Once $\mathcal{E}_0$ is extracted from Eq. 2, standard parameterizations [9] relate it to the shower energy, given by $E_\nu^{meas.}$. Fig. 4 shows the fractional energy resolution for neutrino events that strike a single station for all flavors combined and each flavor separately. It shows that the neutrino energy can be measured to within a factor of 2.4 without a vertex position or flavor ID. The resolution is dominated by the uncertainty in the measured propagation angle with respect to the Cherenkov cone and the unknown inelasticity. We plan to study the time profiles of the Askaryan waveforms more carefully to improve energy estimates.

Multi-station prospects The hexagonal radio array, HRA, consisting of 7 ARIANNA stations, provides additional information for the higher energy (mostly direct) events that can trigger several stations. Flavor ID procedures can be enhanced if, for example, each shower of a double-bang event is detected by separate stations.

4 Summary

Simulation studies show that ARIANNA detects GZK neutrinos between $10^{17.5}$-$10^{19.5}$ eV, roughly independent of flavor. The angular sensitivity is approximately flat over half the sky, and the event rate of events near or just below the horizon is enhanced by tau-regeneration, and merits additional study. The rate of reflected events dominates the rate of direct events, which are largely clustered near the horizon. The energy dependent effective volume per station indicates that 40 events per year are expected for proton dominated GZK models. Finally, initial reconstruction techniques have achieved a fractional energy resolution of 2.4, dominated by the measurement uncertainty in the propagation angle with respect to the Cherenkov cone.

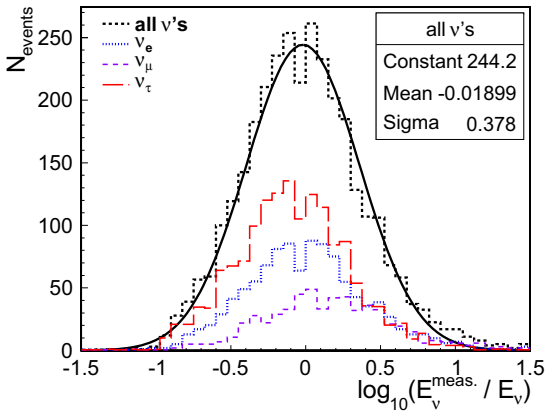

Figure 4: Preliminary fractional energy resolution of a ARIANNA single station

5 Acknowledgments

This work was supported by the U.S. NSF Office of Polar Programs and U.S. NSF Physics Divison, award numbers 0839133 and 0970175, and by the Department of Energy under contract DE-AC-76SF-00098. We also thank the dedicated staff of Raytheon Polar Services for their logistical support of the ARIANNA program.

References

[1] Barwick, S., for ARIANNA Collaboration , 2011, ICRC proc., ID 0976
[2] Gerhardt, L. et al, 2010, Nucl.Inst.Meth.A **624**:85-91
[3] Greisen, K. 1966, PRL, **16**:748 ; Zatsepin, G. T., & Kuz'min, V. A. 1966, JETP Lett., **4**:78
[4] Askar'yan, G. A. 1965, JETP, **21**:658
[5] Wu, F., Nam, J., for ARIANNA Collaboration, 2007, ICRC proc., ID 1111
[6] Engel, R., et al, 2001, Phys.Rev.D, **64**, 093010
[7] Gandhi, R., et al, 1996, Astropart.Phys. **5**:81-110
[8] Halzen, F., & Saltzberg, D., 1998, PRL, **81**:4305-4308
[9] Alvarez-Muñiz, J., et al 2000, Phys.Rev.D, **62**, 63001
[10] Gorham, P. W., et al, 2007, PRL, **99**:171101
[11] Alvarez-Muñiz,J., et al, 1997,Phys.Lett.B411:218
[12] Dowdeswell, J. A. & Evans, S., 2004, Rep.Prog.Phys. **67** 1821
[13] Hanson, J., for ARIANNA Collaboration, 2011, ICRC proc., ID 0340
[14] Balanis, C.A.: 2005, Antenna Theory, 3rd Ed., Wiley.
[15] Wei, H., Chiang, S.-H.W., Kleinfelder, S., Nucl. Sci. Symp. Conf. Record, 2009 IEEE , N13-50.
[16] Alvarez-Muñiz, J., et al, 2010, Phys.Rev.D, **81**, 123009

Heavy Neutrino Decay at SHALON

V.G. SINITSYNA[1], M. MASIP[2],S.I. NIKOLSKY[1], V.Y. SINITSYNA[1]
[1]*P.N. Lebedev Physical Institute, Leninsky pr. 53, Moscow, Russia*
[2]*CAFPE and Departamento de Fosica Teoretica y del Cosmos Universidad de Granada,E-18071 Granada Spain*
sinits@sci.lebedev.ru
DOI: 10.7529/ICRC2011/V04/0170

Abstract: The SHALON Cherenkov telescope has recorded over 2×10^6 extensive air showers during the past 17 years. The analysis of the signal at different zenith angles has included observations from the sub-horizontal direction $\Theta = 97^\circ$. This inclination defines an Earth skimming trajectory with 7 km of air and around 1000 km of rock in front of the telescope. During a period of 324 hours of observation, after a cut of shower-like events that may be caused by chaotic sky flashes or reflections on the snow of vertical showers, we have detected 5 air showers of TeV energies. We argue that these events may be caused by the decay of a long-lived penetrating particle entering the atmosphere from the ground and decaying in front of the telescope. We show that this particle can it not be a muon or a tau lepton. As a possible explanation, we discuss two scenarios with an unstable neutrino of mass $m \approx 0.5$ GeV and $c\tau \approx 30$ m. Remarkably, one of these models has been recently proposed to explain an excess of electron-like neutrino events at MiniBooNE.

Keywords: Extensive Air Showers below the horizon, Earth-skimming neutrino interactions.

Introduction

Cosmic rays have become a very valuable tool in astronomy, as they provide a very *different* picture of the sky. In particular, during the past decades gamma-ray detectors have discovered a large number of astrophysical sources (quasars, pulsars, blazars) in our Galaxy and beyond. Ground based telescopes are designed to detect the Cherenkov light of the shower produced when a 0.1–100 TeV photon enters the atmosphere. The light burst in a photon (or electron) air shower has a profile that can be distinguished from the one from primary protons or atomic nuclei, which are a diffuse background in such observations (see [1, 2] for a review).

Cosmic rays may also offer an opportunity to study the properties of elementary particles. The main objective in experiments like IceCube [3] or Auger [4] is to determine a flux of neutrinos or protons as they interact with terrestrial matter. These interactions involve energies not explored so far at particle colliders, so their study should lead us to a better understanding of that physics. In addition, the *size* of the detector and its distance to the interaction point is much larger there than in colliders, which may leave some room for unexpected effects caused by long-lived particles. It could well be that in the near future cosmic rays play in particle physics a complementary role similar to the one played nowadays by cosmology (in aspects like dark matter, neutrino masses, etc.).

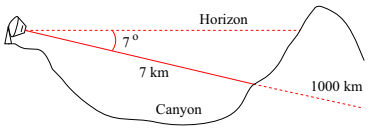

Figure 1: Configuration at $\theta = 97^o$.

In this paper we describe what we think may be one of such effects. It occurs studying the response of the SHALON telescope [5] to air showers from different zenith angles, in a sub-horizontal configuration where the signal from cosmic rays should vanish.

The SHALON mirror telescope

SHALON is a gamma-ray telescope [6, 7]. It has been operating since 1992 [5, 7, 8]. During this period it has detected gamma-ray signals from well known and also from new sources of different type: Crab Nebula, Tycho's SNR, Geminga, Mkn 421, Mkn 501, NGC 1275, SN2006 gy, 3c454.3 and 1739+522 [8].

SHALON is located at 3338 meters a.s.l. in the Tien-Shan mountain station. It has a mirror area of 11.2 m^2 and a large field of view above 8^o, with an image matrix of 144 PMT and $< 0.1^o$ angular resolution. The recording of Cherenkov light is performed in 50 nsec intervals, which is enough to acquire complete information about the air shower while preventing additional light-striking. The telescope is calibrated according to the observations of EAS of cosmic ray at 0° - zenith angle. The cosmic ray shower

Table 1: The atmosphere depth at different zenith angles

Zenith angle, Θ°	Atmosphere depth, g/cm^2	Number of Cherenkov burst per hour
0°	670	1100 ± 210
72°	2250	7 ± 1.14
76°	3000	1.8 ± 0.5
84°	5950	0.5 ± 0.01

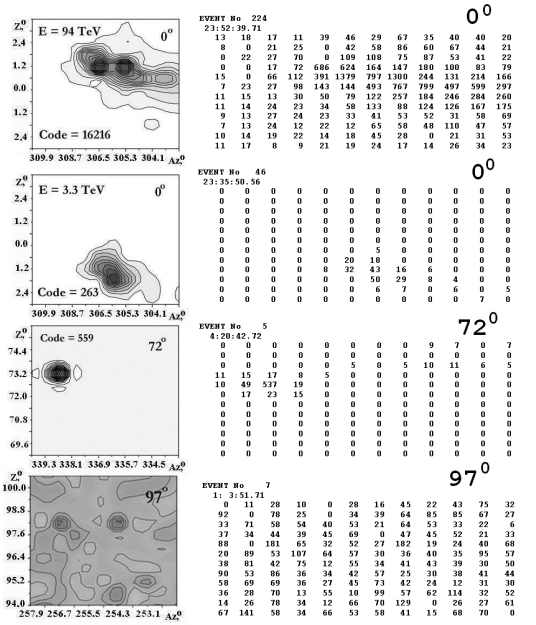

Figure 2: The examples of showers recorded in PMT matrix at different zenith angles. The amplitude of gray - scale shower images is proportional to the ADC count. The number, named CODE shows the range of detected signals in the ADC counts, which are proportional to shower energy.

image detected in the SHALON telescope, generally is elliptic spot in the light receiver matrix, written in the ADC counts (CODE) (the numbers at fig. 2 right).

Observations at large zenith angles have been aimed on study of spectra of the air showers induced by cosmic rays crossing through different atmosphere thickness and events accompanying the passing of EAS and cosmic ray particles near horizon. The observation at large zenith angles 72^o, 76^o, 84^o showed that the efficiency of Cherenkov light detection drops essentially as a zenith angle increases, perhaps because of dissipation and absorption in the atmosphere. So, the comparison of observation results shown that at the zenith angle 84° the number of observed showers is ~ 25 times less than expected by estimation with neglecting by absorption and dissipation of Cherenkov photons in the atmosphere (table 1, fig. 2).

Cherenkov bursts below the horizon

The study of extensive air showers at large zenith angles included observations at the sub-horizontal direction $\theta = 97^o$ [5, 8]. The configuration of the telescope is depicted in Fig. 1. SHALON Cherenkov mirror telescope is located at 3338 m a.s.l. The mountain range lies in the east direction and is more than 4300 m a.s.l. The mountain range is about 20 km long. The mountain slope has a structure which is irregular on the scales less than typical shower size; it is covered with the forest. The thickness of matter in the telescopic field of view is from 2000 to 800 kms; viewed mountain slope area is $> 7 \times 10^5\ m^2$. For telescope located about 7kms away from the mountain slope horizontally, the shadow of mountain is about 7° in elevation. In actual conditions the mirror telescope placement the distance till the opposite slope of the gorge is ~ 7 km or ~ 16.5 radiation units of length, that is quite enough for the development of an electromagnetic cascade till the structure characteristic for the rarefied atmosphere. Observations at 97° zenith angle have been done in cloudless nights in absence of artificial lights and dry air. During 324 hours of observation at 97° zenith angle 323 short-range bursts were recorded. In accordance with the existing ideas and estimations [5, 11, 10] an appearance of electron-photon cascade from upward direction in current SHALON experiment conditions, which are above described, can be connected with passing of weakly interacting particles through rock and earth matter. The identity of upward neutrino initiated showers to cosmic ray ones in frames of concerning experiment has been performed in accordance to the following parameters used in the gamma-ray astronomy. The parameters used to characterize the shower image are image maximum position (x_{max}, y_{max}); length, width; the relation of two previous described Hillas parameters: $Length/Width$; two parameters sensible to the shower shape: $Int0$, $Int1$; The $Int0$ is the ratio of Cherenkov light intensity in pixel with maximum pulse amplitude to the light intensity in the eight surrounding [8]; The $Int1$ is the ratio of Cherenkov light intensity in pixel with maximum pulse amplitude to the light intensity in the in all the pixels except for the nine in the center of the matrix. In addition, the selection criteria we are using ($Int0$, $Int1$, $Length/Width$) are of the relative nature to describe 2-D shower structure, which is also different in current experiment conditions from vertical one by less than 10%. The parameter proportional to the energy of the shower is Code.

The SHALON databank (since 1992) contains a millions of verified showers from vertical cosmic ray observations with their parameters, so the selection of the showers with a set of parameters of any sample can be performed. Reconstruction of shower coming direction using the analysis of shower shape and position of shower maximum (in case of non-gamma shower) is performed with accuracy $< 0.5^\circ$ which is enough to judge on whether it upward shower or near horizontal. Horizontal and down going shower is out of field of view because of narrow-beaming of Cherenkov telescope relative to ice or water neutrino telescopes.

During 324 hours of observations 5 events were detected (figs. 3 left) which have expected angular characteristics of a light burst of an electron-photon cascade developing within a telescope observation angle. These showers

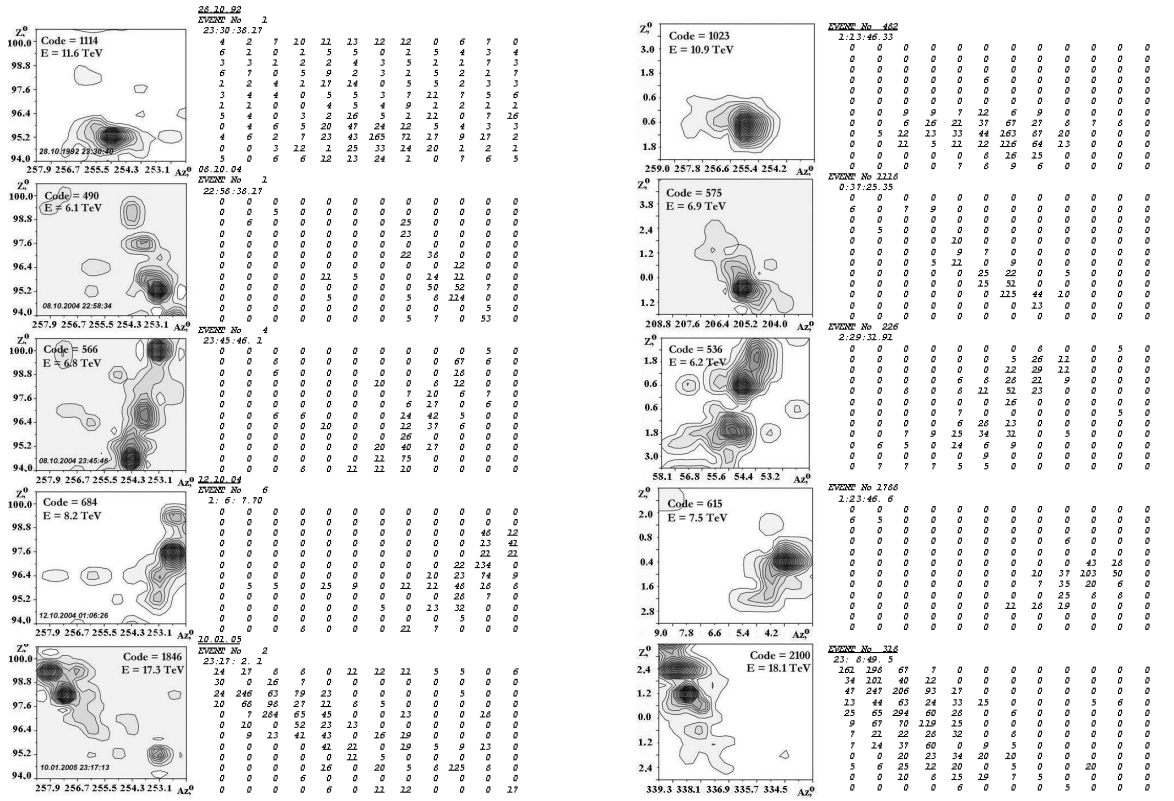

Figure 3: left - Cherenkov Radiation of Extensive Air Showers Observed at 97° Zenith Angles by SHALON; right - Cherenkov Radiation of Extensive Air Showers Observed at 0° Zenith Angles by SHALON

have energy in the range of about $6 - 17.5$ TeV. These 5 events have form characteristics and parameters similar (within 10% error) to those observed at 0° zenith angle (figs. 3 right). These cascades look like the usual extensive air showers generated in atmosphere with narrow light shape. The background for this events can be some reflections of cosmic ray EAS in the mountain slope. First of all it could be a reflection of showers initiated by particles born in interaction of very high energy cosmic rays and rock matter nucleons. The energy of detected showers is more than 6 TeV. There is no albedo particles of such high energies. One more source of particles with high transverse energy is jet production. The reflection from snow which can mimed the EAS shape is excluded due to the irregular and woody structure of opposite slope (in addition: there is no snow there till the start of November). The probability of hadronic jet production with energy of observed showers is ten orders of magnitude less than one for detection of shower generated by secondary particles of UHE neutrino interaction.

All other 318 events of detection of short-range light bursts in the atmosphere have not a narrow angle light direction and are chaotically distributed along the whole matrix or its part of a light-receiver (see figs. 2 for 97°, no other type of shower image were found among the 318 mentioned pictures). These events may be interpreted as a reflection of a Cherenkov burst from a snow mountain slope or as an ionization luminescence of the atmosphere while an extensive air showers transition within a telescope observation angle.

Earth-skimming neutrino interactions

The flux of sub-horizontal events is around 6×10^{-6} times the flux of TeV cosmic rays reaching the atmosphere. Such a large flux seems to eliminate the possibility that these events are due to neutrino interactions in the air or within the last ≈ 20 cm of rock. The interaction length of a 10 TeV neutrino is $\approx 10^5$ km [12]. This implies that only one out of 10^9 of them will interact to produce such an event. The expected neutrino flux from pion and kaon decays at 10 TeV is a per cent fraction of the primary proton flux, whereas the flux from the prompt decay of charmed hadrons, although uncertain, should be still smaller at these energies [13]. Therefore, the expected number of events from atmospheric neutrino interactions is 10^5 times smaller than the one observed. On the other hand, a flux of primary (non-atmospheric) neutrinos large enough would be inconsistent with observations at neutrino telescopes.

Another possibility that can be readily excluded is the decay in the air of a muon or a tau lepton produced inside the rock. A 10 TeV muon could emerge if it is produced ≈ 1 km inside the rock [12] (one out of 10^5 incident neutrinos will produce a muon there). However, the muon decay length at TeV energies is around 10^4 km, so the probability

that it decays in the air in front of the telescope is again too small. The neutrino fluxes required to explain the events from μ decays or from ν interactions are then similar (and excluded). The probability for tau lepton production in the rock and decay in the air is not higher. The tau becomes *long-lived* at $\approx 10^8$ GeV. At 10 TeV it should be produced within the last meter of rock ($c\tau\gamma \approx 0.5$ m), which reduces very much the number of events.

Heavy neutrino decay

Therefore, we have to explore possible explanations based on new physics. The ideal candidate should be a long-lived massive particle, neutral, frequently produced in air showers, and very penetrating: able to cross 1000 km of rock and decay within the 7 km of air in front of the telescope. If this particle has (possibly suppressed) couplings to the W and/or Z bosons, its mass m_h should be larger than m_μ (to decay in the last 7 km of air) and smaller than m_τ (to cross 1000 km of rock without decaying). Notice that if its decay length at 10 TeV is $c\tau\gamma \approx 1000$ km, at GeV energies it will tend to decay far from the detectors in colliders.

An obvious possibility is a sterile neutrino. We take two Weyl spinors n and n^c and add a Dirac mass term together with a Yukawa coupling to the lepton family $L = (\nu_l\ l)$,

$$-\mathcal{L}_\nu = m_n\ nn^c + y_\nu\ h^\dagger L n^c + \text{h.c.} \qquad (1)$$

Then the Higgs VEV v induces mixing between n and ν_l:

$$-\mathcal{L}_\nu \supset m_n\ nn^c + m_{EW}\ \nu_l n^c = m_h\ \nu_h n^c\ , \qquad (2)$$

where $m_{EW} = y_\nu v/\sqrt{2}$, $m_h = \sqrt{m_n^2 + m_{EW}^2}$, $\nu_h = c_\alpha n + s_\alpha \nu_l$, $s_\alpha = m_{EW}/m_h$, and the orthogonal combination $-s_\alpha n + c_\alpha \nu_l$ remains massless. The mixing implies couplings of ν_h to the W and Z gauge bosons; the first one will appear suppressed by $U_{lh} = s_\alpha$, whereas the flavour-changing (heavy to light) Z coupling will be proportional to $c_\alpha s_\alpha$.

A first ν_h model that we would like to discuss has been recently proposed by Gninenko [14] to explain an anomaly at MiniBooNE [15]. He claims that the excess of electron-like events in the interactions of the $\langle E\rangle \approx 800$ MeV ν_μ beam could be caused by the decay of a heavy neutrino if $m_h \approx 0.5$ GeV, $c\tau_h \leq 30$ m, and $|U_{\mu h}|^2 \approx 10^{-3}$. This explanation requires a large transition magnetic moment [16], $\mu_{tran} \approx 10^{-10}\mu_B$, which implies a dominant decay mode

$$\nu_h \to \gamma\nu\ . \qquad (3)$$

The final photon would convert into a e^+e^- pair with a small opening angle that would be indistinguishable from an electron in MiniBooNE. At the same time, this dominant decay channel could make the required value of $U_{\mu h}$ consistent with bounds $|U_{\mu h}|^2 \leq 10^{-5}$ from BEBC [17], CHARM [18] and CHARM2 [19], as these experiments look for decays into final states with charged particles ($\nu_h \to ee\nu, \mu e\nu, \mu\pi$).

It is easy to see that such a particle could have an impact on the SHALON events. At 10 TeV its decay length is $\lambda_h \approx 600$ km. If ν_h is produced in the atmosphere with that energy, the probability that it crosses $\lambda \approx 1000$ km of rock and decays within the $\Delta\lambda \approx 7$ km of air in front of the telescope is

$$p = e^{-\lambda/\lambda_h}\left(1 - e^{-\Delta\lambda/\lambda_h}\right) \approx 0.002 \qquad (4)$$

This implies that the atmospheric flux of heavy neutrinos should be a 1/1000 fraction of the TeV flux of primary cosmic rays. This large flux seems difficult to achieve because ν_h is not produced in pion or kaon decays (as $m_h > m_{\pi,K}$), it appears only in a $|U_{\mu h}|^2 \approx 10^{-3}$ fraction of charmed hadron decays into muons.

A slightly more frequent production rate could be expected in a second model, where ν_h has a sizeable component along the tau neutrino. NOMAD [20] has set limits $|U_{\tau h}|^2 \leq 10^{-2}$ from $D_s \to \tau\nu_h$, and then $\nu_h \to \nu_\tau ee$, but they apply only to neutrinos lighter than $m_{D_s} - m_\tau \approx 0.19$ GeV. Cosmological and supernova bounds on $U_{\tau h}$ apply to lighter values of m_h as well [21]. On the other hand, LEP bounds cover just the range $m_h > 3$ GeV [22] (decays in the detector of lighter neutrinos are too rare). Therefore, a possible candidate could have a 0.2–0.4 GeV mass, $|U_{\tau h}|^2 \approx 0.1$, and negligible mixings with the other two families. The dominant decay channels would be into $\nu_\tau\pi^0$ and into $\nu_\tau ee$, $\nu_\tau\mu\mu$. If its decay length at the TeV energies of the sub-horizontal events is around 1000 km, then the probability of decay in the air in front of SHALON is ≈ 0.003. Its production in air showers would be through tau decay; one can expect $|U_{\tau h}|^2 \approx 0.1$ heavy neutrinos from each tau produced in the atmosphere. These tau leptons would mainly come from the prompt decay of charmed D_s mesons, and also from mesons containing a bottom quark. The flux required, a per cent of the TeV proton flux, seems still too large. Notice, however, that there are also large uncertainties in the flux and energy of the sub-horizontal events, or in the tau production rate in the atmosphere by cosmic rays [13].

Summary and discussion

When a cosmic ray enters the atmosphere it produces an extended air shower with thousands of secondary particles. Obviously, if there is any new physics it will be contained in a fraction of these events. Now, if this *exotic* physics includes a long-lived particle, we think that there is the potential for its discovery in cosmic ray experiments. Generically, to be detectable the particle must *survive* after the rest of the shower has been absorbed by the atmosphere (*e.g.*, a long-lived gluino in horizontal air showers [23]) or the ground (a stau in neutrino telescopes [24]). In particular, a long-lived neutral particle could propagate to the center of a neutrino telescope and start there a contained shower when it decays. However, this event would look indistinguishable from a standard neutrino interaction.

In this paper we discuss several air showers obtained at SHALON in a configuration (see Fig. 1) where the expected number of events is zero. Around 1000 km of rock absorb the atmospheric flux of any standard particles but neutrinos. Neutrino interactions in the rock are frequent, but they are not observable as they *disappear* in just half a meter of soil. A few muons could be produced during the last km and emerge from the rock, but then the probability of muon decay within the 7 km of air in front of the telescope is too small. The crucial difference with a neutrino telescope is that here the probability of a *visible* ν interaction (in the air or the last centimeters of rock) is negligible.

We argue that these events may correspond to the decay of a neutral particle after it is produced in the atmosphere and has crossed 1000 km of rock. We have studied a couple of models where this particle is a heavy neutrino, and have concluded that although the required production rate seems higher than the expected one, due to a number of uncertainties on the flux and the energy of the exotic events or on the production of charmed particles in the atmosphere, none of these possibilities should be excluded.

Acknowledgements.– The SHALON Experiment has been supported by RFBR 06-02-17364 and by the Program of the Russian Academy of Sciences "Neutrino Physics" 06, 08, 09. The work of M.M. has been supported by MEC of Spain (FPA2006-05294) and by Junta de Andalucía (FQM-101 and FQM-437).

References

[1] T. C. Weekes, arXiv:0811.1197 [astro-ph].
[2] H. J. Völk and K. Bernloehr, arXiv:0812.4198 [astro-ph].
[3] A. Achterberg, et al. [IceCube Collaboration],: Astropart. Phys. 2006, **26**: 155.
[4] J. Abraham, et al., [Pierre Auger Collaboration],: Nucl. Instrum. Meth. A, 2004, **523**: 50.
[5] V. G. Sinitsyna [SHALON Experiment],: in Proc. of Toward a Major Atmospheric Cherenkov Detector-II, Calgary, July 17-18 1993, ed. R. C. Lamb, 91, 1993.
[6] S. I. Nikolsky and V. G.Sinitsyna [SHALON Experiment],: VANT, Ser. TFE, 1987, 1331, 30.
[7] V. G. Sinitsyna, Prepared for 6th GeV - TeV Gamma Ray Astrophysics Workshop: Toward a Major Atmospheric Cerenkov Telescope, Snowbird, Utah, 13-16 Aug 1999.
[8] V. G. Sinitsyna et al., [SHALON Experiment],: Nucl. Phys. Proc. Suppl. 2003, **122**: 247 ; Nucl. Phys. Proc. Suppl. 2008, **175-176**: 455, 544; Nucl. Phys. Proc. Suppl. 2009, **196**: 251, 433, 437, 442.
[9] V. Y. Sinitsyna et al., [SHALON Experiment],: in Proc. of the 28th International Cosmic Ray Conference, July 31-August 7, 2003. Trukuba, Japan. Editors: T. Kajita et al., 2369, 2004.
[10] L.K. Resvanis, Nucl.Phys.B (Proc.Suppl.), 2006, **151**: 279.
[11] D. Fargion, ApJ, 2002, **570**: 909.
[12] C. Amsler et al., [Particle Data Group],: Phys. Lett. B, 2008, **667**: 1.
[13] C. G. S. Costa Astropart. Phys. 2001,**16**: 193.
[14] S. N. Gninenko, "The MiniBooNE anomaly and heavy neutrino decay," arXiv:0902.3802 [hep-ph].
[15] A. A. Aguilar-Arevalo et al., [The MiniBooNE Collaboration],: Phys. Rev. Lett. 2007, **98**: 231801.
[16] R. N. Mohapatra and P. B. Pal: "Massive neutrinos in physics and astrophysics. Second edition," World Sci. Lect. Notes Phys. 1998, bf60; 1.
[17] A. M. Cooper-Sarkar et al. [WA66 Collaboration],: Phys. Lett. B, 1985, **160**: 207.
[18] F. Bergsma et al. [CHARM Collaboration],: Phys. Lett. B, 1986,**166**: 473.
[19] P. Vilain et al., [CHARM II Collaboration],: Phys. Lett. B, 1995, **343**: 453.
[20] P. Astier et al., [NOMAD Collaboration],: Phys. Lett. B, 2001, **506**: 27. [arXiv:hep-ex/0101041].
[21] A. D. Dolgov, S. H. Hansen, G. Raffelt and D. V. Semikoz, Nucl. Phys. B, 2000, **590**: 562.
[22] O. Adriani et al., [L3 Collaboration],: Phys. Lett. B, 1992, **295**: 371.
[23] J. I. Illana, M. Masip and D. Meloni, Phys. Rev. D, 2007, **75**: 055002.
[24] M. Ahlers, J. I. Illana, M. Masip and D. Meloni JCAP, 2007, **0708**: 008.

32ND INTERNATIONAL COSMIC RAY CONFERENCE, BEIJING 2011

Search for a diffuse flux of high-energy muon neutrinos with the ANTARES neutrino telescope

FABIAN SCHÜSSLER[1] ON BEHALF OF THE ANTARES COLLABORATION
[1] *Commissariat à l'énergie atomique et aux énergies alternatives*
Institut de recherche sur les lois fondamentales de l'Univers
91191 Gif-sur-Yvette Cedex, France
fabian.schussler@cea.fr
DOI: 10.7529/ICRC2011/V04/0237

Abstract: We present the search for the diffuse flux of astrophysical muon neutrinos using data collected by the ANTARES neutrino telescope. We introduce a novel method to estimate the energy of high-energy muons traversing the ANTARES detector and discuss detailed comparisons between data and Monte Carlo simulations. Using data recorded in 2008 and 2009 a search for a high-energy excess over the expected atmospheric neutrino background is presented and stringent limits on the diffuse flux of astrophysical muon neutrinos in the energy range 20 TeV - 2.5 PeV are derived.

Keywords: neutrino astronomy, neutrino telescopes, diffuse flux

1 Introduction

Despite enormous efforts throughout the last century, the mystery of the origin of high-energy cosmic rays remains unsolved. Over the last years it became more and more obvious that multiple messengers will be needed to achieve this task. Fortunately fundamental particle physics processes like the production and subsequent decay of pions in interactions of high-energy particles predict clear links between high-energy cosmic rays and high-energy neutrinos as well as gamma rays. The detection of astrophysical neutrinos and the identification of their sources is one of the main aims of large neutrino telescopes operated in ice at the South Pole (IceCube) and in water at Lake Baikal and in the Mediterranean Sea (ANTARES).

1.1 The ANTARES neutrino telescope

The ANTARES detector [1] became fully equipped and operational in 2008. The detector is composed of 12 detection lines placed at a depth of 2475m off the French coast near Toulon. The detector lines are arranged on the seabed in an octagonal configuration, covering a base of 180×180 m^2 and are about 450m high. They hold a total of 885 optical modules (OM), 17" glass spheres housing each a 10" photomultiplier tube. The OMs look downward at 45° in order to optimize the detection of upgoing, i.e. neutrino induced, tracks. The geometry and size of the detector make it sensitive to neutrinos in the TeV-PeV energy range. A schematic layout is shown in Fig. 1.

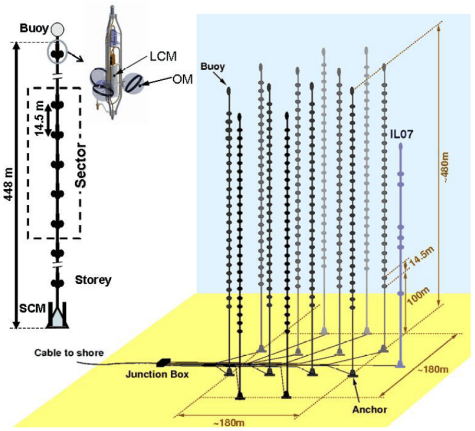

Figure 1: Schematic view of the ANTARES detector.

1.2 Neutrino detection and dataset

The neutrino detection relies on the emission of Cherenkov light by high-energy muons originating from charged current neutrino interactions near and inside the instrumented volume. All detected signals are transmitted via an optical cable to a shore station, where a farm of CPUs filters the data for coincident signals or *hits* in several adjacent OMs. The muon direction is then determined by maximising a likelihood which compares the times of the hits with the expectation from the Cherenkov signal of a muon track.

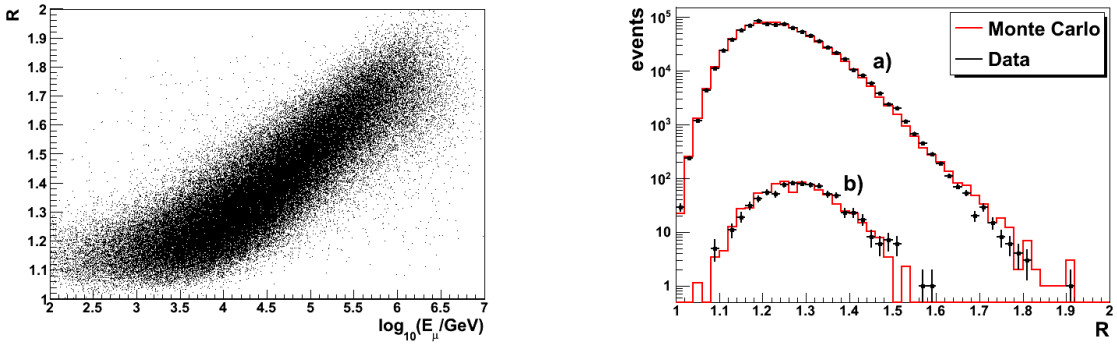

Figure 2: Left plot: Correlation between the energy estimator R and the generated muon energy after all quality cuts. Right plot: Distribution of the R energy estimator of data (markers) and simulated atmospheric muons normalized to the data (histograms) applying only loose quality cuts. Good agreement of the shape is found for both downgoing muons (a) and events mis-reconstructed as upgoing (b).

We analyse here data taken with the ANTARES detector between 12/2007 and 12/2009. Related to the construction and maintenance efforts, this period includes data from a detector comprised of 9, 10 and 12 active detection lines. Data runs were selected according to a set of basic quality criteria, which require for example low environmental background noise. The selection corresponds to a total live time of 334 days (136 days with 9 lines, 128 days with 10 lines and 70 days with 12 lines).

2 Diffuse astrophysical neutrino flux

The measured flux of high-energy cosmic rays has been used to derive upper bounds for the expected diffuse neutrino flux [2, 3]. For the TeV to PeV energy range considered here, this flux is typically assumed to originate from particle interactions at or close to the cosmic ray acceleration sites. Although only weakly constrained, the neutrino energy spectrum is typically modelled by a simple E^{-2} power law.

2.1 Background discrimination

Two main backgrounds for the measurement of the flux of these astrophysical neutrinos can be identified: downgoing atmospheric muons which have been mis-reconstructed as upgoing and atmospheric neutrinos originating in cosmic ray induced air showers at the opposite side of the Earth. Both backgrounds can at least partially be discriminated using various parameters like the quality of the event reconstruction or an estimator for the energy of the muon. To optimize the selection criteria detailed Monte Carlo (MC) simulations have been used. The atmospheric muon flux has been simulated with the MUPAGE package [4]. Generated atmospheric neutrinos are weighted corresponding to the 'Bartol' parametrisation [5]. Due to the lack of information on the production of charm mesons in high-energy hadronic interactions, the presence of an additional component at high energies (above $\sim$ 10 TeV) is possible. Among the models considered in [6] the Recombination Quark Parton Model (RQPM) was used. It gives the largest 'prompt' contribution to the atmospheric neutrino flux. Both event types, atmospheric muons and neutrinos, are processed with the full ANTARES detector simulation and reconstruction chain. Special care has been taken to reproduce the changing detector configuration during the analysed data taking period and the details of the data acquisition by including for example afterpulses in the PMT simulations. The simulated instrumental and environmental background noise has been extracted for each of the detector configurations from a representative real data-taking run.

2.2 Atmospheric muon rejection

Atmospheric muons are recorded with the ANTARES detector at a rate of several Hz and dominate the detector trigger rate. To remove a large majority of them from the dataset the selected events have to fulfil the following basic quality criteria:

- detection with at least two detector lines
- more than 60 hits available for the reconstruction
- reconstructed zenith angle $\theta < 80°$, i.e. upgoing tracks

To fully suppress mis-reconstructed atmospheric muons, an additional 2-dimensional cut has been derived. It combines the quality parameter Λ which is derived from the likelihood value of the track fitting algorithm and the number of hits used in the fitting procedure $N_{\rm hit}$. The events have to pass the selection

$$\Lambda > \begin{cases} -4.59 - 5.88 \cdot 10^{-3}\, N_{\rm hit} & \text{for} \quad N_{\rm hit} \leq 172 \\ -5.60 & \text{for} \quad N_{\rm hit} > 172 \end{cases}$$

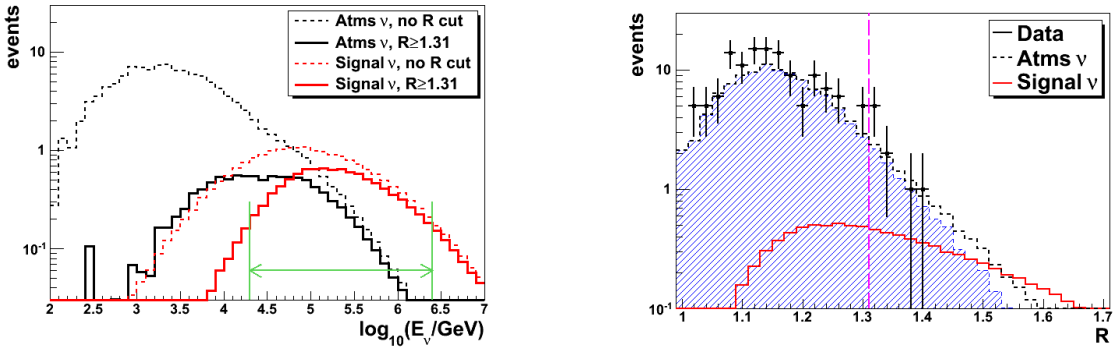

Figure 3: Left plot: Energy distribution for the Bartol+RQPM atmospheric neutrino flux and a E^{-2} astrophysical signal with arbitrary normalisation after all quality cuts. The horizontal arrow denotes the interval in which 90% of the signal events is expected. Right plot: Distribution of the energy estimator R for data (markers), the Bartol atmospheric neutrino flux (filled histogram) and the 'prompt' contribution (RQPM model, dashed histogram). The signal at the level of the derived upper limit is shown as the full, red line together with the cut at $R > 1.31$ (vertical, dashed line).

Applied to Monte Carlo simulations, these cuts completely remove the $2 \cdot 10^8$ reconstructed tracks induced by atmospheric muons and reduce the contribution from atmospheric neutrinos (Bartol + RQPM) from $7 \cdot 10^3$ to 116 events [7].

2.3 Energy estimator

As the flux of astrophysical neutrinos is expected to follow a harder spectrum ($\propto E^{-2}$) than that of the atmospheric neutrino background it should become visible as an excess of high-energy events. This discrimination requires an estimation of the neutrino, or as best approximation, the muon energy. Various energy estimators are under study within the ANTARES collaboration [8]. Here we exploit the structure of the arrival times of photons created along the muon track at the OMs. This time structure is sensitive to the energy as higher energy muons have a higher probability to create electromagnetic showers along the track. The light emitted by these showers is responsible for delayed hits in the OMs with respect to the detected Cherenkov photons. A robust parameter sensitive to delayed photons is the mean number of hit repetitions R within an event. It is calculated by averaging the number of hits R_i recorded by an OM within a 500 ns time window over all OMs contributing to the reconstructed muon track. The clear correlation with muon energy is shown for simulated events in Fig. 2, left plot. The estimator has been extensively studied both on MC and on (atmospheric muon dominated) data (e.g. Fig. 2, right plot) and an average HWHM resolution after the discussed quality criteria of $\log(E_{\rm rec}/E_{\rm true}) = 0.4$ could be determined.

2.4 Optimisation of the event selection

The final discrimination between the atmospheric neutrino background and the astrophysical signal is achieved by a cut in the R variable. This cut has been optimized before un-blinding the data by minimizing the Model Rejection Factor (MRF) [9]. Taking into account all possible fluctuations of the number of background events $n_{\rm B}$, the average upper limit $\bar{\mu}_{90\%}(n_{\rm B})$ of background-only pseudo-experiments is derived. The optimal value of the cut in R is then determined by minimizing the MRF given as $\bar{\mu}_{90\%}(n_{\rm B})/n_{\rm S}$, where $n_{\rm S}$ is the number of expected signal events from an E^{-2} test spectrum. The optimum has been found when selecting events above $R_{\rm cut} = 1.31$.

The determination of the energy estimator cut allows to define the energy range to which the analysis will be sensitive. We define this range as the interval containing 90% of the signal events and obtain 20 TeV $< E_\nu <$ 2.5 PeV (see Fig. 3, left plot).

2.5 Low energy region and systematic uncertainties

Before un-blinding the data in the defined region $R > 1.31$ the distribution of the selected data events below this cut has been compared to the corresponding Monte Carlo simulations. Whereas 125 events are selected from data, the Bartol flux parametrisation combined with the RQPM model for the prompt contribution predicts 105 events. The observed difference is well within the systematic uncertainty of the atmospheric neutrino flux given as $25 - 30\%$ [10] and has been corrected before un-blinding the high-energy region by applying a scale factor $k = 105/125 = 1.19$ to the MC predictions.

Further systematic uncertainties on the number of expected events in the high-energy signal region include

- the contribution of prompt events derived as maximal deviation between the models discussed in [6] of $^{+1.7}_{-0.3}$ events. The maximal value (1.7 events) is used in the following.

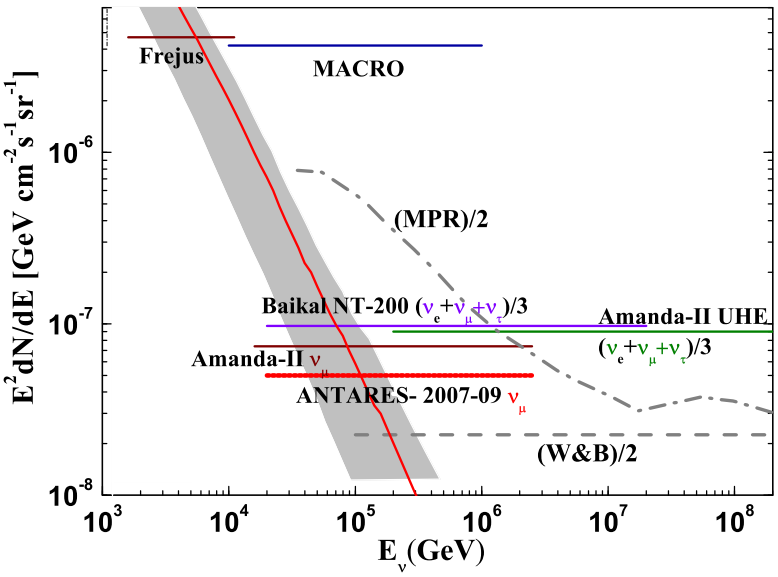

Figure 4: The upper limit for a E^{-2} diffuse high-energy $\nu_\mu + \bar{\nu}_\mu$ flux derived from data of the ANTARES neutrino telescope compared to previous measurements and phenomenological upper bound predictions.

- uncertainties in the spectral shape of the atmospheric neutrino flux which is related to uncertainties in the primary cosmic ray energy spectrum. By varying the spectral index of the neutrino spectrum by ± 0.1 independently below and above ≈ 10 TeV we obtained a sys. uncertainty of ± 1.1 events.
- uncertainties in the details of the description of the detector and environmental parameters like the angular acceptance of the OMs, details of PMT afterpulses and water properties like absorption and scattering lengths which lead to a total uncertainty of 5%.

3 Results

Applying the discussed quality and energy selection criteria to the simulated dataset gives a background estimation of $n_\mathrm{B} = 10.7 \pm 2$ events in the high-energy region. In the analysed dataset of the ANTARES detector 9 events were selected. Including the systematic uncertainty on the background expectations following the method discussed in [11] we derive the 90% c.l. upper limit on the number of signal events as $\mu_{90\%}(n_\mathrm{B}) = 5.7$. The corresponding upper limit on the neutrino flux is given by $\phi_{90\%} = \phi \cdot \mu_{90\%}/n_\mathrm{S}$, where n_S is the number of events expected from the flux ϕ. We obtain [12]:

$$E^2\phi_{90\%} = 5.3 \times 10^{-8}\ \mathrm{GeV}^{-2}\mathrm{s}^{-1}\mathrm{sr}^{-1} \qquad (1)$$

As can be seen in Fig. 4, the derived limit is competitive with previous results and further constrains models of the diffuse flux high-energy $\nu_\mu + \bar{\nu}_\mu$ flux.

References

[1] M. Ageron *et al.* (ANTARES Collaboration), ANTARES: the first undersea neutrino telescope, to appear in NIM A (2011)
[2] E. Waxman, J. Bahcall, Phys. Rev. D 59 (1998) 023002
J. Bahcall, E. Waxman, Phys. Rev. D 64 (2001) 023002
[3] K. Mannheim, R.J. Protheroe, J.P. Rachen, Phys. Rev. D 63 (2000) 023003
[4] Y. Becherini, A. Margiotta, M. Sioli, M. Spurio, Astropart. Phys. 25 (2006) 1
G. Carminati, M. Bazzotti, A. Margiotta, M. Spurio, Comp. Phys. Comm. 179 (2008) 915
[5] V. Agrawal, T.K. Gaisser, P. Lipari, T. Stanev, Phys. Rev. D 53 (1996) 1314
[6] C.G.S. Costa, Astropart. Phys. 16 (2001) 193
[7] S. Biagi, proceedings CRIS 2010 (Nucl. Phys. B proc. suppl. 212-214)
[8] D. Palioselitis for the ANTARES Collaboration, Muon energy reconstruction and atmospheric neutrino spectrum unfolding with the ANTARES detector, these proceedings, 2011
[9] G.C. Hill, K. Rawlins, Astropart. Phys. 19 (2003) 393
[10] Barr, G. D., Robbins, S., Gaisser, T. K. and Stanev, T., Phys. Rev. D 74 (2006) 094009
[11] J. Conrad, et al., Phys. Rev. D 67 (2003) 012002
[12] J.A. Aguilar *et al.* (ANTARES Collaboration), Physics Letters B 696 (2010) 16

32ND INTERNATIONAL COSMIC RAY CONFERENCE, BEIJING 2011

Autocorrelation analysis of ANTARES data

FABIAN SCHÜSSLER[1] ON BEHALF OF THE ANTARES COLLABORATION
[1] *Commissariat à l'énergie atomique et aux énergies alternatives*
Institut de recherche sur les lois fondamentales de l'Univers
91191 Gif-sur-Yvette Cedex, France
fabian.schussler@cea.fr
DOI: 10.7529/ICRC2011/V04/0238

Abstract: Clustering of neutrino arrival directions would provide hints for their astrophysical origin. The two-point autocorrelation method is sensitive to a large variety of cluster morphologies and, due to its independence from Monte Carlo simulations, provides complementary information to searches for the astrophysical sources of high energy muon neutrinos. We present the analysis of the autocorrelation function as a function of the angular scale of data collected during 2007-08 with the ANTARES neutrino telescope.

Keywords: neutrino astronomy, neutrino telescopes, point sources, autocorrelation

1 Introduction

The key question to resolve the long standing mystery of the origin of cosmic rays is to locate the sources and study the acceleration mechanisms able to produce fundamental particles with energies orders of magnitude above man-made accelerators. Over the last years it has become more and more obvious that multiple messengers will be needed to achieve this task. Fundamental particle physics processes like the production and subsequent decay of pions in interactions of high energy particles predict that the acceleration sites of high energy cosmic rays are also sources of high energy gamma rays and neutrinos. The detection of astrophysical neutrinos and the identification of their sources is one of the main aims of large neutrino telescopes operated at the South Pole (IceCube), in Lake Baikal and in the Mediterranean Sea (ANTARES).

1.1 The ANTARES neutrino telescope

Whereas physics data taking started already during the deployment phase, the ANTARES detector [1] became fully equipped and operational in 2008. The detector is composed of 12 detection lines placed at a depth of 2475m off the French coast near Toulon. The detector lines are about 450m long and hold a total of 885 optical modules (OMs), 17" glass spheres housing each a 10" photomultiplier tube. The OMs look downward at 45° in order to optimize the detection of upgoing, i.e. neutrino induced, tracks. The geometry and size of the detector makes it sensitive to neutrinos in the TeV-PeV energy range. A schematic layout is shown in Fig. 1.

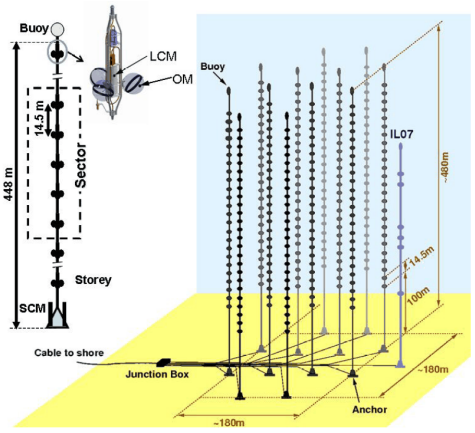

Figure 1: Schematic view of the ANTARES detector.

1.2 Neutrino detection

The neutrino detection relies on the emission of Cherenkov light by high energy muons originating from charged current neutrino interactions inside or near the instrumented volume. All detected signals are transmitted via an optical cable to a shore station, where a farm of CPUs filters the data for coincident signals or *hits* in several adjacent OMs. The muon direction is then determined by maximising a likelihood which compares the times of the hits with

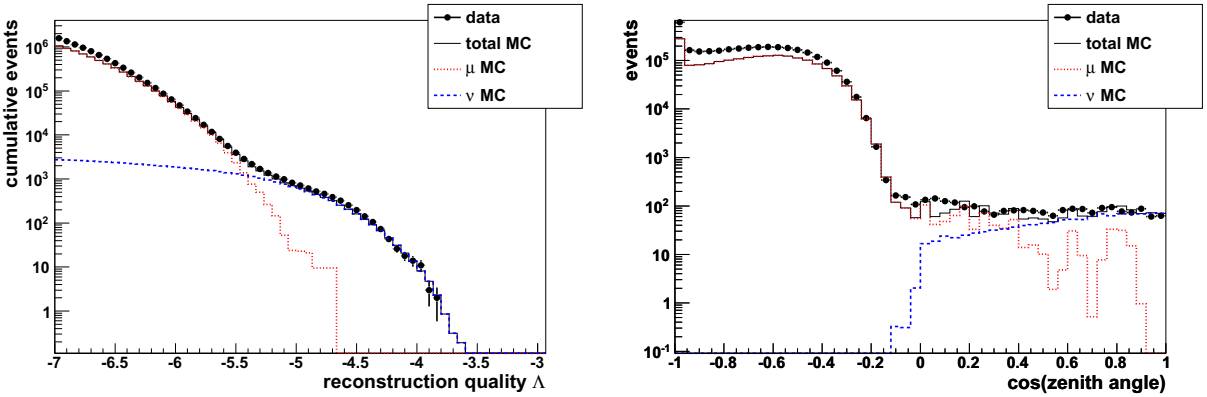

Figure 2: Distribution of the quality parameter Λ (left plot) and the cosine of the reconstructed zenith angle (right plot) of the selected data events (markers) compared to Monte Carlo simulations of atmospheric muons (red, dotted line) and atmospheric neutrinos (blue, dashed line).

the expectation from the Cherenkov signal of a muon track.

1.3 Astrophysical neutrinos

Two main backgrounds for the search for astrophysical neutrinos can be identified: downgoing atmospheric muons which have been mis-reconstructed as upgoing and atmospheric neutrinos originating in cosmic ray induced air showers at the opposite side of the Earth. Depending on the requirements of the analysis both backgrounds can at least partially be discriminated using various parameters like the quality of the event reconstruction or an estimator for the deposited energy [2].

In addition, analysing the reconstructed arrival directions of the events allows to search for an excess over the uniform atmospheric backgrounds. Despite important efforts, no clear signature for point sources of astrophysical neutrinos has been found so far [3, 4, 5, 6]. Both the distribution and morphologies of sources potentially emitting neutrinos in the TeV energy range are yet unknown but are possibly very inhomogeneous with most of them being located in the Galactic disk and spatially extended (e.g. shell type supernova remnants like RXJ1713 [7]). It seems therefore interesting to study the intrinsic clustering of the arrival directions of neutrinos. Possible analysis biases are naturally avoided as no prior information about the potential sources is required. Covering a large angular range, i.e. neutrino emission regions of very different sizes, this study complements the searches for point like sources and, if successful, would provide hints for underlying, yet unresolved, source morphologies and source distributions.

2 Autocorrelation analysis

The most commonly used method to detect intrinsic clusters within a set of N events is the standard 2-point autocorrelation distribution. It is defined as the differential distribution of the number of observed event pairs N_{p} in the data set as a function their mutual angular distance $\Delta\Omega$. To suppress statistical fluctuations that would reduce the sensitivity of the method, we analyse here the cumulative autocorrelation distribution defined as

$$\mathcal{N}_{\mathrm{p}}(\Delta\Omega) = \sum_{i=1}^{N} \sum_{j=i+1}^{N} H(\Delta\Omega_{ij} - \Delta\Omega), \qquad (1)$$

where H is the Heaviside step function.

2.1 Data set

The analysed data set has been recorded by the ANTARES neutrino telescope in 2007 and 2008. During this period the detector was in its construction phase and has been operated in various setups ranging from 5 active lines at the beginning of 2007 to a fully operational detector of 12 lines since mid 2008. After applying a run selection removing for example periods without precise detector alignment information, the dataset corresponds to about 300 effective days. Comprising mainly atmospheric muons, about 100 million events were reconstructed with the standard ANTARES reconstruction algorithm. Basic selection criteria include a cut on the reconstructed zenith angle θ to ensure that only upgoing muon tracks are selected ($\cos(\theta) > 0$) and a cut on the angular uncertainty β given by the covariance matrix of the final likelihood fit ($\beta < 1^\circ$). The final selection criteria is a cut on the fit quality parameter Λ, which is derived from the value of the maximal likelihood itself. Before unblinding the data, this cut has been optimized by means of MC simulations to yield the best average upper limit on the neutrino flux in the search for point like sources [5, 6]. 2190

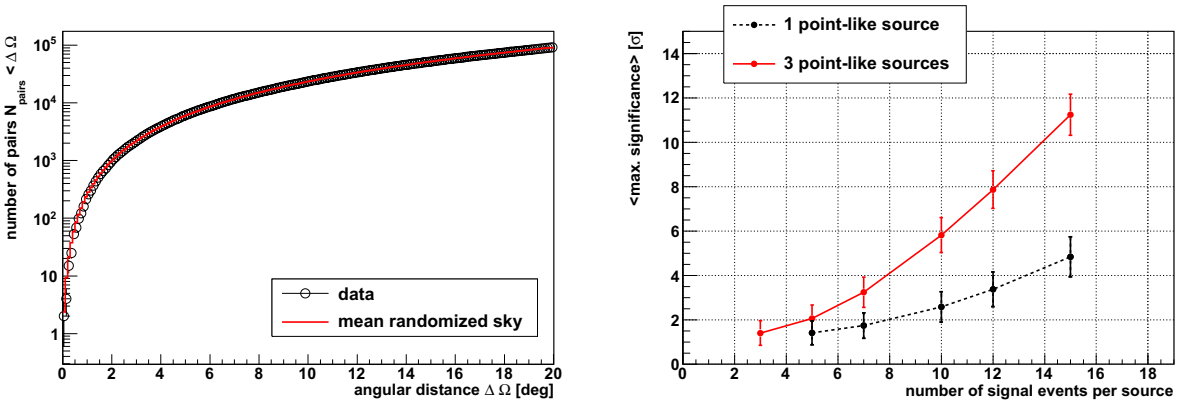

Figure 3: Left: Cumulative autocorrelation distribution of the selected dataset (open markers) shown in comparison with the reference distribution (red solid line). Right: Performance of the algorithm to detect a single or multiple point-like sources.

events pass the final criterion $\Lambda > -5.4$. The Λ and zenith angle distributions of events passing all quality criteria (except the ones shown in the plot) are shown in figure 2.

Following eq. 1, the cumulative autocorrelation distribution of the selected events has been determined. It is shown in the left plot of figure 3.

2.2 Reference autocorrelation distribution

To detect structures in the sky distribution of the analysed events we need a reference autocorrelation distribution to compare with. This reference has been determined by scrambling the data themselves, a method which allows to avoid systematic uncertainties introduced by the use of Monte Carlo simulations. The scrambling method uses the local coordinates (zenith and azimuth) and the detection time T_i of all selected data events. While keeping the pairs of zenith/azimuth for all events in order to avoid losing information about possible correlations between them, the detection time is drawn randomly from another event within the same detector configuration in order to keep track of the changing asymmetry of the detector. Using all selected events, a randomized sky map with the same number of events as in the data and naturally the same sky coverage is constructed. This randomized sky is then analysed in exactly the same way as the data to derive the autocorrelation function. The randomization process is performed about 10^6 times and the derived autocorrelation distributions are averaged in order to suppress statistical fluctuations. The resulting reference distribution is shown as a red dotted line in the left plot of figure 3.

2.3 Comparison between data and reference

Structures in the sky distribution of our data will show up as differences between the autocorrelation distributions of the data and the reference distribution. The comparison between them is performed by using the formalism introduced by Li&Ma [8]. This formalism results in the raw significances of the differences as a function of the cumulative angular scale which is shown in figure 4. As the comparison is performed bin-by-bin and as we scan over different angular scales, this result has to be corrected for the corresponding trial factor. We apply the method proposed by Finley and Westerhoff [9] and perform about 10^5 pseudo experiments in which the autocorrelation distributions of randomized sky maps are compared with the reference distribution. The probability to obtain the same or higher significance as the maximum deviation observed in the data is calculated and given as final p-value of the analysis.

2.4 Performance and sensitivity

The performance of the algorithm has been determined using mock data sets for which we scrambled the selected data events as described above. While keeping the total number of events in the toy model constant and taking into account the angular resolution, we added predefined source structures with various sizes and source luminosities. These mock data sets where then analysed in exactly the same way as described above. As can be seen in the right plot of figure 3, the algorithm is sensitive enough to obtain a 3σ evidence in the exemplary case of 3 point like sources emitting each about 6 events. This source luminosity is at the detection threshold of the dedicated search for a point like excess in the same dataset [5, 6], which underlines the complementarity of the two methods.

An important free parameter of the analysis is the binning of the autocorrelation distribution as it will determine the sensitivity to certain angular scales and which is connected to the angular resolution. For the used quality selection an average angular resolution of 0.5° has been determined from Monte Carlo simulations. Using toy simulations with various source scenarios an optimal binning of 0.1° has been determined.

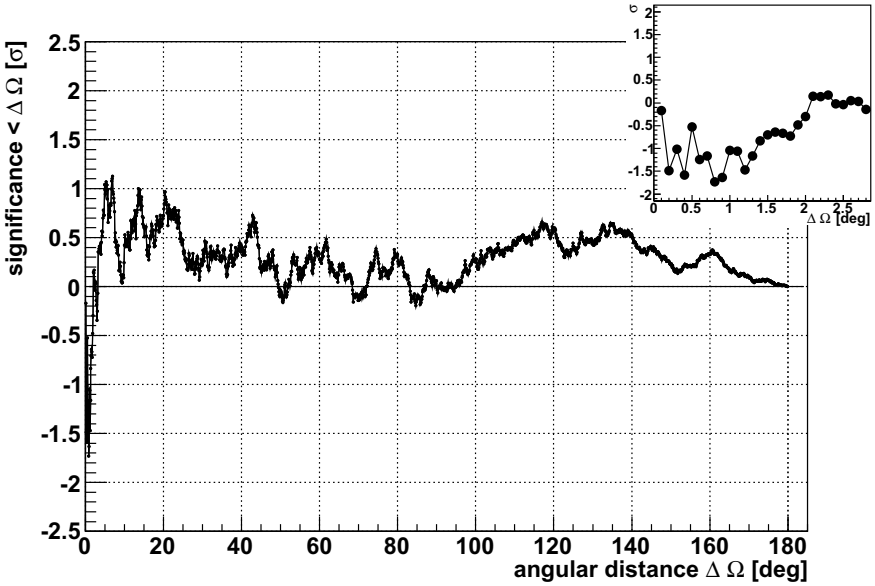

Figure 4: The significance of intrinsic clustering of data taken with the ANTARES neutrino telescope in 2007/2008. The trial factor is not corrected for. The inset shows an enlarged view of the significance for small angular distances.

2.5 Results and discussion

The described analysis has been applied to the 2090 selected data events recorded by the ANTARES neutrino telescope between 2007 and 2008. The uncorrected significance as a function of the cumulative angular scale is shown in figure 4. A maximum deviation between the data and the reference distribution of $1.1\ \sigma$ is found for an angular scale $< 7^\circ$. Correcting for the scanning trial factor this corresponds to a p-value of $55\ \%$ and is therefore not significant.

In the search for the sources of high energy cosmic rays, the detection of astrophysical sources of neutrinos may play a crucial role. Various experiments are currently taking data or are in a preparatory phase to achieve this goal and the recorded data is scrutinized in numerous ways in order to extract a maximum of information. We presented here the first search for intrinsic clustering of data recorded with the ANTARES neutrino telescope. The data, taken during the deployment phase of the detector, do not show evidence for deviations from the isotropic arrival direction distribution expected for the background of atmospheric neutrinos and contamination by mis-reconstructed atmospheric muons.

References

[1] M. Ageron *et al.* (ANTARES Collaboration), ANTARES: the first undersea neutrino telescope, to appear in NIM A, 2011

[2] D. Palioselitis for the ANTARES Collaboration, Muon energy reconstruction and atmospheric neutrino spectrum unfolding with the ANTARES detector, these proceedings, 2011

[3] R. Abbasi *et al.* (AMANDA Collaboration), Search for point sources of high energy neutrinos with final data from AMANDA-II, PRD 79, 062001, 2009

[4] R. Abbasi *et al.* (IceCube Collaboration), Time-integrated Searches for Point-like Sources of Neutrinos with the 40-string IceCube Detector, APJ 732, 18-34, 2011

[5] M. Ageron *et al.* (ANTARES Collaboration), Point-like source search with 2007-2008 data, in preparation, 2011

[6] C. Bogazzi for the ANTARES Collaboration, Searching for point sources of high energy cosmic neutrinos with the ANTARES telescope, these proceedings, 2011

[7] F. Aharonian *et al.* (HESS Collaboration), Primary particle acceleration above 100 TeV in the shell-type supernova remnant RX J1713.7-3946 with deep HESS observations, A&A 464, 235-243, 2007

[8] T.-P. Li and Y.-Q. Ma, Analysis methods for results in gamma-ray astronomy, APJ 272, 317-324, 1983

[9] C. Finley and S. Westerhoff, On the evidence for clustering in the arrival directions of AGASA's ultrahigh energy cosmic rays, APP 21, 359-367, 2004

LUNASKA simultaneous neutrino searches with multiple telescopes

J. D. BRAY[1,2], R. D. EKERS[2], C. W. JAMES[3], P. ROBERTS[2], A. BROWN[2], C. J. PHILLIPS[2], R. J. PROTHEROE[1], J. E. REYNOLDS[2], R. A. MCFADDEN[4], M. AARTSEN[1]
[1]*School of Chemistry & Physics, Univ. of Adelaide, SA, Australia*
[2]*CSIRO Astronomy & Space Science, Epping, NSW, Australia*
[3]*Department of Astrophysics, IMAPP, Radboud University Nijmegen, The Netherlands*
[4]*ASTRON, 7990 AA Dwingeloo, The Netherlands*
justin.bray@adelaide.edu.au
DOI: 10.7529/ICRC2011/V04/0240

Abstract: The most sensitive method for detecting neutrinos at the very highest energies is the lunar Cherenkov technique, which employs the Moon as a target volume, using conventional radio telescopes to monitor it for nanosecond-scale pulses of Cherenkov radiation from particle cascades in its regolith. Multiple-antenna radio telescopes are difficult to effectively combine into a single detector for this purpose, while single antennas are more susceptible to false events from radio interference, which must be reliably excluded for a credible detection to be made. We describe our progress in excluding such interference in our observations with the single-antenna Parkes radio telescope, and our most recent experiment (taking place the week before the ICRC) using it in conjunction with the Australia Telescope Compact Array, exploiting the advantages of both types of telescope.

Keywords: UHE neutrinos, lunar Cherenkov technique

1 Introduction

The particle cascades induced in dense media by UHE (ultra-high energy; >EeV) cosmic rays and neutrinos may be detected through the Askaryan effect [1], which results in a nanosecond-scale coherent radio pulse. Dagkesamanskii and Zheleznykh suggested that ground-based radio telescopes could be used to monitor the upper layers of the Moon, which are a suitable radio-transparent target material, to use the Moon as a neutrino detector [2].

Compared to similar experiments exploiting the Askaryan effect to search for UHE particles in terrestrial volumes of ice [3] or salt [4], this technique has a larger potential aperture (as the Moon is a large target), but has a higher threshold energy for a particle to be detectable (as the Moon is far away). It also has the advantage that suitable instruments, in the form of radio telescopes, already exist; but these are also used for other experiments, so they are only intermittently available for use for UHE particle detection.

A significant difficulty with this technique is distinguishing between a real event and a spurious pulse of RFI (radio frequency interference) produced by artificial electrical equipment. Without the ability to do this reliably, it is possible to set a limit to the UHE particle flux based on the strength and/or number of observed pulses, but it is not possible to confidently attribute a particular pulse to a particle cascade, and hence to claim the detection of a UHE particle.

2 Types of experiment

Current experiments employing this technique have several factors in common. They all monitor the signal from a radio telescope in real time, keeping a buffer of the most recent data. If a potential event is detected, this triggers the permanent storage of the buffered data, which can then be examined in more detail.

These experiments vary, however, in the details of the real-time algorithm used to identify a potential event. Apart from steps including dedispersion, interpolation, etc., they can be divided into two types according to whether they use their radio telescope, which may consist of one or several antennas, in an incoherent or a coherent fashion.

2.1 Incoherent experiments

An incoherent experiment makes use of a radio telescope consisting of multiple antennas, each of which acts as an independent detector. The radio pulse from a UHE particle interaction on the Moon will be seen by all antennas, with relative arrival times indicating its arrival direction. Experiments of this type include RESUN [5] and previous LUNASKA observations with the ATCA (Australia Telescope Compact Array) [6].

The requirement that a pulse must be seen by all antennas, with relative arrival times indicating that it originated from

the Moon, provides an effective discriminant against false events from RFI. However, the sensitivity of this type of experiment is limited by the sensitivity of a single antenna.

2.2 Coherent experiments

This type of experiment coherently combines the incoming radio waves across the entire collecting area of a radio telescope before checking the signal for a possible pulse. The telescope may consist of either a single large antenna or an array. In the latter case, the signals from separate antennas must be combined electronically, which requires special-purpose digital hardware.

Due to the larger effective collecting area, this approach results in improved radio sensitivity, allowing it to detect pulses from lower-energy UHE particles. However, a larger antenna or array of antennas forms a narrower beam, allowing it to observe only a fraction of the Moon and reducing its aperture to UHE particles. This drawback can be offset by using multiple beams directed at different parts of the Moon. For a single antenna, this is achieved by placing multiple receiver feeds at the antenna focus. For an array, it involves combining the signals from separate antennas at a different set of relative delays for each beam.

A real event should appear as a pulse in only one beam: the beam directed towards the region of the Moon where it occurred. This is used to exclude false events from RFI, which generally appear in multiple beams. However, previous experiments have found this to be a weaker discriminant than the RFI rejection scheme used in incoherent experiments, whether using a single antenna [7] or an array [8], so they have been limited by the RFI background.

3 This experiment

The work described here is a development of a previous experiment of the coherent type described above, using a single large antenna: the 64 metre Parkes radio telescope. The previous experiment used four beams, three being directed at the Moon, with the fourth used purely for RFI rejection. One beam was always on the limb of the Moon closest to Centaurus A, to maximise directional sensitivity to UHE particles from that potential source [9], as in a previous experiment [10]. More pulses were observed than expected from Gaussian noise, which may be due to remnant RFI; but the possibility of real events cannot be excluded [7].

The purpose of this experiment is to determine whether this excess of observed pulses includes any genuine UHE particle interaction events, by observing simultaneously with a second telescope and searching for coincident pulses. The second telescope was the ATCA, an array of which we used five antennas in a compact configuration. The frequency range of the ATCA receivers was 1.1–3.1 GHz, which encompasses the 1.2–1.5 GHz range of the Parkes receiver. The ATCA antennas were pointed at the same location as a single Parkes beam, as shown in figure 1.

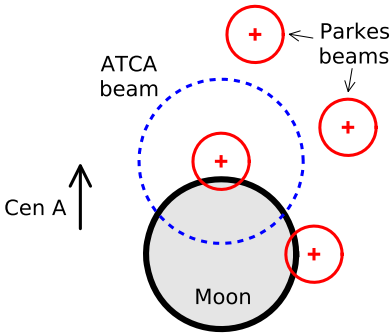

Figure 1: Typical beam pointings relative to the Moon (shaded) for the Parkes (solid) and ATCA (dashed) telescopes. Crosses indicate the orientation of the orthogonal linear polarisations of the Parkes receiver. The two off-Moon Parkes beams are for RFI rejection; the other beam positions are a compromise between exposure to the Moon, and reducing the thermal noise received from the Moon to increase the sensitivity. The ATCA beam is placed to be able to confirm a possible detection in the Parkes beam sensitive to UHE particles from the direction of Centaurus A.

To match the sensitivity of the Parkes telescope, we require a coherent combination of the signals from the five ATCA antennas. However, we were not able to form, in real time, the multiple combined signals that would be required. Instead, we used the detection of a pulse at Parkes as a trigger to store buffered data on all ATCA antennas, which can then be retroactively combined to search for a coincident pulse.

Essentially, this experiment uses each of the involved telescopes in a coherent manner: the Parkes telescope is a single antenna, so it is inherently coherent, while the multiple antennas of the ATCA are coherently combined. The combination between the two telescopes, however, is incoherent: the signal from each telescope is examined for a pulse independently. The sensitivity is similar to the previous experiment using the Parkes telescope alone, as a pulse must exceed the trigger threshold on this telescope in order to be recorded. However, the use of a second telescope to confirm potential events should allow complete rejection of the RFI background, allowing much greater confidence if a coincident pulse is found.

This experiment was conducted during 4-7 August, immediately prior to the 32nd International Cosmic Ray Conference. We have not yet determined whether there were any coincident pulses between the Parkes and ATCA telescopes during the observation period. However, we have established that we were successful in performing several types of calibration required for this type of experiment.

4 Calibration

This experiment required careful calibration of the delays between the antennas of the ATCA, and between the Parkes and ATCA telescopes, which are separated by 300 km. The first of these is required for normal use of the ATCA, and the second is a routine procedure in VLBI (Very Long Baseline Interferometry). However, in our case they must be accomplished using only the short buffers which are captured in this experiment.

4.1 ATCA calibration

To coherently combine the signals from separate antennas of the ATCA, the relative delays must be calibrated to within a small fraction ($\sim 1/20$) of the inverse of the bandwidth. Since we aim to find pulses corresponding to those detected by the Parkes telescope in the frequency range 1.2–1.5 GHz, we require timing precision of ~ 0.2 ns.

Achieving this requires cross-correlation between antennas of a broad-band signal such as noise from an astronomical source. For this purpose we used the quasar 3C273, as it was unresolved by our array, and bright enough for a strong cross-correlation within the maximum buffer size that could be captured with our system (6 ms).

These buffers of baseband data also allow calibration of the relative phase of each antenna, which is also required in order to coherently combine the data from multiple antennas. In fact, this phase calibration is required in order to obtain delays which meet our precision criterion, as shown in figure 2. Phase calibration can be checked for consistency via the requirement that the phases around any closed loop of antennas must sum to zero: applying this, we find that these sums vary from zero by $\pm 2.5°$, which indicates negligible error.

4.2 Parkes-ATCA calibration

It was necessary to calibrate the relative timing between the Parkes and ATCA telescopes for two reasons. The first is to be able to determine, if a pulse is found in the ATCA data corresponding to a pulse detected at Parkes, whether the arrival time indicates that it originated from the Moon. If the timing offset is known precisely, there is a ~ 4 μs window within which the ATCA pulse could arrive, corresponding to the width of the Parkes beam. If there is uncertainty in the timing offset, this search window must be extended, resulting in a higher threshold for significance and hence reduced sensitivity.

The second reason for this calibration is to ensure that the correct data are stored. Depending on the position of the Moon on the sky, the relative arrival times of a pulse could vary by about 1 ms. In normal operation, however, we only store a 200 μs segment of the buffer at the ATCA. This segment must be selected from the buffer based on the current position of the Moon. The precision required for this purpose is only $\pm$ 100 μs, to ensure that the correct time is within the range of the stored data.

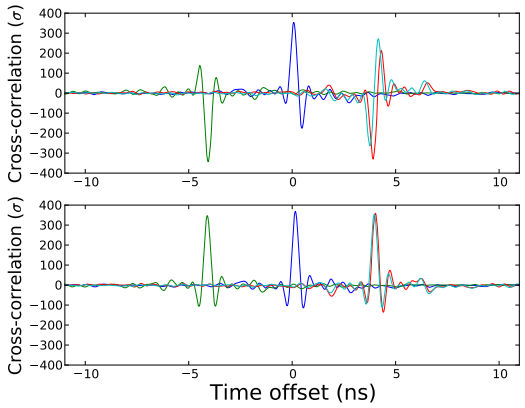

Figure 2: Sample cross-correlations between antenna 1 of the ATCA and the other four antennas, from a single 6 ms buffer while observing 3C273. Fourier interpolation has been performed, and only one polarisation is shown. Without phase corrections (top panel), the exact time offset is unclear. With phase corrections (bottom panel), the peaks are well-defined, and their positions are stable to ± 0.09 ns between this and other buffers. The structure away from the peaks, which deviates from an idealised sinc function, may be due to the extended structure of 3C273, or other sources in the field of view.

This calibration is performed in a similar way to the ATCA internal calibration, but with a cross-correlation between buffers captured at the Parkes and ATCA telescopes. Our system at the Parkes telescope has a maximum buffer size of 8 μs, considerably less than at the ATCA, which reduces the strength of the correlation and requires that we use a stronger calibrator source. In addition, the source must be compact enough to be unresolved on the 300 km Parkes-ATCA baseline, which limits the range of suitable astronomical objects.

Due to the lower required precision, however, a narrow-band signal is sufficient for this purpose. As our source, we used BeiDou-1C, a Chinese navigational satellite which emits strongly in the range 1220-1245 MHz. We determined its position with a TLE-format ephemeris [11] and the PyEphem astronomical library [12]. The timing precision we achieved, shown in figure 3, is ~ 50 ns, which corresponds roughly to the theoretical limit of the inverse bandwidth. There will be an additional error from uncertainty in the satellite ephemeris, which we expect to be less than this.

5 Lunar satellite interference

We detected narrow-band interference at a frequency of 2.27 GHz, varying with a period of 133 minutes (see figure

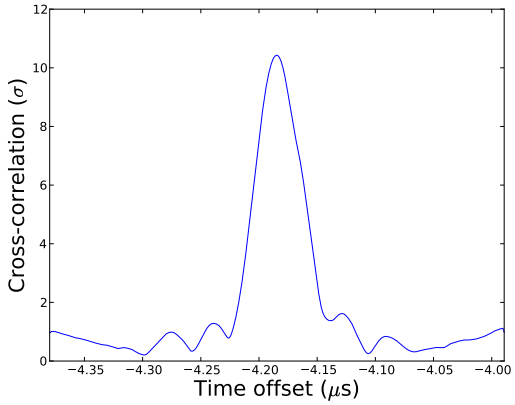

Figure 3: Cross-correlation between Parkes and antenna 1 of the ATCA from a single pair of corresponding buffers while observing BeiDou-1C, discarding ATCA data from outside the Parkes frequency range. The result has been rectified and smoothed with a Gaussian of width 10 ns. The time offset is relative to the arrival time predicted by the satellite ephemeris; the 4.2 μs offset is consistent between observations and hence is a systematic effect which can be removed. The width of the peak indicates that we have achieved timing precision of $\sim$ 50 ns.

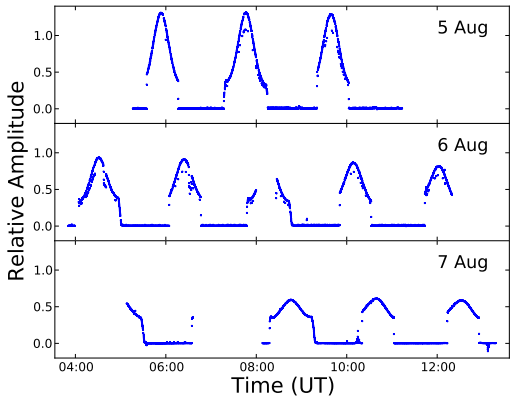

Figure 4: Intensity of narrow-band interference at 2.27 GHz, relative to the underlying noise spectrum. The behaviour is as expected for a lunar satellite: it peaks as the satellite orbits through the telescope beam, and falls to zero when the satellite is occulted by the Moon. The variation from one day to the next is due to the changed pointing of the telescope (see section 3) relative to the fixed orbit of the satellite.

4). These figures correspond respectively to the communications frequency and orbital period of the NASA Lunar Reconnaissance Orbiter (LRO) [13].

This narrow-band interference is simple to remove from the data. However, there is the possibility that an electrical system on the LRO (or another lunar satellite) may be capable of producing nanosecond-scale broad-band radio pulses. Unlike terrestrial interference, such a pulse would be seen by both telescopes used in this experiment, with relative arrival times indicating that it originated from the Moon. This makes it difficult to distinguish from a real UHE particle-induced Askaryan pulse.

We are investigating the feasibility of such pulses being generated by the hardware of a lunar satellite. If this is feasible, then it will be necessary to compare the position of any detected pulse, as determined from its arrival times, with the simultaneous position of all lunar satellites. The position of a satellite may be obtained either from a published ephemeris, or from interferometry on its communications signal.

6 Conclusion

We have demonstrated the ability to search for lunar Askaryan pulses with two radio telescopes simultaneously, with good timing calibration between them. This allows coincidence detection to confirm the lunar origin of a detected pulse, which is a prerequisite for our experiment to reliably detect a UHE particle interaction on the Moon.

7 Acknowledgements

The Australia Telescope Compact Array and Parkes telescope are both part of the Australia Telescope which is funded by the Commonwealth of Australia for operation as a National Facility managed by CSIRO. This research was supported by the Australian Research Councils Discovery Project funding scheme (project number DP0881006).

References

[1] G. A. Askaryan, Sov. Phys. JETP, 1962, **14**: 441-443
[2] R. D. Dagkesamanskii, I. M. Zheleznykh, Sov. Phys. JETP Lett., 1989, **50**: 259-261
[3] P. W. Gorham et al., Phys. Rev. D, 2010, **82**: 022004
[4] A. Connolly, Proc. 4th ARENA, Nantes, 2010
[5] T. R. Jaeger et al., Astropart. Phys., 2010, **34**: 293-303
[6] C. W. James et al., Phys. Rev. D, 2010, **81**: 042003
[7] J. D. Bray et al., in prep.
[8] S. Buitink et al., A&A, 2010, **521**: A47+
[9] Pierre Auger Collaboration (Abreu et al.), JCAP06, 2011, **022**
[10] C. W. James et al., MNRAS, 2011, **410**: 885-889
[11] `http://celestrak.com/NORAD/elements/`
[12] `http://rhodesmill.org/pyephem/`
[13] `http://lunar.gsfc.nasa.gov/`

32ND INTERNATIONAL COSMIC RAY CONFERENCE, BEIJING 2011

Study on possible correlation between events observed by the ANTARES neutrino telescope and the Pierre Auger cosmic ray observatory

JELENA PETROVIC[1] FOR THE ANTARES COLLABORATION
[1]*Nikhef, The Netherlands*
jelenap@nikhef.nl

DOI: 10.7529/ICRC2011/V04/0291

Abstract: According to the theory of hadronic acceleration, ultra high energy cosmic rays are expected to be accompanied by gamma-rays and neutrinos from pion decays formed in the interactions of protons with photons. While gamma-rays have been linked to astrophysical sources by many experiments (H.E.S.S, MAGIC, Fermi), no point source of UHECRs or neutrinos have been found so far. In this contribution, we present the results of multimessenger stacking sources analysis developed to investigate the correlation of arrival directions of neutrino candidate events and UHECRs. This analysis has been applied on neutrino candidate events detected during 2007-08 by the ANTARES telescope (ANTARES collaboration 2011), and 69 ultra-high energy cosmic rays observed by the PAO (The Pierre Auger Collaboration 2010).

Keywords: Multimessenger, Neutrinos, Cosmic-rays, ANTARES telescope, Pierre Auger Observatory

1 Introduction

Finding point sources of both UHECRs and neutrinos is a very challenging task, as both messengers have many down-sides. UHECRs are rare and do not point back to their sources, since they are scrambled by galactic and intergalactic magnetic fields [1, 2, 3, 4, 5, 6, 7, 8, 9, 10, 11, 12, 13, 14, 15, 16]. Also, due to the interaction with the cosmic microwave background photons, their range may be limited to the distance of about 100Mpc or less [17, 18, 19, 20, 21]. However, they are detectable with large shower arrays, like the Pierre Auger Observatory (PAO), which so far reported the observation of few tens of events above 55EeV [21, 22]. On the other side, cosmic neutrinos, as neutral and weak interacting particles, should point back to their sources and their traveling distances should not be limited, but at the same time they are very difficult to detect. Currently operating neutrino telescopes ANTARES and IceCube have not yet observed excess above the atmospheric neutrino flux coming from air showers [23, 24].

Previously, the Pierre Auger Observatory (PAO) reported an anisotropy in the arrival directions of UHECRs [21] and indicated a correlation with Active Galactic Nuclei (AGN) from the VCV catalog [25]. The correlation was the most significant for 27 cosmic rays with energies higher than 57EeV and AGNs at distances less than 75Mpc. The suggested correlation with the nearby AGN sources mostly following the location of the supergalactic plane decreased in the subsequent analysis [22] with 69 events at energies above 55EeV, observed until 31st December 2009.

In this paper, we investigate the correlation of arrival directions of 2190 neutrino candidate events detected by 5-12 line ANTARES neutrino telescope, and 69 UHECRs observed by the PAO. This stacking sources analysis is developed for a blinded set of neutrino events. Blinding was performed by scrambling in right ascension. At the end, the analysis was done with the unblinded neutrino dataset.

2 The ANTARES telescope and data samples

The ANTARES neutrino telescope is located in the Mediterranean Sea, about 40km off the southern coast of France (42 48N, 6 10E), at a depth of 2475m. It was completed in 2008, and its final configuration is a three-dimensional array of 885 photomultipliers in glass spheres (optical modules), distributed along twelve lines. These photomultipliers detect Cherenkov photons, from relativistic muons produced in neutrino interactions nearby the detector. The total instrumented volume of the ANTARES telescope is about $10^7 \mathrm{m}^3$. The data acquisition system of the detector is based on "all-data-to-shore" concept, in which signals from the photomultipliers above a given threshold are digitized and sent to shore for processing.

The data used in this analysis were collected during 2007 and 2008, while the detector was operating with 5 to 12 lines. For a part of that period, data acquisition was interrupted for the employment of new lines, and in addition, some periods were excluded due to high bioluminescence-induced optical background. The resulting effective live time is 304 days. The final data sample consists of 2190 up-

going (zenith angle up to 90°) neutrino candidate events. No selection was done based on the energy reconstruction. The angular resolution was estimated to be 0.5±0.1 degrees. Details of data reconstruction, effective area, angular resolution and the dataset are given in [24].

This sample of neutrino candidate events was correlated with UHECR events recorded with the PAO surface detectors between January 1st 2004, and 31st December 2009. Those events have zenith angles below 60 degrees, and reconstructed energy above 55EeV. 69 events satisfy these cuts, and they are all in the ANTARES telescope field of view, as the field of view for the ANTARES telescope and the PAO greatly overlap.

3 Background simulations

A Monte Carlo set with 10^6 skies is generated, each with 2190 neutrinos and 69 cosmic rays. In each of the million skies the position of the UHECRs is fixed according to the PAO dataset, and the positions of 2190 neutrinos are obtained from the blinded 5-12 line dataset scrambled in right ascension. The numbers of neutrinos within bins of any size, centered on 69 UHECR events can be counted, probability density functions can be calculated and fitted with Gaussian distributions, giving the mean neutrino count expected from the randomized background samples, and the standard deviation of the neutrino count.

Figure 1 shows an example count of neutrinos within bins of 1-10 degree size. The count of events is done by adding neutrinos for which the minimum angular distance to UHECRs is smaller than the bin size. In this way, a double counting of neutrino events is avoided. After optimizing the bin, the significance of observed number of neutrino events within 69 bins can be calculated by comparison with the distributions for the pure background MC samples. After optimizing the bin, and unblinding the data, the significance of observed number of neutrino events within 69 bins can be calculated by comparison with the distributions for the pure background MC samples.

4 Signal simulations

Simulation of sources with E^{-2} spectrum and equal flux strength from each 69 UHECR direction was performed. Flux values from 0.5×10^{-8}GeV cm^{-2} s^{-1} to 10×10^{-8}GeV cm^{-2} s^{-1} are considered. Further, for each flux, the event rate per source is determined, using the effective area for 5-12 lines and the live time given in [24]. For every source, the amount of signal neutrinos is determined according to the Poisson distribution with the event rate per source R as mean value.

$$R = t \int_{10^2\mathrm{GeV}}^{10^7\mathrm{GeV}} \Phi(E_\nu) A_{eff}(E_\nu) dE_\nu$$

where t is a live time of the ANTARES detector, Φ is the flux from each individual UHECR direction, and A_{eff} is the ANTARES telescope effective area.

Signal neutrinos are randomly generated following a Gaussian distribution centered on the measured UHECR coordinates, and the ANTARES telescope resolution [24].

$$\exp\left(-(x_1(\alpha,\delta)-\mu)^2/(2\sigma_1^2)\right) \rightarrow x_2(\alpha,\delta)$$
$$\exp\left(-(x_2(\alpha,\delta)-\mu)^2/(2\sigma_2^2)\right) \rightarrow x_{fin}(\alpha,\delta)$$

where x_i = x_i (α, δ) are neutrino coordinates, $x_{fin}(\alpha,\delta)$ are the final signal neutrino coordinates, σ_1 is the tolerance value for the magnetic deflection, and σ_2 is the ANTARES telescope angular resolution. The width of the tolerance value accounting for a magnetic deflection Gaussian is chosen to be 3 degrees, based on the PAO results [22,25].

The same amount of background neutrinos is removed from a declination band of 10 degrees centered on each UHECR to ensure that every random sky has 2190 events, and to keep the neutrino declination distribution profile close to the observed profile. The angular resolution of PAO air shower reconstruction is about 0.9 degrees, less than the expected magnetic deflection, so it is not considered additionally.

5 Sensitivity and bin optimization

Although it is not possible to know the actual upper limit that will result from an experiment until looking into unblinded data, Monte Carlo predictions can be used to calculate the average upper limit, or so called Feldman-Cousins sensitivity [26, 27], that would be observed after hypothetical repetition of the experiment with expected background n_b, and no true signal $n_s = 0$. Over an ensemble of experiments with no true signal, the background n_b will fluctuate to different n_{obs} values with different Poisson probabilities, and upper limits μ_{90}.

The "mean upper limit" is the sum of these expected upper limits, weighted by their Poisson probability of occurrence:

$$\overline{\mu^{90}}(n_b) = \sum_{n_{obs}=0}^{\infty} \mu^{90}(n_{obs}, n_b)\,(n_b^{n_{obs}}/n_{obs})\,e^{-n_b}$$

Over an ensemble of identical experiments, the strongest constraint on the expected signal flux corresponds to a set of cuts that minimizes the so called "model rejection factor" μ_{90}/n_s and at the same time minimizes the mean flux upper limit that would be obtained over the hypothetical experimental ensemble.

The described Feldman-Cousin's approach with the Rolke extension [28] was used to calculate the mean upper limit on E^{-2} flux per source, for a 90% confidence level, from 10^6 background samples, as a function of a search bin, as shown on a Figure 2.

The search bin that minimizes the mean upper limit for 3 degrees tolerance value accounting for a magnetic deflection is found to be 4.9 degrees.

6 Discovery potential

With the bin size optimized and fixed, it is possible to estimate the probability of making a 3σ or a 5σ discovery given a certain signal flux. This is done by taking the chosen significance from the background MC samples, and comparing this to MC samples with signal of a certain flux. The number of skies with signal, that have more neutrinos in the given bin than the chosen significance from background only, is counted and gives a direct measure of the discovery potential for that particular flux.

Figure 3 shows the discovery potential for 3σ (dashed line) and 5σ (solid line) discovery, for an optimized bin of 4.9 degree bins, and a tolerance value accounting for a magnetic deflection of 3 degrees. Around 125 signal events on the whole sky are needed for a 5σ discovery in 50% of trials, and around 75 events are needed for a 3σ hint. Those values correspond to source flux values of about 1.29×10^{-8} GeV cm^{-2} s^{-1} and 2.16×10^{-8} GeV cm^{-2} s^{-1} respectively.

7 Results from the unblinded data

To analyze the level of correlation between the distribution 69 UHECRs reported by the Pierre Auger Observatory, and ANTARES neutrino candidates, we unblinded 2190 neutrino events. The significance of observed correlation is determined with the help of randomized background samples, using the bin size of 4.9 degrees.

The most probable count for the optimized bin size of 4.9 degrees, or the mean background expectation from the randomized samples is 310.49 events (in all 69 bins, i.e. on the whole sky), with the standard deviation of 15.22 events.

After unblinding 2190 ANTARES neutrino candidate events, a count of 290 events within 69 bins is obtained. On Figure 4, neutrino candidates are represented with crosses and neutrino candidates correlating with observed UHECRs are highlighted as large triangles. The observed number of correlated neutrino events is beneath expected (negative correlation), with the significance of about 1.35σ. This result is compatible with a background fluctuation. The corresponding upper flux limit, assuming the equal flux from all UHECR sources, is 4.96×10^{-8} GeV cm^{-2} s^{-1}.

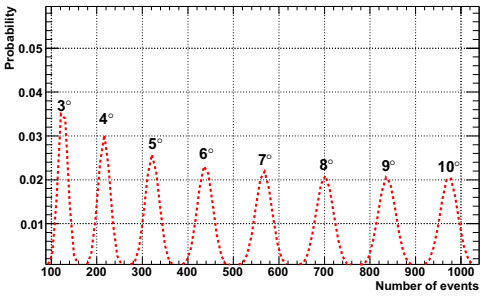

Figure 1: The probability density functions (PDFs) of the number of neutrino events in 1-10° bins centered on 69 UHECRs observed by the Pierre Auger Observatory. The counts were obtained from the background only Monte Carlo simulations, each with 2190 neutrino events blinded by scrambling the observed events in right ascension.

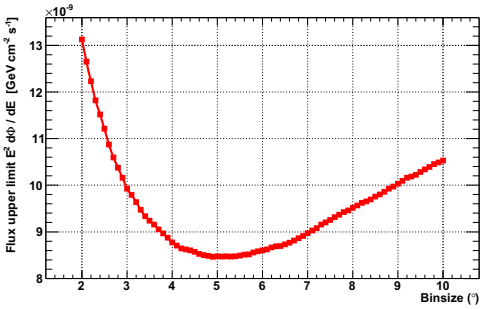

Figure 2: The mean upper flux limits as a function of the search bin size. The minimum flux value for magnetic field deflection tolerance value of 3 degrees is obtained for 4.9° search bin.

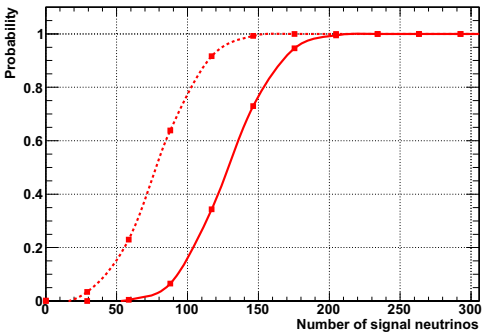

Figure 3: The discovery potential of 3σ (dashed line) and 5σ (solid line) as a function of number of signal neutrino events on the whole sky derived from the signal source flux.

References

[1] Stanev, T. 1997, Astrophysical Journal, **479**: 290
[2] Medina Tanco, G. A., de Gouveia dal Pino, E.M., & Horvath, J. E. 1998, Astrophysical Journal, **492**: 200
[3] Harari, D., Mollerach, S., & Roulet, E. 1999, Journal of High Energy Physics, **8**: 22

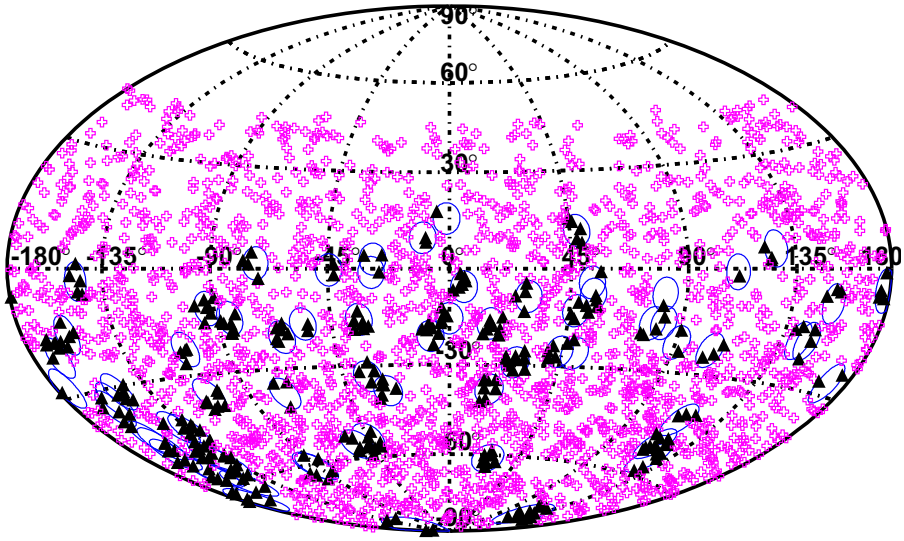

Figure 4: Crosses represent ANTARES neutrino events outside of 4.9 degree bins centered on UHECRs observed by the PAO, and triangles represent ANTARES neutrino events correlating with observed UHECRs.

[4] Kalashev, O. E., Kuzmin, V. A., & Semikoz, D. V. 2001, Modern Physics Letters A, **16**: 2505
[5] Alvarez-Muniz, J., Engel, R., & Stanev, T. 2002, Astrophysical Journal, **572**: 185
[6] Tinyakov, P. G. & Tkachev, I. I. 2002, Astroparticle Physics, **18**: 165
[7] Prouza, M. & Smida, R. 2003, Astronomy & Astrophysics, **410**: 1
[8] Yoshiguchi, H., Nagataki, S., & Sato, K. 2004,Astrophysical Journal, **607**: 840
[9] Tinyakov, P. G. & Tkachev, I. I. 2005, Astroparticle Physics, **24**: 32
[10] Kachelrie M., Serpico, P. D., & Teshima, M. 2007, Astroparticle Physics, **26**: 378
[11] Takami, H. & Sato, K. 2008, Astrophysical Journal, **681**: 1279
[12] Dolag, K., Grasso, D., Springel, V., & Tkachev, I. 2005, Journal of Cosmology and Astro-Particle Physics, **1**: 9
[13] Sigl, G., Miniati, F., & Enin, T. A. 2004, Physical Review D, **70**: 043007
[14] Kotera, K. & Lemoine, M. 2008, Physical Review D, **77**: 123003
[15] Das, S., Kang, H., Ryu, D., & Cho, J. 2008, Journal of Physics Conference Series, **120**: 062025
[16] Takami, H. & Sato, K. 2010, Astrophysical Journal, **724**:1456
[17] Greisen, K. 1966, Physical Review Letters, **16**: 748
[18] Zatsepin, Z. & Kuzmin, V. 1966, Zh. Eksp. Teor. Fiz. Pisma Red., **4**: 144
[19] Abbasi, R. U., Abu-Zayyad, T., Amann, J. F., et al. 2004, Physical Review Letters, **92**: 151101
[20] Takeda, M., Hayashida, N., Honda, K., et al. 1998, Physical Review Letters, **81**: 1163
[21] The Pierre Auger Collaboration. 2008, Astroparticle Physics, **29**: 188
[22] The Pierre Auger Collaboration. 2010, Astroparticle Physics, **34**: 314
[23] The IceCube collaboration. 2009, Astrophysical Journal, **701**: 47
[24] The ANTARES collaboration. 2011, astro-ph/11080292
[25] Veron-Cetty,M.-P. & Veron, P. 2006, Astronomy & Astrophysics, **455**: 773
[26] Feldman, G. J. & Cousins, R. D. 1998, Physical Review D, **57**: 3873
[27] Hill, G. C. & Rawlins, K. 2003, Astroparticle Physics, **19**: 393
[28] Rolke, W. A., Lopez, A. M., & Conrad, J. 2005, Nuclear Instruments and Methods in Physics Research A, **551**: 493

Searching for Point Sources of High Energy Cosmic Neutrinos with the ANTARES telescope

CLAUDIO BOGAZZI[1] ON BEHALF OF THE ANTARES COLLABORATION
[1]*FOM Instituut voor Subatomaire Fysica Nikhef, Science Park 105, 1098 XG Amsterdam, The Netherlands*
claudiob@nikhef.nl
DOI: 10.7529/ICRC2011/V04/0295

Abstract: ANTARES is currently the largest neutrino detector on the Northern Hemisphere. It consists of a tridimensional array of 885 photomultipliers arranged on 12 vertical lines, placed at a depth of 2475 meters in the Mediterranean Sea near Toulon, France. The telescope, completed in 2008, detects the Cherenkov radiation of muons produced by high energy neutrinos interacting in or around the detector. Muon tracks are then reconstructed using a likelihood-based algorithm. One of the main goals of the experiment is the search for high-energy neutrinos from astrophysical point-like sources. Due to its location, ANTARES is sensitive to up-going neutrinos from many potential galactic sources in the TeV to PeV energy regime. New results from an unbinned method as well as the sensitivity of the detector are presented.

Keywords: ANTARES, Neutrino telescopes, Point source search

1 Introduction

One of the main questions in astroparticle physics is the origin of high energy Cosmic Rays (CRs). In the last decade progress has been made related to energy spectrum and composition [1]. However, the origin of CRs remains unknown. Many acceleration sites have been suggested, such as supernova remnants, microquasars and active galactic nuclei [2]. The final signature of these cosmic accelerators are gamma rays and high energy neutrinos produced through hadronic interactions. The observation of a point-like source of neutrinos would then offer a unique occasion to study the mechanism of CRs acceleration.

1.1 The ANTARES detector

The ANTARES detector is located at a depth of 2475 m in the Mediterranean Sea, 42 km from Toulon in the south of France ($42°48N, 6°10E$). It consists of a tridimensional array of 885 optical sensors arranged on 12 vertical lines. Each line comprises up to 25 detection storeys each equipped with 3 downward-looking 10-inch photo-multipliers (PMTs), oriented $45°$ to the line axis. The spacing between storeys is 14.5 m while the lines are spaced by 60-70 m. A buoy at the top of the line keep them to stay vertical.

The telescope operates by detecting Cherenkov light emitted by charged particles that result from neutrino interactions in or around the detector. The arrival time and amplitude of the Cherenkov light on the PMTs are digitized into 'hits' [3] and transmitted to shore.

2 Data Selection

The data analysed in this work were collected between January 31st 2007 and December 30th 2010. The total livetime of the analysis is 813 days of which 183 days were with 5 lines, while for the remaining 630 days the detector consisted of 9, 10 and 12 lines

The reconstruction of the muon track is achieved using the time and position information of the hits. The algorithm is based on a maximum likelihood method [4] where a multi-stage fitting procedure is applied in order to maximise the likelihood of the observed hit times as a function of the muon direction and position. The quality of the reconstruction is defined by the variable Λ, which is based on the maximisation of the log-likelihood [4]. Figure 1 shows the cumulative distribution of Λ for upward-going events with the simulated contributions of atmospheric muons and neutrinos. Atmospheric muons are simulated with the MUPAGE package [5]; neutrinos are instead generated with the GENNEU [6] package and the Bartol model [7].

Neutrino candidates events are selected requiring an upward going track, i.e. zenith angle $< 90°$, and a value for the lambda variable $\Lambda > -5.2$. The latter is obtained by optimizing the background reduction and the signal efficiency, in terms of the discovery potential. Another cut is then applied in order to reject mis-reconstructed atmospheric downward going muons using the information of the uncertainty on the reconstructed muon track direction obtained from the fit. This value is required to be $\leq 1°$. The final sample consists of 3058 events; from the simula-

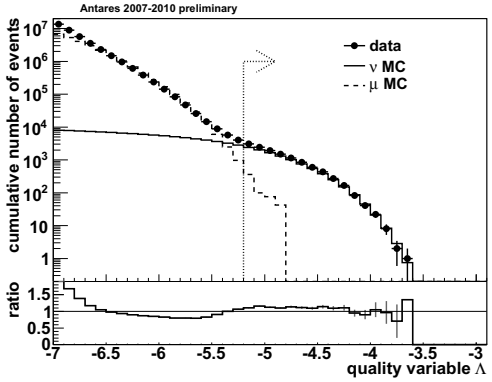

Figure 1: Cumulative distribution of the reconstructed quality variable Λ. The dashed line is for simulated atmospheric muons while the solid line corresponds to simulated atmospheric neutrinos. The bottom plot shows the ratio between data and Monte Carlo.

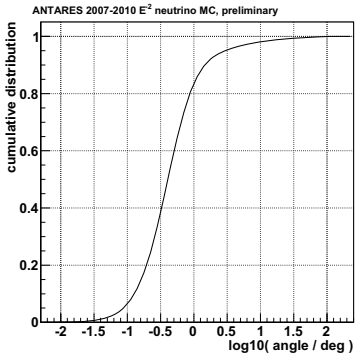

Figure 2: Cumulative distribution of the angle between the reconstructed muon direction and the true neutrino direction for simulated upward going neutrinos that pass the cuts described in Section 2 assuming a E_ν^{-2} neutrino spectrum.

tions 84% of them are estimated to be neutrinos, while the rest are mis-reconstructed atmospheric muons.

3 Detector Performance

The angular resolution and the acceptance of the detector have been obtained from simulation. The systematic uncertainty on the angular resolution has been computed following the procedure described in [9] by smearing the hit times according to a Gaussian with a width of σ_t in order to artificially deteriorate the simulated timing accuracy. The study leads to exclude an additional smearing of 3 ns which was found to be incompatible with data at the 2σ level where σ is the uncertainty on the flux model [8]. The best agreement between data and Monte Carlo is obtained for $\sigma_t = 2 \pm 0.5$ ns. This value is indeed used for the simulations presented in this paper.

3.1 Angular resolution

Figure 2 shows the cumulative distribution of the angle between the reconstructed muon direction and the generated neutrino direction for neutrino events where we assumed an energy spectrum proportional to E_ν^{-2} with E_ν the neutrino energy. The median of this angular error is 0.46 degrees.

3.2 Acceptance

The acceptance for signal neutrinos is also estimated using simulations. In the search, we deal with fluxes of the form of

$$\frac{dN}{dE} = \phi(\frac{E_\nu}{GeV})^{-2} GeV^{-1} s^{-1} cm^{-2}, \qquad (1)$$

where ϕ is the flux normalisation. The acceptance, A, is defined as the constant of proportionality between ϕ and

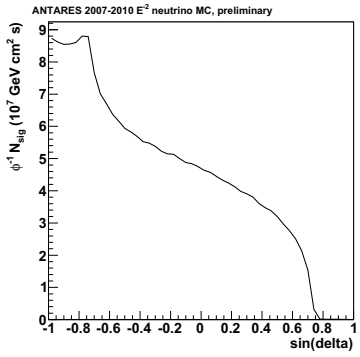

Figure 3: Acceptance, i.e. the constant of proportionality between the normalisation factor for an E^{-2} flux and the selected number of events.

the number of selected events. Figure 3 shows exactly this proportionality: for a source at a declination of -90 (0) degrees, $A = 8.8(4.8) \times 10^7$ GeV cm^2 s. Systematic uncertainties on the acceptance are constrained by the agreement between the simulated atmospheric neutrino sample and data. For the computation of the flux limits an uncertainty of 15% is assumed.

4 Search method

The algorithm used on the analysis is based on the likelihood of the observed events which is defined :

$$\log \mathcal{L}_{\rm s+b} = \sum_i \log[\mu_{\rm sig} \times \mathcal{F}(\beta_i(\delta_s, \alpha_s)) \times \mathcal{N}(N_{hits}^{i,sig}) + \mathcal{B}_i \times \mathcal{N}(N_{hits}^{i,bkg})] + \mu_{\rm tot},$$

where the sum is over the events, $\mathcal{F}$ is the point spread function, i.e. the probability density of reconstructing an

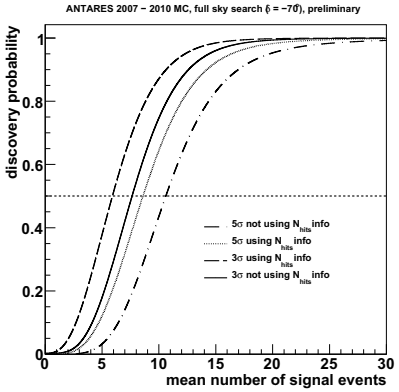

Figure 4: Probability for a 3σ (dashed and solid lines) and 5σ (dotted and dashed-dotted lines) discovery as a function of the mean number of signal events for the case where we use the number of hits information in the likelihood (dashed and dotted lines) and for the case where we do not use it (solid and dashed-dotted lines) for the full sky search. In this case the signal was added at a declination of -70°.

event i at a distance β_i from the true source declination and right ascension δ_s, α_s; $\mathcal{B}$ is a parametrization of the background rate, obtained from the observed declination distribution of the events; μ_{sig} is the mean number of detected events that the source produces and μ_{tot} represents the total number of expected events and $\mathcal{N}(N^i_{hits})$ is the probability for an event i to be reconstructed with N_{hits} number of hits (this probability was not included in the analysis with 2007 and 2008 data [9]).

In order to compute the test statistic the free parameters of the likelihood are maximized. We have now to distinguish between the two different analysis presented in this paper: in the candidate list search only the μ_{sig} are fitted while in the full sky search we have in addition the source coordinates (δ_s, α_s) to fit. In both cases the results of the fit are the maximum likelihood value $\mathcal{L}^{max}_{s+b}$ and the estimates of the free parameters. The test statistic is then defined as:

$$\mathcal{Q} = \mathcal{L}^{max}_{s+b} - \mathcal{L}_b \qquad (2)$$

where $\mathcal{L}_b$ is the likelihood computed for the background only case. The higher $\mathcal{Q}$ the more the data are compatible with signal.

Just using the number of hits information in the likelihood let us to gain a 25% (22%) factor for the 3 (5) σ discovery probability as shown in Figure 4 for the full sky search.

5 Results

As mentioned above two different analyses have been done. The first one is a full sky survey with no assumptions about the source position. In the second analysis, we made a search for a signal excess in an *a priori* defined spot in the sky corresponding to the position of some interesting astrophysical objects.

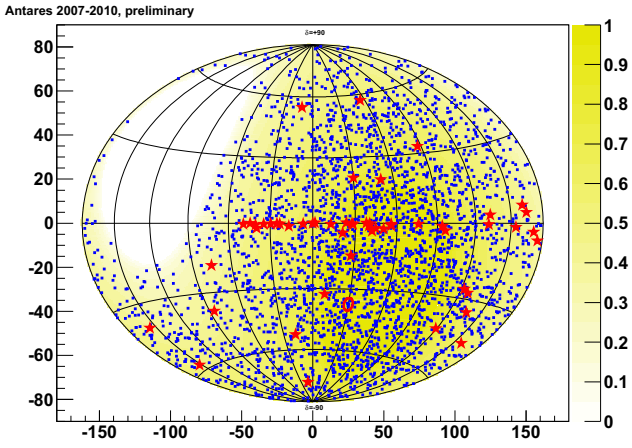

Figure 5: Galactic skymap showing the 3058 data events. The position of the most signal-like cluster is indicated by the circle. The stars denote the position of the 51 candidate sources.

5.1 Full sky search

In the full sky search, no significant clusters of neutrino candidates were found. The most signal-like cluster is located at $\alpha_s, \delta_s = (-46.5°, -65.0°)$. The fit assigns 5 events above the background. The value of the test statistic for this cluster is 13.0 which yields to a p-value of 2.6%. Figure 5 shows a sky map of the selected events in galactic coordinates with the location of the most signal like cluster.

5.2 Candidate list search

The results of the search in the direction of 51 pre-defined candidate sources are shown in Table 1. None of the sources have a significant excess of events. The most signal-like candidate source is HESS J1023-575 where the post-trial p-value is of 41%. Figure 6 shows the 90% confidence level limits on ϕ using the Feldman-Cousins prescription [10] and assuming an E^{-2} neutrino spectrum for each of the source candidates as a function of the source declination. The sensitivity of this analysis is also presented, defined as the median expected limit and resulting in a factor 2.7 better than the one obtained with data collected during 2007 and 2008 only [9]. Limits from other experiments are also shown. However, it should be noted that for this spectrum, ANTARES detects most events at energies around 10 TeV while the limits in the Southern Hemisphere published by the IceCube Collaboration [11] apply to the PeV region.

source	$\alpha_s(^\circ)$	$\delta_s(^\circ)$	p	$\phi^{90\%\mathrm{CL}}$
HESS J1023-575	155.83	-57.76	0.41	6.6
3C 279	-165.95	-5.79	0.48	10.1
GX 339-4	-104.30	-48.79	0.72	5.8
Cir X-1	-129.83	-57.17	0.79	5.8
MGRO J1908+06	-73.01	6.27	0.82	10.1
ESO 139-G12	-95.59	-59.94	0.94	5.4
HESS J1356-645	-151.00	-64.50	0.98	5.1
PKS 0548-322	87.67	-32.27	0.99	7.1
HESS J1837-069	-80.59	-6.95	0.99	8.0
PKS 0454-234	74.27	-23.43	1.00	7.0
IceCube hotspot	75.45	-18.15	1.00	7.0
PKS 1454-354	-135.64	-35.67	1.00	5.0
RGB J0152+017	28.17	1.79	1.00	6.3
Geminga	98.31	17.01	1.00	7.3
PSR B1259-63	-164.30	-63.83	1.00	3.0
PKS 2005-489	-57.63	-48.82	1.00	2.8
HESS J1616-508	-116.03	-50.97	1.00	2.7
HESS J1503-582	-133.54	-58.74	1.00	2.8
HESS J1632-478	-111.96	-47.82	1.00	2.6
H 2356-309	-0.22	-30.63	1.00	3.9
MSH 15-52	-131.47	-59.16	1.00	2.6
Galactic Center	-93.58	-29.01	1.00	3.8
HESS J1303-631	-164.23	-63.20	1.00	2.4
HESS J1834-087	-81.31	-8.76	1.00	4.3
PKS 1502+106	-133.90	10.52	1.00	5.2
SS 433	-72.04	4.98	1.00	4.6
HESS J1614-518	-116.42	-51.82	1.00	2.0
RX J1713.7-3946	-101.75	-39.75	1.00	2.7
3C454.3	-16.50	16.15	1.00	5.5
W28	-89.57	-23.34	1.00	3.4
HESS J0632+057	98.24	5.81	1.00	4.6
PKS 2155-304	-30.28	-30.22	1.00	2.7
HESS J1741-302	-94.75	-30.20	1.00	2.7
Centaurus A	-158.64	-43.02	1.00	2.1
RX J0852.0-4622	133.00	-46.37	1.00	1.5
1ES 1101-232	165.91	-23.49	1.00	2.8
Vela X	128.75	-45.60	1.00	1.5
W51C	-69.25	14.19	1.00	3.6
PKS 0426-380	67.17	-37.93	1.00	1.4
LS 5039	-83.44	-14.83	1.00	2.7
W44	-75.96	1.38	1.00	3.1
RCW 86	-139.32	-62.48	1.00	1.1
Crab	83.63	22.01	1.00	4.1
HESS J1507-622	-133.28	-62.34	1.00	1.1
1ES 0347-121	57.35	-11.99	1.00	1.9
VER J0648+152	102.20	15.27	1.00	2.8
PKS 0537-441	84.71	-44.08	1.00	1.3
HESS J1912+101	-71.79	10.15	1.00	2.5
PKS 0235+164	39.66	16.61	1.00	2.8
IC443	94.21	22.51	1.00	2.8
PKS 0727-11	112.58 -	11.70	1.00	1.9

Table 1: Results of the candidate source search. The source coordinates and the p-values (p) are shown as well as the limits on the flux intensity $\phi^{90\%\mathrm{CL}}$; the latter has units $10^{-8}\mathrm{GeV}^{-1}\mathrm{cm}^{-2}\mathrm{s}^{-1}$.

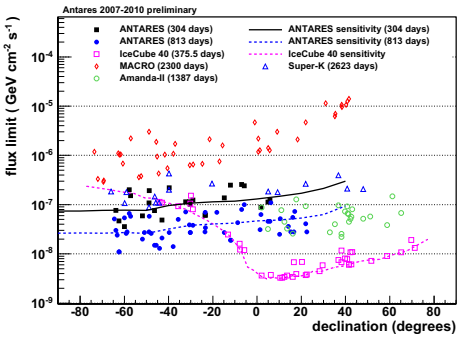

Figure 6: Limits set on the normalisation ϕ of an E_ν^{-2} spectrum of high energy neutrinos from selected candidates (see Table 1). Also shown is the sensitivity, which is defined as the median expected limit. In addition to the present result, several previously published limits on sources in both the Southern and Northern sky are also shown.

6 Conclusions

A search of high energy cosmic neutrinos has been performed. Data were taken during the first four years of operation when ANTARES consists of 5 line for most of the first year considered and 9, 10 and 12 for the rest. A measurement of the angular resolution using MonteCarlo data yields to 0.46 degrees. Neither the full sky search nor the candidate list search show a significant excess of events therefore limits have been obtained on the neutrino flux.

References

[1] E. Waxmann, to be published in Astronomy at the Frontiers of Science, 2011, ed. J. P. Lasota, Springer.
[2] J. K. Becker, Physics Reports, 2008, **458**: 173-246.
[3] J. A. Aguilar *et al.* , Nucl. Instr. Meth., 2010, **A622**: 59-73.
[4] A. Heijboer, 2004, PhD Thesis, http://antares.in2p3.fr/Publications.
[5] G. Carminati, M. Bazzotti, A. Margiotta and M. Spurio, Comp. Phys. Comm., **179**: 915.
[6] D. Bailey, 2002, PhD Thesis, http://antares.in2p3.fr/Publications.
[7] V. Agrawal, T. K. Gaisser, P. Lipari, T. Stanev Phys. Rev. D, 1996, **53**: 1314-1323.
[8] G. D. Barr *et al.* , Phys. Rev. D, 2006, **74**(9): 094009.
[9] S. Adrian-Martinez *et al.* (ANTARES Collaboration), arXiv:1108.0292v1 [astro-ph.HE], submitted to Astrophysical Journal Letters.
[10] G. J. Feldman and R. D. Cousins, Phys. Rev. D, 1998, **57**(7):3873-3889.
[11] R. Abbasi *et al.* , Astrophys. J., 2011, **732**: 18.

32ND INTERNATIONAL COSMIC RAY CONFERENCE, BEIJING 2011

Update for 2010 of the results of the search for neutrino bursts from core collapse supernovae at the Baksan Underground Scintillation Telescope

R.V. NOVOSELTSEVA[1], M.M. BOLIEV[1], V.I. VOLCHENKO[1], G.V. VOLCHENKO[1], I.M. DZAPAROVA[1], M.M. KOCHKAROV[1], YU.F. NOVOSELTSEV[1], V.B. PETKOV[1], P.S. STRIGANOV[1], A.F. YANIN[1]
[1]*Institute for Nuclear Research, Russian Academy of Sciences, Moscow, 117312 Russia*
R.V. Novoseltseva rivinov@yandex.ru
DOI: 10.7529/ICRC2011/V04/0298

Abstract: The results of 30 years of neutrino sky coverage at the Baksan Underground Scintillation Telescope are presented. The investigation of afterpulses related to inelastic muon interactions has been performed. The upper bound on collapse frequency in our Galaxy was found 0.088 y^{-1} (90% CL).

Keywords: neutrino, undeground detectors

1 Introduction

Neutrino burst from the core collapse of a massive star in our Galaxy would be detected by existing detectors. Together they will provide detailed information on the neutrino flux, energy and the dynamics of the collapse. Furthermore, neutrino detection would be the only way, apart from gravitational waves, to obtain information of the inner layers of the star. Until now, the only supernova source of neutrinos that has been observed is the supernova SN1987A [1, 2, 3, 4]. Registered events generated by SN1987A neutrino confirmed predictions of the supernovae theory.

2 Theoretical models

The theoretical models for the neutrinoradiation parameters expected during the gravitational core collapse of a massive star and the cooling newborn neutron star forecast: neutrinos carry away about 99% of the gravitational binding energy released in the collapse $\epsilon_{tot} = 3 \times 10^{53}$ erg; this energy is roughly equipartitioned between the six neutrino flavors; typical ranges for the average energies of the time-integrated neutrino spectra $\langle E_{\nu_e} \rangle$ = 10-12 MeV, $\langle E_{\overline{\nu}_e} \rangle$ = 11-17 MeV, $\langle E_{\nu_x} \rangle$ = 15-24 MeV and the duration of the neutrino burst does not exceed 20 sec ([5] and refs. therein), [6].

The SN 1987A neutrino observations provided a confirmation of the overall picture of core-collapse and neutron-star formation. The signal duration was about ten seconds, which is within time scale predicted by the diffusive neutrino energy transport in a nuclear-density hot compact star. The energies in the ten MeV range, representatives of the temperature at the "neutrino sphere," roughly agreed with expectations.

However a registration of significant event cluster in the LSD experiment [2] gives rise to non-standard two-stage scenario of stellar collapse. The scenario has been proposed to incorporate both neutrino pulses from SN1987 in a self-consistent two-stage hydrodynamical model of the gravitational collapse [7]. The mean neutrino energy (during the first stage) in this model is $\overline{E}_{\nu_e} = 30 - 40$ MeV [8].

Another model of type II supernova explosion has been proposed in 2007 [9]. This model has taken into account large-scale convection caused by non-equilibrium neutronization of matter in the central region of protoneutron star. The large-scale convection provides high yield of high energy neutrinos from the central region of presupernova. The average energy of neutrinos is 30-50 MeV which is more than in the case of diffusion.

The Baksan underground scintillation telescope has been searching for neutrino burst from supernova explosions since June 30, 1980.

3 The Baksan Underground Scintillation Telescope (BUST)

3.1 The Baksan Neutrino Observatory

The Baksan Neutrino Observatory located in the Northern Caucasus consists of facilities at different depths, dimensions and scopes. The underground facilities are placed in the first excavation in the world specifically built for scientific purposes. The experimental activities started in the 70s.

3.2 BUST

BUST is placed at the effective depth of 850 m of w.e. [10]. The facility has dimensions of $17 \times 17 \times 11$ m^3 and consists of four horizontal and four vertical planes. Planes are covered with standard autonomic modules (detectors). Each module ($70 \times 70 \times 30$ cm^3 in size) is filled with organic liquid scintillator on the basis of white spirit ($C_nH_{2n+2},\ n \simeq 9$), viewed by one photomultiplier with a photocathode of 15 cm in diameter. The scintillator was developed at the Institute for Nuclear Research [11] and it remains one of the best in the world. The long term stability of the scintillator has been checked in practice - BUST has been operated since 1977. The total number of modules is 3180. The mass of the scintillator of the facility is 330 tons. Three lower horizontal planes (the internal planes) have 1200 standard detectors and 130 tons of scintillator.

The information from each detector is transferred through three channels concurrently:

- an anodic channel (which serves to generate triggers and measure signal amplitudes of up to 2.5 GeV),

- a pulse channel with an energy threshold of 8 MeV (the most probable muon energy release in the module is 50 MeV),

- a logarithmic channel with an energy threshold of 500 MeV.

The last essential change of the condition of event's selection at the facility, amidst other various changes performed since 1977, was in 2001 year; since March, 2001 all events have been written down without exception.

Dead time of BUST is $\simeq 1$ ms. The timing accuracy is 0.2 ms. Synchronization of the clock is performed by GPS signal approximately 20 times per calendar day.

4 The method of neutrino burst detection in the Baksan experiment

Since the cross-section for inverse β decay reaction on protons

$$\overline{\nu}_e + p \rightarrow n + e^+ \tag{1}$$

exceeds the cross-sections for other neutrino flavors and targets, the neutrino signal from a supernova explosion is recorded with $\overline{\nu}_e$ events.

If the mean antineutrino energy is 11 -17 MeV [5, 6] the range of positrons (produced in reaction (1)) will be as a rule, in the volume of one detector only. In such a case the signal from a supernova explosion will appear as a series of events from singly triggered detectors. Singly triggered detector means that the one pulse channel at the facility has been operated (below as "1 from 3180"). The search for the signal from the neutrino burst involves selecting a cluster of single events during τ = 20 s (according to the standard collapse models the burst duration does not exceed 20 s).

Calculation of the detection efficiency for e^- (e^+) η_1 shows that the efficiency depends on the electron energy. $\eta_1 = 0.7$ if the electron energy $E_e = 10$ MeV and $\eta_1 = 0.9$ if $E_e = 20$ MeV [12].

To evaluate the expected number of events at BUST from neutrino burst, we assume that 1) the distance from the star is 10 kpc (approximately the distance to the Galactic center, but in an arbitrary direction), 2) the total energy radiated in neutrinos is $\epsilon_{tot} = 3 \times 10^{53}$ erg and 3) we leave out a possible influence of oscillations.

If the energy of the $\nu_i(\overline{\nu}_i)$ ($i = e, \mu, \tau$) flux is equal to

$$1/6 \times \epsilon_{tot} \tag{2}$$

the expected number of single events from reaction (1) will be $N^H_{ev} \simeq 38 \times \eta_1$, where η_1 denotes the detection efficiency of e^+ and the symbol "H" indicates that the hydrogen is the target.

The models [8, 9] called for further investigations of response at BUST. According to [8, 9] the mean neutrino energy is $\overline{E}_\nu = 30 - 50$ MeV, therefore the reactions on the carbon of the scintillator begin to work:

$$\begin{aligned} &\nu_i + {}^{12}C \rightarrow {}^{12}C^* + \nu_i, \quad E_{th} = 15.1\ MeV, \\ &i = e, \mu, \tau, \\ &{}^{12}C^* \rightarrow {}^{12}C + \gamma, \quad E_\gamma = 15.1\ MeV \end{aligned} \tag{3}$$

and

$$\begin{aligned} &\nu_e + {}^{12}C \rightarrow {}^{12}N + e^-, \quad E_{th} = 17.34\ MeV, \\ &{}^{12}N \rightarrow {}^{12}C + e^+ + \nu_e, \quad \tau_N = 15.9\ ms, \end{aligned} \tag{4}$$

τ_N is the lifetime of the nucleus ^{12}N.

Reaction (3) allows us to measure the total neutrino flux with the energy $E_\nu > 15.1$ MeV.

If the energy $\overline{E}_\nu = 30$ MeV, the expected number of events for reactions (3) and (4) can be estimated (under condition (2)) by formulae

$$N^C_{ev2} = 16 \times \eta_2, \quad (E_\gamma = 15\ MeV), \tag{5}$$

$$N^C_{ev3} = 30 \times \eta_3, \quad (E_\nu = 30\ MeV), \tag{6}$$

The radiation length for our scintillator is 47 g/cm^2, therefore $\eta_2 \approx 0.2$. In reaction (4) the sum of energies $E_{e^+} + E_\nu$ is 17.3 MeV, therefore $\eta_3 \approx 0.5 - 0.7$.

In reaction (4) BUST can detect both an electron with energy $E_e = E_\nu - 17$ MeV and a positron if the energy release from each particle is > 8 MeV. In such a case, the reaction (4) has the distinctive signature of two signals separated by $5 - 45$ ms time interval (dead time of BUST is $\simeq 1$ ms).

In the case of very high energy neutrinos we consider also the neutrino interaction with the iron of the facility. The lower part of the overlap between horizontal scintillator planes is the 8 mm iron layer. This can be used as the target in the reaction

$$\nu_e + {}^{56}Fe \rightarrow {}^{56}Co^* + e^-, \quad E_{th} = 4.056\ MeV, \tag{7}$$

(cobalt emerges in excited state).

Under condition (2) the expected number of events from reaction (7) (neutrinos arrive from above) is

$$N_{ev}^{Fe} = 6.3 \times \eta_{Fe}(26\ MeV), \tag{8}$$

$\eta_{Fe}(26\ MeV) \approx 0.4$ is the detection efficiency of e^- with the energy 26 MeV produced into the 8 mm iron layer.

It should be noticed, if $\overline{E}_{\nu_e} = 30 - 40$ MeV a noticeable percentage of neutrino reactions (7) will cause triggering of two detectors.

To summarize, if the average neutrino energies are $30 - 40$ MeV, the number of events induced by neutrino at BUST is increased by $\approx 50\%$.

The cluster of events at BUST would be considered to be a serious candidate for collapse detection if nine or more single events were observed within 20 s sliding time interval in the internal planes of the facility (130 ton of scintillator). To search for such rare events requires careful consideration of noises.

5 Background events

The background for this task is due to a number of reasons.

1. One of them is cosmic ray muons when a single muon is only registered by one detector ("1 from 3180") due to spatial gaps between modules of the telescope, and also in the case of one muon energy release < 8 MeV.

2. Other sources of the background come from radioactive isotopes induced by cosmic ray muons (see subsection "Inelastic muon interaction with the matter of the detector").

3. Since our experiment is based on the detection of a single recoil electron, any radioactive decay with similar energy deposition can mimic a neutrino events.

4. The ghost signals from detectors add to the noise.

The total count rate from single events in the Baksan experiment is $f_i = 0.02 s^{-1}$ in internal planes (1200 detectors) and $f_e = 1 s^{-1}$ in external ones (1980 detectors). Therefore three lower horizontal planes are used as a target (i.e. the fired detector is located in one of three internal planes).

We suppose that background events are fitted by Poissons' law. So the background events imitate the expected signal (k single events in the internal planes within sliding time interval τ) with a count rate

$$p(k) = f_i \times exp(-f_i\tau)\frac{(f_i\tau)^{k-1}}{(k-1)!} \tag{9}$$

The treatment of experimental data over a period of 2001 - 2010 y (the period with equal conditions for recording of the events) shows that the single event distribution is in good agreement with Poissons' law.

At present we are also studying events with two triggered detectors of BUST. The count rate of such events in internal planes is $\approx 4 \cdot 10^{-3} s^{-1}$.

5.1 Inelastic muon interaction with the matter of the detector

Some part of the background events can be connected with inelastic muon interactions which can produce unstable nuclei whose disintegration brings into operation only one detector. To separate such events, afterpulses following large energy deposition ($\geq$ 500 MeV) in the detector were studied.

The events "1 from 3180" are afterpulses for this case. The events with energy deposition of ($\geq$ 500 MeV) are cascades with a lot of detectors (the number of the pulse channels up to 3000); at least one logarithmic channel has been operated (the number of them up to a few tens).

The events are analyzed, which have had on the internal planes of the facility one or more detectors with energy release of $E \geq 500$ MeV (event of type "a"), and then a single events were selected among these detectors (i.e. afterpulses) within interval Δt (event of type "b").

The distribution of events of type "b" in Δt is well described by exponent $A * exp((-\Delta t)/\tau)$ with $\tau = 21.8 \pm 2.16$ ms. This value of τ is in good agreement with lifetime of the nucleus ^{12}B: $\tau(^{12}B)$ = 20.4 ms.

^{12}B can appear as the result π^- interacting with carbon of the scintillator ($\pi^-$are produced in inelastic muon interactions)

$$^{12}C + \pi^- \rightarrow ^{12}\ B + \pi^o \tag{10}$$

and then disintegrate in reactions

$$^{12}B \rightarrow ^{12}\ C + e^- + \overline{\nu}_e \tag{11}$$

The peak of energy deposition spectrum of type "b" events with $\Delta t \leq$ 1s corresponds to energy deposition $E = 13.3$ MeV which is in close agreement with typical energy of an electron in process (10) ($E_e = 13.37$ MeV). Events with larger energy depositions are interpreted as the path of a single muon when only one detector is hit in BUST (naturally, such muons give some contribution at smaller values of energy deposition).

The energy deposition spectrum of "b" events with $\Delta t \leq$ 0.1 s (i.e. the contribution of muons has been reduced by 10 times) has the peak at the same energy. This apparently indicates that the peak results from ^{12}B decay.

Assuming that N_{a-b} is $\simeq 10\%$ of the total number of reactions (10,11) we obtain the estimation for the fraction of detector's operation related to ^{12}B decay $fr(^{12}B) = 0.013$.

6 Conclusions

Investigations of BUST response to neutrinos of 30 - 40 MeV have been performed. The number of events induced by neutrino in BUST has been found to be increased by $\approx 50\%$.

Afterpulses related to inelastic muon interactions have been studied. Discrimination of such afterpulses does not lead to noticeable reduction of the background.

The Baksan experiment searching for neutrino bursts is in progress since the mid-1980s [12], [13]. The total live time for the period of 30.06.1980 to 31.12.2010 is T = 26.2 years. No burst candidates have been detected during this period. Let f_{col} be the mean frequency of collapses, then the probability of absence collapse during the time interval T is (according to the Poisson law) $\exp(-f_{col}T)$. An upper bound on the mean frequency of gravitational collapses in the Galaxy at 90% CL can be obtained with the help of the expression $\exp(-f_{col}T) = 0.1$, therefore

$$f_{col} < 0.088y^{-1} \quad (90\%\, CL). \tag{12}$$

$Acknowledgements$.This work was supported by the "Neutrino Physics and Neutrino Astrophysics" Program for Basic Research of the Presidium of the Russian Academy of Sciences.

The work is partially supported by the Federal Targeted Program of Ministry of Science and Education of Russian Federation "Research and Development in Priority Fields for the Development of Russia's Science and Technology Complex for 2007-2013", contract no. 16.518.11.7072.

References

[1] K.S.Hirata, T.Kajita, M.Koshiba et al., Phys. Rev. Lett., 1987, **58**: 1490
[2] M. Aglietta et al., Europhys. Lett., 1987, **3**: 1315
[3] R.M.Bionta, G.Blewitt, C.B.Bratton et al., Phys. Rev. Lett., 1987, **58** : 1494
[4] E.N.Alekseev, L.N.Alekseeva, V.L.Volchenko, et al., Pis'ma Zh.Eksp.Teor.Fiz.,1987, **45**: 461; E.N.Alexeyev, L.N.Alexeyeva, I.V.Krivosheina et al., Phys. Lett.,1988, **B205**: 209
[5] Keil M. T., G. G. Raffelt, and H.-T. Janka, Astrophys. J. ,2003, **590** : 971; Raffelt G.G. Contribution to Proc. Neutrino 2006, Santa Fe, New Mexico. arXiv:astro-ph/0701677 (2007)
[6] T. Totani, K. Sato, H. E. Dalhed and J. R. Wilson, Astrophys. J., 1998, **496**: 216
[7] Imshennik V.S. Space Sci.Rev., 1995, **74**: 325
[8] Imshennik V.S., Ryazhskaya O.G. Astronomy Letters, 2004, **30**: 17
[9] I.V.Bajkov, V.M. Suslin, V.M. Chechetkin, V.Bychkov, L. Stenflo, Astronomicheskij jurnal, 2007,**84** (4): 308 -316
[10] Alexeyev E.N. et al. Proc. of 16 ICRC,Kyoto, 1979, **10**: 276.
[11] Voevodskii, A.V., Dadykin, V.A., and Ryazhskaya, O.G., Prib. Tekh. Eksp., 1970, **1**: 85
[12] Alexeyev E.N. et al. JETP, 1993, **104**: 2897-2911
[13] Novoseltseva R.V. et al., Proc. of 31th ICRC, 2009, icrc 0366

32ND INTERNATIONAL COSMIC RAY CONFERENCE, BEIJING 2011

Search for Galactic Cosmic-Ray Accelerators with the Combined IceCube 40-strings and AMANDA Detector

THE ICECUBE COLLABORATION
[1] *see special section of these proceedings*

Abstract: During the season 2008/2009, IceCube took data as a combined detector with AMANDA embedded into the 40-string array. With a smaller spacing between the sensors compared to IceCube, AMANDA improved the effective area below a few TeV and acted as a first generation low-energy extension of IceCube. The data obtained in this configuration is used to search for neutrino sources within the Galaxy. The TeV γ-ray spectra of some potential galactic cosmic-ray accelerators show cut-offs in the energy spectrum at energies of a few TeV. In the case of transparent TeV γ-ray sources, high-energy neutrinos will follow similar spectra and an improved effective area below a few TeV improves the sensitivity for these of sources.

Several tests including a scan of the galactic plane in the Northern Hemisphere and a dedicated analysis for the Cygnus region are presented. In the absence of a significant signal, upper limits are reported. The results provide the most restrictive upper limits for the Cygnus region obtained so far. Depending on the assumed energy cut-off, the upper limits obtained with this analysis are only a factor of two to three above the expected neutrino flux if all the TeV γ-rays observed in the region were of hadronic origin. This implies that during the coming years, IceCube will be able to either detect neutrinos from the Cygnus region, or to constrain the nature of the high-energy γ-ray emission in the region, and thus the fraction of interacting cosmic rays produced in one of the most active parts of the Galaxy.

Corresponding authors: Sirin Odrowski[1] (*Sirin.Odrowski@mpi-hd.mpg.de*), Elisa Resconi[2],[3](*Elisa.Resconi@mpi-hd.mpg.de*), Yolanda Sestayo[1] (*Yolanda.Sestayo@mpi-hd.mpg.de*)
DOI: 10.7529/ICRC2011/V04/0320

[1] Max-Planck-Institut fuer Kernphysik, 69117 Heidelberg, Germany

[2] T.U. Muenchen, 85748 Garching

[3] Friedrich-Alexander Universitaet Erlangen-Nuernberg, 91058 Erlangen

Keywords: neutrino astronomy, IceCube

1 High-Energy Neutrino Production in the Galaxy

One of the primary goals of the IceCube experiment [1] is the detection of astrophysical sources of high-energy neutrinos. A neutrino signal uniquely identifies the sites of hadron acceleration and interaction and thereby the sites of cosmic-ray production.

If protons are accelerated to sufficiently high energies in (galactic) sources, high-energy neutrinos can be produced through proton-proton interactions with the ambient gas. If such sources are transparent and the γ-ray emission from high-energy electrons is small compared to the total γ-ray emission, the high-energy neutrino spectra can be inferred from the γ-ray spectra [2].

Several objects within the Galaxy such as supernova remnants and pulsar wind nebulae, binary systems and the collective winds of massive stars might accelerate protons up to PeV energies [3]. Even though γ-rays up to several TeV have been observed from several of these objects, many of the observed γ-ray spectra have energy cut-offs below 10 TeV and/or their energy spectra are significantly steeper than an E^{-2} spectrum as expected from shock acceleration. A search for neutrino emission from within the Galaxy thus requires an approach that is optimized to retain a high efficiency for neutrinos with energies below 10 TeV. The predicted neutrino flux from galactic sources is very low and single point-like sources might elude a detection in the near future. In star forming regions, it is however possible that several (weak) sources produce an integrated signal strong enough for a discovery. In particular the Cygnus region as the most active part of the Galaxy in the Northern Hemisphere is of primary interest to IceCube in this context.

2 Methods and Targets

At energies between a few hundred GeV and a few TeV, the field of view of the 2008/2009 configuration of Ice-

Cube is restricted to the Northern Hemisphere where the atmospheric muon background is suppressed by several orders of magnitude by the shielding provided by the Earth. Within this field of view, a search for point-like, steady high-energy neutrino sources has been performed. We search for a significant excess of neutrinos over the uniform background of atmospheric neutrinos by a maximum likelihood ratio hypothesis test, described in [4]. The search is performed on a 0.25° grid covering the galactic plane within the field of view ($37.5^\circ < l < 212.5^\circ$, $-5^\circ < b < 5^\circ$). Since the angular grid size is smaller than the angular resolution of the detector, this search may be regarded as an unbinned analysis. The energy term in [4] is omitted as it is not relevant for soft spectra sources.

In addition, the same likelihood ratio hypothesis test is applied to six prominent γ-ray sources: the Crab Nebula, LSI +61 303, CasA, W51, SS433 and IC443. The sources were chosen due to their brightness in γ-rays and/or the presence of target material for proton-proton interactions in or near the sources.

To search for high-energy neutrino emission within the Cygnus region, a dedicated test based on a 2-point correlation function has been developed [5]. A search for a spatial clustering of events inside a 7°x11° region ($72^\circ < l < 83^\circ$, $-3^\circ < b < 4^\circ$) around the most active part of the Cygnus region is performed. The method is able to take advantage of extended emission regions and the emission of any sources within the region. If applied to the data sample used in this work, the discovery flux per point source is lower than in a standard search if more than two point sources are present within the region.

The analyzed data set is dominated by atmospheric neutrinos. Any potential astrophysical signal presents only a very small contribution in number of events. A data driven background estimation can thus be obtained by randomizing the arrival directions of the events, compatible with a homogeneous spatial distribution. All statistical tests reported here use this technique for the construction of their respective null hypothesis.

3 The Combined IceCube 40-string and AMANDA Detector

The full IceCube [1] neutrino telescope at the South Pole consists of a volume of approximately one cubic kilometer of clear Antarctic ice instrumented with light sensors. This instrumentation allows to detect muons from charged current interactions of neutrinos. 5160 digital optical modules are deployed in the ice along 86 strings that hold 60 optical modules each. The detector has been built in several stages and new strings have been added each Antarctic summer since 2004/2005.

AMANDA [8] is located at the same site as IceCube and consists of 677 optical modules deployed on 19 strings, most of them at depths between 1500 and 2000 m. Both the vertical and horizontal spacing of the optical modules in AMANDA are smaller than in IceCube. This provides a lower energy threshold and a higher collection efficiency for muons below a few TeV. As AMANDA is the precursor experiment to IceCube, many of the techniques employed in IceCube were developed and tested in AMANDA [9]. AMANDA took data as a stand-alone neutrino telescope until December 2006. Since 2007, AMANDA is fully surrounded by IceCube strings and was integrated into the IceCube data acquisition system as a low-energy extension of the IceCube detector until 2009 [10].

In the combined data taking mode, AMANDA initiates a read-out of IceCube whenever a multiplicity trigger condition in AMANDA is fulfilled. The data collected from both parts of the combined detector is then merged into a single event and reconstructions can be applied to either the full event information or to the IceCube or AMANDA information separately. The analysis presented here uses the information from both IceCube and AMANDA.

4 Neutrino Sample

The targets of this analysis are soft-spectrum sources or sources with high-energy cut-offs below the PeV range within the Galaxy. The event selection is thus aimed to improve the effective area for neutrino energies below this scale. This is achieved both through the use of AMANDA as an embedded array inside the 40 IceCube strings and through an event selection optimized for a larger acceptance of events below 10 TeV compared to the analysis presented in [11].

The current analysis uses data collected from April 5, 2008 to May 20, 2009. Both parts of the combined IceCube-AMANDA detector operated very stably during this time. For IceCube $\sim$ 375 days of data were collected. AMANDA was decommissioned before the end of the IceCube 40-string data taking period and $\sim$306 days of combined IceCube-AMANDA data were collected . The main causes for detector downtime were scheduled operations in the course of the integration of new strings into the detector.

The dominant class of recorded events are atmospheric muons incident from the atmosphere above the detector. The majority of this background is suppressed by a cut on the reconstructed direction such that only events from the Northern Hemisphere are accepted. Even after this cut, the atmospheric muons dominate over the atmospheric neutrinos by several orders of magnitude as a fraction of atmospheric muons are not well-reconstructed and as such end up as up-going muons. In particular coincidences between two muons from different air showers can mimic up-going events. An event selection is then applied to reduce this background by rejecting events with poor reconstruction quality and/or events with a high probability to be composed of two separate particles. An overview of reconstruction quality estimators and other event parameters that allow to distinguish signal from background is given in [11]. A subset of these parameters is used in this work.

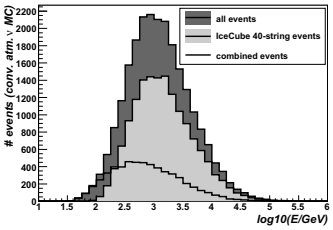

Figure 1: Energy distribution of atmospheric neutrino events in the combined IceCube 40-strings and AMANDA point source sample. Events with AMANDA trigger ("combined events") peak at lower energies than events with IceCube trigger. 90% of the events are contained in a central interval from 130 GeV to 7.5 TeV.

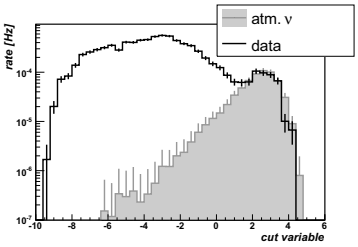

Figure 2: Distribution of the main cut variable for IceCube-triggered events before final cuts are applied. Shown are the data in black and atmospheric neutrino simulation based on the atmospheric neutrino flux model of [6] in gray. The final cut is placed at 1.0 as result of an optimization of the discovery potential [7].

The data collected in 2008/2009 contains events that triggered AMANDA, events that triggered IceCube and events that triggered both detectors. Most analyses performed on the data sample, such as [11], use only the events that triggered IceCube. The approach presented here extracts a neutrino sample from all three kinds of events. Combined IceCube-AMANDA events are selected by different event selection criteria than events that only have an IceCube trigger, as outlined below.

IceCube events without AMANDA trigger are selected by a series of one-dimensional cuts on event quality parameters followed by a multivariate classification based on the Neyman-Pearson rule (see for example [12]). The probability density functions for five quality parameters are generated from atmospheric muon-dominated data as background and from atmospheric neutrino simulation and combined in the cut. The main cut variable is the likelihood ratio between the atmospheric neutrino and the atmospheric muon hypothesis. The distribution of this main cut variable is shown in Figure 2 for data and for atmospheric neutrino simulation. For combined IceCube-AMANDA events, the Neyman-Pearson rule is not applied because a series of a series of one-dimensional cuts resulted in a similar performance for these events.

The energy distribution at the final event selection level is shown in Figure 1. The combined IceCube-AMANDA events peak at lower energies. The angular resolution of the sample depends on the energy of the events. An unbroken E^{-3} power law spectrum has been used to benchmark the performance of the analysis. For this very soft spectrum, a median angular resolution of 1.2° is achieved. From simulation of single and double coincident cosmic-ray air showers with CORSIKA [13], the atmospheric muon contamination of the cleaned data sample used in this analysis is estimated between 2% and 3%.

19797 neutrino candidates are selected from IceCube and AMANDA triggered events. This sample is predominantly background atmospheric neutrinos, which cannot be distinguished from the cosmic neutrino signal on an event-by-event basis [1]. These events are analyzed with the hypothesis tests described in the previous section to search for spatial clustering of events over the uniform atmospheric neutrino background.

5 Results

The results of the galactic plane scan are presented in Figure 3, from which it is seen that all observations are compatible with the background expectation. The largest clustering of events was observed at $(85.5^\circ, -2, 0^\circ)$ with a (pre-trial) probability to observe an equal or stronger excess at this position of 0.0935% due to background fluctuations only. Accounting for the trials introduced by the repetition of the test along the galactic plane, an equivalent or more significant observation is made in 88.02% of randomized data samples. Thus the observed excess in the scan is consistent with fluctuations of background. Also the results for the six γ-ray sources are compatible with the background expectation and preliminary 90% flux upper limits are summarized in Table 1 assuming a power-law with a spectral index of 3. The preliminary limits do not include the systematic uncertainty of the signal efficiency. The strongest preliminary flux limit can be set for Cas A at a flux of $5.9 \cdot 10^{-11}$ TeV^{-1} cm^{-2} s^{-1}. The upper limits are calculated using the approach of Feldman and Cousins [15].

With 55 events observed within the box defined around the most active part of the Cygnus region compared to a background expectation of 60 events, strong flux upper limits could be extracted for this region. Assuming an $E^{-2.6}$ spectrum as was fit to the MILAGRO γ-ray observations [16], a preliminary 90% flux upper limit of $3 \cdot 10^{-11}$ TeV^{-1}cm^{-2}s^{-1} (without systematic uncertainties) is obtained provided the astrophysical signal from the region has an exponential energy cutoff at or above 1 TeV.

1. An exception could be the use of a veto against atmospheric neutrinos as proposed in [14]

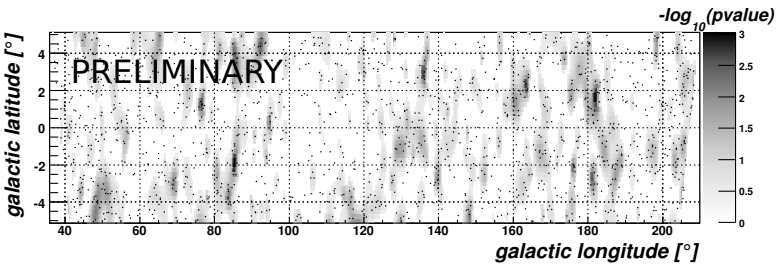

Figure 3: Result of the galactic plane scan using data collected by IceCube 40-strings as a combined detector with AMANDA. The significance of the observation at each grid point is expressed by the (pre-trial) pvalue which is shown together with the distribution of the events shown as black dots. The most significant excess of events is located at $(85.5°, -2, 0°)$ with a (pre-trial) pvalue of 0.000935 (-log10(pvalue)=3.03). The probability to observe a similar or stronger excess of events at any point of the galactic Plane is 88.02%. No neutrino sources have been detected.

	ra	dec	ns	upper limit
Crab	83.63°	22.01°	0	7.3
CasA	350.85°	58.82°	0	5.9
LSI +61 303	40.13°	61.23°	1.6	7.8
SS433	287.94°	4.983°	0	9.7
IC443	94.18°	22.53°	0	7.3
W51	290.82°	14.15°	0.6	8.3

Table 1: Position, best fit number of source events (ns) and **preliminary** 90% upper limits on the flux of muon neutrinos for each of the tested objects in units of 10^{-11} TeV^{-1} cm^{-2} s^{-1}. The upper limits are calculated without systematic uncertainties under the assumption of an E^{-3}-spectrum.

6 Outlook

The installation of the IceCube detector has been completed in 2010 and IceCube is now taking data in its final configuration of 86 strings. The collaboration continues to search for neutrino sources within and outside of the Galaxy. With the substantially larger detector, the sensitivity to galactic neutrino sources will improve significantly with respect to the analysis presented here.

In particular IceCube's observations of the Cygnus region will enter an interesting regime in the next few years. We have shown that the IceCube 40-string/AMANDA limits for the Cygnus region are only a factor of two to three above the expected flux if all of the γ-rays in the region were of hadronic origin. Applying the same test to the data obtained with larger configurations of IceCube, it will thus be possible to either detect neutrino emission in this region or to constrain the hadronic component in the γ-ray emission.

AMANDA has been decommissioned in 2009 and replaced by the DeepCore extension of IceCube. The positioning of a more densely instrumented volume in the deepest and clearest ice around the central IceCube string offers several advantages with respect to AMANDA. In particular, it offers the possibility to use veto techniques that allow the suppression of downgoing atmospheric muons and might open the Southern Hemisphere to neutrino astronomy below several tens of TeV from the South Pole.

References

[1] IceCube collaboration, Astroparticle Physics 20 (2004) 507.
[2] S. R. Kelner, F. A. Aharonian, Physical Review D, 2008, **78**(3): 034013-1 - 034013-16
[3] S. Gabici, F. A. Aharonian, Astrophysical Journal, 2007, **665**(2): L131 - L134
[4] J. Braun et. al., Astroparticle Physics, 2008, **29**(4): 299 - 305
[5] Y. Sestayo, PhD Thesis, Universitaet Heidelberg, 2010
[6] G. D. Barr et. al., Phys. Rev. D, 2004, **70**(2): 023006-1 - 023006-13
[7] G. Hill et. al., Proceedings of PHYSSTAT05, Oxford, UK, 2006, 108-111
[8] AMANDA collaboration, Nature, 2001, **410**: 441-443
[9] AMANDA collaboration, Nuclear Instruments and Methods in Physics Research A, 2006, **556**(1): 169 - 181
[10] A. Gross et. al. for the IceCube collaboration, Proceedings of the 30th International Cosmic Ray Conference, Merida, Mexico, 2007 : 12531256, http://arxiv.org/abs/0711.0353
[11] IceCube collaboration, Astrophysical Journal, 2011, **732**(1): 1 - 16
[12] A. R. Webb, Statistical Pattern Recognition, John Wiley & Sons, Ltd, 2002
[13] D. Heck et. al., Forschungszentrum Karlsruhe Report FZKA, 1998 **6019**)
[14] S. Schoenert et. al., Phys Rev. D, 2009, **79**(4): 043009-1 - 043009-5
[15] G. J Feldman, R. D. Cousins, Phys. Rev. D ,1998, **57**(7): 38733889
[16] A. A. Abdo et. al., Astrophysical Journal, 2007, **658**(1): L33 - L36

32ND INTERNATIONAL COSMIC RAY CONFERENCE, BEIJING 2011

Study of South Pole ice transparency with IceCube flashers

THE ICECUBE COLLABORATION[1]
[1]*See special section in these proceedings*

Abstract: The IceCube observatory, 1 km^3 in size, is now complete with 86 strings deployed in the antarctic ice. IceCube detects the Cherenkov radiation emitted by charged particles passing through or created in the ice. To realize the full potential of the detector the properties of light propagation in the ice in and around the detector must thus be known to the best achievable accuracy. This report presents a new method of fitting the ice model to a data set of in-situ light source events collected with IceCube. The resulting set of derived ice parameters is presented and a comparison of IceCube data with simulation based on the new model is shown.

Corresponding author: Dmitry Chirkin (*dima@icecube.wisc.edu*)
IceCube Reseach Center, University of Wisconsin, Madison, WI 50703, U.S.A.

DOI: 10.7529/ICRC2011/V04/0333

Keywords: IceCube, ice properties, ice transparency, scattering, absorption, photon propagation

1 Introduction

The properties of photon propagation in a transparent medium can be described in terms of the average distance between successive scatters and the average distance to absorption (local scattering and absorption lengths), as well as the angular distribution of the new direction of a photon relative to old at a given scattering point. These details are used in both the simulation and reconstruction of IceCube data, thus they must be known to the best possible accuracy. This work presents a new, *direct fit* approach to determine these ice properties, which is different from the method described in [4]. A global fit is performed to a set of data with in-situ light sources (see Figure 1) covering all depths of the detector, resulting in a single set of scattering and absorption parameters of ice, which describes these data best. Figure 2 shows examples of experimental data used for this analysis.

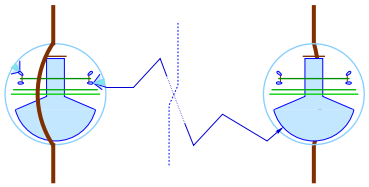

Figure 1: Simplified schematics of the experimental setup: the flashing sensor on the left emits photons, which propagate through ice and are detected by a receiving sensor on the right.

2 Flasher dataset

In 2008, IceCube consisted of 40 strings as shown in Figure 3, each equipped with 60 equally spaced optical sensors, or digital optical modules (DOMs). Each of the DOMs consists of a 10" diameter photomultiplier tube (PMT) [2] and several electronics boards enclosed in a glass container [3]. One of the boards is the "flasher board", which has 6 horizontal and 6 tilted LEDs, each capable of emitting $\sim 7.5 \cdot 10^9$ photons at $\sim 405 \pm 5$ nm in a 62 ns-wide pulse.

The PMT output signal is digitized into "waveforms" using the faster, ATWD, and slower, fADC, sampling chips [1]. The ATWD is configured to collect 128 samples with 3.3 ns sampling rate, and the fADC records 256 samples with 25 ns sampling rate. The DOMs transmit time-stamped digitized PMT signal waveforms to computers at the surface.

In a series of several special-purpose runs, IceCube took data with each of 60 DOMs on string 63 flashing in a sequence. For each of the flashing DOMs at least 250 flasher events were collected and used in this analysis. All 6 horizontal LEDs were used simultaneously at maximum brightness and pulse width settings, creating a pattern of light around string 63 that is approximately azimuthally symmetric.

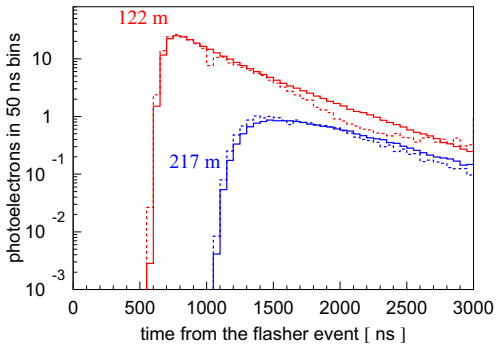

Figure 2: Example photon arrival time distributions at a sensor on one of the nearest strings (122 m away), and on one of the next-to-nearest strings (217 m away). Dashed lines show data and solid lines show simulation based on the model of this work (with best fit parameters). The goal of this work is to find the best-fit ice parameters, which describe these distributions as observed in data simultaneously for all pairs of emitters and receivers.

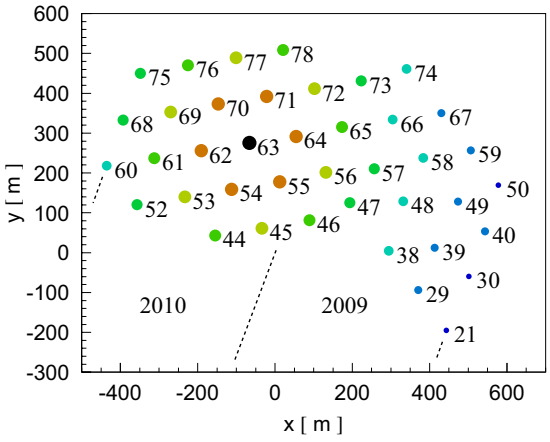

Figure 3: IceCube 40-string configuration as operated in 2008. String 63 (of DOMs that were used as flashers) is shown in black. IceCube parts installed in the following years (2009, 2010 as shown in the figure) lie in regions indicated approximately with dashed lines.

The pulses corresponding to the arriving photons were extracted from the digitized waveforms and binned in 25 ns bins, from 0 to 5000 ns from the start of the flasher pulse (extracted from the special-purpose ATWD channel of the flashing DOM). To reduce the contribution from saturated DOMs (most of which were on string 63 near the flashing DOM) [2] the photon data collected on string 63 was not used in the fit.

3 Ice parametrization

The ice is described by a table of parameters $b_e(405)$, $a(405)$, related to scattering and absorption at a wavelength of 405 nm at different depths. The width of the vertical ice layers (10 m) was chosen to be as small as possible while maintaining at least one receiving DOM in each layer. Coincidentally it is the same as the value chosen in [4].

The geometrical scattering coefficient b determines the average distance between successive scatters (as $1/b$). It is often more convenient to quote the effective scattering coefficient, $b_e = b \cdot (1 - \langle \cos\theta \rangle)$, where θ is the deflection angle at each scatter, $\langle\rangle$ denote the expectation value. The absorption coefficient a determines the average distance traveled by photon before it is absorbed (as $1/a$).

4 Simulation

The detector response to flashing each of the 60 DOMs on string 63 needs to be simulated very quickly, so that simulations based on many different sets of coefficients $b_e(405)$ and $a(405)$ could be compared to the data.

A program called PPC (photon propagation code [7]), was written for this purpose. It propagates photons through ice described by a selected set of parameters $b_e(405)$ and $a(405)$ until they hit a DOM or get absorbed. No special weighting scheme was employed, except that the DOMs were scaled up in size (a factor 5 to 16, depending on the required timing precision), and the number of emitted photons was scaled down by a corresponding factor $(5^2 - 16^2)$.

The probability distribution $f(\theta)$ of the photon scattering angle θ is modeled by a linear combination of two functions commonly used to approximate scattering on impurities:

$$f(\theta) = (1 - f_{\mathsf{SL}}) \cdot \mathsf{HG} + f_{\mathsf{SL}} \cdot \mathsf{SL},$$

where HG is the Henyey-Greenstein function [4]:

$$p(\cos\theta) = \frac{1}{2} \frac{1 - g^2}{[1 + g^2 - 2g \cdot \cos\theta]^{3/2}}, \quad g = \langle \cos\theta \rangle,$$

and SL is the simplified Liu scattering function [8]:

$$p(\cos\theta) \sim (1 + \cos\theta)^{\alpha}, \quad \text{with} \quad \alpha = \frac{2g}{1 - g}.$$

f_{SL} determines the relative fraction of the two scattering functions and it determines the overall shape. Figure 4 compares these two functions with the prediction of the Mie theory with dust concentrations and radii distributions taken as described in [4]. The distributions of photon arrival time are substantially affected by the "shape" parameter f_{SL} (as shown in Figure 5). f_{SL} is also a global free parameter in the fitting procedure.

The value of $g = 0.9$ was used in this work (cf. $g = 0.8$ in [4]). Higher values (as high as ~ 0.94 [4, 6]) are predicted by the Mie scattering theory, however, these result

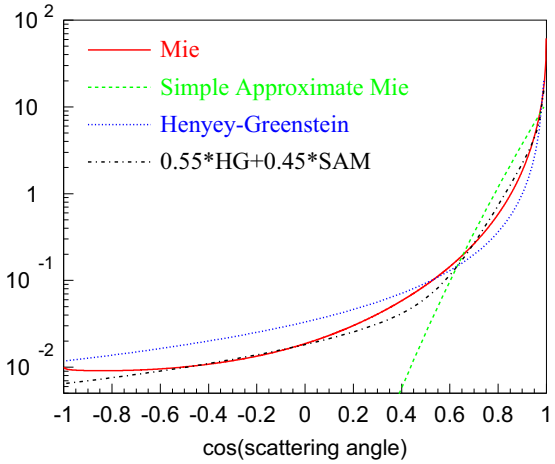

Figure 4: Comparison of the Mie scattering profiles calculated at several depths of the South Pole ice with the Henyey-Greenstein (HG) [4] and simplified Liu (SL) [8] scattering functions, all with the same $g = 0.943$.

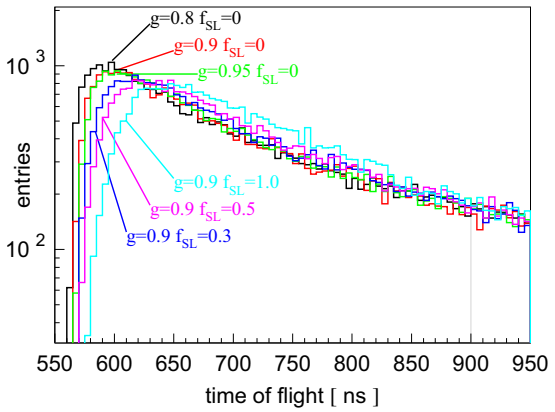

Figure 5: Photon arriving time distributions at a DOM 125 m away from the flasher, simulated for several values of $g = \langle \cos\theta \rangle$ and f_{SL}. The difference in peak position simulated with $g = 0.8$ and $g = 0.9$ is of the same order (~ 10 ns) as that between sets simulated with different values of the shape parameter f_{SL}.

in slower simulation, while yielding values of the effective scattering b_e and absorption a coefficients that change by less than 3% as determined in [4], which could also be concluded from Figure 5.

5 Fitting the flasher data

Data from all pairs of emitter-receiver DOMs (located in the same or different ice layers, altogether $\sim$ 38700 pairs) contributed to the fit of $\sim$ 200 ice parameters (scattering and absorption in 10 m layers at detector depths of 1450 to 2450 m).

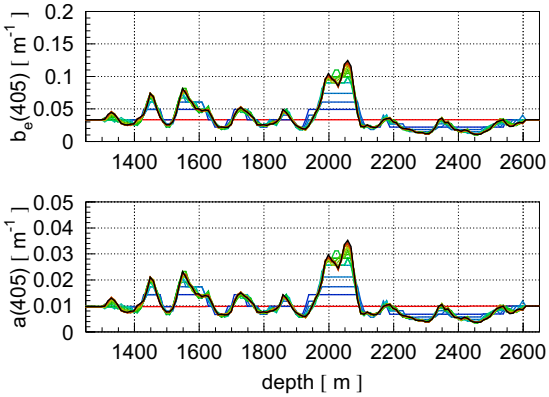

Figure 6: Values of $b_e(405)$ and $a(405)$ vs. depth for subsequent steps of the minimizer. The "converged" black curve shows fitted values after the last of the 20 steps of the minimizer.

The photon counts $d(t_i)$ and $s(t_i)$ observed in time bins in n_d data and n_s simulated flasher events are compared to each other using a likelihood function

$$\mathcal{L} = \prod \frac{(\mu_s n_s)^s}{s!} e^{-\mu_s n_s} \cdot \frac{(\mu_d n_d)^d}{d!} e^{-\mu_d n_d} \cdot \frac{1}{\sqrt{2\pi}\sigma} \exp \frac{-(\log \mu_d - \log \mu_s)^2}{2\sigma^2} \cdot R.$$

The product is over all emitters and all time bins of receivers. $\mu_d(t_i)$ and $\mu_s(t_i)$ are the expected values of photon counts per event in data and simulation, and are determined by maximizing $\mathcal{L}$ with respect to these. The first two terms in the product are the Poisson probabilities, and the third term describes the systematic uncertainties inherent in the simulation. The last term R represents regularization constraints of the solution values with depth and with each other.

Starting with the homogeneous ice described with $b_e(405) = 0.042$ m^{-1} and $a(405) = 8.0$ km^{-1} (average of [4] at detector depths) the maximum of $\mathcal{L}$ is found in $\sim$ 20 steps. At each iteration step the values of $b_e(405)$ and $a(405)$ are varied in consecutive ice layers, one layer at a time. Five flashing DOMs closest to the layer, which properties are varied, are used to estimate the variation of the $\mathcal{L}$. Figure 6 shows ice properties after each of 20 steps of the minimizer. The general agreement of the model and data is good as shown in Figure 2.

6 Dust logger data

Several dust loggers [5] were used during the deployment of seven of the IceCube strings to result in a survey of the structure of ice dust layers with extreme detail (with the effective resolution of $\sim$ 2 millimeters). These were then matched up across the detector to result in a *tilt map* of the

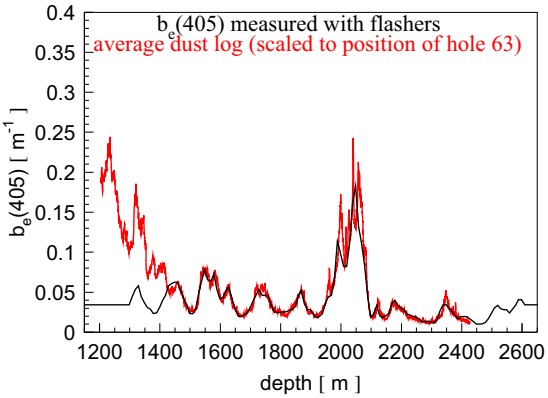

Figure 7: Comparison of the average dust log with the effective scattering coefficient $b_e(405)$ measured with the flasher data.

South Pole ice, as well as a high-detail *average dust log*, a record of a quantity proportional to the dust concentration vs. depth. Additionally, the EDML (East Dronning Maud Land, see [5]) ice core data was used to extend the dust record to below the lowest dust-logger-acquired point.

The correlation between the effective scattering coefficient measured with the IceCube flasher data and the average dust log (scaled to the location of string 63) is excellent, as shown in Figure 7. Within the depth range 1450 m - 2450 m instrumented with DOMs all major features match, have the right rise and falloff behavior, and are of the same magnitude. Some minor features are washed out in the flasher measurement.

Having established the correlation with the average dust log, the EDML-extended version of the log was used to build an initial approximation to the fitting algorithm described in the previous section. This resulted in a solution that is determined by the scaled values of the extended log (instead of by the somewhat arbitrary values of the initial homogeneous ice approximation) in the regions where the flasher fitting method has no resolving power, i.e., above and below the detector.

7 Results

The effective scattering and absorption parameters of ice measured in this work are shown in Figure 8 with the $\pm 10\%$ gray band corresponding to $\pm 1\sigma$ uncertainty at most depths. The uncertainty grows beyond the shown band at depths above and below the detector. The value of the scattering function parameter $f_{\mathrm{SL}} = 0.45$ was also determined.

Figure 8 also shows the AHA (Additionally Heterogeneous Absorption) model, which is based on the ice description of [4] extrapolated to cover the range of depths of IceCube and updated with a procedure enhancing the depth structure of the ice layers.

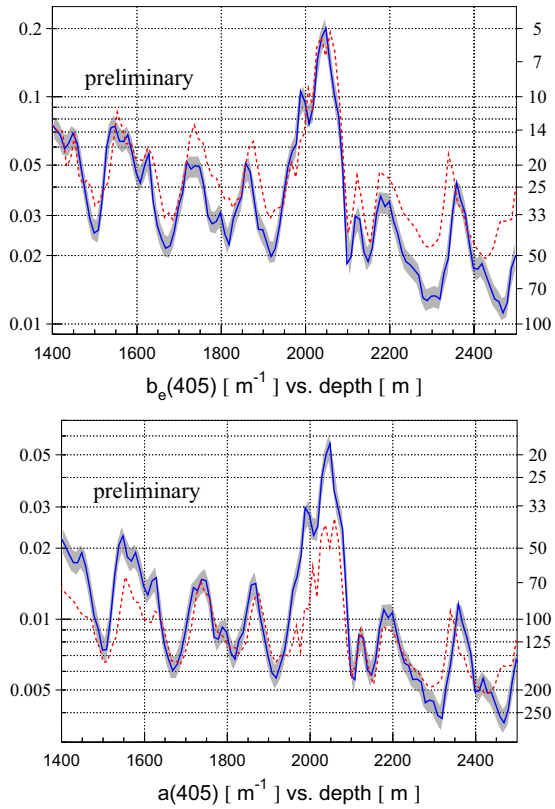

Figure 8: Values of $b_e(405)$ and $a(405)$ vs. depth for converged solution shown with solid lines. The updated model of [4] (AHA) is shown with dashed lines. The uncertainties of the AHA model at the AMANDA depths of 1730 ± 225 m are $\sim 5\%$ in b_e and $\sim 14\%$ in a. The scale and numbers to the right of each plot indicate the corresponding effective scattering $1/b_e$ and absorption $1/a$ lengths in meters.

References

[1] R. Abbasi et al., Nucl. Instrum. Methods A, 2009, **601**: 294-316.
[2] R. Abbasi et al., Nucl. Instrum. Methods A, 2010, **618**: 139-152.
[3] A. Achterberg et al., Astropart. Physics, 2006, **26**: 155.
[4] M. Ackermann et al., J. Geophys. Res., 2006, **111**: D13203.
[5] R. C. Bay et al., J. Geophys. Res., 2010, **115**: D14126.
[6] D. Chirkin., 2002, Mie scattering code and plots: http://icecube.wisc.edu/~dima/work/ICESCA.
[7] D. Chirkin., 2010, photon propagation code: http://icecube.wisc.edu/~dima/work/WISC/ppc.
[8] Pingyu Liu., Phys. Med. Biol., 1994, **39**: 1025.

32ND INTERNATIONAL COSMIC RAY CONFERENCE, BEIJING 2011

Neutrino triggered high-energy gamma-ray follow-up with IceCube

THE ICECUBE COLLABORATION[1]
[1]*See special section in these proceedings*

Abstract: We present the status of a program for the generation of online alerts issued by IceCube for gamma-ray follow-up observations by Air Shower Cherenkov telescopes (e.g. MAGIC). To overcome the low probability of simultaneous observations of flares of objects with gamma-ray and neutrino telescopes a neutrino triggered follow-up scheme is developed. This mode of operation aims at increasing the availability of simultaneous multi-messenger data which can increase the discovery potential and constrain the phenomenological interpretation of the high energy emission of selected source classes (e.g. blazars). This requires a fast and stable online analysis of potential neutrino signals. We present the work on a significance based alert scheme for a list of phenomenologically selected sources. To monitor the detector and the alert system reliability, monitoring systems have been implemented on different levels. We show data from the first weeks of running this system.
Corresponding authors: Robert Franke[2] (*robert.franke@desy.de*), Elisa Bernardini[2] (*elisa.bernardini@desy.de*)
[2]*DESY Zeuthen, 15738 Zeuthen, Germany* DOI: 10.7529/ICRC2011/V04/0334

Keywords: IceCube, neutrino, NToO, blazars

1 Introduction

The major aim of neutrino astrophysics is to contribute to the understanding of the origin of high energy cosmic rays. A point-like neutrino signal of cosmic origin would be an unambiguous signature of hadronic processes, unlike γ-rays which can also be created in leptonic processes. The detection of cosmic neutrinos is however very challenging because of their small interaction cross-section and because of a large background of atmospheric neutrinos. Parallel measurements using neutrino and electromagnetic observations (the so-called "multi-messenger" approach) can increase the chance to discover the first neutrino signals by reducing the trial factor penalty arising from observation of multiple sky regions and over different time periods. In a longer term perspective, the multi-messenger approach also aims at providing a scheme for a phenomenological interpretation of the first possible detections.

The search of occasional flares with a high-energy neutrino telescope is motivated by the high variability which characterizes the electromagnetic emission of many neutrino candidate sources. Recent results obtained by the IceCube Collaboration [1] indicate that high-energy neutrino telescopes have reached a sensitivity to neutrino fluxes comparable to the observed high energy gamma-ray fluxes of Blazars in the brightest states (e.g. the flares of Markarian 501 in 1997 [2] and Markarian 421 in 2000/2001 [3]). With the assumption that the possibly associated neutrino emission would be characterized by a flux enhancement comparable to what is observed in gamma-rays in such states, neutrino flares could be extracted from the sample of neutrino-like events with a reasonable significance.

These astrophysical neutrinos can be searched for in several ways. Here we present a methods for a neutrino point source search that looks for events coming from a restricted angular region, which could be identified with a known astrophysical object. Finding neutrino point sources in the sky means to locate an excess of events from a particular direction over the background of cosmic-ray induced atmospheric neutrinos and muons. These events might present additional features that distinguish them from background, for example a different energy spectrum or time structure. For sources which manifest large time variations in the emitted electromagnetic radiation, the signal-to-noise ratio can be increased by searching for periods of enhanced neutrino emission (a time-dependent search). Of special interest is the relation of these periods of enhanced neutrino emission with periods of strong high-energy γ-ray emission. However, as Imaging Air Cherenkov Telescopes (IACTs) have a small field-of-view and are not continuously operated such correlation studies are not always possible to do after the fact. Therefore it is desirable to ensure the availability of simultaneous neutrino and high-energy γ-ray data for periods of interests. This is achieved by an online neutrino flare search that alerts a partner IACT ex-

periment when a possible neutrino flare from a monitored source is detected.

Such a Neutrino Triggered Target of Opportunity program (NToO) using a list of pre-defined sources was developed already in 2006 using the AMANDA array to initiate quasi-simultaneous gamma-ray follow-up observations by MAGIC [4]. We present here a refined and enhanced implementation using the IceCube neutrino detector.

IceCube is a one cubic kilometer neutrino detector operating in the glacial ice at the geographical South Pole. It consists of 86 strings equipped with 5160 digital optical modules (DOMs). Each DOM contains a photomultiplier tube to detect Cherenkov light of charged ultra-relativistic particles.

2 Neutrino event selection

The basis for the neutrino event selection is an on-line filter that searches for high-quality muon tracks. The full-sky rate of this filter is about 35 Hz for IceCube in its 2010/2011 configuration with 79 deployed strings. This rate is strongly dominated by atmospheric muons. As the computing resources at the South Pole are limited one can not run more elaborate reconstructions at this rate, so a further event selection has to be done. This so called Online Level2 filter selects events that were reconstructed as upgoing ($\theta > 80°$, $\theta = 0°$ equals vertically down-going tracks) with a simple likelihood reconstruction that only takes into account the arrival time of the first photon at each Digital Optical Module. By requiring a good reconstruction quality the background of misreconstructed atmospheric muons is reduced. The parameters used to assess the track quality are the likelihood of the track reconstruction, the number of unscattered photons with a small time residual w.r.t. the Cherenkov cone and the distribution of these photons along the track. The reduced event rate of approximately 3.6 Hz can then be reconstructed with more time intensive reconstructions, like a likelihood fit seeded with different tracks (iterative fit) and a likelihood-fit that takes into account the total number of photo-electrons registered in each module (multi-photoelectron fit). Based on this reconstruction the final event sample is selected by employing a zenith angle cut of $\theta > 90°$ for the multi-photoelectron fit and further event quality cuts based on this reconstruction. These cuts are optimized to achieve a good sensitivity for flares of different time durations. The event selection results in a median angular resolution of $0.48\,°$ for an E^{-2} signal neutrino spectrum, the median resolution for events with $E > 10^6$ GeV is $< 0.4\,°$. For each event an angular uncertainty estimate is calculated.

The resulting event rate compared to the rate of atmospheric neutrinos as predicted by Monte Carlo as a function of zenith angle can be seen in Figure 1.

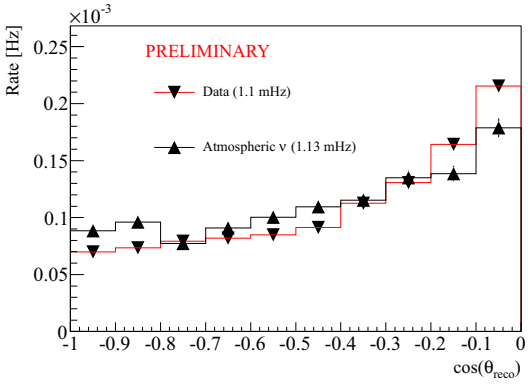

Figure 1: Comparison of the rate of selected events to the predicted rate of atmospheric neutrinos based on Monte-Carlo for IceCube in its 2010/2011 configuration with 79 deployed strings. The atmospheric neutrino prediction is based on the Bartol conventional flux model and the Naumov prompt flux model.

3 The time-clustering algorithm

The timescale of a neutrino flare is not fixed a-priori and thus a simple rolling time window approach is not adequate to detect flares. The time clustering approach that was developed for an unbiased neutrino flare search [6] looks for any time frame with a significant deviation of the number of detected neutrinos from the expected background. The simplest implementation uses a binned approach where neutrino candidates within a fixed bin around a source are regarded as possible signal events. To exploit the information that can be extracted from the estimated reconstruction error and other event properties like the energy an unbinned maximum-likelihood method is under development.

If a neutrino candidate is detected at time t_i around a source candidate the expected background $N_{\mathrm{bck}}^{i,j}$ is calculated for all other neutrino candidates j with $t_j < t_i$ from that source candidate. To calculate $N_{\mathrm{bck}}^{i,j}$ the detector efficiency as a function of the azimuth angle and the uptime has to be taken into account. The probability to observe the multiplet (i, j) by chance is then calculated according to:

$$\sum_{k=N_{\mathrm{obs}}^{i,j}-1}^{\infty} \frac{(N_{\mathrm{bck}}^{i,j})^k}{k!} e^{-N_{\mathrm{bck}}^{i,j}} \qquad (1)$$

where N_{obs} is the number of detected on-source neutrinos between t_j and t_i. It has to be reduced by 1 to take into account the bias introduced by the fact that one only does this calculation when a signal candidate is detected. As typical flares in high energy gamma-rays have a maximal duration of several days we constrain our search for time clusters of neutrinos to 21 days.

If the cluster with the highest significance exceeds a certain threshold (e.g. corresponding to $3\,\sigma$) the detector stability

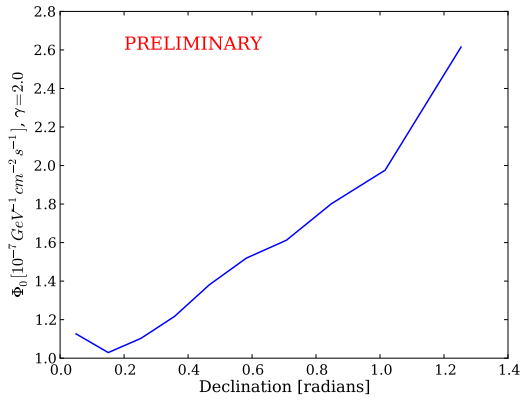

Figure 2: Neutrino flux needed from a given source declination to trigger a flare with a significance of $3\,\sigma$ with a probability of 50%. The neutrino spectrum is assumed to be an unbroken power law with a spectral index of -2.

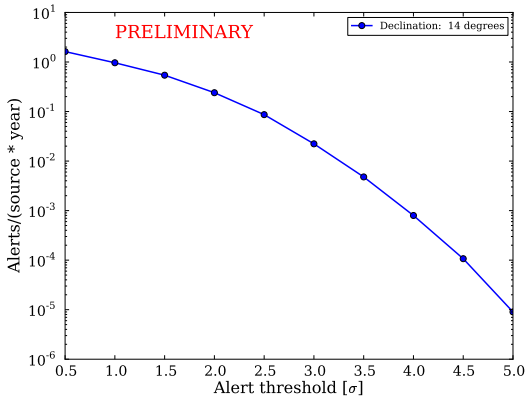

Figure 3: Expected number of accidental background alerts per year for a source at a declination of $14°$ as a function of the alert threshold expressed in units of standard deviations corresponding to a one-sided p-value.

will be checked and an alert will be sent to a Cherenkov telescope to initiate a follow-up observation. Figure 2 shows the flux needed as a function of declination for a neutrino spectrum with a spectral index of -2 to trigger a flare with a significance of $3\,\sigma$ with a probability of $50\,\%$.

To not overwhelm the partner experiment with follow-up requests one has to know the number of accidental background alerts caused by atmospheric neutrinos. This is shown in Figure 3 as a function of the alert threshold.

4 Stability monitoring

Data quality is very important for any online alert program to minimize the rate of false alerts due to detector or data aquisition (DAQ) instabilities. IceCube has a very extensive monitoring of the DAQ system and South Pole on-line processing. However, most of the information is only available with a certain delay after data-taking and thus not useful for a follow-up program which requires fast alerts. To ensure that alerts are triggered by neutrino multiplets that were detected during stable running conditions a simple but powerful stability monitoring scheme has been developed. It is based on a continuous measurement of the relevant trigger and filter rates in time bins of 10 minutes. These rates are inserted into an SQL database at the South Pole and are generally accessible a few minutes after the respective time bin ended. The rates and ratios of rates relevant for the selection of good quality neutrino-induced muon tracks are compared to an exponential running average of these rates to detect significant deviations. The running average is necessary as slow seasonal changes in the atmosphere and faster weather changes influence the rate of atmospheric muons which dominate the Level-2 rate. This system was tested off-line on data from IceCube in its 59-string configuration and proved to correlate very well with the extensive off-line detector monitoring. The fraction of data that has to be discarded because it was flagged as bad by this method was about $1.6\,\%$.

To generate a sufficient number of alerts to monitor the alert generation and forwarding itself we add 2000 so-called monitoring sources to the sourcelist (see Section 5). They are randomly distributed over the northern sky. To guarantee blindness for these sky locations the alerts for the monitoring sources are generated from blinded data events. The blindness is achieved by using the previous event time in the transformation from detector to sky coordinates for the current event instead of its own time. Due to the low event rate on the order of 10^{-3} Hz this results in a sufficient random shift of the event right ascension.

5 Sources

For a test run of this program we used selection criteria based on FERMI measurements [5]. For the galactic sources we choose sources that were observed in TeV and had a FERMI variability index > 15. Blazars were chosen according to the following criteria:

- Redshift < 0.6
- Fermi variability index > 15
- Spectral index as observed with FERMI < 2.4 (BL Lacs only)
- FERMI flux $1 - 100$ GeV $> 1 \cdot 10^{-9}$ph cm^{-2} s^{-1} (BL Lacs only)
- FERMI flux $0.1 - 1$ GeV $> 0.7 \cdot 10^{-7}$ph cm^{-2} s^{-1} (FSRQs only)

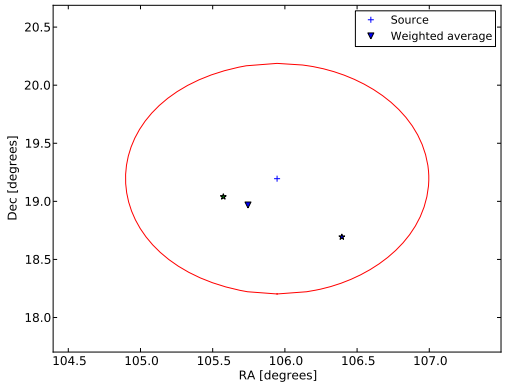

Figure 4: Angular distribution of events (star symbols) for one of the alerts that were generated during a test run of this follow-up program from March, 21st 2011 till May, 13th 2011 (see Section 7). The events contributing to this alert were blinded using the procedure described in this paper. The weighted average of the contributing events is calculated using an event-by-event angular resolution estimator. The circle indicates the size of the on-source bin.

These criteria are motivated by a compilation of different hadronic models that provide the guidelines to identify the most promising neutrino candidate sources. 22 sources (one galactic source, three FSRQs and 18 BL Lac objects) were selected according to these criteria in the northern hemisphere ($\delta > 0$).

6 Technical design of the alert system

After the alerts for this follow-up program are generated at the South Pole they are sent to the University of Wisconsin via the Iridium satellite communication system. This low bandwidth connection allows to send short messages from the South Pole without any significant delay. Once the message arrives in the North it is checked to see whether it represents a real alert or a test alert from a monitoring source. If it is a real alert, the alert is forwarded to the partner experiment. Depending on the technical setup this can happen e.g. via email or a dedicated socket connection.

All alerts (real and test) are filled into a database and a monitoring web page is updated. Each alert can be reviewed and basic information like the coordinates of the contributing events can be inspected. This allows a fast human inspection of alerts, even before the full IceCube event data arrives in the North. For each generated alert the time and space distribution of the contributing events can be inspected (see Figure 4). Furthermore global properties of the alerts, like their rate, significance and time length distribution are plotted and monitored.

The total time delay between the time the (latest) neutrino event is detected by IceCube and the moment it is forwarded to the partner experiment is on the order of several minutes ($\sim$ 10 min). This time is dominated by the delay until the detector rate is available in the database and the event processing time in the South Pole system.

7 Testrun results and Outlook

The system described here was tested online with the IceCube 79-string configuration from March, 21st 2011 till May, 13th 2011. During the test run neutrino triggers were generated online but not forwarded to any IACT. 199 alerts were generated during this test run for all sources combined, including the monitoring sources, while 219 where expected for a 52 day period. Besides statistical fluctuations, part of the discrepancy is also due to the limited event history available during the first days of running the program.

We plan to run this neutrino triggered high-energy gamma follow-up program using IceCube in its final 86-string configuration. Several enhancements are possible and planned. A maximum-likelihood based significance calculation taking into account an event-by-event angular reconstruction uncertainty estimation and an energy estimation of the event will further improve the sensitivity to neutrino flares.

References

[1] J.L. Bazo Alba *et al.* for the IceCube Collaboration, Proc. 31st ICRC, 2009, arXiv:0908.4209
[2] F. Aharonian *et al.* , A&A, 1999, **349**: 11-28
[3] F. Aharonian *et al.* , A&A, 2002, **393**: 89-99
[4] M. Ackermann *et al.* , Proc. 29th ICRC, 2005, arXiv:astro-ph/0509330.
[5] The Fermi LAT Collaboration, Astrophys.J.Suppl., 2009, **183**: 46-66
[6] K. Satalecka *et al.* for the IceCube collaboration, Proc. 30th ICRC, 2007

32ND INTERNATIONAL COSMIC RAY CONFERENCE, BEIJING 2011

Ross Ice Shelf Thickness, Radio-frequency Attenuation and Reflectivity: Implications for the ARIANNA UHE Neutrino Detector

JORDAN C. HANSON[1], FOR THE ARIANNA COLLABORATION
[1]*Department of Physics and Astronomy, University of California at Irvine, Irvine, CA 92697*
jchanson@uci.edu
DOI: 10.7529/ICRC2011/V04/0340

Abstract: The ARIANNA high energy neutrino detector is planned to be deployed on the surface of the Ross Ice Shelf to search for astrophysical neutrinos. Collisions with nuclei in the ice generate showers of particles that emit short pulses of radiation, created by the Askaryan mechanism, in the frequency range of 100 MHz to 1 GHz. The ARIANNA site is located about 65 miles from McMurdo Station, the main hub of US Antarctic operations, and is protected from ambient RF interference by a geologic formation known as Minna Bluff. In this work, we report preliminary results for the frequency interval 90-180 MHz from site studies of the field attenuation length (averaged over depth), and reflection and polarization properties of the saltwater-ice boundary.

Keywords: ARIANNA, Antarctica, GZK, neutrino astronomy, Ross Ice Shelf, attenuation length

1 Introduction

The Antarctic Ross Ice Shelf Antenna Neutrino Array (ARIANNA) is designed to detect ultra-high energy (UHE) cosmogenic neutrinos, via the Askaryan effect [1, 2, 3, 4, 5]. When a neutrino interacts in bulk matter with an index of refraction, the resulting hadronic and electromagnetic cascades can produce coherent GHz radiofrequency (RF) pulses. High energy scattering processes and positron anihilation cause a negative charge excess to build up in the cascades, creating an effective radiating dipole moment. This radiation is coherent, since the coherent radiated power from Chernekov radiation scales quadratically with the charge of the emitter [6], and the wavelengths are set by the lateral size of the shower initiated by the original neutrino interaction. Simulation studies show that the signal pulses from high energy neutrinos usually arrive at ARIANNA surface receivers by first reflecting from the ice-water interface at the bottom of the Ross Ice Shelf (RIS), and then propagating through the bulk ice [7]. Relatively few neutrino signals propagate directly from the interaction vertex to the surface receivers. Therefore, the sensitivity and capabilities of ARIANNA depends on the ice properties such as the attenuation length and reflection efficiency. In this work, we report on several key properties of the ARIANNA site.

The ARIANNA detector consists of an array of autonomous stations deployed on the surface of the RIS, viewing 513 km^3 of glacial ice centered at (77° 44' 523" S, 165° 02' 414" E) in western Antarctica. Prior studies of the electromagnetic properties of the ARIANNA site have measured the electric field attenuation length by using vertically reflected pulses and assumed a value for the reflection coefficient from the ice-water boundary at the bottom [11]. In this work, we examine reflected pulses over several baselines to determine both the field attenuation length and reflection coefficient. We also show that the reflected pulse preserves its polarization orientation. Measurements of the reflection coefficient have been made independently [8, 9], revealing strongly reflected RF pulses in regions free of sub-glacial flow lines and sea-ice freezing zones. ARIANNA is in Moore's Bay, which is far from glacial irregularities [8] and in good RF isolation. For a similar study of attenuation lengths performed in ice located in a different region of Antarctica, see Besson (2008) [10].

We quantify absorptive losses experienced by an electromagnetic wave by adding an imaginary component to the dielectric constant, parameterized by

$$\alpha = -8.686(\pi\nu/c)(\sqrt{\epsilon'}tan\ \delta) \ \ (\mathrm{dB/m}) \qquad (1)$$

Here, the vacuum speed of light is c, ν is the frequency in Hz, ϵ' is the real part of the dielectric and the loss tangent tan δ is the imaginary part of the dielectric over the real part ϵ''/ϵ'. The electric field attenuation length is then defined as [11]

$$L_\alpha = 1/\ln\sqrt{10^{\alpha/10}} \qquad (2)$$

which is the distance the electromagnetic wave travels before decreasing in amplitude by a factor e^{-1}.

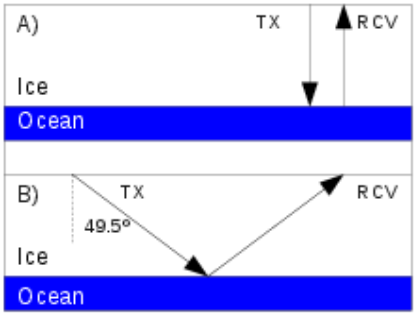

Figure 1: A) A schematic of the direct bounce experimental geometry. B) The angled bounce experimental geometry.

2 Experimental Methods

To create broad band RF pulses for propagation through the ice shelf, a short duration (1 ns wide), kilovolt pulse is delivered from the HYPS Pockel Cell Driver to a log-periodic dipole array (LPDA) transmitter (105 MHz-1300 MHz), supplied by Creative Design Corp (CLP5130-2). These antennas are directional, with a gain of 6-7 dBi. An identical LPDA serves as a receiver. Along with a precise measurement of the ice-shelf depth at the ARIANNA site, we have the S11 and voltage standing wave ratio (VSWR) parameters for the antennas as they couple to the dielectic properties of the snow around them [5]. The lowest frequency measurable by the LPDA in snow decreases to approximately 80 MHz because the wave speed slows down in the snow, while the antenna response remains constant. The VSWR is close to one for all relevant frequencies in this work. The signal from the receiver is filtered with both a NHP-50+ highpass filter and a NLP-1200+ lowpass filter, and amplified by a 1 GHz Miteq AM-1660 low-noise amp before being recorded on a Tektronix oscilloscope with 1 GHz bandwidth. We also attenuate by 20 dB where appropriate to obtain manageable signal amplitudes.

Figure 1 shows two distinct reflection geometries employed in these studies for the antennas, both of which are buried in the low density firn snow and pointed down. The direct bounce configuration (1a) is indicated by the vertical path between the transmitter and receiver antennas, which are separated by 18.7 m. The radio pulse travels 576 m to the water-ice interface and reflected back to the surface for a total path length of 1152 m. The angled bounce configuration (1b) is similar to the direct bounce, where the are antennas oriented vertically downward, but the separation between the two antennas is increased to 977 m, which increases the total path length to 1510 m (see Table 1). The unattenuated signal amplitude is determined by rotating the LPDA antennas to point toward each other through the surface snow while separated by 18.7 m. The path length for this test is the shortest of the three configurations. In practice, R, G, and the exponential factor are set to 1 in eqn. (4). Since the signal in this test is relatively strong, the amplifier is removed for this measurement.

The analysis presented here focuses on the frequency range between 90 MHz and 180 MHz, where the measured power was well above thermal noise for the three configurations. It assumes that losses due to RF scattering in the ice medium are negligible for the frequencies of interest, and that the field reflection coefficient does not depend significantly on incidence angle of the two reflection configurations. We verified with a noise source that cable losses are negigible at these frequencies.

The Friis equation relates the power received (P_r) to the transmitted power (P_t) in a lossless medium at a given wavelength. For two identical antennas, separated by a distance d, it becomes

$$P_r = \frac{G_a^2 \lambda^2}{(4\pi)^2 d^2} = \frac{P_0}{d^2} \tag{3}$$

where G_a is the intrinsic gain of the antenna and λ is the electromagnetic wavelength. The factor P_0 can be treated as a constant at each frequency for all configurations since the variation in LPDA intrinsic gain is small for the frequency interval of this study. P_0 was determined from the short distance configuration with the antennas rotated to point toward each other. To account for absorption losses and possible losses upon reflection, the Friis equation is modified to

$$P_r = \frac{P_0 R G^2}{d^2} \exp\left(-2\frac{d}{\langle L_\alpha \rangle}\right) \tag{4}$$

The factor R is the reflection coefficient, defined for power. The factor of 2 is required in the exponential if $\langle L_\alpha \rangle$ is the electric field attenuation length, rather than a quantity associated with the power. The brackets around $\langle L_\alpha \rangle$ indicate that the attenuation length is averaged over the full depth of the ice, and thereby integrated over the temperature dependence of the path[1]. Following convention, the reflection coefficient for the electric field is then $R^{1/2}$. The factor G^2 accounts for the difference in relative antenna gain for each antenna. G is 1 for the direct bounce, where the returned signal is aligned along the receiver boresight. The orientation of the antennas remained vertical for the angled bounce configuration, so the signal pulses were emitted and received at an angle of 49.5°. At this angle in the H-plane of the antennas, G = 0.80.

1. This temperature dependence arises from the modest temperature dependence of the imaginary part of the dielectric constant of bulk ice, which is roughly one part in a thousand.

Year/site	Delay (ns)	Depth (m)
2006 [11]	6783 ± 10	577.5 ± 10
2009 [12]	6745 ± 15	572 ± 6
2010 [this work]	6772 ± 15	576 ± 10

Table 1: The result from this work was produced using the same $n(z)$ model as the result in the first row. The larger final uncertainties come from using slightly larger uncertainties on the index of refraction of bulk ice.

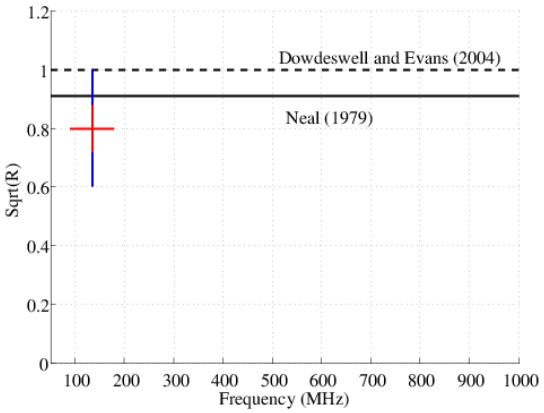

Figure 2: Expected field reflection coefficient $R^{1/2}$ vs. frequency, for an ideal flat surface. The longest vertical error bar indicates 95% confidence. The horizontal error bar indicates the range of frequencies used in this analysis.

3 Data and Analysis

3.1 Depth of the Ice Shelf

The thickness of the ice at the ARIANNA site can be determined by the round-trip travel time and knowledge of the index of refraction, $n(z)$, as a function of depth. For depths greater than 65-75 m, the ice is uniform with $n = 1.78$. At shallower depths, the mass density of the firn is characterized with an exponential dependence [11]. Along with the linear dependence between index of refraction and mass density, we have a complete description of $n(z)$ in the firn ice. Table 1 summarizes the calculations of ice thickness at the ARIANNA site. The 2009 and 2010 measurements were performed at the same geographical location on the ice shelf, whereas the 2006 measurement was performed at a location about 1 km from the 2009 and 2010 tests. The round trip travel times agree to within two standard deviations. The uncertainties in the depth measurements include statistical errors in the round trip travel time and index of refraction in the uniform ice, and systematic errors due to the functional variation of $n(z)$. The larger errors associated with the 2006 and 2010 depths are due to slightly larger uncertainties for the index of refraction in the bulk ice.

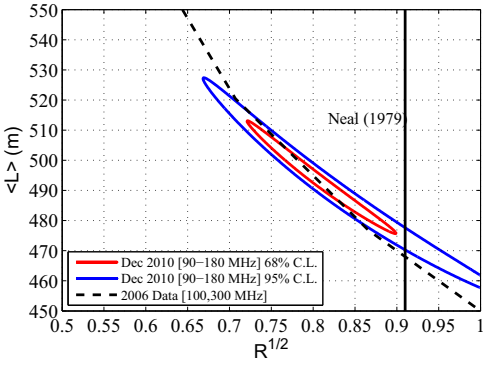

Figure 3: Contour plot of the depth averaged attenuation length $\langle L_\alpha \rangle$ in (m) vs. $R^{1/2}$ showing 1 and 2-σ errors. Dashed curve was obtained from [11], as explained in the text. Vertical line indicates theoretical expectation of $R^{1/2}$ = 0.91 from [9].

3.2 Attenuation Length, Reflectivity and Signal Polarization

After correcting for the geometrical effects of path length for the three different configurations and relative antenna gain, the field reflection coefficient $R^{1/2}$ and $\langle L_\alpha \rangle$ are treated as free parameters in eqn. (4). The statistical errors in P_r were obtained from the rms fluctuation over the entire frequency band. The 1 and 2-σ contours in figure 3 were obtained from a reduced chi-squared fit. The contours match the dashed curve, which was derived by varying the reflection coefficent $R^{1/2}$ assumed in [11] for the quoted attenuation lengths at 100 and 300 MHz. The attenuation length is determined to be 495 ± 15 m at 68 % C.L., in agreement with previous values from 2006 [11], and the field reflection coefficient $R^{1/2} = 0.80 \pm 0.08$ at 68% C.L., in agreement with a theoretical expectation ($R^{1/2}$ = 0.91) for an ideal ice-saltwater interface [9].

Our measurements indicate that the field reflection coefficient at the ARIANNA site is compatible with an ideal flat surface, although values as small as 0.7 are also permitted. The reflection coefficient is not expected to vary significantly with frequency for specular reflection, as shown in figure 2. If the permittivity of sea-water is assumed to be very large for 100-1000 MHz, then the field reflection coefficient is 1 with no frequency dependence (the upper horizontal line in figure 2) [12]. In addition, muli-path effects are safely ignored in this analysis because the maximum duration of our signal pulses (100 ns) is small compared to the total propagation time.

The radio pulse from the neutrino interaction is perfectly linearly polarized, with the orientation perpendicular to the direction of the propagation of the pulse. It lies in the plane defined by the neutrino direction vector and propagation vector. Therefore, the polarization information helps to determine the direction of the neutrino, and reflected signals must retain a known correlation with the intial polarization.

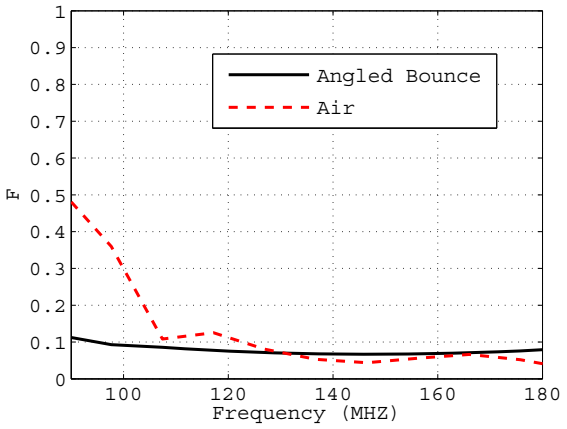

Figure 4: Polarization fraction, F, is shown as a function of frequency for transmission through air (dashed line) and for the angled bounce configuration at the ARIANNA site (solid line).

We investigate this by compariing the co-polarized power, $P_{||}$, to the cross-polarized power, $P_{\perp}$ for the angled bounce configuration. The fraction of cross-polarized power to total power is

$$F = \frac{P_{\perp}}{P_{||} + P_{\perp}} \quad (5)$$

Figure 4 compares F for the angled bounce configuration (solid curve) to a study performed in air (dashed curve). Due to imperfections in the LPDA antennas, some power will leak into the cross-polarized configuration, representing a lower limit to F. This is estimated by air measurements with the LPDA antennas oriented to point toward each other, and separated by 10 m to avoid near-field effects. The sudden rise to a value of 0.5 (the value of F for unpolarized noise) at frequencies below 105 MHz is due to the antenna response. In air, the VSWR of the LPDA increases dramatically below 105 MHz, whereas the VSWR for LPDAs buried in snow remains low down to 80 MHz [5]. The good agreement between the angled bounce configuration and the air studies suggests that little power is transferred from the co-polarized direction to the cross polarized direction after reflection from the water-ice boundary.

4 Conclusion

Preliminary studies of the site properties in the frequency band 90-180 MHz confirm large field attenuation lengths (495 $\pm$ 15 m), and show that the reflection coefficient is compatible with theoretical expectations for a smooth saltwater-ice interface ($R^{1/2} = 0.80 \pm 0.08$), and signal polarization is preserved. Further work is required over multiple baselines to distinguish the smooth water-ice hypothesis from potential small losses due to surface roughness at the ARIANNA site. We note that Neal [9] reported very small levels of surface roughness at sites in the RIS characterized by large reflection coefficients at 60 MHz. Such small effects will have little, if any, impact on signal attenuation and time profiles if similar values for vertical rms fluctuations from flatness and horizontal correlation lengths are found at higher frequencies.

5 Acknowledgements

This work was supported by the U.S. NSF Office of Polar Programs and the U.S. NSF Physics Division, award numbers 0839133 and 0970175, and by the Dept. of Energy under contract DE-AC-76SF-00098. We also thank the dedicated staff of Raytheon Polar Services for their logistical support of the ARIANNA program.

References

[1] Askaryan,G., Soviet Physics JETP, 1962, **14**: 441-442
[2] Barwick,S. (ARIANNA Collab.), J. Phys.: Conf. Ser., 2007, **60**: 276-283
[3] Hoffman, K. *et al.* (ARA Collab.) J. Phys.: Conf. Ser., 2007, **81**(1): 012022
[4] Gorham, P. *et al.* (ANITA Collab.), Phys. Rev. D, 2010 **82**: 022004
[5] Gerhardt, L. *et al.* Nucl. Inst. and Meth., 2010 **624**(1): 85-91
[6] Gorham, P. *et al.* (ANITA Collab.), Phys. Rev. 2007, **99**: 171101
[7] ARIANNA Collaboration, paper 0144, these proceedings.
[8] Neal, C.S., J. Glaciology, 1979, **24**(90): 295-307
[9] Neal, C.S., Annals of Glac., 1982, **3**: 216-221
[10] Besson, D. *et al.* Astropar. Phys., 2008, **2**: 130-157
[11] Barrella, T. *et al.* J. Glaciology, 2011 **57**(201): 61-66
[12] Dowdeswell, J.A. and Evans, S. Rep. Prog. Phys. **67**: 1821

32ND INTERNATIONAL COSMIC RAY CONFERENCE, BEIJING 2011

Test of a multi-PMT digital optical module on the ANTARES site

VLAD POPA[1], FOR THE KM3NET CONSORTIUM
[1]*Institute for Space Sciences, R-077125, Bucharest - Magurele, Romania*

vpopa@spacescience.ro

DOI: 10.7529/ICRC2011/V04/0386

Abstract: KM3NeT will be a multi-cubic-kilometer neutrino telescope, to be deployed in the near future in the Mediterranean Sea. The KM3NeT design is based on the previous experience of the ANTARES, NEMO and NESTOR projects, and brings many innovative solutions, amongst which is the concept of a digital multi PMT optical module. We intend to soon test a prototype of such a module at the ANTARES site. We report on the technical aspects of the integration of a multi PMT optical module for evaluation within the operating ANTARES deep-sea infrastructure and discuss the status of the KM3NeT project.

Keywords: Neutrino telescopes, KM3NeT, ANTARES, multi-PMT optical module, background measurements

1 Introduction

Neutrino astronomy, the missing link in reaching the multi-messenger astronomy goal, justifies the efforts to build very large volume neutrino telescopes in both Earth hemispheres. Today there are two such instruments: IceCube, at the South Pole – with an instrumented volume approaching one cubic kilometer - and a smaller one in the Mediterranean Sea, ANTARES. KM3NeT will be the next very large volume neutrino telescope (about 6 km^3) in the Mediterranean Sea, with the main role to search for neutrino point sources in the Southern sky, including the Galactic Plane. The E.U. FP6-funded KM3NeT Design Study has been completed with the publication of a conceptual design report [1] and a technical design report [2]. The E.U. FP7-funded Preparatory Phase will end in February 2012. The next step is the construction and deployment of a prototype of a full size KM3NeT detection unit, with only the two uppermost of the 20 storeys active. KM3NeT will implement various innovative solutions with respect to its predecessors, among them the multi-photomultiplier Digital Optical Module (DOM). We report on our intention to deploy a hybridized optical module which can operate with the existing ANTARES readout system, and discuss the reasons and means to do that.

2 KM3NeT optical modules and layout.

Neutrino telescopes are designed to detect the Cherenkov light emitted by relativistic charged particles (muons) in water or ice. The common choice is to use large photomultipliers (PMTs), each one in its own optical module (OM). As an example, Fig. 1 shows a detail of part of an ANTARES line. Three "storeys" are visible. Each storey is

Figure 1. An image of ANTARES OMs mounted on 3 storeys. The large PMTs are visible inside the glass spheres. The LCMs (the cylinders) are also visible.

made of 3 OMs, each containing a 10" PMT, and a Local Control Module (LCM) housing the electronics.
The KM3NeT structure will be completely different. Each DOM (Digital Optical Module) will house 31 3" PMTs, the calibration instrumentation and all acquisition electronics [3], all inside a 17" pressure glass sphere. Furthermore, the PMT signals will be digitized inside the PMT bases (developed by NIKHEF, Amsterdam) [4, 5]. Fig. 2 shows a prototype of a KM3NeT digital optical module.

Figure 2. View of a KM3NeT prototype DOM.

The multi PMT digital optical modules will be mounted on 6 meter long bars (the equivalent of the ANTARES storeys), as shown in Fig. 3.

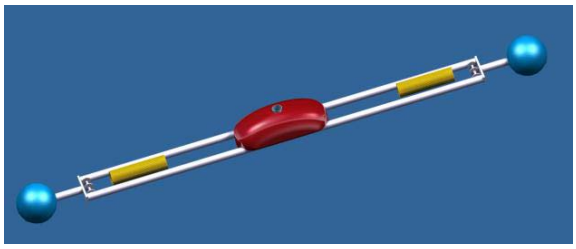

Figure 3. The final design of a KM3NeT bar, supporting 2 DOMs; also showing the central syntactic foam buoyancy device and cable spools.

Each "detector unit" (DU) consists in a flexible tower of 880 m height, made of 20 bars (storeys) with 40 m space between them. Each bar will be oriented perpendicular to its neighbors. Fig. 4 suggests the KM3NeT DU geometry. The detection units will be grouped in "building blocks". A building block will represent about one third of the full detector. A possible footprint of such a building block is presented in Fig. 5. This is one of the layouts under investigation, the final choice is due in the near future.

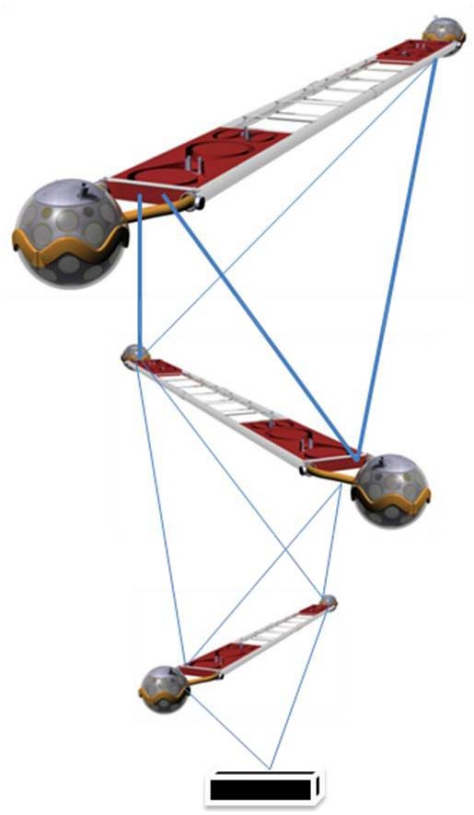

Figure 4. A sketch (not in scale) showing the orthogonal layout of a KM3NeT DU. Only 3 of the 20 storeys (in an intermediate design) are represented.

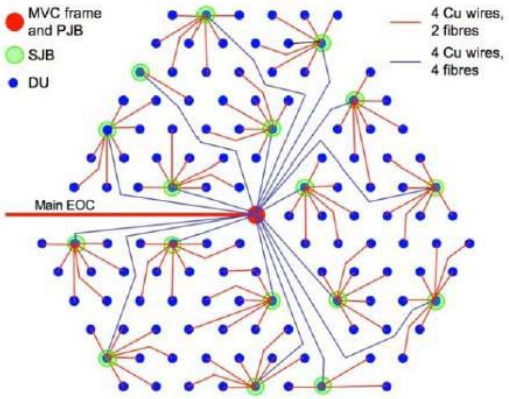

Figure 5. A possible layout of a building block. The primary junction box (PJB) is at the center of the structure, and secondary JBs (SJBs) are distributed in a star geometry. 7 DUs are connected to each SJB. The main electro – optical cable (EOC) connecting the building block to the shore station is also visible.

3 Testing a multi-PMT digital optical module in ANTARES

The task of KM3NeT software development (Monte Carlo simulations, reconstruction algorithms, etc.) needs as crucial input the knowledge of the response of the multi-PMT DOMs to the environmental background (^{40}K radioactivity and bioluminescence). The precursor experiments, ANTARES [6], NEMO [7] and NESTOR [8] used large PMTs, so local background coincidences were seen as large pulse signals. The recovery and redeployment of the ANTARES instrumentation line would offer the opportunity to test a multi – PMT digital optical module in the ANTARES site. The main motivation of this project is to measure the hit coincidence rates as a function of the space angle between the axes of the PMTs. This will be achieved by selecting / deselecting various PMTs inside the hybridized OM through software commands from the shore counting room. It will ease the KM3NeT software development prior the prototype deployment.

The multi-PMT DOM used for this purpose should be a hybridized one. Signals delivered by the PMT bases are already digitized, whereas the ANTARES data acquisition system (DAQ) is conceived to collect analog signals from the OMs and digitize them inside the LCMs, using "Analogue Ring Samplers" (ARS) custom ASICs [9] which sample the PMT pulses in amplitude and produce the digital signal sent to the shore station.

The hybridized DOM contains only eight 3" PMTs, all mounted in the lower hemisphere of the module. The compatibility with the ANTARES DAQ is ensured by a specially designed summing board, developed at ISS, Bucharest. This board has multiple tasks:

- to combine the digital signals from two or more PMTs in the DOM and deliver an "analog" output signal compatible with the ARS input;
- to ensure the "slow control" of the device (to receive commands from the shore station concerning the PMT combination for each run, to transmit information on the acquisition status and control of the PMT high voltage);
- to ensure the power to all components inside the DOM.

Fig. 6 illustrates the principle of the analogue summing process. For simplification, only three PMTs are represented here.

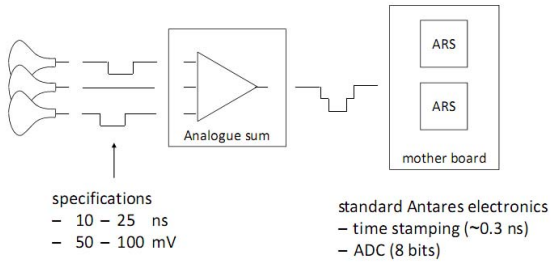

Figure 6. The principle of the analogue summing board.

4. Conclusions

While this paper was being written, various components of the hybrid multi-PMT digital optical module were in the final stage of development and testing. We intend to integrate the device on the ANTARES instrumentation line, to be redeployed on the ANTARES site (2500 m depth, about 40 km South of Toulon, France) later this year. The complexity of the instrumentation line redeployment as well as the time constraints imposed by the sea operations might limit our window of opportunity at the ANTARES site. With this in mind we are considering an alternative integration of the hybrid optical module into an ANTARES line which is being independently prepared for deployment to test the recently deployed deep sea infrastructure at the NEMO site (near Capo Passero, Sicily), later this year.

Acknowledgements.

The KM3NeT project was funded by the E.U. under the FP6 grant 011937 and continues under the E.U FP7 grant 212525.

We acknowledge the ANTARES Collaboration for their commitment to assist us in completing this project.

The Romanian group is supported by ANCS under contract 107EU/2011

References

[1] P. Bagley et al.: 2008, Conceptual Design Report for KM3NeT, ISBN 978-90-6488-031-5

[2] P. Bagley et al.: 2010, Technical Design Report for KM3NeT, ISBN 978-90-6488-033-9

[3] P. Kooijman et al., Nuclear Instruments and Methods in Physics Research Section A, 2011, **626-627**, Supplement 1; S139-S141

[4] P. Timmer, E. Heine and H. Peek, J. Inst, 2010, **5**; DOI: 10.1088/1748-0221/5/12/C12049

[5] D. Gajanana, V. Gromov, P. Timmer, E. Heine and R. Kluit, J. Inst, 2010, **5**; DOI: 10.1088/1748-0221/5/12/C12040

[6] M. Ageron et al. (ANTARES Coll.), Nucl. Instr. and Meths. in Phys. Res. A, 2007, **581**: 695-708

[7] G. Riccobene et al. (NEMO Coll.), Nucl. Instr. and Meths. in Phys. Res. A, (2004) **518**: 220-222
[8] G. Aggouras (NESTOR Coll.), Nucl. Instr. and Meths. in Phys. Res. A (2005), **552**: 420-439
[9] J.A. Aguilar et al., Nucl. Instr. and Meths. in Phys. Res. A, 2007, **570**: 107-116

32ND INTERNATIONAL COSMIC RAY CONFERENCE, BEIJING 2011

Optical follow-up program of IceCube multiplets - testing for soft relativistic jets in Core-collapse Supernovae

THE ICECUBE COLLABORATION[1], CARL AKERLOF[2], FANG YUAN[3], WEIKANG ZHENG[2]
[1]*see special section in these proceedings,* [2]*University of Michigan, Ann Arbor,* [3]*Australian National University*

Abstract: Transient neutrino sources such as Gamma-Ray Bursts (GRBs) and Supernovae (SNe) are hypothesized to emit bursts of high-energy neutrinos on a time-scale of $\lesssim 100\,\mathrm{s}$. To increase the sensitivity to detect those neutrinos and identify their sources, an optical follow-up program for neutrinos detected with the IceCube observatory has been implemented. If a neutrino multiplet, i.e. two or more neutrinos from the same direction within 100 s, is found by IceCube a trigger is sent to the Robotic Optical Transient Search Experiment, ROTSE. The 4 ROTSE telescopes immediately observe the corresponding region in the sky in order to detect an optical counterpart to the neutrino events of IceCube. Data from the first year of operation of the optical follow-up program have been searched for a signal from supernovae. No statistically significant excess in the rate of neutrino multiplets has been observed and further no coincidence with an optical counterpart was found during the first year of data taking. This allows us to restrict current models predicting a high-energy neutrino flux from soft jets in core-collapse SNe. For the first time a stringent limit on the hadronic jet production in core-collapse SNe is derived.

Corresponding Author: Anna Franckowiak[3] (*franckowiak@physik.uni-bonn.de*) DOI: 10.7529/ICRC2011/V04/0445
[3]*Universität Bonn*

Keywords: neutrinos, supernovae, gamma-ray bursts

1 Introduction

High-energy astrophysical neutrinos are produced in proton interactions of charged cosmic rays with ambient photon or baryonic fields (for reviews see [1]). Acceleration of protons to very high energies takes place in astrophysical shocks. Neutrinos escape the acceleration region and propagate through space without interaction, while protons are deflected in magnetic fields and no longer point back to their source. Unlike gamma-rays, neutrinos are solely produced in hadronic processes and could therefore reveal the sources of the highest energy charged cosmic rays. Gamma-ray bursts could provide the environment and the required energy to explain the production of the highest energy cosmic-rays and hence are a plausible candidate. Recent observations imply a common physical origin of long GRBs and core-collapse supernovae (CCSNe): a massive stellar explosion (see [2] for a review). According to the collapsar model [3], long GRBs (duration $\gtrsim 2\,\mathrm{s}$) have their origin in the collapse of a massive, rapidly rotating star into a black hole surrounded by an accretion disk. Relativistic jets with Lorentz boost factors of 100-1000 form along the stellar axis. This GRB-SN connection gives rise to the idea that GRBs and SNe might have the jet signature in common and a certain fraction of core-collapse SNe might host soft relativistic jets. SN jets are suggested to be equally energetic and more baryon-rich, hence they are only mildly relativistic. Such soft relativistic jets would become stalled in the outer layers of the progenitor star, leading to essentially full absorption of the electromagnetic radiation emitted by the jet and at the same time an efficient production of high-energy neutrinos [4, 5]. This motivates a search for neutrino emission, as neutrinos would be able to escape from within the star.

The IceCube neutrino detector, located at the geographic South Pole, is built to detect high-energy astrophysical neutrinos [6]. So far GRB neutrino searches have been performed offline on AMANDA [7] and IceCube [8] data, triggered by gamma-ray satellite detections. Furthermore, a dedicated search for a neutrino signal in coincidence with the observed X-ray flash of SN 2008D has been conducted by IceCube [9] in order to test the soft jet scenario for CC-SNe. Neither the GRB nor the SN neutrino searches led to a detection yet, but set upper limits to the possible neutrino flux.

Early SN detections, as in the case of SN 2008D, are very rare since X-ray telescopes have a limited field of view. However, neutrino telescopes cover half of the sky at any time. If neutrinos produced in soft relativistic SN jets are detected in real time, they can be used to trigger follow-up observations [10]. This is realized with the optical follow-up program presented here. Complementary to the offline

searches, the optical follow-up program is an online search independent of satellite detections. It is sensitive to transient objects, which are either gamma-dark or missed by gamma-ray satellites. In addition to a gain in significance, the optical observations may allow to identify the transient neutrino source, be it a SN, GRB or any other transient phenomenon producing an optical signal. Hence it enables us to test the plausible hypothesis of a soft relativistic SN jet and sheds light on the connection between GRBs, SNe and relativistic jets.
In order to implement the optical follow-up program an online neutrino event selection was developed at the neutrino detector IceCube. The data are processed online by a computer farm at the South Pole. A multiplicity trigger selects neutrino burst candidates and the directional information is transferred to the four ROTSE telescopes, which start the follow-up immediately and continue observations for several days. The obtained optical data are analyzed in order to search for an optical supernova counterpart.

2 IceCube

The IceCube neutrino telescope has been under construction at the geographic South Pole since 2004 and was completed in the Antarctic summer of 2010/11. It is capable of detecting high energy neutrinos with energies above 100 GeV and is most sensitive to muon neutrinos within the energy range from TeV to PeV. High-energy muon neutrinos undergoing charged current interactions in the ice or the underlying rock produce muons in neutrino-nucleon interactions. The muon travels in a direction close to that of the neutrino and emits Cherenkov light. The deep ultra clear Antarctic ice is instrumented with light sensors thus forming a Cherenkov particle detector. After its completion it comprises a volume of $1\,\mathrm{km}^3$ with 5160 digital optical modules (DOMs) attached to 86 vertical strings at a depth of 1450 m to 2450 m [6]. Each DOM consists of a 25 cm diameter Hamamatsu photomultiplier tube (PMT) and supporting hardware inside a glass pressure sphere. Here we present the analysis of the data taken from the start of the follow-up program on 2008/12/16 to 2009/12/31. Initially 40 IceCube strings were taking data. In May 2009 an additional 19 strings were included. This corresponds to an uptime of 121 days with 40 and 186.4 days with 59 strings. In the following the deployment stages will be referred to as IC40 and IC59.

2.1 Online System

In order to rapidly trigger optical telescopes the first online analysis of high-energy neutrinos detected by IceCube was developed and implemented. Unlike in the offline analyses, which are performed on an entire dataset (usually ~ 1 year of data) with time consuming reconstructions on a large computer cluster, the data are processed online by a computer cluster at the South Pole. The processing includes event reconstruction and basic event selection. The first year of data presented here was taken with a latency of 6-8 h. With the start of operations with 79 strings the processing was upgraded reducing the latency to a few minutes. After the parallel processing the data arrive on a dedicated machine (analysis client), where a sophisticated event selection is applied based on the reconstructed event parameters. A multiplicity trigger selects neutrino burst candidates (see section 2.2). No further reconstruction algorithms need to be applied at the analysis client allowing a very fast filtering of the events ($\ll 1$ s). The directional information is transferred to Madison, Wisconsin, via the Iridium satellite network within about 10 s. From there the message is forwarded to the four ROTSE telescopes via the internet through a TCP-socket connection for immediate follow-up observations. The stability and performance of the online system is constantly monitored in order to allow a fast discovery of problems. To achieve this, test alerts are produced at a much higher rate (~ 100 test alerts per day compared to 25 real alerts per year) by the same pipeline and are also send to the North. Their rate and delay time distributions are monitored using an automatically generated web page.

2.2 Neutrino Event Selection

The background in a search for muon-neutrinos of astrophysical origin can be divided into two classes. One consists of atmospheric muons, created in cosmic ray air showers, entering the detector from above. The other is given by atmospheric neutrinos which have their origin in meson decays in cosmic ray air showers. The expected neutrino signal according to the soft jet SN model can be calculated as a function of two model parameters: the boost Lorentz factor Γ and the jet energy E_{jet} [9]. Signal events are simulated following the predicted neutrino flux spectrum in order to develop and optimize selection criteria to distinguish signal and background events. Restricting the search to the Northern hemisphere and imposing requirements on the event reconstruction quality (e.g. the number of hits with small time residual or the likelihood of the reconstruction) allows a suppression of the mis-reconstructed muon background. To suppress the background of atmospheric neutrinos, which we cannot distinguish from the soft SN neutrino spectrum, we require the detection of at least two events within 100 s and an angular difference between their two reconstructed directions of $\Delta\Psi \leq 4^\circ$. The choice of the time window size is motivated by the jet penetration time. The observed gamma-ray emission from long GRBs has a typical length of 50 s, which roughly corresponds to the time for a highly relativistic jet to penetrate the stellar envelope. The angular window $\Delta\Psi$ is determined by the angular resolution of IceCube and was optimized along with the other selection parameters. The final set of selection cuts has been optimized in order to reach a multiplet rate of ~ 25 per year corresponding to the maximal number of alerts accepted by ROTSE. The final data stream consists of 37% (70%) atmospheric neutrinos for IC40 (IC59). Combining the neutrino measurement with the optical measure-

ment allows the cuts to be relaxed yielding a larger background contamination and at the same time a higher signal passing rate. A doublet is not significant by itself, but may become significant when the optical information is added. Each multiplet is forwarded to the ROTSE telescopes. The doublet direction is calculated as a weighted mean from the single reconstructed directions comprising the multiplet. The single events are weighted with $1/\sigma^2$, where σ is the reconstruction error estimated by the paraboloid fit, which fits a paraboloid to the likelihood landscape around the minimum defined by the best fit. The resolution of the doublet direction is $\sim 0.8^\circ$.

3 Search for Optical Counterparts

The IceCube multiplet alerts are forwarded to the robotic optical transient search experiment (ROTSE), which consists of four identical telescopes located in Australia, Texas, Namibia and Turkey [11]. The telescopes stand out because of their large field of view (FoV) of $1.85^\circ \times 1.85^\circ$ and a rapid response with a typical telescope slew time of 4 sec to move the telescope from the standby position to the desired position. The telescopes have a parabolic primary mirror with a diameter of 45 cm. To be sensitive to weak sources no bandwidth filter is used. ROTSE is most sensitive in the R-band (~ 650 nm). The wide field of view is imaged onto a back-illuminated thinned CCD with 2048×2048 $13.5\,\mu$m pixels. For a 60 sec exposure at optimal conditions the limiting magnitude is around $m_R \approx 18.5$, which is well suited for a study of GRB afterglows during the first hour or more and SN light curves with peak magnitude ≤ 16. The corresponding FWHM (full width at half maximum) of the stellar images is less than 2.5 pixels (8.1 arcseconds). Observations are scheduled in a queue and are processed in the order of their assigned priority. IceCube triggers have second highest priority after GRB follow-ups triggered by the GRB Coordinate Network (GCN).

Once an IceCube alert is received by one of the telescopes, the corresponding region of the night sky will be observed within seconds. A predefined observation program is started: The prompt observation includes thirty exposures of 60 seconds length. Follow-up observations are performed for 14 nights. This was extended on 2009/10/27 to 24 nights, with daily observations for 12 nights and then observations during every second night up to day 24 after the trigger was received. Eight images with 60 seconds exposure time are taken per night. The prompt observation is motivated by the typical rapidly decaying light curve of a GRB afterglow, while the follow-up observation of 14 (or 24) nights permits the identification of a rising SN light curve. In the initial phase with IC40 and IC59, the online processing latency of several hours made the search for an optical GRB afterglow unfeasible. We therefore focus on the SN light curve detection in the ROTSE data.

Image correction and calibration are performed at the telescope sites. The images of each night are combined in order to obtain a deeper image. A reference image is subtracted from each combined image using the algorithm developed by [12]. As deep images are usually not available for the positions we would like to observe, we initially choose the deepest image of our observing sequence as the reference image. In 40% of the alerts we took another deep image roughly one year later. Both SN light curves and GRB afterglows would have faded after a few weeks, and would not be present in the newly taken reference image.

All extracted objects found in the subtracted images are candidates for variable sources. However, bad image quality, failed image convolution, bad pixels and other effects frequently cause artifacts in the subtraction process, requiring further selection of the candidates. A candidate identification algorithm including a boosted decision tree is applied to classify sources according to geometrical and variability criteria. The final candidates are summarized on a web page and are inspected visually by several trained persons, who have to classifly the candidate as a SN, a variable star or a subtraction artifact. SN candidate identification by the human eye works well as shown in the galaxy zoo SN project [13]. The visual scanning was performed by three individual persons to ensure no good candidate was missed and to avoid false positives.

4 Results

This paper presents the results from the analysis of data taking in the period of 2008/12/16 to 2009/12/31. Table 1 shows the number of detected and expected doublets and triplets for the IC40 and the IC59 datasets as well as the number of detected and expected optical SN counterparts. The IceCube expectation based on a background only hypothesis was obtained from scrambled datasets. To correctly incorporate detector asymmetries, seasonal variations and up-time gaps we used the entire IC40 and IC59 datasets and exchanged the event directions randomly while keeping the event times fixed. The number of doublets shows a small excess, which corresponds to a $2.1\,\sigma$ effect and is thus not statistically significant. The expected number of randomly coincident SN detections, $N_{\mathrm{SN}}^{bg} = 0.074$, is based on an assumed core-collapse SN rate of 1 per year within a sphere with radius 10 Mpc, i.e. $2.4 \cdot 10^{-4}\,\mathrm{y}^{-1}\,\mathrm{Mpc}^{-3}$, and a Gaussian absolute magnitude distribution with mean of -18 mag and standard deviation of 1 mag for CCSN [14]. In total 31 alerts were forwarded to the ROTSE telescopes. Five could not be observed be-

Table 1: measured and expected multiplets

	SN	Doublets		Triplets	
		IC40	IC59	IC40	IC59
measured	0	15	19	0	0
expected	0.074	8.55	15.66	0.0028	0.0040

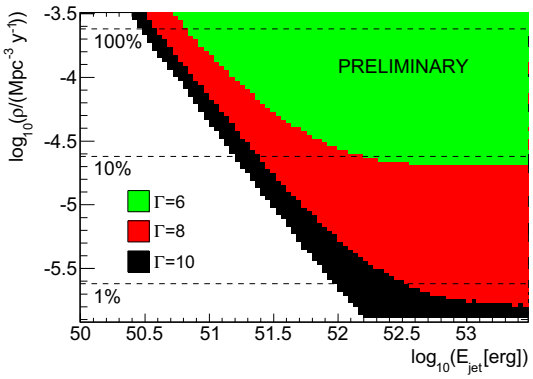

Figure 1: Limits on the choked jet SN model [5] for different boost Lorentz factors Γ as a function of the rate of SNe with jets ρ and the jet energy $E_{\rm jet}$ (colored regions are excluded at 90% CL). Horizontal dashed lines indicate a fraction of SNe with jets of 100%, 10% or 1%.

cause they were too close to the sun. For two alerts no good data could be collected. Seven alerts were discarded because the corresponding fields were too close to the galactic plane and hence too crowded. Thus 17 good optical datasets remained for the analysis. The data were processed as described above. No optical SN counterpart was found in the data.

We obtain the confidence level for different combinations of SN model parameters [5] by using a pre-defined test statistic based on a likelihood function. The limit is calculated for the jet boost Lorentz factors $\Gamma = 6, 8, 10$ as a function of the rate of SNe with jets ρ and the jet energy $E_{\rm jet}$. Systematic errors related to the simulated neutrino sensitivity and the SN sensitivity are included in the limit calculation. The 90% confidence regions for each Γ-value are displayed in the $E_{\rm jet}$-ρ-plane in figure 1 (colored regions are excluded at 90% CL). Including the optical information into the limit calculation improved the limit and allows tests of 5-25% smaller CCSN rates. The largest improvement is obtained for small jet energies and large CCSN rates. The most stringent limit can be set for high Γ-factors. Less than 4.2% of all SNe have a jet with $\Gamma = 10$ and a typical jet energy of $E_{\rm jet} = 3 \cdot 10^{51}$ erg. This is the first limit on CCSN jets using neutrino information.

5 Summary and Outlook

The optical follow-up program of IceCube neutrino multiplets realized by the four ROTSE telescopes proves the feasibility of the program. The technical challenge of analyzing neutrino data in real time at the remote location of the South Pole and triggering optical telescopes has been solved. First meaningful limits to the SN slow-jet hypothesis could be derived already after the first year of operation. Especially in cases of high boost Lorentz factors of $\Gamma = 10$ stringent limits on the soft jet SN model are obtained. Soderberg *et al.* [15] obtain an estimate on the fraction of SNe harboring a central engine from a radio survey of type Ibc SNe. They conclude that the rate is about 1%, consistent with the inferred rate of nearby GRBs. Our approach is completely independent and for the first time directly tests hadronic acceleration in CCSN, while the radio counterpart is sensitive to leptonic acceleration.

The volume of the IceCube detector has now increased to a cubic kilometer yielding a larger sensitivity to high-energy neutrinos. In addition the acquired uptime is growing continuously. The delay of processing neutrino data at the South Pole has been reduced significantly from several hours to a few minutes. This results in the possibility of a very fast follow-up and allows the detection of GRB afterglows, which fade rapidly below the telescope's detection threshold.

Because of the successful operation of the optical follow-up program with ROTSE, the program was extended in August 2010 to the Palomar Transient Factory (PTF) [16], which will provide deeper images and a fast processing pipeline including a spectroscopic follow-up of interesting SN candidates. Furthermore an X-ray follow-up by the Swift satellite of the most significant multiplets has been set up and started operations in February 2011 [17].

References

[1] Anchordoqui, L.A. and Montaruli, T., Ann. Rev. Nucl. Part. Sci., 2010, **60**: 129-162
[2] Woosley, S.E. and Bloom, J.S., Ann. Rev. Astron. Astrophys., 2006, **44**: 507-556
[3] MacFadyen, A. and Woosley, S.E., Astrophys.J., 1999, **524**: 262
[4] Razzaque, S. and Meszaros, P. and Waxman, E., Mod. Phys. Lett., 2005, **A20**: 2351-2368
[5] Ando, S. and Beacom, J.F., Phys. Rev. Lett., 2005, **95**: 061103
[6] Achterberg, A. *et al.* , Astropart. Phys., 2006, **26**: 155-173
[7] Achterberg, A. *et al.* , Astrophys.J., 2008, **674**: 357-370
[8] Abbasi, R. *et al.* , Phys.Rev.Lett., 2011, **106**: 141101
[9] Abbasi, R. *et al.* , Astron.Astrophys., 2011, **527**: A28
[10] Kowalski, M. and Mohr, A., Astropart.Phys., 2007, **27**: 533-538
[11] Akerlof, C. W. *et al.* , Publ. Astron. Soc. Pac., 2003, **115**: 132-140
[12] Yuan, F. and Akerlof, C.W., astro-ph/0801.0336, 2008
[13] Smith, A.M. *et al.* , astro-ph/1011.2199, 2010
[14] Richardson, D. and Branch, D. and Baron, E., Astron. J., 2006, **131**: 2233-2244
[15] Soderberg, A.M. *et al.* , Nature, 2010, **463**: 513-515
[16] Rau, A. *et al.* , Publ. Astron. Soc.Pac., 2009, **121**:1334-1351
[17] IceCube Collaboration, paper 535, these proceedings

32nd International Cosmic Ray Conference, Beijing 2011

Search for supernova neutrino bursts with the Large Volume Detector

W.Fulgione[1,2], A.Molinario[1,2,3], C.F.Vigorito[1,2,3]
on behalf of the LVD collaboration

[1] *INFN, sezione Torino, via Pietro Giuria 1, Torino, Italy*
[2] *INAF, IFSI-TO, Corso Fiume 4, Torino, Italy*
[3] *Dipartimento di Fisica Generale, Università di Torino, Italy*
fulgione@to.infn.it
DOI: 10.7529/ICRC2011/V04/0513

Abstract: The Large Volume Detector (LVD) in the INFN Gran Sasso National Laboratory, Italy, is a 1 kt liquid scintillator neutrino observatory mainly designed to study low energy neutrinos from gravitational stellar collapses in the Galaxy. The experiment has been taking data since June 1992, under increasing larger mass configurations. The telescope duty cycle, in the last ten years, has been greater than 99%. We have searched for neutrino bursts analysing LVD data in the last run, from May 1^{st}, 2009 to March 27^{th}, 2011, for a total live time of 696.32 days. The candidates selection acts on a pure statistical basis, and it is followed by a second level analysis in case a candidate is actually found in the first step. We couldn't find any evidence for neutrino bursts from gravitational stellar collapses over the whole period under study. Considering the null results from the previous runs of data analysis, we conclude that no neutrino burst candidate has been found over 6314 days of live-time, during which LVD has been able to monitor the whole Galaxy. The 90% c.l. upper limit to the rate of gravitational stellar collapses in the Galaxy results to be 0.13 events / year.

Keywords: Supernova - Neutrino - Core collapse - Neutrino detection

Gravitational stellar collapses (GSC) are astrophysical events of great interest. The modeling of the physical processes is still in evolution, but it is in general accepted that the role of neutrinos is critical to allow the supernova to form out of a collapse [1].
The confirmed detection of the neutrino signal from the SN1987A, which was located in the Large Magellanic Cloud, marked the beginning of a new era in neutrino astrophysics [2, 3, 4] and, in spite of some unresolved controversies [5], opened the way to neutrino astronomy. Even in the lack of a complete theory of the core collapse supernova explosion the correlated neutrino emission is believed to be well established and should be detected with different active detectors at the time next event will occur within the Milky Way boundaries.

All the experiments aiming at the detection of neutrino bursts from core collapse supernovae have to face the extremely low frequency of this events. One core collapse supernova is expected to happen within the borders of the Galaxy every 30-50 years [6]. This implies the ability to set up detectors which last several years with a very high duty cycle. Another crucial point is that, in the absence of others detectable signals, neutrino telescopes must be able to recognize the neutrino burst from the background with very high reliability.

1 The Large Volume Detector (LVD)

The Large Volume Detector (LVD), located in the hall A of the INFN Gran Sasso National Laboratory, Italy, is a neutrino observatory with 1000 tons of liquid scintillator as an active target. The major purpose of LVD is the search for neutrinos from GSC in our Galaxy [7]. The detector consists of an array of 840 scintillator counters, 1.5 m^3 each, organized in a compact structure (dimensions $13 \times 23 \times 10$ m^3). The whole array is divided in three identical towers with independent power supply, trigger and data acquisition. In turn, each tower consists of 35 modules hosting a cluster of 8 counters. Each counter is viewed from the top by three photomultipliers (PMTs).

The main interaction expected in the liquid scintillator, at the typical energies of neutrino from GSC (some tens of MeV), is the inverse beta decay (IBD): $\bar{\nu}_e p, e^+ n$. It gives two detectable signals: the prompt one due to the e^+ (visible energy $E_{\rm vis} \simeq E_{\bar{\nu}_e} - Q + m_e = E_{\bar{\nu}_e} - 0.789$ MeV), followed

by the delayed one from the neutron capture on proton, $E_\gamma = 2.23$ MeV, with a mean capture time, in one LVD counter, of $\tau = 185 \pm 5\,\mu s$. The trigger condition for the experiment is the coincidence above threshold H of all three PMTs of any counter. If a trigger occurs, the threshold is lowered to a level L for ~ 1 ms in all the counters of the same module of that which gave the trigger, in order to look for the delayed γ pulse from neutron capture on proton. The energy release in one counter to get a 50% probability to generate a H trigger is $E_H = 4$ MeV, if the average over all the counters is considered. For the L triggers it is $E_L < 0.5$ MeV.

The duty cycle of LVD has been on average $\geq 99\%$ since 2001. It is shown in figure 1 (in black) together with the active mass (in red). Beyond the active scintillator ($M = 1$ kt) the iron supporting structure of the detector ($M = 0.85$ kt) can also act as a passive target for neutrino and products of the interactions can be detected.
Besides interactions with free protons LVD is also sensitive to charged current interactions with carbon and iron nuclei through:
- ν_e ^{12}C,^{12}N e^-, (physical threshold $E_{\nu_e} > 17.3\ MeV$) observed through two signals: the prompt one due to the e^- ($E_d \simeq E_{\nu_e} - 17.3$MeV) followed by the signal from the β^+ decay of ^{12}N (mean life $\tau = 15.9$ ms);
- $\bar{\nu}_e$ ^{12}C,^{12}B e$^+$, (physical threshold $E_{\bar{\nu}_e} > 14.4\ MeV$) observed through two signals: the prompt one due to the e^+ ($E_d \simeq E_{\bar{\nu}_e} - 14.4\,\mathrm{MeV} + 2m_ec^2$) followed by the signal from the β^- decay of ^{12}B (mean life $\tau = 29.4$ ms);
- ν_e ^{56}Fe,^{56}Co e^-, where the mass difference between the nuclei is $\Delta_{m_n} = m_n^{\mathrm{Co}} - m_n^{\mathrm{Fe}} = 4.055$ MeV, and the first Co allowed state at 3.589 MeV; the efficiency for electron and gammas, also produced in the interaction, to reach the scintillator with energy higher than $\mathcal{E}_H$ has been simulated [8]; on average, the detectable electron energy is $E_d \simeq 0.45 \times E_\nu$.
- $\bar{\nu}_e$ ^{56}Fe,^{56}Mn e^+.
And neutral current interactions through:
- $\overset{(-)}{\nu}_\ell$ ^{12}C, $\overset{(-)}{\nu}_\ell$ ^{12}C* ($\ell = e, \mu, \tau$), (physical threshold $E_\nu > 15.1\ MeV$), whose signature is the monochromatic photon from carbon de-excitation ($E_\gamma = 15.1$ MeV);
- $\overset{(-)}{\nu}_\ell$ ^{56}Fe, $\overset{(-)}{\nu}_\ell$ ^{56}Fe* ($\ell = e, \mu, \tau$), (physical threshold $E_\nu > 7.6\ MeV$);
- $\overset{(-)}{\nu}_\ell$ e^-, $\overset{(-)}{\nu}_\ell$ e^-, which yields a single signal due to the recoil electron.

To evaluate the number of detected events in LVD for a neutrino burst from GSC we consider a parameterized model, whose parameters have been determined by a maximum likelihood procedure on the data from SN 1987A [9]. From this model the average $\bar{\nu}_\mathrm{e}$ energy is $\bar{E}_{\bar{\nu}_\mathrm{e}}$=14 MeV, the total radiated energy $E_b = 2.4{\cdot}10^{53}$ erg, assuming energy equipartition and normal mass hierarchy for neutrino oscillations. If we set the distance of the collapsing star to D =10 kpc, we get that a total of 300 triggers are expected in LVD with a 1 kt active mass, 85% of which are due to IBD. The energy spectrum would have a mean value of 18 MeV.

2 The search for supernova neutrino bursts

The analysis presented here considers the period from May 1^{st}, 2009 to March 27^{th}, 2011, for a total live time of 696.32 days. All the triggers with energy in the interval 7-100 MeV are selected. A cut on crossing muons is applied excluding the triggers in different counters in coincidence within 250 ns. Some quality cuts are included to avoid electronic noise that can affect data and to exclude counters with unstable counting rate. They are described in detail in [10]. The total rate after these selections is 0.2 s^{-1}.

The neutrino burst candidates selection acts on a pure statistical basis. The algorithm is based on the search for clusters of triggers within a fixed time window, $\Delta t = 20$ s. The candidate is simply characterized by its multiplicity m, i.e., the number of pulses detected in Δt. All the other characteristics of the cluster, detailed time structure, energy spectra, ν flavor content and topological distribution of signals inside the detector are left to a subsequent independent analysis. In detail, the time sequence of total duration T, is scanned through a *sliding window* of duration $\Delta t = 20$ s, that is, it is divided into $N = 2 \cdot \frac{T}{\Delta t} - 1$ intervals, each one starting in the middle of the previous one (in this way the maximum unbiased time window is 10 s). The frequency of clusters of duration 20 s and multiplicity $\geq m$, i.e., the imitation threshold due to background, is:

$$F_{im}(m, f_{bk}) = N \cdot \sum_{\mathrm{k\geq m}}^{\infty} P(k; \frac{20 \cdot f_{bk}}{s^{-1}})\ \mathrm{ev \cdot day^{-1}} \quad (1)$$

where: f_{bk} is the background counting rate of the detector for $\mathrm{E}{\geq}\mathrm{E}_{\mathrm{cut}}$; $P(k, f_{bk}\Delta t)$ is the Poisson probability to have clusters of multiplicity k if $(f_{bk}\Delta t)$ is the average background multiplicity, and N =8640 is the number of trials per day. This search for neutrino burst candidates is performed simultaneously for trigger energies E > 7 MeV ($f_{bk} = 0.2$ Hz) and E > 10 MeV ($f_{bk} = 0.03$ Hz), being $N^{'} = 2N$ the effective number of trials.

We can choose different values of F_{im}, to which a different minimum multiplicity of the cluster corresponds. We check, for various F_{im}, the delay between a selected cluster and the following one. Then we

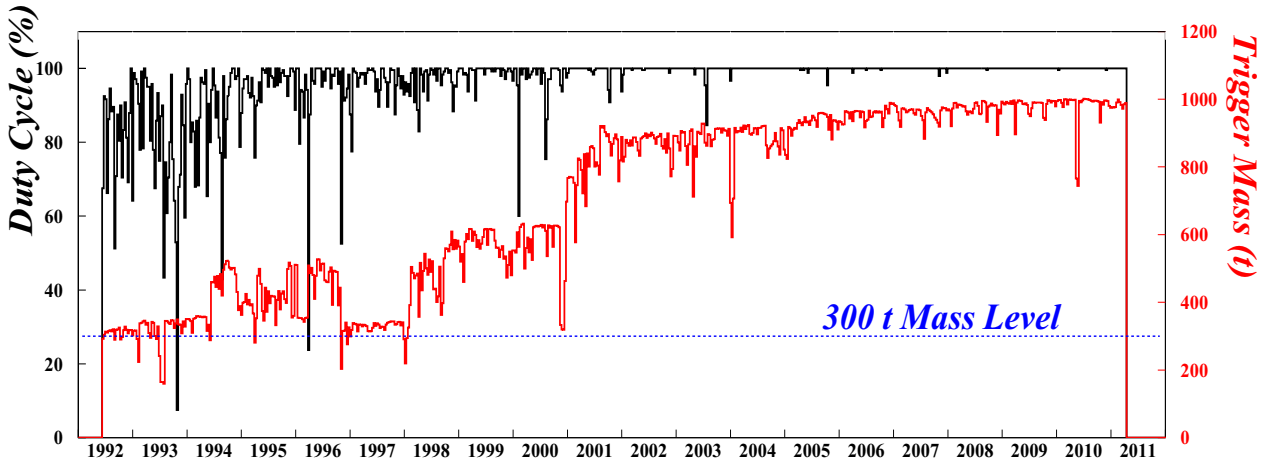

Figure 1: Duty cycle (in black) and active mass (in red) as a function of time, updated to March 27^{th} 2011. The 300 t mass level is marked by the blue horizontal line.

compare the resulting distribution with the expectations from Poisson statistics (figure 2). At the level of $F_{im} < 1$ year^{-1} we found two clusters, and both of them had a $F_{im} \sim 1$ y^{-1}.

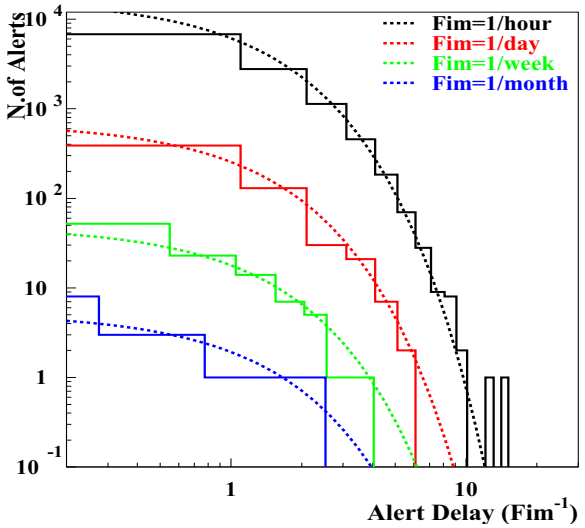

Figure 2: Distribution of the observed time delay between alerts selected at different imitation threshold (F_{im}) from 1 hour^{-1} up to 1 month^{-1} , compared with the expected distribution (dashed lines)at the corresponding threshold. A the level of $F_{im} < 1$ year^{-1} we found two clusters (observed $F_{im} \sim 1$ y^{-1}).

The good agreement among predicted distributions and results from data means that the background is understood and under control. Given this condition we may define as *neutrino burst candidates* those clusters which would be produced by background fluctuations less than 0.01 $year^{-1}$.

After this pure statistical selection a complete study of selected clusters is planned, to test their consistency with the expectations for real GSC neutrino bursts. In particular this second level analysis focuses on:

1. *The topology of the cluster*, i.e., how the events of the cluster are distributed inside the detector. LVD can identify the counter where an event occurred. We expect that a neutrino burst would distribute uniformly in the detector, while events from the background favour external counters over the internal, more shielded, ones.

2. *The number and temporal distribution of n-captures signal.* As a real GSC neutrino burst would mainly interact through IBD, we do expect that n-capture signals after the triggers are actually present. Moreover, their temporal distribution should be exponential decreasing with a mean time $\tau \sim 185\,\mu$s.

3. *The energy spectrum.* Events from a GSC neutrino burst peak at around 20 MeV, while the events from the background reach their maximum just at the energy threshold (7 MeV or 10 MeV).

We applied the statistical selection of clusters with $F_{im} < 0.01$ $year^{-1}$. We couldn't select any over the whole period under study, so no evidence for a neutrino burst from GSC is found.

Run	Start	End	Time (days)	Mass (t)
1	Jun.6^{th} 1992	May 31^{st} 1993	285	310
2	Aug.4^{th} 1993	Mar.11^{th} 1995	397	390
3	Mar.11^{th} 1995	Apr.30^{th} 1997	627	400
4	Apr.30^{th} 1997	Mar.15^{th} 1999	685	415
5	Mar.16^{th} 1999	Dec.11^{th} 2000	592	580
6	Dec.12^{th} 2000	Mar.24^{th} 2003	821	842
7	Mar.25^{th} 2003	Feb.4^{th} 2005	666	881
8	Feb.4^{th} 2005	May 31^{st} 2007	846	936
9	May 31^{st} 2007	Apr.30^{th} 2009	699	967
10	May 1^{st} 2009	Mar.27^{th} 2011	696	981
Σ	Jun.6^{th} 1992	Mar.27^{th} 2011	6314	721

Table 1: LVD data runs

3 Discussion and conclusions

We may consider the null results for the search of GSC neutrino bursts over the whole period of data taking of the experiment, from June 6^{th}, 1992 to March 27^{th}, 2011, for a total of 6314 days live-time. It results that the 90% c.l. upper limit to the rate of gravitational stellar collapses in our Galaxy is 0.13 events/year. The summary of the features of all LVD data runs is reported in table 1.

The selection method, as it follows from equation 1, defines a candidate as any cluster of $m \geq m_{min}$ signals within a window of $\Delta t = 20s$. For a known background rate, $m_{min} - f_{bk}\Delta t$ is the minimum number of neutrino interactions required to produce a supernova alarm at a selected F_{im} threshold. We consider the number of signals expected from a SN1987A-like event occurring at different distances, for $E_{\rm cut} = 7$ and $E_{\rm cut} = 10$ MeV and for two values of the detector active mass, $\rm M_{act} = 300$ t and $\rm M_{act} = 1000$ t. Taking into account Poisson fluctuations in the cluster multiplicity, we derive the detection probability as a function of the distance shown in figure 3 (lower scale) for LVD working stand-alone. The detection probability as a function of neutrino luminosity in terms of percentage of SN1987A at the distance of 10 kpc is shown in the upper scale (see details in [10]). It results that LVD is able to monitor the Galaxy ($D \leq$ 20kpc) at full efficiency for both energy thresholds (7 MeV and 10 MeV) when the active mass is greater than 300 t.

In conclusion, LVD has been monitoring the Galaxy since 1992 in the search for neutrino bursts from gravitational stellar collapses with an high duty cycle (greater than 99% in the last ten years). No GSC neutrino burst candidate has been found over 6314 days of live-time, the resulting 90% c.l. upper limit to the rate of gravitational stellar collapses in the Galaxy ($D \leq 20$ kpc) is 0.13 events / year.

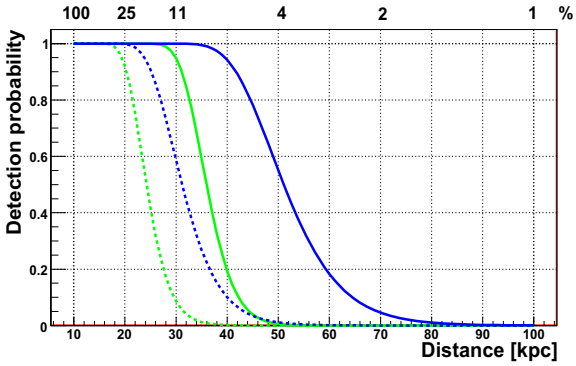

Figure 3: Detection probability versus distance (lower scale) and percentage of SN1987A signal at 10 kpc (upper scale) for Ecut = 7-10 MeV (light green and dark blue lines, respectively) and M = 300 t (dotted) and 1000 t (continuous) for LVD stand alone.

References

[1] H.A.Bethe, J.R.Wilson, The Astrophysical Journal, 1985, **295**: 14-23
[2] K.Hirata et al. (Kamiokande Collaboration), Physical Review Letters, 1987, **58**: 1490
[3] R.M.Bionta et al. (IMB Collaboration), Physical Review Letters, 1987, **58**: 1494
[4] E.N.Alekseev et al., J. Exp. Theor. Phys. Lett., 1987, **45**: 589
[5] M.Aglietta et al. (LSD collaboration), Europhys. Lett., 1987, **3**: 1315
[6] R.Diehl et al., Nature, 2006, **439**: 45
[7] M.Aglietta et al. (LVD Collaboration), Il Nuovo Cimento, 1992, **A 105**: 1793
[8] N.Yu.Agafonova et al., Astroparticle Physics, 2007, **27**: 254-270
[9] G.Pagliaroli, F.Vissani, M.L.Costantini, A.Ianni, Astroparticle Physics, 2009, **31**: 163-176
[10] N.Yu.Agafonova et al., Astroparticle Physics, 2008, **28**: 516-522

32ND INTERNATIONAL COSMIC RAY CONFERENCE, BEIJING 2011

SWIFT Follow-Up of IceCube neutrino multiplets

THE ICECUBE COLLABORATION[1], SWIFT COLLABORATORS[2]
[1]*See special section in these proceedings,* [2] *see [1]*

Abstract: The search for neutrinos of astrophysical origin is among the primary goals of the IceCube neutrino telescope. Point source candidates include galactic objects such as supernova remnants (SNRs) as well as extragalactic objects such as Active Galactic Nuclei (AGN), Supernovae (SNe) and Gamma-Ray Bursts (GRBs). To increase the sensitivity of the search for high-energy neutrinos from SNe and especially GRBs an X-ray follow-up with the Swift satellite has been developed. Upon the detection of two or more neutrinos from a common direction and within a short span of time, IceCube will trigger the satellite to scan the same direction for a transient X-ray counterpart, e.g. an X-ray GRB afterglow. In addition to typical GRBs the program is sensitive to SN shock breakouts, slightly off-axis GRBs and orphan GRB afterglows. The online event selection in IceCube as well as the X-ray observation strategy will be presented.

Corresponding Author: Andreas Homeier[3] (*ahomeier@icecube.wisc.edu*), Miles Smith[4,5] (*msmith@astro.psu.edu*)
[3]*University of Bonn*
[4]*Swift Mission Operations Team*
[5]*Penn State University*

DOI: 10.7529/ICRC2011/V04/0535

Keywords: Neutrino, GRB, Swift, X-ray, Multimessenger

1 Introduction

1.1 Scientific Motivation

It may be possible to observe high energy neutrinos from astrophysical sources similar to GRBs that are not detectable via prompt electromagnetic emissions. Such objects could be GRBs with narrow jets that don't point directly towards earth [2] or choked GRBs [3] for which the jet may fail to penetrate the stellar envelope. In these cases, despite the lack of prompt γ-rays, the source is likely to be visible in X-rays from shock breakout after 10^3 s, and to exhibit an optical counterpart similar to that seen in core collapse supernovae [4]. While no firm estimate exists, the number of these dark bursts might be up to 100 times larger than γ-bright bursts [5]. Therefore, the search for transient neutrino sources can play an important role in the search for (γ-dark) GRBs, and may provide insights into the origin of the high energy cosmic rays. While an optical follow-up can be conducted by ground based telescopes (e.g. ROTSE [6]), satellites such as Swift are uniquely capable of rapid follow up with X-ray observations.

NASA's Swift Explorer Mission is ideally suited for studying the electromagnetic radiation from violent astrophysical events, such as GRBs. Three telescopes are supported by the Swift platform. A wide field of view instrument, the Burst Alert Telescope (BAT), monitors for the prompt γ-rays from a GRB. In response to a burst, Swift will slew into position to image the BAT error region with the X-Ray Telescope (XRT) and UltraViolet and Optical Telescope (UVOT). In this program the XRT will be used.

1.2 Overview of the program

The X-ray Follow-Up with Swift is a multimessenger approach developed by the Swift and the IceCube collaborations to detect GRBs. It uses the IceCube neutrino telescope at the South Pole to look for signal-like neutrino-multiplets (i.e. at least two neutrinos from the same direction within 100 seconds) to trigger follow-up observations with the Swift satellite in the X-ray band. The implementation of the program makes use of the existing neutrino event selection of the Optical Follow-Up Program [7] (OFUP) at the South Pole. Neutrino multiplets are reconstructed and identified online in quasi-real time with a typical latency of about 5 minutes. This low latency opens the possibility to search for fast decaying X-ray afterglows from (GRBs). Additional latency is expected on the Swift side, due to communication constraints with the spacecraft, the orbital position of Swift, and human-in-the-loop requirements for spacecraft commanding. Depending on the visibility of Swift to a ground relay station, the additional delay will be between 30 minutes to 4 hours. It is worth noting that the typical X-ray afterglow associated with long GRBs is visible to Swift for days and sometimes weeks.

2 Alert chain

Swift is in high demand amongst the scientific community. Hence only limited observing time is available for the IceCube follow-up program. The current implementation of the OFUP program results in about 25 neutrino-multiplet triggers per year in IceCube. Most of these are due to background consisting of atmospheric neutrinos and about 25 % atmospheric muons. For short Swift follow-ups, the number of IceCube alerts can be decreased to approximately 7/year with very little loss in signal efficiency. This is achieved by using a likelihood method, as described in section 2.1. Extensive follow-ups over a time span of at least a week can then be performed at a rate of about one per year based on a quick evaluation of the first available X-ray data, as described in section 3.1.

2.1 IceCube candidate event selection

For the optical follow-up program, the singlet data rate achieved by the OFUP filter [7] is $R_s \approx 2mHz$, reaching a 75% pure (atmospheric) neutrino sample. Using this data sample, multiplets are selected if more than one neutrino is detected within $\Delta t = 100s$ and from the same direction within the reconstruction uncertainty of $\Delta\Psi = 3.5°$. These two conditions reduce the detected number of coincident neutrinos from the isotropic background of atmospheric neutrinos to about 25 false positives per year.

Given the limited observing time available with Swift, an additional test-statistic was developed to select the subset of these multiplet triggers which are most likely to have astrophysical origins and be detectable by Swift follow-up observations. As the derivation is beyond the scope of this paper, it is only described and motivated here. We begin with the following definitions:

$$\begin{aligned} \sigma_q^2 &= \sigma_1^2 + \sigma_2^2 \\ \sigma_w^2 &= \left(\frac{1}{\sigma_1^2} + \frac{1}{\sigma_2^2}\right)^{-1} \\ cos\psi &= \hat{r}_1 \cdot \hat{r}_2 \end{aligned} \tag{1}$$

where $\sigma_{1/2}$ are the reconstruction uncertainties of the participating neutrinos that arrive from the (reconstructed) directions $\hat{r}_{1/2}$ with an angular difference of ψ. Assuming a circular follow-up region, the test statistic

$$d = \frac{\psi^2}{\sigma_q^2} + 2\ln(2\pi\sigma_q^2) - 2\ln\left(1 - e^{-\frac{\theta_A^2}{2\sigma_w^2}}\right) + 2\ln\left(\frac{\Delta t}{100s}\right) \tag{2}$$

tends to small values for signal-like doublets and larger values for background-like events (figure 1). It takes various effects into account.

- The first two terms act together. While the first term favors events with a small angle ψ, indicating neutrinos from the same direction and possibly source, it also introduces a penalty for small reconstruction uncertainties. The qualitative explanation is that two neutrinos for which the error regions do not overlap are more likely background than signal. As a consequence the first term tends also to small values for large combined reconstruction uncertainties σ_q. The second term counteracts this effect, introducing a penalty for large uncertainties. Thus, the two first terms favor well reconstructed events from the same direction.

- The third term introduces the tiled Swift field of view with a radius of $\theta_A \approx 0.5°$. It favors those events with small errors for which, in the case of a signal, the reconstructed doublet direction is expected to be relatively close to the source direction, thus minimizing the possibility of observing a region of space during a follow-up which does not include the actual source within the FoV and supporting the first two terms in selecting well reconstructed events. The value of θ_A reflects a tiled field of view of Swift (section 2.2).

- The time difference Δt between two neutrinos is considered in the fourth term. Normalized to the 100 s time window of the trigger, small values are reached for small time differences assuming they are an indicator for a neutrino bundle of an astrophysical source.

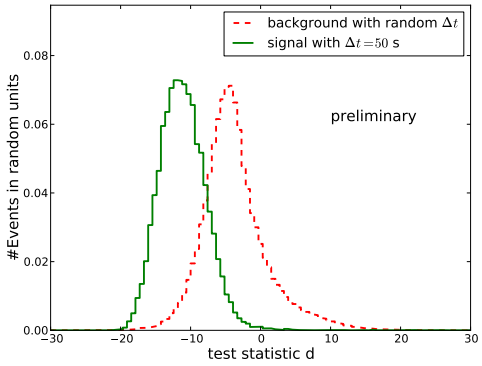

Figure 1: The distribution of the test statistic used for down-selection of OFU alerts, shown here for signal from astrophysical sources with an E^{-2} spectrum (solid line) and background doublets (dashed line). For background, Δt is assumed to be evenly distributed over 0 - 100s while a signal with $\Delta t = 50$ s is assumed.

2.2 Swift Follow-Up

IceCube provides a median position resolution for selected events of less than one degree. However, the XRT field of view is only 0.4^o in diameter, which will cover only a fraction of the IceCube space angle distribution. Due to this

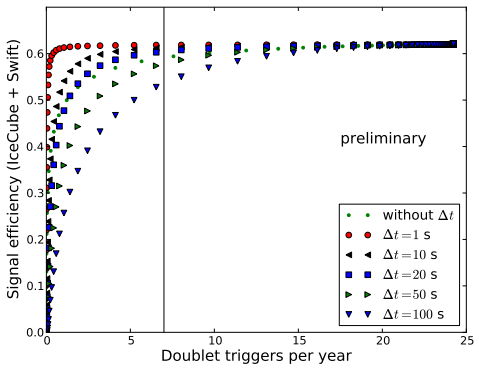

Figure 2: Displayed on the y-axis is the signal efficiency with which a real E^{-2} source that passed the OFUP selection criteria will pass the test statistic and lie within Swift's FoV. This is plotted vs the estimated number of doublet triggers per year. The effect of the Swift field of view is included, only accepting events within the FoV and reducing the acceptance to a maximum of 63%. It is displayed for four different cases assuming a signal with a time difference between the arriving signal neutrinos of Δt. The aim is to reduce the background to seven alerts per year.

limited coverage by the XRT field of view, we are forced to tile the follow-up region with seven pointings of Swift, thus creating an artificially larger field of view. Assuming a neutrino signal following an E^{-2} spectrum and centering the telescope pointings on the reconstructed direction, the fraction of sources that are actually positioned in the observed tiled field of view if is found to increase thus from only about 20% to 63% by tiling the follow-up region. At the same time the observation time for one pointing is reduced limiting the search to bright sources that are easily discovered in less than 1000 sec.

Figure 2 shows the signal efficiency for an astrophysical source with an E^{-2} spectrum relative to the optical follow-up filter as a function of the estimated number of doublet triggers per year. Starting with loose cuts on the test statistic (high positive values in figure 1) and 25 false positives a year, one can see the drop in the number of false positives as well as signal efficiency for tighter cuts (lower values of d in figure 1) reducing the background to zero doublets per year.

Based on figure 2 we decided to aim for triggering seven observable alerts for follow-up per year as the best compromise between background reduction and signal efficiency. This reduces the background by 72% while, in the case of an E^{-2} spectrum, there is only a loss of 10% (14%) for events arriving with a time difference of 50 (100) seconds relative to the maximum acceptance. Almost all doublets with a shorter time difference will pass the cut.

3 Expected Results

Swift orbits the Earth every 96 minutes, with the IceCube trigger region becoming visible each orbit for approximately 2000 sec. The spacecraft will be commanded to automatically observe the seven tiled fields as soon as they rise above the Earth limb, providing approximately 285 every orbit until a total of approximately 2000 sec per tile is achieved, typically taking between 12 hours and a full day to complete. In this way, any X-ray sources visible to Swift will be observed multiple times, generating a light curve. This information is critical for interpreting the nature of the source, possibly identifying a GRB via a typical GRB afterglow.

Two different significance tests are proposed. The level 1 test (section 3.1) provides a relatively quick test on the first day of data collected by Swift, to decide whether to initiate a multi-day follow-up program. The level 2 test (section 3.2), made on the full data set, provides a threshold for claiming a joint Swift-IceCube discovery of an X-ray afterglow in coincidence with an astrophysical neutrino source. The level 1 test is presented in its final form here, while the level 2 test is still under development.

3.1 Level-1 Significance Test

After several orbits, Swift may have detected one or more X-ray sources, with a position uncertainty that is typically on the order of a few arcsec, limited by the Swift XRT point spread function. The source position and an initial measurement of the flux are used to assess whether this is significantly above the expected X-ray background. The expected number of background X-ray sources depends strongly on the flux threshold. We will consider an X-ray source to have passed the level 1 significance test if it satisfies any of the following criteria for an (extra) galactic search.

A **Uncatalogued Sources:** The level 1 source is not in proximity to a catalogued X-ray object (i.e. not within $N\sigma$ ($N = 3$) of the combined Swift and catalog position uncertainty), is brighter than a flux threshold $S_A = (5 \cdot 10^{-12})1 \cdot 10^{-10}$ erg/(cm^2 s), and occurs in a region of the sky where the ROSAT Bright Source Catalog would have observed it had it been in its current state when surveyed.

B **Variable Sources:** The source is brighter than a flux threshold $S_B = (5 \cdot 10^{-13})1 \cdot 10^{-11}$ erg/(cm^2 s) and exhibits significant variability across the first day of Swift data, with the p-value of a fit to a flat light curve being lower than some critical value $P = 0.001$.

C **Active Catalogued Sources:** The level 1 source is within $N = 3\,\sigma$ uncertainty of the position of a catalogued object but the new measurement is $M = 10\times$ brighter than it appears in the catalog.

D **Poorly Catalogued Sources:** A source lies outside of the region covered by the ROSAT Bright Source Catalog (due to the low exposure time of ROSAT in that region) but is observed to be $\overline{M} = 10\times$ brighter than the threshold set by ROSAT for that region.

It is noted that there are significantly more serendipitous X-ray backgrounds in proximity to the galactic plane. As such, the analysis is carried out with different thresholds depending on galactic latitude (GL). Specifically, a higher threshold is used if $|GL| < 20^{\circ}$.

Our intended goal is that the level 1 test will allow no more than one false positive per year. If an X-ray source passes the level 1 test, then additional Swift data is accumulated over the following ≈ 1 week, to determine a light curve and spectrum for the source. The full data set is then utilized for the level 2 test.

The level 1 tests will first be applied once two observations have been made on each tile (i.e. after two Swift orbits). The analysis will continue on the accumulating data until the level 2 observations are triggered or a total of 2000 sec have been observed for each tile. Otherwiese no further obserations or analysis will be carried out.

3.2 Level-2 Significance Test

Should an X-ray source be discovered that passes the level 1 test described above, a dedicated observing program will be initiated for that source. The tiled observations will be discontinued and Swift will take up a pointed observing mode, with the source at the center of a single XRT field of view (0.4° diameter). The level 2 test will determine the significance of all data accumulated over ≈ 1 week, in conjunction with the IceCube trigger data. Backgrounds will be significantly reduced from level 1 to level 2 by examining the larger data set, looking at additional features for transient behavior like the slope of the light curve.

It is anticipated that, for a given class of transient X-ray sources (GRB afterglow, AGN activity, etc), unambiguous identification of a source will be limited by an irreducible background of similar but unrelated events. A first estimate, based on the rate of BAT-triggered GRBs and the average light curve behavior, predicts that serendipitous GRB afterglows will be discovered only once per 3000 years with the Swift-IceCube program.

Numerous studies have placed limits on the number of untriggered GRBs, typically of order 100 times the rate of regular GRBs [5, 8, 9]. This would place a limit on the Swift-IceCube level-2 false positive rate of once per 30 years.

4 Current Status and Outlook

The program was approved by the IceCube collaboration at the beginning of 2011 and is running since February, 11^{th}. Until the middle of May, one alert has been forwarded to Swift. The total latency between the neutrino events and the first observation by Swift was 90 minutes. All steps in the alert chain worked as planned and the event will be included in the final analysis of the program.

In the full km^3 sized IceCube detector a mean of about 10 neutrinos from GRBs per year and hemisphere are predicted to be detectable [10]. If the neutrino flux is equally distributed amongst the GRBs, then we estimate a combined Swift and IceCube detection rate for γ-bright GRBs of 0.013 per year. This number was derived by folding in various detection efficiency factors like, for example, the filter efficiency of the OFU program and the probability to classify the source with Swift. In the case where a 2-year joint Swift-IceCube program results in no detection, a conservative upper limit on the γ-dark GRB rate of 90 times the γ-bright GRB rate (90% c.l.) can be placed. This upper limit will improve significantly for model dependent analysis where a large fraction of the neutrinos are concentrated in a subset of the bursts [11].

A future extension to single neutrino events, applying a stringent high energy cut, is planned as an additional stream. Avoiding the doublet criteria for triggering a follow-up leads to an improved signal efficiency. Initial estimates suggest a detection rate of 0.25 γ-bright GRBs per year and a 2-year upper limit on the γ-dark GRB rate of 4.5 times the γ-bright GRB rate (90% c.l.). This limit is within the current theoretical prediction given in [5].

References

[1] "http://astroteilchen.physik.uni-bonn.de/∼homeier/SwiftCollaborators/SwiftC.pdf"
[2] R. Yamazaki, K. Ioka, T. Nakamura, K. Toma , Adv. Sp. Res., 2006, **38**:1299
[3] P. Meszaros, Rept.Prog.Phys., 2006, **69**: 2259-2322
[4] S. Ando, J. F. Beacom, Phys. Rev. Lett., 2005,**95**: 171101-1 - 171101-4
[5] T. Totani, A. Panaitescu, The Astrophysical Journal, 2002, **576**: 120-134
[6] C. W. Akerlof et al., arXiv:astro-ph/0210238v1, 2002,
[7] A. Franckowiak for the IceCube collaboration, ICRC proceedings, 2011
[8] J. Greiner et al., Astronomy and Astrophysics Supplement, 1999, **138**: 441-442
[9] Achterberg et al., The Astrophysical Journal, 2007, **664**: 397-410
[10] M. Kowalski, A. Mohr, Astropart. Phys., 2007, **27**: 533-538
[11] J. Becker, M. Stamatikos, Francis Halzen, Wolfgang Rhode, arXiv:aastro-ph/0511785v1, 2005

32ND INTERNATIONAL COSMIC RAY CONFERENCE, BEIJING 2011

Muon energy reconstruction and atmospheric neutrino spectrum unfolding with the ANTARES detector

D. PALIOSELITIS[1] ON BEHALF OF THE ANTARES COLLABORATION
[1]*Nikhef (Nationaal instituut voor subatomaire fysica), Science Park 105, 1098XG Amsterdam, The Netherlands*
dimp@nikhef.nl
DOI: 10.7529/ICRC2011/V04/0541

Abstract: Measurement of the atmospheric muon neutrino spectrum is important since it is a test on the expected conventional atmospheric neutrino fluxes as well as on the prompt contribution from charm decay. In addition to that, it forms the irreducible background for high energy cosmic neutrinos searches. A number of methods have been developed within the ANTARES collaboration for the estimation of the energy of muon tracks traversing the detector. These include a maximum likelihood method, an approach based on neural networks as well as an estimator based on the energy loss of the muon along its track. The reconstructed muon energy can be used to calculate the energy spectrum of the atmospheric neutrinos by using a singular value decomposition approach on regularized unfolding. The most recent results on the energy reconstruction and spectrum deconvolution will be presented.

Keywords: Neutrino telescope, atmospheric neutrinos, energy reconstruction, unfolding

1 Introduction

The ANTARES detector is a high energy neutrino telescope deployed in the Mediterranean sea, 40 km off the coast of Toulon in France. It consists of a three dimensional array of photomultiplier tubes designed to detect light produced by charged particles crossing the instrumented volume. Its main scientific goal is the detection of astrophysical high energy neutrinos.

When a neutrino interacts with a nucleon in the area close to or inside the instrumented volume, it produces a detectable signature. ANTARES is optimized to detect muons produced by the charged current neutrino interaction with nuclei in the surrounding medium. The detection principle is based on the Čerenkov light produced by charged particles when they traverse a medium with a velocity higher than the speed of light. This light is detected by the photomultiplier tubes, housed into glass spheres called optical modules (OMs). The OMs record information about the charge and time of each hit. The position of each OM is provided by an acoustic positioning system. This information allows for both directional [1, 2] and energy reconstruction.

The majority of neutrino candidate events detected with ANTARES is expected to be due to atmospheric neutrinos, coming from the decay of pions and kaons produced by cosmic ray interactions in the atmosphere. Neutrinos produced by this mechanism constitute the so-called "conventional" component of the atmospheric neutrino spectrum. At higher energies, the decay lengths of these mesons are longer than their path lengths in the atmosphere thus leading to a suppression of produced neutrinos. The "prompt" decay of charmed mesons, produced at high energies, provides an additional contribution to the atmospheric neutrino flux at the higher energies end of the spectrum [3]. The prompt neutrino spectrum is less steep than the conventional atmospheric neutrino spectrum. Measurement of the atmospheric neutrino spectrum can therefore provide valuable information on the prompt component which is expected to dominate the atmospheric neutrino flux at energies above $\sim 10\,\mathrm{TeV}$. Downgoing atmospheric muons, produced by cosmic rays interactions in the atmosphere constitute an enormous background to neutrino candidate events. This background is reduced by selecting well-reconstructed upgoing events since the muons cannot cross the Earth. The atmospheric neutrinos cannot be rejected this way, resulting in an irreducible background for high energy neutrino searches of galactic or extragalactic origin. Fortunately, a cosmic diffuse neutrino flux is expected to fall as E_ν^{-2} while the atmospheric neutrino spectrum is steeper, proportional to $E_\nu^{-3.7}$. This allows the extraction of the cosmic neutrino flux statistically by measuring eventual changes in the slope of the measured neutrino energy spectrum. The presence of a prompt component can be established in the same way.

In the present paper, three methods developed within the ANTARES collaboration aiming at the reconstruction of the muon energy are presented in section 2. At the end of this section their performance is presented and discussed. Section 3 contains a description of the unfolding procedure that will be used to reconstruct the atmospheric neutrino

energy spectrum. A test of the method on a neutrino Monte Carlo sample is performed.

2 Energy reconstruction

Relativistic muons passing through matter lose energy by means of various processes. The most common one is ionization of water molecules. Above 1 TeV radiative processes start dominating, leading to an almost linear dependence of the energy loss per unit length on the energy of the muon. Pair production, bremsstrahlung radiation and photonuclear interactions are the processes that are responsible for the increase of energy losses at higher energies. The stochastic nature of these phenomena requires the use of a mean energy loss per unit length approximation described by

$$-\frac{dE}{dx} = a(E) + b(E)E. \quad (1)$$

The first term in this equation is almost constant and accounts for the ionization energy losses while the second term describes the stochastic energy loss phenomena that dominate the energy losses above $1\,\mathrm{TeV}$.

The three strategies presented in the following are attempting to reconstruct the muon energy by basically inverting numerically equation 1 and using the amount of light detected by the telescope as an estimate for the muon energy loss. Technically, the first strategy uses a maximum likelihood method, the second a neural network, whereas the third uses only analytical approximations. In addition to these three energy reconstruction strategies, an energy estimator based on the average number of multiple hits recorded on the same OM during the event has been used for the diffuse flux search by the ANTARES collaboration [4, 5]. The results presented in this section are expectations from a realistic simulation of the detector, including detailed OM electronics response, photon tracking and optical background generation.

2.1 Maximum likelihood method

The first method presented here is based on a maximum likelihood estimation of the energy of the muon. We define a function which gives the likelihood that the observed time t and amplitude A of each hit on the OMs are the result of a given muon track. The likelihood function is defined as

$$\mathcal{L}(E) = \prod_{i}^{N_{OM}} P_i(E), \quad (2)$$

with the product running over all OMs within 300 m from the track and $P_i(E)$ the probability for individual OMs to record a hit of a certain amplitude or not. The form of $P_i(E)$ is given by

$$P(A;\langle n\rangle) = \sum_{\mathrm{n=1}}^{\mathrm{n_{max}}} P_p(n;\langle n\rangle)\cdot P_g(A;n), \quad (3)$$

$$P(0;\langle n\rangle) = e^{-\langle n\rangle} + P_{\mathrm{threshold}}(\langle n\rangle). \quad (4)$$

Equation 3 describes the probability of observing a certain amplitude A, given that the expected number of photoelectrons is $\langle n\rangle$. $P_p(n;\langle n\rangle)$ is the Poissonian probability of having n photoelectrons given that the expectation is $\langle n\rangle$, while the probability of n photoelectrons in the photocathode producing an amplitude A is given by $P_g(A;n)$ and is assumed to be a Gaussian. Equation 4 represents the Poissonian probability of having no photoelectrons, when the expectation is $\langle n\rangle$ photoelectrons, to which the probability P_{th} that the produced photoelectrons give amplitudes below the threshold of the electronics is added. The best energy estimate $\hat{E}$ is found by minimizing the negative logarithm of the likelihood function $\mathcal{L}(E)$. The energy dependence of the likelihood function is included in the expected number of photoelectrons $\langle n\rangle\,(E)$, which is calculated using the probability density functions of the photon arrival times on the OMs. In addition to the muon energy, these density functions depend on the track geometry i.e. distances of each OM to the track and the OM orientation compared to the track. A linear fit is applied to determine the relation between the energy estimate $\hat{E}$ and the true muon energy E_μ.

2.2 Artificial neural networks

A second method used to determine the muon energy is based on neural networks. An artificial neural network (ANN) is a simulated collection of interconnected nodes where each node produces a certain response to a set of input signals. A number of input parameters x_i are given to the input layer of the network. The values of the input parameters are transmitted to the nodes of the next layer, where a connection weight w_{ij} is assigned for each input x_i connected to a node j. The method described here implements a feed-forward neural network i.e. the nodes are grouped in layers and information flows only in one direction, from the input layer to the output node. Three hidden layers are being used in the ANN energy reconstruction method. The input to the j^{th} node of a layer is given by

$$z_j = \sum_i w_{ij}x_i + w_0, \quad (5)$$

where w_0 is the bias of the node. The summation is performed on the nodes of the previous layer, and its output is given by an activation function $g_j(z_j)$. The back propagation algorithm is used to determine the weights w_{ij} and the bias w_0 that optimize the performance of the neural networks method by minimizing an error function. The training is performed on Monte Carlo simulation samples. The network is a mapping from the space of input variables x_i onto a space of output variables y_i. The only output in the present method is the energy of the muon. The space, time and charge distributions of the recorded hits, the number of hits per OM at different distances from the muon track as well as various geometrical parameters such as the track direction and the distance from the track to the center of gravity of the detector are used as input parameters. The

optical background rate has also been proven to be a useful input parameter. The ANN energy reconstruction method uses a total of 56 input parameters.

2.3 dE/dx estimator

This method [6] is based on the construction of an energy loss dE/dx estimator ρ. The estimator is constructed as

$$\rho = \frac{\sum_{i=1}^{N_{\rm hits}} A_i}{L_\mu \cdot \epsilon}, \qquad (6)$$

where the sum of all hit amplitudes in the event is divided by the muon path length L_μ in the detector sensitive volume and the detector acceptance ϵ. The sensitive volume extends 2.5 effective attenuation lengths λ away from the instrumented volume. The acceptance ϵ is given by

$$\epsilon = \frac{1}{N_{OM}} \sum_{j=1}^{N_{OM}} \frac{\alpha(\theta)}{r_j} e^{\frac{-r_j}{\lambda}}, \qquad (7)$$

where N_{OM} is the number of OMs in the detector and $\alpha(\theta)$ is the photomultiplier tube's angular efficiency. The term $\frac{1}{r_j} e^{\frac{-r_j}{\lambda}}$ describes the number of photons reaching the OM after traveling distance r_j in water. The detector acceptance ϵ measures the fraction of light which can be seen by the OMs. An interpolation between tabulated values of the estimator ρ and the true muon energy E_μ is used to determine the relation between them.

2.4 Energy reconstruction performance

In order to study the performance of an energy reconstruction algorithm, one has to look at the mean and standard deviation of the $\log_{10}\frac{E_{\rm reco}}{E_{\rm true}}$ distribution. Since the performance is dependent on the muon energy these distributions are examined as function of the true energy. For all three methods presented here, these distributions are well described by a Gaussian fit. The mean of the Gaussian fit shows how far away is the energy estimate from the true energy while the standard deviation represents the resolution. A mean of the fit very close to zero and a small standard deviation indicate a high performance of the method. The bias and the resolution of the three methods as a function of the muon energy are shown in figures 1 and 2. For this study the true Monte Carlo track has been used, in an attempt to decouple the performance of the energy reconstruction from the quality of the track fit. The overestimation of the true energy by the maximum likelihood and dE/dx methods for lower energies, as shown in figure 1, is due to the fact that for muon energies lower than a few TeV the energy loss is almost constant, making it difficult to distinguish between e.g. a 100 Gev and a 500 GeV muon. The optical background from potassium decay in sea water and bioluminescence can affect the performance below the critical energy since these low energy events

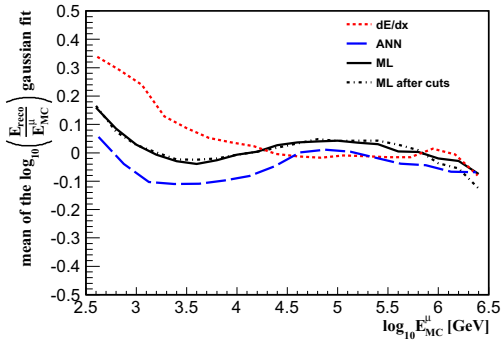

Figure 1: Mean of the gaussian fit on $\log_{10}\frac{E_{reco}}{E_{MC}}$ distribution as a function of the true muon energy for the different methods. A perfectly unbiased energy reconstruction is characterized by zero mean.

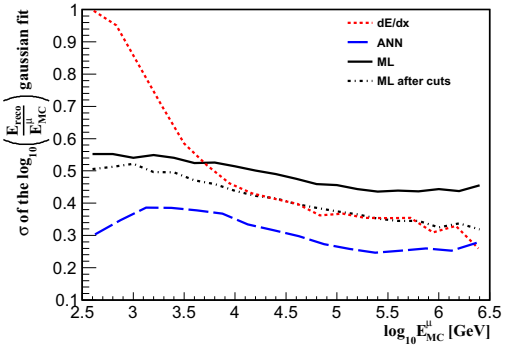

Figure 2: Standard deviation of the gaussian fit on $\log_{10}\frac{E_{reco}}{E_{MC}}$ distribution as a function of the true muon energy for the different methods. A small standard deviation corresponds to a good resolution.

do not produce sufficient light and the effect of the optical background noise is more pronounced. The resolution of the energy reconstruction methods presented here is below 0.5 in $\log_{10}E\,[GeV]$ at energies above 5-10 TeV. The maximum likelihood and artificial neural networks methods have a more stable behavior with the neural network approach reaching as low as 0.25 at higher energies.

The impact of using the reconstructed track was estimated for the maximum likelihood method, using tracks reconstructed with the standard ANTARES reconstruction strategy [2] and selected to increase the population of well reconstructed tracks and minimize the atmospheric muon background events. The selection efficiency, estimated from simulation, varies between 10% at 1 TeV and 20% at 100 TeV with almost 99% purity. The median angular resolution is 0.25° above 1 TeV. The performance of the energy reconstruction using the reconstructed track is shown in figures 1 and 2, indicated as "ML after cuts" in the legend.

3 Atmospheric neutrino spectrum deconvolution

The atmospheric neutrino spectrum cannot be reconstructed by just assigning each event to the corresponding estimated energy bin. This is due to the limited resolution of the energy reconstruction. The atmospheric neutrino spectrum is steeply falling so events with overestimated energy will introduce a large distortion on the spectrum at high energies. This can be overcome by the use of unfolding techniques [7]. The unfolding is performed following the method presented in [8], using the package *RooUnfold* [9].

The unfolding problem can be formulated as follows. The true neutrino spectrum $x(E)$ is distorted by a number of different factors. The energy that is measured is only part of the muon energy, depending on the part of its track that is visible by the detector. An additional distortion comes from the fact that the muon carries only a fraction of the parent neutrino energy. Finally, the limited resolution of the energy reconstruction itself contributes further to the distortion of the spectrum. Let $y(E)$ be the vector of the measured spectrum, then in matrix notation the problem is expressed as $y(E) = Rx(y)$. R is called the response matrix and describes the effect of the detector and the reconstruction on the true spectrum. The response matrix is constructed by means of Monte Carlo simulation. A simple matrix inversion turns out to be a naive attempt to solve the problem since statistical fluctuations in the data vector $x(E)$ will give a highly oscillating solution $y(E)$ with large errors. The problem can be located and addressed by performing a singular value decomposition on the matrix $R = USV^T$. This is equivalent to expressing the solution vector as a sum of terms weighted by the inverse singular values of the matrix S. The small singular values are responsible for enhancing the statistically insignificant coefficients in the solution. These coefficients can be damped out by imposing an additional constraint on the smoothness of the solution $y(E)$. Since there is no reason to expect abrupt irregularities in the spectrum, the solution is not allowed to exhibit significant bin to bin variations. Various methods exist to decide the amount of regularization one should impose on the solution in order to have the optimal trade off between bias towards the expected solution and the size of the covariance matrix.

The unfolding method was tested using the results from the maximum likelihood energy reconstruction on a realistic 12 line configuration Monte Carlo dataset, equivalent to 3 years of data taking livetime. The response matrix was constructed assuming the atmospheric neutrino flux parametrizations from [10, 11] while the fluxes used to generate the test data are taken from [12, 13]. After unfolding to the neutrino spectrum at the detector level, the atmospheric neutrino flux (figure 3) can be determined by including the effects of neutrino propagation through the Earth and detector efficiency. The method succeeds in reconstructing the "true" Monte Carlo neutrino spectrum.

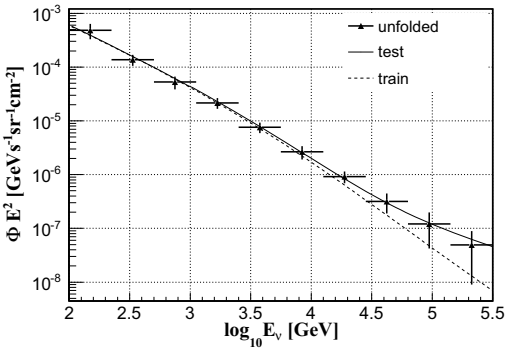

Figure 3: Application of the unfolding method on a realistic Monte Carlo dataset for the determination of the atmospheric neutrino flux weighted with E_ν^2. Systematic effects are not included. See text for explanation of the fluxes.

4 Conclusions

Three different methods for muon energy reconstruction currently under evaluation in ANTARES have been described. Their precision varies from 0.25 to 0.5 in $\log_{10}E\,[GeV]$ above 5-10 TeV when the true track geometry is used as an input. This resolution may be improved for particular classes of events, especially in the case of the maximum likelihood and dE/dx methods. The results of the maximum likelihood reconstruction on a simulated dataset have been used to test the unfolding method. Systematic uncertainties are under study and have not been included in these proceedings.

References

[1] ANTARES Collaboration, Astroparticle Physics vol.34, 9:652-662, 2011
[2] A. Heijboer, PhD Thesis, Univ. van Amsterdam, 2004
[3] R. Enberg, M. H. Reno, I. Sarcevic, Phys. Rev. **D78**:043005, 2008
[4] ANTARES Collaboration, Phys. Lett. **B696**:16, 2011
[5] F. Schüssler for the ANTARES Collaboration, these proceedings, 2011
[6] A. Romeyer, PhD Thesis, Universitè Paris VII, 2003
[7] J. D. Zornoza, PhD Thesis, Univ. de Valencia, 2005
[8] A. Hoecker and V. Kartvelishvili, Nucl. Inst. & Meth. in Phys. Res. **A372**:469-48, 1996
[9] T. Adye, Unfolding algorithms and tests using RooUnfold, arXiv:1105.1160v1
[10] M. Honda, T. Kajita, K. Kasahara, S. Midorikawa, T. Sanuki, Phys. Rev. **D75**:043006, 2007
[11] A.D. Martin, M.G. Ryskin, A.M. Stasto, Acta Phys. Pol. **B34**,3273, 2003
[12] G. D. Barr, T. K. Gaisser, P. Lipari, S. Robins and T. Stanev, Phys. Rev. **D70**:023006, 2004
[13] C.G.S. Costa, Astropart. Phys. **16**:193, 2001

32ND INTERNATIONAL COSMIC RAY CONFERENCE, BEIJING 2011

Search for point sources with the ANTARES neutrino telescope using the EM algorithm

JUAN PABLO GÓMEZ-GONZÁLEZ[1], ON BEHALF OF THE ANTARES COLLABORATION.
[1] *IFIC - Instituto de Física Corpuscular, Edificios de Investigación de Paterna, CSIC - Universitat de València, Apdo. de Correos 22085, 46071 Valencia, Spain.*
jpablo@ific.uv.es
DOI: 10.7529/ICRC2011/V04/0678

Abstract: The ANTARES detector, currently the largest deep-sea neutrino telescope in the Northern Hemisphere, consists of a three-dimensional array of 885 optical modules arranged over 12 detection lines anchored at a depth of 2475 m in the Mediterranean Sea, 40 km offshore from Toulon (France). The photomultiplier tubes detect the Cherenkov light induced by the charged particles produced in the interaction of cosmic neutrinos with the matter surrounding the detector. The trajectories of the resulting muons are reconstructed with high precision, revealing the direction of the incoming neutrinos. The main scientific goal of ANTARES is the search for high energy neutrinos coming from astrophysical sources. This contribution describes a point source search using a dedicated clustering algorithm, based on the analytical maximization of the likelihood. The results of shuch analysis using four years of data will be presented.

Keywords: ANTARES, neutrino telescopes, point source search, EM algorithm.

1 Introduction

The ANTARES neutrino telescope [1] started data taking in 2007 and is fully operational since 2008. Located at 40 km off the coast of Toulon it consists of 12 detection lines anchored to the seabed at a depth of 2475 m and sustained vertically by means of buoys. Each line has 25 floors (or storeys) composed by a triplet of photomultiplier tubes (PMTs) housed in pressure resistant glass spheres called optical modules (OMs). The OMs are facing downward at 45° from the vertical for an increased detection- efficiency for up-going neutrinos.

This three-dimensional photo-detector array detects the Cherenkov light emitted by the charged leptons originated in the interaction of high energy neutrinos with the matter surrounding the detector. The tracks of the produced muons can be reconstructed using the position and timing information of the hits arriving to the PMTs. An accurate timing and position calibration [2] of the detector OMs is necessary in order to achieve the best attainable angular resolution.

The main goal of the experiment is the detection of high energy neutrinos from extraterrestial origin, and one of the most promising ways of establishing their existence is the search for point sources. Here, we present such a search using data collected between years 2007 and 2010 for a total of 813 days of livetime. In section 2 the track reconstruction method and data selection criteria are described. The detector performance is reviewed in section 3. The clustering algorithm applied in this analysis is explained in section 3. Finally the search results are presented in section 4.

2 Data selection and track reconstruction

Data runs used in this analysis were recorded in the first four years of detector operation. Taking into account the time spent on sea operations (like the deployment of new lines) and sporadic data taking problems of the detector, the total livetime of the analysis is 813 days; about 77% of this data were collected using 9, 10 and 12 detection lines, while the remaining 183 days correspond to data gathered with the initial 5-lines configuration.

The reconstruction method [3] is based on the maximization of the likelihood function describing the probability density function (PDF) for the residuals, defined as the difference between the measured hit time and the expected arrival time of the hits. The goodness of the track reconstruction is described by the Λ parameter, which is basically the log-likelihood of the fitted track. This parameter can be used to eliminate badly reconstructed tracks by selecting an appropriate cut on the Λ value. The corresponding cumulative Λ distribution for events reconstructed as upgoing is shown on Figure 1. The contribution from the different components of the expected background is also included. The simulation reproduces well the data.

For this analysis atmospheric muons were simulated using the MUPAGE package [4], while the atmospheric neutrinos were generated with the GENNEU [5] package according to the Bartol model [6].

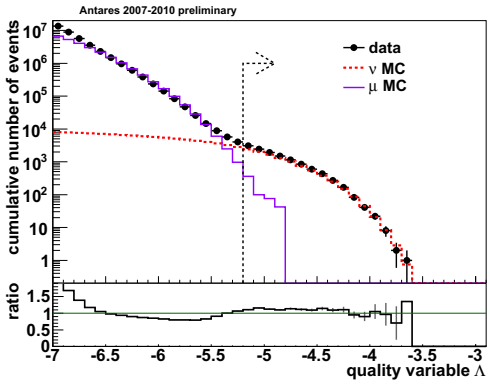

Figure 1: Cumulative distribution of the quality of the reconstruction parameter for data and MC upgoing events.

A cut on the quality of the reconstruction at $\Lambda \geq$ -5.2 was found to be the optimal for the search discovery potential using muon tracks recostructed as upward going ($\theta < 90°$). Additionally, the uncertainty on the muon direction estimated from the fit is required to be $\leq 1°$. The selected sample contains 3058 events, out of which it is estimated from MC simulations that about 84% are neutrino events and only 16% downgoing atmospheric muons mis-reconstructed as upgoing.

3 Detector performance

The two main parameters describing the performance of a neutrino telescope are the angular resolution and the acceptance. Both parameters are estimated from simulations. Figure 2 shows the cumulative angular resolution for upgoing neutrino events following an E^{-2} spectrum and complying the selection criteria described in Section 2. The plot shows that roughly 80% of the signal events are reconstructed with an angular error less than $1°$, being the median value of the reconstruction error equal to $0.46 \pm 0.1°$. The uncertainty on this value has been computed considering all the effects leading to a deterioration of the detector timing resolution [7]. In addition, the uncertainty on the absolute orientation of the detector, which is estimated to be of the order of $0.1°$, is also taken into account in the limits computation (see section 4).

The acceptance allows us to relate the detected event-rate with the neutrino flux of the source at the Earth, and it is shown on Figure 3 as a function of the sinus of the declination considering a flux normalization $\phi = 10^{-8} GeV^{-1} cm^{-2} s^{-1}$. Based on the agreement between data and simulations a 15% systematic error on the detection efficiency has been considered for the limits calculation.

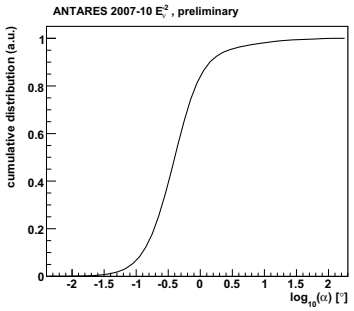

Figure 2: Cumulative angular resolution for E^{-2} upgoing neutrinos selected for this analysis.

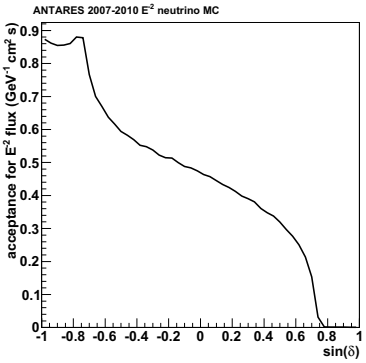

Figure 3: Detector acceptance as a function of the sinus of the declination.

4 Clustering method

Point source clustering techniques try to identify and separate events coming from real sources from background events. The Expectation-Maximization (EM) algorithm [8] used in this analysis is a pattern recognition algorithm that analytically maximizes the likelihood in finite mixture problems. These mixture models are different groups of data described by different density components. In the case of a search for neutrino point sources [9] the mixture problem can be expressed as:

$$p(\mathbf{x}) = \pi_{bg} P_{bg}(\delta) + \pi_{sg} P_{sg}(\mathbf{x}; \mu; \mathbf{\Sigma}) \cdot (P_{sg}^{nhits} / P_{bg}^{nhits}) \quad (1)$$

where π_{bg} and π_{sg} are the so-called mixing proportions, $\mathbf{x} = (\alpha, \delta)$ is the position of the signal event in equatorial coordinates, $\mu = (\mu_\alpha, \mu)$ and $\mathbf{\Sigma} = (\sigma_\alpha, \sigma)$ are, respectivly, the mean and the covariance vector of the Gaussian distribution, and P^{nhits} is the probability for an event to be reconstructed using $nhits$ number of hits.

In this analysis the expected density distributions of background and signal events are parametrized. The pdf describing the background is obtained from the declination

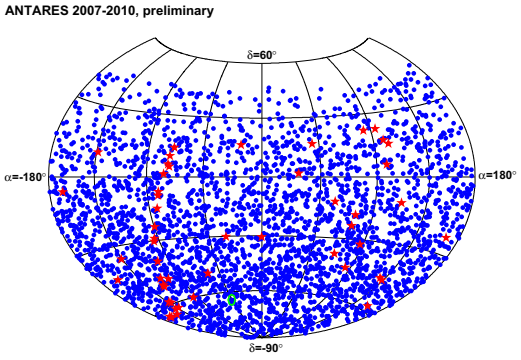

Figure 4: Skymap with the equatorial coordinates of the 3058 events selected. The position of the most significant cluster is denoted by the green circle and the coordinates of the candidate list sources are indicated with the stars.

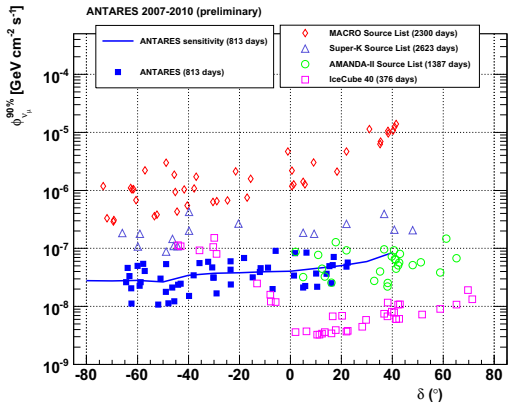

Figure 5: Limits on the E_ν^{-2} flux for the 51 sources in the candidate list search. Upper limits previously reported by other neutrino experiments for both Northern and Southern sky are shown. The ANTARES sensitivity computed in this analysis is also included.

distribution of data events, while the source signals are supposed to follow a two-dimensional Gaussian distribution.

The EM algorithm works in two steps. In the first step called "Expectation" the expected value of the complete data log-likelihood is computed for a given set of parameters. In the "Maximization" step a new set of parameters that maximizes the likelihood is found. In our case, the parameters to be maximized are the two components of the Gaussian width, the expected number of signal events and, in the full sky search (see next section), the coordinates of the signal source.

After likelihood maximization the so called test-statistic, defined as the likelihood ratio of the two mixture models, is computed. Lower values of this quantity indicate that data is more likely to be produced by the background, while larger values are more likely to be produced by the presence of the searched signal.

5 Results

Two different searches for point sources have been considered in this analysis. In the first approach a blind survey is done looking everywhere in the whole ANTARES visible sky. The second search used a catalog of candidate sources to look for presence of signal at particular locations in the sky. The candidate list of sources includes both galactic and extra-galactic sources known to be gamma-ray emitters. The detector visibility and PSF was taking into account when defining the list.

No significant excess of events was found neither in the full sky search, nor in the candidate list search. The most signal-like cluster was found at ($\delta = -64.87°$, $\alpha = -46.49°$) in the all sky survey. For this cluster a 2.6% excess p-value is found.

The locations (in equatorial coordinates) of the most significant cluster, the 3058 events selected and the 51 candidate sources are shown on figure 4. Upper limits [1] on the E^{-2} neutrino flux spectrum are reported in table 1 and in figure 5 as a function of the declination for the sources in the candidate list. The ANTARES sensitivity (defined as the median value of the expected limit) it is shown, as well as limits reported by other neutrino experiments included for comparison.

6 Conclusions

This contribution presented the analysis of 813 days of livetime using data collected in the first four years of the ANTARES neutrino telescope operation. No statistically significant excess of events has been found neither in the search using a candidate list of interesting sources, nor in the full sky search. The most significant cluster, with a post-trial probability of 2.6 % was found at coordinates $\delta = -64.87°$, $\alpha = -46.49°$. Some of the most stringent limits to E_ν^{-2} flux were obtained for sources located in the ANTARES field of view. Using a different search method the results presented here are consistent with the main analysis [10] reporting upper limits for the 51 candidate sources using the Feldman-Cousins prescription.

I greatfully acknowledge the financial support of MICINN (FPA2009-13983-C02-01 and MultiDark CSD2009-00064) and of Generalitat Valenciana (Prometeo/2009/026).

1. Here we follow the Neyman prescription.

Source	ra (°)	δ (°)	Q	p-value	ϕ^{90CL}
3C 279	-165.95	-5.79	1.97	0.04	9.1
GX 339-4	-104.30	-48.79	1.62	0.06	5.4
HESS J1023-575	155.83	-57.76	1.49	0.07	5.4
MGRO J1908+06	-73.01	6.27	1.12	0.09	8.5
RGB J0152+017	28.17	1.79	1.16	0.09	8.3
ESO 139-G12	-95.59	-59.94	1.02	0.11	5.0
ICECUBE	75.45	-18.15	0.74	0.14	6.8
PSR B1259-63	-164.30	-63.83	0.63	0.16	4.6
PKS 0548-322	87.67	-32.27	0.41	0.19	5.9
PKS 1454-354	-135.64	-35.67	0.39	0.20	5.6
1ES 1101-232	165.91	-23.49	0.35	0.21	6.0
Cir X-1	-129.83	-57.17	0.30	0.22	4.1
Geminga	98.31	17.01	0.25	0.22	7.1
H 2356-309	-0.22	-30.63	0.02	0.34	4.7
PKS 0454-234	74.27	-23.43	0.00	1	4.3
HESS J1356-645	-151.00	-64.50	0.00	1	2.6
HESS J1837-069	-80.59	-6.95	0.00	1	2.0
PKS 2005-489	-57.63	-48.82	0.00	1	1.8
HESS J1616-508	-116.03	-50.97	0.00	1	3.0
HESS J1503-582	-133.54	-58.74	0.00	1	2.6
HESS J1632-478	-111.96	-47.82	0.00	1	1.1
MSH 15-52	-131.47	-59.16	0.00	1	2.3
Galactic Center	-93.58	-29.01	0.00	1	1.7
HESS J1303-631	-164.23	-63.20	0.00	1	3.3
HESS J1834-087	-81.31	-8.76	0.00	1	4.7
PKS 1502+106	-133.90	10.52	0.00	1	2.2
SS 433	-72.04	4.98	0.00	1	2.1
HESS J1614-518	-116.42	-51.82	0.00	1	1.1
RX J1713.7-3946	-101.75	-39.75	0.00	1	1.5
3C454.3	-16.50	16.15	0.00	1	2.5
W28	-89.57	-23.34	0.00	1	2.4
HESS J0632+057	98.24	1.81	0.00	1	2.3
PKS 2155-304	-30.28	-30.22	0.00	1	3.2
HESS J1741-302	-94.75	-30.20	0.00	1	3.2
Centaurus A	-158.64	-43.02	0.00	1	2.5
RX J0852.0-4622	133.00	-46.37	0.00	1	2.1
Vela X	128.75	-45.60	0.00	1	1.2
W51C	-69.25	14.19	0.00	1	3.6
PKS 0426-380	67.17	-37.93	0.00	1	3.4
LS 5039	-83.44	-14.83	0.00	1	3.2
W44	-75.96	1.38	0.00	1	3.4
RCW 86	-139.32	-62.48	0.00	1	2.1
Crab	83.63	22.01	0.00	1	4.9
HESS J1507-622	-133.28	-62.34	0.00	1	1.1
1ES 0347-121	17.35	-11.99	0.00	1	3.9
VER J0648+152	102.20	15.27	0.00	1	5.0
PKS 0537-441	84.71	-44.08	0.00	1	2.4
HESS J1912+101	-71.79	10.15	0.00	1	3.7
PKS 0235+164	39.66	16.61	0.00	1	1.2
IC443	94.21	22.51	0.00	1	1.7
PKS 0727-11	112.58	-11.70	0.00	1	4.6

Table 1: Results for the 51 sources used in the candidate list search. The equatorial coordinates of the sources, Q values, number of fitted signal events, pre-trial p-values and upper limits on the E_ν^{-2} flux ($10^{-8} GeV^{-1} cm^{-2} s^{-1}$) are shown.

References

[1] M. Ageron et. al., *ANTARES: the first undersea neutrino telescope*, 2011, arXiv:1104.1607v1.

[2] J. A. Aguilar et al., *Time Calibration of the ANTARES neutrino Telescope.*, Astroparticle Physics, 2011, **34**, 539-549.

[3] A. Heijboer, *Track reconstruction and point source searches with ANTARES*, PhD thesis, Universitet van Amsterdam, 2004, available at http://antares.in2p3.fr/Publications/index.html#thesis.

[4] G. Carminati et al., *Atmospheric MUons from PArametric formulas: a fast GEnerator for neutrino telescopes (MUPAGE)* , Comput. Phys. Commun. 179, 915-923 (2008) XXX

[5] D. Bailey, *Monte Carlo tools and analysis methods for understanding the ANTARES experiment and predicting its sensitivity to dark/matter, PhD thesis, Oxford University*, 2002, available at http://antares.in2p3.fr/Publications/index.html#thesis.

[6] P. Lipari et al., Phys. Rev. D, 1996, **53**, 1314.

[7] S. Adrián-Martínez et. al., *First Search for Point Sources of High Energy Cosmic Neutrinos with the ANTARES Neutrino Telescope* submitted to Astrophysical Journal Letters, arXiv:1108.0292v1.

[8] A. P. Dempster, N. M. Laird, and D.B. Rubin, J. Royas Statistical Soc. Series **B38**, 1997.

[9] J. A. Aguilar and J. J. Hernández-Rey, Astrop. Phys. **29** (2008).

[10] C. Bogazzi, *Search for point sources of high energy cosmic neutrinos with the ANTARES telescope*, these proceedings, 2011.

32ND INTERNATIONAL COSMIC RAY CONFERENCE, BEIJING 2011

Studying Cosmic Ray Composition around the knee region with the ANTARES Telescope.

CHING-CHENG HSU [1]
[1]*NIKHEF*

cchsu@nikhef.nl

DOI: 10.7529/ICRC2011/V04/0679

Abstract: The composition of the cosmic rays in the "knee" region ($\approx 10^4$ TeV/nucleus) of the all particle spectrum is considered to be the result of the particle acceleration and propagation from the astrophysical sources. The steeply falling CR spectrum makes a direct measurement of the composition difficult, but it can be inferred from the measurements of the showers generated by the interaction of the primary cosmic ray with the Earth atmosphere. In particular the characteristics of the muon bundles produced in the showers depend on the primary CR nature. The ANTARES telescope is situated 2.5 km under the Mediterranean Sea off the coast of Toulon, France. It is taking data in its complete configuration since May 2008 with nearly 900 photomultipliers installed on 12 lines. The trigger rate is a few Hz dominated by atmospheric muons. A method using a multiple layered neural network as a classifier was developed to estimate the relative contribution of proton and iron showers to the CR spectrum from the energy and multiplicity distribution of the muon tracks reaching the ANTARES detector. The performance of the method estimated from simulation will be discussed.

Keywords: Cosmic Ray, Knee, Composition, Antares

1 Introduction

Although the main goal of ANTARES telescope is to look for high energy neutrinos coming from the deep space, it also provides us opportunities to study cosmic ray physics. One of the most important topics is to distinguish the different chemical compositions around knee region of its spectrum. The cosmic ray spectrum is known as a power law with power index about -2.7 up to few PeV. Then the slope changes to -3.1 until the energy around 4×10^{18} eV [1]. The *knee* was first observed by the MSU group in 1970s, then has been confirmed by many groups afterward. The origin of the *knee* could be generally summarized into either astrophysical origin or particle physics origin. Nevertheless it is still a puzzle and generally believed to be a key issue to the problem of the origin of galactic cosmic rays.

Most people attributed the knee to the sudden reduction in Galactic trapping efficiency. A popular explanation is that the knee is associated with an upper limit of acceleration energy by galactic supernovae. Another popular scenario is the leakage of particles from the Galaxy, since the Larmor radius of a proton in the galactic magnetic field increases with its energy and finally exceeds the thickness of the galactic disk. Additionally, there are a minority of theorists who proposed that the knee is due to a single, recent and local supernova remnant (SNR) or a rapidly rotating pulsar interacting with radiation from its parent SNR.[2]

If the knee is caused by the maximum energy attained during the acceleration process or it is due to leakage from the Galaxy, the energy spectra for individual elements with charge Z would exhibit a cut-off at an energy $E_c^Z = \mathrm{Z} \times E_c^p$, where E_c^p is the cut-off energy of protons. The sum of the flux of all elements with their individual cut-off makes up the all-particle spectrum. In this picture the knee is related to the proton cut-off and the steeper spectrum above the knee is a consequence of the subsequent cut-off of heavier elements, resulting in a relatively smooth spectrum above the knee [3].

2 Composition Model

In the so-called polygonato model, the general form for the flux of primary nuclei of charge Z and energy E_0 is

$$\frac{d\phi_Z}{dE_0} = \phi_Z^0[1 + (\frac{E_0}{E_{trans}})^{\epsilon_c}]^{\frac{-\Delta\gamma}{\epsilon_c}}$$

where the transition energy E_{trans} could be determined according to three different scenarios. The parameter ϵ_c determines the smoothness of the transition, and γ_c is the hypothetical slope beyond the knee. E_{trans} is the cut-off energy. Under the polygonato model: three different scenarios are proposed :

- Rigidity dependent: From the astrophysical point of view, a rigidity dependent cut-off $E_{trans} = \hat{Ep} \cdot \mathrm{Z}$ is the most likely description if we take into account the acceleration and propagation of the cosmic rays.

- Mass dependent: This model predicts that the change in the power law index depends on the mass E_{trans} = $\hat{Ep}$ × A instead of the charge. This scenario leads to a steeper energy spectrum after the cut-off. The sharp cut-off would be hard to explain on astrophysical reasons. Maybe a nearby source or a new type of interaction in the atmosphere could yield such cut-off [3].

- Constant Composition: E_{trans} = $\hat{Ep}$. The knee is explained by a common steepening in the energy spectrum; it occurs for all the particles at the same energy.

So far, the best measurement of the compositions around the knee region was done by KASCADE [4]. The measured primary energy spectra show that the knee in the all particle spectrum is due to a steepening of the light elements spectra.

3 Analysis Strategies

The ANTARES detector is located at 40 km off the coast of Toulon, France, at a depth of 2475 m in the Mediterranean Sea. It consists of 12 exible strings, each with a total height of 450 m, separated by about 60 m. They are anchored to the sea bed and kept near vertical by buoys at the top of the strings. Each string carries a total of 75 10-inch Hamamatsu photo multipliers (PMTs) housed in glass spheres, the so-called optical modules (OM) [5]. The OMs are arranged in 25 storeys (three optical modules per storey) separated by 14.5 m. The detector was starting taking data in 2007 and was fully completed in May 2009.
Since ANTARES is deeply buried under the sea, only the muon components from the air shower will survive at detector level. The muons will emit Cherenkov radiation only when passing through the sea water, which can be detected using photomultiplier tubes. To be registered by the ANTARES detector, muons have to travel at least 2.5 km of sea water and still be energetic enough to trigger the detector. The energy threshold for vertical down-going muon is around 500 GeV. At large zenith angles, the threshold increases because of the increasing depth of the sea water. The muon bundles properties (such as multiplicity) is strongly related to the primary energy and species of the nuclei. However, the ANTARES detector cannot resolve individual muons from a muon bundle. Hopefully, the topology of the hit distributions in space and time could give pertinent information about the properties of the muons in the bundles. Two useful analysis methods are combined and then applied on MC samples in this analysis. The first one is a cluster finding algorithm, and the second one is an electromagnetic shower searching algorithm[6].
In both analysis methods, we rotate our coordinate system such that the z axis is along the reconstructed muon track axis. We define the plane which is passing through the detector center and perpendicular to the reconstructed track

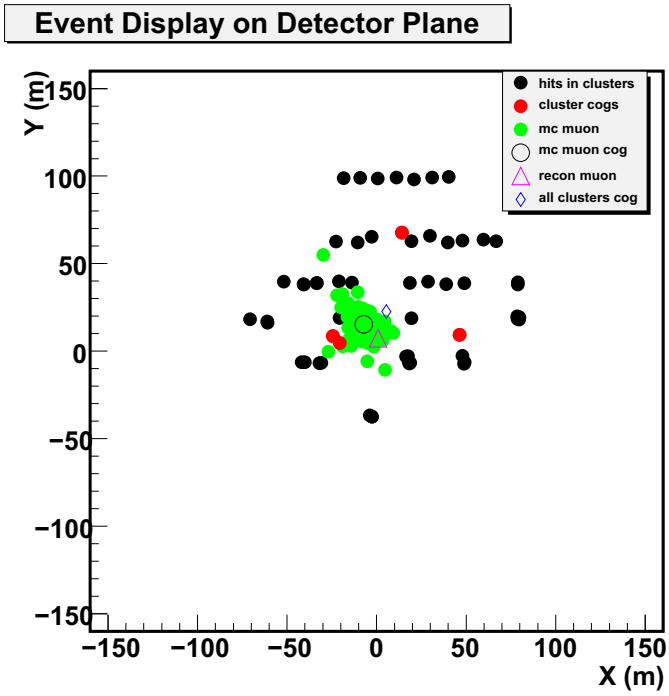

Figure 1: Typical patterns produced by muons bundles originating from primary protons(left) and iron nuclei with the same energy of muon bundle pattern on the detector plane.

as *detection plane*. Fig. 1 shows the snapshot of muon bundle patterns on the detector plane from the same primary energy of proton and iron nuclei. The projections of all the hits positions on the detection plane are also calculated, including the time correction information.

In the cluster finding algorithm, the clusters are formed if the hits fulfill the following three conditions:

- $\mid T_i - T_j \mid \leq \mid r_i - r_j \mid$ /C/n_g where T_i and T_j are the time for any two hit pairs in the hit cluster. r_i and r_j are the associated positions of these two hits.

- Any two hits within clusters should be in the same or neighboring strings or floors.

- $\mid T_i - T_j \mid \leq \mid (z_i - z_j) \mid$/C + d × $tan\theta_c$ /c + T_{ext}, where T_{ext} are maximum extra time, here we set 20 ns; T_i and T_j are again time informations of two hits. z_i and z_j are the rotated Z positions of two hits.

In order to quantify the cluster patterns from cosmic showers initiated by different groups of elements, we try to parametrize the hit patterns. There are two kinds of parameters in our analysis:

- Cluster-wise parameters: The parameters which are related to each individual clusters, for instances, the

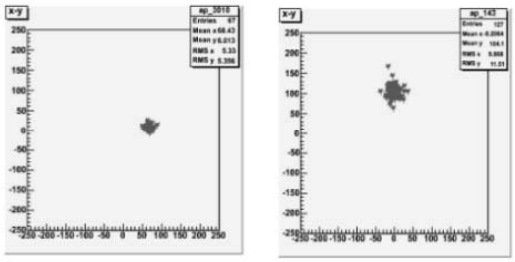

Figure 2: The hit patterns projection on the detector plane and then parametrized by cluster algorithm.

"Size" (total number of photoelectrons in one cluster), the Area: the area which contains 90 % of the hits...

- Event-wise parameters: The parameters which are related to all different clusters within one event, such as the Center of Gravity(C.O.G.) of all the clusters, X_{COG}, total number of clusters $N_{cluster}$ ...

In total, we have about 25 event-wise parameters and 12 cluster-wise parameters. One example of pattern after parametrization superimposed with reconstruction position of the muon tracks(bundles) is presented in Fig 2.

On the other hand, the ANTARES electromagnetic shower searching method gives us additional information about the muon bundles. The high energy muons suffer from catastrophic energy losses. Once it happens, electromagnetic showers are initiated either by γ or e^+ and e^- pairs. The radiation length of the electron is about 30 cm/gm^2. The spacing between optical modules and strings is large compared to the shower extent. Instead of projection hits information on the detector plane, we project all the hits on the reconstructed axis and search for the peak using the T-Spectrum function in ROOT package. The details of the algorithm could be found in [6]. Two more parameters are obtained by this methods. They are the number of showers N_{shower} and the amplitude of the baseline $N_{baseline}$ from the algorithm.

Combining the cluster-finding and shower-finding algorithms, we have in total 37 parameters. Each parameter gives different discrimination powers for the chemical species. To achieve multi-dimensional comparisons, we use the existing package "TMVA" (Toolkit for Multivariate Data Analysis with ROOT) for this analysis [8]. TMVA is a toolkit which hosts a large variety of multivariate classification algorithms. Training, testing, performance evaluation and application of all available classifiers is carried out simultaneously.

Several methods are implemented inside TMVA packages. In order to cross check the results, four different methods were chosen for this analysis. They are Multilayer Perception (MLP), (MLPBNN), (TMlpANN) and k-Nearest Neighbour (k-NN). The performances of multivariate analysis are sensitive to correlation of the training parameters. Thus, to reduce the un-important parameters is necessary. We input each parameter into the analysis individually and then we kept only the top five rank of the parameters which gave us the most distinguished power. These five parameters are N_{hit}, $N_{cluster}$ and N_{npe}, representing number of hits, clusters, and photoelectrons from cluster-finding algorithm. N_{shower} and Base are the numbers of showers and the number of photoelectrons of the baseline from EM shower-finding algorithm.

Efficiency	P Purity	Fe Purity	P eff.	Fe eff.
30%-70%	0.7	0.66	0.68	0.77
1.8%-92.8%	0.76	0.62	0.61	0.81

Table 1: The estimated purity and rejecting efficiency for two different combinations of pseudo-data sets.

4 Analysis on MC samples

A full MC simulation was adopted in this analysis. The air showers induced by the primary nuclei with energy ranging from 1 to 10^5 TeV /nucleon and zenith angle between 0° and 85° using the CORSIKA software (Version 6.2) [7] and the hadronic interaction model QGSJET.01c. All muons reaching the sea level, with energies larger than threshold energy, are propagated through sea water to the detector. At last, muons are transported through the ANTARES sensitive volume, Cherenkov light is produced and the detector response is simulated. Background noises were added afterward. The trigger is done by standard ANTARES trigger. The muon direction and position are reconstructed using a multi-stage fitting procedure, which basically maximizes the likelihood of the observed hit times as a function of the muon direction and position[9].

We further divide the MC samples into 3 independent subsets for training, testing and evaluating in TMVA analysis. The relative sizes of the three subsets are 40%, 30% and 30%. Each event is with proper weight according to different spectrum models. The iron component is selected as source of signal and the rest of the four groups of elements are tagged as sources of background. The "pure" signal distributions are obtained, if we assume that the all coming cosmic rays are iron. On the other hand, the souces of the background samples are coming from the superposition of the rest of four groups of elemetns assuming all cosmic rays are from individual element. The distributions of N_{shower} and $N_{cluster}$ assuming the all particle spectrum are proton and iron are shown in Fig 3.

We carefully checked the output of neural network from test samples in order to avoid the over-training effects.

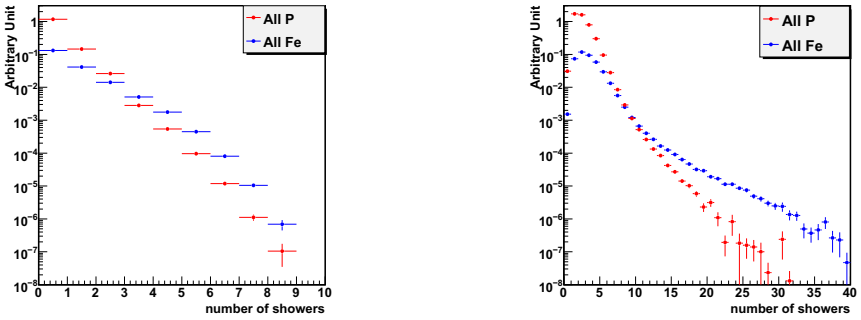

Figure 3: The relative distribution of N_{shower} and $N_{cluster}$ parameters after the reconstruction quality cut assuming that all the particles from cosmic rays are proton and iron.

5 Results and Conclusions

The training and test events fed into the neural network were subjected to a series of cuts. The main quality cut is the so-called Λ cut [9] in order to keep good quality on reconstructed events. For testing the method, we mixed proton and iron components from our pseudo-data set with $\approx$ 30%-70% and 1.8%-98.2%, individually. All the training, testing and psedo-data are applied on the same analysis chains and cuts. The output of neural network training on the proton and iron components is shown on the Fig 4. The green curve region (left) corresponds to the true proton events, while the red curve region (right) corresponds to the true iron events. The blue curve in the plot shows the psedo-data events with the 1.8%-98.2% configuration. The purity and rejecting efficiency for proton and iron are listed in the Table 1 if we cut on the MLP output value at 0.45, where the S/$\sqrt{S+B}$ is maximized. In addition, instead of applying a cut on the MLP output value. we adjust proton and iron distibutions as a whole to fit the psedo-data distribution ("Template fitting" in roofit). We found that the χ^2/ndf are 23.6/21 and 18.1/21 for the two configurations, respectively. The fitted numbers from the two-component model are satisfatory. In the future, we are planing to add more chemical compositions in the backgrounds and add magnesium in the source category. We have developed a method to estimate the ratio of the heavy elements in the triggered cosmic ray events based on the information from the muon tracks and electromagnetic showers in ANTARES detector. To combine all the discrimination powers from established multi-parameters needs the help from multi-variate analysis (neural network). The estimated ratio from heavy elements will be used as an input for calculating the true ratios between elements in original cosmic ray spectra. Further calculating the efficiencies from triggers, combinations of different cuts and effective areas are necessary and will be done. The analysis of ANTARES real data with the goal of deriving ratio between different groups of elements in the cosmic ray spectra is ongoing and will yield results in the near future.

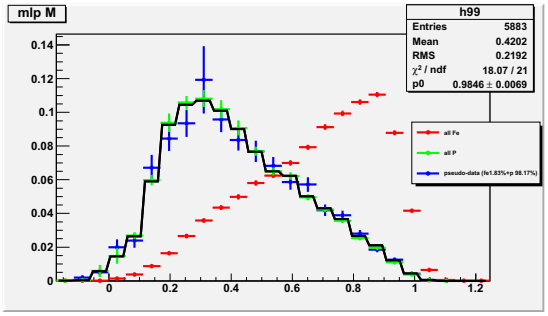

Figure 4: Output computed by the neural network in the presence of a mixture of proton and iron components from the pseudo-data sets. The green curve region (left) corresponds to the true proton events, while the red curve region (right) corresponds to the true iron events. The artificial mixture of pseudo-data is in blue.

References

[1] Bluemer, J. and Engel, R. and Hoerandel, J. R. Prog. Part. Nucl. Phys. 2009 **63**: 293-338
[2] Wibig, Tadeusz and Wolfendale, Arnold W. astro-ph/1012.4562 2010
[3] Hoerandel, J. R. Astropart. Phys. 2004 **21**: 241-265
[4] T. Antoni *et al.* [The KASCADE Collaboration] Astropart. Phys. **24** (2005) 1
[5] ANTARES Collaboration 2011 **astro-ph/1104.1607** :
[6] Mangano, Salvatore Nucl. Instrum. Meth. A **588** (2008) 107
[7] D. Heck et al. Forschungszentrum Karlsruhe Report FZKA, **6019** 2998
[8] A. Hoecker, P. Speckmayer, J. Stelzer, J. Therhaag, E. von Toerne, and H. Voss, PoS ACAT **040** (2007), arXiv:physics/0703039
[9] A Heijboer. PhD Thesis, available from http://antares.in2p3.fr/Publications/index.html
[10] First Author et. al.: year, Book Name, ed. Editor, Publisher

The Pierre Auger Observatory and ultra-high energy neutrinos: upper limits to the diffuse and point source fluxes

YANN GUARDINCERRI[1] FOR THE PIERRE AUGER COLLABORATION[2]
[1]*Facultad de Ciencias Exactas y Naturales, Universidad de Buenos Aires, Buenos Aires, Argentina*
[2]*Observatorio Pierre Auger, Av. San Martín Norte 304, 5613 Malargüe, Argentina*
(Full author list: http://www.auger.org/archive/authors_2011_05.html)
auger_spokespersons@fnal.gov
DOI: 10.7529/ICRC2011/V04/0682

Abstract: With the Surface Detector of the Pierre Auger Observatory, we can detect ultra-high energy neutrinos in the sub-EeV energy range and above. Neutrinos of all flavours can interact in the atmosphere and induce inclined showers close to the ground (down-going). The sensitivity of the Surface Detector to tau neutrinos is further enhanced through the "Earth-skimming" mechanism (up-going). Both types of neutrino interactions can be identified through the broad time structure of the signals induced in the Surface Detector stations. Two independent sets of identification criteria were designed to search for down and up-going neutrinos in the data collected from 1 January 2004 to 31 May 2010, with no candidates found. Assuming a differential flux $f(E_\nu) = kE_\nu^{-2}$, we place a 90% CL upper limit on the single flavour neutrino flux of $k < 2.8 \times 10^{-8}$ GeV cm^{-2} s^{-1} sr^{-1} in the energy interval 1.6×10^{17} eV $- 2.0 \times 10^{19}$ eV based on Earth-skimming neutrinos and $k < 1.7 \times 10^{-7}$ GeV cm^{-2} s^{-1} sr^{-1} in the energy interval 1×10^{17} eV $- 1 \times 10^{20}$ eV based on down-going neutrinos. We also show that the Auger Observatory is sensitive to ultra-high energy neutrinos from a large fraction of the sky, and we place limits on the neutrino flux from point-like sources as a function of declination, and in particular from the active galaxy Centaurus A.

Keywords: UHE neutrinos, cosmic rays, Pierre Auger Observatory

1 Introduction

Essentially all models of Ultra High Energy Cosmic Ray (UHECR) production predict neutrinos as the result of the decay of charged pions, produced in interactions of the cosmic rays within the sources themselves or in their propagation through background radiation fields [1, 2]. Neutrinos are also copiously produced in top-down models proposed as alternatives to explain the production of UHECRs [1].

With the surface detector (SD) of the Pierre Auger Observatory [3] we can detect and identify UHE neutrinos (UHEνs) in the 0.1 EeV range and above. "Earth-skimming" tau neutrinos [4] are expected to be observed through the detection of showers induced by the decay products of an emerging τ lepton, after the propagation and interaction of a ν_τ inside the Earth. "Down-going" neutrinos of all flavours can interact in the atmosphere and induce a shower close to the ground [5].

This contribution updates both, Earth-skimming [6, 7, 8] and down-going [8] analyses with data until the 31 May 2010 and shows, for the first time, the sensitivity of the Pierre Auger surface detector to neutrinos from point-like sources.

2 Identifying neutrinos in data

Identifying neutrino-induced showers in the much larger background of the ones initiated by nucleonic cosmic rays is based on a simple idea: neutrinos can penetrate large amounts of matter and generate "young" inclined showers developing close to the SD, exhibiting shower fronts extended in time. In contrast, UHE particles such as protons or heavier nuclei interact within a few tens of g cm^{-2} after entering the atmosphere, producing "old" showers with shower fronts narrower in time. In Fig. 1 we show a sketch of these two kinds of showers together with an Earth-skimming shower and a ν_τ interacting in the Andes, which can also be identified.

Although the SD is not directly sensitive to the nature of the arriving particles, the 25 ns time resolution of the FADC traces, with which the signal is digitised in the SD stations, allows us to distinguish the narrow signals in time expected from a shower initiated high in the atmosphere from the broad signals expected from a young shower. Several observables can be used to characterise the time structure and shape of the FADC traces. They are described in [9] where their discrimination power is also studied.

In this work we use two different sets of identification criteria to select neutrinos. One is used to define Earth-

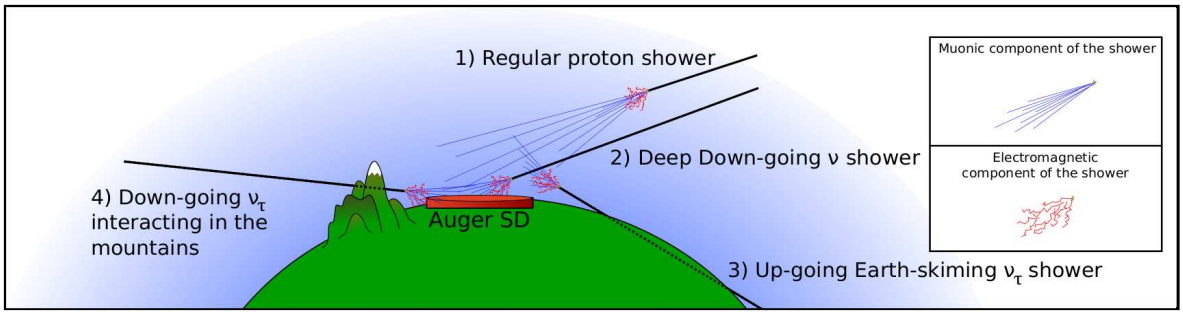

Figure 1: Sketch of different inclined showers which can be detected by the Pierre Auger Observatory. (1) An inclined shower induced by a proton interacting high in the atmosphere whose electromagnetic component is absorbed and only the muons reach the detector. Inclined showers presenting significant electromagnetic component at the detector level: (2) a deep down-going ν shower; (3) an Earth-skimming ν_τ shower; (4) and a ν_τ interacting in the mountains.

skimming tau neutrinos and the other for down-going neutrinos. They are given in Table 1 and described in the following.

Table 1: Criteria to select Earth-skimming ν_τ and down-going ν. See text for details.

	Earth-skimming	Down-going
Inclined Showers	N° of Stations ≥ 3 $L/W > 5$ $0.29\frac{\text{m}}{\text{ns}} < V < 0.31\frac{\text{m}}{\text{ns}}$ RMS(V)$< 0.08\frac{\text{m}}{\text{ns}}$ -	N° of Stations ≥ 4 $L/W > 3$ $V < 0.313\frac{\text{m}}{\text{ns}}$ $\frac{\text{RMS}(V)}{V} < 0.08$ $\theta_{rec} > 75°$
Young Showers	ToT fraction>0.6	Fisher discriminator based on AoP

The analyses start with the inclined shower selection (down-going:$\theta > 75°$ and Earth-skimming $\theta < 96°$). These showers usually have elongated patterns on the ground along the azimuthal arrival direction. A length L and a width W are assigned to the pattern and a cut on their ratio L/W is applied. We also calculate the apparent speed V of an event using the times of signals at ground and the distances between stations projected onto L. Finally, for down-going events, we reconstruct the zenith angle θ_{rec}.

Once we have selected inclined showers we look for young showers. A station having signals extended in time usually has a Time over Threshold (ToT) local trigger while narrow signals have other local triggers [3, 10]. The Earth-skimming analysis identifies young showers placing a cut on the fraction of ToT stations (ToT fraction). For down-going events, to optimize the discrimination power, we use the Fisher discriminant method using AoP (area of the FADC trace over its peak value, which gives an estimate of the spread in time of the signal) as input variables. The advantage of the Fisher discriminant is that it allows us to place an optimized cut to reject backgrounds from regular hadronic showers, and that it provides an a priori measure of how neutrino-like a possible candidate is.

3 Exposure and limit on the diffuse flux

The Earth skimming and down going criteria are applied to data collected from 1 Jan 04 to 31 May 10, and from 1 Nov 07 to 31 May 10, respectively. The down-going sample is smaller than the Earth-skimming one because data from 1 Jan 04 to 31 Oct 07 was used as a training sample for the Fisher discriminator [1]. Due to the fact that the Observatory was continuously growing during the construction phase (2004 - 2008) and that the SD is a dynamic array (some stations can occasionally be not operative), the previous periods correspond to 3.5 yr (Earth-skimming) and 2 yr (down-going) of data of a full SD array. No neutrino candidates were found and an upper limit on the diffuse flux of ultra-high energy neutrinos can be placed.

For this purpose the exposure of the SD array to UHE neutrinos is calculated. For down-going neutrinos, this involves folding the SD array aperture with the interaction probability and the identification efficiency, and integrating in time, taking into account changes in the array configuration due to the installation of new stations and other changes. The identification efficiency ε for the set of cuts defined above depends on the neutrino energy E_ν, the slant depth D from ground to the neutrino interaction point, the zenith angle θ, the core position $\vec{r} = (x, y)$ of the shower in the surface S covered by the array, and the time t through the instantaneous configuration of the array. Moreover it depends on the neutrino flavour (ν_e, ν_μ, or ν_τ), and the type of interaction – charged (CC) or neutral current (NC) – since the different combinations of flavour and interaction induce different types of showers. The efficiencies ε were obtained through MC simulations of the first interaction between the ν and a nucleon with HERWIG [11], of the development of the shower in the atmosphere with AIRES [12], and of the response of the surface detector array, see [9] for more details. Assuming a 1:1:1 flavour

1. In the case of Earth-skimming analysis, data from 1 Nov to 31 Dec 04 was used as a test sample and excluded from the search sample.

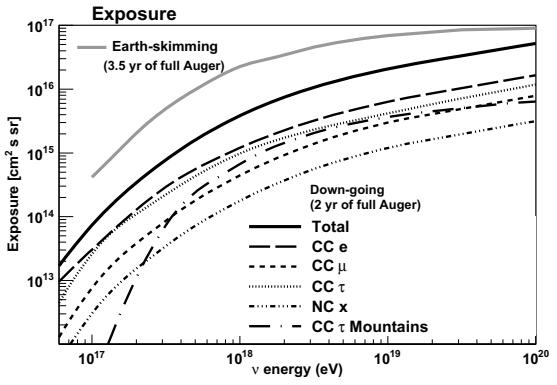

Figure 2: Exposure of the surface detector of the Pierre Auger Observatory for Earth-skimming neutrino initiated showers (3.5 yr of full Auger) and for down-going neutrino initiated showers for all the considered channels as a function of neutrino energy (2 yr of full Auger).

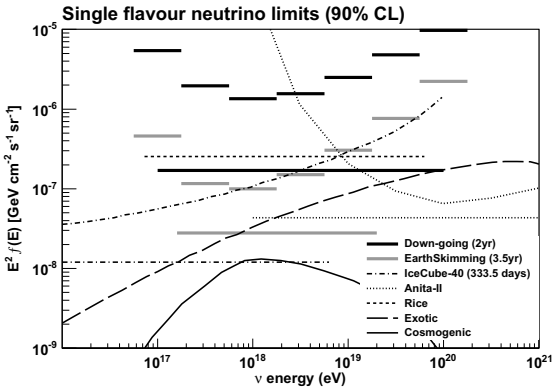

Figure 3: Differential and integrated upper limits (90% C.L.) from the Pierre Auger Observatory for a diffuse flux of down-going ν (2 yr of full Auger) and Earth-skimming ν_τ (3.5 yr of full Auger). Limits from other experiments are also plotted [16]. Expected fluxes are shown for cosmogenic neutrinos [17] and for a theoretical exotic model [18].

ratio, the total exposure can be written as:

$$\mathcal{E}^{\rm DG}(E_\nu) = \frac{2\pi}{m}\sum_i \left[\sigma^i(E_\nu)\int dt\, d\theta\, dD\, dS \right. \\ \left. \sin\theta\, \cos\theta\, \varepsilon^i(\vec{r},\theta,D,E_\nu,t)\right] \quad (1)$$

where the sum runs over the 3 neutrino flavours and the CC and NC interactions, m is the mass of a nucleon, and σ^i is the ν cross section with a nucleon. For ν_τ we have taken into account the possibility that it produces a double shower in the atmosphere triggering the array – one in the ν_τ CC interaction itself and another in the decay of the τ lepton. Furthermore, we consider the possibility of a ν_τ interacting in the Andes inducing a shower through the decay products of the τ lepton.

For the Earth-skimming neutrinos the procedure is described in Ref [7].

In Fig. 2 we show both the Earth-skimming and down-going exposures for the respective search periods.

Several sources of systematic uncertainties have been taken into account and their effect on the exposure evaluated. For down-going neutrinos there is $[-30\%, 10\%]$ systematic uncertainty in the exposure due to the neutrino-induced shower simulations and the hadronic models. Another source of uncertainty comes from the neutrino cross section which is $\sim 10\%$ [13]. For the Earth-skimming showers the systematic uncertainties are dominated by the tau energy losses, the topography and the shower simulations [7].

Using the computed exposures and assuming a typical $f(E_\nu) = k \cdot E_\nu^{-2}$ differential neutrino flux and a 1:1:1 flavour ratio, an upper limit on the value of k can be obtained. We use a semi-Bayesian extension [14] of the Feldman-Cousins approach [15] to include the uncertainties in the exposure. The updated single-flavour 90% C.L. limit based on Earth-skimming neutrinos is: $k < 2.8 \times 10^{-8}$ GeV cm^{-2} s^{-1} sr^{-1} in the energy interval 1.6×10^{17} eV $- 2.0 \times 10^{19}$ eV and the updated single-flavour 90% C.L. limit based on down-going neutrinos is: $k < 1.7 \times 10^{-7}$ GeV cm^{-2} s^{-1} sr^{-1} in the energy interval 1×10^{17} eV $- 1 \times 10^{20}$ eV. These results are shown in Fig. 3 including the limit in different bins of width 0.5 in $\log_{10} E_\nu$ (differential limit) to show at which energies the sensitivity of the Pierre Auger Observatory peaks. The expected number of events from a cosmogenic [17] (neutrinos produced by the interaction of cosmic rays with background radiation fields) and an exotic model [18] (neutrinos produced due to the decay of heavy particles) are given in Table 2.

4 Limits to point-like sources

As we found no candidate events in the search period, we can place a limit on the UHE neutrino flux from a source at declination δ.

A point source moves through the sky so that it is visible from the SD of the Pierre Auger Observatory with zenith angle $\theta(t)$ which depends on the sidereal time t. For an observatory located at a latitude λ the relation between the zenith angle and the declination of the source δ is given by:

$$\cos\theta(t) = \sin\lambda\, \sin\delta + \cos\lambda\, \cos\delta\, \sin(\omega t - \alpha_0) \quad (2)$$

with $\omega = 2\pi/T$, where T is the duration of one sidereal day and α_0 depends on the right ascension.

The sensitivity to UHEνs is limited to large zenith angles so the rate of events from a point source in the sky depends strongly on its declination. The point-source exposure $\mathcal{E}^{\rm PS}(E_\nu, \delta)$ can be obtained in a similar way as the diffuse exposure but avoiding the integration in solid angle and taking into account that the probability of neutrino

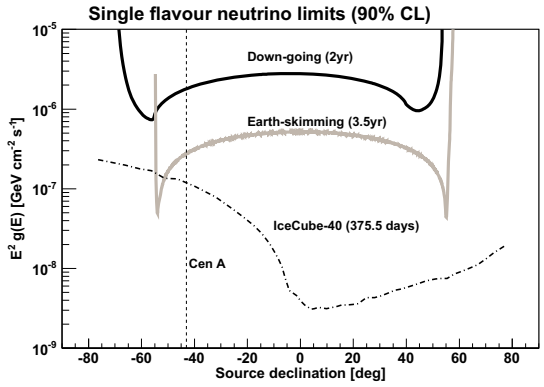

Figure 4: Neutrino flux limits to a E^{-2} differential neutrino flux from a point source as a function of the declination of the source, as obtained with the SD of the Pierre Auger Observatory for 1.6×10^{17} eV $- 2.0 \times 10^{19}$ eV (Earth-skimming) and 1×10^{17} eV $- 1 \times 10^{20}$ eV (down-going). Also shown is the limit obtained by IceCube [19] that applies below 10^{17} eV (or lower depending on declination).

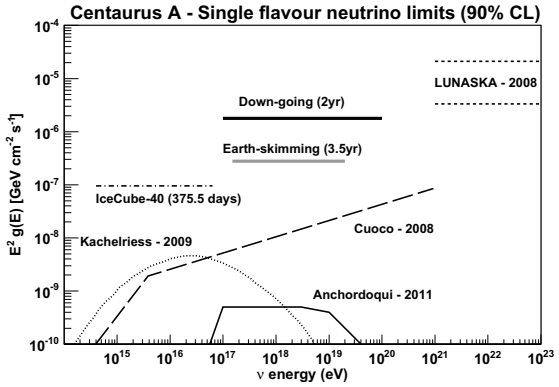

Figure 5: Limits on Cen A coming from the Earth-skimming and down-going analyses. Also shown are limits from IceCube [19] and LUNASKA [20] in different energy ranges and three theoretical predictions [21].

identification ε depends on θ, while the θ of the source depends on sidereal time through Eq. (2). Also ε itself depends explicitly on time because the configuration of the SD array changes with time.

We perform the integration over time and we obtain the point source exposure which depends not only on E_ν but also on δ. Assuming now a point source flux which decreases in energy as $g(E_\nu) = k^{\rm PS} \cdot E_\nu^{-2}$ and a 1:1:1 flavour ratio, we can obtain a point source upper limit $k^{\rm PS}(\delta)$.

In Fig. 4 we show the value of $k^{\rm PS}$ as a function of the declination of the source. In both Earth-skimming and down-going analyses the sensitivity has a broad "plateau" spanning $\Delta\delta \sim 100^\circ$ in declination. We also show the sensitivity of IceCube which is at a lower neutrino energy.

In Fig. 5 we show the constraints on k for the case of the active galaxy Centaurus A (CenA) at a declination $\delta \sim -43^\circ$. We also show three models of UHEν production in the jets and the core of CenA [21]. The expected number of events from each of these models with the current exposure is given in Table 2.

Table 2: Expected number of events for two diffuse neutrino flux models and two CenA neutrino flux models.

Diffuse flux model	Earth-skimming	Down-going
Cosmogenic	0.71	0.14
Exotic	3.5	0.97
CenA flux model	**Earth-skimming**	**Down-going**
Cuoco *et al.*	0.10	0.02
Kachelriess *et al.*	0.006	0.001

References

[1] F. Halzen *et al.*, Rep. Prog. Phys., 2002, **65**:1025-1078.
[2] R. Engel *et al.*, Phys. Rev. D, 2001, **64**: 093010.
[3] The Pierre Auger Collaboration, Nucl. Instrum. Meth., 2004, **A523**: 50-95.
[4] X. Bertou *et al.*, Astropart. Phys, 2002, **17**: 183-193.
[5] K. S. Capelle *et al.*, Astropart. Phys., 1998, **8**: 321-328.
[6] The Pierre Auger Collaboration, Phys. Rev. Lett., 2008, **100**: 211101.
[7] The Pierre Auger Collaboration, Phys. Rev. D, 2009, **79**: 102001.
[8] J. Tiffenberg, for the Pierre Auger Collaboration, Proc. 31st ICRC, Łódź, Poland, 2009. arXiv:0906.2347 [astro-ph].
[9] D. Gora, for the Pierre Auger Collaboration, Proc. 31st ICRC, Łódź, Poland, 2009. arXiv:0906.2319 [astro-ph].
[10] The Pierre Auger Collaboration, Nucl. Instrum. Meth., 2010, **A613**: 2939.
[11] G. Corcella *et al.*, JHEP, 2001, **0101**: 010.
[12] S. Sciutto, http://www.fisica.unlp.edu.ar/auger/aires
[13] A. Cooper-Sarkar, S. Sarkar, JHEP, 2008, **0801**: 075.
[14] J. Conrad *et al.*, Phys. Rev. D, 2003, **67**: 012002.
[15] G. J. Feldman, R. D. Cousins, Phys. Rev. D, 1998, **57**: 3873-3889.
[16] The IceCube Collaboration, Phys. Rev. D, 2011, **83**: 092003; The ANITA Collaboration, Phys. Rev. D, 2010, **82**: 022004, Erratum arXiv:1011.5004v1 [astro-ph]; I. Kravchenko *et al.*, Phys. Rev. D, 2006, **73**: 082002.
[17] M. Ahlers *et al.*, Astropart. Phys., 2010, **34**: 106-115.
[18] D. Semikoz, G. Sigl, JCAP, 2004, **0404**:003.
[19] The IceCube Collaboration, ApJ., 2011, **732**: 18.
[20] C. W. James *et al.*, Mon. Not. R. Astron. Soc., 2011, **410**: 885-889.
[21] A. Cuoco, S. Hannestad, Phys. Rev. D, 2008, **78**: 023007; M. Kachelriess *et al.*, New J. Phys., 2009, **11**: 065017; L. A. Anchordoqui arXiv:1104.0509 [hep-ph].

Searches for high-energy neutrinos in coincidence with gravitational waves with the ANTARES and VIRGO/LIGO detectors

VÉRONIQUE VAN ELEWYCK[1], FOR THE ANTARES COLLABORATION[2]
[1]*AstroParticule et Cosmologie (APC), CNRS: UMR7164-IN2P3-Observatoire de Paris-Université Denis Diderot-Paris VII-CEA: DSM/IRFU, France*
[2]*http://antares.in2p3.fr*
elewyck@apc.univ-paris7.fr

Abstract: Cataclysmic cosmic events can be plausible sources of both gravitational waves (GW) and high-energy neutrinos (HEN). Both GW and HEN are alternative cosmic messengers that may traverse very dense media and travel unaffected over cosmological distances, carrying information from the innermost regions of the astrophysical engines. Such messengers could also reveal new, hidden sources that were not observed by conventional photon astronomy.

A neutrino telescope such as ANTARES can determine accurately the time and direction of high energy neutrino events, and a network of gravitational wave detectors such as LIGO and VIRGO can also provide timing/directional information for gravitational wave bursts. Combining these informations obtained from totally independent detectors can provide original ways of constraining the processes at play in the sources, and also help confirming the astrophysical origin of a HEN/GW signal in case of concomitant observation.

This contribution describes the first GW+HEN joint search conducted with the ANTARES and LIGO/VIRGO detectors using concomitant data taken in 2007 during the VIRGO VSR1 and LIGO L5 science runs, while ANTARES was operating in a 5-line configuration. The specific strategies developed in ANTARES for the selection of HEN candidates used in the joint search will be discussed, together with the possible methods for the combination of HEN and GW data currently under investigation. Perspectives will also be given for the analysis of the data taken during the 2009 VIRGO/LIGO science run conducted with upgraded detectors (VIRGO+, eLIGO and ANTARES 12-lines) providing enhanced sensitivity both to HENs and GWs.

Keywords: neutrino astronomy; gravitational waves

(Paper not received. Talk can be download from: http://icrc2011.ihep.ac.cn/paper/proc/content_v4.htm)

32ND INTERNATIONAL COSMIC RAY CONFERENCE, BEIJING 2011

Search for a diffuse flux of astrophysical muon neutrinos with the IceCube Detector

THE ICECUBE COLLABORATION[1]
[1] *See special section in these proceedings*

Abstract: The discovery of a cumulative flux of high-energy neutrinos from the sum of all cosmic sources in the Universe is one of the central goals of the IceCube experiment. The experimental signature of isotropically distributed astrophysical sources is an excess of high-energy neutrinos with a characteristic angular distribution over the background of less energetic neutrinos produced when cosmic rays interact with the Earth's atmosphere. Such searches are challenging because of systematic uncertainties in these fluxes and the detector response. The distribution of reconstructed neutrino energies is analyzed using a likelihood aproach that takes into account these uncertainties and simultaneously determines the contribution of an additional diffuse extraterrestrial neutrino component. This analysis is applied to the data measured with the IceCube detector in its 40 and 59-string configurations, covering the period from April 2008 to May 2010. No evidence for an astrophysical neutrino flux was found in the 40-string analysis. The upper limit obtained for the period from April 2008 to May 2009 is $d\Phi/dE \leq 8.9 \cdot 10^{-9}\,\mathrm{GeV}^{-1}\,\mathrm{cm}^{-2}\,\mathrm{s}^{-1}\,\mathrm{sr}^{-1}$ at 90% confidence level in the energy region between 35 TeV and 7 PeV. For the 59-string data from May 2009 to May 2010, an improved analysis technique including the angular distribution in the likelihood approach is presented. The preliminary sensitivity is $d\Phi/dE \leq 7.2 \cdot 10^{-9}\,\mathrm{GeV}^{-1}\,\mathrm{cm}^{-2}\,\mathrm{s}^{-1}\,\mathrm{sr}^{-1}$.

Corresponding authors: Anne Schukraft[2] (*schukraft@physik.rwth-aachen.de*), Sean Grullon[3] (*sean.grullon@icecube.wisc.edu*), Marius Wallraff[2] (*mwallraff@physik.rwth-aachen.de*)
[2]*III. Physikalisches Institut, RWTH Aachen University, D-52056 Aachen, Germany*
[3]*Dept. of Physics, University of Wisconsin, Madison, WI 53706, USA*

DOI: 10.7529/ICRC2011/V04/0736

Keywords: IceCube, neutrino astronomy, AGN

1 Introduction

The study of cosmic rays is one of the main aspects of current research in astroparticle physics. Despite all efforts, charged cosmic rays have not yet revealed their sources. A candidate source class is active galactic nuclei, which are believed to accelerate particles up to energies of several EeV by the mechanism of Fermi acceleration, e.g., in the vicinity of their central supermassive black holes. Through hadronic interactions with the surrounding matter and radiation, high-energy neutrinos can be produced. Unlike charged cosmic rays and photons, neutrinos propagate almost unaffected by magnetic fields or intervening matter through the universe. This makes them an ideal messenger particle for astrophysics.
The neutrino telescope IceCube was built at the geographic South Pole with the purpose of detecting neutrinos with energies from several tens of GeV to EeV [1]. It consists of 86 strings each equipped with 60 optical sensors, distributed over an area of roughly 1 km^2 and instrumented in depths from 1.5 to 2.5 km in the Antarctic ice. This huge volume is necessary to compensate for the very low interaction probability of neutrinos with matter. After seven years of construction, the IceCube telescope was completed in December 2010 and is currently the largest detector of its kind in the world.
The detection principle is based on the observation of secondary charged leptons and hadrons produced in interactions of neutrinos in the surrounding ice and rock. These emit Cherenkov light which is detected by IceCube's optical sensors. From the number of photo-electrons and their arrival times, detected by the optical sensors, the neutrino's initial direction and energy are reconstructed. Although no specific neutrino emitting sources have been discovered yet, it is believed that the combined flux of many weak sources distributed all over the sky could be detected with IceCube. This flux would exceed the flux of cosmic ray induced atmospheric neutrinos at high energies and would arrive almost isotropically from all directions. Since it would not be possible to identify individual neutrino sources, this analysis is known as a search for a diffuse neutrino flux.

2 Neutrino Event selection

The first step in the searches for a diffuse astrophysical neutrino flux is to select a sample of neutrino events with high

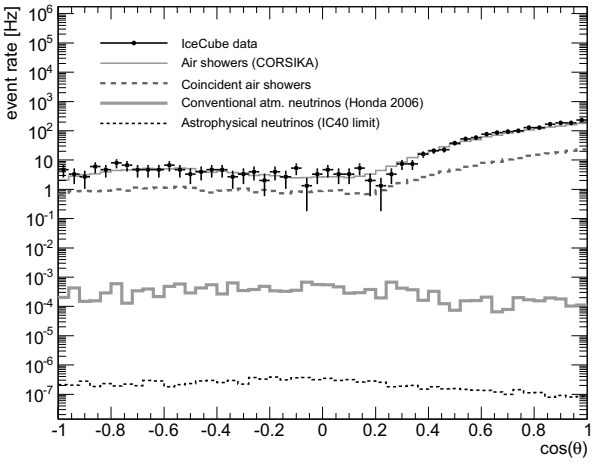

Figure 1: Reconstructed zenith angle distribution of one day of experimental data, and of simulated muons from air showers and neutrino-induced muons with the 59-string configuration at trigger level. The distribution of astrophysical neutrinos is normalized to the 40-string analysis upper limit.

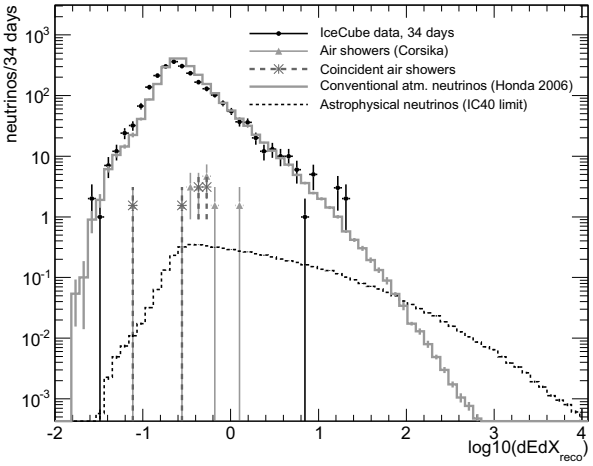

Figure 2: Distribution of the reconstructed muon energy loss for 10% of the 59-string data after neutrino selection.

purity. This contribution presents two searches for a diffuse neutrino flux with data from two consecutive years during the construction of IceCube. Both analyses focus on the selection of high-energy secondary muon tracks. Data was taken from April 2008 to May 2009 in the 40-string configuration and from May 2009 to May 2010 with 59 deployed strings. The event selections and analysis techniques are very similar. The analysis of the 59-string sample has not been finalized.

The reconstructed zenith angle distribution of detected events is shown in Fig. 1. The dominant background in this analysis are muons from cosmic-ray air showers. At trigger level, they outnumber the detected neutrino-induced muons by several orders of magnitude. In contrast to neutrinos, muons are easily absorbed by the Earth. Therefore, muons produced in the atmosphere enter the detector from above and are primarily reconstructed as downward going tracks, while muons originating from neutrinos interacting with the matter surrounding the detector come from all directions.

To reject a large amount of air shower background the analysis is restricted to upward reconstructed muon tracks. The remaining background is misreconstructed air-shower-induced muon tracks, containing a large fraction of muons arriving from coincident but independent air showers. For the further selection, an algorithm searches for patterns separated in space and time in the ensemble of recorded light-sensor pulses. This allows rejection of coincident events as well as tracks associated with random noise hits.

For the selection of a high-purity upward-going neutrino sample, the remaining data is reduced by a series of quality-criteria applied to reconstructed variables like the directional estimate of the reconstruction. They are described in detail in [5]. The final event sample consist of 12877 neutrino candidate events for the 40-string configuration and about 25000 expected events for the 59-string configuration after finalization of the analysis. Based on Monte Carlo simulation, the expected contamination of remaining background events is less than 1%.

Figure 2 shows the distribution of the reconstructed average energy losses for the selected muon tracks along their path in the detector. The experimental data is largely consistent with the expectation from atmospheric neutrinos. Most interesting for this analysis are events with high energy depositions.

3 Analysis method

The irreducible background for astrophysical neutrino searches consists of conventional atmospheric neutrinos. These neutrinos are produced in the decay of pions and kaons in cosmic-ray air showers in the Earth's atmosphere. They are described by an energy spectrum following a power law of about $d\Phi/dE \propto E^{-3.7}$ and by a characteristic zenith angle distribution related to the meson's path through the atmosphere. Another – not yet observed – type of atmospheric background are so called prompt neutrinos. Prompt neutrinos originate from the decay of heavier mesons, typically containing a charm quark[3]. They are produced at a higher cosmic-ray energy threshold and because of their comparably short lifetimes their energy distribution is predicted to follow a harder energy spectrum of $d\Phi/dE \propto E^{-2.7}$ with an almost isotropic angular distribution.

The aim of this analysis is to identify a possible astrophysical component in the neutrino sample. An astrophysical flux can be distinguished from a conventional atmospheric

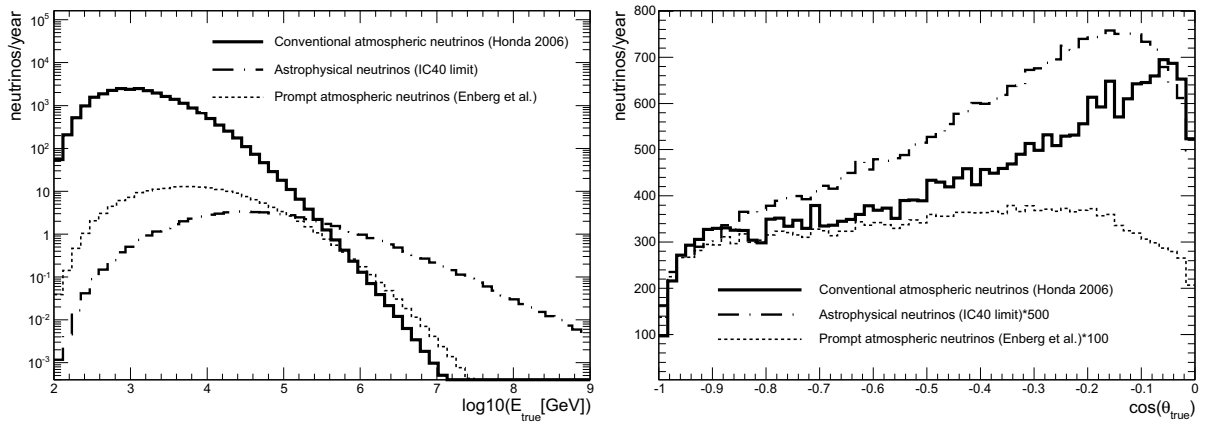

Figure 3: Expected energy (left) and zenith (right) distribution for detected conventional atmospheric neutrinos, prompt atmospheric neutrinos and astrophysical neutrinos in the IceCube detector with 59 strings. Left: The astrophysical neutrino flux is normalized to the upper limit (90% CL) of the 40-string analysis presented here. Right: The astrophysical and prompt fluxes have been renormalized for better visualization.

flux by its harder energy spectrum. Assuming shock acceleration in the extragalactic sources, an astrophysical neutrino flux would follow a $d\Phi/dE \propto E^{-2.0}$ power law (see Fig. 3). With the presumption of isotropically distributed sources over the whole sky, the arrival directions of these neutrinos would be isotropic. Their energy spectrum being harder than that of conventional atmospheric neutrinos, prompt neutrinos are an important background in a search for a diffuse flux.

Relative to the 40-string analysis[5], the ongoing 59-string analysis improves the sensitivity to an astrophysical flux by considering directional information in addition to energy. Figure 3 shows the expected zenith angle distribution of arrival directions when considering the energy-dependent absorption in the Earth, the angular detector acceptance and event selection efficiency. The significant differences in angular distribution for neutrinos of different origin adds separation power between the three components.

A likelihood method is applied to the experimental data to fit for the contributions of conventional atmospheric neutrinos, prompt atmospheric neutrinos and astrophysical neutrinos. In the 40-string analysis, the corresponding one-dimensional probability density functions (pdf) of the reconstructed energy are used to determine the probability for an astrophysical and prompt component. For the 59-string analysis, two-dimensional pdfs of reconstructed energy loss and zenith angle are used to account for both parameters and their correlation. Systematic uncertainties are taken into account by incorporating nuisance parameters in the likelihood function. These uncertainties are discussed in the next section.

The test statistic is a profile likelihood based on a likelihood ratio of the best fit of all physics and nuisance parameters to the experimental data compared to a fit of only the nuisance parameters for each point in the physics parameter space. Confidence regions are constructed according to the Feldmann & Cousins approach by generating a large number of random experiments based on Monte Carlo simulations[7]. In order to estimate the sensitivity of the analysis to a signal of diffuse astrophysical neutrinos, random experiments assuming the zero-signal hypothesis are generated.

4 Systematic uncertainties

A challenge in the search for a diffuse neutrino flux is the treatment of systematic uncertainties. Unlike other analyses of IceCube data, the background cannot be estimated from an off-source region in the experimental data. Therefore, the background estimation relies on a full-chain detector simulation. Inputs are, amongst others, air showers simulated with CORSIKA [4] and atmospheric neutrinos based on [2, 3]. More details can be found in [5, 6].

Main uncertainties at high energies are the conventional and prompt atmospheric neutrino flux predictions, the calculated neutrino cross sections and in particular the modeling of the detector response. Examples for the latter are the optical properties of the Antarctic glacial ice and the absolute efficiency of the optical sensors. The influence of these uncertainties on the final result is determined by studying simulations with different settings of these parameters. Some uncertainties, such as in the spectral index of atmospheric neutrinos, are taken into account with nuisance parameters in the likelihood fit. Additional information on the sytematic uncertainties can be found in [5, 6].

One possibly significant uncertainty not taken into account in the 40-string analysis is the effect of the knee in the cosmic-ray spectrum on the energy spectrum of conventional atmospheric neutrinos. This leads to an expected steepening of the neutrino spectrum above several tens of

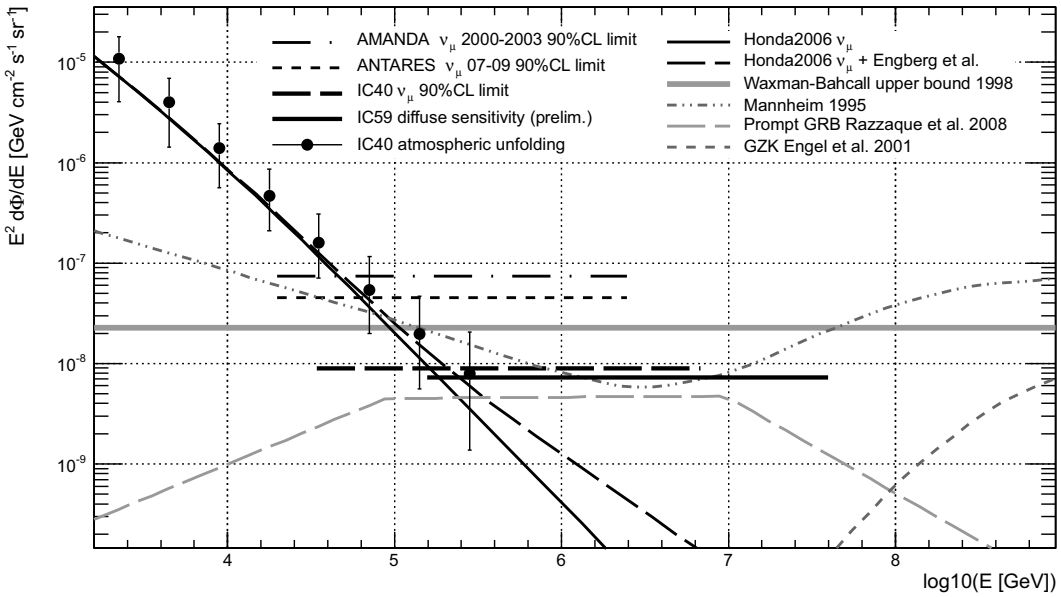

Figure 4: Limits and predictions for diffuse muon neutrino fluxes. The thin black lines show the expected flux for atmospheric neutrinos without and with an additional prompt component together with the unfolded atmospheric neutrino spectrum by IceCube[6]. The black horizontal lines represent 90%-confidence-level upper limits from different experiments [8, 9, 5]. The gray curves represent theoretical flux predictions for AGN models [11], gamma ray bursts [12] and GZK neutrinos [13]. The thick gray line shows the Waxman-Bahcall upper bound [10].

TeV, which is within the energy range relevant for this analysis but which has so far not been included in our simulations. The systematic uncertainties related to such a neutrino knee will be incorporated into the 59-string analysis using parameterizations of the measured cosmic-ray spectra.

5 Results

The result of the 40-string diffuse neutrino search has been published in [5]. The measured energy distribution is consistent with the expectation from conventional atmospheric neutrinos only. No prompt atmospheric nor astrophysical flux component was found. A small underfluctuation relative to the expectation was observed in the high-energy tail. This results in an upper limit on an astrophysical neutrino flux $d\Phi/dE \propto E^{-2.0}$ of $d\Phi/dE \leq 8.9{\cdot}10^{-9}\,\mathrm{GeV}^{-1}\,\mathrm{cm}^{-2}\,\mathrm{s}^{-1}\,\mathrm{sr}^{-1}$ integrated over the energy range between 35 TeV and 6.9 PeV with 90% confidence. This is currently the most constraining limit on a diffuse astrophysical neutrino flux and about a factor of two below the Waxman-Bahcall upper bound for an astrophysical neutrino flux [10]. At the same confidence level, a prompt atmospheric flux at 70% of the most probable flux predicted by Enberg et al.[3] was ruled out.

The higher statistics of the neutrino sample from the larger 59-string detector improves the sensitivity to astrophysical fluxes by about 35% compared to the 40-string analysis. The additional gain from using directional information is about 10% and results in a sensitivity of $d\Phi/dE \leq 7.2{\cdot}10^{-9}\,\mathrm{GeV}^{-1}\,\mathrm{cm}^{-2}\,\mathrm{s}^{-1}\,\mathrm{sr}^{-1}$ (Fig. 4). A further gain of roughly 10% in sensitivity for astrophysical fluxes is expected when taking into account the effect of the knee in the cosmic-ray spectrum.

References

[1] A. Achterberg et al., Astropart. Physics, 2006, **26** (155)
[2] M. Honda et al., Phys. Rev. D, 2007, **75** (043006)
[3] R. Enberg et al., Phys. Rev. D, 2008, **78** (043005)
[4] D. Heck et al., CORSIKA: A monte carlo code to simulate extensive air showers, Tech. Rep. FZKA, 1998
[5] R. Abbasi et al., arXiv:1104.5187v1, 2011 (submitted)
[6] R. Abbasi et al., Phys. Rev. D, 2011, **83** (012001)
[7] G. Feldman and R. Cousins, Phys. Rev. D., 1998, **57** (3873)
[8] A. Achterberg et al., Phys. Rev. D, 2007, **76** (042008)
[9] S. Biagi, Search for a diffuse flux of muon neutrinos with the antares telescope, Conference presentation at NEUTRINO 2010 Athens, Greece (2010)
[10] E. Waxman and J. Bahcall, Phys. Rev. D., 1998, **59** (023002)
[11] K. Mannheim, Astropart. Phys, 1995, **3** (295)
[12] S. Razzaque and P. Meszaros, Phys. Rev. D, 2003, **68** (083001)
[13] R. Engel, D. Seckel, and T. Stanev, Phys. Rev. D, 2001, **64** (093010)

Search for astrophysical neutrino-induced cascades using IceCube-40

THE ICECUBE COLLABORATION[1]
[1]*See special section in these proceedings*

Abstract: IceCube is the first cubic-kilometre scale neutrino observatory dedicated to detecting astrophysical neutrinos. A large contribution to the expected neutrino signal is from electromagnetic and hadronic showers (cascades) initiated by charged current ν_e interactions, and neutral current ν_e, ν_μ and ν_τ interactions. Cascade energy is reconstructed with better resolution than muons, and the atmospheric background is lower. The energy spectrum of astrophysical neutrinos is expected to be harder than that of atmospheric neutrinos, so an astrophysical neutrino signal could be observable as a break in the cascade energy spectrum.

Cascades are difficult to detect due to a large background coming from atmospheric muons and muon bundles, many orders of magnitude larger than the cascade signal. Large statistics, advanced reconstruction methods and machine learning techniques are required to isolate cascade events within the data. There is growing evidence for neutrino-induced cascade events in IceCube in several analyses that were carried out using data from April 2008 to May 2009, when 40 IceCube strings were operational. This is the largest instrumented volume, and yields the most sensitive search for a diffuse flux of astrophysical neutrinos using cascades to date.

Two of the IceCube-40 analyses are described in these proceedings. The high energy analysis measures four background events, and sets a 90% confidence level limit for all flavour astrophysical neutrino flux of 9.5×10^{-8} $\mathrm{GeVsr^{-1}s^{-1}cm^{-2}}$ over the energy range 89 TeV to 21 PeV. The mid energy analysis observes 14 cascade candidate events. The background to these events is under investigation. Three of the observed events have reconstructed energies above 100 TeV.

Corresponding authors: Stephanie Hickford[2] (*stephanie.hickford@pg.canterbury.ac.nz*), Sebastian Panknin[3] (*sebastian.panknin@icecube.wisc.edu*)
DOI: 10.7529/ICRC2011/V04/0759
[2]*Department of Physics and Astronomy, University of Canterbury. Private Bag 4800, Christchurch, New Zealand*
[3]*Institut für Physik, Humboldt-Universität zu Berlin, Newtonstr. 15, 12489 Berlin*

Keywords: IceCube; neutrinos; cascades

1 Introduction

High energy neutrino production is predicted to occur in regions of the universe containing astrophysical objects that emit large amounts of energy [1]. The same regions are predicted to emit the highest energy cosmic rays, whose origins are yet unknown. These are dense regions where large gravitational forces generate relativistic jets, accelerating charged particles. This is associated with objects such as supernovae, gamma ray bursts, and active galactic nuclei. High energy neutrinos originating from these objects may be observed as a diffuse flux by detectors such as IceCube.

A large proportion of the expected diffuse flux which interacts with nucleons in the detector results in particle showers (cascades). IceCube is capable of detecting cascades produced from all flavours of neutrinos. Cascade energy is reconstructed with better resolution than that from track-like particles such as muons, since cascades are fully contained in the detector. Also cascades have lower atmospheric neutrino background flux. The astrophysical flux has a harder energy spectrum than that of atmospheric neutrinos, which makes diffuse searches a promising route for observing a break in the energy spectrum of neutrinos from astrophysical sources. A previous cascade analysis in IceCube [2] has shown progress towards a detection of atmospheric neutrinos, and set a limit of 3.6×10^{-7} $\mathrm{GeVsr^{-1}s^{-1}cm^{-2}}$ on astrophysical neutrinos (assuming a 1:1:1 flavour ratio) for the energy range 24 TeV to 6.6 PeV, using the 22 string IceCube detector. There are several cascade analyses using the larger 40 string IceCube detector: two low energy analyses described in other proceedings at this conference [3, 4], and the two high energy analyses described here. The goal of these high energy analyses is to search for astrophysical neutrino-induced cascades.

2 IceCube-40 Data

IceCube is a Cherenkov neutrino detector located at the South Pole. The detector is comprised of Digital Optical Modules (DOMs) [5] situated on strings deployed deep

in the Antarctic ice. The DOMs house photomultiplier tubes (PMTs) [6], along with data acquisition software, in a pressure vessel. There are 60 DOMs on each string which detect Cherenkov light from charged particles traveling through the ice. The analyses described here uses data from when the detector was still under construction, when 40 strings were deployed and acquiring data. Figure 1 shows the IceCube-40 detector configuration.

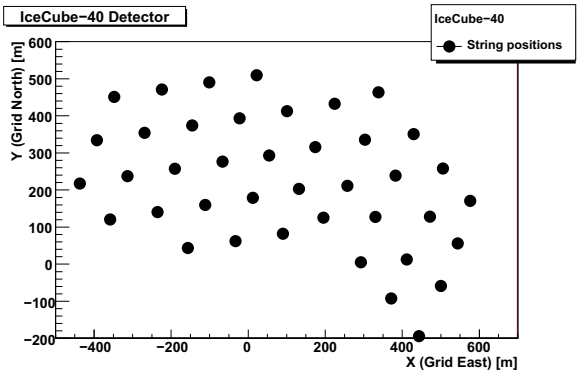

Figure 1: IceCube-40 detector configuration.

The IceCube-40 detector was operational from 6^{th} April 2008 to 20^{th} May 2009. During physics runs all event information was sent from DOMs to the surface for processing if the trigger condition was met. The trigger condition requires 8 DOMs to be hit within 5000 ns. The IceCube-40 physics dataset contains 374 days of data.

3 Analysis

The analyses presented here [10, 11] search for an E^{-2} neutrino flux within the IceCube-40 dataset. These searches use cuts on reconstructed event variables, reducing the background from atmospheric muons to isolate cascade events originating from astrophysical sources.

Neutrino interactions of all flavours were simulated to predict the expected signal. This was done using Monte Carlo simulations with an energy spectrum of E^{-1}. These simulated events were then re-weighted for atmospheric and astrophysical neutrino spectra. The atmospheric re-weighting uses the Bartol model [7] for the conventional neutrino flux, and the Sarcevic model [8] for the prompt neutrino flux. The astrophysical re-weighting uses an E^{-2} spectrum.

The dominant background to these analyses comes from atmospheric muons, simulated using Monte Carlo techniques with CORSIKA [9]. The simulation was used to train machine learning algorithms to develop cuts to separate signal from background.

3.1 Filter Levels of Mid Energy Analysis

The first level of filtering is run online at the pole in order to reduce the data volume to an acceptable level for transfer via satellite. The pole filter for the cascade stream during IceCube-40 consisted of two cuts placed on reconstructed variables. The first variable is a fit to the hit timing, and is placed to reject track-like events with a high velocity, and keep cascade-like events with low velocities. The second variable uses the hit topology of the event defined by Tensor of Inertia eigenvalues. The cut rejects elongated track-like events, and keeps highly spherical cascade-like events by cutting on the ratio of lowest eigenvalue to the sum of the three. After the data is transferred, level 2 processing is run, which consists of further reconstructions used in higher level filtering.

The level 3 filter reduces the background further in order to run more advanced reconstruction algorithms. This filter was applied only to events with a reconstructed cascade energy below 10 TeV, where the background is most dominant. The first cut variable is the reconstructed zenith direction assuming a plane-wave track topology. Events coming from above the horizon ($\theta_z < 80°$) are removed. The second cut variable is the reduced log likelihood. This variable is derived from the likelihood that an event is a cascade, based on the hit pattern in the detector. Events less likely to be cascades are removed.

The level 4 filter reduces the background further to run more sophisticated reconstructions with better variable resolutions. There are three cuts at this level. The first cut is on the reconstructed energy, placed at 2.5 TeV. The two further cuts at this level are on Spatial Distance and Fill Ratio reconstructions. The Spatial Distance cut splits the event into two parts based on the timing of hits, with the vertex position from each half reconstructed separately. If the event is a spherical cascade-like event the two vertex positions are expected to be at the same location in the detector. If the event is an elongated track-like event the two vertex positions will be located far apart. This cut requires that the two reconstructed vertex positions be within 40 m of each other. The Fill Ratio cut defines a sphere based on the radius from the mean position of hit DOMs around the reconstructed vertex of an event, and looks at the ratio of DOMs hit within this sphere over the total number of DOMs. If the event is a spherical cascade-like event the fill ratio is expected to be close to one. If the event is an elongated track-like event the fill ratio will be much less than one. This cut requires at least 40% of DOMs within the sphere to have hits.

The level 5 filter consists of containment cuts. These cuts are necessary as most of the remaining background events are located at the edges of the detector. The first containment cut is on the reconstructed vertex position. This cut requires that the vertex of the event be more than 50 m inside the top and bottom of the detector, and inside the outer ring of strings (string containment). The second containment cut is on the charge received by each DOM. This cut requires that the DOM with the largest charge be located on an inner string (DOM charge containment). The effect of these containment cuts is shown in Figure 2. After these cuts are applied, background and signal simulation are fed

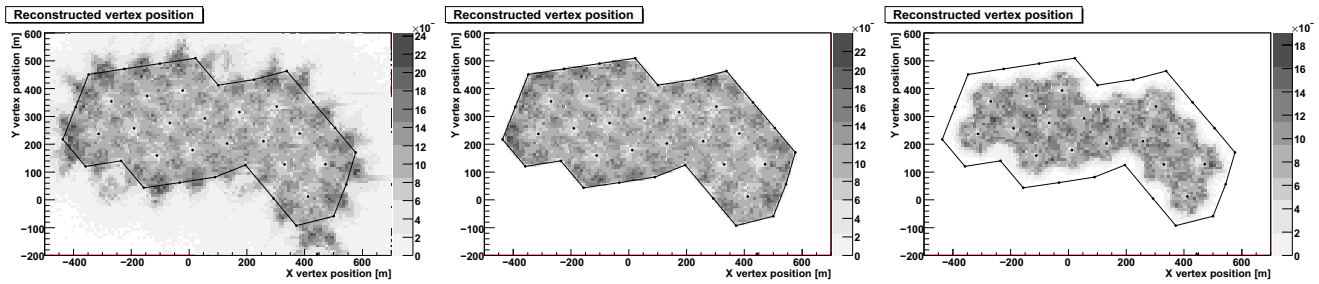

Figure 2: IceCube-40 detector in xy coordinates, black dots are the string positions. Each figure shows the reconstructed vertex for simulated E^{-2} signal. **a)** Before containment, **b)** after string containment, **c)** after DOM charge containment.

into a machine learning algorithm. Multivariate analysis (TMVA) [12] is used, which assigns a boosted decision tree (BDT) response score to each event. This BDT response has a strong separation power. The variables used for machine learning are:

- **Z vertex position** Reconstructed event depth.
- **Zenith track direction** Reconstructed zenith angle.
- **Log likelihood** Likelihood event arises from a muon.
- **Linefit velocity** Particle speed to create hit pattern.
- **Eigenvalue ratio** Topology of event.
- **Fill ratio** Ratio of DOMs hit in sphere around vertex.
- **Time split** Difference in time of two halves of event.
- **Containment** Event distance from detector centre.

The level 6 filter is the final level of cuts. There are two cuts at this level: the BDT response from multivariate analysis, and the reconstructed energy. These cut values are optimised using the Feldman-Cousins [13] method. The BDT response cut is 0.2, and the energy cut is 25 TeV.

3.2 Filter Levels of High Energy Analysis

This analysis was designed to quickly reach a result, and thus accepted a higher energy threshold [11]. It follows the mid energy analysis to level 3, then a BDT was trained using ten variables connected to shape, fit quality and position of the event. Each variable has a correlation of less than 30% to reconstructed energy, so BDT score and energy can be used as quasi-independent variables to suppress background in the final level. These cuts were optimised for sensitivity [14], based only on simulation. The background is very sensitive to cosmic ray composition, ice and detector properties. In addition, limited statistics for rare events made the background prediction fragile. The atmospheric muon prediction is $0.72 \pm 0.28(\mathrm{stat}) \pm^{1.54}_{0.49}(\mathrm{sys})$ events, with a large systematic error that is based on a detailed comparison of simulation with data. The systematic uncertainty will be reduced with future simulation. The signal prediction for an all flavor E^{-2} flux of 10^{-7} $\mathrm{GeVsr}^{-1}\mathrm{s}^{-1}\mathrm{cm}^{-2}$ is $7.93 \pm 0.13(\mathrm{stat}) \pm 1.47(\mathrm{sys})$ events (assuming a flavor ratio of 1:1:1).

4 Results

4.1 High Energy Analysis

In the high energy analysis four events were found. After careful inspection, all events look similar to background from atmospheric muons. Due to the systematic error this result is compatible with a null hypothesis. A limit at 90% confidence level on the astrophysical neutrino flux was set using the method of Rolke et. al. [15]:

$$\Phi_{\mathrm{lim}}\mathrm{E}^{-2} \leq 9.5 \times 10^{-8}\mathrm{GeVsr}^{-1}\mathrm{s}^{-1}\mathrm{cm}^{2}. \qquad (1)$$

The energy range containing 90% of the signal is 89 TeV to 21 PeV. A comparison with model predictions and other analyses limits is shown in Figure 3.

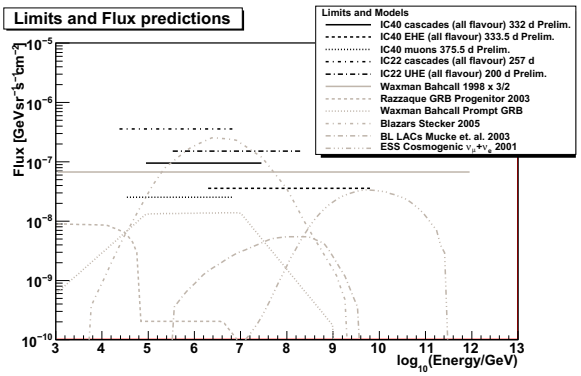

Figure 3: Limits and flux predictions for an all flavor diffuse flux. Black lines indicate limits, this high energy analysis is the solid line. The current best limit is given by the IceCube-40 diffuse search using muon neutrinos [16]. Theoretical models are thin grey lines.

4.2 Mid Energy Analysis

In the mid energy analysis a total of 14 events were observed. Of these, four events contained early hits, with timing from before the cascade. This could indicate a background event due to an atmospheric muon interaction, a muon neutrino interaction, or muon production within the

cascade. The background prediction is under investigation. The remaining events contain no evidence of early hits, and after visual inspection appear to be high quality cascade candidate events, including three that have reconstructed energies above 100 TeV.

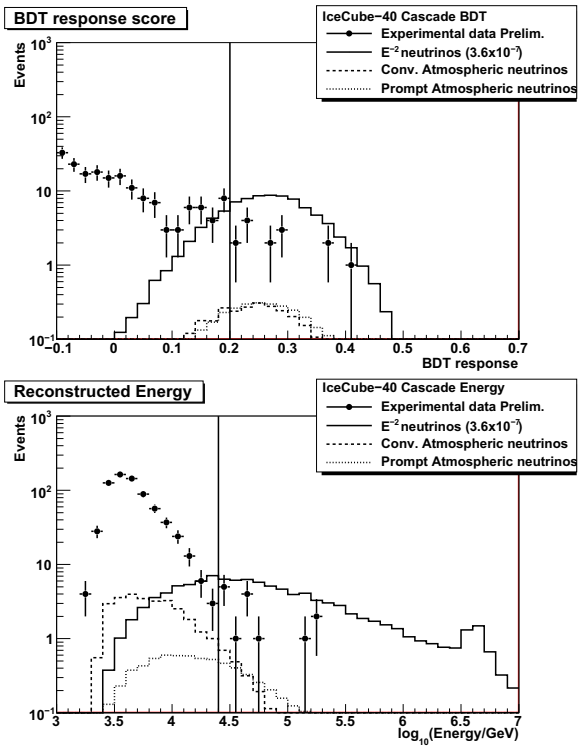

Figure 4: Distributions with final cut values shown by the vertical lines. **a)** BDT response, **b)** Energy spectrum.

Figure 4 shows the BDT response and energy spectrum distributions. Experimental data, E^{-2} signal prediction, and expectation from atmospheric cascades are shown. E^{-2} signal assumes a flux of 3.6×10^{-7} $\mathrm{GeVsr}^{-1}\mathrm{s}^{-1}\mathrm{cm}^{-2}$, the limit set by previous IceCube-22 cascade analyses [2]. The vertical line on these distributions indicates the cut value of 0.2 for BDT response and 25 TeV for reconstructed energy. On the right hand side of these cut values are the 14 events, which lie above the prediction from atmospheric cascades. Figure 5 shows a cascade event in IceCube-40 observed by the mid energy analyses. This event has a BDT response of 0.236, and a reconstructed energy of 144 TeV.

5 Summary

Results of the searches for an E^{-2} astrophysical neutrino flux with IceCube-40 are presented. The high energy analysis observed four background events and set a limit of 9.5×10^{-8} $\mathrm{GeVsr}^{-1}\mathrm{s}^{-1}\mathrm{cm}^{-2}$. The mid energy analysis observed 14 events. The majority of these events appear to be good cascade candidates, while four contain evidence of muon tracks. These four events could be background

Figure 5: Cascade event in IceCube-40. Small dots are position of DOMs, circles show light received, where size indicates number of photons.

events, or muons from muon neutrino interaction or within the cascade. Using atmospheric neutrino models Bartol and Sarcevic, 1.8 conventional events and 2.1 prompt events are predicted from atmospheric neutrinos. The events are currently being investigated by performing more extensive background simulations.

References

[1] F. Halzen, AIP Conf. Proc., 2009, **1182**: 14-21
[2] R. Abbasi et. al., ArXiv e-prints 1101.1692, Jan 2011
[3] IceCube Collaboration, paper 1097, these proceedings
[4] IceCube Collaboration, paper 0324, these proceedings
[5] R. Abbasi et. al., Nucl. Instrum. Meth., 2009, **A601**: 294-316
[6] R. Abbasi et. al., Nucl. Instrum. Meth., 2010, **A618**: 139-152
[7] G.D. Barr, T.K. Gaisser, P. Lipari, S. Robbins, T. Stanev, Phys. Rev., 2004, **D70**: 023006
[8] R. Enberg, M.H. Reno, I. Sarcevic, Phys. Rev., 2008, **D78**: 043005
[9] D. Heck et. al., FZKA, 1998, 6019
[10] S. Hickford, PhD Thesis, 2011 (in preparation)
[11] S. Panknin, PhD Thesis, 2011 (in preparation)
[12] A. Hocker et. al., PoS ACAT 2007, 040
[13] G.J. Feldman and R.D. Cousins, Phys. Rev., 1998, **D57**: 3873-3889
[14] G.C. Hill and K. Rawlins, Astropart. Phys., 2003, **19**: 393-402
[15] W.A. Rolke, A.M. Lopez, J. Conrad, Nucl. Instrum. Meth., 2005 **A551**: 493-503
[16] R. Abbasi et. al., ArXiv e-prints 1104.5187, Apr 2011

32ND INTERNATIONAL COSMIC RAY CONFERENCE, BEIJING 2011

Limits on Neutrino Emission from Gamma-Ray Bursts with the 59 String IceCube Detector

THE ICECUBE COLLABORATION[1]
[1]*see special section in these proceedings*

Abstract: IceCube is the first neutrino telescope that has sensitivity to the TeV neutrino flux from GRBs below theoretical predictions and hence is able to put constraints on the model parameters and the cosmic-ray flux from GRBs above 10^{18} eV. The analysis of data from the IceCube 59-string configuration presented here is a dedicated search for neutrinos produced via $p\gamma$-interactions in the prompt phase of the GRB fireball. Yielding no significant excess above the background, the result from this analysis is then combined with the IceCube 40-string configuration result and a stringent limit on the model is set. The combined limit is 0.22 times the predicted neutrino flux. Finally, the implications for the fireball model are discussed.

Corresponding Author: Peter Redl (redlpete@umd.edu), University of Maryland DOI: 10.7529/ICRC2011/V04/0764

Keywords: IceCube, GRB, fireball model, neutrino

1 Introduction

Gamma-ray Bursts (GRBs) are prime candidates for the production of the highest energy cosmic rays because of the enormous energy that is released in such an event [1] ($\mathcal{O}(10^{51} - 10^{54}\mathrm{erg} \times \Omega/4\pi)$ in gamma rays, where Ω is the opening angle of a possible beamed emission). If the prime engine accelerates protons and electrons with similar efficiencies this would be sufficient energy to account for the observed ultra high energy cosmic rays. The observed gamma-rays would originate from high energy electron synchrotron emission and inverse Compton scattering, while high energy neutrons would escape the fireball's magnetic field and later decay to protons, which would be responsible for the high energy cosmic ray flux seen on Earth. The observation of high energy gamma-rays confirms the presence of high energy electrons in the fireball; however, because high energy protons are deflected in inter-galactic and the Galactic magnetic fields no direct observation of protons from GRBs is possible. Nevertheless, if high energy protons are present in the fireball along with high energy electrons it is reasonable to assume that pions will be produced through $p\gamma$ interactions near the source, which would give rise to neutrinos. Guetta et al. [2] gives a detailed account of the expected neutrino flux from such interactions and is the model that is used for the theoretical neutrino prediction in this paper. Previous searches with IceCube and other experiments have given null results, with the most recent search done in IceCube achieving a 90% upper limit that is slightly below the predicted model flux [3]. In this contribution, a further improved limit is presented, which is then combined with the previous one.

2 IceCube

IceCube is a km^3-scale neutrino detector at the South Pole sensitive to TeV-scale neutrinos and above. Construction of the detector finished in December, 2010. IceCube detects Cherenkov light emitted by secondary charged particles produced in neutrino nucleon interactions and uses that information to reconstruct neutrinos. The finished detector is made up of 5160 optical modules (DOMs), with 60 optical modules placed on each of the 86 strings. The results presented here were obtained with the 59-string configuration of IceCube, which took data from 05/20/09 to 05/31/10. IceCube is able to detect all known neutrino flavors; however, in this analysis the focus was on ν_μ. Furthermore, IceCube is sensitive to the entire sky; however, because of the large cosmic-ray muon background in the southern sky, this analysis only considers events that were reconstructed as coming from the northern sky and consequently, only GRBs in that part of the sky were analysed. In this region, the best sensitivity for ν_μ can be achieved in part because of the good angular resolution for muons (0.7° for $E_\nu \gtrsim 10$ TeV) and the low background. The background consists of mis-reconstructed muons (a reducible background) and atmospheric neutrinos (an irreducible background). Both backgrounds have a softer spectrum than the predicted neutrinos from GRBs so event

energy information can be used to improve the signal to background ratio.

3 Event Reconstruction

Events in IceCube are reconstructed by fitting the spatial and temporal Cherenkov light hit pattern observed by the DOMs in a muon event using a maximum likelihood method [4][5]. In the energy range that IceCube is sensitive to, neutrinos have sufficiently high energy for the charged current interaction between the neutrino and the nucleon to be forward and hence the muon and neutrino move in a nearly collinear manner, which enables the determination of the neutrino direction from the reconstructed muon. The shape of the likelihood space near the maximum gives an estimate of the reconstruction error of the fit [6]. In addition to knowing the direction of the neutrino, knowing the energy helps to separate signal from background. The stochastic nature of the muon energy loss in the ice, and the fact that many tracks originate outside of the detector makes it impossible to measure the energy of a muon at the neutrino-interaction point directly. Nevertheless, it is possible to measure the energy loss rate of a muon as it traverses the detector, which is correlated to the energy of the muon inside the detector for energies $\gtrsim$ 1 TeV [7]. The energy resolution achieved in this way is 0.3 to 0.4 in $\log_{10}(E)$.

4 The GRB sample

During the IC59 data taking period, 105 GRBs were observed in the northern sky and reported via the GRB Coordinates Network (GCN) [8]. Of those GRBs 9 had to be removed, because IceCube was not taking physics data. GRB090422 and GRB090423 happened during 59-string test runs before the official start of the IceCube-59 runs and were included in the final GRB list as well, which brings the final catalog to 98 GRBs. The GRB localization is taken from the satellite that has the smallest reported error. The start (T_{start}) and stop (T_{stop}) times are taken by finding the earliest and latest time reported for gamma emission. The fluence, and gamma-ray spectral parameters are taken preferentially from Fermi (GBM), Konus-Wind, Suzaku WAM, and *Swift* in this order. The gamma-ray spectra reported by the satellites were used to calculate the neutrino spectra and flux as outlined in Appendix A of [2]. The neutrino energy spectrum was calculated as a power law with two breaks, with the first break corresponding to the break in the photon spectrum and with the second break corresponding to synchrotron losses of muons and pions (Fig 1). GCN does not always report values for all of the parameters used in the neutrino spectrum calculation. In that case average values are used for the parameters not measured by the satellites. GRBs are classified into two groups: long soft bursts, which are all bursts with a duration longer than 2 seconds and short-hard bursts, which are all bursts with a duration of less than 2 seconds. Average parameters from [3] were used.

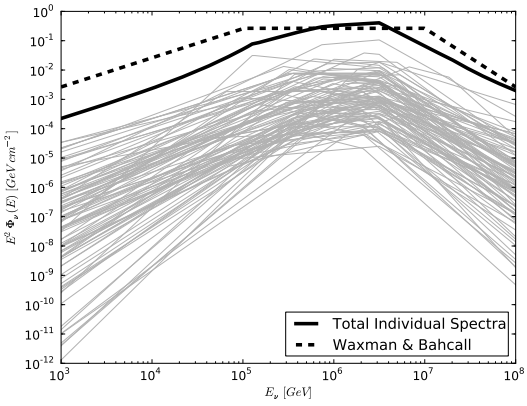

Figure 1: Neutrino spectra of the GRBs used in this analysis. The thin lines represent the individual bursts while the solid thick line represents the sum of all bursts. Finally, the dashed line shows the Waxman 2003 [9] prediction normalized to the number of GRBs observed.

5 Analysis

The analysis presented here was designed to be sensitive to neutrino production from $p\gamma$ interactions in the prompt phase of the fireball. To separate signal from background a Boosted Decision Tree [10] was trained. The analysis was then optimized for discovery with respect to the Boosted Decision Tree score. The optimized value resulted in a final data sample of 85% atmospheric neutrinos and 15% miss-reconstructed cosmic ray muons in the off time data sample (any events not within ± 2 hours of a GRB). An unbinned maximum likelihood search [11] was performed and each event passing the boosted decision tree cut was assigned a probability of being a signal event from a GRB or a background event. The final likelihood is the product of three PDFs based on the location of an event with respect to a GRB, the timing information of the event with respect to the prompt gamma-ray emission, and the energy. The directional signal PDF is a two-dimensional Gaussian:

$$\mathrm{PDF}_i^S(\vec{x}) = \frac{1}{2\pi(\sigma_i^2 + \sigma_{GRB}^2)} e^{\frac{|\vec{x}_i - \vec{x}_{GRB}|^2}{2(\sigma_i^2 + \sigma_{GRB}^2)}} \qquad (1)$$

where σ_i is the directional uncertainty for the i^{th} event and σ_{GRB} is the uncertainty of the GRB location as reported by GCN. $|\vec{x}_i - \vec{x}_{GRB}|$ is the angular difference between the reconstructed muon direction and the GRB location reported by GCN. The background spacial PDF was constructed from off-time data, taking into account the direction-dependent acceptance of the detector.

The time PDF is flat over the duration (T_{100}) of the burst and falls off smoothly as a Gaussian on either side. The

width, σ, of the Gaussian is equal to the T_{100} of the burst with a minimum of 2 s and a maximum of 25 s .

The third component of the likelihood is an energy PDF. In previous analyses, a single energy PDF for the whole northern sky was used [3, 11]. However, because the Earth is opaque to neutrinos above $\sim$ 100 TeV, the northern sky was split into three zenith regions in order to account for this effect. The signal energy PDFs were computed from the reconstructed muon energy-loss (dE/dx) from signal simulation and averaged over all GRBs in a region. The energy background PDF was computed from the dE/dx distributions of all off-time data in each region.

The final likelihood is maximized by varying the assumed number of signal events n_s and a test statistic λ is computed from the likelihood ratio $L(n_s = \hat{n}_s)/L(n_s = 0)$, where $\hat{n}_s$ is the number of signal events for the maximized likelihood. A distribution, λ, for the background-only case is constructed from off-time data by scrambling it in time a sufficient number of times. By comparing the λ value for the on-time data with the background-only distribution a p-value for the measurement is derived, which is a measure for the compatibility of the measurement with the background-only hypothesis.

6 Result

No events were found in the on-time data to be on-source (within 10° of a GRB) and on time with a GRB and the likelihood maximization yielded $\lambda = 0$. In total 24 background events (not necessarily on source) were expected to be in the total time window and 21 were observed (none on-source). From the Guetta et al. model [2] 5.8 signal events were predicted and a final upper limit of 0.46 times the predicted flux can be set. This limit includes a 6% systematic uncertainty. The systematic uncertainty is estimated by varying parameters in the signal simulation and recomputing the limit, with the dominant factor being the efficiency of the DOMs (the uncertainty of the DOM-efficiency is $\sim 10\ \%$).

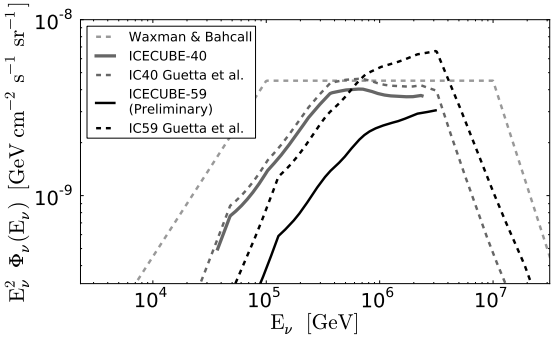

Figure 2: This plot shows the result of this analysis along with the result of the previous analyses. The flux lines from the predictions from Guetta et al. [2] and Waxman 2003 [9] are shown as well.

The corresponding model dependent result presented in a previous analysis [3] sets a limit of 0.82 of the model flux. This limit was obtained using data from the IceCube detector in the 40-string configuration. It is possible to combine this limit with the limit presented in this paper [3], because both analyses obtain a null result. The limits are combined by using signal simulation from each analysis and combining them into one signal simulation data set. From the combined signal data set a new limit is calculated by finding the fraction of total signal flux that would have yielded a *test statistic* that was greater than zero in either analysis in 90% of the cases. This new fractional signal flux is the combined limit and is 0.22 times the flux calculated according to Guetta et al. [2]. Systematic uncertainties were handled by combining the worst limit from each analysis which makes the combined limit conservative with respect to systematic uncertainties. Figure 3 shows the combined limit from these two analyses.

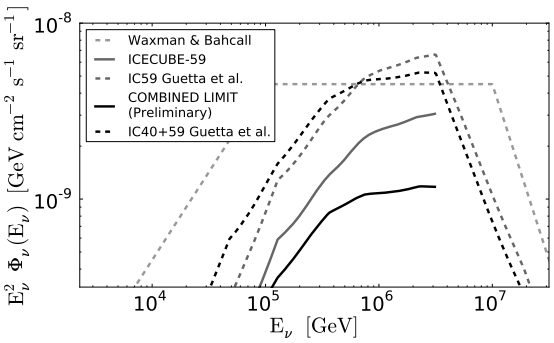

Figure 3: The combined limit of the IC40+59 analysis is shown in addition to the limits and flux predictions displayed in Fig.2.

7 Discussion

Previous results have excluded the neutrino production models outlined in [2] and [9] at a level where it may still have been explained by statistical fluctuations. This analysis is able to exclude the models with high confidence and if the result is combined with the previous result the model in question is strongly disfavored. The caveat is that there are parameters in the model for which average values, or theoretically calculated values are used, because they are not measured (or rarely measured) by the satellites. The bulk Lorentz Factor Γ is one of these values. The lower limit on this value is established by pair production arguments [2], but the upper limit is less clear. Recent papers [12, 13, 14] suggest that Γ can take values of up to 1000 (316 was used in this analysis as well as in [11, 3]). Γ is an important parameter, because in this analysis the GRBs that have the highest neutrino expectation also have the highest energy gamma-rays observed by Fermi's LAT [15]. Because of pair production arguments [2], this indicates higher Γ factors, which implies that the theoretical

brightest GRBs in the neutrino sky would be suppressed in practice. Another unmeasured parameter that could contribute to the non-detection of a neutrino flux from GRBs is the variability of the observed γ-ray light curve, t_{var}. This parameter is assumed to be the characteristic time scale between the collision of different shock fronts in the GRB fireball. Conceptually, if this time is shorter, shock fronts will collide more frequently, causing a greater number of accelerated particles and therefore more neutrinos. Recent limits on t_{var} indicate that if t_{var} is varied by a factor of 10 (either higher or lower) UHECR could still be explained as originating from GRBs [16]. Therefore, t_{var} was varied by a factor of 10 and the limit was recomputed in incremental steps from $0.1 - 10$ times the standard t_{var} value. In Fig. 4 the limit of this analysis is plotted as a function of Γ and t_{var}. It is also useful to ask, how well IceCube will do in

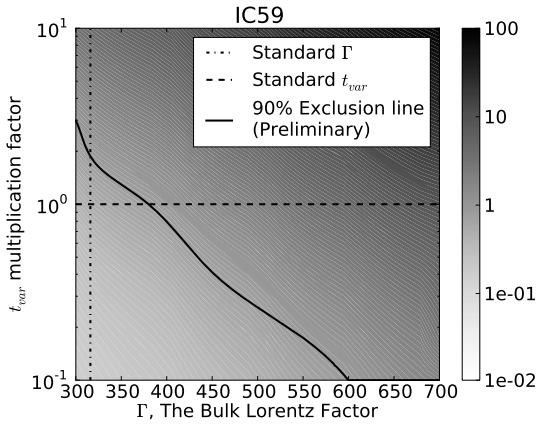

Figure 4: Limit set by the IC59 analysis as a function of the t_{var} multiplication factor and Γ assuming the Guetta et al. model [2]. The gray scale indicates the fraction of the model flux that can be excluded at each point of the phase space at 90% CL. The thick black line indicates where $1\times$ the model can be excluded at 90 % CL, while the dashed lines indicated the standard values used in this analysis. The excluded region is the region found to the left and below the exclusion line.

the 86-string configuration with respect to constraining this parameter space. To get a handle on this the GRB catalog from the 59-string configuration was used to estimate the 86-string sensitivity from Monte Carlo simulations. The result for 3-years of 86-string operation is plotted in Fig. 5. As seen from the plot, 3-years of IceCube-86 can exclude a large portion of the allowed parameter space with the portion that is not excluded being disfavored by theory. The parameters that are treated here are not the only variable parameters in the model that are important to the neutrino flux. However, the above parameters alone could account for the null result seen in IceCube so far. Future observations with the completed IceCube detector will be able to exclude or confirm GRBs as the major sources of UHECR production in a few years.

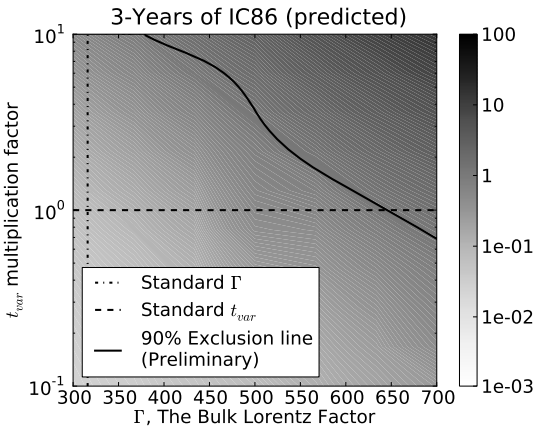

Figure 5: Projected sensitivity of IC86 after 3 years of operation with respect to Γ and t_{var}.

References

[1] E. Waxman. *Phys. Rev. Lett.*, 75:386–389, July 1995.

[2] D. Guetta, D. Hooper, J. Alvarez-Muñiz, F. Halzen, and E. Reuveni. *Astroparticle Physics*, 20:429–455, January 2004.

[3] R. Abbasi et al. *Phys. Rev. Lett.*, 106:141101, 2011.

[4] J. Ahrens, (AMANDA Collaboration), et al. *Nucl. Instrum. and Meth. A*, 524:169–194, May 2004.

[5] N. van Eijndhoven, O. Fadiran, and G. Japaridze. *Astropart. Phys.*, 28:456–462, 2007.

[6] T. Neunhöffer. *Astroparticle Physics*, 25:220–225, April 2006.

[7] Sean Grullon, David Boersma, Gary Hill, Kotoyo Hoshina, and K. Mase. In *Proc. of 30th ICRC, Merida, Mexico*, 2007.

[8] GRB Coordinates Network. `http://gcn.gsfc.nasa.gov`.

[9] E. Waxman. *Nucl. Phys. B Proc. Suppl.*, 118:353–362, April 2003.

[10] Andreas Hoecker, Peter Speckmayer, Joerg Stelzer, Jan Therhaag, Eckhard von Toerne, and Helge Voss. *PoS*, ACAT:040, 2007.

[11] R. Abbasi, (IceCube Collaboration), et al. *ApJ*, 710:346–359, February 2010.

[12] Johan Bregeon et al. *Astrophys. J.*, 729:114, 2011.

[13] En-Wei Liang et al. *Astrophys. J.*, 725:2209–2224, 2010.

[14] Alicia M. Soderberg and Enrico Ramirez-Ruiz. *AIP Conf. Proc.*, 662:172–175, 2003.

[15] NASA. Fermi: Gamma ray space telescope. 2008. `http://fermi.gsfc.nasa.gov/`.

[16] M. Ahlers, M. C. Gonzalez-Garcia, and F. Halzen. *submitted to ApJ*, 2011. arXiv:1105.2326.

32ND INTERNATIONAL COSMIC RAY CONFERENCE, BEIJING 2011

New Background Rejection Methods for the GZK Neutrino Search with IceCube

THE ICECUBE COLLABORATION[1]
[1] *see special section in these proceedings*

Abstract: The detection of cosmogenic (GZK) neutrinos with IceCube requires the ability to discriminate very rare and energetic signal events from an abundant background of cosmic ray induced muons. High energy cosmic ray air showers produce high numbers of muons densely packed around the shower core trajectory. These bundles of muons emit large amounts of Cherenkov light in the ice that constitutes the detection volume. We present several techniques to improve background rejection while keeping a large fraction of the GZK neutrino signal. The differences in the light distributions around a neutrino-induced muon track and a muon bundle are exploited. The photon hit-time pattern in the detector differs slightly for the two event types and is used for identification of muon bundles. The surface array, IceTop, is used to tag the background with high efficiency but limited zenith range. The efficiency of this method was studied using data from the partially completed detector.

Corresponding authors: Jan Auffenberg[2] (*jan.auffenberg@icecube.wisc.edu*), Shirit Cohen[3] (*shirit.cohen@icecube.wisc.edu*), Keiichi Mase[4] (*mase@hepburn.s.chiba-u.ac.jp*)
[2]*University of Madison Wisconsin, 222 W. Washington, Madison, USA*
[3]*Laboratory for High Energy Physics, École Polytechnique Fédéral, CH-1015 Lausanne, Switzerland*
[4]*Chiba University, Yayoi-cho 1-33, Inage-ku, Chiba-shi, Chiba, Japan*

DOI: 10.7529/ICRC2011/V04/0778

Keywords: UHECR; GZK neutrinos; IceCube

1 Introduction

Ultra High Energy Cosmic Rays (UHECRs) with energies above 10^{11} GeV have been observed by several experiments[1, 2]. The origin of UHECRs remains unknown, though there may be indications of a correlation of incoming directions with the close-by extra-galactic source distribution [3]. The elucidation of the origin has been longed for from the first detection. UHECRs interact with cosmic microwave background photons and necessarily generate neutrinos with energies in excess of 10^7 GeV through secondary pion decays (GZK effect). Therefore, the detection of such Extremely High Energy (EHE) neutrinos can shed light on the UHECR origin.

The IceCube detector [4], completed in Dec. 2010, instruments a huge volume of 1 km^3 ultra transparent glacial ice and is suitable to search for rare EHE neutrino events.

The GZK neutrino flux prediction depends on the cosmological source evolution, the source injection spectra and the cosmic ray composition [5]. The expected GZK neutrino event rate in IceCube is about one event per year [5, 6].

The main background for EHE neutrino search comes from muon bundles induced by cosmic ray interactions in the atmosphere. While bundles are much more abundant compared to the expected neutrino signal, their flux decreases steeply with increasing energy. Therefore signal, expected to have a harder energy spectrum, may emerge from the background above a certain critical energy. In addition, muon multiplicity in bundles increases with the primary cosmic ray energy, which leads to more pronounced background-event signatures and to increasing rejection efficiency. Another difference between neutrinos and muon bundles is their arrival direction. While the muon bundle rate decreases with increasing zenith angle, near horizontal directions are favored for GZK events because of the increase of the neutrino cross section at high energies.

The energy and arrival direction information has been used in several EHE neutrino searches [7, 8] producing the best upper limit for EHE neutrinos in the relevant energy range around 10^9 GeV.

In this paper we present methods which are being developed to achieve higher signal efficiency and high-multiplicity muon bundle background rejection using the characteristic differences between the two.

2 Muon Bundle Rejection Techniques

In Extensive Air Showers (EAS), more than thousands of muons can be generated and reach the IceCube detector

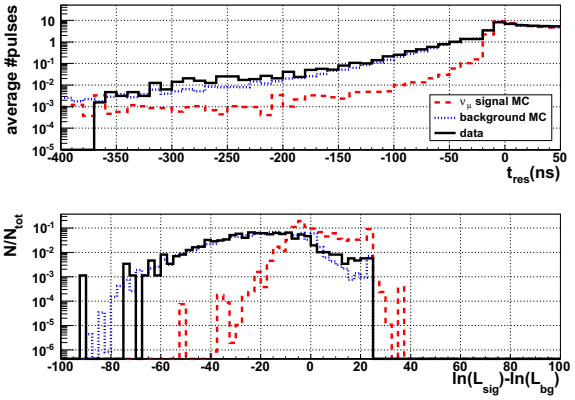

Figure 1: Top: Average number of recorded pulses as a function of the time residual for events with 10,000 <NPE< 30,000. Bottom: negative time residual likelihood ratio distribution for the same events. Dashed red: ν_μ signal simulation, dotted blue: background simulation, black: experimental data.

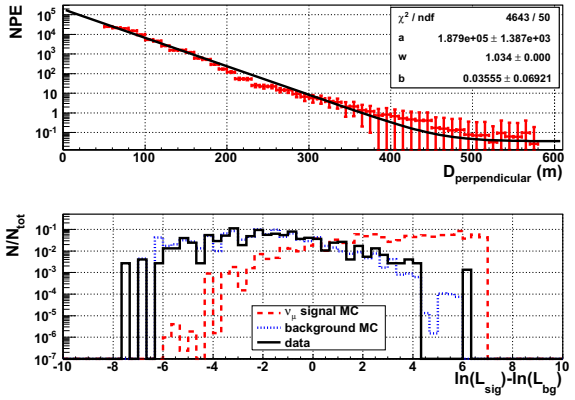

Figure 2: Top: Distribution of detected light perpendicular to a simulated neutrino-induced single muon track (red markers) and the fitted μ function (black) for an event with 100,000 NPE. Bottom: light distribution likelihood parameter ratio distribution for events with 10,000 < NPE < 30,000.

depth, under an ice overburden of about 1500 m. Most of these muons are concentrated in a dense core, but some may have relatively high transverse momenta p_t and are therefore separated from the core of the bundle at the depth of IceCube by a distance $\propto p_t/E_\mu$. Multiple scattering and deflection due to the Earth's magnetic field can increase the separation for near-horizontal events [9]. Observing the separation of single muons within the bundle core is not possible in IceCube as the photon scattering length in ice is too short and the detector's string spacing is too large for this purpose. However, differences in the light distribution around the bundle core compared to that around a single muon can be used to distinguish the two event classes.

2.1 Early Photon Hit Times

The application of a single muon hypothesis track reconstruction [10] to a muon bundle event gives the location and direction of the bundle axis. For each detected Digital Optical Module (DOM) pulse and a given reconstructed track we define the time residual $t_{\rm res}$ as the difference between the measured pulse time and the expected arrival time of an unscattered Cherenkov photon from the single track hypothesis. In the muon bundle case, the light generated by outlying muons may result in pulses with negative $t_{\rm res}$ values, indicating photon arrival times inconsistent with the single track hypothesis. We exploit the density of negative $t_{\rm res}$ pulse distribution by means of a likelihood analysis where signal and muon bundle background hypotheses are compared. The distribution of number of pulses with negative $t_{\rm res}$ values for simulated signal and background, compared to experimental data events for the IceCube 40 string configuration is shown in Fig. 1 (top). The observable NPE refers to the total Number of Photo-Electrons collected in an event by the IceCube DOMs. The resulting likelihood parameter distributions are shown in Fig. 1 (bottom).

2.2 Perpendicular Light Distribution

The amount of detected light at perpendicular distances from a single muon track is a function of the muon energy, ice properties and the detector noise level due to DOM electronics. Its parameterization is described in [11] and is given by

$$\mu(d,\theta,E) = a(\theta,E)\,\omega^{-d/d_0} + b_{\rm noise} \qquad (1)$$

with d: DOM-track distance, θ: string axis-track opening angle, E: energy of the track and $d_0 = 1$ m. Parameter a (in units of NPE) represents the light normalization and is dependent on energy of the track in IceCube, the dimensionless parameter ω describes the shape of the falling light curve and $b_{\rm noise}$ (in units of NPE) gives the expected noise level of the DOMs. Parameters a and ω are both dependent on ice properties which vary with depth [12]. However, it is difficult to resolve the dependency as for each event light is emitted and detected at different ice depths and the dependency is averaged in the fitted parameter values.

Examples for the detected light distribution around a single muon neutrino event and the fitted $\mu(d,\theta,E)$ function are given in Fig. 2 (top). The radial spread of the muons inside the bundle can be up to $\sim$ 50 m, so the perpendicular light distribution at small distances is flatter around a bundle compared to a single muon track. The amount of detected light at larger distances is higher for a single muon track compared to a bundle. This could be because muons in the bundle range out and do not reach the clearest ice at the bottom of the detector and because of large stochastic energy losses in the single muon case. These differences appear mostly in the value of the fitted ω parameter. For

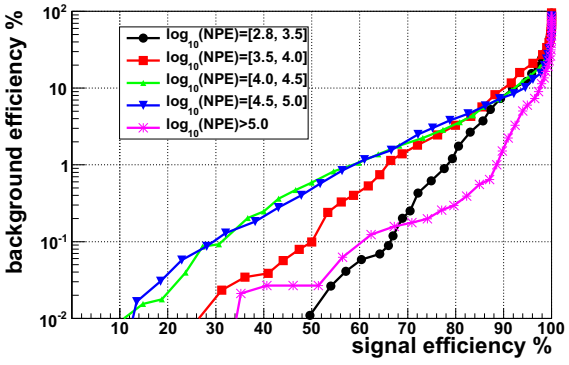

Figure 3: Combined $\Delta \ln(L)$ cut signal efficiency vs. background efficiency. For a signal cut efficiency of 90% the background rejection efficiency ranges from 90%-98% for neutrino energies of $10^{6.5} - 10^{11}$ GeV. The curves refer to samples of events with increasing amount of light detected with the IceCube 40 string detector.

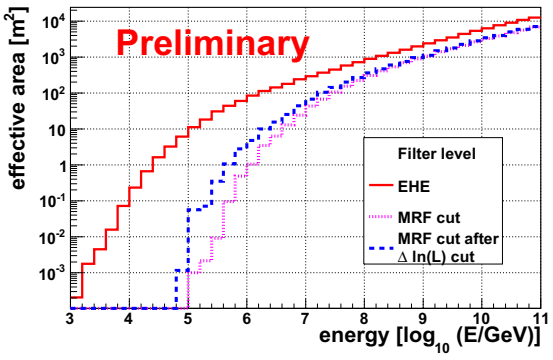

Figure 4: ν_μ effective areas for a simple analysis using a combined $\Delta \ln(L)$ cut on MC simulation of IceCube 40 string configuration. Full red: IceCube EHE events filter level, dotted purple: MRF cut calculated on filter level event sample, dashed blue: MRF cut calculated after applying a combined $\Delta \ln(L)$ cut.

signal and background events in a GZK neutrino search the obtained 2-dimensional distributions of fitted ω versus a values occupy different areas of the phase space. A likelihood parameter comparing signal and muon bundle background hypotheses is constructed and its distributions for the IceCube 40 string configuration simulated and experimental data events are shown in Fig. 2 (bottom).

2.3 Results

The bundle rejection observables described in sections 2.1 and 2.2 were combined in a single likelihood parameter. Background vs signal efficiency is shown in Fig. 3 as a function of a cut on the combined likelihood ratio $\Delta \ln(L)$ defined as $\ln(L_{\rm sig}) - \ln(L_{\rm bg})$. In order to assess the strength of the combined $\Delta \ln(L)$ observable, a cut was set at a fixed $\Delta \ln(L)$ value which gives signal passing rates of $88\% - 97\%$ depending on NPE range. A signal selection NPE threshold was then calculated using the MRF technique [14] on simulated and experimental data that passed both the EHE event filter (NPE > 630) and the combined $\Delta \ln(L)$ cut. The resulting effective areas are shown in Fig. 4.

3 IceTop Veto on Cosmic Ray Showers

An EAS event in the IceCube detector may be preceded by hits recorded in the surface detector IceTop. Therefore another promising technique to discriminate muon bundles from EHE neutrinos is to use IceTop to veto muon bundles. IceTop uses the same DOMs as IceCube to detect the electromagnetic and muonic part of EAS. For the IceTop veto the electromagnetic part plays only a minor role. Inclined EAS are mostly tagged by detection of high p_t muons far away from the shower core.

An efficient IceTop veto against high energy EAS will improve the signal efficiency in a GZK neutrino search. The three main parameters determining the EAS veto efficiency are:

Primary Energy and Composition: The higher the primary energy of the EAS, the higher the probability to see a signal in IceTop, as the number of secondary particles and the lateral extension increases. A higher veto probability for heavier primary particles is expected due to more secondaries.

Distance to IceTop: The shorter the distance of the shower core from IceTop, the higher the probability to detect the event by IceTop. The distance of the shower core can be up to several km, depending on the geometrical hit position in IceCube. This parameter is closely related to the inclination.

Inclination: With increasing inclination the air shower propagates through more atmosphere where the electromagnetic shower component gets attenuated more than the hadronic component. Thus for near-horizontal showers we expect IceTop to detect mainly muons.

Single tank hits in IceTop are used to establish the IceTop veto [13]. These IceTop hits have to be within the time window of several μs of a high energy event that triggered IceCube. In order to find hits in coincidence with the air shower front, we reconstruct the shower front in time and space. Here the center of gravity of the IceCube event and the direction from the track reconstruction are used. A planar shower front is a good approximation to find coincident hits and can be corrected by a parameterization of the shower front curvature. Fig. 5 shows the principal idea of the IceTop veto.

The distribution in Fig. 5 is used to fix the size of the veto time window to 400 ns covering the coincidence peak. For comparison, we take a background time window of the

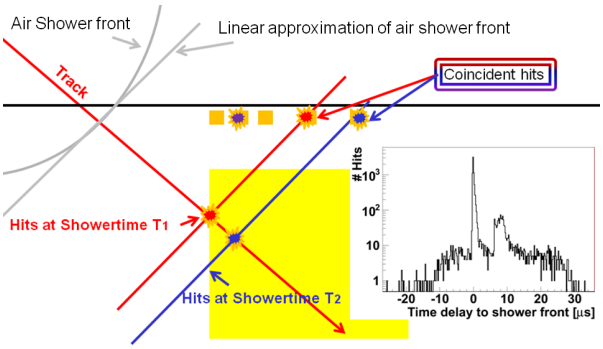

Figure 5: Sketch illustrating the veto principle. The right plot shows the IceTop hit distribution over time relative to the shower front. The sharp peak at $T = 0$ in the plot is caused mainly by coincident IceTop hits. The second peak after the shower front has passed is caused by after-pulses of the photomultipliers.

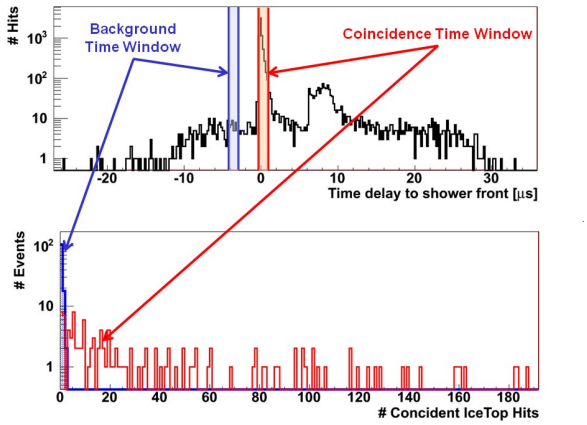

Figure 6: Top: Illustration of the chosen coincidence time windows for events with NPE $>$ 30,000. The background time window contains hits due to background from uncorrelated cosmic ray showers. Bottom: The number of events in the background time window falls steeply as a function of IceTop hits. The distribution for events in the coincidence window is significantly flatter, indicating a preliminary veto efficiency higher than 85% for NPE $>$ 30,000.

same length before the shower front reaches IceCube so that only hits from uncorrelated cosmic ray showers are included. The upper plot of Fig. 6 shows the time window selection strategy. The lower plot shows the number of events as a function of hits for both the random and real coincidence time windows. The ratio of the number of events in the real coincidence time window over the number of events in the random coincidence time window for a given number of hits gives the probability of the event to have correlated hits. Due to the low statistics of the available test data (10% of IceCube data taken in 2010 with 79 string configuration), no detailed systematic analysis of the veto efficiency is possible yet. The random coincident background is following Poisson statistics and is independent of the coincident hits. We assume that our data contains exclusively cosmic ray induced events and neglect all other background contributions. Estimates of the veto efficiency have to take into account the full dependences on energy, inclination, and distance to IceTop. All events with an NPE value exceeding 10^5 in the IceCube 2010 test data fulfill the 99.99% coincidence probability (5 hits in the coincidence time window). We conclude that the high veto efficiency at very high energies makes the IceTop veto a powerful instrument for GZK and diffuse neutrino searches.

4 Possible Future Improvements

Other variables are under investigation with the aim of further improving the sensitivity to EHE neutrinos. The longitudinal distribution of the amount of detected photons has been found to differ between a single muon derived from a neutrino and muon bundles [15]. The observed distribution along muon bundles is rather smooth while the one around single muons fluctuates much more and exhibits DOMs that detect very low PE values, which do not exist in the bundle case. It is important to separate EHE neutrinos passing far away from the detector center from the abundant lower energy muon bundles passing well within the fiducial detector volume since both of them yield similar NPE. Time-over-threshold of the recorded charge for each DOM was found to be a good proxy for the distance of light source from the DOM. This information will be used in a future EHE neutrino search as well as utilizing the IceTop veto power.

References

[1] R. Abbasi et al., Astropart. Phys., 2009, **32**: 53-60.
[2] J. Abraham et al., Phys. Lett. B, 2010, **685**: 239-246.
[3] P. Abreu et al., Astropart. Phys., 2010, **34**: 314-326.
[4] H. Kolanoski, IceCube summary talk, these proceedings.
[5] IceCube Collaboration, paper 0773, these proceedings.
[6] IceCube Collaboration, paper 0949, these proceedings.
[7] R. Abbasi et al., Phys. Rev. D, 2010, **82**: 072003.
[8] R. Abbasi et al., Phys. Rev. D, 2011, **83**: 092003.
[9] L. Gerhardt et al., Proceedings of the 31st ICRC, Lodz, Poland, July 2009. arXiv:0909.0055v.1.
[10] J. Ahrens et al., Nucl. Inst. Meth., 2004 **A524**: 169-194.
[11] M. Ribordy, Nucl. Inst. Meth., 2007, **A574**: 137-143.
[12] M. Ackermann et al., J. Geophys. Res., 2006, **111**: D13203.
[13] R. Abbasi et al., Nucl. Inst. Meth. A, 2009, **601**: 294-316.
[14] G. Hill et al., Astropart. Phys., 2003, **19**: 393-402.
[15] IceCube Collaboration, paper 0085, these proceedings.

32ND INTERNATIONAL COSMIC RAY CONFERENCE, BEIJING 2011

Search for astrophysical neutrinos from extended and stacked sources with IceCube

THE ICECUBE COLLABORATION[1]
[1]*See special section in these proceedings*

Abstract: The combined data of IceCube's 40-string and 59-string configurations spanning over 700 days are used to search for astrophysical neutrinos originating from sources listed in several catalogs. A stacking method which stacks sources and searches for an integrated signal above the estimated background is employed. Very large scale sources such as neutrino emission from the galactic plane and the Fermi bubble region are also used as extended source hypotheses. To perform these searches, a likelihood method that tests the presence of signal using the shape of such sources, their energy spectra and the angular distribution of events is employed.

Corresponding authors N. Kurahashi[2] (*naoko@icecube.wisc.edu*), J.A. Aguilar[2], M. Baker[2], J. Dumm[2], T. Montaruli[2]
[2]*Dept. of Physics, University of Wisconsin, Madison, WI 53706, USA* DOI: 10.7529/ICRC2011/V04/0796

Keywords: Astrophysical neutrinos, Fermi bubbles, galactic plane

1 Introduction

A search for astrophysical neutrinos originating in galactic and extragalactic sources using a likelihood (LH) method extensively described in [1, 2] has been performed recently on IceCube data and is reported in [3]. This method uses energy and directional information that distinguish the softer backgrounds of atmospheric muons and neutrinos from the harder astrophysical neutrinos. Such neutrinos, yet to be observed, could originate in jets and shocks via Fermi acceleration. The background is estimated by scrambling real events in their arrival times (or right ascensions) in the LH method. In this way, the p-value (the fraction of randomized data sets with higher test-statistic values than the real data) comes only from data and has no dependency on the accuracy of the simulation [1]. While Ref. [3] is focused on the LH search for steady emissions from point sources from the whole sky and from selected sources of interest, the work reported in [4] and [5] is focused on extending the likelihood method by utilizing time dependence of emissions (GRBs and AGN flares). The work presented here extends the LH method to the stacking of sources belonging to the same source class and to very extended sources that cover a large fraction of the sky. In this work, as in [1, 3], the median sensitivity and upper limits at a 90% confidence level (CL) are calculated according to teh classical (frequentist) construction of upper limits (Neyman 1937). The discovery potential is the flux required for 50% of trials with simulated signal to yield a p-value less than 2.87×10^{-7} (i.e. 5σ significance if expressed as the one-sided tail of a Gaussian distribution) unless stated otherwise.

The data sample and its selection is described in [3]. For the first time the LH method has been adapted to combine data belonging to different configurations. We combine the data sample collected for 375.5 d in the 40-string configuration of IceCube during the period from 2008 April 5 to 2009 May 20 [1] and data collected during the 59-string configuration for 348.1 d from May 20, 2009 to May 30, 2010 [3]. The total data sample consists of 43,339 (64,230) events with 59 strings in the upgoing (downgoing) hemisphere and 14,121 (22,779) for 40 strings. Hence the total number of events on which this search is performed in the whole sky is 144,469. As shown in [3], depending on the declination the sensitivity of the 40+59-string sample with respect to the 40-string sample published in [1] improves by about a factor of 2.5. A factor of about 4 is achieved in the downgoing vertical region where use of the IceTop detector as a veto for muons leads to a more significant improvement [3]. It is to be noted that the search for astrophysical sources in IceCube extends to the entire sky but the sensitivity is different in the upgoing (Northern sky) and in the downgoing (Southern sky) regions. As a matter of fact, as explained in [1], the upgoing region is dominated by atmospheric neutrinos since muons are filtered by the Earth, while we select high energy muons in the downgoing region since we look for a clustering of astrophysical events characterized by a harder spectrum than atmospheric events.

All searches shown in this proceeding will be unblinded by the time of the conference, hence here we indicate preliminary sensitivities. P-values and corresponding fluxes will be given at the conference.

2 Stacking searches

Stacking multiple sources in neutrino astronomy can enhance discovery potential and further constrain astrophysical models for uniform populations of sources. The stacking method is described in detail in [1] where it is explained how the signal and background are integrated over a set of sources using the same weight for all sources or a weighting scheme from models for specific tests. As shown in [1], the fractional flux needed for discovery for stacked sources compared to single sources at 5σ CL is very close to the inverse of number of stacked sources. The stacking searches we perform were also performed in [1] on the 40-string sample with the exception of one catalog. We perform:

1. A stacking search for 17 Milagro TeV gamma ray sources, 9 of which have been reported as high significance-detections and another 8 which are lower in significance but also confirmed by Fermi[6, 7]. The sources include supernova remnants, pulsars, pulsar wind nebulae, and one unconfirmed hot-spot;
2. It was noticed with an *a posteriori* search [1], that some of the 6 supernova remnants (SNR) observed by Milagro at energies $> 1TeV$ and considered in [8] as interesting potential neutrino emitters are the most significant in the previous list above. When these 6 sources are analyzed as a single sub-group, an a posteriori p-value of 0.02 was found with best fit parameters n_s = number of signal events = 15.2 and γ = spectral index = 2.9. The true trial factor is incalculable from this search with 40 strings since this was done after unblinding. Hence we perform a search for these 6 sources using only the sample of 59-strings in order not to bias the final result;
3. a stacking search for 127 local starburst galaxies [9];
4. a stacking search for five nearby galaxy clusters (GCs), testing four different models for the CR spatial distribution [10]. The GCs we considered are Virgo, Centaurus, Perseus, Coma and Ophiuchus. The parameterization of the models, taken from [10] and described in detail in [1], consider scenarios where CRs are uniformly distributed within the cluster shock radius or the virial radius (Models A and B respectively), an Isobaric Model in which CRs follow the distribution of thermal gas, and a Central AGN Model in which CRs are accelerated in a central AGN. This last case is treated as a point source while other models include the extension of sources in the LH.
5. a stacking search of ultra-high energy cosmic rays (UHECRs) assuming the sources of these UHECRs are also neutrino sources. We include UHECRs observed by the Auger Observatory [11] and the HiReS [12] collaboration.

The UHECR search presented here looks for neutrinos originating from the same direction as observed UHECRs. However, for this search, we fit for the 'extension' of the sources in maximizing the LH. The 'extension' of the sources here represent the possible deflection of the UHECR from their sources which depends on the UHECRs energy and the distance and magnetic field strength they propagate through. The observation of a correlation between UHECR and neutrinos is only possible in proton dominated scenarios since heavy elements would be deflected too much by magnetic fields. This search fits for an average deflection of all events stacked. The average can still be insightful given the similar energies of the UHECRs. Furthermore, the width of a Gaussian centered at the UHECR directions is used as the fit variable, accounting for the possible event-by-event directional variation between the UHECRs and neutrinos. This search, like all other LH searches performed, incorporates the neutrino event point spread function of the IceCube detector as well. After fitting for the 'extension' of sources, we test a model describing the deflections of UHECRs in extragalactic magnetic fields [13] and constrain the degenerate parameter space of distance and B-field intensity assuming that UHECRs are protons. The Auger sample contains 69 events with reconstructed energy above 55 EeV [11] with angular resolution better than 0.9° for events that trigger more than 6 stations, and the HiRes sample contains 13 events [12] in the same energy range with angular resolution of 0.8° in stereo mode. The energy scale for these events is known at the level of 20%. In order to reduce the galactic magnetic field contribution, expected to be larger than the intergalactic one, UHECR events that cross the galactic plane are removed so the fitted extension represents the intergalactic magnetic deflection alone.

The sensitivities for these searches are shown in Tab. 1.

3 The Galactic plane

Neutrinos and photons are expected to be produced in the galactic plane via interaction of cosmic rays with the interstellar medium (ISM). Diffused cosmic rays are confined for million years in the galaxy and their spectrum is hence expected to approach $E^{-2.7}$ with a composition that becomes heavier above the knee at a few PeVs. The low density of the ISM allows secondary mesons to decay before reaching their interaction length, thus preserving the cosmic ray spectrum in their decay products and also fixing the ratio of neutrinos to photons. The Milagro collaboration have reported observation of TeV gamma-rays from the galactic plane [19], showing good agreement with the GALPROP model. The GALPROP code propagates cos-

Catalog	Data sample	Fit par.	Sensitivity	Disc. Pot.
Milagro 17	I+II	γ+n_s	0.28 $\times$ $E2$	1.05 $\times E2$
Milagro 6	II	γ+n_s	0.66 $\times$ FM	3.20 $\times FM$
Starbursts 127	I+II	γ+n_s	0.96 $\times$ $E2$	3.44 $\times E2$
GC - Model A	I+II	γ+n_s	1.39 $\times$ FM	4.85 $\times FM$
GC - Model B	I+II	γ+n_s	2.58 $\times$ FM	8.98 $\times FM$
GC - Isobaric	I+II	γ+n_s	1.26 $\times$ FM	4.84 $\times FM$
GC - AGN	I+II	γ+n_s	0.63 $\times$ FM	2.36 $\times FM$
UHECR	I+II	γ+σ+n_s	4.01 $\times$ $E2$	12.8 $\times E2^*$

Table 1: Median sensitivities of the stacking searches (90% CL) and the discovery potentials (p-value $< 2.87 \times 10^{-7}$) given as a sum of flux required from the sources in each catalog. Data sample I (II) represents data taken with the 40-string (59-string) configuration. Fit parameters are the spectral index γ, the extension of the sources σ, and the number of signal events n_s. $E2$ indicate units of E^2dN/dE [10^{-11} TeV cm^{-2} s^{-1}], while FM indicates the scaling to the predicted flux profile. *For UHECR, p-value $< 1.35 \times 10^{-3}$ (3σ significance of one-sided Gaussian) is used for discovery potential calculation.

mic rays in the galaxy with assumptions of the distribution of cosmic ray sources [15]. The Fermi telescope has prodcued a detailed map of the observed gamma-ray emission from the galactic plane region [17]. The GALPROP code and a fit for the cosmic ray flux are then used to separate the contribution from neutral pion decays, which the neutrino emission map should closely follow. We use this Fermi model of the relative flux of pion decays as the spacial template in the LH analysis for neutrinos from the galactic plane. Fig. 1 shows the relative neutrino signal strength expected in the 59-string IceCube configuration assuming a source emission pattern of the Fermi model. The strongest emission is expected near the galactic center and extends along the plane. However, because the center belongs to the Southern (downgoing) hemisphere, the signal strength is expected to be highest at the closest region on the plane to the galactic center that belongs to the Northern (upgoing) hemisphere, due to IceCube's background and event selection as described in the Introduction section. The LH analysis will combine data from both the 40 and 59-string configurations. One noteworthy issue is that while the Fermi model used here provides a relative flux expected from different regions of the sky, it does not provide the absolute scale of the predicted flux. Therefore, a detailed calculation of the neutrino flux must be made, or older flux predictions [16] must be used to translate event counts in IceCube into fluxes. The flux calculations of [16] predict 21 neutrino events in the combined 40-string and 59-string data.

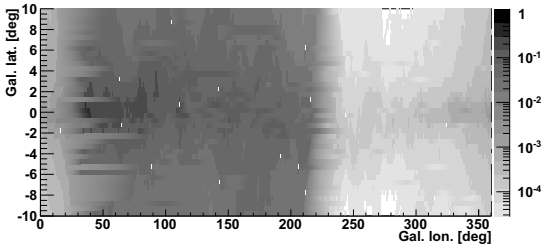

Figure 1: Relative signal strength from different parts of the sky expected from the galactic plane to be seen with the 59-string IceCube detector, plotted in galactic coordinates *(preliminary)*. The center belongs in the Southern (downgoing) hemisphere, so the signal strength is highest at the closest region on the plane to the galactic center that belongs to the Northern (upgoing) hemisphere as expected.

4 The Fermi Bubbles

Recently evidence has emerged of enormous features in the γ-ray sky observed by the Fermi-LAT instrument: bilateral "bubbles" of emission centered on the core of the Galaxy and extending to around 10 kpc from the Galactic plane. These structures are coincident with a nonthermal microwave "haze"' and an extended region of X-ray emission [18]. The bubbles γ-ray emission is characterized by a hard and relatively uniform spectrum, relatively uniform intensity, and an overall luminosity of $\sim 4 \times 10^{37}$ erg/s. The γ-ray luminosity between 1-100 GeV is measured to be around an order of magnitude larger than the microwave luminosity and more than an order of magnitude lower than the X-ray luminosity. In [20] the bubbles are explained as due to a population of relic cosmic ray protons and heavier ions in the energy range of $10 - 1000$ GeV trapped for timescales of about 10^{10} yrs undergoing pp collisions on the bubbles low density plasma that produce secondaries which in turn produce γ-rays and neutrinos. Accounting for ionization losses by sub-relativistic protons and adiabatic energy losses at all energies, bubble protons lose a total of about 10^{39} erg/s in steady state, precisely accounting for the CR power injected at the galactic center. This is compatible with observations in γ-rays around the galactic center by Fermi and at higher energies by HESS [20]. While in the galactic plane diffusive confinement of the CRs leads to a steepening of the steady-state spectrum to $\propto E^{-2.7}$, in the bubbles there is no energy-dependent confinement effect. So, given the almost energy-independent

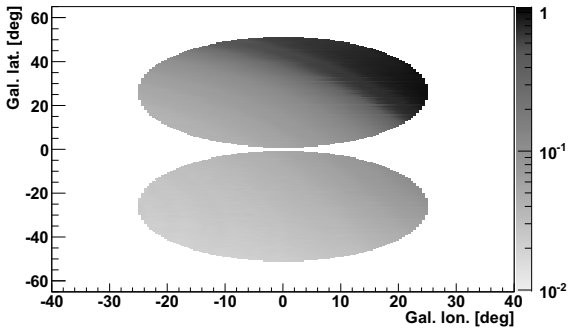

Figure 2: Relative signal strength expected from Fermi bubbles with the 59-string IceCube detector, plotted in galactic coordinates *(preliminary)*. Most of the signal is expected from the corner of the bubble that is in the Northern (upgoing) hemisphere when transformed to equatorial coordinates.

pp loss time, the observed spectrum of the CRs is as at the injection at their acceleration sites (evidently $\propto E^{-2.1}$) mirrored by the bubble $\gamma-$ rays. If the bubbles are a reservoir of CRs it is possible to think that the primary spectra reach energies above the knee and with a very hard neutrino spectrum. This makes these sources extremely interesting for neutrino telescopes.

The bubbles are parameterized as circular regions of 25° radii emitting a uniform flux of neutrinos per steradian. In Fig. 2, the relative signal strength expected from each region is simulated using the 59-string configuration of the IceCube detector. As expected, a part of one bubble that dips below the horizon in equatorial coordinates as seen by IceCube (upgoing hemisphere) has the largest expected signal. Thus the exact sensitivity of IceCube to the Fermi bubbles depends on the characterization of the shape of the bubbles. However, despite the extensive shape-fittings of the gamma emission performed in [18], due to the intrinsic haziness of the structure, the dependence on the fitting of other emission mechanisms contributing to the observed gamma-ray structure, and the unknown energy dependence of the shape at the high-energy region of our interest, we conclude that using a simple model of two circular neutrino-emission regions is adequate for an initial LH analysis. The LH analysis will combine data from both the 40 and 59-string configurations. Using this circular parameterization and assuming a continuous flux of $3.5 \times E^2 dN/dE$ [10^{-10} TeV cm^{-2} s^{-1}], motivated by an optimistic gamma-ray flux calculation [20], 164 events are expected in the combined 40 and 59-string configuration of IceCube.

References

[1] R. Abbasi *et al.*, 2011, Astrop. J. **732**:18.
[2] J. Braun *et al.*, 2008, Astropart. Phys. **29**: 299.
[3] IceCube Collaboration, 0909, these proceedings.
[4] IceCube Collaboration, 0784, these proceedings.
[5] IceCube Collaboration, 0289, these proceedings.
[6] A. A. Abdo *et al.*, 2009, Astrop. J. **700**: L127-L131.
[7] A. A. Abdo *et al.*, 2007, Astrophys. J. **664**L91.
[8] F. Halzen, A. Kappes & A. OMurchadha, 2008, Phys. Rev. **D78**: 063004.
[9] J. K. Becker, P. L. Biermann, J. Dreyer & T. M. Kneiske, 2009, arXiv:0901.1775.
[10] K. Murase, S. Inoue & S. Nagataki, 2008, Astrop. J. Letters **689**: L105.
[11] P. Abreu *et al.*, 2010, Astrop. Phys. **34**: 314.
[12] R. Abbasi *et al*, 2008, Astrop. Phys. **30**: 175.
[13] F. A. Aharonian, S. R. Kelner, A. Y. Prosekin, 2010, Phys. Rev. **D82**:043002.
[14] S. Hoover *et al.*, arXiv:1005.0035.
[15] Moskalenko *et al.*, `http://galprop.stanford.edu`, 2010.
[16] G. Ingelman & M. Thunman, 1996, Phys. Rev. D **54**: 4385
[17] Fermi-LAT Collaboration, `http://fermi.gsfc.nasa.gov/ssc/data/access/lat/BackgroundModels.html`, 2010.
[18] D. P. Finkbeiner, 2004, Astrop. J. **614**: 186; M. Su, T. R. Slatyer, & D. P. Finkbeiner, 2010, Astrop. J. **724**: 1044.
[19] A. A. Abdo *et al.*, 2008, Atrophys. J. **688:** 1078.
[20] R. M. Crocker & F. Aharoanian, 2011, Phys. Rev. Lett. **106**: 101102; F. Aharonian *et al.*, aXiv:1105:0131.

32ND INTERNATIONAL COSMIC RAY CONFERENCE, BEIJING 2011

Recent Results from the Antares Deep-sea Neutrino Telescope

AART HEIJBOER[1], ANTARES COLLABORATION
[1]*Nikhef, Amsterdam*
aart.heijboer@nikhef.nl

DOI: 10.7529/ICRC2011/V04/0858

Abstract:

The Antares observatory is currently the largest neutrino telescope in the Northern Hemisphere. Located at a depth of 2.5 km in the Mediterranean Sea, it aims to detect high energy neutrinos that are expected from cosmic ray acceleration sites. The status of the experiment will be discussed, including a broad target-of-opportunity program. The latest results will be presented, including searches for a diffuse high-energy cosmic neutrino flux, neutrinos from Gamma Ray Bursts, and for (galactic) point-like sources.

Keywords: Antares, neutrino

1 The Antares Neutrino Detector

Cosmic Rays are thought to originate in Galactic and extra-Galactic sources that accelerate protons and other nuclei up to high energies. Identification of the responsible objects could be achieved by detecting the distinct signatures of these cosmic accelerators, which are high energy neutrinos and gamma rays produced through hadronic interactions with ambient gas or photoproduction on intense photon fields near the source. While gamma rays can be produced also by directly accelerated electrons, the detection of high-energy neutrinos from these objects would provide unambiguous and unique information on the sites of the cosmic accelerators and hadronic nature of the accelerated particles.

The ANTARES Collaboration has constructed a neutrino telescope [1] at a depth of about 2475 meters deep, offshore Toulon, France. Neutrinos are detected by Photomultiplier tubes (PMTs), housed in pressure resistant glass spheres, which are regularly arranged on 12 detection lines. Each line accommodates up to 25 triplets of PMTs, located between 100 and 350 m above the sea bed. The lines are connected to the shore via a central junction box and a single, 40 km electro-optical cable, which provides both power and an optical data link. On shore, a computer farm runs a set of trigger algorithms to identify events containing Cherenkov light from high energy muons within the data stream, which otherwise consists mostly of signals from radioactive decay and bioluminescence. The selected events are stored for offline reconstruction. In 2007, the first 5 detector lines became operational, followed, in May 2008, by the completion of the full 12-line detector.

The reconstruction of muon tracks is based on the arrival time of the Cherenkov photons on the PMTs. For high energy neutrinos, the angular resolution is determined by the timing accuracy, which is limited by the transit time spread of the PMTs (1.3ns). Time calibration is performed by a number of independent systems, including LED and laser beacons [2] located throughout the detector. The relative inter-line timing has been calibrated using the time residuals measured in a large number of down-going reconstructed muon events, in addition to the optical beacon systems. The positions of the PMTs vary with time because of the sea currents. Using an acoustic positioning system, combined with information from internal compasses and tiltmeters, the positions of the PMTS are determined every 2 minutes with an accuracy of ~ 10 cm.

Most of the analyses described here use a muon track reconstruction algorithm (based on [3]) that consists of multiple fitting steps. The final step is based on a full likelihood description of the arrival times of the detected Cherenkov photons, which also accounts for background light. The achieved angular resolution is, by necessity, determined from simulations. However, several aspects of the simulations were confronted with data in order to constrain the possible systematic effects in the timing resolution that would result in a deteriorated angular resolution. The angular resolution (i.e. the median angle between the neutrino and the reconstructed muon) was found to be 0.4 ± 0.1 (sys) degrees for the detector with all 12 lines operational. Studies of the detector and the optical water properties [4] are ongoing and may help to further improve and constrain the angular resolution in the near future. Moreover, a study to observe the shadow of the moon using down-going muons

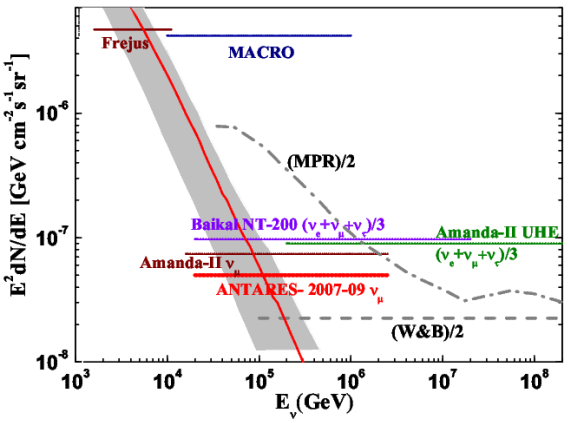

Figure 1: Upper limit on the diffuse neutrino flux of HE neutrinos obtained from the 2007-2009 ANTARES data, compared to theoretical predictions 6 and to limits set by other neutrino telescopes. (see [5] for references).

might in the future provide additional information on the (absolute) pointing accuracy [19].

In the following, a selection of results recently obtained by the Antares experiment will be summarized; many of them are discussed in more detail in dedicated contributions to this conference.

2 Searches for high energy cosmic sources

Searches for cosmic neutrinos and their sources comprise a main goal of the Antares experiment. Various searches for high energy cosmic neutrinos have been performed using the first years of data.

2.1 Search for a diffuse neutrino flux

A search for a diffuse cosmic neutrino flux has been conducted using 334 live-days of data collected in 2008 and 2009 [5]. Such a flux results in an excess of high energy events over the irreducible background of atmospheric neutrinos. A measure of the energy is provided by an observable R, which measures the number of PMTs that detect multiple photons separated in time. The distribution of the R variable agrees well with the background-only simulations and shows no evidence for a contribution from a cosmic diffuse E^{-2} flux, which would result in an excess of high-R events. Consequently, a 90% C.L. limit on such a flux is obtained in the energy range 20 TeV - 2.5 PeV. The limit is shown in figure 1 together with previously published limits from other experiments.

2.2 Point source search

Cosmic point-like source of neutrinos have been searched for using 813 live-days of data from 2007 up to and including 2010 [17]. An earlier version of the analysis is described in [18]. Event selection criteria have been applied which optimize both the sensitivity and the discovery potential. Events are required to be reconstructed as upward-going and to have a good reconstruction quality, quantified by a variable based on the reduced log-likelihood of the track fit, and an angular error estimate better than 1°. The resulting event sample consists of 3058 neutrino candidates, of which $\sim 84(16)\%$ is expected to be atmospheric neutrinos (muons misreconstructed as upward-going). To search for point sources, the analysis uses an unbinned maximum likelihood method, which exploits the knowledge on the angular resolution[1] of 0.5° and the rate of background events as a function of the declination.

Two different versions of the search were conducted: in the 'full-sky' search, the full visible sky is searched for point sources. In the 'candidate search', neutrinos are searched for only in the direction of 24 a-priori selected candidate source-locations, corresponding to know gamma ray objects of interest. Neither search yields a significant excess of events over the background: the post-trial p-values are 2.5% (for a cluster of events at $\alpha, \delta = (-46.5^\circ, -65.0^\circ)$ for the full sky search and 41% for the most signal-like source in the candidate source list (HESS J1023-575). Limits have been extracted on the intensity[2] of an assumed E^{-2} neutrino flux from the candidate sources. They are shown in Figure 2. The limit computation is based a large number of generated pseudo experiments in which systematic uncertainties on the angular resolution and acceptance are taken into account.

These limits are more stringent than those from previous experiments in the Northern hemisphere (also indicated in the figure) and competitive with those set by the IceCube observatory [8] for declinations $< -30^\circ$. The various experiments are sensitive in different energy ranges, even though they all set limits on E_ν^{-2} spectra. For this spectrum, ANTARES detects most events at energies in a broad range around 10 TeV, which is a relevant energy range for several galactic source candidates.

An independent point source analysis was performed using a different search method based on the 'EM-algorithm' [9]. This cross-check yielded similar results as the likelihood based analysis described above.

The sample of neutrino candidates from the previous search [18] has been used for additional studies, which are also reported on at this conference:

1. Since part of the data in this analysis was taken by a 5-line detector, the resolution is slightly worse than the 0.4° mentioned earlier for the full detector.

2. The limits are on ϕ, which is defined by the the following expression for the neutrino flux: $dN/dE = \phi \times (E/\mathrm{GeV})^{-2}\ \mathrm{GeV}^{-1}\mathrm{cm}^{-2}\mathrm{s}^{-1}$.

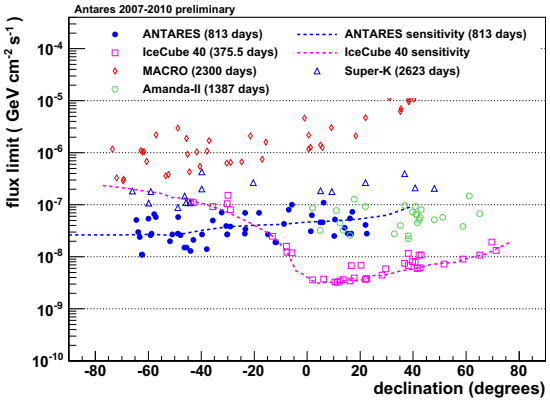

Figure 2: Limits set on the normalisation of an E_ν^{-2} spectrum of high energy neutrinos from selected candidates. Also shown is the sensitivity, which is defined as the median expected limit. In addition to the present result, several previously published limits on sources in both the Southern and Northern sky are also shown (see [17] for references).

- An auto-correlation analysis [6] was performed in order to test for unexpected (larger scale) structures in the neutrino candidate sample. No such structures were found.
- An analysis has been performed to search for directional correlations between the neutrino candidate events and 69 published ultra-high energy cosmic rays events detector by the Pierre Auger Observatory [7]. The data were found to contain no such correlations.

3 Multi-messenger Astronomy

Several analyses are performed in ANTARES, which focus on coincident measurement of neutrinos with a variety of external measurements. A selection is described below.

3.1 Neutrinos from flaring blazars

In addition to the time-integrated searches described above, a time-dependent point source search has been conducted to looks for neutrinos in correlation to the variable gamma-ray emission from blazars measured by the LAT instrument on-board the Fermi satellite. By restricting the search to the 'high state' (typically 1-20 days) of the gamma emission, the background is reduced compared to the time-integrated point source search. An analysis using 60 days of live time collected during 2008 is presented in [11]; no significant excess above the expected background was observed.

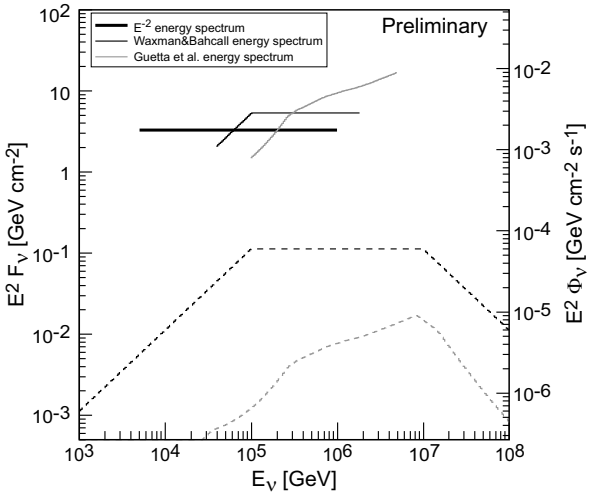

Figure 3: The upper limits (solid lines) for 37 GRBs obtained by the muon track search for the specified neutrino flux models (dashed lines) of gamma-ray bursts. The limits were placed using data taken during 2007, when the telescope consisted of 5 detector lines.

3.2 Neutrinos from GRBs

Various models predict high energy neutrinos to be emitted by Gamma Ray Burst events. Restricting the neutrino search to the duration (i.e. T_{90}) of the GRB virtually eliminates all background events. Hence, the detection of only a few events could already constitute a discovery. Two such searches [12] have been performed. The first uses the muon-neutrino channel, exploiting the good angular resolution of the detector to demand directional correlation in addition to the time. This search has so far been performed using 37 GRBs and ANTARES data from 2007 (5 detector lines). No neutrino events were found in the a-priori-defined search cone and limits on the neutrino flux were obtained; see figure 3.

The second search is ongoing and searches for 'shower' events, which are the result of a localized energy deposition in the detector. These events can be produced by e.g. electron neutrinos which produce an electromagnetic shower, or by neutral current interactions of all neutrino flavours. A reconstruction algorithm for these events has been developed. The sensitivity of this analysis to GRB neutrinos of all flavours is presented in [12].

3.3 Optical follow-up of ANTARES events.

To search for transient sources of neutrinos with an optical counterpart, a system has been setup to enable fast optical observations in the direction of detected neutrino events. A reconstruction algorithm that does not require full alignment information [10] is run online and alerts are produced for network of small automatic optical telescopes.

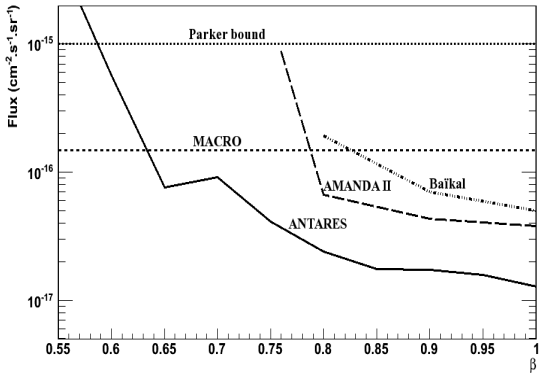

Figure 4: Flux upper limit (90 % C.L.) on up-going magnetic monopole for relativistic velocities ($0.55 \leq \beta \leq 0.995$) is compared to the published upper limits set by other experiments are also shown (see [14] for references) as well as the theoretical Parker bound.

Such alerts are produced for very high energy neutrinos or for multiple neutrinos that coincide in time and direction. Since February 2009, ANTARES has sent 37 alert triggers to the TAROT and ROTSE telescope networks, 27 of them have been followed. First results on the analysis of the resulting optical images to search for GRB and core-collapse SNe will be shown at the conference [11].

Another combination of measurements consists of correlating neutrino events with the signals from the gravitational wave detectors LIGO and VIRGO. A joint analysis is being performed that searches for a gravitational wave signal in coincidence with a sample of neutrino candidate events detected by ANTARES in 2007 [13].

4 Searches for Exotic physics

Antares is also searching for signatures of physics beyond the Standard Model. An analysis is performed that looks for neutrinos produced by Dark Matter particles annihilating in the Sun and the Galactic center [15].

Magnetic Monopoles with masses between 10^{10} and 10^{14} traversing the detector volume would be detected as a very bright track. A search for this signature has been conducted [14] and a limit on the flux of monopoles with $\beta > 0.55$ has been obtained; see Figure 4. This limit is more stringent than those from previous experiments.

Another hypothetical form of matter is formed by Nuclearites: particles composed of strange quark matter. The signature is a slow-moving (e.g. $10^{-3}c$) bright point traversing the detector. The searches are described in [16].

5 Conclusion

The first deep-sea neutrino telescope, ANTARES, has been taking data for four and a half years now. A large number of analysis are being performed, looking for astrophysical signals of neutrinos, either stand-alone or by looking for coincident observations with a variety of other experiments. The geographical position, combined with the good angular resolution allow ANTARES to explore, in particular, Galactic neutrino sources in the relevant energy range. In addition, several analyses are aimed at detecting signals from non-standard model particles.

The successful operation of ANTARES, and analysis of its data, is an important step towards KM3NET [20] a future km3-scale high-energy neutrino observatory and marine sciences infrastructure planned for construction in the Mediterranean Sea.

References

[1] M. Ageron et al. Nucl. Instr. Meth.,arXiv:1104.1607 [astro-ph.IM].
[2] J.A. Aguilar et al, Astropart. Phys. 34 (2011) 539549
[3] A. Heijboer, PhD Thesis, university of Amsterdam, 2004.
[4] S. Mangano for the ANTARES collaboration, these proceedings
[5] J.A. Aguilar et al, Physics Letters B 696 (2010) 16; also F. Schüssler for the ANTARES collaboration, these proceedings.
[6] F. Schüssler for the ANTARES collaboration, these proceedings.
[7] J. Petrovic for the ANTARES collaboration, these proceedings
[8] R. Abbasi et al, Astrophysical Journal 732 (2011) 18
[9] J.P. Gomez for the ANTARES collaboration, these proceedings
[10] J.A. Aguilar et al, Astropart. Phys. 34 (2011) 652-662
[11] D. Dornic for the ANTARES collaboration, these proceedings
[12] C. Reed for the ANTARES collaboration, these proceedings
[13] V. Van Elewyck for the ANTARES collaboration, these proceedings
[14] N. Pimente for the ANTARES collaboration, these proceedings
[15] G. Lambard for the ANTARES collaboration, these proceedings
[16] V. Poppa for the ANTARES collaboration, these proceedings
[17] C. Bogazzi for the ANTARES collaboration, these proceedings
[18] S. Adrin-Martnez et al, arXiv:1108.0292v1, submitted to ApjL
[19] C. Riviere for the ANTARES collaboration, these proceedings
[20] P. Kooijman for the KM3NeT collaboration, these proceedings; also www.km3net.org

32ND INTERNATIONAL COSMIC RAY CONFERENCE, BEIJING 2011

Constraints on the origins of the ultra-high energy cosmic-rays using the IceCube diffuse neutrino limits : An analytical approach

SHIGERU YOSHIDA[1], AYA ISHIHARA[1,2]
[1]*Department of Physics, Graduate School of Science, Chiba University, Japan*
[2]*Research Fellow, Japan Society for the Promotion of Science, Japan*
syoshida@hepburn.s.chiba-u.ac.jp
DOI: 10.7529/ICRC2011/V04/0954

Abstract: Astrophysical neutrinos are expected to be produced in the interactions of the ultra-high energy cosmic-ray protons with surrounding photons. Therefore astrophysical neutrino model fluxes are highly dependent on characteristics of the cosmic-ray sources, such as their cosmological distributions and the photon field in each sources. We study possible constraints on the properties of cosmic-ray sources in a model-independent way using the recently obtained upperlimit on the diffuse flux of neutrinos with energies above 100 PeV by the IceCube detector. The semi-analytic formula is derived to estimate the fluxes of cosmogenic neutrinos as functions of source evolution parameter and source extension in redshift. Then the obtained formula enables us to convert the upperlimits on the neutrino fluxes into the constraints on the cosmic-ray sources. It is found that the recently obtained upperlimit on the cosmogenic neutrinos by IceCube tightly constrains the very high source evolution scenarios. The derived analytic formula also shows that the future limits from the $1\mathrm{km}^3$ scale detectors such as IceCube and KM3NET are able to further constrain the the ultra-high energy cosmic-rays sources with evolutions comparable to the cosmic star formation rate.

Keywords: Ultra-high energy cosmic rays; neutrinos

1 Introduction

The origin of the ultra-high energy cosmic-rays (UHECRs) has still been a long-standing puzzle in astro-particle physics. The recent observations by the Auger collaboration [1, 2] and by the HiRes collaboration [3] indicated that the most energetic population seems propagating from extra-galactic space, but identification of the astronomical object classes responsible for UHECR emission is far from being established. A part of the difficulties arises from our poor knowledges about mass composition of UHECRs and (inter-)galactic magnetic field configuration, both of which strongly influences UHECR particle trajectories from their origin to the earth. From this view point, neutrinos secondary produced by UHECR nucleons provide complementary informations on the UHECR origin. They are penetrating over cosmological distances without being deflected by cosmic magnetic field. The intensity of the "cosmogenic" neutrino [4] produced by the GZK mechanism, the collisions of UHECR nucleons with the cosmic microwave background (CMB) photon via photo-produced π meson decay as $\pi^{\pm} \to \mu^{\pm}\nu_{\mu} \to e^{\pm}\nu_e\nu_{\mu}$, carries information on distribution of the UHECR sources [5]. Measurement or upperlimit of these ultra-high energy neutrino flux leads to direct constraints on UHECR origin without relying on uncertain estimation of magnetic fields and extra-galactic background light (EBL), in contrast to the constraints by the diffuse photon flux [6]. Estimations of the neutrino fluxes with the entire parameter space of cosmogenic neutrinos are able to convert the observationally obtained upperlimits of neutrino flux into the constraints on the UHECR sources.

In this work, we derive the analytical formula to approximately calculate intensities of the secondary produced neutrinos such as the cosmogenic neutrinos. The comparison of the predicted intensity assuming various parameters on the UHECR source distribution such as its evolution to the recently published upperlimit [7] and the future sensitivity [8] on detection of cosmic neutrino flux in energy range around EeV ($= 10^9$ GeV) by the IceCube neutrino observatory then conduces to model independent constraints on the UHECR origins. Our approach aims at bounding the UHECR source evolution and its redshift dependence in as much comprehensive way as possible without introducing any models on specific astronomical objects such as the star formation evolution. Using the analytical formula is especially suitable for this purpose as it allows to calculate neutrino intensities in the full phase space of the source evolution without an intensive computational task. It also provides an easy-to-handle tool to approximately calculate neutrino intensity as benchmark estimation to interpret the present and future results of ultra-high energy cosmic neutrinos by IceCube and KM3NET [9].

2 Analytical function to calculate ν flux

2.1 Formulation

The neutrino flux per unit energy dJ_ν/dE_ν is generally obtained by

$$\frac{dJ_\nu}{dE_\nu} = \frac{c}{H_0} n_0 \int_0^{z_{max}} dz \frac{\psi(z)}{(1+z)\sqrt{\Omega_m(1+z)^3+\Omega_\lambda}} \int_0^z dz_\nu \frac{dN_{p\to\nu}}{dE_\nu dL}(E_\nu(1+z_\nu), z_\nu, z)\,\frac{dt_\nu}{dz_\nu}. \quad (1)$$

The first integral adds neutrinos generated by cosmic ray protons emitted from sources at redshift z. $\psi(z)$ represents the cosmic evolution of the spectral emission rate per comoving volume. The second integral calculates total neutrino flux originated in a single source at redshift z by summing up neutrinos generated by the UHECR interactions at redshift $z_\nu(\leq z)$. $dN_{p\to\nu}/dE_\nu dL$ is the yield of produced neutrinos with energy of E_ν per unit UHECR propagation length. It is determined by the UHECR intensity from the source at z, the CMB photon density, and the photo-pion interaction dynamics, for example, in case of the cosmogenic neutrino production. H_0 is the Hubble constant, c is the speed of light, n_0 represents the UHECR local source density at the present universe, *i.e.,* $z = 0$, which is determined by the observed UHECR flux in the end. Following our policy of the present analysis valuing comprehensiveness and simplicity, we parameterize $\psi(z)$ as $(1+z)^m$ so that the parameter m can represent "scale" of the cosmic evolution often used in the literature.

The integrations in Eq. 1 are found to be semi-analytically computable for the cosmogenic neutrino model when the following approximations are introduced.

1. neglect the contribution of UHECR colliding with IR/O background.
2. consider photo-pion production only from the Δ resonance region.
3. simplify the kinematics of the photo-pion production as a single pion production.
4. approximate the energy attenuation length, $\lambda_{\rm GZK}$, of UHECRs as a constant with energies above 10^{20} eV.

Then we get

$$\frac{dJ_\nu}{dE_\nu} = (\alpha-1)E_{\rm GZK}^{\alpha-1} F_{\rm CR} \frac{c}{H_0}\frac{k_{\rm B}T}{8\pi^2\hbar^2c^3}\left(\frac{s_R-m_p^2}{4k_{\rm B}T}\right)^{-(\alpha+2)} \sigma_{\gamma p}^R \frac{s_R \Delta s_R}{\sqrt{(s_R+m_\pi^2-m_p^2)^2-4s_R m_\pi^2}}\frac{3}{1-r_\pi}\zeta, \quad (2)$$

as the neutrino all-flavor intensity. Here $F_{\rm CR}$ is the UHECR intensity with energy above the reference GZK energy $E_{\rm GZK} = 10^{20}$eV, α is the spectral index of UHECRs, $k_{\rm B}$ is the Boltzmann constant, T is the CMB temperature, $s_R = 1.47$ GeV^2 is the Lorentz-invariant Mandelstam variable, the square of invariant mass, at the Δ resonance, $\Delta S_R = 0.6$ GeV^2 is the width of the Δ resonance, $\sigma_{\gamma p}^R = 2.1\times10^{-28}$cm^2 is the photo-pion production cross section of channel $\gamma p \to n\pi^+$, $r_\pi = m_\mu^2/m_\pi^2 \simeq 0.57$ is the muon-to-pion mass squared ratio. ζ is the term to account the evolution dependence and given by

$$\begin{aligned}\zeta &= e^{-2}\frac{1}{\gamma_m}\Omega_m^{-\frac{\alpha+m}{3}} \Bigg[(\Omega_m(1+z_{up})^3+\Omega_\lambda)^{\frac{\gamma_m}{3}}\left(x_0^{-(\alpha+1)}\ln(\frac{\eta_R^+}{\eta_R^-})+ x_1^{-(\alpha+3)}e^{-\frac{1}{x_1}}\left\{\ln(x_1\frac{s_R-m_p^2}{4k_{\rm B}TE_\nu(1+z_{up})^2}\eta_R^- r_\pi) +\frac{2}{\gamma_m}\right\}\right) - (\Omega_m+\Omega_\lambda)^{\frac{\gamma_m}{3}}x_0^{-(\alpha+1)}\ln(\frac{\eta_R^+}{\eta_R^-}) \\ &\quad -(\Omega_m(1+z_{down})^3+\Omega_\lambda)^{\frac{\gamma_m}{3}}x_1^{-(\alpha+3)}e^{-\frac{1}{x_1}} \left\{\ln(x_1\frac{s_R-m_p^2}{4k_{\rm B}TE_\nu(1+z_{down})^2}\eta_R^- r_\pi)+\frac{2}{\gamma_m}\right\}\Bigg] \quad (3)\\ \gamma_m &\equiv \frac{2(\alpha+m)-3}{2} \\ \eta_R^\pm &\equiv \frac{s_R+m_\pi^2-m_p^2}{2s_R} \pm \frac{\sqrt{(s_R+m_\pi^2-m_p^2)^2-4s_Rm_\pi^2}}{2s_R}\end{aligned}$$

Here $x_0 = 0.275$, and $x_1 = 0.16$ are the numerical constants. The bounds of the redshifts, z_{up}, and z_{down} are associated with z_{max} in Eq. 1, the maximum redshift of the UHECR sources, but depend also on neutrino energy E_ν due to kinematics of the π decay and the redshift energy loss. They are given by

$$z_{up} = \begin{cases} 1 & x_1\frac{s_R-m_p^2}{4k_{\rm B}T}\eta_R^+ r_\pi \leq E_\nu \\ \left(x_1\frac{s_R-m_p^2}{4k_{\rm B}TE_\nu}\eta_R^+ r_\pi\right)^{\frac{1}{2}} & x_1\frac{s_R-m_p^2}{4k_{\rm B}T(1+z_{max})^2}\eta_R^+ r_\pi \leq E_\nu \leq x_1\frac{s_R-m_p^2}{4k_{\rm B}T}\eta_R^+ r_\pi \\ 1+z_{max} & E_\nu \leq x_1\frac{s_R-m_p^2}{4k_{\rm B}T(1+z_{max})^2}\eta_R^+ r_\pi \end{cases} \quad (4)$$

$$z_{down} = \begin{cases} 1+z_{max} & E_\nu \leq x_1\frac{s_R-m_p^2}{4k_{\rm B}T(1+z_{max})^2}\eta_R^- r_\pi \\ \left(x_1\frac{s_R-m_p^2}{4k_{\rm B}TE_\nu}\eta_R^- r_\pi\right)^{\frac{1}{2}} & x_1\frac{s_R-m_p^2}{4k_{\rm B}T(1+z_{max})^2}\eta_R^- r_\pi \leq E_\nu \leq x_1\frac{s_R-m_p^2}{4k_{\rm B}T}\eta_R^- r_\pi \\ 1 & x_1\frac{s_R-m_p^2}{4k_{\rm B}T}\eta_R^- r_\pi \leq E_\nu \end{cases} \quad (5)$$

The UHECR intensity F_{CR} in Eq. 2 is taken from the measurement of the HiRes experiment [3] in the present study and obtained to be 1.76×10^{-21} cm^{-2} sec^{-1} sr^{-1}. Note that the case when the evolution function $\psi(z)$ becomes constant above a certain redshift can be also analytically calculated with a minor modification into ζ.

2.2 Validity assessment of the analytical method

The introduced approximations to derive the analytical formula induce a certain inaccuracy. Nevertheless we illustrate a key point that the formula reasonably describes the flux in energy regime from $\sim$ 100 PeV up to $\sim$ 10 EeV, the central energy range of the IceCube cosmogenic neutrino search [7, 10]. The contribution of neutrino generation by UHECR colliding IR/O becomes only sizable in energy region below 100 PeV [11]. The neutrinos from

photo-produced pions above the Δ resonance are mostly visible only in the lower energy range below 100 PeV [12], and the single pion production is the most dominated channel in the Δ resonance. The detailed behavior of UHECR proton propagation in extra-galactic space is not a deciding factor in neutrino intensity below 10 EeV because these neutrinos are mostly generated at cosmological distances away, which is substantially much longer than the UHECR proton energy attenuation length in the CMB field. This fact deeply involves the well known findings that the cosmogenic flux above 10 EeV is sensitive to E_{max}, the maximal injection energy of UHECR protons from their sources, and the spectral index of UHECR spectrum α, but the flux below 10 EeV is rather insensitive to these parameters, but mostly determined by the source evolutions which describes history of the UHECR emissivity in the cosmological time scale [5, 13]. Reference [11] has extensively scanned many parameter space of the cosmogenic neutrinos with a numerical Monte-Carlo method and shown that the intensity around 1 EeV is indeed robust against E_{max} and models of transition between the Galactic and extra-galactic cosmic-ray components. Reference [6] has also calculated ν fluxes under the various parameter space that is consistent with the UHECR observed spectrum and exhibited that the neutrino intensities below 10 EeV for the similar source evolutions agree each other well within a factor of two in various α and the different transition scenario unless one does not make extreme assumption (for example, very hard UHECR spectrum with transition to extra-galactic component in higher energies). These observations are also suggested by the fact that the neutrino intensities at O(EeV) predicted by the relatively old works [5, 12] assuming harder UHECR spectrum of $\alpha = 2.0$ and higher E_{max}, and those by the recent works [6, 11] giving the nod to $\alpha \sim 2.5$ are consistent within a factor of two for comparable scale of the source evolution.

For further demonstration, we compared the cosmogenic neutrino integral flux above 1 EeV obtained by the full numerical calculations with that given by the present analytical formula with the same/comparable source evolution parameters. The results are listed in Table 1. We use $\alpha = 2.5$ in the analytical formula. They are comparable each other for wide range of parameters mostly within a factor of two. The similar agreement is found in the intensity at 100 PeV. It is confirmed that the present formula provides a reasonable estimate of the neutrino flux from $\sim$ 100 PeV to $\sim$ 10 EeV with uncertainty of factor of two. This uncertainty reflects the possible range of intensity of the extra-galactic UHECR component allowed by the observed UHECR spectrum, and the accuracy of the approximations in derivation of the analytical formula.

ν Flux Model	Integral Flux F($E_\nu \geq 1$ EeV) [/cm^2 sec sr]
Ahlers *et al.* [6]	
$m = 2.0, z_{max} = 2.0$	1.85×10^{-18}
The analytical formula	
$m = 2.0, z_{max} = 2.0$	4.50×10^{-18}
Kotera *et al.* [11]	
SFR1	1.07×10^{-17}
The analytical formula	
$m = 3.4 (z \leq 1.0)$	
const. $(1 \leq z \leq 4)$	1.02×10^{-17}
Ahlers *et al.* [6]	
$m = 4.6, z_{max} = 2.0$	3.39×10^{-17}
The analytical formula	
$m = 4.6, z_{max} = 2.0$	3.88×10^{-17}
Kalashev *et al.* [13]	
$m = 5.0, z_{max} = 3.0$	7.38×10^{-17}
The analytical formula	
$m = 5.0, z_{max} = 3.0$	1.04×10^{-16}
Kotera *et al.* [11]	
FR II	6.74×10^{-17}
The analytical formula	
$m = 5.02 (z \leq 1.5)$	
const. $(1.5 \leq z \leq 2.5)$	5.04×10^{-17}

Table 1: Cosmogenic ν fluxes predicted by the model-dependent full numerical calculations and those given by the present analytical formula with the corresponding parameters on source evolution.

3 Constraints on UHECR origin with the IceCube diffuse neutrino flux limit

We estimate expected event rate with the IceCube neutrino observatory by using the derived formula. The analytical function is valid in the IceCube cosmogenic neutrino detection energy range distributed around 1 EeV [7] . Convolution of Eq. 2 and the IceCube neutrino effective area [7, 8] gives the event rate for the entire phase space of the evolution parameter m and the maximal redshift z_{max}. The Feldman-Cousins upper bound [14] then defines the excluded region on the m-z_{max} plane at a given confidence level. Figure 1 displays the resultant constraint. The shaded region represents the factor of two uncertainty in the analytical estimation discussed in the previous section. The IceCube 2008-2009 observation has already started to limit UHECR source class with strong evolution $m \geq 4.5$. This bound may be still weaker than that by the Fermi diffuse γ-ray flux measurement [6], but the limit by neutrinos is more solid against uncertainty of the assumptions of E_{max}, inter-galactic magnetic field, and the EBL intensity, while the Fermi limit strongly depends on these parameters and it is more difficult to extract constraint on the UHECR source evolution. The full IceCube 5 year observation would certainly probe the most interesting region of the source evolution phase space where the powerful astronomical objects like radio galaxies and GRBs are included.

4 Discussion

The present analysis indicated that five year observation by the IceCube observatory would fully scan the parameter space on the source evolution in which many of the

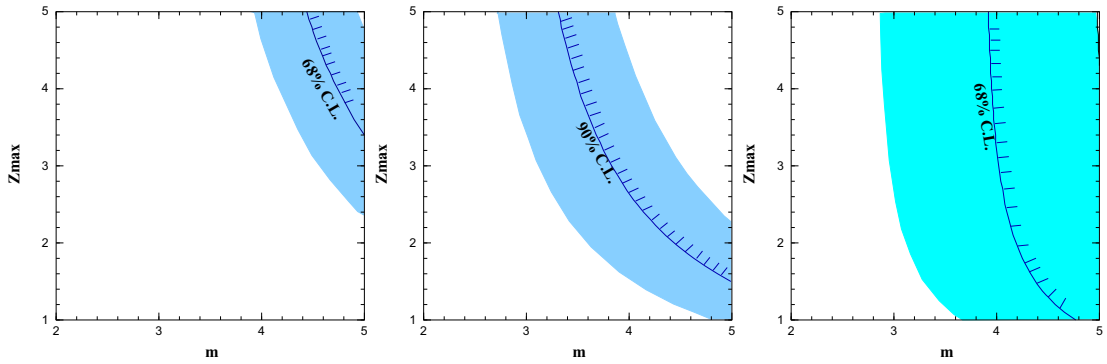

Figure 1: Constraints on the UHECR source evolution m and z_{max} by the IceCube 2008-2009 flux limit [7] (left) and by the full IceCube 5 year sensitivity [8] (middle). The upper right region is excluded by null detection of ν events. The shaded regions represent uncertainties in the present analytical estimation. The right panel shows the full IceCube 5 year constraint when the emission rate per comoving volume becomes constant above $z \geq 1.0$.

proposed UHECR astronomical sources are distributed. A null neutrino observation would imply that either UHECR sources are local with $z_{max} \leq 1$, or only very weakly evolved with $m \leq 3$, or the UHECRs are not proton dominated but heaver nuclei like irons after all. The first two possibilities may lead to speculation about the highest energy particle radiation from an entirely different and probably dimmer class of objects. The last possibility has already been suggested by the measurement of the depth of maximum of airshowers by the Auger collaboration [15]. Neutrino search in ultra-high energies provides a complementary constraint on the proton fraction of UHECRS in this case [16].

The largest uncertainty in the present analytical formula at the lower energy range ($\sim$100 PeV $\leq E_\nu \leq \sim$ 1 EeV) arises from our neglect of the IR contribution to the cosmogenic neutrino production. While photo-produced pions from UHECRs interaction with the IR background are major origin of neutrinos with energies below 10 PeV, they are relatively minor contribution in the higher energies we have mainly discussed from aspect of the cosmogenic neutrino detection by IceCube. Size of the IR contribution has been different among the various numerical calculations in the literature, indicating that prediction of the IR contributions above 100 PeV is not very straightforward. For example, the calculation in Ref. [11] exhibits higher contribution of the IR background, while the effect is very suppressed in Ref. [6] mainly due to the introduction of the minimal energy of extra-galactic UHECR population. The variance is consistent with the factor of two uncertainty we assigned to the intensity predicted by the analytical formula. Note that the neglect of the IR background always leads to conservative constraint on the UHECR source evolution and that the IR background yield itself is not firmly understood [17].

References

[1] Pierre Auger Collaboration, J. Abraham *et al.* , Science, 2007, **318**: 938.
[2] Pierre Auger Collaboration, J. Abraham *et al.* , Phys. Rev Lett. 2008, **101**: 061101.
[3] High Resolution Fly's Eye Collaboration, R. U. Abbasi *et al.* , Phys. Rev Lett. 2004, **92**: 151101.
[4] V. S. Beresinsky, G. T. Zatsepin, Phys. Lett. 1969, **28B**: 423.
[5] S. Yoshida, M. Teshima, Prog. Theor. Phys. 1993, **89**: 833.
[6] M. Ahlers *et al.* , Astropart. Phys., 2010, **34**: 106.
[7] IceCube collaboration, R. Abbasi *et al.* , 2011, Phys. Rev. D **83**: 092003.
[8] A. Ishihara for IceCube Collaboration, *these proceedings*.
[9] http://www.km3net.org/
[10] IceCube Collaboration, R. Abbasi *et al.* , 2010, Phys. Rev. D **82**: 072003.
[11] K. Kotera, D. Allard, A. V. Olinto, 2010, JCAP **10** 013.
[12] R. Engel, D. Seckel, and T. Stanev, Phys. Rev. D **64**, 093010 (2001).
[13] O. E. Kalashev, V. A. Kuzmin, D. V. Semikoz, G. Sigl, Phys. Rev. D, 2002, **66**: 063004.
[14] G. J. Feldman, R. D. Cousins, 1998, Phys. Rev. D **57**: 3873.
[15] Pierre Auger Collaboration, J. Abraham *et al.* , 2010, Phys. Rev. Lett., **104**: 091101.
[16] M. Ahlers, L. A. Anchordoqui, S. Sarkar, 2009, Phys. Rev. D **79**: 083009.
[17] D. S. Fixsen *et al.* , 1998, Astrophys. J. **508**:123.

Evaluating gadolinium for use in Super-Kamiokande

LLUÍS MARTÍ MAGRO[1] FOR THE SUPER-KAMIOKANDE COLLABORATION
[1]*Kamioka Observatory, Institute for Cosmic Ray Research, University of Tokyo, 456 Higashi-Mozumi, Kamioka, Hida, Gifu, 506-1205 Japan*
martillu@suketto.icrr.u-tokyo.ac.jp
DOI: 10.7529/ICRC2011/V04/0966

Abstract: Neutron tagging in water Cherenkov detectors like Super-Kamiokande has enormous advantages, e.g. in the detection of galactic supernovae and the diffuse supernova neutrino background [DSNB]. For DSNB, where the signal measurement is limited by large backgrounds, neutron tagging is indispensable. Gadolinium, with its large neutron capture cross section and the resulting delayed 8 MeV gamma cascade has been proposed in GADZOOKS! and would make it possible. However, the addition of a gadolinium compound has potential effects that are being evaluated at EGADS, a dedicated gadolinium R&D facility at the Kamioka Observatory. EGADS features a 200 ton tank, water filtration systems, transparency measuring equipment, and 240 50-cm PMTs.

Keywords: Super-Kamiokande, neutron tagging, Cherenkov detector, supernova, neutrino, gadolinium

1 Introduction and Motivation from Diffuse Supernova Neutrino Background

The SK detector is a very versatile detector. It has the best proton lifetime limit, observed atmospheric and solar neutrino oscillations and accelerator neutrinos [1, 2, 3, 4]. Studies on the Diffuse Supernova Neutrino Background (DSNB), neutrinos from all previous core-collapese supernovae in the universe, have also been performed and SK also has the best limit [5]. Here, the inverse beta decay (IBD):

$$\bar{\nu}_e + p \rightarrow e^+ + n \quad (1)$$

plays a central role, since $\bar{\nu}_e$ has a cross section two orders of magnitude larger than for ν_e elastic scattering. At SK we can currently detect effectively the positron only. The observation of the DSNB is limited by two irreducible backgrounds: at low energies by invisible muon decay (muons below Cherenkov threshold that decay into electrons) and at high energies by atmospheric neutrinos. The lower energy threshold is defined by our ability to remove spallation events.

In pure water, the neutron from the IBD is captured by hydrogen and yields a 2.2 MeV gamma, which is very difficult to detect. However, if we could detect the neutron capture, the coincidence detection of positron and neutron (delayed) would enormously reduce those backgrounds. In 2003, John F. Beacom and Mark R. Vagins proposed the addition of gadolinium in GADZOOKS! [6]. The cross section for neutron capture on Gd is about 5 orders of magnitude larger than on hydrogen and yields an 8 MeV gamma cascade. Because of the much larger cross section, with the addition of just 0.2% of gadolinium sulfate, $Gd_2(SO_4)_3$, about 90% of the neutrons would be captured on Gd.

Another very important feature is that this is the only technique that can be used in large detectors while keeping costs relatively low.

Galactic Supernova Neutrinos

The benefits of neutron tagging are of course applicable to galactic supernova neutrinos. Adding 0.2% of gadolinium sulfate will make it possible to tag IBD events individually and extract their spectrum. Since this is the most numerous reaction, being individually tagged implies that we will reduce the background for other reactions. An important consequence of this is that now, our supernova pointing accuracy from neutrino elastic scatters is expected to increase by a factor of about 2 [7].

Another benefit of the background reduction will be that it will allow us to observe neutrinos from the cooling phase of the supernova to much later times.

Reactor Neutrinos

Reactor $\bar{\nu}_e$ neutrinos are observed from the IBD reaction too. Since the reactor signal dies away above 8 MeV, the DSNB signal above 10 MeV will unaffected by the reactor flux. The great advantage of SK compared to KamLAND is its larger fiducial volume which translates into a much larger statistics.

It has been calculated [8] that we could achieve a high precision of the solar neutrino mixing parameters within a few years measuring reactor antineutrinos. SK with Gd would

dramatically improve the precision in Δm^2_{12}, while the improvement in $sin^2\theta_{12}$ although not as substantial, would be significant.

2 EGADS R&D Project

Given the added value that this technique would mean to water Cherenkov detectors and specifically the tremendous improvement that it would mean to SK, many efforts have been invested in making it possible. Shortly after the GADZOOKS! paper appeared, tests on the filtration system and materials aging started. Since 2009 a new project has been funded to build a facility that mimics the SK conditions and has given more momentum. This project is called EGADS, Evaluating Gadolinium's Action on Detector Systems, and aims to show that the idea works.

Since the project was funded in 2009 a new hall near the SK detector has been built. Here, a 200 ton stainless steel tank is now in place with its own water system and other ancillary equipment. This water tank has been filled with pure water and under these conditions the water filtration system has been tested. In the near future, we plan to install 240 50-cm PMTs and its own data acquisition system, see Figure 1. After all the equipment has been deployed we will be able to answer all the questions related to: Gd loaded water filtration system, material effects, Gd loaded water transparency, neutron background and techniques on how to add or remove Gd. I will briefly discuss them here.

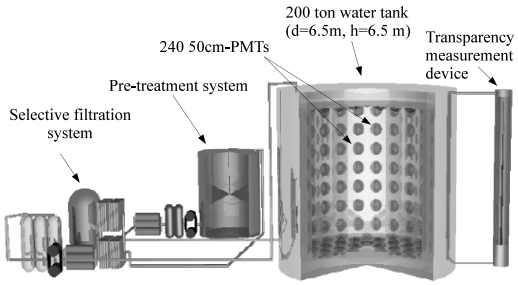

Figure 1: Schematic view of EGADS (Evaluating Gadolinium's Action on Detector Systems), from left to right: selective filtration system, pre-treatment system, water tank and UDEAL.

Water Transparency: the water transparency is a very important parameter in a water Cherenkov detector. Because dissolved substances may reduce the transparency directly or indirectly (by degrading detector materials), it is necessary to monitor it continuously. A device to measure the water transparency had been developed first at the University of California, Irvine (UCI), and now a similar device, UDEAL (Underground Device Evaluating Attenuation Length) has been installed at EGADS, see Figure 2.

This device consists of three basic components: a beam injector and intensity monitor (upper part), pipe (middle) and transmitted light instrument (below the pipe). The beam injector has seven different wave lengths (λ = 337nm, 375nm, 405nm, 445nm, 473nm, 532nm and 595nm). One wave length is used at a time. Part of the beam is directed through the pipe, while part of it goes into an integrating sphere with UV enhanced photodiode. The pipe is filled to a given height with water and therefore, when the beam reaches the lower integrating sphere, its intensity changes. Measurements of the beam intensities at different wave lengths and water heights enables us to measure the water transparency and its dependence with the wave length.

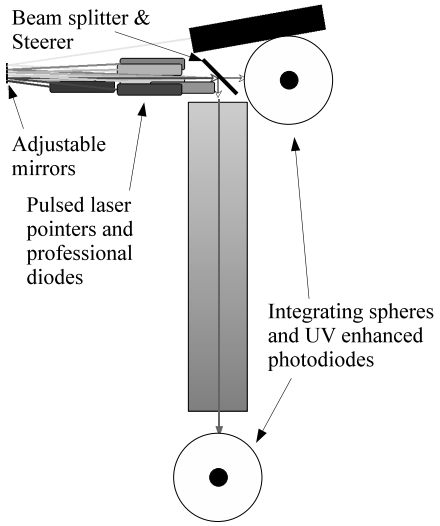

Figure 2: Schematic view of UDEAL (Underground Device Evaluating Attenuation Length): beam injector and intensity monitor (top), pipe (middle) and transmitted light measurement instrument (bottom).

The pure water in the 200 ton tank has been circulated through the water system for months and monitored at three different positions of the 200 ton tank (bottom, centre and top) with good quality transparency data and very consistent results from UDEAL. These data show that the pure water has a good transparency and comparable to the pure SK water. One example can be seen in Figure 3. These data were taken from the 200 ton tank bottom for three wave lengths: 337nm, 375nm and 405nm. The 200 ton tank was filled with pure water and soon the water attenuation length started to decrease. As soon as the water filtration system ran continuously the water attenuation length increased and became stable.

Selective Water Filtration System: Since the water quality is of major importance in water Cherenkov detectors this is the pillar of the EGADS project. In order to ensure a good water transparency, the water filtration system should remove all impurities in water except Gd. Long before the EGADS project started, a prototype had been developed

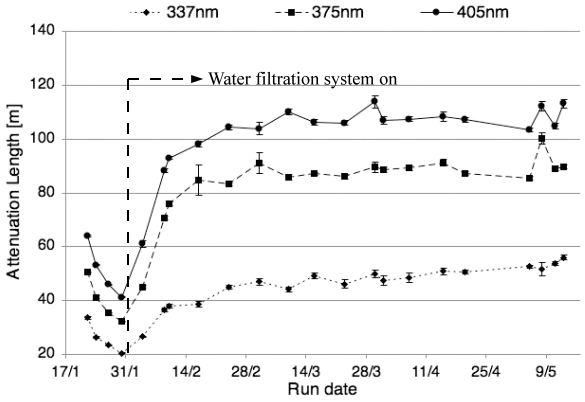

Figure 3: Water attenuation length for pure water from the 200 ton tank (bottom) for three wave lenghts: 337nm, 375nm and 405nm. The water attenuation length decreases first and then increases as soon as the water filtration system ran continuously.

and tested at UCI. The water system achieved a good transparency while retaining almost all the Gd (over 99.9% per pass). The strategy is to filter out all the impurities in water larger and smaller than Gd, thus creating a band-pass filter, that removes everything but Gd. This is achieved by filtering first with an ultra-filter which removes impurities larger than Gd. Its product goes then to nano-filters where their reject collects particles of about the size of Gd while the product goes through a reverse osmosis (RO) filter to remove smaller impurities. Finally, the RO product (pure water) and the nano-filter reject (Gd and any similar-sized impurities) are then returned to the tank.

The water system for EGADS was installed last January and has been running since then, keeping the water quality high and comparable to the SK pure water, i.e. the water attenuation is similar although slightly smaller than the ultra-pure SK water.

Material Effects: adding Gd can influence the material ageing. We need to ensure that adding a Gd solution will not corrode or easily age detector materials. Metallic Gd is not soluble in water and gadolinium(III) chloride, $GdCl_3$, was proposed in the past. However, a test with one kiloton water tank with 0.2% of $GdCl_3$ showed that although $GdCl_3$ did not decrease water transparency, chlorine lifted old rust already present in the one kiloton tank. Our best candidate now is gadolinium sulfate, $Gd_2(SO_4)_3$.

Studies at the Okayama University have tested $Gd_2(SO_4)_3$ with several materials under different conditions, e.g. pH and temperature, with promising results.

Neutron Background: currently at SK neutrons are invisible but once we add Gd ambient neutrons will become visible. The present amount of neutrons at SK is very low. However, adding a Gd solution has to be done with care since it may add neutron background, specially important are those produced in the fiducial volume. It is therefore very important to keep this background under control since it would affect the trigger rates and current analyses.

A Gd batch has been sent to the Laboratorio Subterraneo de Canfranc (LSC), Spain, and measured with a very low background germanium detector. Concentrations of 15 and 1 ppb of uranium and thorium, respectively, were found. A detailed analyse shows that the largest neutron source is the ^{238}U chain and specially its spontaneous fission. This chain represents $\approx 70\%$ of the neutron background. Its neutron production spectrum is shown in Figure 4. Therefore, if we could remove uranium efficiently we would greatly reduce the neutron background.

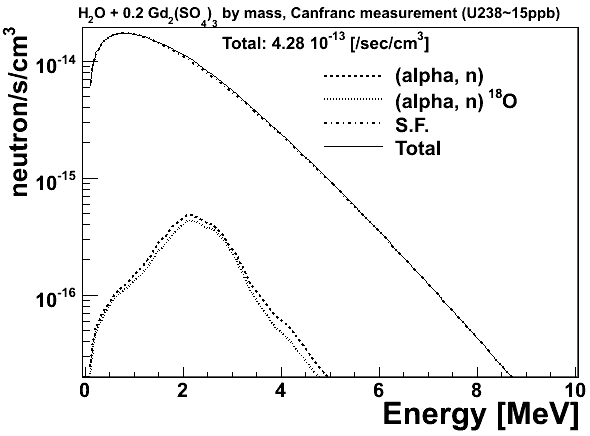

Figure 4: Neutron background per cubic centimetre spectrum for the ^{238}U chain (15ppm). The spontaneous fission (dash-doted line) is the largest contribution.

From the other chains, ^{235}U and ^{232}Th, the ^{235}U chain is the next most important contribution. However, removing uranium would not substantially decrease the neutron background for this chain because, the ^{235}U spontaneous fission is not the main source of neutrons here and the ^{235}U chain activity would be sustained by protactinium (^{231}Pa).

Taking into account the U/Th chains with the above concentration, the total neutron yield in the SK inner detector is $\approx$ 1800/day. To reduce it, tests with the resin Amberjet4400 (AJ4400) have been done. This resin can reduce the amount of U and Th. However, it has been seen that after an extensive use of AJ4400 the Th concentration is not significantly reduced, while the U concentration drops to less than 1% of the original concentration.

With the resin AJ4400 and taking into account the capabilities of the SK water system to reduce U/Th and Rn we estimate that the neutron yield can be reduced at least to about 600 neutrons/day.

How to Add/Remove Gd: a pre-mix 15 ton tank has also been installed together with a pre-treatment system. The 15 ton tank has a stirrer to facilitate the dissolution of gadolinium sulfate in water. The pre-treatment system includes the AJ400 resin to reduce U concentration. The dilution of Gd

into water is easier if the pH is lowered. For this purpose, a relatively small amount of sulfuric acid, H_2SO_4 will be used to facilitate its dilution.

It is also important to monitor how uniformly can we dissolve Gd. For this purpose, samples will be taken at several locations and the Gd concentration will be measured. The concentration can be measured with an atomic absorption spectrometer (AAS) with a precision of $\approx 5\%$.

Techniques to efficiently remove Gd from water have also been studied as we must not release Gd into the environment. Currently, we use a resin that is capable of removing Gd. Detailed studies about the efficiency of this method are being carried out. So far, we know that the Gd concentration after processing a 0.2 % $Gd_2(SO_4)_3$ solution is below the ppm level.

3 EGADS Schedule

In the next few months we will make very decisive steps. Very soon we will circulate Gd in our system. The water filtration system has proven to keep a high pure water quality. We expect this to be the case when we add gadolinium sulfate into the water once we retune it to the new situation. Preparations for PMT installation are being done too: installation and PMT structures, wiring, PMT pre-calibration, etc.

4 Summary

Many advantages are expected from neutron tagging in a light water detector. Being able to clearly identify $\bar{\nu}_e$ from the coincidence detection of positron and neutron from $\bar{\nu}_e + p \rightarrow e^+ + n$ reactions (and similarly for $\bar{\nu}_\mu$) would allow us to start new studies in antineutrino spectroscopy. This will have dramatic implications in Supernova, reactor and solar neutrinos.

This has motivated a very intensive R&D program to study the feasibility of antineutrino tagging in SK. The coincidence detection in $\bar{\nu}_e + p \rightarrow e^+ + n$ reactions will be possible by adding 0.2% of gadolinium sulfate. The decisive test is being now performed using a 200 ton tank, EGADS project. This includes: the water filtration system, ageing test of detector systems in presence of Gd, its impact on the water transparency and the uniformity of the solution.

Once this program is completed we will be prepared to add Gd into SK and start a new era in many fields of neutrino physics.

References

[1] H. Nishino *et al.* [Super-Kamiokande Collaboration], Phys. Rev. Lett., 2009, **102**: 141801.

[2] Y. Fukuda *et al.* [Super-Kamiokande Collaboration], Phys. Rev. Lett., 1998, **81**: 1562

[3] S. Fukuda *et al.* [Super-Kamiokande Collaboration], Phys. Lett., 2001, **B 539**: 179.

[4] M.H. Ahn *et al.* [K2K Collaboration], Phys. Rev. Lett., 2003, **90**: 041801.

[5] M. Malek *et al.* [Super-Kamiokande Collaboration], Phys. Rev. Lett., 2003, **90**: 061101.

[6] J. F. Beacom and M. R. Vagins, Phys. Rev. Lett., 2004, **93**: 171101.

[7] P. Vogel and J. F. Beacom, Phys. Rev., 1999, **D60**: 053003.

[8] S. Choubey and S. T. Petcov, Phys. Lett., 2004, **B594**: 333-346.

ARIANNA – A New Concept for High Energy Neutrino Detection

STEVEN W. BARWICK[1], FOR THE ARIANNA COLLABORATION
[1]*University of California, Irvine, CA 92697*
barwick@hep.ps.uci.edu

DOI: 10.7529/ICRC2011/V04/0976

Abstract: Dedicated high-energy neutrino telescopes based on optical Cherenkov techniques have been scanning the cosmos for about a decade. Consequently, neutrino flux limits have improved by several orders of magnitude in the TeV-PeV energy interval. At higher energies, detectors using radio Cherenkov techniques have produced aggressive limits on the neutrino flux. In this paper, we describe a novel concept for the next generation of astrophysical neutrino detection, called ARIANNA, which takes advantage of unique geophysical features of the Ross Ice Shelf in Antarctica. ARIANNA, based on the radio Cherenkov technique, is designed to improve the sensitivity to neutrinos with energies in excess of 10^{17} eV by at least a factor of 10 relative to current limits. We describe the physics motivation for ARIANNA, which includes a measurement of the GZK neutrino flux, whose existence is relatively secure but frustratingly small, and the search for non-standard particle physics. We outline our plans to construct the Hexagonal Radio Array, the first stage of ARIANNA that was approved by the US NSF in mid 2010.

Keywords: ARIANNA, Antarctica, neutrino, EHE, UHE, GZK, astronomy, sources, detector, Ross Ice Shelf, diffuse

1 Detector Description

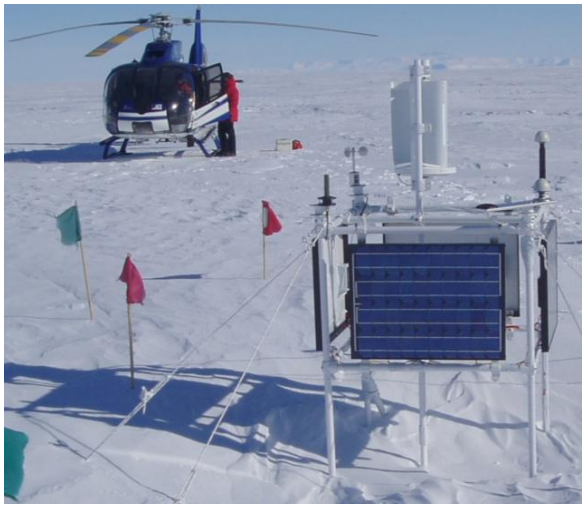

Figure 1: Prototype ARIANNA station deployed in Antarctica in December 2009. Radio receivers and electronics (marked by flags) are buried under snow and not visible.

The primary mission of the ARIANNA array will be to establish the absolute cosmogenic neutrino flux produced by the interaction of cosmic rays with CMB. The extreme energies and solely weakly-interacting nature of cosmogenic neutrinos (from this perspective, neutrinos are the purest of nature's known particles) provides a wonderful laboratory to search for new physics beyond the scope of the standard model of particle physics. The goals of this project also provide a complementary strategy to those adopted by the teams of researchers who are now using the Large Hadron Collider (LHC) to search for new physics.

The idea of using a surface array of radio receivers to search for astrophysical sources has a long history [1]. The ARIANNA (Antarctic Ross Iceshelf ANtenna Neutrino Array) concept [2,3] utilizes the enormous Ross Ice Shelf near the coast of Antarctica to increase the sensitivity to ultrahigh energy cosmogenic neutrinos by roughly an order of magnitude when compared to the sensitivity of existing detectors and those under construction. ARIANNA exploits a fortuitous natural phenomenon: the water-ice interface at the bottom of the Ice Shelf reflects radio signals with remarkable fidelity [4]. Consequently, the reflected conical Cherekov pulses can be detected from neutrinos traveling in any downward direction that interact in the ice. The reflected (and direct) radio pulses are detected by autonomous antenna stations located near the top of the ice surface, which greatly simplifies deployment of a large array. Moreover, shadowing produced by the gradient in the index of refraction near the surface is mitigated by the mostly vertical paths taken by the reflected pulses.

ARIANNA capitalizes on several additional features of the site itself: it is geographically close to McMurdo, the major US base in Antarctica, and it exhibits low levels of anthropogenic radio noise. Simulation tools were developed from a relatively mature simulation

package utilized by the ANITA collaboration [5]. Radio emission is estimated via standard parameterizations that were validated at accelerators. For concreteness, each station consists of 4-8 single-polarization log-periodic dipole antenna (LPDA) with gain (~7), bandwidth (108 MHz-1.3 GHz) and angular sensitivity specified by the manufacturer. The receiver antennas are arranged symmetrically with a diameter of 6m, point vertically down, and embedded in the topmost several meters of the ice shelf with a surface density of 0.3 g/cm^3. As discussed in the next section, due to theoretical imprecision we must allow for substantial flexibility in detector sensitivity. Initially, ARIANNA stations can be deployed on a sparse 31x31 grid with 1 km spacing to maximize collecting power – viewing ~0.5 Teraton of ice - and since they are located on the surface, can be redeployed with a smaller separation (~0.3km) to maximize angular and energy resolution once the flux is known. The surface area and configuration of the array can be adjusted to follow science.

The high sensitivity of ARIANNA results from nearly six months (or possibly more with the addition of wind power or fuel-based electric generators) of continuous operation, low energy threshold (~3x10^{17} eV), and a view of more than half the sky (declination +20 to -90 degrees).

2 Science Motivation

Somewhere out in space, cosmic rays are born at extremely high energy. During their travels from the most distant recesses of the Universe, the highest energy cosmic rays collide with photons [6] in the microwave background to create "cosmogenic" or "GZK" neutrinos [7]; potent new messengers with remarkable properties. They provide a novel opportunity to help unravel the origins of the cosmic rays [8]. More dramatically, the neutrino "beam", which interacts solely by the weak force, can be exploited to attack the question of what lies beyond our current understanding of the physical world, as defined by the standard model of elementary particle physics. ARIANNA can probe for physics beyond the standard model [2] by measuring the neutrino cross-section at center of mass energies near 100 TeV with good precision. Unfortunately, despite tremendous growth in instrumental sensitivity over the past decade, no detector has yet observed a source that emits neutrinos with energies above 100 GeV due their small fluxes and incredibly weak interaction with matter. We believe that the ARIANNA concept has sufficient power to dramatically improve the odds of success at cosmogenic energies.

During the past decade, Antarctica has emerged as one of the preferred locations to construct and operate high energy neutrino telescopes. Neutrinos interact so infrequently that a realistic detector must encompass or survey an enormous number of target nuclei, and the target medium must be transparent to the electromagnetic signals generated by the interaction. Several large projects (AMANDA [9], ANITA [10], IceCube [11], and RICE [12] and newer proposals such as ARA[29]) exploit the fact that Antarctic ice is transparent to radio and optical emission. At the very highest energies, the most secure prediction for a measurable flux of neutrinos arises from the "GZK mechanism" [6], which involves the collision between cosmic rays and cosmic microwave photons. The subsequent neutrino production at energies between 10^{17}eV-10^{20}eV from the GZK mechanism is called "GZK neutrinos" or "cosmogenic neutrinos" [7]. Recently, the Auger [13] and HiRes [14] collaborations have reported strong evidence for GZK suppression in cosmic ray spectra, thereby increasing confidence in the existence of cosmogenic neutrinos.

Since the now confirmed GZK mechanism is based on widely accepted tenets and measurements, the predictions for the neutrino flux is perhaps the most secure of any in high energy neutrino astronomy. Neutrinos are uncharged and only interact weakly. Consequently neutrinos can travel unimpeded from the most distant sources and point back to their origin. In particular, GZK neutrinos are produced within a few tens of Mpc of the cosmic ray source, so it is expected that GZK neutrinos will point back with sub-degree accuracy. Moreover, the neutrino energy spectrum helps to break model degeneracy between source distribution and evolution [8]. Thus, the scientific promise of high energy neutrino astronomy remains as exciting, compelling and elusive as ever.

Despite the recent exciting developments from Auger and HiRes, there remains significant theoretical imprecision in the estimating the energy spectrum of cosmogenic neutrinos due to uncertainty associated with the elemental composition and injection spectra of the cosmic rays, source evolution, and cosmology. Representative) predictions for the cosmological neutrino flux are shown in Table 1. Many authors assume pure proton composition injected with an energy spectrum proportional to E^{-2}. Different assumptions for source evolution, injected energy spectrum and cutoff at high energies account for the variation, and predictions almost 1 order of magnitude higher exist [18]. Given the current level of uncertainty, it is plausible that the flux is too low for currently operating instruments. The next generation of UHE neutrino telescopes must be flexible and powerful enough to observe potentially very small fluxes.

When ultra-high energy neutrinos interact in a dense medium, such as the ice in the Ross Ice Shelf, the enormous cascade of secondary particles emit an intense sub-nanosecond pulse of coherent Cherenkov radiation at *radio* wavelengths. This emission mechanism, known as the Askaryan effect [15], was experimentally confirmed in ice and other media less than a decade ago [16,17]. The effect arises from the excess of negative charge that builds up as electrons are swept out by the development of the cascade. The longer wavelengths of the broadband emission from the collective motion of the net charge will add coherently, producing a short duration, intense radio pulse. The shower dimensions determine the wavelengths of coherent emission, typically less than 5 GHz, but absorption in the media tend to limit the upper frequencies to ~1 GHz.

Cosmogenic neutrinos, which can be thought of as a "beam" that interacts solely by the weak force, collide with nuclei in the ice with center of mass energies

at ~100 TeV, and thereby provide an opportunity to study physics at energies above that which is available at current or planned accelerator facilities. Several ideas exist in the literature to measure the neutrino cross-section at extremely high energy [19], but in practice, suffer from limited statistical precision. ARIANNA has sufficient collecting power to ensure adequate statistics to determine the cross-section from the angular dependence of the measured flux near the horizon [9] using the opacity of the ice and earth. Thus, ARIANNA is sensitive to models incorporating extra dimensions and other proposed extensions to the standard model that impact the interaction length of the neutrino.

ν Model	N_ν	MRF
Cosmogenic(GZK):		
ESS-Fig 9 [20] -p	40	0.05
Y-QSO [23] -p	23	0.1
Y-GRB [23] -p	51	0.044
WB [24] -p	16	0.14
Ahlers et al. [25] -p	12	0.19
Ave et al. -max [26]- Fe	3	0.75
Non-cosmogenic:		
AGN-MPR [27]	154	0.015
AGN-M [28]	62	0.037

Table 1: ARIANNA event rates (N_ν) and MRF for cosmogenic flux models that span the range of flux predictions. We also include a short, representative set of AGN and GRB models. MRF computed assuming zero neutrinos observed. Predictions are excluded for MRF<1. Computed for 1 year. HRA event rate (see section 3) is factor 400 smaller.

Although we have focused on cosmogenic neutrino production, it is not the only potential source of neutrino messengers at ARIANNA energies. The sources of cosmic rays may also produce neutrinos directly. ARIANNA can survey the southern half the sky for point sources of high-energy neutrinos from AGN or GRB with unprecedented sensitivity (see Table 1) for energies between 10^{17}-10^{19} eV. It would also be sensitive to novel, if somewhat unlikely, components of cosmology such as topological defects produced in the Big Bang. Of course, we recognize that the study of ultrahigh energy neutrinos with a uniquely sensitive instrument could reveal completely unexpected phenomena.

The scientific advantages of ARIANNA are summarized as follows:

(1) ARIANNA increases the sensitivity for the detection of GZK neutrinos by more than an order of magnitude when compared to present limits. Simulations indicate that the full ARIANNA detector can observe **~40 events per year** of operation based on a widely-used prediction for the GZK neutrino flux (Fig. 9 of Ref [20]).

(2) The "low" energy threshold of ARIANNA, combined with high statistics, provides an unparalleled opportunity to measure the flux over a broad interval of the GZK neutrino energy spectrum, rather than just the low energy or high-energy tail of the spectrum. Neutrino energy spectra provide critical constraints on source evolution, distribution, and cosmic ray injection spectra. ARIANNA can test models that assume that the extragalactic cosmic rays are mixed elemental composition [26].

(3) Point source sensitivity is expected to reach $E^2(dN/dE) \sim 3\times10^{-9}$ GeV/cm^2/s after one year, and uniquely test some models with spectra that strongly deviate from E^{-2} power laws.

(4) As mentioned, ARIANNA can probe for physics beyond the standard model by measuring the neutrino cross-section at center of mass energies of 100 TeV, a factor 10 larger than available at the LHC [2]. Preliminary studies indicate that the cross-section can be measured with a precision of 25%, benefiting from the large statistical sample of 400 events spanning $>2\pi$ solid angle. In another example, recent papers [30, 31] have pointed out that small violation of Lorentz-invariance can dramatically impact the energy spectrum of cosmogenic neutrinos, emphasizing the need for a high statistics measurement of the energy spectrum.

3 Hexagonal Radio Array (HRA)

In September 2010, NSF agreed to support the construction of seven ARIANNA stations arranged in a hexagonal pattern (plus one in the center) over a period of four years. The separation between stations in the hexagonal radio array (HRA) is 1 km. NSF also agreed to operate a long-range wireless link to transfer data from the ARIANNA site to the northern hemisphere. We plan to (1) continue to investigate physics and anthropogenic backgrounds over a two year period, (2) improve our knowledge of the attenuation and reflection properties of the ice shelf, (3) procure station components, (4) integrate subsystems, (5) deploy and commission the autonomous stations, and (6) evaluate the performance of the data acquisition and control systems based on the "advanced ATWD" integrated circuit [21]. The advanced ATWD combines trigger decisions in the time domain with high speed digitiziation that requires relatively low power and provides good dynamic range and linearity.

A prototype single-channel waveform capture board incorporating the new digitizer was successfully tested at the ARIANNA site in 2010. The fidelity and functionality of the prototype DAQ electronics meets project requirements. Our plan to develop the 8-channel data acquisition electronics, and communication and calibration subsystems build upon the successful development and testing of the existing single-channel waveform capture system, thus minimizing the chance of inadvertent incorporation of hardware and software design errors. Stations will be deployed in a phased approach with sufficient time to evaluate and iterate between deployment seasons.

3.1 Prototype station

The ARIANNA concept was initially validated by *in situ* measurements of the radio properties at the site in Moore's Bay, Antarctica [22]. Following concept validation, the ARIANNA team deployed a prototype station (see ref. [3] for technical specifications) - the primary technical component of the array- in December 2009

(shown in Fig. 1) to assess the mechanical and electrical robustness of the electronic components, especially during the sunset and sunrise periods of the Antarctic year. The prototype station collects waveform data and autonomously transmits housekeeping information to ARIANNA collaborators using an Iridium modem and high-speed wireless internet installed by Raytheon Polar Services. It consists of 4 log-periodic dipole array (LPDA) antennas and provides a wealth of information on technical issues associated with the ARIANNA concept. The station computer controlled a set of relays to turn on the various systems in the station. When fully operational, the station consumes 25W of power, but near sunset, it was reduced to 14W by operating communication systems only when required.

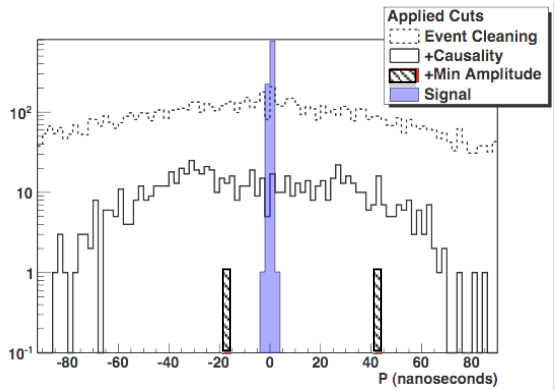

Figure 2: Planarity for simulated signal (filled histogram) and data events as a function of selection criteria. At the final cut level (stripe), no events remain.

We summarize the key findings:

(1) The ambient RF noise conditions are excellent. In over one month of data collected between Jan. 5, 2010 and Feb. 16, 2010 there are no events that were confused with neutrino signal (Fig. 2). After minor cleaning, the triggered events are distributed randomly in time and completely consistent with thermal noise in the ice. The average rates for the trigger condition of 2 of 3 antennas with amplitudes greater than a factor 5 above the rms noise fluctuations were measured to be 10^{-2} Hz.

(2) During Austral summer, solar power is sufficient to operate the station. During the continuous night of winter, wind and/or electric generators may supply power. The measured average wind speed was typically 5-10 knots, with only sporadic periods of winds over 20 knots, typically every 10 days. We installed a larger wind generator (Aerogen-612-F) in December 2010 to continue to evaluate wind as a possible source of power during the winter months.

(3) In Fig. 2, the planarity variable P sums the time differences for the four baselines between neighboring antennas (the diagonal baselines were not used in this analysis). The nearly planar wavefront expected from a neutrino signal would sum to approximately zero in this variable as shown by the solid black histogram. The P values for triggers from thermal noise are more diffusely distributed. The event cleaning removes a small sample of events with periodic time structure associated with Iridium communication and writing events to flash drive memory. Selection criteria based on straightforward timing causality and amplitude minimums remove all but 2 events and none in the signal region. The analysis of the triggered events indicate that the ARIANNA site has low anthropogenic sources of RF noise that mimic neutrino signals, which is expected because the site is shielded from narrow band transmitters at McMurdo by a high ridge known as Minna Bluff.

(4) A heartbeat and calibration transmitter demonstrated timing resolutions of 0.1ns per receiver channel and monitored slow drifts of absolute time delays.

Acknowledgements

This work was supported by the U.S. NSF Office of Polar Programs and U.S. NSF Physics Division, award numbers 0839133 and 0970175, and by the Department of Energy under contract DE-AC-76SF-00098. We also thank the dedicated staff of Raytheon Polar Services for their logistical support of the ARIANNA program.

References

[1] Gusev G , Zheleznykh I M, JETP Lett. **38** (1983) 611.
[2] Barwick S W, J. Phys. Conf. Ser. **60**(2007)276.
[3] Gerhardt L, *et al.,* Nucl. Inst. Meth. **A624**, 85 (2010)
[4] Hanson J, for ARIANNA, paper 0340, these proc.
[5] Dookayka K, for ARIANNA, paper 0144, these proc.
[6] Greisen K 1966 *Phys. Rev. Lett*. **16** 748; Zatsepin G T and Kuzmin V A 1966 *JETP Lett.* **4** 78.
[7] Stecker F W 1973 *Astrophys. Space Sci*. **20** 47; Berezinsky V S and Smirnov A 1975 *Astro. Spa. Sci.* **32** 461.
[8] Seckel D and Stanev T 2005 *PRL* **95** 141101.
[9] Ahrens J, *et al.* 2004 *Phys. Rev. Lett.* **92** 071102.
[10] Gorham P W, *et al.* Phys. Rev. **D82** (2010) 022004.
[11] Achterberg A *et al.* 2006 Astropart. Phys. **26** 155.
[12] Kravchenko I, *et al.* 2006 *Phys. Rev* **D73** 082002.
[13] Auger Collaboration, 2010 Phys. Lett. **B685** 239.
[14] Abbasi R U, *et al.,* (HiRes), PRL **100**(2008)101101.
[15] Askaryan G A 1965 *JETP* **21** 658.
[16] Saltzberg D, *et al*. 2001 *Phys. Rev. Lett*. **86** 2802.
[17] Gorham P W, *et al.* 2007 PRL **99**: 171101.
[18] Kalashev O, *et al*, 2002 Phys. Rev. D**66** 063004
[19] Kusenko A and Weiler T 2002 *PRL* **88** 161101; Anchordoqui L A, *et al*., 2006 *PRL* **96** 021101.
[20] R. Engel, *et al.* , Phys. Rev. **D64**(2001)093010.
[21] Huang W, Wood S, and Kleinfelder S, , Conf. Record of IEEE Nucl. Sci. Symp. N13-50 (2009).
[22] Barrella T, Barwick S W, and Saltzberg D, 2011 J. Glac. **57**:61.
[23] Yuksel H& Kistler M, 2007 Phys. Rev. **D75**:083004
[24] Waxman E, Science **315**(2005)63.
Waxman E and Bahcall J, Astrop. 2000, J. **541**:707.
[25] Ahlers M, *et al.,* Phys. Rev. 2005, **D72**:023001.
[26] Ave M, *et al*., 2005 *Astropart. Phys*. **23** 19.
[27] K. Mannheim, *et al*., 2001 Phys. Rev. **D63**:023003
[28] Murase K, Phys. 2008 Phy. Rev. **D 78**: 101302(R).
[29] Allison P*, et al*., arXiv:1105.2854
[30] Scully S & Stecker F, Astrop. Phys. 34, 575 (2011).
[31] Mattingly D M, *et al*., Phys. JCAP02 007 (2010).

32ND INTERNATIONAL COSMIC RAY CONFERENCE, BEIJING 2011

Searches for Neutrinos from GRBs Using the ANTARES Telescope

REED, C.[1], BOUWHUIS, M.[1], PRESANI, E.[1] FOR THE ANTARES COLLABORATION
[1]*National Institute for Subatomic Physics (Nikhef), Amsterdam, The Netherlands*
cjreed@nikhef.nl
DOI: 10.7529/ICRC2011/V04/1085

Abstract: Multiple searches for neutrinos in correlation with gamma-ray bursts (GRBs) using data from the ANTARES neutrino telescope have been performed. One search uses data taken during 2007, at which time the telescope consisted of 5 detector lines, to measure the number of neutrino-induced muons in correlation with 37 GRBs that occurred during the data-taking period. While no correlations are observed, upper limits have been placed on the flux of neutrinos for different GRB models. A second search uses an alternative method to identify the shower at the neutrino-interaction vertex. This search is particularly sensitive to electron-neutrinos, but is able to observe neutrinos of any flavor. The sensitivity of this method to measure correlations between neutrinos and prompt photons emitted by GRBs is presented for a typical neutrino flux model.

Keywords: ANTARES, neutrino, telescope, gamma-ray burst, GRB

1 Introduction

First discovered in the 1960's, a gammy-ray burst (GRB) is observed as an extremely luminous flash of photons from a seemingly random point in the sky. The energy spectrum of these photons can be parametrized by a broken power law of the form $dN/dE \propto E^{\alpha}$, where $\alpha \approx -1$ below the break energy (typically around an MeV) and $\alpha \approx -2$ above it [1]. The large energy output of a typical GRB, around 10^{52} erg, combined with the GRB occurrence rate, about one per galaxy per million years, makes gamma-ray bursts a candidate source of high energy cosmic rays [2]. If GRBs are indeed accelerating hadrons, then these hadrons can be expected to suffer inelastic collisions with particles found in the acceleration regions, typically shock waves in relativistic jets [3, 4, 5]. Such hadronic interactions would ultimately yield mesons that decay to produce high-energy neutrinos.

The ANTARES telescope seeks to observe such cosmic neutrinos. For this purpose, the sea water of the Mediterranean Sea is used both as a target and Čerenkov medium. Neutrinos interacting with a nucleus in or around the instrumented volume will produce a hadronic shower at the collision vertex and will also produce an energetic lepton in the case of a charged-current interaction. These relativistic charged particles will produce Čerenkov radiation which can then be measured by photo-sensitive detection units in the ANTARES telescope. Neutrinos with an energy of around 10 TeV or higher will yield leptons traveling along the same trajectory as the neutrino. The source of such a neutrino can then be identified through its correlation with the neutrino's arrival time and/or direction.

To measure the light produced by charged particles generated in neutrino interactions, the ANTARES telescope consists of 12 detector lines that hold photo-sensitive units. Each line is anchored to the sea floor at a depth of 2475 m and supports 25 triplets of photo-multiplier tubes (PMTs) spaced evenly along the line in 14.5 m intervals. Further details of the detector configuration can be found in Ref. [6]. The detector lines are not rigid and are therefore affected by sea currents. The position and orientation of each PMT is determined by multiple positioning systems, described in reference [7].

While the sea water around the telescope is extremely dark, ANTARES can and does detect photons that are not due to neutrino interactions. The main sources of such background signals are (a) down-going muons produced by the interactions of cosmic rays with the Earth's atmosphere, (b) the decay of the radioactive isotope $^{40}\mathrm{K}$ present in the sea water and (c) light emitted by living organisms in the water. The latter two sources produce random signals in each photo-detection unit at a rate which varies with the sea current and is around 60-150 kHz per PMT. This background is reduced through the application of triggering algorithms that select potential neutrino events [8]. The so-called atmospheric muons form a background which is reduced after the trigger as part of a neutrino analysis procedure, as described in the following sections. With the search for transient sources such as gamma-ray bursts, the vast majority of the atmospheric-muon background can be reduced simply by demanding that a potential neutrino event correlates in time to the a priori known time of the source flare.

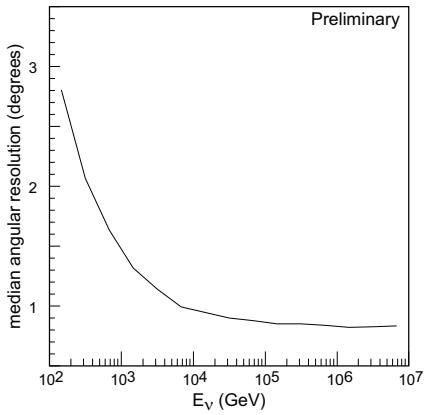

Figure 1: The angular resolution for muon tracks passing the selection described in the text, as a function of the neutrino energy.

2 Muon Track Search

Data taken by the ANTARES telescope during 2007 has been analyzed to search for neutrino-induced muons arriving in correlation with prompt photons from gamma-ray bursts. The prompt photon signals were detected by external satellite experiments, and were mainly long-duration GRBs detected by Swift [9, 10]. During this data-taking period, the ANTARES telescope was still under construction and consisted of only 5 detector lines. Muon candidates are extracted from raw data using a trigger algorithm that searches for a collection of causally-connected hits consistent with photons emitted by a muon traversing the detector [8]. The average trigger rate during the data-taking period was 1 Hz.

The muon trajectory is determined by a reconstruction package that uses probability density functions (PDFs) describing the expected photon arrival times, of both signal and background photons, to find the local muon position and direction that maximizes the likelihood that the observed hit times correspond to the expected times [11, 12]. Potential neutrino- induced muons are required to have an up-going trajectory (to reject muons from atmospheric cosmic-ray showers) and to have a good fit quality. The fit quality is estimated using two parameters, one based on the (log of the) value of the likelihood function, Λ, and one based on the angular precision calculated by the fit procedure, σ_f.

The distribution of these parameters observed in the data is well reproduced by simulations of the background due to atmospheric muons and neutrinos. While signal neutrinos have been simulated for several different spectra, a single set of cuts on the quality parameters is found to provide a good separation of signal from background events. The angular resolution for simulated muons passing these cuts is shown in Fig. 1.

The good angular resolution for muon tracks allows the direction, in addition to the time, of neutrino candidate events to be used in the search for correlations with gamma-ray bursts. The candidate tracks are required to point back to the GRB position to within 2°, and to occur during the arrival of prompt photons, i.e. during the T_{90} observed by the satellite. With these criteria, the expected background rate is found to be about 1.0×10^{-7} Hz. Of the remaining background events, 90% are due to (misreconstructed) atmospheric muons from showers above the detector and 10% to atmospheric neutrinos producing up-going muons.

This search for muons produced by neutrinos in correlation with gamma-ray bursts has been applied to the data taken during the flares of 37 GRBs that occurred during 2007. No neutrino candidate events are observed in correlation with the GRBs. The limits placed on the total $\nu_\mu + \bar{\nu}_\mu$ flux of these bursts at the 90% confidence level, using the Feldman-Cousins recipe [13], for three different GRB models are presented in Fig. 2. In addition to a general E^{-2} spectrum, two GRB neutrino spectra have been explored, both based on the fireball model. The Waxman-Bahcall model is that described in Ref. [14], and all GRBs are assumed to follow the same spectrum. The model of Guetta *et al.* is described in Ref. [15]. For this model, the neutrino spectrum of each GRB has been calculated separately using the (satellite) measured GRB parameters.

The reliability of the simulations used in this analysis has been studied in depth. The uncertainty with the largest impact arises from the efficiency and angular acceptance used for PMTs in the simulations. Reducing the efficiency of the tubes by 15% results in a 12% reduction of the acceptance of the telescope to E^{-2} muon-neutrinos, without affecting its angular resolution. A degradation of the PMT timing of only a few nanoseconds in the simulations is found to be incompatible with muon data. Such studies allow a conservative estimate of 15% to be placed on the uncertainty of the angular resolution of the telescope. Uncertainties on PMT timing can also reduce the acceptance of the telescope. The aggregate effect of the PMT timing and efficiency results in an uncertainty of 15% on the relative acceptance of ANTARES to cosmic muon-neutrinos.

3 Collision Vertex Shower Search

An additional search method has been developed to search for neutrinos of any flavor in correlation with gamma-ray bursts. This is done by locating the shower(s) produced at the vertex of the collision between the neutrino and a nucleus in or around the detector. Such a deep inelastic scattering will produce a hadronic shower irrespective of the neutrino flavor. In the case of electron neutrinos undergoing a charged current interaction, an electromagnetic shower is also produced at the vertex by the resulting electron or positron. Such showers occurring during the prompt photon emission of a GRB are then sought. This analysis is the first to seek to measure neutrinos of multiple flavors in the ANTARES data.

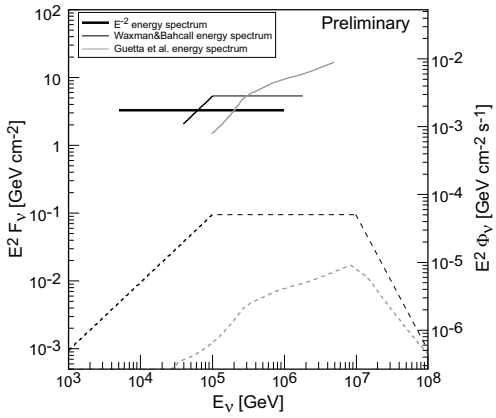

Figure 2: The upper limits on the total $\nu_\mu + \bar{\nu}_\mu$ flux of 37 GRBs, obtained by the muon track search, are shown by the solid lines for different flux models. Two of the flux models are shown by the dashed lines. The expected Waxman-Bahcall flux [14] is shown in black and the expected Guetta *et al.* flux [15] is shown in gray. The limits have been placed using data taken during 2007, when the telescope consisted of 5 detector lines.

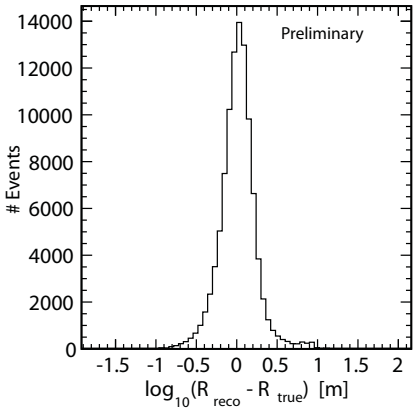

Figure 3: The spacial resolution of the shower reconstruction algorithm, determined using special calibration data in which LED beacons were flashed.

As the extent of the vertex shower is small compared to the spacing between detection units in the telescope, photons radiated by charged particles in the shower appear to originate from the same point in space and time. A simple procedure to reconstruct the position and time of the vertex shower has been developed. This reconstruction is applied to candidate neutrino events that have passed at least one trigger criteria. In addition to the trigger algorithm described in Sect. 2, a second trigger condition in which clusters of time-correlated hits in neighboring PMT triplets are sought has been applied. This second trigger algorithm was implemented during the 2008 data taking period.

The shower vertex position and time is then determined by minimizing the difference between the expected photon arrival times and the measured hit times. The arrival time of photons is assumed to depend only on the distance traveled from the shower vertex. The resolution of this reconstruction procedure has been studied using special calibration data taken by ANTARES in which LED beacons were used to obtain a burst of photons originating from a single point. The spacial resolution of the shower reconstruction is found to be around 1 m, as shown in Fig. 3, and the timing resolution around 2.4 ns.

A sample of reconstructed showers from triggered events will contain many electromagnetic showers produced by the stochastic energy loss of atmospheric muons traversing the telescope. Neutrino-induced showers are extracted from this background by placing cuts on quality parameters. The most discriminating variable is found to be the number of direct hits, $N_{DirHits}$: the number of selected hits having a time residual better than 15 ns. In addition, requiring the number of detector lines used in the fit to be greater than two is found to further reduce the atmospheric muon background. The cut on $N_{DirHits}$ has been determined by finding the value that minimizes the flux of a GRB required to discover a source with T_{90} =100 s at the 5σ level in 50% of test cases. The GRB flux used during cut optimization is assumed to follow the Waxman-Bahcall flux [14].

While a rare occurrence, a sparking PMT could produce a signal with a similar profile to that of a neutrino-induced shower. To eliminate such events, showers are rejected if they are reconstructed too close to any PMT. This cut effectively reduces the fiducial volume of the telescope by about 2%, but since the detector is capable of measuring high-energy neutrino-induced showers from far outside the instrumented volume, the ultimate effect on the sensitivity is much less.

The expected rate of background events passing the full set of quality cuts has been estimated from data taken during 2007-2008 in which no GRB was observed by a satellite experiment. During this time, the ANTARES telescope was under construction and data was taken while the telescope consisted of 5, 9, 10 and 12 detector lines. The average rate of surviving background events over the 2007 (5 line) and 2008 (9-12 lines) periods are found to be 4.4×10^{-5} Hz and 6.8×10^{-5} Hz, respectively. Note that the background is much larger than that obtained by the muon track search method described in Sect. 2, due to the lack of directional information. With the simple shower reconstruction, the field of view of the telescope cannot be restricted to the region of sky around the GRB.

The (Neyman) sensitivity of the vertex shower search method to observe the total flux of neutrinos and antineutrinos of all three flavors from GRBs [14] has been calculated. The sensitivity obtained for the 2007 and 2008 data taking periods, averaged over the viewable sky, is shown in Fig. 4. For the 2007 period, the detector con-

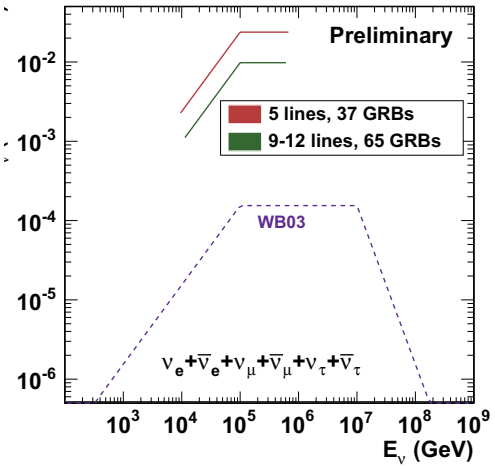

Figure 4: The sensitivity of the shower vertex search method applied to the average ANTARES detector as it was during the 2007 and 2008 data taking periods to the total neutrino and anti-neutrino flux of GRBs. The neutrino spectra are assumed to follow the Waxman-Bahcall spectrum [14].

sisted of 5 lines and the sensitivity is shown for the same 37 GRBs studied in Sect. 2. For the 2008 period, the sensitivity is shown for 65 GRBs and averaged over the 9, 10 and 12 line detector configurations.

The impact of systematic uncertainties in the detector simulations are under study. A significant effect comes from the possibility that the efficiency of each PMT is not accurately reproduced in the simulations. This is being studied by reducing the efficiency with which signal photons are converted to hits. Other simulation properties have also been studied by varying the Čerenkov light propagation, altering the high energy shower generation and using different models of the neutrino-nucleus cross sections. These effects lead to a reduction of the sensitivity of the shower analysis that is currently estimated to be 10-20%.

4 Summary

Two methods have been developed that can be used to search for a detectable flux of neutrinos emitted by gamma-ray bursts. Both methods attempt to measure neutrinos arriving at the Earth in conjunction with the prompt photons emitted by GRBs (as observed by external satellite experiments). For both methods, muons and neutrinos generated by the interaction of cosmic-rays with the Earth's atmosphere form a substantial background that must be reduced.

The first method reduces this background by measuring the trajectory of the muon produced by muon-neutrino interactions. The muon is demanded to be well reconstructed and to come from within 2° of the GRB. It has been applied to data taken by the ANTARES telescope during 2007, when the experiment consisted of 5 detector lines. No neutrino events are observed in correlation with 37 selected GRBs of 2007. Limits on the maximum flux that would have only a 10% chance to produce no events in the telescope have been calculated.

The second method seeks to measure the shower generated at the neutrino collision vertex and is the first analysis of ANTARES to be sensitive to neutrinos of any flavor. Showers produced by the stochastic energy loss of atmospheric muons are rejected by studying the topology of the shower event. Due to the lack of directional information available from the shower reconstruction, the background rate of this method is higher than that of the muon analysis. The sensitivity of the ANTARES telescope as it was during 2007-2008 to showers from a flux of neutrinos from GRBs has been determined.

References

[1] Band, D. et al., Astrophys. J., 1993, **413**: 281–292
[2] Waxman, E., Phys.Rev.Lett., 1995, **75**: 386–389
[3] Rhoads, J., Astrophys.J., 1997, **487**: L1
[4] Rees, M. and Meszaros, P., Astrophys.J., 1994, **430**: L93–L96
[5] Meszaros, P. and Rees, M., Astrophys.J., 1993, **405**: 278
[6] The ANTARES Collaboration, arXiv:1104.1607, 2011
[7] Brown, A. et al., arXiv:0908.0814, 2009
[8] Aguilar, J. et al., Nucl. Instrum. Meth., 2007, **A570**: 107–116
[9] Gehrels, N. et al., AIP Conf.Proc., 2004, **727**: 637–641
[10] Burrows, D. et al., Space Sci. Rev., 2005, **120**: 165
[11] Heijboer, A.: 2004, Track Reconstruction and Point Source Searches with ANTARES, PhD Thesis
[12] Heijboer, A. et al., arXiv:0908.0816, 2009
[13] Feldman, G. and Cousins, R., Phys.Rev., 1998, **D57**: 3873–3889
[14] Waxman, E. and Bahcall, J., Phys.Rev., 1999, **D59**: 023002
[15] Guetta, D. et al., Astropart.Phys., 2004, **20**: 429–455

32ND INTERNATIONAL COSMIC RAY CONFERENCE, BEIJING 2011

Search for atmospheric neutrino induced particle showers with IceCube 40

THE ICECUBE COLLABORATION[1]
[1]*See special section of these proceedings*

Abstract: One of the guaranteed fluxes under study by the IceCube neutrino telescope are neutrinos originating from cosmic ray induced air showers. These neutrinos come from the decay of π and K mesons (the conventional flux) and from the decay of charmed mesons (the prompt flux). Although several flux predictions exist, the electron neutrino flux has been measured only up to GeV energies. At TeV energies, where atmospheric neutrinos are an inevitable source of background events for astrophysical neutrino searches, the prompt flux becomes important and the flux predictions vary greatly. The detection of electromagnetic and hadronic particle showers, which are not only produced by electron neutrinos but which can be found in the final states of charged and neutral current interactions of all neutrino flavours, remains challenging. Given the sensitivity to all neutrino flavours, the good energy resolution that will be possible with fully contained shower events and the possibility to isolate the prompt from the conventional flux, the prospects of this detection channel are very promising. This poster will present an analysis done on a data sample collected with IceCube in its 40 string configuration as it was running from 2008 to 2009. The development of the event selection on a small part of the sample will be discussed.

Corresponding Author: Eike Middell[2] (eike.middell@desy.de)
[2]DESY Zeuthen, Platanenallee 6, 15738 Zeuthen, Germany

DOI: 10.7529/ICRC2011/V04/1097

Keywords: atmospheric neutrinos, IceCube, particle showers

1 Observing Neutrinos at the South Pole

The possibility to measure or constrain the flux of astrophysical neutrinos could help to solve a number of questions of which one of the most prominent, the question of the origin of cosmic rays, remains unanswered nearly a century after their discovery. Experiments that aim at the detection of these neutrinos must compensate for the small interaction cross sections and the low expected fluxes with increased size. With this year's completion of IceCube [1], the biggest neutrino detector to date, such an experiment is now available. For the experiment a cubic kilometer of glacial ice below the geographical South Pole was instrumented with photomultiplier tubes in order to detect the Cherenkov light of charged secondaries generated in neutrino interactions.

During the last 7 austral summers 86 holes were melted 2.5 km deep into the ice and into each a cable holding 60 so-called Digital Optical Modules (DOMs) has been deployed. The light sensors on 78 of these strings form a grid with a horizontal spacing of 125 m and a vertical distance of 17 m. As the spacing basically determines the energy threshold, the detector center was augmented with the denser DeepCore infill array between 2009 and 2010. The data-taking started already during the construction phase. This work uses data recorded between April 2008 and May 2009 when 40 strings were operational (IceCube 40).

IceCube's main physics goal is the detection of astrophysical neutrinos at energies above 100 GeV. These neutrinos must be isolated from the much larger flux of leptons created in cosmic ray induced air showers [2]. Among these a huge number of muons originating mostly from pion and kaon decays form the biggest part of the background. In the same air showers also atmospheric neutrinos are created [3]. In order to separate them from the astrophysical neutrinos a good understanding of their energy spectrum, flavour ratios and angular distribution will be helpful. This in turn is tightly coupled to our knowledge of the cosmic ray composition and hadronic interactions at energies that are out of reach of accelerator experiments.

The atmospheric neutrino spectrum is expected to consist of two components, the conventional flux from decaying pions and kaons [4, 5] and the prompt neutrinos from decays of short lived charmed mesons [6, 7]. The existing flux predictions for the latter vary widely and current measurements of the muon neutrino flux [8] are not yet able to resolve any prompt from the conventional component (see Fig. 1). Compared to muon neutrinos the flux of atmospheric electron neutrinos is lower and falls with a similar steep power law. Taking advantage of the lower energy threshold of the DeepCore array, IceCube has recently

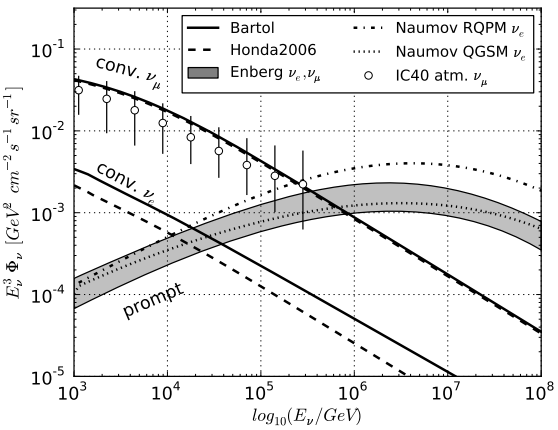

Figure 1: Different flux predictions for atmospheric neutrinos (taken from [4]-[7]) compared to a measurement of the atmospheric ν_μ-flux with IceCube 40 [8].

detected atmospheric neutrino induced showers around a mean energy of 40 GeV [9]. However, at TeV energies this measurement remains challenging, and only recently an analysis on the same IceCube 40 dataset started to find several promising candidate events [10]. In the energy spectrum of neutrino induced particle showers the prompt component is expected to emerge from the conventional at about 10^5 GeV which is about an order of magnitude lower than for muon neutrinos (see Fig. 1 and [11]). This makes shower events a suitable tool to isolate the prompt component.

2 Neutrino Induced Particle Showers

The events of interest in this study are particle showers emerging from deep-inelastic neutrino nucleon scattering. Particle showers can be found in the final states of charged current (CC) electron and tau neutrino interactions and in all neutral current (NC) interactions. Since IceCube cannot distinguish ν_e and low-energy ν_τ CC interactions from all-flavour NC interactions, analyses tailored to this event signature are effectively sensitive to all neutrino flavours. In NC interactions neutrinos deposit only parts of their energy so they show up as less energetic cascades. This leads to a lower effective area for muon neutrinos.

At TeV energies the particle showers have lengths of a few meters. But due to the large DOM spacing and the scattering of light in the ice showers appear as nearly point-like light sources. This results in spherical hit patterns which at higher energies appear significantly different from the hit patterns of muon tracks.

The separation from the muonic background is mostly impeded by the fact that high energetic muons stochastically undergo catastrophic energy losses in the form of bremsstrahlung showers along the track. Because of the considerable energy deposition these bright electromagnetic showers change the appearance of the track and make them less distinguishable from the searched signal. This has also a connection to the cosmic ray composition because proton air showers produce more often single highly energetic muons than for e.g. iron showers. From the latter often whole bundles of muons reach the detector and traverse the detector nearly in parallel. As the individual muons will have their stochastic energy losses at different positions, the whole bundle appears sufficiently different from a single particle shower and is easier to reject. Extensive simulations performed in the context of similar analyses done on the IceCube 22 dataset confirmed this effect albeit with low statistics. Those muons which passed all cuts were originating from proton air showers [12].

For electromagnetic showers the light yield scales linearly with energy. It has been shown in a Monte Carlo study that for electron neutrino interactions with energies of 10 TeV-1 PeV and well contained interaction vertices the energy may be reconstructed with a precision of about $\Delta \log_{10}(E_\nu) = 0.13$ [17].

3 Event Selection

In order to minimize statistical bias a blind analysis is performed. From the 364 days of usable data, 32 days are chosen to develop the event selection. The data was sampled uniformly over the year in order to reflect seasonal variations in the muonic background rate. Secondly, a large background sample of simulated muons from more than 10^{12} air showers were generated. A version of CORSIKA [13] with the Sibyll interaction model was adapted for IceCube and used to simulate the Hörandel polygonato cosmic ray spectrum [14]. Additionally more statistics of protons are currently produced in order to study the impact of composition uncertainties on the background prediction. For the expected signal interactions electron, muon and tau neutrinos were generated with a collaboration-internal simulation package that is based on ANIS [15].

The IceCube 40 detector operated at a trigger rate of about 1300 Hz. An online event selection based on two quickly calculable variables selected events at a rate of 16 Hz. A straight line fit through all hit DOMs at position $\vec{x}_i$ and time t_i yields a parametrization of the form $\vec{x}_i = \vec{x}_0 + \vec{v} \cdot (t_i - t_0)$ where the parameter $|\vec{v}|$ denotes how fast the hit pattern evolves. The second variable uses an analogy to classical mechanics in which it interprets the hit pattern as a rigid body and the recorded amount of light in each DOM as a mass. Spherical hit patterns can then be selected by calculating the eigenvalues of the tensor of inertia and requiring that all three eigenvalues are nearly of the same size. This online filter starts to get efficient above an energy threshold of about 1 TeV and is optimized for the search for the expected astrophysical E^{-2} flux for which it yields an efficiency of about 73%. For the less energetic atmospheric electron neutrino flux the efficiency is only about 35%.

The selected events were transmitted via satellite to institutes in the North where more elaborate track and vertex likelihood reconstructions can be performed. They provide a sufficient angular resolution for incident muons and with the likelihood value of the vertex reconstruction a quality parameter to select particle showers. Based on the vertex reconstruction also an energy estimator that considers the depth dependent optical properties of the ice [16] is run. Cuts based on these variables reduce the data rate to 2 Hz while keeping about 60% of the atmospheric ν_e signal. According to a predicted atmospheric neutrino flux [5] the sample contains at this point about 1200 ν_e and 10000 ν_μ (CC+NC) events which are still buried below $50 \cdot 10^6$ atmospheric muon events. The effective areas up to this cut level are shown in Fig. 2.

All passing events are fed into a more elaborate likelihood reconstruction [17]. This takes into account the full timing and amplitude information of the recorded light as well as tabulated results of detailed simulations of how light propagates in the ice [18]. For showers this provides estimates for the time and position of the interaction as well as the amount of deposited energy. Also the track reconstruction is repeated with an iterative optimization strategy in order to avoid local minima of the likelihood and to improve the angular resolution for background events [19].

So-called split reconstructions, which split the recorded photons by time into two sets and reconstruct each set individually, provide further information about the event due to the different timing behaviour of tracks and showers. For a track, later hits are downstream along the track while for particle showers they are centered around the vertex but at larger distance.

Based on an argument that shower induced hit patterns should be spherical another cut variable can be constructed. For an imaginary sphere with a given radius and centered at the reconstructed vertex one can calculate the fill ratio N_{hit}/N_{sphere}, where N_{sphere} denotes the number of all DOMs in the sphere and N_{hit} the number of triggered DOMs. This is especially useful to reject events containing several coincident atmospheric muons because the hit patterns of e.g. two coincident but well separated tracks can have many untriggered DOMs in between.

In order to further reduce the muonic background, DOMs at the surface of the instrumented volume are used to veto tracks that appear to enter and traverse the detector. Events for which the first triggered light sensor is located on the outer layer of the detector are rejected. Together with the requirement that the reconstructed vertex is located inside the fiducial volume, this forms a strict containment cut.

Finally those variables that still provide separation power are combined with a machine learning algorithm. In the TMVA framework [20] a boosted decision tree is trained which provides a final cut variable to select particle showers. Current investigations suggest that this event selection is able to remove the remaining background while keeping the prospect to find a few atmospheric neutrinos in the whole sample.

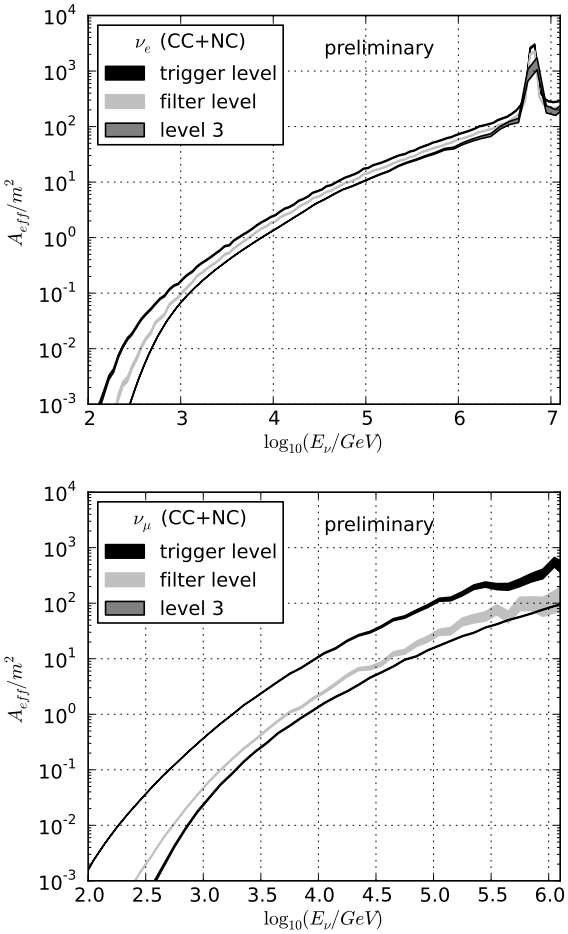

Figure 2: Effective areas for electron and muon neutrinos for the early stages of the analysis. The width of the bands denotes the statistical error. This differs between cut levels because datasets of different size have been used. The peak at 6.3 PeV for electron neutrinos is due to the Glashow resonance. The drop in effective area for muon neutrinos between trigger and online filter level illustrates the effect of tailoring the analysis to neutrino induced particle showers. At the presented cut levels the contribution of muon tracks from charged current interactions is still present. Therefore the effective area is still higher for muon than for electron neutrinos.

However, this statement relies on the Monte Carlo background prediction which has to be scrutinized before unblinding. Accordingly, studies of the systematic uncertainties in the simulated background sample (like for example a lighter cosmic ray composition) are ongoing and will be presented together with the final event selection at the conference.

References

[1] H. Kolanoski, IceCube summary talk, these proceedings.
[2] L. Anchordoqui and T. Montaruli, Ann. Rev. of Nuclear and Particle Science, 2010, **60**:129-162.
[3] T.K. Gaisser and M. Honda, Ann. Rev. of Nuclear and Particle Science, 2002, **52**:153-199.
[4] G.D. Barr *et al.*, Phys. Rev. D, 2004, **70**:023006.
[5] M. Honda *et al.*, Phys. Rev. D, 2007, **75**:043006.
[6] E.V. Bugaev *et al.*, Il Nuovo Cimento, 1989, **12C**:41-73.
[7] R. Enberg *et al.*, Phys. Rev. D, 2008, **78**:043005.
[8] R. Abbasi *et al.*, Phys. Rev. D, 2011, **83**:012001.
[9] IceCube Collaboration, paper 0324, these proceedings.
[10] IceCube Collaboration, paper 0759, these proceedings.
[11] J.F. Beacom and J.Candia, JCAP, 2004, **11**:009.
[12] R. Abbasi *et al.*, arXiv:1101.1692v1,2011
[13] D. Heck *et al.*, Forschungszentrum Karlsruhe, 1998, Report No. FZKA 6019.
[14] J. R. Hörandel, Astropart. Phys., 2003, **19**:193-220.
[15] A. Gazizov, M. Kowalski, Comput.Phys.Commun., 2005, **172**:203-213.
[16] M. Ackermann *et al.*, J.Geophys. Res.,2006 , **111**:D13203
[17] E. Middell, Proc. of the 31st ICRC, 2009, paper 0708
[18] J. Lundberg *et al.*, Nucl. Instrum. Meth. A, 2007, **581**:619-631.
[19] J. Ahrens *et al.*, Nucl.Instrum.Meth.A,2004,**524**:169-194.
[20] A. Hoecker *et al.*, arXiv:physics/0703039, 2007.

32ND INTERNATIONAL COSMIC RAY CONFERENCE, BEIJING 2011

Supernova detection with IceCube and beyond

THE ICECUBE COLLABORATION[1]
[1]*See special section in these proceedings*

Abstract: In its current configuration, IceCube is a formidable detector for supernovae. It can detect subtle features in the temporal development of MeV neutrinos from the core collapse of nearby massive stars. For a supernova at the galactic center, its sensitivity matches that of a background-free megaton-scale supernova search experiment and triggers on supernovae with about 200, 20, and 6 standard deviations at the galactic center (10 kpc), the galactic edge (30 kpc), and the Large Magellanic Cloud (50 kpc). Signal significances are reduced due to the noise floor and correlations between background hits. In this paper we discuss ways to improve the signal over background ratio with an improved data acquisition. We also discuss methods to track the average neutrino energy by multiple hit detection from individual interacting neutrinos. The latter relies on the ability to reject coincident hits from atmospheric muons.

Corresponding authors: V. Baum[1], L. Demirörs[2], L. Köpke[1], M. Ribordy[2] (*mathieu.ribordy@epfl.ch*) , M. Salathe[2], L. Schulte[1]
DOI: 10.7529/ICRC2011/V04/1137
[1]*Institute of Physics, University of Mainz, Staudinger Weg 7, D-55099 Mainz, Germany*
[2]*Laboratory for High Energy Physics, École Polytechnique Fédérale, CH-1015 Lausanne, Switzerland*

Keywords: IceCube, supernovae

1 Introduction

It was recognized early by [1] and [2] that neutrino telescopes offer the possibility to monitor our Galaxy for supernovae. IceCube is uniquely suited for this measurement due to its location and 1 km^3 size. The noise rates in IceCubes photomultiplier tubes average around 540 Hz since they are surrounded by inert and cold ice with depth dependent temperatures ranging from $-43\,^\circ$C to $-20\,^\circ$C. At depths between $(1450 - 2450)$ m they are partly shielded from cosmic rays. Cherenkov light induced by neutrino interactions will increase the count rate of all light sensors above their average value. Although this increase in individual light sensor is not statistically significant, the effect will be clearly seen once the rise is considered collectively over many sensors.

The 5160 photomultipliers are installed in modules called digital optical modules (DOMs) and arranged in two configurations: IceCube, with 17 m (125 m) vertical spacing between DOMs (horizontal spacing between strings), and DeepCore with 7 m (72 m) spacings and equipped with high quantum efficiency DOMs, where $\epsilon_{\mathrm{DeepCore}} = 1.35\epsilon_{\mathrm{IceCube}}$ [3, 4]. With absorption lengths exceeding 100 m, photons travel long distances in the ice such that each DOM effectively monitors several hundred cubic meters of ice. The inverse beta process $\bar{\nu}_e + p \rightarrow e^+ + n$ dominates supernova neutrino interactions with $\mathcal{O}(10\,\mathrm{MeV})$ energy in ice or water, leading to positron tracks of about $0.55\,\mathrm{cm} \cdot E_\nu/\mathrm{MeV}$ length for $E_\nu \leq 10$ MeV. Considering the approximate E_ν^2 dependence of the cross section, the light yield per neutrino roughly scales with E_ν^3. The detection principle was demonstrated with the AMANDA experiment, IceCubes predecessor [5]. Since 2009, IceCube has been sending real-time datagrams to the Supernova Early Warning System (SNEWS) [6] when detecting supernova candidate events.

Currently, the supernovae search algorithms are based on count rates of individual DOMs stored in 1.67 ms time bins. We plan to introduce an improved data acquisition system that will allow to store all IceCube hits for supernova candidates. We discuss below some of the improvements that we expect to be achieved using this additional information. In addition, the collaboration is discussing future extensions of the detector that would also improve the supernova detection capacity.

2 Current performance

IceCube is the most precise detector for analyzing the neutrino lightcurve of close supernovae. A paper, discussing the detector and physics performance, is close to being published. Figure 1 shows the expected significance for the detection of a supernovae as function of distance (left) and presents the expected rate distribution for the Lawrence-

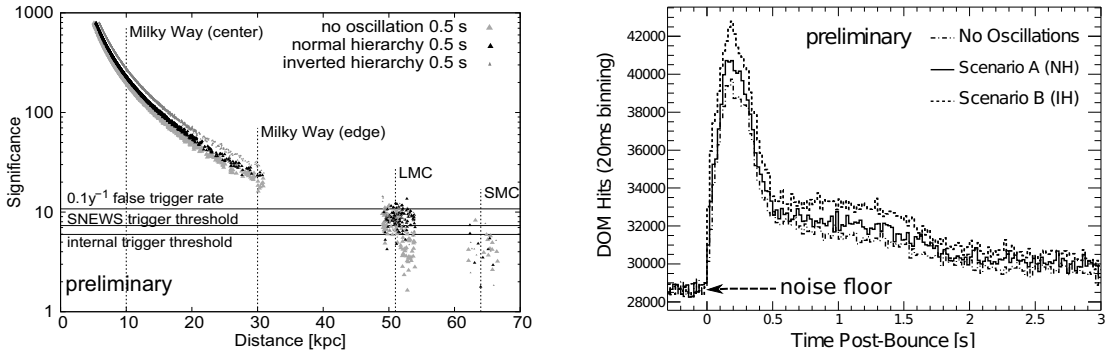

Figure 1: Left: Expected significance versus distance assuming the Lawrence-Livermore model [9] for three oscillation scenarios. The significances are increased by neutrino oscillations in the star by typically 40% in case of an inverted hierarchy. The Magellanic Clouds as well as the center and the edge of the Milky Way and various trigger thresholds are marked. For the Milky Way, the supernova progenitor distribution follows the prediction from [7], for the Magellanic Clouds it is assumed to be uniform. Right: Expected rate distribution at 10 kpc supernova distance assuming normal and inverse hierarchies.

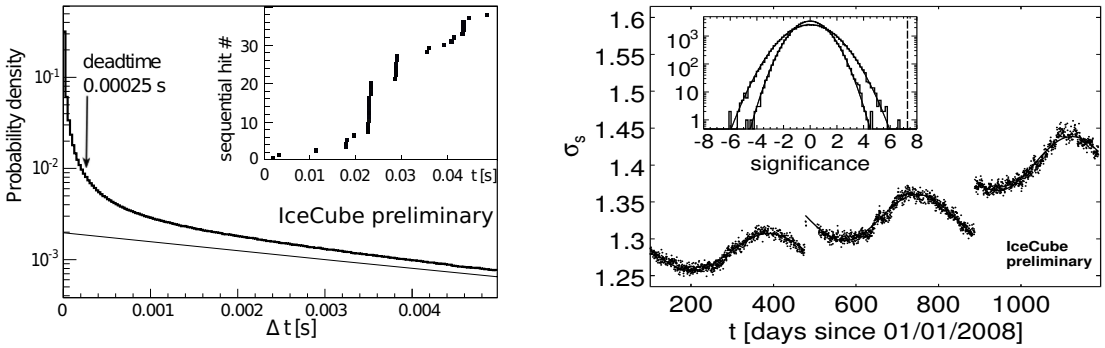

Figure 2: Left: Measured probability density distribution of time differences between pulses for noise (bold line) and the expectation for a Poissonian process fitted in the range $15\,\mathrm{ms} < \Delta T < 50\,\mathrm{ms}$ (thin line). The excess is due to bursts of correlated hits, as indicated by the 50 ms long snapshot of hit times shown in the inset. Right: Measured width of the significance distribution as function of time during IceCube construction with 40 (left), 59 (middle) and 79 (right) deployed strings. The inset shows the significance distribution before (wide distribution) and after (narrow distribution) suppression of hits due to atmospheric muons (79 strings). The current trigger threshold for SNEWS alarms is indicated by a dashed line.

Livermore model [9] (right). The rate distribution demonstrates the excellent resolution of details in the neutrino light curve. This includes the possibility to distinguish the neutrino hierarchy, provided that the astrophysical model is well known and $\sin^2\Theta_{13} > 1\,°$[7]. The present noise floor is indicated in Fig. 1 (right) which leads to a fast deterioration of the signal significance particularly at larger distances. In addition, the expected signal significance in IceCube is somewhat reduced due to two types of correlations between pulses that introduce supra-Poissonian fluctuations. The first correlation involves a single photomultiplier tube. It comes about because a radioactive decay in the pressure sphere can produce a burst of photons lasting several μs. The second correlation arises from the cosmic ray muon background; a single cosmic ray shower can produce a bundle of muons which is seen by hundreds of DOMs. The observed time difference between noise hits deviates from an exponential distribution expected for a Poissonian process (see Fig. 2, left). The inset shows a hit sequence from a single DOM, clearly indicating the bursting behavior. A significant fraction of these bursts can be rejected by an artificial non-paralyzing deadtime, currently adjusted to $\tau = 250\,\mu$s, which decreases the average optical module noise rate to 285 Hz, while keeping $\approx 87\%/(1 + r_{\mathrm{SN}} \cdot \tau)$ of supernova induced hits with rate r_{SN}.

Due to remaining correlated pulses from radioactive decays and atmospheric muons, the measured sample standard deviation in data taken with 79 strings is ≈ 1.3 and ≈ 1.7 times larger than the Poissonian expectation for 2 ms and

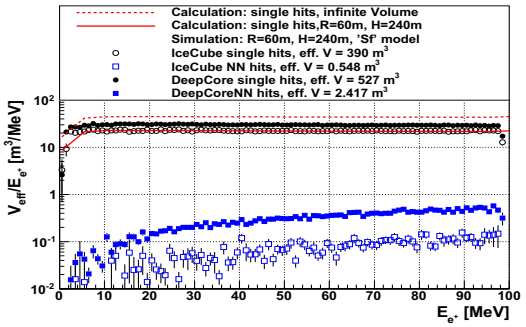

Figure 3: Effective volume per optical module and positron energy versus positron energy. Due to the chosen generation volume, the single hits effective volumes (circles) are about a factor of two too small. This is illustrated by the calculations taken from [11] (lines). The nearest neighbor coincidence modes (squares) are shown here without cut on the coincidence time. The effective volumes given in the legend are calculate according to the "Sf" model from [12] with an integration time of 4 s.

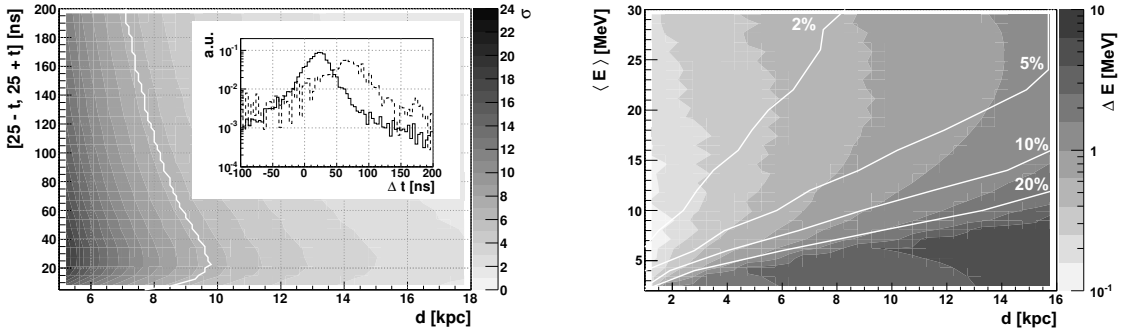

Figure 4: Left: Significance as a function of distance d and the allowed time window $[25\,\mathrm{ns} - t, 25\,\mathrm{ns} + t]$ between hits in two neighboring DOMs 7 m apart (DeepCore). The time difference distribution is shown in the inset in solid for DeepCore and dashed for IceCube. The maximum distance of about 10 kpc is reached for $t = 25\,\mathrm{ns}$ for a significance threshold of 6.7 (white line). Right: Energy resolution ΔE as a function of distance d and average energy of the emission spectrum $\langle E \rangle$. The white line show several $\Delta E/E$ contours.

500 ms time bins, respectively. For the analysis, we define the significance $\xi = \Delta\mu/\sigma_{\Delta\mu}$, where $\Delta\mu$ is the most likely collective rate deviation of all optical module noise rates from their running average. $\sigma_{\Delta\mu}$ is the corresponding deviation calculated from the data, thus accounting for non-Poissonian behavior in the dark rates. The significance should be centered at zero with unit width. Fig. 2 (right plot) shows that this is not the case; instead the width changes with the season and increases with the size of the instrumented detector. This behavior is linked to the seasonal change of the muon flux. While atmospheric muons contribute to the count rates of individual DOMs by only 3%, these hits are correlated across the detector, thus broadening the significance distribution and giving rise to a seasonal dependence of the trigger rate. At present, it is possible to subtract roughly half of the hits introduced by atmospheric muons from the total noise rate offline, as the number of coincident hits in neighboring DOMs is recorded for all triggered events. The width of the significance distribution then decreases to about 1.06, close to the expectation (see inset of Fig. 2 (right plot)).

A data acquisition that records all hits in case of a supernova trigger will permit further improvements. The time resolution on the onset of the burst will no longer be restricted by the 1.67 ms time bins in which the rates are recorded, hits associated to triggered atmospheric muons can be fully rejected, and more sophisticated methods to minimize correlated pulse bursts, e.g. by eliminating the initial hits of the bursts while keeping photomultiplier related afterpulses, can be applied. However, as the significance improves only with $1/\sqrt{N_{\mathrm{background}}}$, a much more drastic reduction of background is required in order to improve the detection significance at the edge of our galaxy, to track the average neutrino energy and maybe even provide some directional capability. This can only be achieved by detecting more than one Cherenkov photon from an interaction and applying a coincidence condition.

3 New opportunities from coincidence rates

The study in this section is motivated by an analytical framework that explores the potential of coincident hit modes [11]. Here, we investigate the "nearest neighbor coincidence hits" mode, with a hybrid GEANT-4/toy Monte Carlo simulation. We chose this mode from other possible multi-hit modes such as multiple hits in one DOM or coincident hits between any DOMs, because it has the best noise suppression potential by requiring a very short time window around the two coincident hits.

Figure 3 shows the positron effective volume per module and positron energy for the two detector configurations and two detection modes: single hits and nearest neighbor coincidence hits. The effective volumes given in the legend are calculated according to the "Sf" model from [12] with an integration time of 4 s. Both modes have a very different energy dependence, which makes the ratio $N_{\rm coinc}/N_{\rm single}$ an observable of the average energy $\langle E \rangle$ of the emission spectrum.

The inset in Fig. 4 shows the smallest time difference between hits in neighboring DOMs for both detector configurations. A cut on this time distribution was found by calculating the detection significance as a function of the supernova distance and the time window, as is shown in Fig. 4 for DeepCore. Applying a time cut of ± 25 ns around the most probable time difference of $T_0 = 25$ ns, a maximum distance of 10 kpc can be reached with the DeepCore DOM separation. A similar cut yields a smaller reach for IceCube due to the larger DOM separation.

To estimate the energy resolution of the energy observable $N_{\rm coinc}/N_{\rm single}$, the ratio was calculated using spectra according to the "Sf" model with average energies between $2 - 30$ MeV. In Fig. 4 (right plot), the deviation ΔE is shown as a function of the supernova distance and the average $\langle E \rangle$. For distance smaller than the trigger threshold (≈ 10 kpc), a resolution of around 5% can be achieved for spectra with an average energy of $10 - 15$ MeV.

The energy resolution depends on the expected noise level for the chosen selection mode. Above, the Poissonian noise levels were scaled up by 1.3, as mentioned in Sec. 2. It is possible that this underestimates the average hit probability for DOMs that were close to atmospheric muons. Preliminary studies show that light from muons can be suppressed by considering only DOMs that were around 300 m or further away from the reconstructed track position. In the worst case, when a track traverses the whole detector volume vertically, this cut reduces the usable volume by $\approx 30\%$. Alternatives to such a cut are being investigated.

4 Possible extensions of IceCube/DeepCore

Discussions on an extension of IceCube/DeepCore have started, which would also improve the supernova detection capability. We used a GEANT-4 simulation to estimate the capabilities of a hypothetic 18 string detector with IceCube DOMs spaced apart a few meters. Fig. 5 shows the effective volumes of single and multiple hits as function of distance between the DOMs. The sizable increase in the active volume of coincidence hits would strongly improve the signal over noise ratio and lead e.g. to a substantial improvement of a supernova detection at the Magellanic cloud.

5 Conclusion

As a supernova detector, IceCube already offers an unmatched ability to establish subtle features in the temporal development of the neutrino flux by tracking the overall count rates of its DOMs. The correlated noise background remains one of the big challenges. The new data acquisition will permit the recording of all hits in case of a trigger signal, thus greatly improving the rejection of correlated noise sources such as atmospheric muons. It will also allow to study the influence of the correlated noise on multiple hit detection modes.

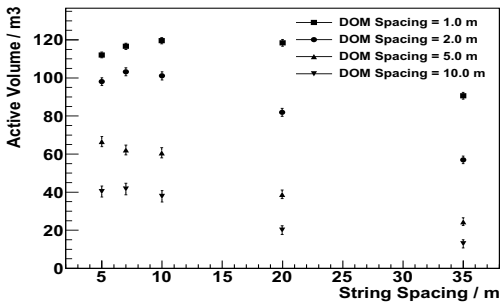

Figure 5: Effective volumes per DOM for multiple hits as function of horizontal and vertical distance between DOMs. The same neutrino spectrum was used as in Fig. 3

One such mode, nearest neighbor coincident hits, was introduced in this paper and shows great potential to extent the existing capabilities of IceCube by measuring the average neutrino energy. This mode also has the potential to be sensitive to the neutrino direction. Other multi-hit modes will be studied next. All these modes would greatly benefit from a very dense sub-array with inter-DOM and inter-string distance of a few meters only, extending their reach to several tens of kilo parsec and possibly beyond.

References

[1] C. Pryor, C. E. Roos, M. S. Webster, Astrophys. J. **329**, 335 (1988).
[2] F. Halzen, J. E. Jacobsen, E. Zas, Phys. Rev. **D53**, 7359-7361 (1996).
[3] [IceCube Collab.] J. Ahrens *et al.*, Astropart. Phys. **20**, 507-532 (2004).
[4] [IceCube Collab.] C. Wiebusch, arXiv:0907.2263
[5] J. Ahrens *et al.*, Astropart. Phys. **16**, 345-359 (2002).
[6] P. Antonioli, R. T. Fienberg, F. Fleurot, Y. Fukuda, W. Fulgione, A. Habig, J. Heise, A. B. McDonald *et al.*, New J. Phys. **6**, 114 (2004).
[7] J. N. Bahcall, T. Piran, Astrophys. J. **267**, L77 (1982).
[8] [IceCube Collab.] R. Abbasi *et al.*, in progress
[9] T. Totani, K. Sato, H. E. Dalhed, J. R. Wilson, Astrophys. J. **496**, 216-225 (1998).
[10] A. S. Dighe, M. T. Keil, G. G. Raffelt, arXiv:hep-ph/0303210v3.
[11] M. Ribordy, arXiv:submit/0263088 [astro-ph.IM]
[12] L. Hudepohl, B. Muller, H. -T. Janka, A. Marek, G. G. Raffelt, Phys. Rev. Lett. **104**, 251101 (2010).

32nd International Cosmic Ray Conference, Beijing 2011

Gadolinium doping of the Large Volume Detector

G.Bruno[1,2], W.Fulgione[3,4], A.A.Bergamini Machado[2], A.Mal'gin[5], A.Molinario[3,4,6], A.Porta[3,4], C.F.Vigorito[3,4,6]
[1] *University of L'Aquila, Coppito (AQ), Italy*
[2] *Laboratori Nazionali del Gran Sasso, INFN, s.s. 17bis Km 18+910, Assergi (AQ), Italy*
[3] *INFN, Via Pietro Giuria 1, Torino, Italy*
[4] *INAF, IFSI-TO, Corso Fiume 4, Torino, Italy*
[5] *Institute for Nuclear Research, Russian Academy of Sciences, pr. Shestidesyatiletiya Oktyabrya 7a, Moscow, 117312 Russia*
[6] *Dipartimento di Fisica Generale, Università di Torino, Italy*
amolinar@to.infn.it
DOI: 10.7529/ICRC2011/V04/1149

Abstract: The Large Volume Detector (LVD) in the INFN Gran Sasso National Laboratory (LNGS), Italy, is a ν observatory which has been monitoring the Galaxy since June 1992 to study neutrino bursts from core collapse supernovae. We evaluate how its sensitivity to such events would change if all its liquid scintillator was doped with a small amount of Gadolinium. It results a 90% detection efficiency at the distance of the Large Magellanic Cloud (50 kpc).

Keywords: Neutrino detection - Supernova - Gadolinium doping

1 Introduction

The Large Volume Detector (LVD) [1] is a 1 kton liquid scintillator neutrino telescope located in the INFN Gran Sasso National Laboratory, Italy. The main goal of LVD is the detection and study of neutrino bursts from core collapse supernovae.

LVD consists of an array of 840 scintillator counters, 1.5 m^3 each, filled with 1.2 tons of liquid scintillator. The main interaction expected in the liquid scintillator, at the typical energies of neutrino from core collapse supernova (some tens of MeV), is the inverse beta decay (IBD):

$$\bar{\nu}_e + p \rightarrow e^+ + n \quad (1)$$

which gives two detectable pulses: the prompt one due to the e^+ (visible energy $E_{vis} \simeq E_{\bar{\nu}_e} - Q + m_e = E_{\bar{\nu}_e} - 0.789$ MeV), which acts as the trigger for the experiment, followed by the delayed one from the neutron capture on proton, $E_\gamma = 2.23$ MeV, with a mean capture time, in one LVD counter, of $\tau = 185 \pm 5\,\mu s$. Like other experiments which look for neutrino bursts from core collapse supernovae, LVD has to be able to extract the neutrino burst signal from the background even without the aid of an external trigger. This capability is determined by the signal to noise ratio S/N. It is possible to try to increase S/N by selecting only those triggers which are followed, within a defined time window, by a delayed pulse in the same counter where the trigger itself took place, a condition which allows to extract the IBD. As the detection efficiency of the γ from neutron capture in LVD is relatively low, applying this technique to the present LVD counters would not lead to significant improvements in the sensitivity to supernova neutrino bursts, as discussed in [2]. A possible improvement could be achieved if the liquid scintillator was doped with a little amount of Gadolinium. Two isotopes of this element (^{155}Gd and ^{157}Gd) have a huge cross section for neutron capture (10^4 times that of the proton) and generate a γ photons cascade that can reach energies up to 8 MeV. We want here to discuss how the sensitivity of LVD would change as a detector for $\bar{\nu}_e$ from core collapse supernovae if all its counters were doped with Gd.

2 Neutron capture detection efficiency

A Monte Carlo simulation allowed us to evaluate the efficiency in detecting neutrons from interaction 1 inside one LVD counter both for normal liquid scintillator and for doped one. We found that, in the case of liquid scintillator without Gd doping:

E_{th} [MeV]	η_n (E_{th}) [%]	$R(E_{th})$ [s^{-1}]	$\delta t(\mu s)$	$P(E_{th})$	S/N*
No Gd doping [2]					
0.5	58	200	0.2 - 650	0.13	1.0
With Gd doping					
0.5	80	200	0.2 - 85	0.0168	3.8
1.0	77	91	”	$8{\cdot}10^{-3}$	5.3
1.5	72	42	”	$4{\cdot}10^{-3}$	7.1
2.0	67	19	”	$2{\cdot}10^{-3}$	9.3
2.5	61	9	”	$8{\cdot}10^{-4}$	13.4
3.0	55	4	”	$3\cdot10^{-4}$	19.7

Table 1: Neutron capture detection efficiency, η_n, background rate in one LVD counter, R, time window δt to search for the delayed pulse, probability P of a background delayed pulse after a trigger in the time window δt and signal to noise relative to the case of no Gd doping, S/N*, as a function of the energy threshold E_{th} imposed on the delayed pulse. For the average undoped LVD counter in the first row, for Gd doped liquid scintillator in the following six rows.

1. 17% of neutrons leave the counter without being captured;
2. 20.5% are captured, but the 2.23 MeV gamma quantum leaves the counter without interactions.

Taking also into account all the current features of LVD in terms of trigger condition and considering the finite time window to search for delayed pulses, $\delta t = 0.2\mu s - 3.5 \cdot \tau$ (where 0.2 μs is the time needed to collect photons released in the scintillator [3] and $\tau = 185 \pm 5\,\mu s$ is the mean capture time in LVD counters without Gd), it results that the total efficiency for neutron capture detection without Gd doping is $\eta_n = 58\%$.

When considering in the simulation the liquid scintillator doped with a small ($\sim 0.14\%$ in weight) amount of Gd, we get that:

1. 10% of neutrons leave the counter without being captured;
2. 5% are captured, but the gamma cascade leaves the counter without interactions.

The mean neutron capture time is $\tau_{Gd} = 24.5 \pm 0.5\mu$s, 7.5 times shorter than the mean neutron capture time of the same counter filled with the undoped liquid scintillator. The considered time window to look for delayed pulses in the case of Gd doping is then $\delta t|_{\rm Gd} = 0.2\mu s - 3.5 \cdot \tau_{Gd}$. Taking into account this finite time window, together with the trigger conditions and PMT's quantic efficiency, the total efficiency for neutron capture detection with liquid scintillator Gd doping results to be $\eta_n|_{\rm Gd} = 80\%$.

The first clear result is that Gd doping one LVD counter raises the neutron detection efficiency by a factor 1.4 (from 58% to 80%) with respect to the undoped one. Moreover, the mean neutron capture time shorten of a factor 7.5. This implies a reduction of the same factor of the time window in which we look for the pulse in coincidence, and finally brings to a reduction of background counting rate $\sqrt{R_{bk}}$ of a factor $(7.5)^{1/2}$. The total gain we get when looking for inverse beta decay signals is of a factor 3.8 in the S/N ratio.

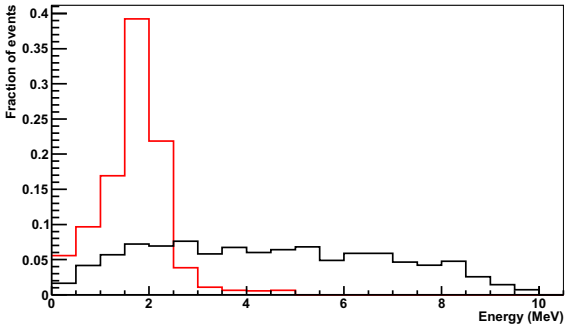

Figure 1: Detected energy distribution, as resulting from the simulation, for neutron capture after an inverse beta decay interaction occurring inside the LVD counter filled with "normal" (red) or Gd doped LS (black).

The shape of the spectrum detected for γ emission after neutron captures on Gd (figure 1, black line) suggests the possibility to add a further cut which only accepts delayed pulses with energy greater than a certain energy threshold E_{th}. In order to evaluate the advantages of this selection criterion we considered the neutron capture detection efficiency, $\eta_n|_{\rm Gd}$, as a function of the imposed E_{th} as obtained by the simulation. It is reported in table 1 as $\eta_n(E_{th})$. Combining these values with the background counting rate over E_{th} in one average LVD counter (third column in the same

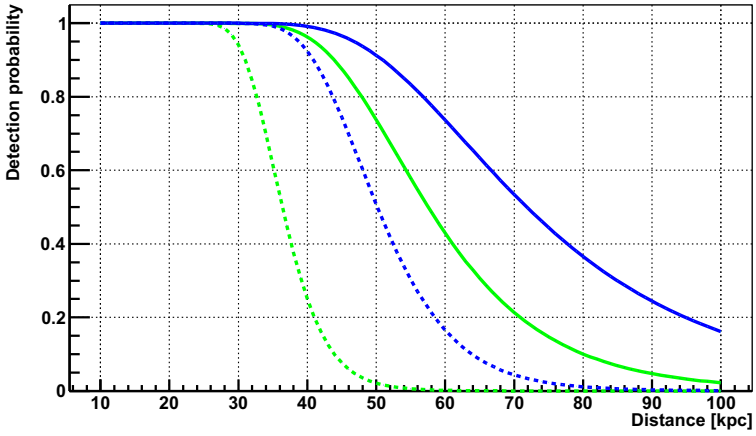

Figure 2: Neutrino burst detection probability versus distance for E_{cut}=7 (light green) or 10 MeV (dark blue) and standard LVD counters (dotted) or Gd doped counters (continuous), with a target mass of M = 1 kton and imitation frequency 1/(100 years).

table, $R(E_{th})$) we can calculate the probability that a trigger is followed in the time window δt by at least one delayed pulse due to background, so to mimic a $\bar{\nu}_e$ interaction, $P(E_{th}) = 1 - e^{-R(E_{th})\cdot\delta t}$. We obtain in this way the signal to noise values relative to the signal to noise we get for the case of no Gd doping, $(S/N)^*$ last column of table 1.

3 Trigger rate increasing

We evaluated how the background counting rate at energies greater than 7 MeV in LVD changes due to Gd doping. Neutrons from natural radioactivity in the rock may be captured on Gd and generate high energy pulses in the detector. We referred to the neutron flux measured in the underground Gran Sasso Laboratory [4]. We simulated the response of one module of LVD, that is a group of eight tanks, to such a neutron flux. The liquid scintillator in the simulation was doped with Gd at 0.14% level, and all neutron interactions, quenching of the liquid scintillator as reported in [5] and energy resolution of LVD counters [6] were taken into account.

In this way we found $f_7|_{Gd} = 1.1$ s^{-1} and $f_{10}|_{Gd} = 0.075$ s^{-1}, for the induced counting rate above 7 and 10 MeV respectively. Considering the present counting rates above the same thresholds over the whole experiment, which are equal to $f_7 = 0.2$ s^{-1} and $f_{10} = 0.03$ s^{-1} [2], we obtained that the total background rate, considering the effect of neutron captures on Gd, should raise to $f_7|_{tot} \leq 1.3$ s^{-1} and $f_{10}|_{tot} \leq 0.105$ s^{-1}.

4 $\bar{\nu}_e$ burst sensitivity

It is possible to calculate the sensitivity to neutrino burst that LVD would achieve if all its liquid scintillator was doped with Gd at a level of 0.14%. We refer for this calculation to the method for neutrino bursts selection described in [2], which relies on the fact, widely discussed in that paper, that the background behaviour in LVD is well described by Poisson statistic. When LVD is operating as a stand-alone detector, the choice is to select as neutrino burst candidates only those clusters which could be produced by background fluctuations less than 0.01 y^{-1}. We took into account that two searches are performed simultaneously, one for the triggers with energy above $E_{cut} = 7$ MeV, and another one for triggers with energy above $E_{cut} = 10$ MeV. We fixed the total number of detectable IBD interactions for a supernova at a distance of $D = 10$ kpc to $N_\nu^0 \sim 230$, referring to a conservative model of neutrino emission from a supernova [7].

We performed the calculation of the sensitivity for both possible trigger selection, $E_{cut} = 7$ MeV and $E_{cut} = 10$ MeV, requesting that a trigger is followed, in the same counter where the trigger itself happened, by a signal in the time window $\delta t = 0.2 - 85\mu s$. We also considered the different possible E_{th} on the delayed pulse, as listed in table 1. We found that the best case for $E_{cut} = 10$ MeV is that with $E_{th} = 2.5$ MeV, when the detection probability drops below 50% when the supernova is more than 72 kpc away. In case $E_{cut} = 7$ MeV we found that the best result (detection efficiency of 50% for supernova at 58 kpc) is obtained when $E_{th} = 2.0$ MeV. The full detection efficiency curves corresponding to these two selections are

drawn in figure 2, in green for $E_{cut} = 7$ MeV, $E_{th} = 2.0$ MeV and in blue for $E_{cut} = 10$ MeV, $E_{th} = 2.5$ MeV. The dotted curves in the same figure are taken from [2] and represent the current detector sensitivity with 1 kton non doped liquid scintillator (green for $E_{cut} = 7$ MeV and blue for $E_{cut} = 10$ MeV).

5 Conclusions

From the results obtained above, it is apparent that LVD is able to monitor the Galaxy with full efficiency both for Gd doped and non doped liquid scintillator. The improvement obtained with Gd doping emerges when considering the possibility to identify a $\bar{\nu}_e$ burst from the Large Magellanic Cloud, about 50 kpc away from us. While for non doped liquid scintillator the efficiency is $\sim 50\%$, and just for $E_{cut} = 10$ MeV, doping with Gd would make it raise to better than 90%, if $E_{cut} = 10$ MeV and $E_{th} = 2.5$ MeV (better than 70% if $E_{cut} = 7$ MeV and $E_{th} = 2.0$ MeV). This sensitivity is comparable to that which we would obtain by doubling the mass of LVD.

6 Notes

This work is going to be published on JCAP.

References

[1] M.Aglietta et al. (LVD Collaboration), Il Nuovo Cimento, 1992, **A 105**: 1793
[2] N.Yu.Agafonova et al., Astroparticle Physics, 2008, **28**: 516-522
[3] N.Yu.Agafonova et al., Instruments and Experimental Techniques, 2010, **53** (6): 800.
[4] P.Belli et al., Il Nuovo Cimento, 1989, **A 101**: 959.
[5] A. Bonardi, M. Aglietta, G. Bruno, W. Fulgione, A.A. Bergamini Machado, Astroparticle Physics, 2010, **34**: 225.
[6] P.Antonioli, W.Fulgione, P.Galeotti, L.Panaro, Nuclear Instruments and Methods, 1991, **A309**: 569.
[7] G.Pagliaroli, F.Vissani, M.L.Costantini, A.Ianni, Astroparticle Physics, 2009, **31**: 163-176

32ND INTERNATIONAL COSMIC RAY CONFERENCE, BEIJING 2011

Near-Field Effects of Cherenkov Radiation Induced by Ultra High Energy Cosmic Neutrinos

CHIH-CHING CHEN

(Paper not received. Talk can be download from: http://icrc2011.ihep.ac.cn/paper/proc/content_v4.htm)

32ND INTERNATIONAL COSMIC RAY CONFERENCE, BEIJING 2011

Determining the high energy neutrino flavor ratio at the astrophysical source

KWANG-CHANG LAI[1,4], M. A. HUANG[2,4], GUEY-LIN LIN[3,4], T. C. LIU[4]
[1]*Center for General Education, Chang Gung University*
[2]*Department of Energies and Resources, National United University*
[3]*Institute of Physics, National Chiao Tung University*
[4]*Leung Center for Cosmology and Particle Astrophysics, National Taiwan University*
kcl@mail.cgu.edu.tw
DOI: 10.7529/ICRC2011/V04/1166

Abstract: We discuss the reconstruction of neutrino flavor ratios at astrophysical sources through the future neutrino-telescope measurements. We demonstrate by a statistical method the accuracies required in the measurements of energy-independent ratios R and S, where R is the number ratio between track and shower events. For energy below a few PeV, shower events consists of electron and tau neutrino events. However, for energies beyond, a tau-lepton behaves like a track similar to a muon. This motivates a new classification of event types and new definitions for R and S. We present our analyses in both types of measurements, R and S, at corresponding energy regime.

Keywords: Astrophysical neutrino, neutrino oscillation, neutrino astronomy.

1 Introduction

The operation of IceCube detector [1] and the R&D effort of KM3Net [2] are important progresses toward a km^3-sized detection capability in the neutrino astronomy [3]. Furthermore the radio and air-shower detectors, such as ANITA [4] and Pierre Auger detector [5] respectively, are also taking the data. These detectors are sensitive to neutrinos with energies higher than those probed by IceCube and KM3Net. Finally, the radio extension of IceCube detector, the ARA [6], is also under consideration. It is expected to detect a score of cosmogenic neutrinos [7] per year.

Most of the astrophysical neutrinos are believed to be produced by decays of charged pions and subsequent decays of muons: $\pi^+ \to \mu^+ + \nu_\mu \to e^+ + \nu_\mu + \nu_e + \bar{\nu}_\mu$ or $\pi^- \to \mu^- + \bar{\nu}_\mu \to e^- + \bar{\nu}_\mu + \bar{\nu}_e + \nu_\mu$. This leads to the neutrino flux ratio $\phi_0(\nu_e) : \phi_0(\nu_\mu) : \phi_0(\nu_\tau) = 1 : 2 : 0$ at the astrophysical source where $\phi_0(\nu_\alpha)$ is the sum of ν_α and $\bar{\nu}_\alpha$ flux. Such a flux ratio results from an implicit assumption that the muon decays into neutrinos before it loses a significant fraction of its energy. However, in some source the muon quickly loses its energy by interacting with strong magnetic fields or with matter [8, 9, 10]. Such a muon eventually decays into neutrinos with energies much lower than that of $\nu_\mu(\bar{\nu}_\mu)$ from $\pi^+(\pi^-)$ decays. Consequently this type of source has a neutrino flavor ratio $\phi_0(\nu_e) : \phi_0(\nu_\mu) : \phi_0(\nu_\tau) = 0 : 1 : 0$, which is referred to as the muon-damped source. The third type of source emits neutrons resulting from the photo-disassociation of nuclei. As neutrons propagate to the Earth, $\bar{\nu}_e$ are produced from neutron β decays [11], leading to a neutrino flavor ratio $\phi_0(\nu_e) : \phi_0(\nu_\mu) : \phi_0(\nu_\tau) = 1 : 0 : 0$.

A natural question in neutrino astronomy is then how well one can identify and distinguish these neutrino sources. The answer to this question depends on our knowledge of neutrino mixing parameters and the achievable accuracies in measuring the neutrino flavor ratio on the Earth such as $R \equiv \phi(\nu_\mu)/\left(\phi(\nu_e) + \phi(\nu_\tau)\right)$ and $S \equiv \phi(\nu_e)/\phi(\nu_\tau)$. In this report, we shall provide an answer to this question with a statistical analysis.

2 Statistical Analysis

Before doing the statistical analysis, we should note that the observables R and S are energy-dependent since R is defined as $N_{\rm track}/N_{\rm shower}$. In very high energy regime, i.e., $E_\nu > 33PeV$, the tau lepton originated from the tau neutrino behaves more like a track rather than a shower while the electron neutrino only give rises to a shower signature. Therefore the more appropriate flux ratio parameters in such a case are $R \equiv \phi(\nu_e)/\left(\phi(\nu_\mu) + \phi(\nu_\tau)\right)$ and $S \equiv \phi(\nu_\mu)/\phi(\nu_\tau)$. For simplicity and clarity, we denote the measurement in the low and high energy regimes as conditions I and II, respectively.

To reconstruct the neutrino flavor ratio at the source with a statistical analysis, we employ the following best-fit values and 1σ ranges of neutrino mixing angles [12]

$$\sin^2\theta_{12} = 0.29^{+0.028,\,0.07}_{-0.024,\,0.06},\ \sin^2\theta_{23} = 0.5^{+0.072,\,0.18}_{-0.09,\,0.16},$$

$$\sin^2\theta_{13} < 0.012(0.047), \tag{1}$$

for our analysis.

The statistical analysis is then performed with the following formula

$$\chi^2 = \left(\frac{R_{\rm th}-R_{\rm exp}}{\sigma_{R_{\rm exp}}}\right)^2 + \left(\frac{S_{\rm th}-S_{\rm exp}}{\sigma_{S_{\rm exp}}}\right)^2 + \sum_{jk=12,23,13}\left(\frac{s^2_{jk}-(s_{jk})^2_{\rm best\,fit}}{\sigma_{s^2_{jk}}}\right)^2 \tag{2}$$

with $\sigma_{R_{\rm exp}} = (\Delta R/R)R_{\rm exp}$, $\sigma_{S_{\rm exp}} = (\Delta S/S)S_{\rm exp}$, $s^2_{jk} \equiv \sin^2\theta_{jk}$ and $\sigma_{s^2_{jk}}$ the 1σ range for s^2_{jk}. Here $R_{\rm th}$ and $S_{\rm th}$ are theoretical predicted values for R and S respectively while $R_{\rm exp}$ and $S_{\rm exp}$ are experimentally measured values. The values for $R_{\rm exp}$ and $S_{\rm exp}$ are generated from input true values of neutrino flavor ratios at the source and input true values of neutrino mixing parameters as given by Eq. 1. We assumes that both ΔR and ΔS are dominated by the statistical errors. In this case, they are related to each other by [13]

$$\left(\frac{\Delta S}{S}\right) = \frac{1+S}{\sqrt{S}}\sqrt{\frac{R}{1+R}}\left(\frac{\Delta R}{R}\right). \tag{3}$$

In our analysis, we scan all possible neutrino flavor ratios at the source that give rise to a specific χ^2 value. Since we have taken$R_{\rm exp}$ and $S_{\rm exp}$ as those generated by input true values of initial neutrino flavor ratios and neutrino mixing parameters, we have $(\chi^2)_{\rm min}$=0 occurring at these input true values of parameters. Hence the boundaries for 1σ and 3σ ranges of initial neutrino flavor ratios are given by $\Delta\chi^2 = 2.3$ and $\Delta\chi^2 = 11.8$ respectively where $\Delta\chi^2 \equiv \chi^2 - (\chi^2)_{\rm min} = \chi^2$ in our analysis.

Let us take the accuracy for measuring R to be $\Delta R/R = 10\%$ in both low and high energy regimes for the damped-muon source. The value for $\Delta S/S$ can be calculated from Eq. 3. The reconstruction of neutrino flavor ratio with the above given $\Delta R/R$ and $\Delta S/S$ is discussed in the follow.

2.1 The reconstruction of initial neutrino flavor ratio by measuring R alone

It is instructive to see how well one can determine the initial neutrino flavor ratio by measuring R alone. We perform such an analysis by neglecting the second term on the RHS of Eq. (2). The 1σ and 3σ ranges for the reconstructed flavor ratios at the source are shown in Fig. 1. It is seen that, with $\Delta R/R = 10\%$, the reconstructed 3σ range of the neutrino flavor ratio almost covers the entire physical region in low energy regime. Hence the possibility of a pion source cannot be ruled out given a true source of the damped-muon source. Clearly it is desirable to measure both R and S to rule out the pion source from the damped-muon source at low energies. On the contrary, we see that the pion source can be ruled out barely at high energies.

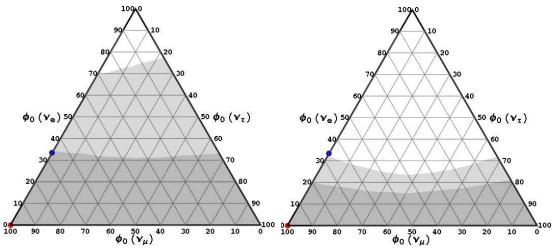

Figure 1: The reconstructed ranges for the neutrino flavor ratios for the damped-muon source with $\Delta R/R = 10\%$. The left and right panels correspond to low and high energy regimes respectively. The numbers on each side of the triangle denote the flux percentage of a specific flavor of neutrino. The red point marks the damped-muon source $\Phi_{0,\mu} = (0,1,0)$ and the blue point marks the pion source $\Phi_{0,\pi} = (1/3, 2/3, 0)$. Gray and light gray areas respectively denote the 1σ and 3σ ranges for the reconstructed neutrino flavor ratios at the source.

2.2 The flavor reconstruction with measurements on both R and S

Then, we perform our statistical analysis with respect to simultaneous measurements of R and S. The accuracy for the measurements on R is $\Delta R/R = 10\%$. Hence $\Delta S/S = 13\%$ for condition I and $\Delta S/S = 9.8\%$ for condition II according to Eq. 3. It is shown, in Fig. 2, that the pion sources can be ruled out from the damped-muon source with the assumed accuracies in both the low and high energy regimes.

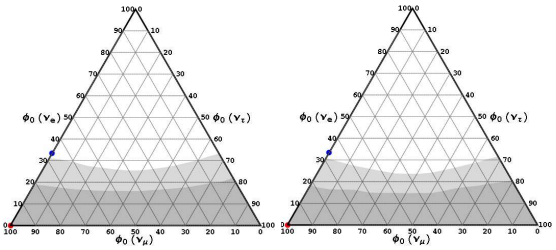

Figure 2: The reconstructed ranges for the neutrino flavor ratios for the damped-muon source with $\Delta R/R = 10\%$. The left and right panels correspond to low and high energy regimes respectively. The numbers on each side of the triangle denote the flux percentage of a specific flavor of neutrino. The red and blue points mark, again, the damped-muon and pion sources respectively. Gray and light gray areas respectively denote the 1σ and 3σ ranges for the reconstructed neutrino flavor ratios at the source.

3 Discussion and Conclusion

In the tri-bimaximal limit of neutrino mixing parameters [14], $\sin^2\theta_{23} = 1/2$, $\sin^2\theta_{12} = 1/3$ and $\sin^2\theta_{13} = 0$, we find $R^{\rm II} = S^{\rm I}/2$ and $S^{\rm II} = 1$. For further simplifications, let us consider astrophysical sources with negligible ν_τ fractions so that $\phi_0(\nu_e) : \phi_0(\nu_\mu) : \phi_0(\nu_\tau) = \alpha : 1-\alpha : 0$ with $0\alpha1$. Fig. 3 shows the flux ratios on the Earth as functions of the initial ν_e fraction α. It is seen that $S^{\rm I}$ and $R^{\rm II}$ are more sensitive to α while $R^{\rm I}$ and $S^{\rm II}$ is either less sensitive to α or completely independent of this parameter.

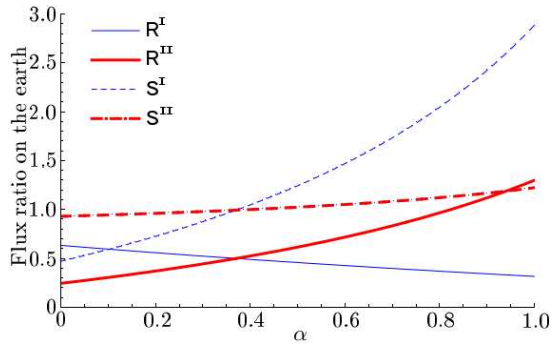

Figure 3: Neutrino flavor ratios on Earth for input sources with flavor ratios of $\phi_0(\nu_e) : \phi_0(\nu_\mu) : \phi_0(\nu_\tau) = \alpha : 1-\alpha : 0$ with $0\alpha1$. The thick and long dashed lines correspond to $R^{\rm II}$ and $S^{\rm II}$ respectively. The thin and short-dashed lines correspond to $R^{\rm I}$ and $S^{\rm I}$ respectively. Apparantly, $S^{\rm I}$ and $R^{\rm II}$ are more sensitive to α.

In this report, we only show ternary diagrams for the assumed damped-muon source due to the limitation of pages. The occasion should vary for the pion source. We have also take into consideration nonzero $\sin^2\theta_{13}$. Since the best-fit value for θ_{13} is non-vanishing suggested by [15], the reconstructed flavor ratios should also depend on the CP phase. For the details of these studies, please see also [16] and [17].

The authors appreciate supports by National Science Council, Taiwan, under the Grant No. 96-2112-M-009-023-MY3, Research and Development Office, National Chiao-Tung Uni- versity and Leung Center for Cosmology and Particle Astrophysics, National Taiwan University.

References

[1] P. Berghaus [for the IceCube Collaboration], arXiv:0812.2883 [astro-ph].
[2] The KM3NeT Collaboration, http://km3net.org.
[3] For a recent review, see V. S. Berezinsky, arXiv:0901.1428 [astro-ph].
[4] P. Gorham *et al.* [ANITA collaboration], arXiv:0812.2715 [astro-ph].
[5] T. P. A. Collaboration, arXiv:0903.3385 [astro-ph.HE].
[6] P. Allison *et al.*, arXiv:1105.2854 [astro-ph.HE].
[7] V. S. Berezinsky and G. T. Zatsepin, Phys. Lett. **28B**, 423 (1969); R. Engel, D. Seckel, and T. Stanev, Phys. Rev. D **64**, 093010 (2001).
[8] J. P. Rachen and P. Meszaros, Phys. Rev. D **58**, 123005 (1998).
[9] T. Kashti and E. Waxman, Phys. Rev. Lett. **95**, 181101 (2005).
[10] M. Kachelriess, S. Ostapchenko and R. Tomas, Phys. Rev. D (2008) **77**, 023007.
[11] L. A. Anchordoqui, H. Goldberg, F. Halzen and T. J. Weiler, Phys. Lett. B (2004) **593**, 42.
[12] M. Maltoni *et al.* New J. Phys. (2004) **6**, 122.
[13] K. Blum, Y. Nir and E. Waxman, arXiv:0706.2070 [hep-ph].
[14] P. F. Harrison, D. H. Perkins and W. G. Scott, Phys. Lett. (2002) **B 530**, 167; Phys. Lett. (2002) **B 535**, 163; Z. Z. Xing, Phys. Lett. (2002) B **533**, 85; X. G. He and A. Zee, Phys. Lett. (2003) B **560**, 87; see also L. Wolfenstein, Phys. Rev. D (1978) **18**, 958; Y. Yamanaka, H. Sugawara and S. Pakvasa, Phys. Rev. D (1982) **25**, 1895 [Erratum-ibid. D (1984) **29**, 2135].
[15] G. L. Fogli, E. Lisi, A. Marrone, A. Palazzo and A. M. Rotunno, Phys. Rev. Lett. (2008) **101**,141801
[16] K.-C. Lai, G.-L. Lin and T. C. Liu, Phys. Rev. D (2009) **80**, 103005.
[17] T. C. Liu, M. A. Huang and G.-L. Lin, arXiv:1004.5154 [hep-ph].

Sensitivity estimates of the TREND radiodetection array to Ultra High energy cosmic neutrinos

THOMAS SAUGRIN[1], V. NIESS[2], D. ARDOUIN[3], C. CÂRLOGANU[2], D. CHARRIER[3], Q. GOU[4], H. HU[4], L. KAI[5], P. LAUTRIDOU[3], O. MARTINEAU-HUYNH[4,1,6], O. RAVEL[3], X. WU[1], J. ZHANG[4], Y. ZHANG[4], M. ZHAO[1], Y. ZHENG[5]

[1]*National Astronomical Observatories of China, Chinese Academy of Sciences, Beijing, P. R. China*

[2]*Clermont Université, Université Blaise Pascal, CNRS/IN2P, Laboratoire de Physique Corpusculaire, BP 10448, F-6300 Clermont-Ferrand, France*

[3] *SUBATECH, Ecole des Mines, CNRS/IN2P3and Université of Nantes, 44307 Nantes, France*

[4]*Key Laboratory of Particle Astrophysics, Institute of High Energy Physics, Chinese Academy of Sciences, Beijing 100049, P. R. China*

[5]*Graduate University of Chinese Academy of Sciences, Beijing 100049, P. R. China*

[6]*Laboratoire de Physique Nucléaire et des Hautes Energies, CNRS/IN2P3 and Université Pierre et Marie Curie, 75252 Paris Cedex, France*

Thomas.saugrin@gmail.com

DOI: 10.7529/ICRC2011/V04/1179

Abstract: The Tianshan Radio Experiment for Neutrino Detection (TREND) is a radio array performing the autonomous detection of Extensive Air Showers (EAS). It is being deployed at 2700m asl on the site of the 21CMA radio-interferometer, in a remote valley of the Tianshan mountain range (XinJiang province, China). This site benefits from excellent radio conditions, the Galactic plane emissions being the dominant background source in the 25-200MHz frequency range, and is surrounded by high mountains, peaking at 5 km asl. This topology could be very well suited for the detection of cosmic tau neutrinos of ultra high energy, through the observation of the nearly horizontal EAS generated by the decay in the air of the converted tau. In this work, we present prospective studies of TREND's sensitivity to such cosmic neutrino fluxes. As a compromise between accuracy and speed, the simulation chain relies on a dedicated hybrid Monte-Carlo scheme for the propagation of the τ through rocks, rendering energy loss fluctuations. Various antenna array layouts are considered.

Keywords: Ultra High Energy Neutrinos; Radio Detection.

1 Introduction

The search for high energy (HE, $E > 10^{12}$ eV) neutrinos of cosmic origin is extremely challenging. The expected astronomical fluxes are low [1], and since neutrinos are purely weak interaction particles their cross section with matter is extremely small even at the highest energies [2]. However, if detected, the same purely weak interacting nature allows probing the very distant Universe, in the light of neutrinos. Various detection techniques have been considered over the last decades with a particular interest in Ultra High Energies (UHE, $E > 10^{18}$ eV), where the transferred energy to the medium becomes macroscopic, allowing for new detection means [3]. In the present work we focus on one of these prospective techniques, exploiting the coherent radio emission of extensive air showers (EAS), enhanced in the Earth geomagnetic field.

At UHE, tau neutrinos converting to τ leptons in rock can initiate EAS. Indeed, at those energies the τ lepton is long lived enough such that it can escape the rocks and disintegrate in the Air. However, this scenario is viable only in the case of Earth-skimming neutrinos with intercepted rock depths of 10-100 km. For downward going neutrinos, the atmosphere is not deep enough to allow neutrino conversion, while for upward going trajectories the τ disintegrates in the rock. Therefore the induced EAS will develop following a quasi-horizontal trajectory. The recently developed radio detection tech-

nique [4, 5] is potentially an efficient way to detect such EAS, since antenna detectors are able to detect radio emission even at large zenith angle. Nevertheless, quasi-horizontal EAS developing in a constant atmosphere density have never been studied experimentally until now since most of the radiodetection arrays are particle-triggered experiments which usually limit the detectable EAS to zenithal angle under 60°.

The TREND experiment is a self-triggering radio detection experiment deployed since 2009 in the Ulastai valley (Tianshan Mountains, Xinjiang autonomous province, China). The complete setup of the experiment is described in another proceeding of this conference [6], but as a self-triggering experiment using omni-directional antennae, TREND is designed to detect EAS coming from all zenithal angle, including the horizon. Moreover, the Ulastai valley is surrounded by high mountains, offering an additional target for neutrino interaction, as well as shielding for high zenithal angle EAS induced by cosmic ray particles. Thanks to its remote location in high altitude (2650m a.s.l.), the experiment site finally offers a remarkably quiet radio environment, and is located in thunderstorm free area [7]. For all these reasons, TREND can be considered as a perfect opportunity to estimate the potentiality of high energy neutrino radiodetection.

The purpose of this work is to provide an end-to-end estimation of the TREND sensitivity to cosmic neutrinos, starting from a τ neutrino down to the electric signal recorded at output of the TREND electronics. The computation is divided in two main steps. First, we consider the neutrino converting to τ in rocks, escaping the latter and decaying in air. For this we rely on a dedicated Monte-Carlo simulation scheme analogous to the one developed by the Pierre Auger Observatory in [8]. The simulation is based on a C++ high level layer embedding standard FORTRAN algorithms. The specific topology of the Ulastai valley as well as the Earth curvature is taken into account. The second step is purely analytical, and was numerically implemented in MATLAB. Candidate τ decays are selected from this simulation and the radiated electric field from the resulting EAS is estimated on the basis of the MGMR radio emission model [9, 10]. The simulated antenna response as well as the measured response of the whole electronics chain allows the computation of the output antenna signal. Furthermore, the electromagnetic background level measured on site is taken into account in order to determine a realistic trigger condition on these EAS.

2 Sensitivity Computation

2.1 Monte-Carlo simulation scheme: from the neutrino to the EAS

The simulation chain is subdivided in C++ packages handling the geometry and physics of the interactions. Concerning the geometric description of the rocky detector medium, the detailed topology of the site is modeled according to the data published by the NASA SRTM survey [11]. The data point cover a grid of ~90 m steps out of which we selected an area of 200×200 km^2, centered on the TREND setup. We assume standard rock composition [12] over the whole area with an average density of 2.65 g/cm^3. The Earth curvature is taken into account by using a Cartesian coordinate frame throughout the whole simulation. The altitude profile is deformed consequently according to the local vertical direction. Candidate neutrinos are injected at the boundaries of the simulation medium, targeting the TREND region. Whenever a neutrino trajectory starts in rocks, it is back-propagated to the atmosphere.

The simulation of the physics starts with the neutrino interaction in rocks. Interactions length for both Charged Current (CC) and Neutral Current (NC) interactions are randomized according to the integrated cross-sections from [2]. The dynamics of the interaction, and consequently the inelasticity, are delegated to PYTHIA. We use PYTHIA 6 [13] together with CTEQ5D (DIS) partons distribution functions from "Les Houches Accord PDF" (LHAPDF). The native FORTRAN code was interfaced to the general simulation scheme as an independent package by embedding it in a C++ layer. The neutrino is further tracked down until (1) its energy falls below a threshold of $E_{\min} = 10^{15}$ eV from NC interactions; (2) it escapes the simulation medium or (3) it converts to a τ lepton by CC interaction.

The proper lifetime of newborn τ leptons is first randomized out of an exponential distribution. Then, the τ is propagated through rock and air until (1) it lives its whole lifetime –as computed in its rest frame- and disintegrates; (2) its energy falls below the threshold, or (3) it escapes the simulation medium. The τ energy loss and proper time spent in rock are simulated with a hybrid Monte-Carlo scheme based on parameterizations of statistical distributions obtained from detailed simulations with GEANT4 [14]. This method allows rendering fluctuations in energy loss while being fast enough. At UHE, photonuclear interactions are the dominant energy loss process for τ lepton. It was coded in GEANT4 following [15]. The other processes considered are multiple scattering, pair production and bremsstrahlung. Due to the large τ mass, they however contribute to lesser extent than photonuclear reactions.

We define the energy loss factor, L_E, and proper time loss factor, L_T, as:

$$E(d) = E_0 e^{-L_E}$$
$$t_0(d) = \frac{d}{c_0 \gamma_0} e^{-L_T} \quad (1)$$

where E_0 is the initial energy of the τ, $E(d)$ its energy at a depth d in the rocks and $t_0(d)$ the proper time spent in its rest frame. We write c_0 the speed of light in vacuum and $\gamma_0 = E_0 / m_\tau$ the initial boost of the τ. For travelled depths shorter than 60 km, the energy loss factors obtained from GEANT4 distributions where found to be gamma distributed, as illustrated in Figure 1. The distribution parameters a and b for a normalized gamma distributions are taken as:

$$\gamma(x;a,b) = \frac{b(bx)^{a-1}e^{-bx}}{\Gamma(a)} \qquad (2)$$

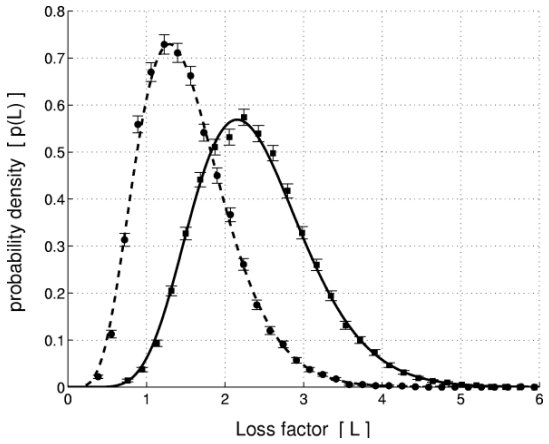

Figure 1 – Loss factors for a τ of primary energy 10^{19} eV at a rock depth of 10 km. Dots are GEANT4 simulation results. The solid line stands for the fit of the energy loss factor by a gamma function while the dotted one is for the fit of the proper time factor.

They depend on the initial τ energy, E_0, and the length, *d*, traveled in the rocks. Furthermore the two loss factors distributions are almost 100% correlated. Consequently, the hybrid simulation scheme resumes to the drawing of a single number out of a gamma distribution in order to randomize both the energy loss and proper time spent by the τ lepton as it reaches a depth *d* in the rocks. For rock depths larger than 60 km this procedure is repeated iteratively by slicing the path in steps of 60 km. Whenever the τ proper lifetime reaches zero or less within the rocks, a zero search algorithm is used to locate the τ decay vertex and its energy at decay.

The τ decays are simulated using PYTHIA interfaced with TAUOLA [16]. Provided that the energy of the daughter τ neutrino is above the energy threshold, it is further tracked down (regeneration scenario). In the case the decay occurs in air, we record the decay vertex location as well as the fraction of energy transferred to showering daughter particles. Taking into account the location of antenna detector elements, a level 0 trigger is then applied to the candidate shower. We require at least one antenna to be in the line of sight of the decay vertex with no rocks in between. We further require this antenna to be within an angular acceptance of 30° of the shower direction of flight, taken from its decay vertex. This allows to filter away showers that would obviously not been detected by the antenna array.

2.2 Signal computation: from the radio emission to the sampled voltage

The estimation of the radio signal radiated by the showers induced by τ decays relies on analytic models implemented in Matlab. The radio signal from the showers is computed using the MGRM model with the full formalism described in [10]. We take into account the 3 dominant sources of emission that are the drift current, the charge asymmetry and the dipolar momentum. So far we however rely on a parameterized description of the longitudinal density, f_z, of electrons and positrons in the shower, from which the 3 source terms are derived. We model f_z by a gamma function, following [17] with parameters and normalization taken according to averaged air shower simulation results for primary protons. Those are in agreement with recent measurements considering uncertainties on the extrapolation of hadronic models [18, 19]. Averaging over QGSP-II, SIBYLL 2.1 and EPOS 1.99 we consider $X_{\max} = 158 + 27.5\ln(E)$ and $N_{\max}/E = 0.47 \cdot E^{0.0142}$, where $X_{\max}$ is in unit $\mathrm{g \cdot cm^{-2}}$ and E in GeV. The longitudinal distribution peak value is normalized to $N_{\max}$ and we further set $b = 0.53/X_0$ which is consistent with simulated air shower profiles in the PeV to EeV energy range. The parameter a falls as $a = bX_{\max} + 1$.

The transverse drift distance, x_d, and drift velocity, v_d, at a given shower age are computed following [8], as:

$$x_d = \frac{C_x}{c_0} < K \cdot L^2 >$$
$$v_d = \frac{C_v}{2} < K \cdot L > \qquad (3)$$

with $K = eB/(\beta m_e)$ and $L = \gamma/(\gamma^2 + \gamma_0^2)X_0/\rho$, where $X_0 = 367\ \mathrm{kg\,m^{-2}}$ is the radiation length in air and ρ the local air density. The air atmosphere was modeled according to data from [20] with mid-latitude winter conditions. The magnetic field at Ulastai is $B = 56.5\ \mu\mathrm{T}$ oriented North and making an angle of 26° with the local vertical. We further recall that the averages in Eq. 3 run over the energy distribution of electrons and positrons in the shower with spectrum modeled following [21]. The factor $\gamma_0 = 13.6\ \mathrm{MeV/m_e}$, rendering multiple scattering, is set following [17]. Finally, the additional factors $C_x = 6.7$ and $C_v = 0.6$ are tuned in order to reproduce the results of [9] for the quoted conditions. Note that the latter relies on Monte-Carlo description of the source terms from shower simulation. We achieve agreement on electric field amplitude within 10% which is satisfactory considering uncertainties introduced by the shower profiles and atmosphere model. Further assuming a pancake thickness of $L_p = 3.9\ \mathrm{m}$ [22] we get a 10-20 % agreement with [23].

The charge excess source term was parameterized according to [22]. We get perfect agreement with results shown in [10, 23] without any tuning. Collecting all terms, Figure 2 shows the expected electric field for a 10^{17} eV horizontal shower developing at 200 m above TREND, at various observation depths down the shower axis. It can be seen that for a given distance to the shower

axis the signal strength actually increases as one gets farther from the shower start, along the shower development direction. This result, which is a priori counter intuitive, results from the fact that the unfiltered radio emission is strongly collimated in the forward region due to the strong Lorentz boost of emitters. Hence, the signal strength is dominated by the angular aperture from which an observer sees the shower axis.

Comparison of various radio antenna designs is beyond the scope of this work. We performed our study with the antennas presently used by TREND, and inspired by the so-called "Butterfly" antennas designed by CODALEMA [24]. The detailed response of theses antennas is simulated with EZNEC, assuming a system bandwidth of 25-250 MHz, and is used to estimate the EAS induced voltage at antenna level. The signal at acquisition level is determined according to the system frequency response, and the standard triggering condition used in TREND (signal amplitude higher than a multiple of the average noise standard deviation) is finally applied. If 5 antennas or more trigger on the shower, the simulated event is considered as a neutrino radio candidate.

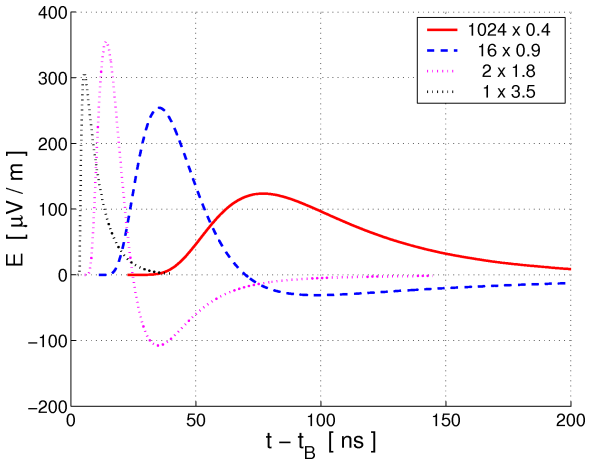

Figure 2 – E-W polarization component of the electric field for a shower propagating from South to North 200 m above the TREND ground. The observer is located at various depths along the shower axis ranging from 0.4 to 3.5 X_{max}. The signal amplitude is scaled accordingly as quoted in the legend.

3 Results for sensitivity estimates

Preliminary sensitivity estimates have been previously obtained with the Monte-Carlo simulation scheme described in section 2.These results, though very encouraging were obtained with a very crude modelisation of the radio signal and antenna response. Current work focuses on interfacing the detailed radio signal computation, as well as defining an antenna design with optimal sensitivity along the horizon. In addition to this, we presently work at identifying possible sources of background events and rejection methods: events generated by human activities at ground level and cosmic-ray induced EAS reconstructed as coming from the horizon are certainly the main sources of concern. For the latter case, mountains act as a screen for EAS with zenith angle larger than 70°, and false identification therefore implies a very large (>5σ) error on the zenith angle reconstruction, given the 2-3° angular resolution in TREND [7]. Radius of curvature of the radio shower front would also help discriminating between (young) neutrino-induced showers and (old) cosmic-ray induced ones. For anthropic background, signal polarization may be the key to discrimination, as it is perpendicular both to the direction of propagation and the geomagnetic field for EAS. A detailed estimation of the TREND sensitivity taking into account these various elements is under progress. It would include efficiency studies of the different steps implied in the detection of a UHE neutrino and various setup configurations would also be investigated.

References

[1] J. N. Bahcall, E. Waxman, Phys.Rev. D **64**, 023002 (2001)
[2] R. Gandhi, *et al.*, Phys. Rev. D **58**, 093009 (1998).
[3] Proceedings of ARENA 2010, Nantes, France. Nucl. Inst. Meth. A, In Press.
[4] D. Ardouin, *et al.*, Astropart. Phys. **31**, 192 (2009).
[5] H. Falcke, *et al.*, Nature **435**, 313 (2005).
[6] T. Saugrin (TREND Collaboration), these Proceedings.
[7] D. Ardouin et al., Astropart. Phys. **34**, 717 (2011).
[8] J. Abraham, *et al.*, Phys. Rev. D **79**, 102001 (2009).
[9] O. Scholten, K. Werner, F. Rusydi, Astropart. Phys. **29**, 94 (2008).
[10] K. Werner, O. Scholten, Astropart. Phys. **29**, 393 (2008).
[11] T.G. Farr, *et al.*, Rev. Geophys. **45** (2007).
[12] http://www.physicalgeography.net/fundamentals/10d.html
[13] T. Sjöstrand, S. Mrenna, P. Skands, JHEP **05**, 026 (2006).
[14] S. Agostinelli, *et al.*, Nucl. Inst. Meth. A **506**, 250 (2003)
[15] S. I. Dutta, Y. Huang, M. H. Reno, Phys. Rev. D **72**, 013005 (2005).
[16] S. Jadach, Z. Was, R. Decker, J. H. Kuehn, Comp. Phys. Commun. **76,** 361 (1993).
[17] K. Nakamura, *et al.* (Particle Data Group), J. Phys. G **37**, 075021 (2010).
[18] J. Abraham, *et al.*, PRL **10**4, 091101 (2010).
[19] R. D. Parsons, *et al.*, Astro. Part. Phys. **34**, 832 (2011).
[20] L. W. Abreu, *et al.*, 'The MODTRAN 2/3 Report and LOWTRAN 7 Model', Prepared by Ontar Corporation for PL/GPOS (1996).
[21] F. Nerling, *et al.*, Astropart. Phys. **24**, 421 (2006).
[22] K. D. de Vries, *et al.*, Astropart. Phys. **34**, 267 (2010).
[23] T. Huege, *et al.*, Proceedings of ARENA 2010, Nantes, France. Nucl. Inst. Meth. A, In Press.
[24] D. Charrier, *et al.*, Proceedings of ARENA 2010, Nantes, France. Nucl. Inst. Meth. A, In Press.

32ND INTERNATIONAL COSMIC RAY CONFERENCE, BEIJING 2011

The Shadow of the Moon in Cosmic Rays measured with IceCube

THE ICECUBE COLLABORATION[1], H. STIEBEL[2]
[1]*See special section in these proceedings*
[2]*Stockholm University, Department of Physics, SE 106 91 Stockholm, Sweden*

Abstract: The observation of a deficit of cosmic rays from the direction of the Moon is an important experimental verification of the absolute pointing accuracy of the IceCube detector and the angular resolution of the reconstruction methods. This Moon shadow in the downward-going muon flux has been observed with a statistical significance of more than 10 sigma in an initial analysis based on a binned counting approach. An unbinned maximum likelihood method was developed to reconstruct the shape and the position of this shadow more precisely, to compare the performance of different reconstruction algorithms and to verify the correctness of the angular error estimate.

Corresponding Authors: D.J. Boersma[3] (*boersma@icecube.wisc.edu*), L.E. Gladstone[4] (*gladstone@icecube.wisc.edu*), J. Blumenthal[3] (*blumenthal@physik.rwth-aachen.de*), H. Stiebel[2] (*hust7801@student.su.se*)
[3]RWTH Aachen University, III. Phys. Institut B, Otto-Blumenthal-Strae, 52074 Aachen, Germany
[4]UW Madison, 222 West Washington Avenue, Madison 53703 WI, USA
DOI: 10.7529/ICRC2011/V04/1235

Keywords: IceCube, cosmic rays, Moon shadow, pointing capability, neutrino astronomy

1 Introduction

IceCube [1] is a cubic kilometer scale Cherenkov detector at the geographical South Pole, designed to search for muons from high energy neutrino interactions. The arrival directions of these muons, which are reconstructed with $\mathcal{O}(1^\circ)$ accuracy, are used to search for point sources of astrophysical neutrinos [2], one of the primary goals of IceCube.

The main component of IceCube is an array of 5160 Digital Optical Modules (DOMs) deployed in the glacial ice at depths between 1450 m and 2450 m. During construction, with the first string of 60 DOMs deployed in January 2005 and the 86th and final string deployed in December 2010, the detector already took high quality data. The data analyzed and reported here were taken in the 40 and 59 string configurations, which were in operation between April 2008 and June 2010, with a configuration switch in May 2009.

For downward-going directions, the vast majority of the detected muons do not originate from neutrino interactions, but from high energy cosmic ray interactions in the atmosphere. While these cosmic ray muons are the dominant background in the search for astrophysical neutrinos, they can be used to study the performance of our detector. In particular, we can verify the pointing capability of IceCube by studying the shadow of the Moon in cosmic ray muons.

Cosmic rays at TeV energies propagate through the solar system nearly uniformly in all directions. The Moon blocks some cosmic rays from reaching the Earth. This creates the shadow of the Moon, a relative deficit of cosmic ray muons from the direction of the Moon.

The idea of a Moon shadow was first proposed in 1957 [3], and has become an established observation for a number of astroparticle physics experiments [4, 5, 6, 7]. Experiments have used the Moon shadow to calibrate detector angular resolution and pointing accuracy [8]. The shift of the Moon shadow due to the Earth magnetic field has also been observed [9].

For an observer at the geographic South Pole, the Moon rises and sets once per orbital period of 27.32 days. The number of cosmic ray induced muons reaching IceCube decreases with increasing declination (i.e. for increasingly horizontal directions), since the Earth and the Antarctic ice sheet filter low energy muons. Therefore, the shadow of the Moon is best observed as far above the horizon as possible, i.e. at low declinations. However, the minimum declination of the Moon in an orbital period varies slowly over time with a period of 18.6 years and is currently increasing. In April 2008, 2009 and 2010 the minimum declination of the Moon was -26.89°, -25.85° and -24.47°, respectively. Fig. 1 shows the energy spectrum of cosmic ray primaries that result in one or more muons triggering IceCube. For the declination greater than -30°, the energy threshold is about 2 TeV.

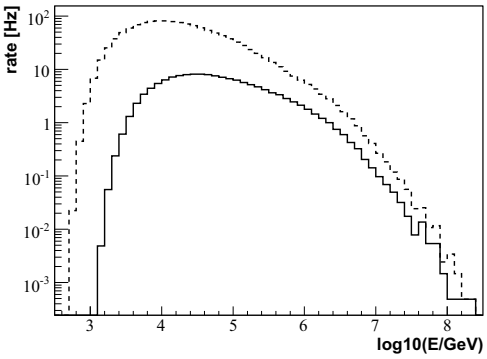

Figure 1: The energy spectrum of cosmic ray (CR) primaries with muons triggering IceCube, as simulated using CORSIKA [10]. Dashed: all events; solid: primaries with $\delta_{\rm CR} > -30^\circ$.

The Moon shadow in cosmic rays was first observed with IceCube using data taken during the first 8 orbital periods in the 40-string configuration, using a binned analysis [11]. In the analysis using the full data sets from the 40-string and 59-string configurations, a log-likelihood based analysis [12] has now been developed to study the point spread function of IceCube for muons.

The observed Moon shadow can be characterized with the following observables:

- The apparent shift of the Moon shadow from its nominal position (as computed from the time at which each muon event was recorded). A shift of order 0.1° is expected due to the Earth's magnetic field. Other contributions to a shift could come from e.g. a possible bias in track reconstruction or an error in the clock used to record the event times.
- The apparent width and ellipticity of the shadow. The apparent radius of the Moon is $\sim 0.25^\circ$, significantly smaller than the estimated angular resolution for muon tracks in IceCube. Hence the width of the shadow provides an experimentalal verification of the angular resolution estimate, which could for instance be different in zenith and azimuth directions.
- The number of shadowed events should be compatible with the measured flux of cosmic-ray induced muons (at the declination of the Moon) and the solid angle subtended by the Moon. Any significantly deviating result would be an indication of a systematic error.

2 Event selection

The trigger rate from cosmic ray muons was about 1.2-1.3 kHz in the 40-string configuration and close to 2 kHz in the 59 string configuration. However, most of those muons detected by IceCube travel nearly vertically, and thus they cannot have come from directions near the Moon.

The online event selection is defined as follows:

- the Moon must be at least 15° above the horizon
- at least 12 DOMs must register each event
- at least 3 strings must contain hit DOMs
- the reconstructed direction must be within 10° of the Moon in declination
- the reconstructed direction must be within $40^\circ / \cos(\delta_\mu)$ of the Moon in right ascension; the $\cos(\delta_\mu)$ factor corrects for spherical projection effects

where δ_μ denotes the declination of the reconstructed track.

The online Moon shadow filter was active (i.e., the Moon was more than 15° above the horizon) for 7-9 days during each 27.3 day orbital period. In that time, between 10M and 20M events were selected, depending on the number of active installed strings, atmospheric conditions and detector stability. This is about one percent of all events triggering IceCube during those days.

The event sample that passed online selection is subject to the same higher level track fitting algorithms as used in the searches for point sources of astrophysical neutrinos. The track likelihood function used in the fit is based on a simplified model of the scattering and absorption of light in ice [13]. In the offline processing, the track fit is repeated using several different seeds. For the majority of the events, this leads to a solution which is close to the online fit with a slightly improved angular resolution, when studied in simulated data. For a fraction of all events, the track fit is ambiguous and the iterative fit may yield a completely different direction.

In the Moon shadow analysis, we characterize each event by the zenith angle difference $\Delta\theta = \theta_{\leftmoon} - \theta_\mu$ (which is equivalent to the the declination difference, thanks to the unique geographic location of the detector) and the azimuth angle difference $\Delta\phi = (\phi_{\leftmoon} - \phi_\mu) \cdot \sin\theta_\mu$ between the direction of the offline reconstructed track and the nominal position of the Moon at the time of the event.

In the analysis, on-source and off-source subsamples are defined using the offline reconstruction. They are again defined by an angular window, namely $|\Delta\theta| \leq 8^\circ$ and $|\Delta\phi + \phi_{\rm off}| \leq 8^\circ$. Here $\phi_{\rm off} = 0^\circ$ for the on-source sample, and $\phi_{\rm off} = \pm 18^\circ$ for the left and right half of the off-source sample, respectively. The on-source samples for the full year data sets of the 40-strings and 59 strings configurations contain 19M and 22M events, respectively.

The per-event directional error estimate is derived from the variation of the track likelihood function near the solution obtained with the track fit [14]. It can be characterized either by the 3 parameters describing the 1σ error ellipse, or by a single average angular error estimate. In this work, we use the latter characterization.

The reliability of the directional error estimate was studied in simulated data, and simple quality selection criteria were developed to ensure that the pull (ratio of real and estimated angular error) is on average equal to unity. Moreover, for numerical stability, only events with an error estimate in the range from 0.075° to 1.5° were accepted. About half of the events in the on-source and off-source samples satisfy all these criteria.

3 Likelihood analysis

An unbinned likelihood analysis was applied to both data sets, using an approach similar to the likelihood approach taken for the IceCube point source searches [2]. The likelihood for the Moon having shadowed n_s events centered around $\vec{x}_s$ out of the on-source data sample is expressed as:

$$L(\vec{x}_s, n_s) = \sum_i^N \log\left(\frac{n_s}{N} S_i + (1 - \frac{n_s}{N}) B_i\right), \quad (1)$$

where $\vec{x}_s = (\Delta\theta, \Delta\phi)$ is the position relative to the nominal Moon position, n_s is the number of signal events, N is the total number of events, S_i is the signal probability density, and B_i is the background probability density. Note that Eq. 1 includes no explicit energy-dependent term; this a major difference between the IceCube Moon analysis and the IceCube point source searches. For the Moon shadow, we expect the number of signal events to be negative, as the Moon produces a deficit.

The signal probability density function S_i was assumed to be Gaussian, with a width given for each event by the estimated error on the reconstructed position [14]. The background probability density function B_i was estimated by using the normalized (Moon-centered) declination distribution obtained from the two off-source regions, and by assuming a uniform distribution in (Moon-centered) right ascension.

The likelihood (1) was maximized at every point $\vec{x}_s$ in an angular grid around the nominal Moon position, allowing the number of "signal" events n_s to vary.

4 Results

The distribution of the reconstructed number of signal events n_s is shown in Figures 2 and 3 as a function of the offset coordinates of the center of the shadow from the nominal Moon position. The shadow of the Moon is observed as a significant deficit centered at the nominal Moon position.

These results are directly compared with the same distributions from the off-source samples, as shown in Fig. 4. The distributions of the off-source samples are consistent with null shadowing effect from the Moon. The RMS values of the n_s distributions obtained for the left and right halves the off-source are considered as two independent estimates of the standard deviation of the background fluctuations.

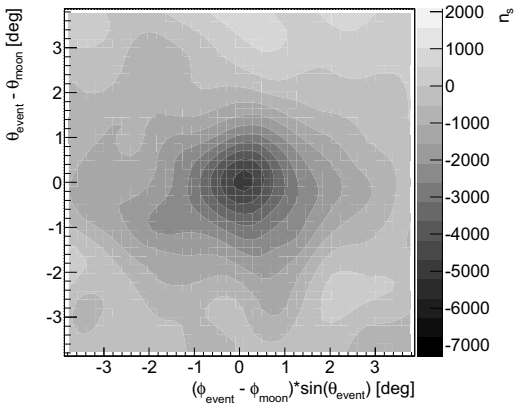

Figure 2: The Moon Shadow from the 40-string configuration *(preliminary)*. See text for details.

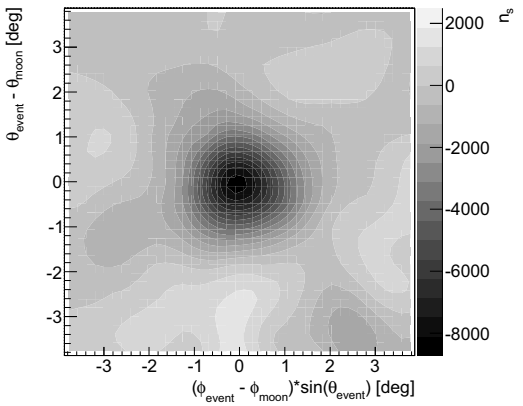

Figure 3: The Moon Shadow from the 59-string configuration *(preliminary)*. See text for details.

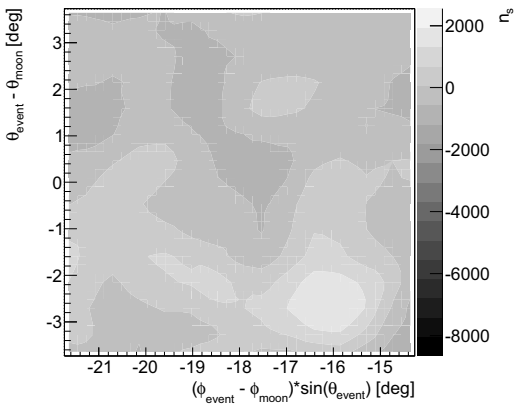

Figure 4: Fluctuation in n_s around the background model in one half of the off-source sample for the 59-string data set *(preliminary)*. See text for details.

	40 strings	59 strings
orbital periods	15	14
expected deficit	5734 ± 76	8192 ± 91
observed deficit	$5326 \pm 544 \pm 498$	$8660 \pm 565 \pm 681$
significance	10-11σ	13-15σ
θ offset	0.0°	0.0°
ϕ offset	0.0°	0.0°

Table 1: Results obtained in the Moon shadow analyses of the 40-string and 59-string data sets. Note that the two uncertainties given for the observed deficit are the estimates for the statistical uncertainty obtained from the left and right half of the off-source data samples; the numbers do *not* specify a systematic error.

The distributions of these values have means compatible with zero, as expected for the off-source regions. The RMS values of these distributions are now used as two independent estimates of the standard deviation of the background fluctuations (see Table 1).

The number of shadowed events found through likelihood maximization are also compared with the *expected* number of shadowed events. The expected number is calculated from the average apparent radius of the Moon and the off-source flux of downward-going muons from the declination of the Moon.

The depth of the observed shadow is compatible with the expected number of shadowed events. The significances of the shadows shown in Figures 2 and 3 are calculated to be 10-11σ and 13-15σ, respectively. The results for both detector configurations are summarized in Table 1.

The larger number of strings is the main reason for the larger significance of the result with the 59-strings configuration. With more optical sensors, more events are recorded, which are reconstructed with better angular resolution. On the other hand, the minimum declination reached by the Moon between April 2008 and May 2009 was more than a degree less than between May 2009 and June 2010. Moreover, the 40-string data sample contains livetime from one more orbital period.

To further confirm our results, the data from the 40-string configuration have also been analyzed using a different track fit algorithm and a corresponding angular error estimate. Simulation studies of this different reconstruction algorithm indicated an average pull of 1.55. Without correcting for this pull, the Moon shadow analysis resulted in a central n_s value of -3574 ± 434, differing by more than 5 standard deviations from the expectation: -6373 ± 80. Redoing the analysis with the angular error estimates rescaled by a factor of 1.55 resulted in a fitted n_s value compatible with expectation.

The log-likelihood-based analysis relies on the error estimate of the reconstructed track direction, ranging in this data sample from 0.075° to 1.5°. If we were not correctly estimating the angular errors, then we would find a shadow depth which is significantly smaller than expectation. The agreement between expected and observed shadow depth is a verification of the directional error estimate of the default track reconstruction algorithm as used in the analyses of the data taken with IceCube in these configurations.

5 Conclusions and Outlook

The shadow of the Moon in cosmic rays has been observed with a significance of more than 10σ in IceCube data collected between April 2008 and June 2010. The shadow depth is compatible with the expected number of shadowed events and has no significant systematic offset. These results confirm the pointing capability of IceCube.

We have started performing an observation of the shadow of the Sun. The shadow depth of the Sun should be comparable to that of the Moon, but a larger offset is expected due to the solar magnetic field. This offset should be correlated to the energy of the observed muons. Furthermore, if there is a component of high energy antiprotons in cosmic rays, then this should result in a faint second shadow with the opposite offset.

References

[1] H. Kolanoski, IceCube summary talk, these proceedings.

[2] J. Braun *et al.*, Astroparticle Physics **29** (2008) 299-305, [arXiv:0801.1604 [astro-ph]].

[3] G.W. Clark, Physical Review **108** (1957) p. 450-457.

[4] A. Karle for the HEGRA collaboration, Ann Arbor Proceedings (1990), High Energy Gamma-Ray Astronomy, p. 127-131.

[5] N. Giglietto, Nuclear Physics B Proceedings Supplements, Volume **61** (1997), Issue 3, p. 180-184.

[6] M.O. Wasco for the Milagro collaboration, 1999, arXiv:astro-ph/9906.388v1.

[7] The Soudan 2 collaboration, 1999, arXiv:hep-ex/9905.044v1.

[8] The Tibet AS Gamma Collaboration, M. Amenomori *et al.*, arXiv:astro-ph/0810.3757v1.

[9] L3 Collaboration, P. Achard *et al.*, Astropart. Phys. **23** (2005) p. 411-434, arXiv:astro-ph/0503472v1.

[10] D. Heck, J. Knapp, J.N. Capdevielle, G. Schatz, T. Thouw, FZKA **6019** (1998).

[11] D.J. Boersma, L. Gladstone, A. Karle, for the IceCube Collaboration, Proceedings of the 31^{st} ICRC, LODZ, POLAND (2009), arXiv:1002.4900.

[12] J. Blumenthal, Diplomarbeit in Physik (2011), Rheinisch-Westfälischen Technischen Hochschule Aachen, available upon request.

[13] G. Japaridze, M. Ribordy, arXiv:astro-ph/0506136v1.

[14] T. Neunhöffer and L. Köpke, Nuclear Instruments and Methods **A558** (2006) p. 561-568.

[15] H. Stiebel, Master Thesis (2011), Stockholm University, available upon request.

32ND INTERNATIONAL COSMIC RAY CONFERENCE, BEIJING 2011

IceCube's In Ice Radio-Frequency extension

THE ICECUBE COLLABORATION[1], E. CHENG[2], L. RUCKMAN[3], G.S. VARNER[3]
[1]*See special section in these proceedings*
[2]*Dept. of Physics, Univ. of Wisconsin, Madison, WI 53703, USA*
[3] *Dept. of Physics and Astronomy, Univ. of Hawaii, Manoa, HI 96822, USA*

Abstract: In preparation for designing a large scale array sensitive to high energy neutrinos (EeV), several Radio Frequency (RF) detectors and calibration equipment were installed with the IceCube neutrino detector at the geographic South Pole between the years 2006–2010. The wide and deep holes drilled for IceCube provided a unique opportunity for deep-ice RF detection studies at depths never surveyed before. The deployed detectors are installed between 5 to 1400 meters deep in the ice, and are sensitive to frequencies in the range of 200 MHz–1 GHz. We will present results of ice properties studies (attenuation length and index of refraction) and environmental noise study.

Corresponding authors: Hagar Landsman(*hagar@icecube.wisc.edu*), Mike Richman(*mike.d.richman@gmail.com*), Kara Hoffman(*kara@umd.edu*)
DOI: 10.7529/ICRC2011/V04/1236

Keywords: Neutrino, Askaryan, GZK, South Pole, ice properties, attenuation

1 Introduction

The concept of high energy neutrino radio frequency detector buried in ice at shallow depths or deployed as a surface array was suggested nearly 30 years ago [1]. The RICE [2] array and the ANITA experiment [3] are already taking advantage of the Askaryan effect and the massive volume of ice in Antarctica for neutrino detection by looking for the coherent radio Cherenkov emission from charge asymmetry in high-energy neutrinos cascades. Future experiments include ARIANNA [4], a surface array on the Ross Ice Shelf, and ARA [5], an in-ice array at shallow depths near the South Pole. Our unique access to IceCube's deep and wide holes have provided us with an opportunity for deploying radio frequency (RF) detectors in the deep Polar ice. These detectors use the communication and time calibration systems developed for IceCube and rely on the experience within the IceCube Collaboration for developing hardware and software and for building and deploying highly-sensitive equipment in the extreme South Pole environment as well as on radio technology expertise from the RICE and ANITA Collaborations. IceCube's deep holes and well-established data handling system provide a unique opportunity for deep-ice RF detection studies.

2 Hardware description

2.1 Full digitization detectors

IceCube's radio extension modules, consisting of several radio frequency (RF) detectors as well as calibration equipment, were installed on IceCube strings during the austral summers between 2006 and 2010 at depths of 5 to $1400\,\mathrm{m}$. Each radio module was installed directly above IceCube's digital optical modules (DOMs). The RF components were mechanically attached to the $\sim 3\,\mathrm{km}$-long IceCube main cable (a 5-cm-diameter cable bundle for communication and power) which simply served as a mechanical support; some of the modules, however, were tapped into one of the auxiliary twisted-pairs within the main cable designed for specialized device operations. The main cable, being a massive conducting object, can shadow the RF antennas.

During the first two seasons five detectors capable of full waveform (WF) digitization were deployed. These so called "clusters" consist of four receiving channels equally spaced over $\sim 40\,\mathrm{m}$ along the IceCube cable, a transmitting channel and a central electronics module. Each receiver channel consists of a broadband dipole antenna (with the gain centered at $\sim 400\,\mathrm{MHz}$ in air and $\sim 250\,\mathrm{MHz}$ in ice), and a set of front-end electronics (housed in a metal tube), including filters (450 MHz notch filter for rejecting constant interference from the South Pole communica-

tion channel, and 200 MHz high-pass filter) and amplifiers (~ 50 dB low-noise amplifier). An additional ~ 20 dB amplification is done at a later stage within the electronic module for a total amplification of ~ 70 dB. A schematic of the 2006–2007 cluster is shown in Figure 1. Three clusters were deployed at depth of ~ 300 m , and two at ~ 1400 m. A detailed description of the electronics installed inside the DRM can be found elsewhere [6, 7].

2.2 Transient detectors

The idea of using an array of simple transient sensors to image the unique spatiotemporal signature of neutrino interactions in Antarctic ice was proposed by Gusev and Zheleznykh nearly thirty years ago [1]. In this type of detector system, the pattern of coincident hits among a large number of sensors provides event confirmation, indication of direction and energy, and information for rejecting sporadic noise on the basis of time-of-arrival and amplitude. Six units of transient-prototype-detector were deployed in the 2009–2010 season. Each unit consists of a discone wide-band omni-directional antenna feeding into a Transient Detector Assembly (TDA), an exploratory device, whose block diagram is shown in Figure 1. Each unit is read out using a control motherboard (MB) developed for the IceCube DOM [8]. The IceCube cable and calibration system also facilitates timing calibration and data handling. The units were deployed in pairs above three IceCube strings, with one unit at $z = -5$ m and the other at $z = -35$ m. The Local Coincidence (LC) capabilities of the IceCube MB are also exploited; when LC is enabled, each TDA pair reads out data only if both units in the pair are triggered in some adjustable time window. The rise-time of the output pulse from these units is on the order of 10–20 ns and is largely independent of amplitude.

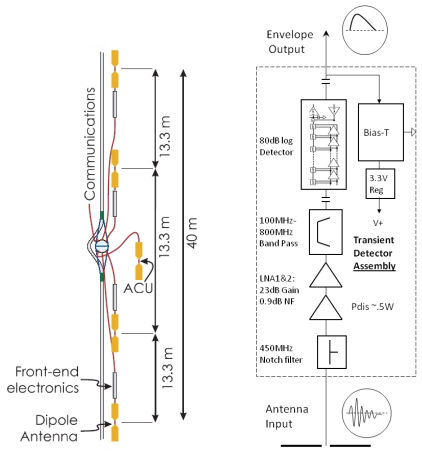

Figure 1: The radio cluster, consisting of the DRM (Digital Radio Module), 4 receiving antennas and 1 transmitting antenna (left); Block diagram of the Transient Detector Assembly (right).

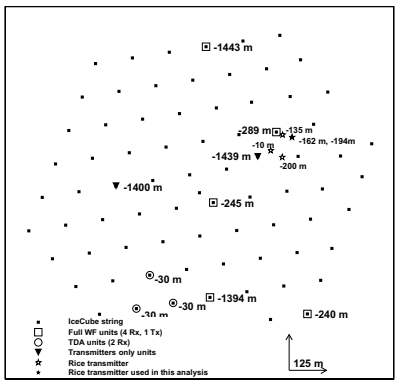

Figure 2: Map of the IceCube radio detector deployments, plotted on top of the full IceCube array. Also shown are the deployment depth of each unit relative to the surface, and the location of the RICE transmitters.

Figure 2 summarizes the in-ice locations and depths of the deployed units.

3 Ice Properties

The properties of ice at radio frequencies determine the feasibility and design of future GZK neutrino detectors. Specifically, the attenuation length affects the spacing between channels and the effective detector volume, whereas uncertainties in the index of refraction determine the reconstruction capabilities and simulation quality.

3.1 Attenuation Length

The attenuation length λ is the distance over which the signal amplitude diminishes by a factor of e due to absorption and/or scattering. In general, λ varies with the density and temperature of a medium and with the frequency of the radiation. In South Pole ice, the density and temperature vary with the depth z, and so the attenuation length is also a function of depth.

The previous in-ice RF attenuation data from the South Pole were obtained by sending signals down into the ice using a surface transmitter and recording the signals reflected from the bedrock below. This measurement provided an average RF attenuation over the round-trip, weighted by the temperature profile along the path [9].

The IceCube Radio Extension provides us with the first opportunity to make a point-to-point attenuation measurement independent of the unknown bedrock reflection coefficient. Of 20 available receiver channels, we use the 6 which have similar amplifiers and electronics. Our sources are RICE antennas which transmit signals from a pulser operated in an on-site lab. The pulse power can be varied by inserting attenuators in the line. The transmitting antennas are similar to the receiving antennas and are located at var-

ious depths down to 220 m, and up to ~ 1400 m away from the receivers (see Figure 2).

The simplest possible relative attenuation measurement would involve broadcasting a signal and measuring the relative power received by antennas at different distances from the transmitter. However, IceCube Radio Extension digitizers have insufficient dynamic range for this approach. Thus, we instead vary the transmitter power, measuring the values which yield the same power at different receivers. The differences between these values are $\Delta\mathcal{L}_{\text{total}}$, the total receiver–receiver difference in losses.

We assume that (in a logarithmic scale) $\Delta\mathcal{L}_{\text{total}} = \Delta\mathcal{L}_{\text{dipole}}(\theta) + \Delta\mathcal{L}_{\text{free space}}(\vec{r}, n(z)) + \Delta\mathcal{L}_{\text{attenuation}}(\vec{r}, \lambda)$. We use a standard dipole pattern for transmitters and receivers: $I(\theta) = (3/8\pi) I_0 \sin^2(\theta)$. The free space losses, which for uniform index of refraction would give the inverse square law, are calculated using ray tracing simulation. After obtaining $\Delta\mathcal{L}_{\text{total}}$ from measurement and $\Delta\mathcal{L}_{\text{dipole}}$ and $\Delta\mathcal{L}_{\text{free space}}$ from simulation, we can calculate the path-averaged attenuation length $\langle\lambda\rangle$: $\Delta\mathcal{L}_{\text{attenuation}} = 10\log_{10} e^{-2\Delta r/\langle\lambda\rangle}$. Figure 3 shows the measurement of pulses from a RICE transmitter. Deep receiver channels show a linear response. Shallow receiver channels have a flatter response for higher power due to saturation; however, for sufficient transmitter attenuation, they also have a linear response.

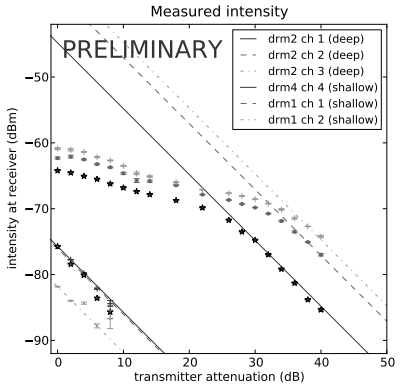

Figure 3: Measured intensity vs. transmitter attenuation.

A linear fit with a slope of -1 is done for the linear region on each curve. The difference between the x-intercepts for any pair of fits is equal to $\Delta\mathcal{L}_{\text{total}}$ for that antenna pair. To date, sufficient data has been taken only with one of RICE transmitters. Preliminary values obtained from this data for $\langle\lambda\rangle$ range from 400 to 700 meters. These numbers are somewhat lower than past results [9]; however, preliminary systematic error estimates suggest that these results will not be inconsistent with each other.

This measurement is ongoing. Our simulation of the effects of reflection and shadowing by an IceCube cable in the vicinity of a broadband dipole antenna is not yet complete. Other remaining work includes estimating other systematics such as receiver gain uncertainties; taking data with additional transmitters; and combining results for $\langle\lambda\rangle$ with existing density and temperature measurements to obtain a model for $\lambda(z)$.

3.2 Index of refraction

Uncertainties in index of refraction lead to uncertainties of the order of a few ns in the time difference measured between two receivers a few meters apart (geometry-dependent); therefore, a precise knowledge of index of refraction is necessary for a sub-ns-resolution detector. The latest index of refraction measurement at the South Pole reported in [10] combines results using the RICE array down to 150 m and ice cores down to 240 m. The model used is of the form $n(z) = n_{\text{deep}} + (n_{\text{shallow}} - n_{\text{deep}})e^{n_c \cdot z}$, where $n_c \approx -0.0132\,\text{m}^{-1}$, $n_{\text{deep}} \approx 1.78$, and $n_{\text{shallow}} \approx 1.35$. The changing index of refraction causes rays to curve in the ice layers, especially in the soft ice layers on top of the glacier (firn), and decreases the angular acceptance of shallow-deployed detectors by causing total reflection of rays propagating between the layers. When looking at possible paths connecting a transmitter and a receiver both in ice there will be either zero or two solutions (direct ray and reflected ray) to the ray-tracing problem. The reflection takes place at the ice-air boundary on the surface, as illustrated in Fig. 4A.

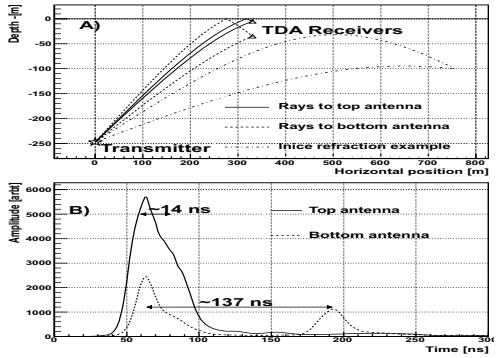

Figure 4: A. Ray Tracing showing the direct- and reflacted-rays solutions. The depths and separation between the transmitter and the receivers in this figure correspond to the transmitter-recievers used in the analysis. B. Average WF collected on the top (solid) and bottom (dashed) antennas of the transient detectors. The time delay between the direct and the refracted ray detected by the bottom antenna is consistent with simulations (137 ns).

The extremely shallow location of the TDA units makes them sensitive to small variations in the index of refraction model, especially to n_{shallow} and n_c. Five out of six TDA units were able to trigger on a calibration pulse transmitted by a calibration antenna from depth of -245 m. The sixth unit that did not see the pulser (Top antenna at hole 8)

was in the shaded area where no solution exists. Limits on the ice model parameters can be set by measuring the trigger time differences between different units as well as the time differences between the direct and reflected ray. This is illustrated in Fig 4B where an average WF from a pulser run for the top and bottom detectors is shown. The expected time delay between the direct and reflected ray for the top antenna was calculated to be about $14\,\mathrm{ns}$, and the direct and reflected peaks are not resolvable. For the bottom antenna the simulated time delay was about $137\,\mathrm{ns}$, in good agreement with the measurement. Figure 5 shows preliminary constraints on n_{shallow} and n_c based on combined time differences measured between detectors.

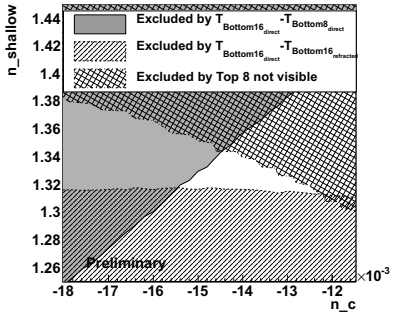

Figure 5: Excluded parameters space for index of refraction based on time delays between hits. This area includes systematic uncertainties from the following uncertainties: timing resolution, slewing, geometry and n_{deep}.

4 Environmental Noise

We have previously shown that timing of elevated noise rates coincided with the periods of winds stronger than $\sim 20\,\mathrm{knots}$ (see Figure 6). Since the South Pole is electrically insulated, electrostatic charge accumulates easily, leading to a discharge causing EMI. There are two possible mechanisms as to how electrostatic charge builds up in strong winds: "precipitation charging" [11] where blowing snow causes structures to charge up; and "snowstorm electrification" [12], where charge separation occurs near the snow surface. A preliminary reconstruction study has pointed to an area around large structures in the Dark Sector as the origin of this interference. Preliminary studies with radio detectors away from the station have shown no such interference, supporting the assumption that the noise is originating from structures and not spotaneous charging of the ice. However, additional data are required since this analysis was preformed early in the austral winter, using limited statistics [5].

We were also sensitive to weather balloon launches, happening twice a day. Since this noise source is well defined in time and frequency, it will not be a problem for future detectors.

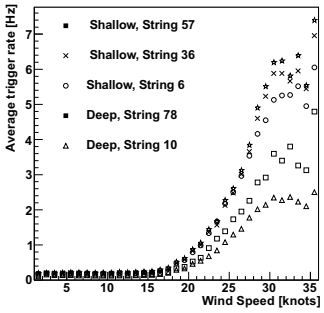

Figure 6: Average trigger rate vs. wind speed for the five clusters described in Section 2.1. The meteorological data were taken from the "Clean Air" automatic weather station, operated by The Antarctic Meteorological Research Center (AMRC) and the Antarctic Automatic Weather Station (AWS) Program [13].

5 Summary

IceCube's mature drilling and data acquisition technology have facilitated the deployment of the first fully digital radio test equipment in South Pole ice as well as deployment to greater depths in South Pole ice than was previously possible. Using the IceCube radio frequency extension, we have obtained tighter constraints on the index of refraction model parameters, and an attenuation length measurement is also underway. We have also been able to characterize and understand the RF noise environment at the Pole. This information will provide a valuable guide for the design of a future GZK neutrino detector.

References

[1] G. A. Gusev, I. M. Zheleznykh, JETP Lett. 38 (1983) 611–614.
[2] I. Kravchenko, et al., Phys. Rev. D73 (2006) 082002.
[3] P. W. Gorham, et al., Phys. Rev. D82 (2010) 022004.
[4] L. Gerhardt, et al., arXiv:1005.5193.
[5] P. Allison, et al., arXiv:1105.2854.
[6] H. Landsman, et al., Nucl. Instrum. Meth. A604 (2009) S70–S75.
[7] H. Landsman, et al., Nucl. Instrum. Meth. In Press, accepted manuscript, (2010) doi:10.1016/j.nima.2010.11.144.
[8] R. Abbasi, et al., Nucl. Instrum. Meth. A601 (2009) 294.
[9] S. Barwick, et al., J. Glaciology 51 (173) (2005) 231.
[10] I. Kravchenko, et al., J. Glaciology 50 (171) (2004) 522.
[11] S. B. Dunham, J. Atmospheric Sciences 23 (1966) 412.
[12] M. Gordon, P. Taylor, Boundary-Layer Meteorology 130 (2009) 97–115.
[13] ftp://amrc.ssec.wisc.edu/pub/southpole/surface_observations.

32ND INTERNATIONAL COSMIC RAY CONFERENCE, BEIJING 2011

Results from the Askaryan Radio Array Testbed Station

THE ARA COLLABORATION[1]
[1]*See special section in these proceedings.*

DOI: 10.7529/ICRC2011/V04/1237

Abstract: The Askaryan Radio Array (ARA) is an ultra-high energy neutrino telescope under development consisting of radio antennas to be deployed in the ice 200 m deep near the geographic South Pole. During the 2010-2011 Austral summer, an ARA testbed station was deployed, consisting of antennas, trigger and readout electronics, and high voltage pulsers, with most components at approximately 20 m depth. The first ARA stations will be deployed in the following two Austral summer seasons. We will present the results from data taken by the testbed this season, including characterizations of the in-ice noise environment, trigger performance, angular resolution, and measurements of the index of refraction and attenuation of radio pulses in the ice. We will conclude with implications of the testbed results for ARA design.

Keywords: neutrino antarctic radio cerenkov

1 Introduction

Neutrinos are unique cosmic messengers as they travel cosmological distances unattenuated and also do not undergo deflections in magnetic fields. Thus they would carry valuable information complementary to that from charged cosmic rays and gamma rays. Apart from solar neutrinos and a small sample of neutrinos from a singular event, SN1987a, neutrinos from beyond the earth's atmosphere remain elusive. However, there is a nearly infallible argument for the existence of a cosmic neutrino flux in the ultra-high energy (UHE) regime (above 10^{18} eV) due to the interaction of UHE cosmic rays with cosmic microwave background photons through what is known as the GZK process [1, 2]. Berezinsky and Zatsepin first noted that this process would produce an observable neutrino flux [3, 4].

Since the expected UHE neutrino flux is rare (of order 10/km^2/year), detection volumes of order 100's of cubic kilometers are necessary. IceCube and Antares are searching for cosmic neutrinos using the visible Cerenkov technique in South Pole ice and Mediterranean sea water respectively [5, 6, 7]. The length over which visible light is scattered or absorbed in these media is on the order of 50 meters. This sets the scale for the sensor spacings, and so detector scales beyond 1 km^3 for that technique are prohibitively expensive. The radio Cerenkov technique allows for much larger detection volumes due to attenuation lengths of approximately 1 km in ice [8]. This technique has been well established over the past two decades [9, 10, 11, 12] and the ANITA experiment, which searches for radio Cerenkov pulses from above the Antarctic ice sheet, places the strongest constraints on the cosmic neutrino flux above $10^{18.5}$ eV [13].

The Askaryan Radio Array (ARA) will use the radio Cerenkov technique to search for UHE neutrinos using antennas deployed in the South Pole ice [14, 15]. It aims to measure a sample of order 100 neutrinos in the UHE regime so that their properties, of interest to both particle physics and astrophysics, can be studied. The proposed first phase of the detector will consist of an array of 37 stations, with 16 antennas each, at a depth of approximately 200 m. The stations will be arranged on a hexagonal grid with a 2 km spacing. The antennas will consist of both vertically polarized, V-pol (bicone, 150 MHz) and horizontally polarized, H-pol (quad-slotted-cylinder, 200-850 MHz) antennas.

2 The Testbed

In January 2011, a first prototype 'testbed' station for ARA was deployed 1.8 km grid East of the IceCube detector, at approximately 30 m depth. It included 10 antennas deployed in the ice and an additional six antennas deployed at the surface. Four V-pol antennas (bicone, 150-850 MHz) and four H-pol antennas (bowtie-slotted-cylinder, 250-850 MHz) and two quad-slotted-cylinders (200-850 MHz) were deployed at approximately 25 m depth. There are also two near-surface discones (150-850 MHz) and two near-surface "batwing" antennas (250-850 MHz). At the surface sit two "fat dipole" (30-300 MHz) antennas. These 16 antennas total were deployed in six boreholes with an approximate trapezoidal geometry and spacing at about 10 m.

The hardware and electronics draws from the strong RICE and ANITA heritage in the collaboration. A low-noise preamplifier is inserted close to the antennas to reduce insertion loss and thermal noise. Along with a second stage amplifier, the total gain is approximately 75 dB. The signals are split into trigger and waveform paths. Each time an event passes the trigger requirements, the RF waveforms for that event are recorded along with associated data such as temperatures, threshold settings, single antenna trigger rates, etc. to a single board computer, then transmitted to a computer at South Pole station over twisted wire pairs via ethernet modem. The data is then transmitted to the northern hemisphere computer archives via satellite link.

A calibration pulser was deployed near the testbed receivers. It pulses at a rate of 1 Hz during all data taking periods and is slaved to a high-precision Rubidium clock to permit signal averaging over multi-km distance scales with picosecond-scale resolution. This allows us to continuously monitor the functionality of the trigger while providing a reference for timing and signal amplitudes.

Three 4 kV, ns-scale pulsers manufactured by FID, Inc. were deployed in deep ice in two of the final holes drilled for IceCube. The furthest pulser from the testbed was at 2.01 km distance along the surface and at approximately 2.45 km depth, for a total distance of 3.16 km through the ice. We took several dedicated runs in mid-January where all three of the deep pulsers were easily observed in the testbed data.

An RF trigger requires that 3 waveforms of the 8 bicone and bowtie-slotted-cylinder antennas at depth exceed a threshold of approximately 3.5 times the RMS thermal noise voltage. This gives a thermal noise trigger rate of typically 0.5-1.0 Hz. In addition, the calibration pulser triggered the system once per GPS second.

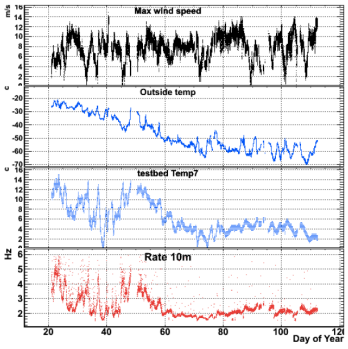

Figure 1: Comparison of trigger rates with environmental variables during ARA testbed data taking. Top: Wind speeds recorded at the South Pole near the site of the testbed. Upper middle: Air temperature near the site. Lower middle: Temperature internal to testbed data acquisition electronics housing. Bottom: Global trigger rate for the ARA testbed, showing a strong correlation with the electronics temperature.

3 Results

3.1 Thermal Noise

Figure 1 shows the testbed trigger rate as compared with three different environmental variables which were monitored continuously during take taking. We monitored the wind speed at the South Pole to check for any correlation of the noise rates with blowing snow and no such correlation was observed. There is however, a clear correlation with the temperature of the testbed electronics. Some correlation is expected due to the temperature dependence of the thresholds. The software has the capability to adjust the thresholds in real time so as to maintain nearly constant trigger rates, but this feature has not yet been enabled.

Figure 2 shows the average Fourier power spectra measured by one of the borehole antennas from a run during a period in late April 2011. For pure thermal noise, the noise level is given by $kT\Delta f$ which is -175dBm/MHz for the electronics temperature $T = 290$ K. The average measured thermal noise levels imply a thermal+system noise temperatures of approximately 325 K.

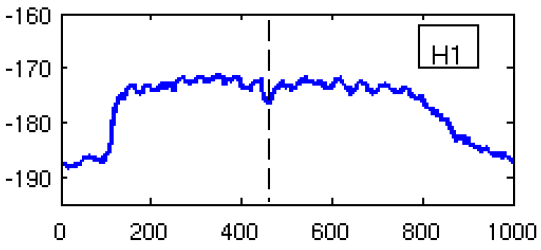

Figure 2: Noise spectra measured with a horizontally polarized antenna in a borehole in the ARA 2010-2011 testbed.

3.2 Galactic Noise

The two surface antennas (one shown in Figure 3), show an increase in thermal noise at frequencies below 150 MHz. This is consistent with being galactic radio noise, whose sky temperature follows a power law given by $T_{\rm sky} = 800\ {\rm K}({\rm f}/100\ {\rm MHz})^{-2.5}$ where f is the frequency. The surface antenna temperatures are an average of the galactic noise temperatures as seen above and that of the ice below. Since the two surface antennas are low frequency dipoles with axis lying parallel to the surface, their nulls sweep the galactic plane over a period of a day. The galactic plane is at approximately 63° declination at the South Pole. Therefore, if the low frequency noise increase is galactic in origin, we should observe a sidereal variation in total noise power, and this is what is observed in Figure 4 for frequencies below 70 MHz. The phase difference in the sin waves

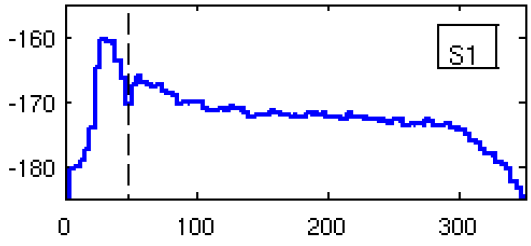

Figure 3: Noise spectra measured with a surface antenna in the ARA 2010-2011 testbed.

from the two antennas is due to an approximately 22° offset in orientation between them.

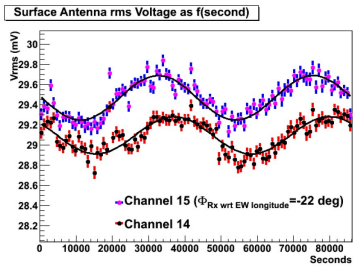

Figure 4: Noise voltage $V_{\rm RMS}$ below 70 MHz as a function of time of day, showing a clear sidereal variation due to the dominance of galactic noise at these frequencies.

3.3 Radio Interference

An important motivation for the testbed was to assess the potential impact of anthropogenic radio noise on ARA data taking. Figure 5 shows the hourly trigger rates during a three month period of ARA testbed data taking. The high rates that occur twice daily until approximately day 65 and once per day after that are due to weather balloon launches, which utilize a ∼400 MHz transponder for data telemetry. These launches result in about 1/2 hour each of event rate saturation, for a total loss of livetime of approximately 5% when the launches occur twice a day. Additionally, incoming and departing aircraft each contribute approximately 20-30 minutes of deadtime. During busy periods with several flights per day, this will contribute an additional 5% or so of deadtime. Other sporadic sources of radio interference have minimal effect on the livetime. The reduction is trigger rates later in the year is due to a migration of trigger thresholds due to decreased temperatures.

3.4 Timing and Event Reconstruction

The local calibration pulsers allow for a continuous monitoring of the trigger functionality as well as a stable reference for timing and signal amplitudes. One of their important functions is to provide a means to determining the

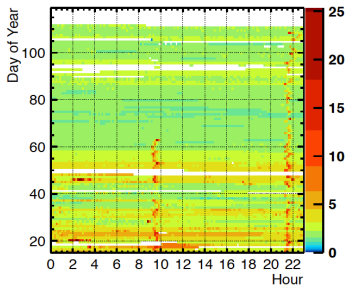

Figure 5: Trigger rates in the ARA testbed by the hour. Top: rates each hour of each day during a three month period in 2011. The regions of white space are times when data transfer from the South Pole was not possible due to bandwidth restrictions.

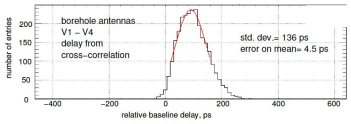

Figure 6: Histogram of delays between pulses received by two different in-ice V-pol antennas. The horizontal offset is arbitrary here.

relative locations of the antennas *in situ* via the relative delays between waveforms at the receivers. Figure 6 shows the relative delay of a pulse between two in-ice V-pol antennas, showing a standard deviation of 136 ps and a standard error of 4.5 ps obtained from a fit to a Gaussian in the peak region. The delays between waveforms were determined by finding the peak of their cross-correlation function. For baselines typically 15 m or more, the angular resolution is of order 0.1° for 136 ps timing error, which is more than adequate for ARA.

For Figure 7, for all of the events on January 29$^{\rm th}$ 2011 we attempted to reconstruct source locations from measured waveforms. Not all timing calibration corrections have yet been implemented. On this day the winds were observed to be high and the South Pole station was open. When a thermal noise fluctuation causes a trigger, the event does not reconstruct to any location because the delays are not causal. RF triggers from the pulser or any RF backgrounds do reconstruct to a particular direction. Figure 6 shows the reconstructed direction of origin relative to the known pulser location for all events that reconstruct on that day. No events were reconstructed beyond the limits shown. Fitting the peak to a Gaussian gives pointing-to-vertex resolutions of 0.27° in ϕ and 0.60° in θ, quite acceptable keeping in mind that the timing calibrations are still in progress and the testbed sits at a shallow depth where there is a light velocity gradient due a depth dependent index of refraction.

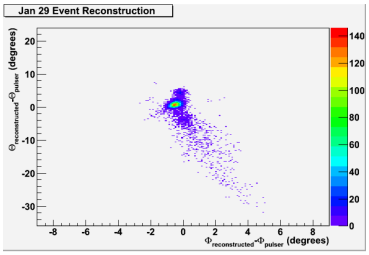

Figure 7: Direction of reconstructed RF signals relative to the known location of the calibration pulser.

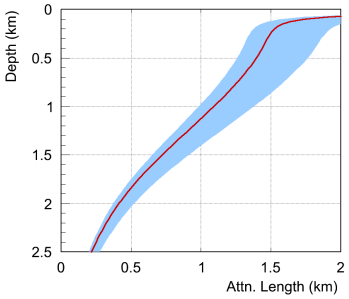

Figure 8: Attenuation length at 300 MHz at all depths in South Pole ice. The normalization of the curve is set by the mean attenuation length measured between the deepest pulser and the testbed antennas.

3.5 Attenuation Lengths

Due to the distance of deep pulsers from the testbed, they provide an opportunity to measure RF loss due to attenuation in the South Pole ice over $\sim$ 3 km. A previous measurement of RF pulses transmitted from the surface and reflected from the bedrock below gave attenuation lengths of order 1 km in the colder ice near the surface [8]. Two of the deep pulsers at intermediate depths $\sim$ 1.5 km completely saturated the amplifiers at the receivers. We therefore used the deepest pulser at 2450 m depth for this measurement.

The Friis formula relates the power transmitted P_t and power received P_r between two antennas (both frequency dependent) $P_r(f) = P_t(f) \cdot G^t \cdot A^r_{\rm eff}/(4\pi r^2) \cdot e^{-2r/L}$ where G_t is the gain of the transmitter, $A^r_{\rm eff}$ is the effective area of the receiver (both absorb antenna coupling efficiencies), $r = 3.14$ km is the distance between the antennas, and L is the field attenuation length.

Due to unexpected difficulties with the high-voltage coupling into the deep pulser transmitters, the received pulse was spread in time over a $\sim$ 20 ns window. However, using lab measurements, we are able to estimate the integrated power in transmission and reception using the observed waveforms in the testbed. Accounting for the antenna responses and beam patterns of the transmitter and receiver, we find an average attenuation length over the transmission distance of $670\ ^{+180}_{-66}$ m. Figure 8 shows the attenuation lengths and systematic uncertainty band as a function of depth, using the models in [16]. In the top 1 km, we find field attenuation lengths that exceed 1 km.

4 Summary

The ARA 2010-2011 testbed station has undergone several months of stable data taking with thermal noise triggers at a rate of a few Hz and deadtime due to RF interference from known sources at approximately 5-10%. The surface antenna see galactic noise at low frequencies, reconstruction has been achieved at the fraction of a degree, and we observe RF field attenuation lengths in the ice of over 1 km in the top km of the ice.

5 Acknowledgements

We are grateful to the National Science Foundation for supporting this research.

References

[1] K. Greisen, Phys. Rev. Lett., 1966, **16**: 748-750.
[2] Zatsepin, G. T. and Kuzmin, V. A., JETP Lett., 1966, **4**: 78-80.
[3] Berezinsky, V. S. and Zatsepin, G. T., Phys. Lett., 1969, **B**(28), 423-424.
[4] Berezinsky, V. S. and Zatsepin, G. T., Sov. J. Nucl. Phys., 1970, **11**: 111.
[5] IceCube, J. Ahrens *et al.*, Astropart. Phys., 2004, **20**: 507.
[6] IceCube, A. Achterberg *et al.*, Astropart. Phys., 2006, **26**: 155.
[7] Antares, O. Kalekin *et al.*, J. Phys. Conf. Ser., 2009, **160**: 012036.
[8] S. Barwick, D. Besson, P. Gorham, D. Saltzberg, J. Glaciol., 2005, **51**: 231.
[9] D. Saltzberg *et al.*, Phys. Rev. Lett. **86**:2802-2805 (2001).
[10] P. W. Gorham, *et al.*, Phys. Rev. D **72**, 023002 (2005).
[11] P. W. Gorham, *et al.*, Phys. Rev. Lett. **99**:171101 (2007).
[12] I. Kravchenko *et al.*, Phys. Rev. D **73**:082002 (2006).
[13] P. W. Gorham *et al.* [The ANITA Collaboration], Phys. Rev. 2010, **D**(82): 022004.
[14] P. Allison *et al.*, Nucl. Instrum. Meth. A **604**, S64 (2009).
[15] P. Allison *et al.*, "Design and Initial Performance of the Askaryan Radio Array Prototype EeV Neutrino Detector at the South Pole," arXiv:1105.2854 [astro-ph.IM].
[16] Price, P.B. *et al.*, "Temperature profile for glacial ice at the South Pole: implications for life in a nearby subglacial lake." Proc. Nat. Acad. Sci. USA, 99(12), 78447847 (2002).

32ND INTERNATIONAL COSMIC RAY CONFERENCE, BEIJING 2011

Estimating the distances of stellar collapses in the galaxy using neutrino bursts

ERNESTO KEMP

(Paper not received. Talk can be download from: http://icrc2011.ihep.ac.cn/paper/proc/content_v4.htm)

Extracting Limits for the Diffuse Non-Electron Neutrino Flux from SNO Data

BRUNO MIGUEZ[1], ERNESTO KEMP[1], ORLANDO L. G. PERES[1,2]
[1] *Instituto de Física "Gleb Wataghin" - Universidade Estadual de Campinas, Campinas-SP, Brasil, 13083-859.*
[2] *The Abdus Salam International Center for Theoretical Physics, I-34100 Trieste, Italy.*
bmiguez@ifi.unicamp.br
DOI: 10.7529/ICRC2011/V04/1310

Abstract: The explosions of all core-collapse supernovae in the past can have originated a diffuse neutrino flux pervading all the universe. The most important factors to weighting this flux are the stellar formation and supernovae occurrence rates. The expected energy spectrum of these neutrinos differ from those from recent supernova mainly by their energy red-shift due the expansion of the universe. These neutrinos have never been observed before. Only upper limits on their fluxes have been reported by the collaborations operating neutrino telescopes. The SNO experiment published an analysis where the total flux of diffuse ν_e has an upper limit of $\phi_e \leq (61-93)\, cm^{-2}.s^{-1}$, depending on a specific supernova model. At the present, the best limit for the diffuse flux of non-electron neutrinos is $\phi_x \leq 10^3 cm^{-2}.s^{-1}$, resulted from an analysis of the Super-Kamiokande data. In this work we have extended the SNO analysis including the elastic scattering on electrons via neutral current interactions to extract information on diffuse flux of the non-electron neutrino flavors (i.e. muon and tau neutrinos). Our analysis yield as limits to non-electron neutrinos flux above to 21 MeV $\phi_x \leq (2.1-17)10^3 cm^{-2}.s^{-1}$ and $\phi_{\overline{x}} \leq (6.5-23)10^3 cm^{-2}.s^{-1}$ as limit to non-electron antineutrinos flux.

Keywords: Supernovae neutrinos, diffuse neutrino background

1 Introduction

The detection of neutrinos from stellar collapses is the only direct source of information from the star's innermost regions. They can yield a lot of astrophysical information like density and temperature profiles of the stellar core, mass and radius of the compact object, total binding energy, time scale of cooling process and characteristics from the particle itself such as electrical charge, mass and number of flavors. However, the low rate of supernovae close enough to the Earth to allow the neutrino detection is an experimental difficulty imposed by the nature of the phenomenon. The only observation made so far is the tens of neutrinos gathered from the SN1987A event [1, 2, 3, 4].

One attempt to bypass this difficulty is the proposal to study the diffuse and steady neutrino flux produced by the neutrinos from all supernovae already exploded in the past, different from a single supernova event, characterized by a neutrino burst. i.e. a transient flux. In the case of the supernovae diffuse neutrino background (SNDB) the expansion of the universe shifts the neutrino spectrum to lower energies imposing an additional difficulty in their detection. Additionally to supernovae and particle physics, the characterization of SNDB have further applications like the possibility to estimate the rates and evolution of stellar formation (including the sub-class of core-collapsing stars), as well as the distribution of mass of core-collapsing stars.

Until now only upper limits for the SNDB were established by diverse collaborations and authors. Today the best limits were obtained by Lunardini and Peres [5] from Super-Kamiokande published data and are close to theoretical predictions within a factor 1-4, suggesting the feasibility of the detection of the SNDB at the present or, more likely, in the next generation of detectors. In this work we present results obtained from the Sudbury Neutrino Observatory - SNO data, by analyzing the neutrino-electron elastic scattering interaction channel $\nu(e^-, e^-)\nu$. In the following we discuss some additional ingredients that must be included in calculations to take into consideration changes in the neutrino spectral characteristics due the neutrino propagation from the source to the detector.

2 The Expected Signal in Detectors

2.1 Diffuse Flux Spectrum

A core-collapse supernova releases $\sim 99\%$ of its binding energy in neutrinos, most of them during the colapsed core cooling phase. The energy spectrum can be aproximately described as a thermal spectrum, given by the equation bellow[1]

1. Other authors suggest a non-thermal behavior with suppression in both low and high tails of the spectrum [6, 7]. In this work we have adopted the thermal approach just by simplicity.

$$\frac{dN_\nu}{dE_\nu} = C\frac{E_\nu^2}{1+e^{\frac{E_\nu}{kT}}} \quad (1)$$

In Eq.1 C is the normalization constant determined by the total energy carried away by neutrinos.

Despite the debates on energy equipartion among different flavors, flux or luminosities normalizations [8], is clear that oscillations leading to interchanges of spectral population among flavors should have impact on the mean energy of the detectable neutrino spectrum. In this work we will consider only the two extreme limits, where i) no oscillations takes place or ii) total permutation $\nu_x \to \nu_e$, where ν_x denotes $(\nu_\mu + \nu_\tau)$ and $\overline{\nu}_x$ their antiparticles. Both cases cover interesting combinations of models of stellar matter density profiles and neutrino oscillations parameters.

The expansion of the Universe reduces the energy of each one of the neutrinos, then reducing the spectral average energy. One neutrino with energy E'_ν produced in the past in a red-shift z is observed today with energy $E_\nu = \frac{E'_\nu}{1+z}$. Thus the energy spectrum that should be observed at the present is given by Eq.1 with E_ν replaced by E'_ν.

Another issue to take into consideration is an aspect linked to stellar evolution. In large time scales the star formation rate, thus the core-collapse supernovae rate $R_{SN}(z)$, are expected to change during the evolution of the Universe. The parametrization we have used in this work is [9]:

$$R_{SN}(z) = \quad R_{SN}(0)(1+z)^\beta \quad z < 1 \quad (2)$$
$$R_{SN}(z) = \quad R_{SN}(z_p)(1+z)^\alpha \quad z > 1 \quad (3)$$

where z_p is a transition *red-shift*, here set in $z_p = 1$.

2.2 Number of Interactions

The differential number density of emmited neutrinos in a supernova with energy between E'_ν and $E'_\nu + dE'_\nu$ in a instant between t e $t + dt$ is [10]:

$$dn_\nu(E'_\nu) = \frac{dN_\nu}{dE'_\nu} R_{SN}(t) dE'_\nu dt \quad (4)$$

We can rewrite Eq.4 changing t by z and adopting the relation between these variables given by the ΛCDM model with conservative parameters.

$$dn_\nu(E_\nu) = \frac{dN_\nu(E'_\nu)}{dE'_\nu} R_{SN}(z) |\frac{dz}{dt}|^{-1}(1+z)dz\, dE_\nu \quad (5)$$

where $\frac{dz}{dt}$ is given by:

$$\frac{dz}{dt} = -H_0(1+z)\sqrt{\Omega_M(1+z)^3 + \Omega_\Lambda} \quad (6)$$

Where $H_0 = 70.4\, km.s^{-1}.Mpc^{-1}$ is the Hubble constant, $\Omega_M = 0.27$ and $\Omega_\Lambda = 0.73$ are respectively the density of dark matter and dark energy in the Universe. Thus, is straightforward to write the expression for the flux of SNDB:

$$\frac{d\Phi_\nu(E_\nu)}{dE_\nu} = \frac{c}{H_0}\int_0^{z_m} \frac{dN_\nu(E'_\nu)}{dE'_\nu} \frac{R_{SN}(z)dz}{\sqrt{\Omega_M(1+z)^3 + \Omega_\Lambda}} \quad (7)$$

To calculate the expected number of interactions in a detector (N_ν), generated by neutrinos of the SNDB with energy between $E_{\nu 1}$ and $E_{\nu 2}$, producing leptons with energy between E_{l1} and E_{l2}, in a given detection channel which the cross section is $(\sigma(E_\nu, E_l))$ and having (N_T) target particles, within an exposure time t_e, and considering the detector efficiency $\epsilon(E_\nu)$, we use:

$$N_\nu = N_T\, t_e \int_{E_{\nu 1}}^{E_{\nu 2}} \int_{E_{l1}}^{E_{l2}} \sigma \times \epsilon \times \frac{d\Phi_\nu}{dE_\nu}\, dE_\nu dE_l \quad (8)$$

3 Limits Estimation

The limit on the flux was calculated using the formalism described above to evaluate the expected number of events in SNO within the exposition time of the published SNO's data [11]. The steps to set the limits for the flux are described in the following.

3.1 Renormalization

We assume to have no prior knowledge on the absolute flux, so we leave the flux normalization constant A as a free parameter, and the flux from Eq.7 was renormalized to the unity, leading to a new function $\Phi_1(E_\nu)$ which determines only the neutrino spectral shape.

$$\frac{d\Phi_\nu}{dE_\nu}(E_\nu) \to A\frac{\frac{d\Phi_\nu}{dE_\nu}(E_\nu)}{\int_{E_1}^{E_2}\frac{d\Phi_\nu}{dE_\nu}(E_\nu)dE_\nu} = A\Phi_1(E_\nu) \quad (9)$$

Now it is possible to rewrite Eq.8, expliciting the constant A:

$$N_\nu = A.N_T.t_e \int_{E_{\nu 1}}^{E_{\nu 2}} \int_{E_{l1}}^{E_{l2}} \beta(E_\nu, E_l)\, dE_\nu dE_l \quad (10)$$

where $\beta = \sigma(E_\nu, E_l) \times \epsilon(E_\nu) \times \Phi_1(E_\nu)$. From Eq.10, for each observed number of interactions in the detector within a time t_e is possible to obtain the proper normalization of the flux A.

3.2 Data Analysis

The experimental SNO observation was the absence of electrons with energy $21 \leq E \leq 35\, MeV$ in the corre-

sponding exposition time. With this result the SNO Collaboration could set the upper limit for the ν_e flux of the SNDB, considering the charged current channel $\nu_e + d \rightarrow e^- + p + p$ and assuming a specific parametrization for the core-collapse neutrino emission [11].

Assuming a Poisson distribution for the number of observed interactions and taking into account that no events were observed ($N_\nu = 0$) we can set the upper limit for the event rate (90% CL):

$$P(0,\lambda) = e^{-\lambda} \Rightarrow \int_0^\lambda e^{-t} dt < 0.9 \Rightarrow \lambda < 2.3 \quad (11)$$

Then, the expectation for the number of interactions consistent with the null result is $E(N_\nu) = \lambda < 2.3$. Since A is a free parameter, then the upper limit for the normalization of the flux can be obtained :

$$A < \frac{2.3}{N_T . t_e \int_{E_{\nu 1}}^{E_{\nu 2}} \int_{E_{l1}}^{E_{l2}} \beta(E_\nu, E_l)\, dE_\nu dE_l} \quad (12)$$

To validate our calculation tools we made a cross-check with the SNO's upper limits in the charged current interaction channel, as shown in the Table 1, where is possible to see the good agreement.

Total Flux Upper Limit ($\nu/cm^{-2}s^{-1}$)			
T_{ν_e} **(MeV)**	SNO Collaboration	This work	Ratio
4	1.1×10^4	1.04×10^4	0.95
6	1.5×10^3	1.45×10^3	0.97
8	6.0×10^2	5.77×10^2	0.96

Table 1: Comparison between the upper limits obtained in this work and in the SNO Collaboration's work [11]. Interaction channel: charged current.

As discussed in Section 2, only extreme cases of neutrino oscillations were analyzed. The most unfavorable scenario which leads to lower event rates, consequently, to higher upper limits, is obtained by considering total permutation $\nu_e \leftrightarrow \nu_x$ or the neutrinospheres having same temperatures ($T_{\nu_x} = T_{\nu_e}$). The opposite case where no oscillation takes place and the relation between the neutrinosphere temperatures is $T_{\nu_x} = 2T_{\nu_e}$ leads to higher event rates and lower limits on the flux. Each case is indicated in the following summary Tables containing the results.

The main goal of this work was achieved considering the $\nu(e^-, e^-)\nu$ elastic scattering channel. Eq.10 was integrated over all neutrino energies that can produce leptons with energy in the observed range ($21 < E_{lep} < 35\,MeV \Rightarrow E_\nu > 21\,MeV$), and using the appropriate cross-section for this interaction. The electron scattering is sensitive to neutrinos from all flavors, but since the SNO's limits are lower, as is possible to be checked from Table1 and by the following discussions, is natural to consider the results from this work as pertaining only to non-electron neutrinos (ν_x). The upper limits to ν_x and $\overline{\nu}_x$ for some typical spectral temperatures are shown in the tables 2 and 3, respectively. These limits are calculated considering only the heavy-water SNO's core as neutrino target.

By using the electron scattering as neutrino interaction channel, is possible to consider not only the D_2O mass, but also to include the 1.7 kton of ultra-pure water as target particles, improving the limit by a factor 2.7. The results for the extended target (heavy-water + ultra-pure water) are shown in the tables 4 and 5, respectively.

Upper limit on ν_x flux (D_2O core) ($\nu/cm^{-2}s^{-1}$)		
T_{ν_e} **(MeV)**	Total permutation $\nu_x \leftrightarrow \nu_e$ or $T_{\nu_e} = T_{\nu_x}$	No oscillation $2T_{\nu_e} = T_{\nu_x}$
4	4.6×10^4	2.7×10^4
6	3.4×10^4	1.9×10^4
8	2.7×10^4	1.4×10^4

Table 2: Upper limits for SNDB ν_x flux. Detector mass: D_2O core. Interaction channel: electron scattering.

Upper limit on $\overline{\nu}_x$ flux (D_2O core) ($\nu/cm^{-2}s^{-1}$)		
$T_{\overline{\nu}_e}$ **(MeV)**	Total permutation $\overline{\nu}_x \leftrightarrow \overline{\nu}_e$ or $T_{\overline{\nu}_e} = T_{\overline{\nu}_x}$	No oscillation $2T_{\overline{\nu}_e} = T_{\overline{\nu}_x}$
4	6.2×10^4	3.5×10^4
6	4.6×10^4	2.4×10^4
8	3.5×10^4	1.8×10^4

Table 3: Upper limits for SNDB $\overline{\nu}_x$ flux. Detector mass: D_2O core. Interaction channel: electron scattering.

Upper limit on ν_x flux ($D_2O + H_2O$) ($\nu/cm^{-2}s^{-1}$)		
T_{ν_e} **(MeV)**	Total permutation $\nu_x \leftrightarrow \nu_e$ or $T_{\nu_e} = T_{\nu_x}$	No oscillation $2T_{\nu_e} = T_{\nu_x}$
4	1.7×10^4	1.0×10^4
6	1.2×10^4	3.5×10^3
8	1.0×10^4	2.1×10^3

Table 4: Upper limits for SNDB ν_x-flux. Detector mass: extended target. Interactions channel: electron scattering

4 Conclusions

We have analyzed published SNO data for the neutrino-electron elastic scattering interaction channel in the energy range $E_\nu > 21\,MeV$ to set limits for the SNDB flux. The analysis was done considering two detector configurations: i) only the heavy-water SNO core; and ii) the so-called extended target configuration, where we have added in the

Upper limit on $\overline{\nu}_x$ flux $(D_2O + H_2O)$ $(\nu/cm^{-2}s^{-1})$		
$T_{\overline{\nu}_e}$ **(MeV)**	Total permutation $\overline{\nu}_x \leftrightarrow \overline{\nu}_e$ or $T_{\overline{\nu}_e} = T_{\overline{\nu}_x}$	No oscillation $2T_{\overline{\nu}_e} = T_{\overline{\nu}_x}$
4	2.3×10^4	1.3×10^4
6	1.7×10^4	8.9×10^3
8	1.3×10^4	6.5×10^3

Table 5: Upper limits for SNDB $\overline{\nu}_x$-flux. Detector mass: extended target. Interactions channel: electron scattering.

calculations the 1.7 kton mass of ultra-pure water of the detector shield.

Considering only the mass of the heavy-water core, we have set the following limits for the SNDB ν_x flux:

$$\Phi(\nu_x) \approx (1.4 - 4.6) \times 10^4 cm^{-2}s^{-1} \quad (13)$$
$$\Phi(\overline{\nu}_x) \approx (1.8 - 6.2) \times 10^4 cm^{-2}s^{-1} \quad (14)$$

Considering the extended target configuration, the limits are:

$$\Phi(\nu_x) \approx (2.1 - 17.0) \times 10^3 cm^{-2}s^{-1} \quad (15)$$
$$\Phi(\overline{\nu}_x) \approx (6.5 - 23.0) \times 10^3 cm^{-2}s^{-1} \quad (16)$$

Even in the extended target analysis we have obtained limits that are one order of magnitude greater than in [5], as can be seen in table 6 and in the plot of Fig. 1. This can be considered quite reasonable and consistent if one compares the difference in mass between the detectors (SK 22.5 kton and SNO 2.7 kton). It is worth to mention that the most stringent experimental limit for the SNDB ν_x flux was obtained by LSD Collaboration [12], which upper value are greater by a factor $\sim 10^3$ to 10^4 when compared to the results of this work (see table 7 and figure 1).

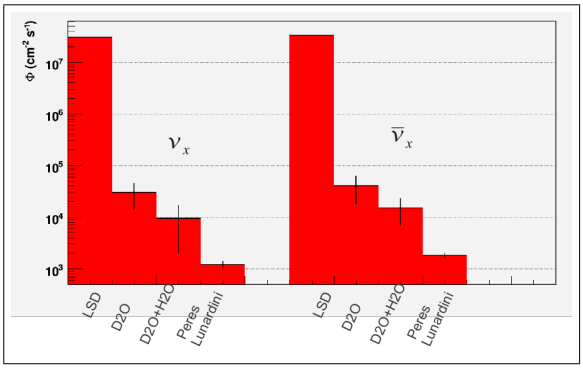

Figure 1: Plot with comparison among different limits for the SNDB flux [12].

In spite of the low flux indicated by current limits, the Super-Kamiokande's limits are greater than some theoretical models by a factor 2 to 5. Thus, the scientific expectations are that some signals from the diffuse flux of neutrinos from past supernovae will be observed soon or the limits should be lowered even more, imposing stronger boundaries in the theoretical models of the physics related to this phenomenon.

ν **Flavor** (E_ν range)	**Flux Limits (90%CL)** $(cm^{-2}s^{-1})$
$\nu_\mu + \nu_\tau \quad (E_\nu > 21MeV)$	$(1.0 - 1.4) \times 10^3$
$\overline{\nu}_\mu + \overline{\nu}_\tau \quad (E_\nu > 21MeV)$	$(1.4 - 1.8) \times 10^3$

Table 6: Best phenomenological limits for the SNDB flux [5].

ν **Flavor** (E_ν range)	**Flux Limits (90%CL)** $(cm^{-2}s^{-1})$
$\nu_e \quad (25 \leq E_\nu \leq 50\,MeV)$	6.8×10^3
$\overline{\nu}_e \quad (20 \leq E_\nu \leq 50\,MeV)$	8.2×10^3
$\nu_\mu + \nu_\tau \quad (20 \leq E_\nu \leq 100\,MeV)$	3.0×10^7
$\overline{\nu}_\mu + \overline{\nu}_\tau \quad (20 \leq E_\nu \leq 100\,MeV)$	3.3×10^7

Table 7: Experimental limits from LSD Collaboration. Adapted from [12].

5 Acknowledgments

This work was supported by the Brazilian agencies Conselho Nacional de Pesquisa e Desenvolvimento - CNPq (National Council for Research and Development) and Fundação de Amparo à Pesquisa do Estado de São Paulo - FAPESP (The São Paulo Research Foundation).

References

[1] Aglietta, M. et al. Europhys. Lett., 1987, **3**, 1315.
[2] Hirata, K., et al., Phys. Rev. Lett., 1987, **58**, 1490.
[3] Bionta, R. M., et al., Phys. Rev. Lett., 1987, **58**, 1494.
[4] Alexeyev, E. N., et al., Pis'ma Zh. Eksp. Teor. Fiz., 1987, **45**, 461[JETPLett., 1987, **45**, 589].
[5] Lunardini, C. and Peres, O. L. G., JCAP, 2008, **8**, 33.
[6] E.S.Myra and A.Burrows, Astrophys.J., 1990, **364**, 222.
[7] Keil, M. T., Raffelt, G. G., and Janka, H.-Thomas, Astrophys.J., 2003, **590**, 971.
[8] Janka, H.-Thomas, Astropart.Phys., 1995, **3**, 377.
[9] Beacom, J. F., and Strigari, L. E., Phys.Rev., 2006, **C73**, 035807.
[10] Ando, S. and Sato, K., New J. Phys., 2004, **6**, 170.
[11] SNO Collaboration, Phys.Rev.Lett., 2001, **87**(7), 071301.
[12] Aglietta, M. et al., Astropart. Phys., 1992, **1**, 1.

32ND INTERNATIONAL COSMIC RAY CONFERENCE, BEIJING 2011

The Askaryan Radio Array

THE ARA COLLABORATION[1]
[1]*See special section in these proceedings.*
kara@umd.edu

Abstract: Ultra high energy cosmogenic neutrinos could be most efficiently detected in dense, radio frequency (RF) transparent media via the Askaryan effect. Building on the expertise gained by RICE, ANITA and IceCube's radio extension in the use of the Askaryan effect in cold Antarctic ice, we are currently developing an antenna array known as ARA (The Askaryan Radio Array) to be installed in boreholes extending 200 m below the surface of the ice near the geographic South Pole. The unprecedented scale of ARA, which will cover a fiducial area of 200 square kilometers, was chosen to ensure the detection of the flux of neutrinos "guaranteed" by the observation of the GZK cutoff by HiRes and the Pierre Auger Observatory. Funding to develop the instrumentation and install the first prototypes has been granted, and the first components of ARA were installed during the austral summer of 2010-2011. Within 3 years of commencing operation, the full ARA will exceed the sensitivity of any other instrument in the 0.1-10 EeV energy range by an order of magnitude. The primary goal of the ARA array is to establish the absolute cosmogenic neutrino flux through a modest number of events. Here we describe the array and the science goals, and describe the current status of the project.

Keywords: ARA, neutrino astrophysics, Askaryan effect, GZK neutrinos

(Paper not received. Talk can be download from: http://icrc2011.ihep.ac.cn/paper/proc/content_v4.htm)

32ND INTERNATIONAL COSMIC RAY CONFERENCE, BEIJING 2011

Ionospheric propagation effects for UHE neutrino detection with the lunar Cherenkov technique

REBECCA MCFADDEN[1,2], RON EKERS[2], JUSTIN BRAY[2,3]
[1]*ASTRON Netherlands Institute for Radio Astronomy, 7991 PD Dwingeloo, The Netherlands*
[2]*CSIRO Astronomy and Space Science, Epping, NSW 1710, Australia*
[3]*Dept. of Physics, School of Chemistry & Physics, Univ. of Adelaide, SA 5005, Australia*
mcfadden@email.astron.nl
DOI: 10.7529/ICRC2011/V04/1322

Abstract: Lunar Cherenkov experiments aim to detect nanosecond pulses of Cherenkov emission produced during UHE cosmic ray or neutrino interactions in the lunar regolith. Pulses from these interactions are dispersed, and therefore reduced in amplitude, during propagation through the Earth's ionosphere. Pulse dispersion must therefore be corrected to maximise the received signal to noise ratio and subsequent chances of detection. The pulse dispersion characteristic may also provide a powerful signature to determine the lunar origin of a pulse and discriminate against pulses of terrestrial radio frequency interference (RFI). This characteristic is parameterised by the instantaneous Total Electron Content (TEC) of the ionosphere and therefore an accurate knowledge of the ionospheric TEC provides an experimental advantage for the detection and identification of lunar Cherenkov pulses. We present a new method to calibrate the dispersive effect of the ionosphere on lunar Cherenkov pulses using lunar Faraday rotation measurements combined with geomagnetic field models.

Keywords: UHE Neutrino Detection, Lunar Cherenkov Technique, Detectors - telescopes, Ionosphere, Lunar Polarisation

The lunar Cherenkov technique [1] uses the moon as a large volume detector for UHE particles interacting in the lunar regolith. This technique was pioneered by Hankins, Ekers and O'Sullivan using the 64-m Parkes radio telescope [2] and is currently being used in experiments by the NuMoon [3, 4], RESUN [5] and LUNASKA [6] collaborations. UHE particles interacting in the Moon's regolith cause cascades of secondary particles which, due to a negative charge excess, produce coherent Cherenkov radiation [7] that may be detected by radio telescopes. The Cherenkov radiation has a broad spectrum which peaks under a few gigahertz with the exact position of the peak determined by de-coherence and/or attenuation effects in the regolith and therefore dependent on shower geometry.

In the time domain this produces a very narrow pulse with no obvious modulation features, however, the pulse is only narrow before propagation as it becomes dispersed by the ionosphere before reaching an earth-based detector. Ionospheric dispersion destroys the coherency of the pulse which reduces the pulse amplitude and subsequent chances of detection. Pulse amplitude may be recovered using dedispersion techniques and this requires an understanding of the dispersion characteristic and current ionospheric conditions.

1 Effects of Ionospheric Dispersion

The ionosphere is a shell of weakly ionized plasma primarily influenced by ultraviolet radiation from the sun. Its Total Electron Content (TEC) is subject to a strong diurnal cycle and is also dependent on the season, the current phase of the 11-year solar cycle and the geometric latitude of observation. The frequency-dependent refractive index of the ionospheric plasma causes a differential additive delay across the bandwidth of a propagating pulse (Equation 1) which results in a loss of coherency and reduction of the received pulse amplitude (Figure 1).

This effect is most dramatic for low frequency experiments such as the NuMoon Westerbork Synthesis Radio Telescope (WSRT) [3] and LOFAR [4] experiments which operate in the 100-200MHz range. The differential delay is given by

$$\Delta t = 0.00134 \times STEC \times (\nu_{\rm lo}^{-2} - \nu_{\rm hi}^{-2}), \qquad (1)$$

where Δt is the duration of the dispersed pulse in seconds, $\nu_{\rm lo}$ and $\nu_{\rm hi}$ are the receiver bandwidth band edges in Hz and $STEC$ is the Slant Total Electron Content in electrons per cm^2 which refers to the total electron content along the line of sight to a particular target object.

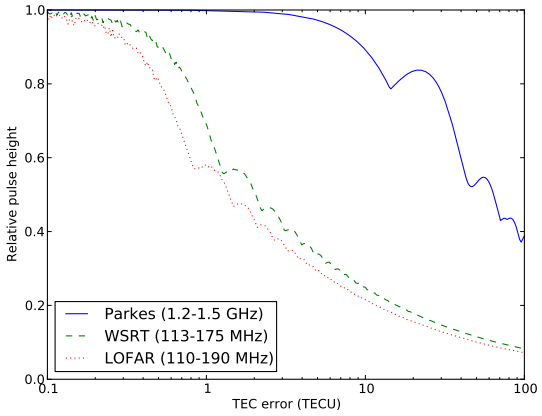

Figure 1: Pulse amplitude loss due to dispersion error for the NuMoon WSRT and LOFAR experiments and the LUNASKA Parkes experiment. This assumes that dispersion was the only mechanism for loss of sensitivity and does not account for other effects such as finite sampling (see [4]) and phase shifts. The Parkes curve assumes downconversion with a high-side local oscillator at 1555 MHz, while the WSRT and LOFAR curves assume direct sampling.

A reduction of the received pulse amplitude not only affects the chances of pulse detection but also the neutrino energy threshold. The amplitude of the pulse at the lunar surface is related to the charge excess in the particle shower. This excess is roughly proportional to the number of particles in the electromagnetic cascade which in turn is proportional to the energy of the shower and the energy of the original neutrino. Therefore as the minimum detectable pulse height is increased, the minimum detectable neutrino energy is also increased.

2 Ionospheric Monitoring

Coherent pulse dedispersion can be used to recover pulse amplitude. This can be implemented via matched filtering techniques and requires an accurate knowledge of the current ionospheric conditions, particularly the instantaneous TEC. Current methods of ionospheric monitoring include using data from Global Positioning System (GPS) satellites and ground-based ionosondes.

TEC Measurements can be derived from dual-frequency GPS signals and are available online from several sources. Until recently these values have not been made available in real time and we have made use of CDDIS TEC data [8] which is sampled at two-hour intervals and published with a few days delay. More recently NASA [9] has made global near real-time TEC maps available at 15-minute intervals and the Australian Bureau of Meterology [10] has done likewise for the Australasia region, although only the latter are also publicly available as data files. Both of these near real-time services produce estimates derived from GPS measurements processed with Kalman filters and combined with the IRI-2007 ionospheric model, which is driven by real-time foF2 observations from IPS ionosondes.

Ionosondes probe the peak transmission frequency (fo) through the F2-layer of the ionosphere which is related to the ionospheric TEC squared. Near real-time TEC measurements can also be derived from foF2 ionosonde measurements and are available hourly from the Australian Bureau of Meteorology [10]. However, there are known inaccuracies in the derivation of the foF2-based TEC estimates as they are empirically derived. Comparison with GPS data shows that the foF2-derived TEC data consistently underestimates GPS TEC measurements (for e.g. Figure 2). This may be attributed to the ground-based ionosondes probing mainly lower ionospheric layers and not properly measuring TEC contribution from the plasmasphere. The error from this effect is estimated to be 1-2 TECU [11] which has a minimal effect on high frequency experiments but for low frequency experiments this corresponds to a reduction in pulse amplitude of almost 60%.

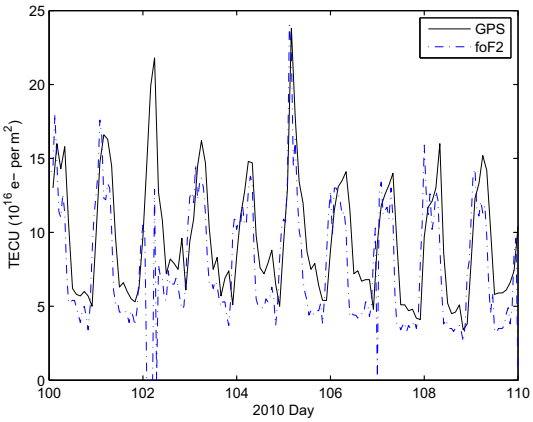

Figure 2: Comparison of VTEC data from dual-frequency GPS and foF2 ionosondes.

Both of the GPS and foF2 TEC products are published as vertical TEC (VTEC) maps which must be converted to STEC estimates to obtain the true total electron content through the slant angle line-of-sight to the Moon. To perform this conversion, the ionosphere can be modeled as a Single Layer Model (SLM) [12] which assumes all free electrons are concentrated in an infinitesimally thin shell and removes the need for integration through the ionosphere. Slant and vertical TEC are related via

$$STEC = F(z)VTEC. \tag{2}$$

where $F(z)$ is a slant angle factor defined as

$$F(z) = \frac{1}{\cos(z')}$$

$$= \frac{1}{\sqrt{1 - \left(\frac{R_e}{R_e+H}\sin(z)\right)^2}}$$

R_e is the radius of the Earth, z is the zenith angle to the source and H is the height of the shell (see Figure 3). The CDDIS also use an SLM ionosphere for GPS interpolation algorithms and assume a mean ionospheric height of 450 km. The slant conversion provides a considerable source of error, however, it is difficult to quantify as it is elevation angle dependent and influenced by horizontal gradients in the ionosphere. Combined with interpolation errors and instrumental biases this error can be as high as 3-10 TECU [11].

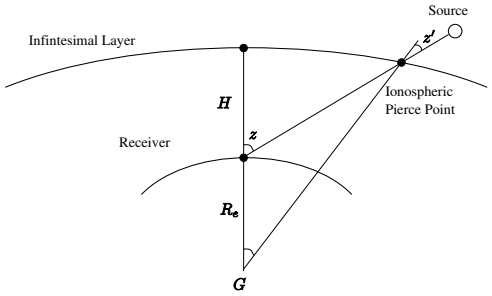

Figure 3: Parameters of the ionospheric Single Layer Model.

3 A New Technique

New methods of ionospheric monitoring are required particularly for the current low-frequency lunar Cherenkov experiments and, as the solar cycle enters a more active phase, accurate pulse dedispersion will become a more important experimental concern at all frequencies.

We have formulated a technique to obtain TEC measurements that are both instantaneous and line-of-sight to the Moon. Ionospheric TEC can be deduced from the Faraday rotation measurements of a polarised source combined with a geomagnetic field model, which are more stable than ionospheric models (IGRF magnetic field values are accurate to better than 0.01% [13]). We propose to use this method with lunar thermal emission as the polarised source which is possible since Brewster angle effects produce a nett polarisation excess in the emission from the lunar limb [14].

Traditional methods of planetary synthesis imaging and polarimetry require a complete set of antenna spacings and enough observing time for earth rotation synthesis. Faraday rotation measurements obtained through synthesis imaging will therefore be averaged over the entire observational period and not contain any information on short-term ionospheric structure. Depending on the chosen experimental strategy, the lunar imaging baseline requirements may also conflict with the unique constraints of a lunar Cherenkov experiment. For UHE particle detection, long antenna spacings may be preferred to minimize the level of lunar noise correlation between antennas or short spacings may be used to minimize the relative geometric delays between antennas. To overcome these limitations we have a developed a method of obtaining lunar Faraday rotation estimates in the visibility domain (i. e. without Fourier inversion to the image plane).

Working in the visibility domain relaxes the array configuration constraints and the need for earth rotation synthesis, allowing measurements to obtained in real time. This technique makes use of the angular symmetry in the polarisation distribution of a planetary object such as the Moon. The intrinsic thermal radiation of a planetary object appears increasingly polarised toward the limb, when viewed from a distant point such as on Earth [14, 15]. The polarised emission is radially aligned and due to the changing angle of the planetary surface toward the limb combined with Brewster angle effects. The angular symmetry of this distribution can be exploited by an interferometer so that an angular spatial filtering technique may be used to obtain real-time position angle measurements directly in the visibility domain. Measured position angles are uniquely related to the corresponding uv angle at the time of the observation and comparison with the expected radial position angles, given the current uv angle of the observation, gives an estimate of the Faraday rotation induced on the Moon's polarised emission. Faraday rotation estimates can be combined with geomagnetic field models to determine the associated ionospheric TEC and subsequently provide a method of calibrating the current atmospheric effects on potential Cherenkov pulses [16].

As a preliminary verification, observations of the Moon were taken using the 22-m telescopes of the Australia Telescope Compact Array with a center frequency of 1384 MHz. Using the angular spatial filtering technique, instantaneous position angle estimates were calculated directly in the visibility domain of the lunar data. Faraday rotation estimates were then obtained by comparing these to the expected uv angles and averaged over small time increments to smooth out noise-like fluctuations. Since the received polarised lunar emission varied in intensity over time, there were nulls during which the obtained position angle information was not meaningful. A threshold was applied to remove position angle measurements taken during these periods of low polarised intensity and baseline averaging was performed as each baseline was affected differently by the nulls. The Faraday rotation estimates were converted to estimates of ionospheric TEC via

$$\Omega = 2.36 \times 10^4 \nu^{-2} \int_{\text{path}} N(s)B(s)\cos(\theta)ds \quad (3)$$

where Ω is the rotation angle in radians, f is the signal frequency in Hz, N is the electron density in m^3, B is the geomagnetic field strength in T, θ is the angle between the direction of propagation and the magnetic field vector and ds is a path element in m.

To evaluate the effectiveness of this technique, the derived TEC estimates were compared against dual-frequency GPS data (Figure 4 *Top*). Slant angle factors were used to convert the GPS VTEC estimates to STEC toward the Moon. Both data sets exhibited a similar general trend, reaching a minimum around the Moon's transit (around 16:00 UT) and rising more rapidly after transit. The steep rise in TEC after transit corresponds to a more active ionosphere at sunrise, as well as an increased path length through the ionosphere as the Moon sets. Before transit, the ionosphere was relatively stable during the night-time hours and it was mainly only the Moon's changing elevation angle which contributed to the changing TEC. The ATCA data underestimated the GPS data, particularly around 14:30–17:00 UT where the STEC estimates may have been influenced by bad data from the shorter baselines (Figure 4 *Bottom*) or due to a TEC contribution from the plasmasphere which is not in the presence of a magnetic field [11]. These observations were taken when the TEC was very low and therefore the relative error in the TEC estimates is large.

4 Conclusions

Accurate dispersion calibration can recover pulse amplitude and increase the chances of pulse detection using the lunar Cherenkov technique. The dispersion effect is frequency dependent and strongest at low frequencies therefore low frequency experiments are the worst affected. However, as the sun enters a more active phase, accurate ionospheric pulse dispersion is becoming a more important experimental concern for lunar Cherenkov experiments at all wavelengths. Several methods of ionospheric monitoring exist including GPS and ionosonde measurements, although these methods include errors which can result in significant loss of pulse amplitude. We have presented a new technique for ionospheric calibration which uses Faraday rotation measurements of the polarised thermal radio emission from the lunar limb combined with geomagnetic field models to obtain estimates of the ionospheric TEC which are both instantaneous and line-of-sight to the Moon. Preliminary comparison to GPS data show that both data sets exhibit similar features which can be attributed to ionospheric events, however, more observations are required to investigate this technique further.

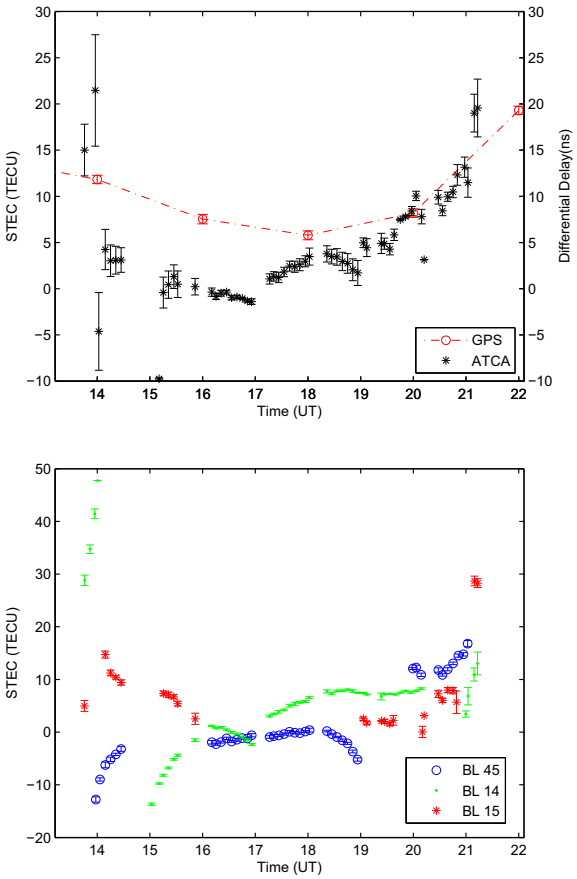

Figure 4: *Top*) Lunar Faraday rotation estimates converted to (*left*) ionospheric TEC values and (*right*) the differential delay across 1.2–1.8 GHz. *Bottom*) TEC values before baseline averaging, for baselines 45 ($61m$), 14 ($107m$) and 15 ($168m$)

References

[1] R. D. Dagkesamanskii, I. M.Zheleznykh, PAZh, 1989, **50**:223
[2] T. H. Hankins, R. D.Ekers, J. D. O'Sullivan, MNRAS, 1996, **283**:1027
[3] S. Ter Veen et. al., Phys. Rev. D, 2010, **82**:103014
[4] K. Singh et. al., submitted 2011
[5] T. R. Jaeger, R. L. Mutel, K. G. Gayley, Astroparticle Physics, 2010, **34**:293-303
[6] C. W. James et. al, MNRAS, **2010**:1425
[7] G. A. Askaryan, Journal of the Physical Society of Japan Supplement, 1962, **17**:C257
[8] http://cddis.nasa.gov/gnss_datasum.html
[9] http://iono.jpl.nasa.gov//latest_rti_global.html
[10] http://www.ips.gov.au/Satellite
[11] C. M. Ho et. al., Radio Science, 1997, **32**:1499-1512
[12] S. Todorova, T. Hobiger, H. Schuh, Advances in Space Research, 2008, **42**:727-736
[13] http://www.geomag.bgs.ac.uk/gifs/igrf.html
[14] C. E. Heiles, F.D. Drake, Icarus, 1963, **2**:281
[15] S. Poppi et. al., American Institute of Physics Conference Series, 2002, **609**:187
[16] R. McFadden, R. Ekers, P. Roberts, Nucl. Instrum. & Methods, 2010, In press

HE.2.4: Theory and calculations

Acceleration of Cosmic Rays in a System of Rotating Stars

KWANG-HUA CHU[1]
[1]*School of Mathematics, Physics, and Biological Engineering, Inner Mongolia University of Science and Technology, Baotou 014010, P.R. China*
qitaichu09@gmail.com
DOI: 10.7529/ICRC2011/V04/0005

Abstract: We theoretically illustrate that the possible acceleration of cosmic rays passing through a kind of amplification channel induced by a system of rotating stars. Our analysis is based on the discrete kinetic model (considering Uehling-Uhlenbeck collision term) which has been used to study the propagation of plane (e.g., acoustic) waves in a system of rotating gases.

Keywords: Kinetic approach, wave amplification

1 Introduction

Cosmic rays : Radiation that enhances with altitude in the atmosphere were discovered by V F Hess in 1912, and it was clear by the early 1930s that this radiation comes from outer space. The all-particle energy spectrum of primary cosmic rays extends from 1 GeV (10^{12} eV) to above 10^{20} eV (100 EeV), the highest energies of known individual particles in the universe [1-3]. The highest-energy particles are so rare that they are detectable only by means of the giant cascades or extensive air showers they create in the atmosphere. Details of how these extensive air showers are observed and of how the parameters of importance are measured can be found in [3]. In spite of many efforts, we have still only a limited understanding of, where these particles are coming from, how they are accelerated to such extremely high energies, how they propagate through interstellar space [2].

The astrophysical environments that are able to accelerate particles up to such high energies, including active galactic nuclei, large scale galactic wind termination shocks, relativistic jets and hot-spots of Fanaroff-Riley radio galaxies, pulsars, magnetars, quasar remnants, starbursts, colliding galaxies, and gamma ray burst fireballs were discussed in [1]. Many researchers believed that cosmic rays are accelerated in a process called diffusive shock acceleration. Suitable astrophysical shocks occur in supernova explosions, and ionized nuclei gain energy as they are repeatedly overtaken by the expanding shock wave. Such mechanisms lead in fact to a power-law spectrum with a maximum energy of about $Z \times 10^{15}$ eV (Z : atomic number), which roughly agrees with the observed steepening (though the theoretically predicted spectrum proves to be steeper than actually observed) [2].

In this short paper, the discrete Uehling-Uhlenbeck equations [4] together with the model of free orientations (θs, the relative direction of scattering of particles w.r.t. to the normal of the propagating plane-wave front) are solved to study the diverse dispersion relations of plane waves in system of rotating stars (or disk-like gases). Anomalous amplification channels could occur for diffusion modes of propagating plane-wave fronts. We propose that the acceleration of cosmic rays passing through this kind of channel might happen.

2 Theoretical Formulations

We make the following assumptions before we investigate the general equations of our model :

(1) Consider a system of rotating stars (or disks) or a gas of identical particles of unit mass and a shape of a disk of diameter d, then each particle (or star) i, $i = 1, \cdots, N$, is characterized by the position of its center q_i and its velocity u_i. We also have the geometric limitations : $|q_i - q_j| \geq d$, $i \neq j$.

(2) Each particle (or star) moves in the plane with velocity belonging to a discrete set $\mathcal{V}$ of 4 velocities with only one speed in the plane. The velocity modulus c is a reference speed depending on the reference frame and specific distribution of particles. c is normally linked to the internal energy of the molecules in thermodynamic equilibrium.

(3) The collisional mechanism is that of rigid spheres, that is, the particles (or stars) scatter elastically and they change their phase states instantaneously, preserving momentum. Only binary collisions are considered, since a multiple collision here is a negligible events.

The collisions between two particles (or stars, say i and j)

take place when they are located at q_i and $q_j = q_i - d\mathbf{n}$, where $\mathbf{n}$ is the unit vector joining their centers. After collisions the particles scatter, preserving momentum, in the directions allowed by the discrete set $\mathcal{V}$. In other words, particles change according to

$$(q_i, u_i) \to (q_i, u_i^*), \qquad (q_j, u_j) \to (q_j, u_j^*).$$

The collision is uniquely determined if the incoming velocity and the impact angle ψ, $\psi \in [-\pi/2,\pi/2]$, are known, which is defined as the angle between u_i and $\mathbf{n}$ or $\mathbf{n}(\psi) = (\cos[\psi+(k-1)\pi/2], \sin[\psi+(k-1)\pi/2])$, $k = 1, \cdots, 4$ ($k = 4$ means during binary encounter there are, in general, two incoming velocities and two departing velocities). From the selected velocities we have two classes of encounters, i.e. (a) $\langle u_i, u_j\rangle = 0$ and (b) $\langle u_i, u_j\rangle = -c^2$, respectively.

(a). In the first class momentum conservation implies only : encounters at $\pi/2$ with exchange of velocities

$$u_i = u^k \to u_i^* = u^{k+1}, \qquad u_j = u^{k+1} \to u_j^* = u^k,$$

in the case $\psi \in [-\pi/2, 0]$, and

$$u_i = u^k \to u_i^* = u^{k+3}, \qquad u_j = u^{k+3} \to u_j^* = u^k,$$

in the case $\psi \in [0, \pi/2]$.

(b) Similarly, $\langle u_i, u_j\rangle = -c^2$;

(i) Head-on encounters with impact angle $\psi = 0$ such that

$$u_i = u^k \to u_i^* = u^{k+2}, \qquad u_j = u^{k+2} \to u_j^* = u^k,$$

(ii) Head-on encounters with impact angle $\psi \neq 0$ such that if $\psi \in [-\pi/2)0]$:

$$u_i = u^k \to u_i^* = u^{k+1}, \qquad u_j = u^{k+2} \to u_j^* = u^{k+3},$$

or if $\psi \in [0, \pi/2]$:

$$u_i = u^k \to u_i^* = u^{k+3}, \qquad u_j = u^{k+2} \to u_j^* = u^{k+1}.$$

For grazing collisions, that is $\langle \mathbf{n}, u_i\rangle = \langle \mathbf{n}, u_j\rangle = 0$, we put $u_i^* = u_i$, $u_j^* = u_j$. Schematic presentation is illustrated in Fig 1. $\mathbf{M}$ and $\mathbf{M}_1$ are the associated angular momenta which have opposite sign.

With general collision rules, we assume that the system of hard-disk gas (star) is composed of identical particles (stars) of the same mass. The velocities of these particles are restricted to, e.g., : $\mathbf{U}_1, \mathbf{U}_2, \cdots, \mathbf{U}_p$, p is a finite positive integer. The discrete number density of particles (or stars) are denoted by $N_i(\mathbf{x}, t)$ associated with the velocity $\mathbf{U}_i$ at point $\mathbf{x}$ and time t. If only nonlinear binary collisions are considered, and considering the evolution of N_i ($i = 1, \cdots, p$), we have

$$\frac{\partial N_i}{\partial t} + \mathbf{u}_i \cdot \nabla N_i = \sum_{j,k,l} A_{kl}^{ij} [N_k N_l (1+\sigma N_i)(1+\sigma N_j) - N_i N_j (1+\sigma N_k)(1+\sigma N_l)] N_i N_j), \qquad (1)$$

where (k, l) are admissible sets of collisions, $i \in \Lambda = \{1, \cdots, p\}$, and the summation is taken over all $j, k, l \in \Lambda$, where A_{kl}^{ij} are nonnegative constants satisfying $A_{kl}^{ji} = A_{kl}^{ij} = A_{lk}^{ij}$: indistinguishability of the particles in collision, $A_{kl}^{ij}(\mathbf{u}_i + \mathbf{u}_j - \mathbf{u}_k - \mathbf{u}_l) = 0$: conservation of momentum in the collision, $A_{kl}^{ij} = A_{ij}^{kl}$: microreversibility condition. Here, σ is a Pauli blocking parameter [4], and, for $\sigma < 0$ (normally, $\sigma = -1$) we can obtain a gas of Fermi-Dirac particles (or stars); for $\sigma > 0$ (normally, $\sigma = 1$) we obtain a gas of Bose-Einstein particles (or stars), and for $\sigma = 0$, we obtain a gas of Boltzmann particles (or stars). The conditions defined for the discrete velocity above requires that elastic, binary collisions, such that momentum and energy are preserved.

Considering binary (two-disk encounter each time) collision only, with $\sigma = 0$, the equation of discrete kinetic models proposed in [4] is a system of $2n(= p)$ semilinear partial differential equations of the hyperbolic type : ($i = 1, \cdots, 2n$,)

$$\frac{\partial}{\partial t} N_i + \mathbf{U}_i \cdot \frac{\partial}{\partial \mathbf{x}} N_i = \frac{2cS}{n} \sum_{j=1}^{n} N_j N_{j+n} - N_i N_{i+n}, \quad (2)$$

where $N_i = N_{i+2n}$ are unknown functions, and $\mathbf{U}_i$ $=c(\cos[\theta + (i-1)\pi/n], \sin[\theta + (i-1)\pi/n])$; c is a reference velocity modulus, S is an effective collision cross-section for the 2-(rotating)disk system, θ is the free orientation parameter (the orientation starting from the positive x-axis to the U_1 direction and is relevant to the (net) induced scattering measured relative to the sound-propagating direction) which might be linked to the external field or the angular momentum or the rotation effects.

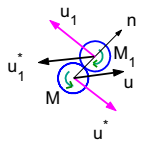

Figure 1: Schematic plot for a collision. $\mathbf{M}$ and $\mathbf{M}_1$ are the associated angular momenta which have opposite sign.

Since passage of the plane (e.g., acoustic) wave causes a small departure from equilibrium (Maxwellian type) resulting in energy loss owing to internal friction and heat conduction, we linearize above equations around a uniform Maxwellian state (N_0) by setting $N_i(t, x) = N_0\ (1 + P_i(t, x))$, where P_i is a small perturbation. (Maxwellian is referred to an equilibrium state here)

Firstly, we have, (say, i=m)

$$\frac{\partial P_m}{\partial t} + \mathbf{U}_m \cdot \frac{\partial P_m}{\partial \mathbf{x}} + 2cSN_0[(P_m + P_{m+n}) = \frac{cSN_0}{n} \sum_{k=1}^{2n} [(P_k + P_{k+n}], \qquad (3)$$

here, $m = 1, \cdots, 2n$. The linearized version of above equation is (set $f_p = 2cSN_0$)

$$\frac{\partial P_m}{\partial t} + \mathbf{U}_m \cdot \frac{\partial P_m}{\partial \mathbf{x}} + f_p(P_m + P_{m+n}) = \frac{f_p}{n} \sum_{k=1}^{2n} P_k. \quad (4)$$

In these equations after replacing the index m with $m + n$ and using the identities $P_{m+2n} = P_m$, then we have

$$\frac{\partial P_{m+n}}{\partial t} - \mathbf{U}_m \cdot \frac{\partial P_{m+n}}{\partial \mathbf{x}} + f_p(P_m + P_{m+n}) = \frac{f_p}{n} \sum_{k=1}^{2n} P_k. \quad (5)$$

Combining above two equations, firstly adding then subtracting, with $A_m = (P_m + P_{m+n})/2$ and $B_m = (P_m - P_{m+n})/2$, we can have ($m = 1, \cdots, 2n$)

$$\frac{\partial A_m}{\partial t} - c\,\cos[\theta + \frac{(m-1)\pi}{n}]\frac{\partial B_m}{\partial x} + 2\,f_p A_m = \frac{2\,f_p}{n} \sum_{k=1}^{2n} A_k, \quad (6)$$

$$\frac{\partial B_m}{\partial t} + c\,\cos[\theta + \frac{(m-1)\pi}{n}]\frac{\partial A_m}{\partial x} = 0. \quad (7)$$

Note that terms of $\partial P_m/\partial y = 0$ as P_m only varies along the wave propagating direction : x-axis direction. From $P_{m+2n} = P_m$, and with $A_m = (P_m + P_{m+n})/2$ and $B_m = (P_m - P_{m+n})/2$, we can have $A_{m+n} = A_m$, $B_{m+n} = -B_m$.

After some manipulations we then have

$$\left(\frac{\partial^2}{\partial t^2} + c^2\cos^2\left[\theta + \frac{(m-1)\pi}{n}\right]\frac{\partial^2}{\partial x^2} + 4cSN_0\frac{\partial}{\partial t}\right) D_m = \frac{4cSN_0}{n} \sum_{k=1}^{n} \frac{\partial}{\partial t} D_k, \quad (8)$$

where $D_m = (P_m + P_{m+n})/2$, $m = 1, \cdots, n$, since $D_1 = D_m$ for $1 = m$ (mod $2n$).

Now we are ready to look for the solutions in the form of plane wave $D_m = a_m \exp[i(kx - \omega t)]$, $(m = 1, \cdots, n)$, with $\omega = \omega(k)$. This could be related to the dispersion relations of 1D forced plane-wave (e.g., ultrasound) propagation (of dilute monatomic hard-sphere gases) problem. So we have

$$\left(1 + ih - 2\lambda^2\cos^2\left[\theta + \frac{(m-1)\pi}{n}\right]\right) a_m - \frac{ih}{n} \sum_{k=1}^{n} a_k = 0, \quad (9)$$

where $\lambda = kc/(\sqrt{2}\omega)$, $h = 4cSN_0/\omega \propto 1/\mathrm{K}_n$ is the rarefaction parameter of the gas; K_n is the Knudsen number which is defined as the ratio of the mean free path of hard-disk gases to the wave length of the plane (e.g., acoustic) wave (here $m = 1, \cdots, n$).

Let $a_m = \mathcal{C}/(1 + ih - 2\lambda^2\cos^2[\theta + (m-1)\pi/n])$, where $\mathcal{C}$ is an arbitrary, unknown constant, since we here only have interest in the eigenvalues of above relation. The eigenvalue problems for different $2 \times n$-velocity model reduces to $F_n(\lambda) = 0$, or

$$1 - \frac{ih}{n} \sum_{m=1}^{n} \frac{1}{1 + ih - 2\lambda^2\cos^2\left[\theta + \frac{(m-1)\pi}{n}\right]} = 0. \quad (10)$$

We solve $n = 2$ case, i.e., 4-velocity case. The admissible collision : $(1, 3) \longleftrightarrow (2, 4)$ for system of rotating disks during binary encounter is shown schematically in Fig. 2. The corresponding eigenvalue equations become algebraic polynomial-form with the complex roots being the results of λs.

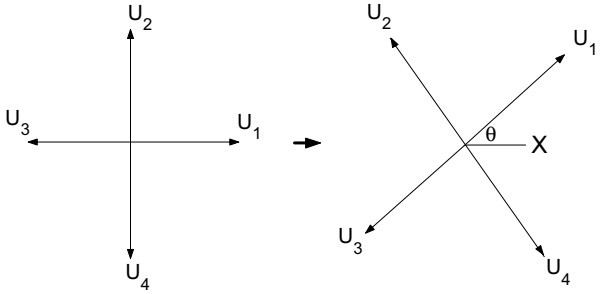

Figure 2: Schematic plot for the regular scattering and the orientational scattering. Plane waves propagate along the X-direction. Binary encounters of U_1 and U_3 and their departures after head-on collisions (U_2 and U_4). Number densities N_i are associated to U_i. θ is the free orientation parameter (the orientation starting from the positive x-axis to the U_1 direction and is relevant to the (net) induced scattering measured relative to the plane wave-propagating direction) which might be linked to the external field or the angular momentum or the rotation effects.

3 Numerical Results and Discussion

Using the mathematical or numerical software, e.g. Mathematica or Matlab, and after intensive validations, we can obtain the complex roots ($\lambda = \lambda_r + \mathrm{i}\,\lambda_i$) for the polynomial equations above. The roots are the values for the nondimensionalized dispersion (positive real part) and the attenuation or absorption (positive imaginary part), respectively. We plot those of $\theta = 0$ into Fig. 3. Curves of branch I

follows the conventional dispersion relation of plane-wave (e.g., ultrasound) propagation in dilute monatomic hard-sphere gases [5]. We remind the readers that θ is relevant to the external field or the angular momentum or the rotation effects and possible effects of $\theta \neq 0$ could be traced in [3]. Curves of branch II, however, show a entirely different trend. The dispersion part seems to follow the diffusion mode reported in [5]. It increases but never reaches to a limit. The anomalous attenuation or amplification might be due to, if any, the intrinsic resonance (an eigen-oscillation) or the implicit behavior of angular momentum relation during 2-(rotating)disk (or star) encounter (each with opposite-sign rotating direction or angular momenta so that the total (net) angular momenta for this two-body encounter is zero) since the latter is absent or of no need in the formulation of 2-body collisions. We note that the direction of the rotational axis of each disk (or star) (ready to encounter) for the collision of 2-(rotating)disk system might be in opposite sign instead of the same sign. We don't know yet at present whether the former or the latter can favor the anomalous attenuation or amplification?

We noticed that some researchers argue that there must be some source of free energy to drive the growth. Meanwhile as argues in [6], the rotational energy of a young pulsar with period P that remains after the supernova explosion is estimated to be $2 \times 10^{50}(10 \text{ ms}/P)^2$ erg. It is an additional energy reservoir for particle acceleration (note that for the energy in a source capable of accelerating particles to 10^{20} eV, considering the energy in the magnetic field (< 0.1 G) : $\gg 10^{57}$ ergs [3]) and in particular it could be the source of very high energy electron-positron pairs. However, the cosmic ray passing through this plane-wave(e.g., acoustic)-amplified channel might be accelerated (neutrinos included)! In fact it was remarked in [7] : *Cosmic rays must be involved in the general Galaxy rotation* $\cdots$. Finally the results presented in Fig. 3 shows that the possible acceleration (due to amplification) is proportional to $h(\propto c\,S\,N_0)$ which is also proportional to Z (a nucleus charge number, considering the effective scattering cross-section S). The latter matches qualitatively with [8] : The PAO data strongly favor the nuclei composition getting progressively heavier at energy $\simeq (4 - 40)$ EeV.

Acknowledgements. The only author is partially supported by 2011-IMUST Starting Funds for Scientific Researcher.

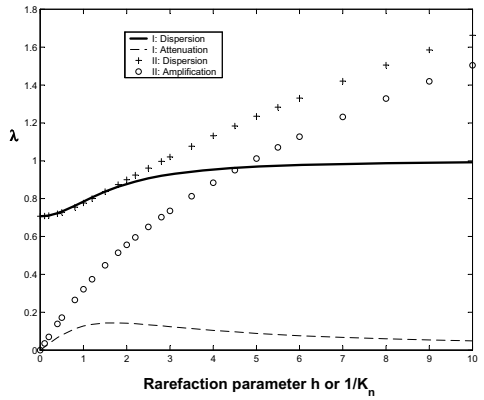

Figure 3: Dispersion relations of branches I and II over a range of h (rarefaction measure). λ_r : phase speed dispersion, λ_i : attenuation or amplification. $\lambda = \lambda_r +$ i λ_i. $\theta = 0$ here. Branch II (diffusion mode) shows anomalous amplification.

References

[1] D.F. Torres, L.A. Anchordoqui, Rep. Prog. Phys., 2004, **67**(9): 1663-1730.

[2] A. Haungs, H. Rebel, M. Roth, Rep. Prog. Phys., 2003, **66**(7): 1145-1206.

[3] M. Nagano, A.A. Watson, Rev. Mod. Phys., 2000, **72**(3): 689-732.

[4] A. K.-H. Chu, Phys. Rev. D, 2005, **71**(10): 103003.
A. K.-H. Chu, Int. J. Mod. Phys. A, 2008, **23**(31): 5081.
A. K.-H. Chu, Int. J. Theor. Phys., 2005, **44**(9): 1429.

[5] R.J. Mason Jr., 1965, Rarefied Gas Dynamics, edited by J.H. de Leeuw, Academic Press, New York, Vol. 1, p. 48.

[6] F. Aharonian, A. Bykov, E. Parizot, V. Ptuskin, A. Watson, arXiv: 1105.0131 (Space Sci. Rev.).

[7] V.I. Ginzburg, V.S. Ptuskin, Rev. Mod. Phys., 1976, **48**(2): 161.

[8] J. Abraham, *et al.* (PAO Collaboration) Phys. Rev. Lett., 2010, **104**(9): 091101. [arXiv: 0906.2319]

Transition Radiation as a Tool for Identification of Primary Cosmic Rays

Kalpana Roy Sinha[1] and Pranayee Datta[2]
[1]Assam Engineering Institute, Guwahati-781003, Assam, India.
[2]Dept. of Electronics and Communication Technology, Gauhati University, Guwahati-781014, Assam, India
kroysinha@yahoo.co.in, pranayee.datta@gmail.com DOI: 10.7529/ICRC2011/V04/0010

Abstract: Production mechanism for radio emission (RE) from extensive air shower (EAS) in the frequency range 10 MHz-200MHz is established to be geosynchrotron mechanism with good Monte Carlo codes and solid experimental verifications. Several groups are being engaged in extensive studies of RE for frequency >10MHz associated with EAS, Extensive Ice Showers (EIS), and Lunar Regolith Showers (LRS). But the region of frequencies <10MHz, although having high potential as source of valuable information because of observation of very high fields in the past, much less attention is being paid. The most promising mechanism for this region is the Transition Radiation (TR) mechanism. When the EAS particles hit the air-ground interface, the EIS particles hit the ice-air interface and the LRS particles hit the LR-vacuum interface, TR is emitted.

As TR is a phenomenon completely different from the mechanisms considered so far for EAS, EIS and LRS by the ongoing project groups, modifications of the existing set up in the light of this mechanism would be beneficial, as this would make possible to observe the same original event from two different approaches.

This paper presents several characteristics of EAS and LRS for different primary particles on the basis of TR mechanism. RE model in the framework of TR is found to exhibit significant characteristics for different primary particles with respect to frequency, shower-size and zenith angle variation. Hence TR mechanism can be utilized as a tool for radio detection of primary particles and ongoing projects may incorporate radio channels for <10 MHz to widen the scope of radio detection of high energy particles.

1 Introduction

Detection of radio emission (RE) from Extensive Air Showers (EAS) initiated by Cosmic Rays (CR) (of primary energy Ep~1016 eV) by Jelley et al. in 1965[1] opened a new era of cosmic ray studies, with most interest centering on the radio detection of high energy particles. Theoretical as well as experimental aspects of the whole spectrum of the radiation from ~50 kHz to ~550 MHz (for mean energy of 1016 eV) have been studied extensively by different groups all over the globe[3][4] in a period of almost five decades since 1965. Production mechanism for RE from EAS is now well established to be geosynchrotron radiation in the frequency band >10MHz [5] and Transition Radiation for <10MHz [2]. From the last quarter of the 20th century, some laboratories are being engaged in detection and investigation of Giant Air Showers (GAS) with Ep > 1019 eV.

Amongst a number of aims of CR studies, identification of primary particle is of utmost importance of current studies. This paper presents several characteristics of RE from EAS and Lunar Regolith Showers (LRS) for different primary particles on the basis of TR mechanism.

2 Method

For a vertical air shower (zenith angle φ=0), the magnitude of the vertical component of the field due to TR is

$$\vec{E}_{aV} = \frac{\in Ne\eta_a \mathrm{k}^2}{2\pi^2 \nu\zeta}\cos^2\theta \qquad (1)$$

Similarly for a vertical LRS (φ=0) the magnitude of the vertical component of the field due to TR is

$$\vec{E}_{lV} = \frac{\in Ne\eta_v \mathrm{k}^2}{2\pi^2 \nu\zeta}\cos^2\theta \qquad (2)$$

Where N = total number of shower particles at the boundary surface,

$\in$ Ne = Excess negative charge,

$$k = \frac{\omega}{c} = \frac{2\pi\nu}{c} = \text{wave number},$$

$$\lambda_{a/v}^2 = \frac{\omega^2}{c^2}\chi_{a/v} - k^2 \quad ; \quad \chi_{a/v} = \in_{a/v}\ \mu_{a/v}$$

$$\lambda_{g/l}^2 = \frac{\omega^2}{c^2}\chi_{g/l} - k^2 \quad ; \quad \chi_{g/l} = \in_{g/l}\ \mu_{g/l}$$

$\in_{a/v}$, $\in_{g/l}$ are dielectric constant of air/vacuum and ground/lunar regolith respectively,

μ_a, μ_g are permeability of air/vacuum air and ground/lunar regolith ground respectively,

$$\eta_{a/v} = \frac{\in_{g/l} / \in_{a/v} - (v/\omega)\lambda_{g/l}}{k^2 - \chi_{a/v}\omega^2/c^2} + \frac{-1 + (v/\omega)\lambda_{g/l}}{k^2 - \chi_{g/l}\omega^2/c^2}$$

$$\zeta = \lambda_{g/l} \in_{a/v} + \lambda_{a/v} \in_{g/l}$$

a stands for air, *v* for vacuum, *l* for lunar regolith and *g* for ground.

$$\tan\theta = Z/R$$

Z = height of the antenna above the ground (earth/lunar)
R = distance of the antenna from the shower axis.

For inclined showers, the variation of field strength with zenith angle is obtained as[2]:

$$\vec{E}_v = \frac{\delta}{a} - 0.1\phi \qquad 20\text{m} \le R \le 50\text{m} \qquad (5)$$

$$\vec{E}_v = \frac{\delta}{b} - 0.1\phi \qquad 50\text{m} \le R \le 90\text{m} \qquad (6)$$

where,
$\delta = (\varepsilon N e \eta_{a/v} k^2/\pi^2 \nu\zeta)\cos^2\theta$;

$a = 3\times10^{-7}N + 1.702$
$b = 4\times10^{-7}N - 2.36$

3 Results:

For different primary particles (P, He, O, Fe and γ) shower size at 872gm cm^{-2} (AUGER level) are obtained from the works of [6,7]. Frequency spectra of vertical component of field strength for GAS are presented in Fig1 and Fig2 for different particles and energies with shower size obtained from ref [6] & [7] respectively.

The variation of field strength with zenith angle for different radial distance of GAS are obtained and shown in Fig 3.

Fig.4 and Fig.5 show the frequency spectra and the variation of field strength with zenith angle for neutrino initiated LRS.

Discussion and conclusion:

Each characteristic of RE adopting TR model (Fig 1,2,3) is found to exhibit distinguishable variations for different primary particles of EAS, viz. P, Fe, O, He, and γ-particle under investigation. Fig 4 and Fig 5 give different characteristics of RE for LRS initiated by ν only. For such characteristics of LRS initiated by cosmic ray particles, theoretical investigations are going on.

As TR is a phenomenon completely different from the mechanisms considered so far for EAS, EIS and LRS by the ongoing project groups, modifications of the existing set up to incorporate an additional radio channel in the light of this mechanism would be beneficial, as this would make possible to observe the same original primary particle from two different backgrounds on the basis of production mechanisms, viz., geosynchrotron & TR (for EAS), Radio Cherenkov Radiation (RCR) & TR (for EIS and LRS).

In view of the above, it is concluded that–

- TR mechanism can be utilized as a tool, in the VLF-LF-MF band, for identification of primary CR.
- On-going projects of EAS & LRS may incorporate radio channels for <10 MHz to widen the scope of radio detection of high energy particles.

4 References:

- J. V. Jelley et al., Nature, 205, p 327-328 (1965).
- K.R. Sinha, Ph.D Thesis, Gauhati University, Guwahati, India, (2010).
- P. Datta et al., RADHEP 2000, UCLA, California, p 98, (2001).
- Beresnyak A. R et al., Astronomy Reports, 49, arXiv:astro-ph/9811011, 127-133, (2005).
- Falcke. H., Detection of Radio Emission from UHECR, Proc. of 30th Interna-tional Cosmic Ray Conference,Merida, Mexico, 6, p 79-93, 2007.
- M. Ambrosio et al., Astroparticle Physics 24, 355-371(2005).
- C. Song for the HiRes Collaboration, Proc 27th ICRC 2, 490-493, (2001)

Fig 1. Frequency spectrum for GAS

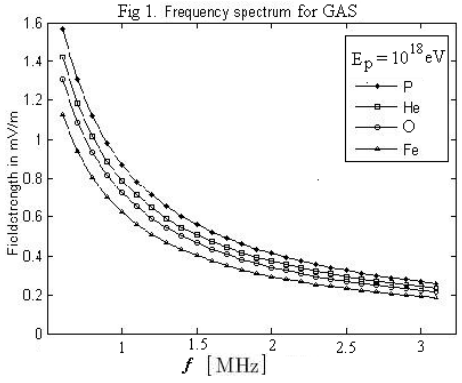

Fig 2. Frequency spectra for GAS

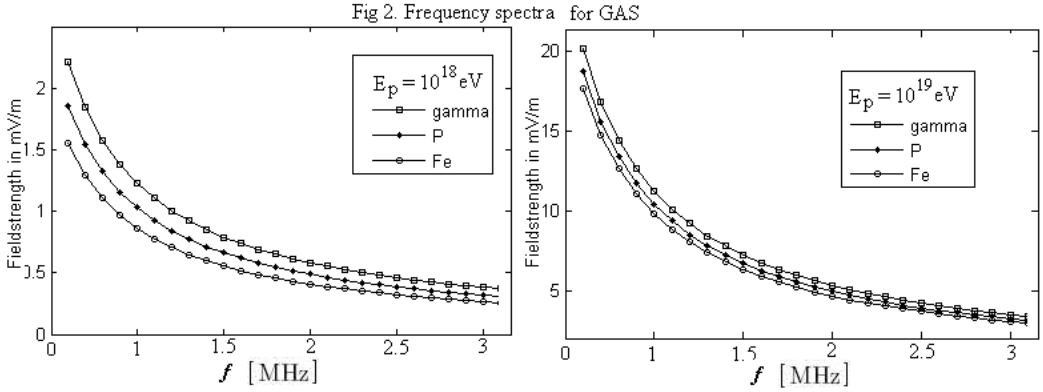

Fig 3. Zenith angle vs field strength for GAS

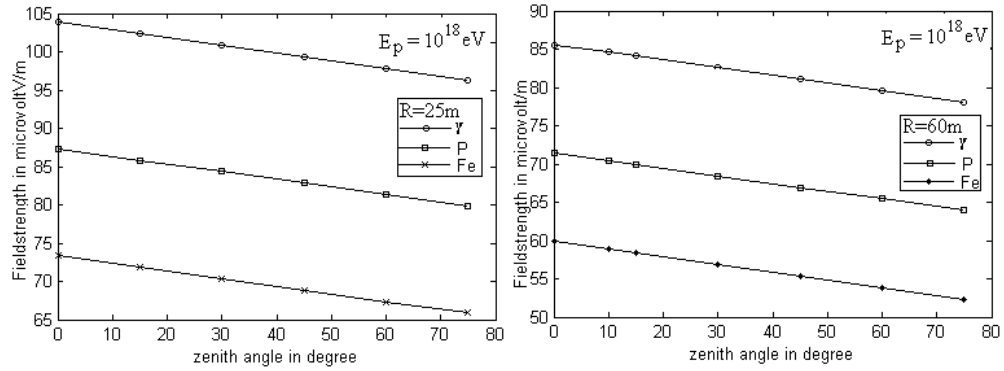

Fig 4. Frequency spectra for LRS

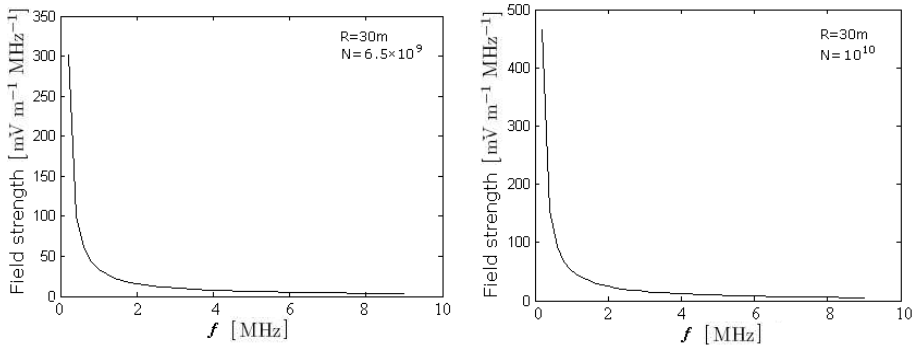

Fig 5.Zenith angle vs field strength for LRS

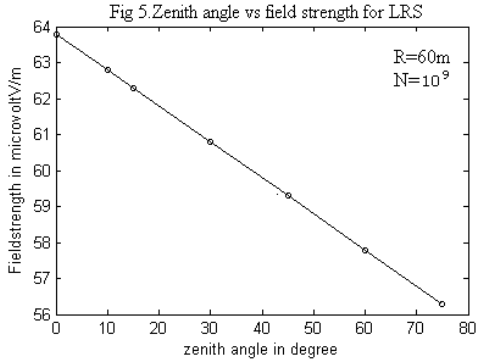

32ND INTERNATIONAL COSMIC RAY CONFERENCE, BEIJING 2011

A simplified model for photohadronic interactions and their application to Active Galactic Nuclei and Gamma Ray Bursts

FELIX SPANIER[1], SVENJA HÜMMER[1], WALTER WINTER[1]
[1] *Institut für Theoretische Physik und Astrophysik, Universität Würzburg*
fspanier@astro.uni-wuerzburg.de
DOI: 10.7529/ICRC2011/V04/0029

Abstract: Up to now the radiation mechanism in Active Galactic Nuclei and Gamma-ray Bursts is not fully understood. A leptonic or hadronic origin is discussed. With the recent progress in the detection of VHE emission from AGN through MAGIC, H.E.S.S. and FERMI a large sample to test emission models is available. One major problem in testing hadronic emission models so far was the lack of a fast method for the computation of photo-hadronic interactions. We present a scheme derived from first principles to calculate the products of photo-hadronic interaction. The possible applications to Active Galactic Nuclei and Gamma-Ray bursts are discussed.

Keywords:

1 Introduction

In the past decade the search for extragalactic very-high energy γ-ray emitters has been booming. With the current generation of Imaging Air-Cerenkov Telescopes and the newest gamma-ray satellite Fermi it has been possible to identify more than 40 extragalactic sources of gamma-rays above 100 GeV. It is especially interesting to find sources at very high redshift due to the increased sensitivity. With this new data available a long standing question has to be raised again: Is the origin of Active Galactic Nuclei radiation leptonic or hadronic?

The leptonic emission model, usually the SSC model using electrons as the source of synchrotron radiation and target for Compton scattering with the very same synchrotron radiation, was very successful in explaining nearby high-peak BL Lac objects. The hadronic model, which is assuming a nonthermal proton population producing charged and neutral pions in photo-hadronic interactions, has been on the market for even longer time, but was rarely used due to its complexity.

The observations of FSRQs suggest that those sources require a hadronic component to explain their spectra (cf. [6]). It is therefore inevitable to provide new numerical models for hadronic emission. One major demand is the ability to model also variable sources. This has been a major problem with the Monte Carlo based models like SOPHIA [1], which are too slow to produce lightcurves in short time. One way to circumvent this problem is to introduce parametrization of the photo-hadronic interaction, as it has been done e.g. by [2]. This parametrization is still based on the Monte Carlo model used in SOPHIA and therefore only allows for physical processes described in the Monte Carlo code. A major problem in this specific approach is that intermediate unstable particles have been integrated out.

As the cooling of these intermediate particles may play an important role especially in sources with a high magnetic field, we are going to follow a different approach for the calculation of photo-hadronic products. From first physics principles an interaction model is derived. A major advantage is the possibility to include new data easily. Intermediate particles are included explicitly.

2 The model

The model we are proposing should fulfill a number of requirements:

- It should yield a detailed prediction for π^+, π^-, and π^0 fluxes separately
- It should be fast enough to be used in time-dependent calculations
- It should include particle physics properties in a transparent way
- It should not be limited to specific proton and photon distributions
- It should yield secondary populations
- It should include the Kaons.

2.1 Basic principles of particle interaction

Two processes are involved in the description of our model: Weak decays like $\pi^+ \to \mu^+ + \nu_\mu$ and the photo-hadronic interaction itself. The decay of particle a into species b is described by the production rate $Q_b(E_b)$, which is given by

$$Q_b(E_b) = \sum_{\rm IT} \int dE_a \, N_a(E_a) \, \Gamma^{\rm IT}_{a\to b}(E_a) \, \frac{dn^{\rm IT}_{a\to b}}{dE_b}(E_a, E_b) \, . \tag{1}$$

where $N_a(E_a)$ is the differential spectrum of parent particles and $\Gamma^{\rm IT}_{a\to b}$ is the interaction or decay rate for the process $a \to b$ as a function of energy E_a. As a number of different processes may be involved they are designated with "IT".

The function $dn^{\rm IT}_{a\to b}/dE_b(E_a, E_b)$ describes the distribution of daughter particles of type b per final state energy interval dE_b. This function can be non-trivial. It contains the kinematics of the decay process, *i.e.*, the energy distribution of the discussed daughter particle. If more than one daughter particle of the same species b is produced, or less than one (in average) because of other branchings, the function has to yield the "multiplicity" of daughter particles per event as a function of energy.

In meson photoproduction, a similar mechanism can be used. The interaction rate Eq. (1) can be interpreted in terms of the incident protons because of the much higher energies in the shock rest frame (SRF). In this case, the interaction rate depends on the interaction partner, the photon, as

$$\begin{aligned} \Gamma^{\rm IT}_{p\,\gamma\to p'\,b}(E_p) \quad &= \quad \int d\varepsilon \int_{-1}^{+1} \frac{d\cos\theta_{p\gamma}}{2} \, (1-\cos\theta_{p\gamma}) \times \\ &\quad \times n_\gamma(\varepsilon, \cos\theta_{p\gamma}) \, \sigma^{\rm IT}(\epsilon_r) \, . \end{aligned} \tag{2}$$

Here $n_\gamma(\varepsilon, \cos\theta_{p\gamma})$ is the photon density as a function of photon energy ε and the angle between the photon and proton momenta $\theta_{p\gamma}$, $\sigma^{\rm IT}(\epsilon_r)$ is the photon production cross section and $\epsilon_r = E_p\varepsilon/m_p(1-\cos_{p\gamma})$ is the photon energy in the nucleon/parent rest frame (PRF) in the limit $\beta_p \approx 1$. The interaction itself, and therefore E_p and ε, is described in the SRF. The daughter particles b are typically π^+, π^-, π^0, or kaons. If intermediate resonances are produced, we integrate them out so that only pions (kaons) and protons or neutrons remain as the final states.

We will assume isotropy $n_\gamma(\varepsilon, \cos\theta_{p\gamma}) \simeq n_\gamma(\varepsilon)$ for the photon distribution. Arbitrary angular distributions would require additional integrations. For isotropic photon distributions the integral over $\cos\theta_{p\gamma}$ can be replaced by one over ϵ_r, we have

$$\Gamma^{\rm IT}_{p\,\gamma\to p'\,b}(E_p) = \frac{1}{2}\frac{m_p^2}{E_p^2} \int_{\frac{\epsilon_{\rm th} m_p}{2E_p}}^{\infty} d\varepsilon \frac{n_\gamma(\varepsilon)}{\varepsilon^2} \int_{\epsilon_{\rm th}}^{2E_p\varepsilon/m_p} d\epsilon_r \, \epsilon_r \, \sigma^{\rm IT}(\epsilon_r) \tag{3}$$

In general, the function $dn^{\rm IT}_{a\to b}/dE_b(E_a, E_b)$ in Eq. (1) is a non-trivial function of E_a and E_b. For photo-meson production in the SRF, the energy of the target photons is typically much smaller than the incident nucleon energy. In this case,

$$\frac{dn^{\rm IT}_{a\to b}}{dE_b}(E_a, E_b) \simeq \delta(E_b - \chi^{\rm IT}_{a\to b} \, E_a) \cdot M^{\rm IT}_b \, . \tag{4}$$

The function $\chi^{\rm IT}_{a\to b}$, which depends on the kinematics of the process, describes what (mean) fraction of the parent energy is deposited in the daughter species. The function $M^{\rm IT}_b$ describes the multiplicity. For our purposes, it will typically be a constant number which depends on interaction type and species b.

Using Eqs. (4) and (3) we find for the photoproduction of pions:

$$Q_b(E_b) = \int_{E_b}^{\infty} \frac{dE_p}{E_p} \, N_p(E_p) \int_{\frac{\epsilon_{\rm th} m_p}{2E_p}}^{\infty} d\varepsilon \, n_\gamma(\varepsilon) \, R_b(x,y) \tag{5}$$

with

$$x \equiv \frac{E_b}{E_p} \, , \quad y \equiv \frac{E_p \, \varepsilon}{m_p} \, , \tag{6}$$

and the "response function"

$$\begin{aligned} R_b(x,y) \quad &\equiv \quad \sum_{\rm IT} R^{\rm IT}(x,y) \\ &\equiv \quad \sum_{\rm IT} \frac{1}{2y^2} \int_{\epsilon_{\rm th}}^{2y} d\epsilon_r \, \epsilon_r \, \sigma^{\rm IT}(\epsilon_r) \\ &\qquad M^{\rm IT}_b(\epsilon_r) \, \delta\left(x - \chi^{\rm IT}(\epsilon_r)\right) \, . \end{aligned} \tag{7}$$

$\epsilon_{\rm th} \lesssim 2y = 2E_p\varepsilon/m_p \lesssim 10^4\,{\rm GeV}$ corresponds to the maximal available center of mass energy, and the $\chi^{\rm IT}$ is the fraction of proton energy deposited in the secondary. Note that $\chi^{\rm IT}(\epsilon_r)$ and $M_b(\epsilon_r)$ are typically functions of ϵ_r, if they only depend on the center of mass energy of the interaction.

For a known response function the secondary spectra may readily be calculated using Eq. (5) for **arbitrary** injection and photon spectra. This is so far similar to [2], but as intermediate particles are retained the resulting function $R(x,y)$ is much simpler. In Fig. 1 we show the cross section as a function of ϵ_r for these interaction types separately, where the baryon resonances have been summed up. Naively, one would just choose the dominating contributions in the respective energy ranges in order to obtain a good approximation for $\sigma^{\rm IT}(\epsilon_r)$. However, the different contributions have different characteristics, such as different π^+ to π^- ratios in the final states, and therefore different neutrino-antineutrino ratios.

2.2 Summary of processes

In summary, we consider the following processes:

Δ-resonance region The dominant resonance process is the $\Delta(1232)$-resonance (at $\epsilon_r = 340\,{\rm MeV}$):

$$p + \gamma \overset{\Delta(1232)}{\to} p' + \pi \, . \tag{8}$$

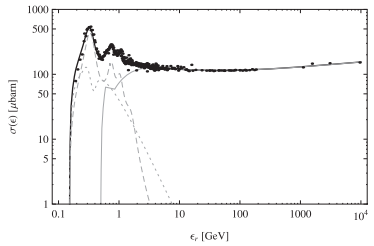

Figure 1: The total $p\gamma$ photo-meson cross section as a function of the photon's energy in the proton rest frame ϵ_r analog to [3] (1μbarn = 10^{-30} cm^2; data, shown as dots, from [4])). The contributions of baryon resonances (dashed), the direct channel (dotted) and multi-pion production (brown) are shown separately.

This process produces neutral (for $p' = p$) or charged (for $p' \neq p$) pions.

Higher resonances The most important higher resonance contribution is the decay chain

$$\gamma + p \overset{\Delta,N}{\rightarrow} \Delta' + \pi\,, \quad \Delta' \rightarrow p' + \pi' \qquad (9)$$

via Δ- and N-resonances. Other contributions, we consider, come from the decay chain

$$\gamma + p \overset{\Delta,N}{\rightarrow} \rho + p'\,, \quad \rho \rightarrow \pi + \pi'\,. \qquad (10)$$

Direct production The same interactions as in Eq. (8) or Eq. (9) can also take place in the t-channel. This mechanism is also called "direct production", because the properties of the pion are already determined at the nucleon vertex.

Multi-pion production At high energies the dominant channel is statistical multi-pion production leading to two or more pions. In SOPHIA [3] this process is described by the QCD-fragmentation of color strings.

The effect of kaon decays is usually small. However, kaon decays may have interesting consequences for the neutrino flavor ratios at very high energies, in particular. Therefore, we consider the leading mode: K^+ production (for protons in the initial state) with the decay channel leading to highest energy neutrinos.

In Fig. 1 we show the total $p\gamma$ photo-meson cross section as a function of ϵ_r, analogously to [3]. In order to fully describe Eq. (7) for each interaction type, we need the kinematics, entering $\chi^{\rm IT}$, the multiplicities $M_b^{\rm IT}$, and the cross section $\sigma^{\rm IT}$.

2.3 Factorized response function

The general expression for the response function eq. 7 may be simplified to avoid computing two integrals. To achieve this $\chi^{\rm IT}(\epsilon_r)$ and $M_b^{\rm IT}(\epsilon_r)$ are assumed to be approximately

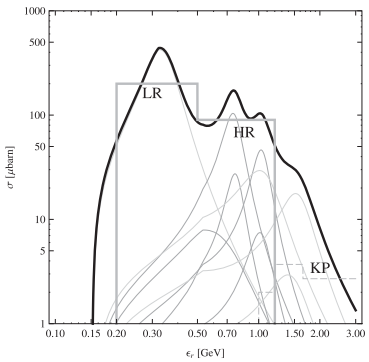

Figure 2: Cross section for the resonances as a function of ϵ_r. Light gray resonances are Δ-resonances, dark gray resonances are N-resonances. The total resonance cross section is shown as thick curve. The simplified model is depicted by the gray boxes. The dashed curve refers to our simplified cross section for kaon production "KP".

constant with respect to ϵ_r. Then it is possible to factorize the response function

$$R^{\rm IT}(x,y) \;=\; \delta(x-\chi^{\rm IT})\, M_b^{\rm IT}\, f^{\rm IT}(y) \text{with}$$
$$f^{\rm IT}(y) \equiv \frac{1}{2y^2}\int_{\epsilon_{\rm th}}^{2y} d\epsilon_r\, \epsilon_r\, \sigma^{\rm IT}(\epsilon_r)\,. \qquad (11)$$

The delta-function describes the energy of the secondary particle and $M_b^{\rm IT}$ is the production rate. It is now relatively easy to evaluate Eq. (5) with Eq. (11):

$$Q_b^{\rm IT} = N_p \left(\frac{E_b}{\chi^{\rm IT}}\right) \frac{m_p}{E_b} \int_{\epsilon_{\rm th}/2}^{\infty} dy\, n_\gamma \left(\frac{m_p\, y\, \chi^{\rm IT}}{E_b}\right)\, M_b^{\rm IT}\, f^{\rm IT}(y)\,. \qquad (12)$$

The simplicity of this scheme is astonishing, with only a single integral the production rate can be readily computed. For the factorization different approaches are possible, the fastest but still sufficiently accurate model is described here (see [5] for more detailed models).

The cross section can be divided into two classes of resonances: The first peak is dominated by the $\Delta(1232)$-resonance (lower resonance – LR), whereas the higher resonances (HR) contribute at larger energies. In addition, the kinematics and the multiplicities are very different.

For the resonances, we define two interaction types LR and HR, as shown in Fig. 2 (boxes). The interaction type LR corresponds to $\Delta_1(1232)$, whereas the interaction type HR contains the higher resonances. The properties of these interaction types are summarized in [5]. The spectra for pions are then calculated fromEq. (12) with a specific set of functions (details also in [5]).

Besides the resonances also the direct production has to be evaluated. Here the same technique applies, but it has to be taken into account that kinematics plays an important role. Therefore the delta-approximation is not a sufficient

approximation, so a broader distribution function is used. Additionally the direct production is split into 3 different one pion interactions and 4 different two pion interactions. A detailed table is shown in [5].

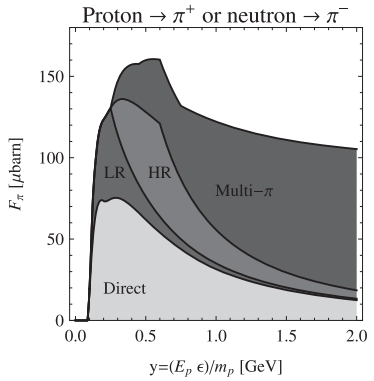

Figure 3: The function $F_\pi(y) \equiv \sum_{\rm IT} M_\pi^{\rm IT}\, f^{\rm IT}(y)$ for charged pion production.

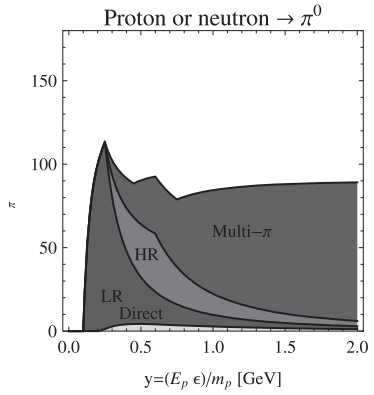

Figure 4: The function $F_\pi(y) \equiv \sum_{\rm IT} M_\pi^{\rm IT}\, f^{\rm IT}(y)$ for neutral pion production.

3 Application to Active Galactic Nuclei

We used our simplified model in a benchmark case which resembles the situation in Active Galactic nuclei. This benchmark is adopted from [1]. The photon spectrum is given by a broken powerlaw with a spectral index -1.6 between 10^{-3} eV and 140 eV and an index of -1.8 between 140 eV and 3600 eV. The proton spectrum is given by powerlaw with index of 2.6 with an exponential cutoff at $2.4 \cdot 10^9$ GeV.

In Fig. 6 the resulting pion and kaon production rates are shown. Additionally the neutrino ratios have been calculated (shown in Fig. 6). A deviation from the SOPHIA code is visible. This can be easily explained by taking into account the spin state of the final muon, which is seemingly not done in SOPHIA.

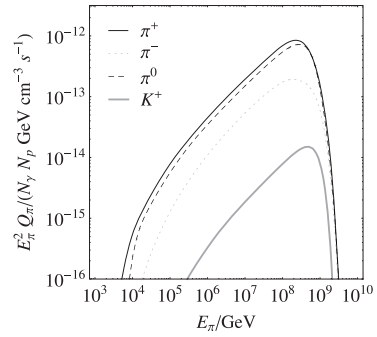

Figure 5: Comparison among the π^+ (upper curve), π^0 (middle curve), and π^- (lower curve) spectra for the AGN benchmark. The grey curve shows in addition the K^+ spectrum. Computed with model Sim-B.

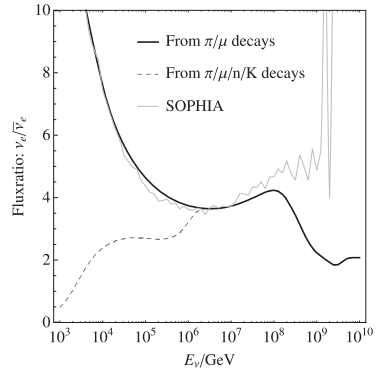

Figure 6: Ratio neutrinos and anti-neutrinos for the AGN benchmark. Also plotted is the result of the SOPHIA code.

4 Conclusion

We presented a simplified model which accounts for the effect of photo-meson production in sources like Active Galactic Nuclei and Gamma-Ray Bursts. The model is much more precise than simple resonance models and much faster than well-known Monte Carlo models.

References

[1] Mücke, A. and Protheroe, R. J., Astropart. Phys., 2001, **15**, 121-136
[2] Kelner, S. R. and Aharonian, F. A. Phys. Rev., 2008, **D78**, 034013
[3] Mücke, A. et al. Comput. Phys. Commun., 2000, **124**, 290-314
[4] Amsler, C. et al. (Particle Data Group), Phys. Lett., 2008, **B667**,1
[5] Hümmer, S. et al., Astrop. J., 2010, **721**, 630-652
[6] Weidinger, M. and Spanier, F., Proceedings of the ICRC, 2011, **submitted**

32ND INTERNATIONAL COSMIC RAY CONFERENCE, BEIJING 2011

High-energy spectrum and zenith-angle distribution of atmospheric neutrinos

S. I. SINEGOVSKY[1], O. N. PETROVA[1], T. S. SINEGOVSKAYA[2]
[1]*Irkutsk State University, Irkutsk, 664003, Russia*
[2]*Irkutsk State Railway University, Irkutsk, 664046, Russia*
sinegovsky@api.isu.ru
DOI: 10.7529/ICRC2011/V04/0487

Abstract: High-energy neutrinos, arising from decays of mesons produced through the collisions of cosmic ray particles with air nuclei, form the background in the astrophysical neutrino detection problem. An ambiguity in high-energy behavior of pion and especially kaon production cross sections for nucleon-nucleus collisions may affect essentially the calculated neutrino flux. We present results of the calculation of the energy spectrum and zenith-angle distribution of the muon and electron atmospheric neutrinos in the energy range 10 GeV to 10 PeV. The calculation was performed with usage of known hadronic models (QGSJET-II, SIBYLL 2.1, Kimel & Mokhov) for two of the primary spectrum parametrizations, by Gaisser & Honda, and by Zatsepin & Sokolskaya. The comparison of zenith angle-averaged muon neutrino spectrum with the measurement data in IceCube experiment make it clear that even at energies above 100 TeV the prompt neutrino contribution is not so apparent because of tangled uncertainties of the strange (kaons) and charm (D-mesons) particle production cross sections. An analytic description of calculated neutrino fluxes is presented.

Keywords: atmospheric neutrinos, high-energy hadronic interactions

1 Introduction

Atmospheric neutrinos (AN) appear in decays of mesons (charged pions, kaons etc.) produced through collisions of high-energy cosmic rays with air nuclei. The AN flux in the wide energy range remains the issue of the great interest since the low energy AN flux is a research matter in the neutrino oscillations studies, and the high energy atmospheric neutrino flux is now appearing as the background noise for astrophysical neutrino experiments [1, 2, 3, 4, 5, 6, 7].

In spite of numerous AN flux calculations are made (for example [8, 9, 10, 11, 12, 13, 14, 15], see also [16, 17] for a review of 1D and 3D calculations of the AN flux) there are questions concerning to the flux uncertainties originated from hadronic interaction models as well as from uncertainties in primary cosmic ray spectra and composition in the "knee" region.

In this work we present results of the atmospheric neutrino flux calculation in the range 10–10^7 GeV made with use of the hadronic models QGSJET-II 03 [18], SIBYLL 2.1 [19] as well as the model by Kimel & Mokhov (KM) [20] that were tested also in recent atmospheric muon flux calculations [21, 22]. We compute here the differential energy spectrum of the conventional neutrinos averaged over zenith angles to compare with the data of the Frejus [1], AMANDA-II [4] and IceCube [5] experiments.

2 Calculations vs. the experiment

The calculation is performed on the basis of the method [23] of solution of the hadronic cascade equations in the atmosphere, which takes into account non-scaling behavior of inclusive particle production cross-sections, the rise of total inelastic hadron-nuclei cross-sections, and the non-power law primary spectrum (see also [15, 21, 22]). Along with major sources of the muon neutrinos, $\pi_{\mu 2}$ and $K_{\mu 2}$ decays, we consider three-particle semileptonic decays, $K^{\pm}_{\mu 3}$, $K^{0}_{\mu 3}$, the contribution originated from decay chains $K \to \pi \to \nu_\mu$ ($K^0_S \to \pi^+\pi^-$, $K^{\pm} \to \pi^{\pm}\pi^0$), as well as small fraction from the muon decays. One can neglect the 3D effects in calculations of the atmospheric muon neutrino flux near vertical at energies $E \gtrsim 1$ GeV and at $E \gtrsim 5$ GeV in case of directions close to horizontal (see [13, 14]). As the primary cosmic ray spectra and composition in wide energy range we use the model recently proposed by Zatsepin & Sokolskaya (ZS) [24], which fits well the ATIC-2 experiment data [25] and supposedly to be valid up to 100 PeV. The ZS proton spectrum at $E \gtrsim 10^6$ GeV is compatible with KASCADE data [26] as well the helium one within the range of the KASCADE spectrum obtained with the usage of QGSJET 01 and SIBYLL models. Alternatively in the energy range $10 - 10^6$ GeV we use the parameterization by Gaisser, Honda, Lipari and Stanev (GH) [17], the version with the high fit to the helium data. Note this version is consistent with the data of the KAS-

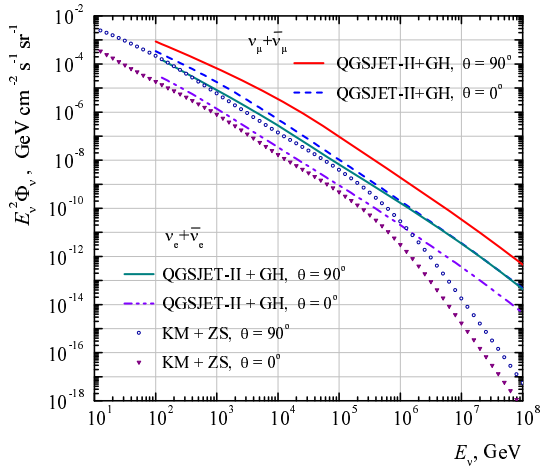

Figure 1: Spectra of the conventional muon and electron neutrinos calculated for vertical and horizontal directions.

CADE experiment at $E_0 > 10^6$ GeV that was obtained (through the EAS simulations) with the SIBYLL 2.1.

Figures 1, 2 display the scale of difference between the conventional $(\nu_\mu + \bar\nu_\mu)$ spectra and $(\nu_e + \bar\nu_e)$ one, calculated with usage of QGSJET-II, SIBYLL and KM model for GH and ZS primary spectra. The difference of neutrino flux predictions related to choice of hadronic models is clearly apparent.

Zenith-angle distributions of the conventional neutrinos, $\phi_{\nu_\mu}(E,\theta)/\phi_{\nu_\mu}(E,0°)$, for the energy range 1-10^5 TeV are shown in Fig. 3. Calculations are made with QGSJET-II and SiBYLL 2.1 models both for GH and ZS (ATIC-2) primary spectra and composition. As was expected, a shape of the angle distribution visibly depends on the neutrino energy (at $E < 100$ TeV) especially for directions close to horizontal. The effect of the hadronic models (as well as

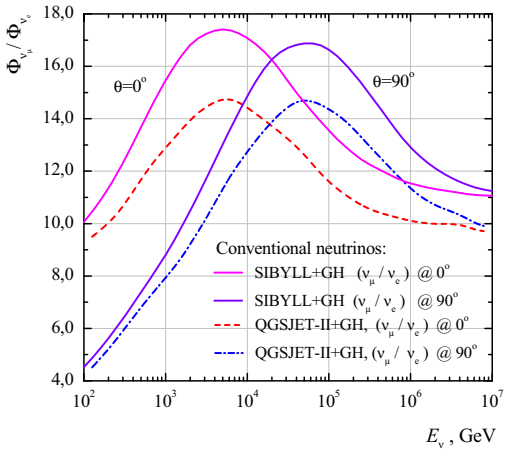

Figure 2: Conventional neutrino flavor ratios calculated with SIBYLL and QGSJET-II hadronic models for the GH primary spectrum.

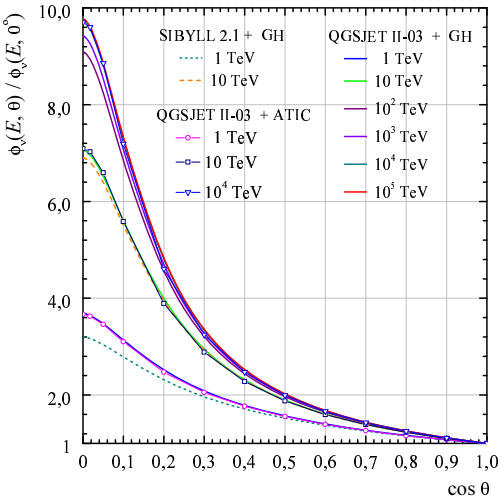

Figure 3: Zenith-angle enhancement of the $(\nu_\mu + \bar\nu_\mu)$ flux.

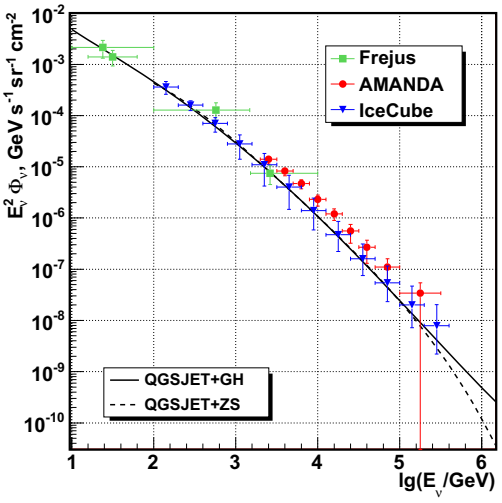

Figure 4: Conventional $(\nu_\mu + \bar\nu_\mu)$ spectrum averaged over zenith angles. Curves: the calculation with usage of QGSJET-II. Symbols: data of experiments, Frejus [1], AMANDA-II [4], IceCube [5].

of the primary spectrum) on the angle distribution is rather weak, while the spectra differences amount to 80% [15].

The calculation of the conventional $(\nu_\mu + \bar\nu_\mu)$ flux averaged over zenith angles as compared with Frejus [1] (squares), AMANDA-II [4] (circles), and IceCube [5] (triangles) measurement data is shown in Figs. 4, 5. Figure 4 displays the conventional $(\nu_\mu + \bar\nu_\mu)$ spectrum (averaged over zenith angles in the range $0° - 84°$) calculated with usage of QGSJET-II model for GH primary spectra and composition (solid line) as well as for ZS one (dashed). The difference in neutrino flux predictions resulted from the primary cosmic ray spectra becomes apparent at high neutrino energies: the flux obtained with QGSJET-II for GH

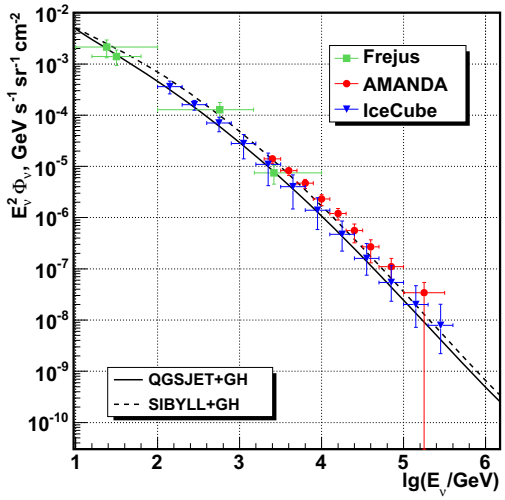

Figure 5: Comparison of the $(\nu_\mu + \bar{\nu}_\mu)$ spectrum calculations with QGSJET-II and SIBYLL 2.1

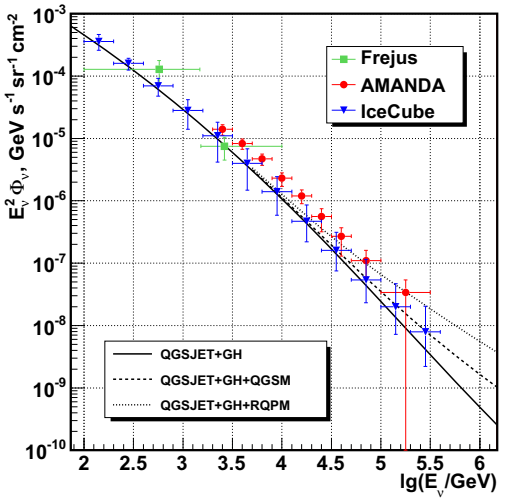

Figure 6: Flux of the conventional and prompt muon neutrinos (case of GH spectrum).

spectrum at 600 TeV is nearly twice as large as that for ZS spectrum. At 1 PeV this discrepancy increases to the factor about five. Comparison of QGSJET-II and SIBYLL presented in Fig. 5 shows that the former seems more preferable to desribe the IceCube measurements at the energies below 40 TeV (conventional neutrinos).

The usage of QGSJET-II and SIBYLL models leads to apparent difference in the neutrino flux, as well as in the case of SIBYLL as compared to KM (unlike the muon flux, where SIBYLL and KM lead to very similar results [21]). On the contrary, the QGSJET-II neutrino flux is very close to the KM one: up to 100 TeV the difference does not exceed 5% for the GH spectrum and 10% for the ZS one at $\theta = 0°$. Note that the muon flux discrepancy in QGSJET-II and KM predictions is about 30% at vertical [21].

Figure 6 shows the sum of the conventional flux (calculated for GH spectrum with usage of QGSJET-II) and prompt muon neutrino flux predictions [27] (see also [11, 16, 28]) due to nonperturbative models, the recombination quark-parton model (RQPM, dotted line) and the quark-gluon string model (QGSM, dashed line). The case of ZS spectrum one can see in Fig. 7. The prompt neutrino fluxes were obtained [27] with NSU primary spectrum [29], therefore they can serve here as upper limits for the prompt neutrino flux due to RQPM and QGSM. It worth noting that evaluation of the prompt neutrino flux obtained with the dipole model [30] is close to the QGSM prediction [27] above 1 PeV. The prompt neutrino flux due to QGSM in the energy range 5 TeV $\leq E_\nu \leq 5 \cdot 10^3$ TeV was approximated by the expression

$$\Phi_\nu^{\rm pr}(E_\nu) = A(E_1/E_\nu)^{3.01}[1 + (E_1/E_\nu)^{2.01}]^{-0.165}, \quad (1)$$

where $A = 1.19 \cdot 10^{-18}$ (GeV cm^2 s sr)$^{-1}$, $E_1 = 100$ TeV. In this range we neglect the weak angle dependence of the prompt neutrino flux.

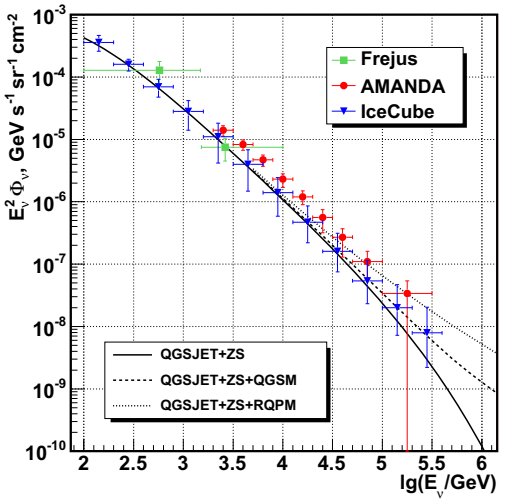

Figure 7: Flux of the conventional and prompt muon neutrinos (case of QGSJET-II + ZS spectrum).

3 Approximation formula

Numerical results of the conventional muon neutrino spectra in the energy range $10^2 - 10^6$ GeV for different zenith angles can be approximated with accuracy $(3 \div 8)\%$ by the formula:

$$\log_{10}[E_\nu^2 \Phi_\nu(E_\nu, \theta)] = \sum_{k=0}^{4} \sum_{n=0}^{3} a_{kn} x^n y^k. \quad (2)$$

Here $\Phi_\nu(E_\nu, \theta)$ is the flux with units of GeV^{-1} s^{-1} sr^{-1} cm^{-2}, $x = \cos\theta$, $y = \log_{10}(E_\nu/\text{GeV})$. Coefficients a_{kn} are given in Tables 1, 2.

Table 1: Coefficients a_{kn} for the QGSJET+GH choice

	n			
k	0	1	2	3
	a_{kn}			
0	0.72550	-6.45625	4.10284	-0.87026
1	-3.21166	6.38522	-3.31293	0.38300
2	1.00337	-2.46611	0.99745	0.01675
3	-0.19397	0.35758	-0.07515	-0.04540
4	0.01211	-0.01753	-0.00135	0.00537

Table 2: Coefficients a_{kn} for the QGSJET+ZS choice

	n			
k	0	1	2	3
	a_{kn}			
0	-3.21881	-7.00088	4.64475	-1.07882
1	1.60632	6.92858	-3.87209	0.60250
2	-1.11835	-2.65863	1.20056	-0.06412
3	0.20848	0.38659	-0.10641	-0.03279
4	-0.01577	-0.01909	0.00037	0.00467

4 Summary

The calculations of the high-energy atmospheric muon neutrino flux demonstrate rather weak dependence on the primary specrtum models in the energy range $10-10^5$ GeV. However the picture appears less steady because of sizable flux differences originated from the models of high-energy hadronic interactions. As it can be seen by the example of the models QGSJET-II and SIBYLL 2.1, the major factor of the discrepancy in the conventional neutrino flux is the kaon production in nucleon-nucleus collisions.

Comparison of calculated muon neutrino flux with the spectrum measured by IceCube shows that QGSJET-II is preferable model irrespective of the primary spectrum choice. The prompt neutrino contribution due to quark qluon string model (QGSM) added to the conventional one lead to better agreement with the IceCube measurement above 100 TeV.

The work supported by Russian Federation Ministry of Education and Science within the Federal Programs "Scientific and educational specialists for innovative Russia" under Contracts 14.740.11.0890, P681, P1242, and "Development of scientific potential in Higher Schools" under grant 2.2.1.1/12360.

References

[1] K. Daum et al. (Frejus Collaboration), Z. Phys. C, 1995, **66**, 417-428.

[2] A. Avrorin et al. Nucl. Instrum. Meth. A, 2011, **626-627**, S13.

[3] V.M. Aynutdinov et al. Russ. Phys. J. 2010, **53**, 601-610.

[4] R. Abbasi et al. (IceCube Collaboration), Astropart. Phys. 2010, **34**, 48-58.

[5] R. Abbasi et al. (IceCube Collaboration), Phys. Rev. D, 2011, **83**, 012001.

[6] T. Montaruli, for the IceCube Collaboration, Nucl. Phys. B (Proc. Suppl.) 2011, **212-213**, 99-108.

[7] S. Biagri, for the ANTARES Collaboration, Nucl. Phys. B (Proc. Suppl.) 2011, **212-213**, 109-114;
A. Margiotta et al. Nucl. Phys. B (Proc. Suppl.) 2009, **190**, 121-126.

[8] L.V. Volkova, Sov. J. Nucl. Phys. 1980, **31**, 784-790.

[9] A.V. Butkevich, L.G. Dedenko, I.M. Zheleznykh, Sov. J. Nucl. Phys. 1989, **50**, 90-99.

[10] P. Lipari, Astropart. Phys. 1993, **1**, 195-227.

[11] V.A. Naumov, T.S. Sinegovskaya, S.I. Sinegovsky, Il Nuovo Cim. A, 1998, **111**, 129-147.

[12] G. Fiorentini, V.A. Naumov, F.L. Villante, Phys. Lett. B, 2001, **510**, 173-188.

[13] G.D. Barr et al. Phys. Rev. D, 2004, **70**, 023006.

[14] M. Honda et al. Phys. Rev. D, 2004, **70**, 043008.

[15] A.A. Kochanov, T.S. Sinegovskaya, S.I. Sinegovsky, arXiv:0906.0671v2;
S.I. Sinegovsky, A.A. Kochanov, T.S. Sinegovskaya, arXiv:1010.2336v1.

[16] V.A. Naumov, hep-ph/0201310.

[17] T.K. Gaisser, M. Honda, Annu. Rev. Nucl. Part. Sci. 2002, **52**, 153-199.

[18] S.S. Ostapchenko, Nucl. Phys. B (Proc. Suppl.) 2006, **151**, 143-146;
S. Ostapchenko, Phys. Rev. D, 2006, **74**, 014026.

[19] R.S. Fletcher et al. Phys. Rev. D, 1994, **50**, 5710-5731;
E.-J. Ahn et al. Phys. Rev. D, 2009, **80**, 094003.

[20] A.N. Kalinovsky, N.V. Mokhov, Yu.P. Nikitin, 1989. Passage of high-energy particles through matter, New York, USA: AIP (1989) 262 p.

[21] A.A. Kochanov, T.S. Sinegovskaya, S.I. Sinegovsky, Astropart. Phys. 2008, **30**, 219-233.

[22] S.I. Sinegovsky et al. Int. J. Mod. Phys. A, 2010, **25**, 3733-3740; arXiv:0906.3791.

[23] V.A. Naumov, T.S. Sinegovskaya, Phys. Atom. Nucl. 2000, **63**, 1927-1935.

[24] V.I. Zatsepin, N.V. Sokolskaya, Astronomy & Astrophys. 2006, **458**, 1-5; Astron. Lett. 2007, **33**, 25-33.

[25] A.D. Panov et al., Bull. Russ. Acad. Sci. Phys. 2007, **71**, 494-497; astro-ph/0612377.

[26] T. Antoni et al., Astropart. Phys. 2005, **24**, 1-25; W.D. Apel et al. Astropart. Phys. 2009, **31**, 86-91.

[27] E.V. Bugaev et al. Nuovo Cim. C, 1989, **12**, 41-73.

[28] E.V. Bugaev et al. Phys. Rev. D, 1998, **58**, 054001.

[29] S.I. Nikolsky, I.N. Stamenov, S.Z. Ushev, Sov. Phys. JETP, 1984, **60**, 10-21.

[30] R. Enberg, M.H. Reno, I. Sarcevic, Phys. Rev. D, 2008, **78**, 043005.

Study the Module Power Supply's Performance

XIANGDONG SHENG[1], SHAORU ZHANG[2], LIZHI ZHAO[3], JINGHONG XIAO[2], SHAOJIE LI[2], FOR THE LHAASO COLLABORATION
[1]*Institute of High Energy Physics, Chinese Academy of Sciences, Beijing, 100049, P.R. China.*
[2]*College of Physics Science And Information Engineering, Hebei Normal University, Shijiazhuang, 050016, P.R. China.*
shaoruzhang@126.com
DOI: 10.7529/ICRC2011/V04/0642

Abstract: The LHAASO detectors would be operated at Yangbajing, under the condition of high altitude (4300m, 0.6atm) and large dynamic temperature variation (from -25°C to 40°C). To keep the gains of the photomultiplier tubes used stable within 5%, it is required that the temperature coefficient and ripple index of the power supplies should be less than 0.01%/℃ and 0.01%, respectively. Different types of power supplies were tested in an environment simulation system, where the temperature and air pressure are controllable, three of which meet the requirements and are chosen as the candidates.

Keywords: Power supply, photomultiplier tube, temperature coefficient, ripple index.

1 Introduction

The Large High Altitude Air Shower Observatory (LHAASO) project [1] is proposed to study gamma ray astronomy from 40GeV to 1PeV by searching for cosmic ray sources using gamma rays above 30TeV, survey in the whole northern sky for gamma ray sources above 100GeV and gamma ray source observation using high resolution telescopes. Cosmic ray physics from 10TeV to 1EeV in energy spectrum for individual composition above 10TeV and energy spectrum and composition above 100PeV will be studied.

Ground-based Extensive Air Shower (EAS) detector is the only choice to cover the wide (about 8 orders of) energy range. The proposed detector consists of the following components[2]:
• a 1km^2 EAS array (KM2A),
• 4 water Cerenkov detector arrays (WCDAs),
• a 5000m^2 shower core detector array (SCDA),
• a wide field of view (FOV) Cerenkov/fluorescence telescope array (WFCA) and
• 2 large imaging Cerenkov telescopes (LIACTs).

A prototype array of 5% size of LHAASO had been built at the Yangbajing Cosmic Ray Observatory and used to simultaneously measure cosmic rays with the ARGO-YBJ experiment.

The LHAASO detectors would be operated at Yangbajing, under the condition of high altitude (4300m, 0.6atm) and large dynamic temperature variation (from -25°C to 40°C). Even under such a condition, PMTs are required to be operated stably. To keep the gain variations of the photomultiplier tubes within 5%, it is required that the temperature coefficient and ripple index of the power supplies should be less than 0.01%/℃ and 0.01%, respectively. To do that, it's important to choose a suitable voltage source from several kinds of high voltage source.

Based on the requirement of the LHAASO detectors for power supply, two kinds of power supplies can be chosen as the candidates. They are linearity power supply and switch power supply. Linearity power supply can offer stable analogue output. The ripple index is small. However, linearity power supply firstly transforms the input to AC high voltage through a transformer which can increase the bulk and weight of the power supply. Moreover, the transfer efficiency is low (only 30%), and the dissipation power is large. Comparing with linearity power supply, the bulk and weight of the switch power supply is small (less 20% ~ 30% than linearity power supply), because it doesn't need any transformer. Its dissipation power is small, and the transfer efficiency is high (more than 75%). However, the ripple index is large.

Considering energy saving, we chose switch power supply as the candidate power supply for LHAASO detectors, as the LHAASO detectors will be operated for

a long time. Different types of power supplies were tested in an environment simulation system, where the temperature and air pressure are controllable. They are Power supply of CENTRE, LION, and DONGWEN, respectively. Three types of them can meet the requirements and are chosen as the candidates. Power supply of LION has been adopted to supply power for the prototype array of 5% size of LHAASO at the Yangbajing Cosmic Ray Observatory. The successful function confirmed our choice.

2 Test System

In order to choose a suitable voltage source from several kinds of high voltage sources, different types of power supplies were tested in an environment simulation system, where the temperature and air pressure are controllable. Figure 1 is the experimentation box.

Figure 1. The experimentation box

According to the actual working environment of high voltage power supplies, the temperature in experimentation box varies from -40 to 50°C. High voltage power supplies and PMTs are put into the box. At the certain temperature, since it needs several hours for the power supplies and PMTs to reach stabilization, the output voltage and ripple index of power supplies were tested after two hours. Moreover, reading data errors had been eliminated through recording data time after time.

3 Test Results

Based on the requirement of the LHAASO detectors for power supplies, the outputs of power supplies were adjusted to 1500V. Each high power supply needs a low voltage DC source to provide energy, and the voltage of this DC source should be equal to 24V.

For the sake of comparing the performance among the three types of power supplies, all high voltage sources are supplied by the same low voltage DC source, which is made by Shanghai Mingwei.

Figure 2 is the temperature performance of the low voltage DC source. It can be seen from the results that the variation of output voltage is less than 1V when the temperature is changed from -40ºC to 50ºC. That is to say this voltage variation can meet the requirement of high voltage power supply for low voltage source (DC 24V±2V).

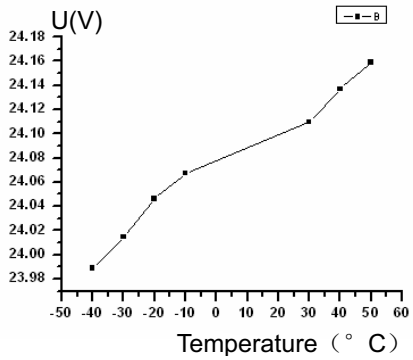

Figure 2. Temperature performance of the low voltage DC source.

3.1 Temperature Coefficient

The CHANGZHOU TONGHUI TH1961 is adopted to test the voltage. This is a high quality digital tabletop multimeter. It will provide precise results in its many application areas. The display has a resolution of 6½ digits (max. count 1.200.000). The DC voltage accuracy is 0.0035%.

The temperature coefficients of three types of power supplies were tested in the experimentation box. Figure 3 is the temperature coefficient.

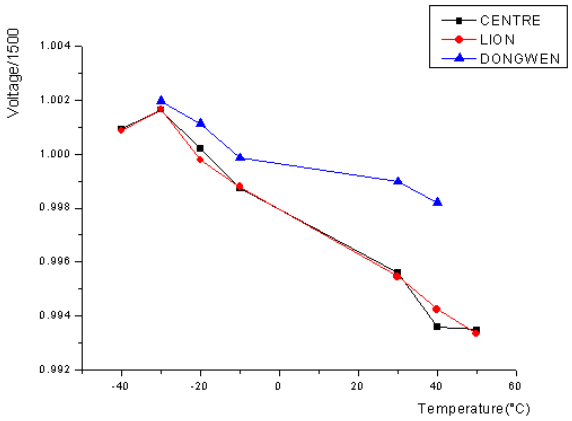

Figure 3. The temperature coefficient.

It can be seen from the results that the temperature coefficient of every type of power supply is about 0.01%/ºC. It can satisfy the requirement.

3.2 Ripple Index

The SUZHOU TONGCHUANG TC2290B is adopted to test the ripple index. This is a 2 Channels AC Millivolt meter. The measured voltage range is from 30uV~100V, the accuracy is +/- 3% of full scale, and the frequency response is 5Hz~2MHz. The input resistor and capacitor are 2MΩ and 20PF, respectively.

The ripple index of three types of power supplies were tested in the experimentation box. Figure 4 is the ripple index.

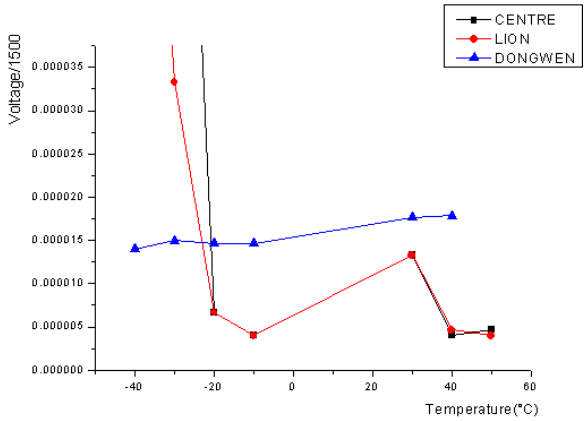

Figure 4. Ripple index.

It can be seen from the results that the ripple index of CENTRE and LION are less than 0.01%, and DONGWEN is less than 0.002%. They can satisfy the requirement.

3.3 Temperature Coefficient and Ripple Index at 0.8atm

The temperature coefficient and the ripple index at 0.8atm are also tested. Figure 5 and Figure 6 are temperature coefficient and the ripple index of DONGWEN, respectively.

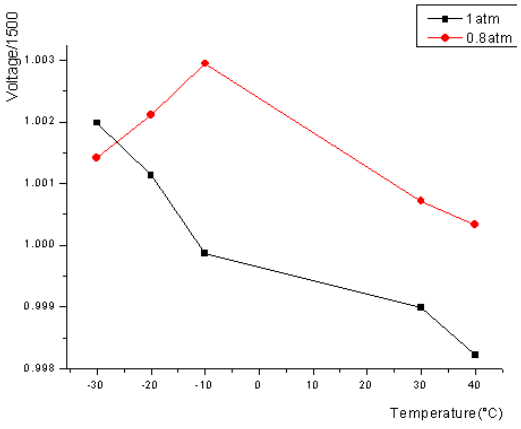

Figure 5. Temperature coefficient of DONGWEN power supply at 0.8atm.

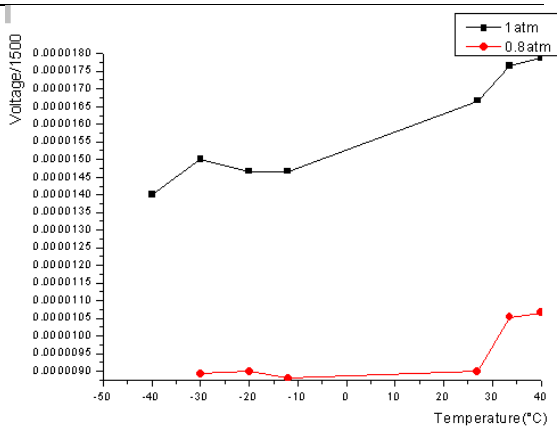

Figure 6. Ripple index of DONGWEN power supply at 0.8atm.

According to these results, we can see that the temperature coefficient is less than 0.008%/ºC, the ripple index is less than 0.001% even if the operation environment is changed.

3.4 Performance with Load Variation

Generally, a voltage divider is used for a PMT operation to apply interstage voltage to the dynodes of a PMT [3]. A voltage divider usually consists of a series of connected resistors and some capacitors, it is called resistor base. Figure 7 shows its schematic drawing. In this figure, symbols of K, Dyn and P mean cathode, dynode and anode, respectively. Resistors divide a total applied voltage and supply constant voltages to the dynodes. Capacitors supply electric charge to each output pulse to keep constant interstage voltages in short term.

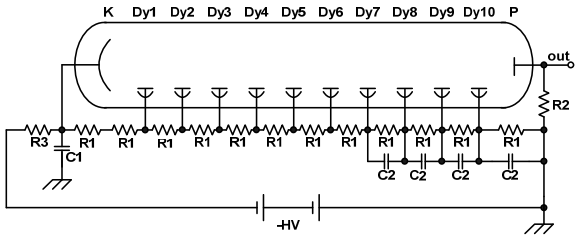

Figure 7. Schematic drawing of a voltage divider.

The performance with load variation of every power supply at 40ºC is also tested. Table 1 is the performance with load variation under different operation conditions. During the course of testing, DC voltage source, high voltage power supply, and PMT are all put into the experimentation box, because they will operate together when the LHAASO project is running.

From Table 1, we can conclude that the output voltage will fluctuate when the load varies. But the range of voltage fluctuation is less than 0.048%, which can be accepted.

voltage	LION(1atm)	DWEN(1atm)	DWEN(0.8atm)
open circuit	1498.68966	1499.01759	1498.55852
only with PMT	1498.1272	1498.29618	1498.33177
with PMT and photons	1498.7648	1498.50362	1498.14458

Table 1. The performance with load variation.

4 Conclusion

The LHAASO project is being built at Yangbajing so that the evolution of galaxies and the acceleration mechanisms in gamma ray sources can be thoroughly understood. It is well known that the altitude is very high and the temperature variation is large at Yangbajing. It is essential to find out a type of appropriate power supply for the LHAASO detectors. So the detectors can be operated stably. Different types of power supplies were tested in an environment simulation system, where the temperature and air pressure are controllable. The experimental results show that three types of them meet the requirements and are chosen as the candidates. These results are advantageous to the in-depth development of the LHAASO project and the test of the high energy physics.

Acknowledgments

This work is partly supported by the Knowledge Innovation Fund (H85451D0U2) of IHEP, Beijing.

References

[1] Cao, Z. et al., for the LHAASO Collaboration, Proceedings of 31th ICRC (2009).
[2] He, H. et al., for the LHAASO Collaboration, Proceedings of 31th ICRC (2009).
[3] Hamamatsu Catalog, “Photomultiplier Tubes” (Cat. No. TPMO 0002E).

32ND INTERNATIONAL COSMIC RAY CONFERENCE, BEIJING 2011

The endpoint formalism for the calculation of electromagnetic radiation and its applications in astroparticle physics

T. HUEGE[1], C. W. JAMES[2], H. FALCKE[2,3], M. LUDWIG[4]
[1]*Karlsruher Institut für Technologie, Institut für Kernphysik, Campus Nord, 76021 Karlsruhe, Germany*
[2]*Department of Astrophysics, IMAPP, Radboud University Nijmegen, P.O.Box 9010, 6500GL Nijmegen, The Netherlands*
[3]*ASTRON, Postbus 2, NL-79900AA Dwingeloo, the Netherlands*
[4]*Karlsruher Institut für Technologie, Institut für Experimentelle Kernphysik, Campus Süd, 76128 Karlsruhe, Germany*
tim.huege@kit.edu
DOI: 10.7529/ICRC2011/V04/0653

Abstract: We present the "endpoint" formalism for the calculation of electromagnetic radiation and illustrate its applications in astroparticle physics. We use the formalism to explain why the coherent radiation from the Askaryan effect is not in general Cherenkov radiation, as the emission directly results from the time-variation of the net charge in the particle shower. Secondly, we illustrate how the formalism has been applied in the air shower radio emission code REAS3 to unify the microscopic and macroscopic views of radio emission from extensive air showers. Indeed, the formalism is completely universal and particularly well-suited for implementation in Monte Carlo codes in the time- and frequency-domains. It easily reproduces well-known "classical mechanisms" such as synchrotron radiation, Vavilov-Cherenkov radiation and transition radiation in the adequate limits, but has the advantage that it continues to work in realistic, complex situations, where the "classical mechanisms" tend to no longer apply and adhering to them can result in misleading interpretations.

Keywords: electromagnetic radiation, modelling, Monte Carlo simulations, cosmic rays, neutrinos

1 Introduction

Processes leading to the emission of electromagnetic radiation can be very complex. To get a grasp of these processes, physicists often revert to "classical named radiation mechanisms" such as synchrotron radiation, transition radiation or Vavilov-Cherenkov radiation and try to apply these concepts to the problem at hand. However, it turns out that this strategy can often yield misleading results. Usually, the classical mechanisms only apply to idealized problems involving, e.g., infinite particle tracks, and their application to complex realistic situations can cloud the view for the complete picture.

Here, we propose a formalism suitable for the calculation of electromagnetic radiation from any kind of particle acceleration, which lends itself very well to the implementation in Monte Carlo codes, and necessitates no simplifying approximations to the underlying processes. In this "endpoint formalism", presented in detail in Ref. [1], the trajectory of individual particles is described as a series of points at which particles are accelerated instantaneously, leading to discrete radiation contributions which can then be easily superposed.

The endpoint formalism can be applied in both the frequency and time domains, and correctly reproduces the aforementioned classical named processes. Furthermore, we demonstrate how the application of the endpoint formalism has provided essential insights for radio emission processes in astroparticle physics.

2 The endpoint formalism

The endpoint formalism relies on the fact that any trajectory of a charged particle undergoing acceleration can be decomposed into a series of discrete "acceleration events" joined by straight tracks. The error introduced by this procedure can be made arbitrarily small by applying the decomposition on scales as small as necessary.

Furthermore, each of the acceleration events during which the velocity vector of a charged particle changes, can again be decomposed into two "endpoints", one corresponding to the instantaneous acceleration of the particle from its velocity to rest and the second corresponding to the instantaneous acceleration of the particle from rest to its new velocity.

The electromagnetic radiation associated with these endpoints can be calculated with a simple formula, which lends itself well to application in Monte Carlo simulations. (For derivations of the stated equations we kindly refer the reader to [1].)

2.1 Frequency domain

The electric field seen by an observer at position $\vec{x}$ and observing frequency ν from an individual endpoint is given by:

$$\vec{E}_{\pm}(\vec{x},\nu) = \pm\frac{q}{c}\frac{e^{ikR(t'_0)}}{R(t'_0)}\frac{e^{2\pi i\nu t'_0}}{1-n\vec{\beta}^*\cdot\hat{r}} \cdot \hat{r}\times[\hat{r}\times\vec{\beta}^*] \quad (1)$$

where $k = 2\pi\nu n/c$, q denotes the particle charge, n is the medium refractive index, $\vec{r}$ gives the line of sight from observer to particle, $R = |\vec{r}|$ and t'_0 corresponds to the (retarded) time at which the endpoint radiates. $\vec{\beta}^*$ denotes the non-zero velocity associated with the endpoint. '$\pm$' is positive when the acceleration is from rest to $\vec{\beta}^*$ and negative when the acceleration is from $\vec{\beta}^*$ to rest.

2.2 Time domain

Likewise, the electric field an observer sees from an endpoint in the time domain is given by:

$$\vec{E}_{\pm}(\vec{x},t) = \pm\frac{1}{\Delta t}\frac{q}{c}\left(\frac{\hat{r}\times[\hat{r}\times\vec{\beta}^*]}{(1-n\vec{\beta}^*\cdot\hat{r})R}\right) \quad (2)$$

Here, the result has to be interpreted as the electric field time-averaged over a time scale Δt, the adequate choice of which is dictated by the time resolution of interest.

2.3 Example application

In Fig. 1 we illustrate the electromagnetic radiation associated with the acceleration of individual charged particles as calculated using the endpoint formalism in the frequency domain. In the figure, the emission from processes such as the instantaneous acceleration of a particle from rest ('acceleration'), the deflection of a relativistic electron by 20° ('deflection'), the deceleration of a relativistic electron to rest ('slow-down'), and the reversal of direction of a mildly relativistic electron ('reversal'), is shown. Typical effects such as the beaming of radiation for relativistically moving charges and the shock wave behaviour near the Cherenkov angle occurring in media with a refractive index different from unity turn up naturally in this calculation.

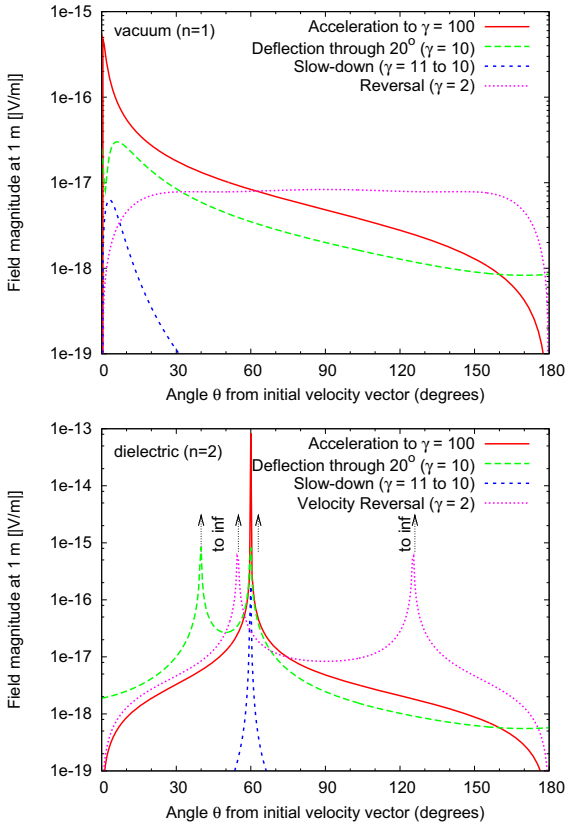

Figure 1: Electric field magnitude resulting from the acceleration of a relativistic electron in four simple cases (see text) in (top) vacuum and (bottom) a dielectric with refractive index $n = 2$, as calculated using Eq. (1).

3 Application to classical mechanisms

To demonstrate that the endpoint formalism can reproduce "classical named radiation mechanisms", we briefly illustrate its application to the processes of synchrotron radiation and Vavilov-Cherenkov radiation.

3.1 Synchrotron radiation

While the term "synchrotron radiation" usually implies relativistic particles revolving continuously in a magnetic field, here we look at a particle undergoing precisely one revolution. To describe this situation using the endpoint formalism, the helical particle track is decomposed into a series of straight tracks joined by "kinks" in which the particle is accelerated instantaneously. As explained earlier, each kink in turn is represented by two endpoints with contributions $\vec{E}_-$ and $\vec{E}_+$, describing the instantaneous deceleration to rest followed by the instantaneous acceleration to the new velocity (in this case with the same magnitude, but different direction).

Using either of equations (1) and (2), the emission radiated during the particle revolution can then be calculated as the superposition of the individual endpoint contributions. Care has to be taken to describe the particle motion on a fine-enough spatial scale, as dictated (respectively) by the maximum frequency/minimum time interval of interest. The results for both the frequency- and time-domain are shown in Fig. 2. Note that calculating the result for one domain by an FFT of the result of the other domain yields the same result, but is usually much more involved than performing a direct endpoint calculation.

Comparing these results with the established theory of synchrotron radiation confirms that the endpoint formalism

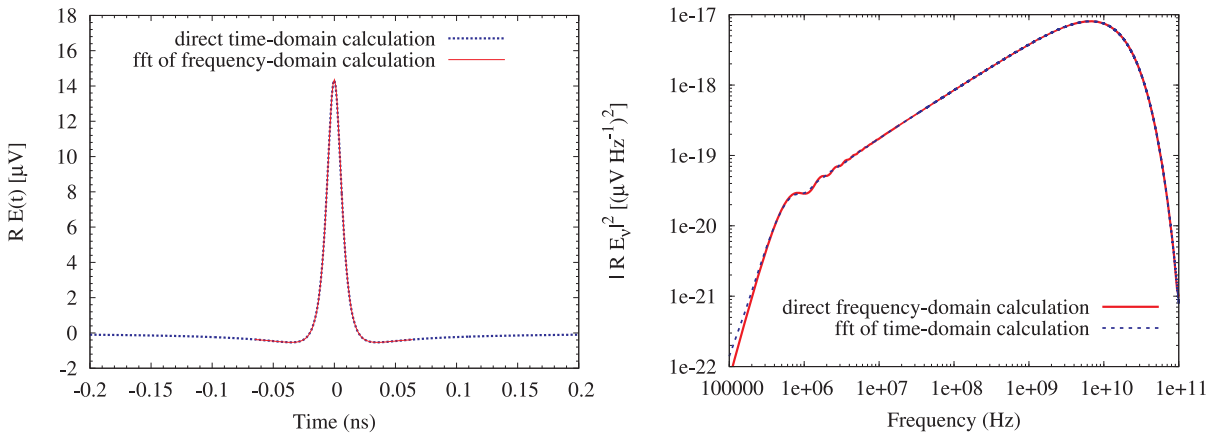

Figure 2: Time-trace of a synchrotron pulse produced by a single gyration of an electron with $\beta = 0.999$ and gyration radius $r = 100$ m (top), and power frequency spectrum of the emitted radiation (bottom). In each case, the direct calculations (time- and frequency-domain respectively) are shown in comparison with the results generated by fast-Fourier-transforming data from the other domain.

can reproduce the well-known theory. (For further details please refer to Ref. [1].)

3.2 Vavilov-Cherenkov radiation

In the scientific literature, the term "(Vavilov)-Cherenkov radiation" is often used somewhat imprecisely, but typically refers to the original calculation of Frank and Tamm in the case of charged particles propagating through a dielectric medium along infinite tracks [2]. There is no acceleration associated with this particle movement, and therefore this "true" Vavilov-Cherenkov emission cannot be described with the endpoint formalism discussed here.

However, in realistic situations particle tracks are not infinite. When trying to calculate the emission associated with particles propagating through a medium on finite tracks, the emission is usually calculated using "track segments", and, as first calculated by Tamm [3], the far-field result near the Cherenkov angle turns out to be proportionate to the total length of track traversed.

Using the endpoint formalism, we regard the radiation as contributions from the endpoints of the track segments. Calculating the radiation based on equation (1), we can derive (cf. Ref. [1] for details):

$$\vec{E}_{\rm track}(\vec{x},\nu) \approx \frac{q\beta\sin\theta}{c}\frac{e^{i(kR+2\pi\nu t_1)}}{R} \times\left(\frac{1-e^{2\pi i\nu(1-n\beta\cos\theta)\delta t}}{1-n\beta\cos\theta}\right)\hat{E} \quad (3)$$

where θ denotes the angle between the particle velocity vector and the line of sight from observer to endpoint, t_1 denotes the (retarded) time of the start of the track, δt is the track length divided by c, and an approximation was made for observer distances large with respect to the track length.

This result corresponds (within a factor of 2 arising from a different definition of the Fourier transform) to the "Vavilov-Cherenkov radiation formula" of Eq. 12 in Zas, Halzen, and Stanev [4], with $\mu_r = 1$ and $q = -e$. These authors also show that their result — and, by extension, ours — produces the same emitted power as Tamm's calculation. Indeed, it has previously been shown that the radiation from a finite particle track consists of both endpoint contributions *and* a "true" Vavilov-Cherenkov contribution from the track itself, the latter of which is negligible at most angles in the far-field [5].

In other words, although the ZHS code is commonly understood as calculating "the Vavilov-Cherenkov radiation" from a particle cascade in a dense medium, it actually calculates the radiation from the endpoints of finite particle tracks. As the particle cascade exhibits a variation of the negative charge excess during its evolution, the endpoint contributions of the individual tracks do not cancel and a net contribution arises. This radiation due to the time-variation of the net charge is a central, yet not generally appreciated aspect of the Askaryan radiation [6] process of cascades in dense media. Thus, we expect that the most recent results on "Čerenkov radio pulses" from straight track segments [7], wherein the authors use a method based on calculating the vector potential, is generally applicable to all radiation processes.

4 Applications in astroparticle physics

We have developed the endpoint formalism in the context of astroparticle physics and hereby illustrate how it has helped us to achieve a better understanding of radio emission processes relevant for cosmic ray and neutrino detection.

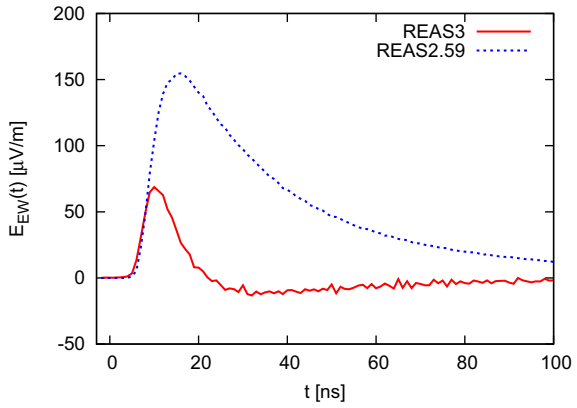

Figure 3: A radio pulse simulated with REAS3 (solid red line) compared with the radio pulse simulated with REAS2.59 (blue dashed line). REAS3 is based on the endpoint formalism.

4.1 Radio emission from air showers

Radio emission from extensive air showers has been under intense study over the recent decade. To interpret the data gathered by experiments, a good understanding of the underlying emission mechanism is vital. A significant number of models have been developed in recent years, but different models gave different results. In particular, there was a discrepancy between microscopic Monte Carlo based approaches such as REAS2 [8] and the macroscopic MGMR model [9]. It became clear that in the microscopic time-domain treatments, a radiation contribution associated with the time-variation of the number of charged particles had been neglected. Using the endpoint formalism in the time-domain in REAS3 [10], it could be understood in detail how the superposition of the individual particle emissions can be carried out consistently. Consequently, the different models could be reconciled [11] — a breakthrough in the modelling of radio emission from extensive air showers. The importance of the correction introduced by the endpoint formalism is illustrated in Fig. 3.

4.2 Radio emission in the lunar regolith

Numerous projects aim at detecting cosmic rays or neutrinos via radio emission radiated from showers initiated in the lunar regolith. For a long time it has been the general understanding that the radio emission would vanish if the particle shower occurred close to the surface of the moon due to the so-called "formation zone effect" (first investigated in this context by Ref. [12]). The argument is that the refractive index close to the surface effectively approaches unity and that therefore Vavilov-Cherenkov emission has to vanish.

As has been argued above, however, the emission produced by showers in dense media (the Askaryan radiation) is dominated by radiation from the endpoints of individual particle tracks. The fact that the shower grows and declines again means that there is a net radiation contribution due to the variation of the net charge, which leads to radiation irrespective of the refractive index of the medium. A suppression of the emission due to the presence of the surface still occurs due to refractive effects at the surface — however, this effect applies equally to both shallow and deep cascades, and is taken into account in experimental simulations.

5 Conclusions

We have developed an endpoint formalism for the calculation of electromagnetic radiation in arbitrarily complex radiation processes. The formalism is universally applicable and can be implemented easily in calculations both in the time and frequency domains.

Classical named radiation processes such as synchrotron radiation or Vavilov-Cherenkov radiation can be successfully reproduced using the endpoint formalism. However, unlike such descriptions, the endpoint formalism does not make any simplifying assumptions which often break down in realistic situations.

We have successfully used the endpoint formalism to address problems in astroparticle physics. In particular, we were able to calculate the radio emission from extensive air showers using the endpoint formalism, and thereby reconcile discrepancies existing between earlier modelling approaches. Also, the endpoint formalism illustrates that Askaryan radio emission in the lunar regolith does not vanish even if the particle cascade develops close to the surface, as the net growth and decline of the shower will produce radio emission even for a refractive index approaching unity.

References

[1] C. W. James, H. Falcke, T. Huege, M. Ludwig, Phys. Rev. E (submitted), arXiv:1007.4146
[2] I.M. Frank and I.E. Tamm, Dokl. Akad. Nauk SSSR **14**, 109 (1937).
[3] I.E. Tamm, J.Phys.Moscow **1**, 439 (1939).
[4] E. Zas, F. Halzen, and T. Stanev, Phys. Rev. D **45**, 362 (1992).
[5] G.N. Afanasiev, V.G. Kartavenko, and Y.P. Stepanovsky, J.Phys.D **32**, 2029 (1999).
[6] G.A. Askaryan, Sov. Phys. JETP, **14**, 441 (1962); **48**, 988 (1965).
[7] J. Alvarez-Muñiz, A. Romero-Wolf, E. Zas, Phys.Rev. D **81**, 123009 (2010).
[8] T. Huege, R. Ulrich, R. Engel, Astrop. Phys., 2007, **27**: 392-405
[9] O. Scholten, K. Werner, F. Rusydi, Astrop. Phys., 2008, **29**: 94-103
[10] M. Ludwig, T.Huege, Astrop. Phys., 2010, **34**: 438-446
[11] T. Huege, M. Ludwig, O. Scholten and K.D. deVries, ARENA Nantes, France (2010), Nucl. Instr. Meth. A in press, doi:10.1016/j.nima.2010.11.041
[12] P.W. Gorham, K.M. Kiewer, C.J. Naudet, D.P. Saltzberg, and D.R. Williams, RADHEP 2000, arXiv:astro-ph/0102435 (2001).

Atmospheric Neutrino Flux with JAM interaction model

MORIHIRO HONDA[1], TAKAAKI KAJITA[1,2], KATSUAKI KASAHARA[3] SHOUICHI MIDORIKAWA[4] JUN NISHIMURA[3] ATSUSHI OKADA[3]
[1]*Institute for Cosmic Ray Research, University of Tokyo, Kashiwa, Chiba, 277-8582 Japan.*
[2] *Institute for the Physics and Mathematical of the Universe, the University of Tokyo, 5-1-5 Kashiwa-no-ha, Kashiwa, Chiba 277-8582, Japan.*
[3]*Research Institute for Science and Engineering, Waseda University, 3-4-1 Okubo Shinjuku-ku, Tokyo, 169-8555, Japan.*
[4]*Faculty of Engineering, Aomori University, Aomori, 030-0943 Japan.*
[5]*Institute of Space and Astronomical Science, JAXA, Sagamihara, Japan.*
mhonda@icrr.u-tokyo.ac.jp
DOI: 10.7529/ICRC2011/V04/0988

Abstract: We report the improvement of the prediction for the lower energy atmospheric neutrino flux ($\lesssim$1 GeV), with the JAM interaction model, which is used in PHITS (Particle and Heavy-Ion Transport code System). We show that when a interaction model can reproduce the observed muon flux at the balloon altitude in a good accuracy, it calculate the atmospheric neutrino flux in the similar accuracy at low energies. When we apply a proper modification to the JAM interaction model, it can reproduce the muon flux observed by BESS at the balloon altitude.

Keywords: atmospheric, neutrino, muon, interaction

1 Introduction

We have calculated atmospheric neutrino fluxes using a 3D scheme, and refined it in previous works [1, 2]. In those calculation, we tested the interaction model with the atmospheric muon. With the "modified" DPMJET-III constructed from the output of DPMJET-III [3], we could reproduce the observed atmospheric muon spectra quite well above 1 GeV/c at sea level and mountain altitudes, but the agreement below 1 GeV/c is not as good. For the "Modification", see Ref. [4]. At balloon altitudes, in particular, the calculated muon fluxes are obviously lower than the observed ones. This seems to be due to the secondary spectra of DPMJET-III, which our simple modification procedure cannot correct. The disagreement was not resolved without violating the agreement at higher momenta.

Instead of a more sophisticated modification method, we searched for an interaction model which has a better nature at low energies, and found the interaction model called JAM, which is used in PHITS (Particle and Heavy-Ion Transport code System) [5]. The JAM interaction model could reproduce the muon flux at balloon altitude better than the DPMJET-III after some modification[4]. Apart from the atmospheric muon flux, it is notable that the hadronic interactions of protons on thin N_2 and O_2 targets have been studied in detail by the HARP experiment, aiming to improve the calculation of atmospheric neutrino fluxes [6]. We examine JAM also with the HARP data, and find the JAM agrees a little better than DPMJET-III.

Constructing "modified" JAM from the output of JAM, we use it to calculate the atmospheric neutrino flux for projectile energy below 32 GeV, and the inclusive DPMJET-III above that. We use essentially the same calculation scheme with that Ref. [2], including the primary flux and the geomagnetic models, except for the hadronic interaction model. The change of interaction model does not change the zenith angle dependence of the atmospheric neutrino fluxes and the $(\nu_\mu + \bar{\nu}_\mu)/(\nu_e + \bar{\nu}_e)$ ratio visibly from the previous calculations, but increased the absolute value of the atmospheric neutrino flux below 1 GeV. Note, we estimate the error of the atmospheric neutrino flux below 1 GeV, also using the atmospheric muon flux at the balloon altitude.

2 Calculation of Atmospheric Neutrino Flux

2.1 Interaction Model and Primary Cosmic Ray Model

For the hadronic interaction model, we used the DPMJET-III in the former calculation [2], since it reproduce the relatively higher energy muon flux observed at sea level. However, using this interaction model, we could not reproduce the observed low energy muon flux by BESS [7] at balloon altitude. Looking for a better interaction model for

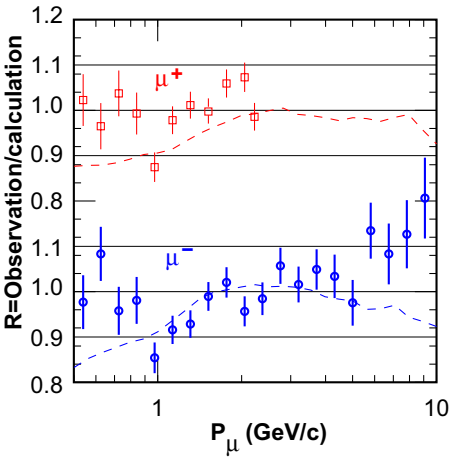

Figure 1: Comparison of the muon flux observed at the balloon altitudes (5–2 g/cm^2) at Fort Sumner and the one calculated with the modified-JAM in ratio. Dashed lines are the ratios of calculations with DPMJET-III to the one with JAM.

the cosmic rays at low energies, we find JAM interaction model, which is used in PHITS (Particle and Heavy-Ion Transport code System) [5], and could reproduce the atmospheric muon flux at balloon altitude reasonably well (Fig. 1). Note, the JAM interaction model show a little better agreement with the HARP experiment.

In the comparison of modified-JAM and the modified DPMJET-III at 10 GeV, we find that modified-JAM shows slightly higher spectra than modified-DPMJET-III in $x(\equiv E_{secondary}/E_{projectile})\lesssim 0.2$, where those energies are kinetic energy. This is the reason for the higher atmospheric muon flux below 1 GeV/c with the modified-JAM. And, our modification method cannot modify DPMJET-III to have this high x-spectra for $x\lesssim 0.2$ and also keep the high spectra for $x\gtrsim 0.2$ required by the observed muon flux above 1 GeV.

We use the same primary flux model shown in Fig. 2, which is also used in Refs [1, 2]. It is based on AMS and BESS data, with a spectral index of -2.71 above 100 GeV for protons. Note, we also use the US-standard '76 model of the atmosphere [9], and the IGRF2005 geomagnetic model [8], as we estimate the results would not be visibly different by the change of these to more recent models.

2.2 3D Calculation Scheme

The scheme 3D calculating the atmospheric neutrino fluxes is almost the same as that for the previous calculations [1, 2], except for the interaction model.

We consider the surface of the Earth is a sphere with a radius of $R_e = 6378.180$ km. In addition, we assume three more spheres; the injection sphere, the simulation sphere, and the escape sphere. We take the radius of the injection sphere as $R_{inj} = R_e + 100$ km, the radius of simulation

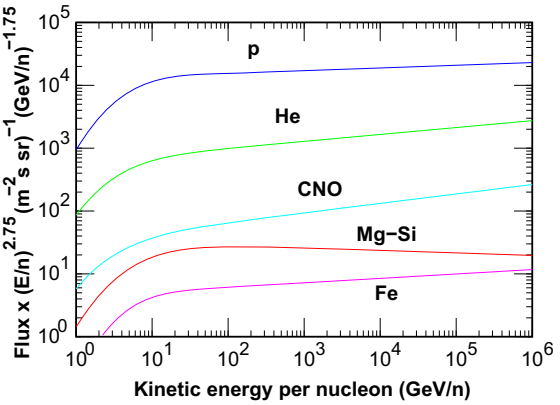

Figure 2: Primary flux model for the chemical compositions used in our calculation

sphere as $R_{sim} = R_{esc} = 10 \times R_e = 63781.80$ km. Note, the radius of the simulation sphere is now the same as that of escape sphere.

Cosmic rays are sampled on the injection sphere uniformly toward the inward direction, following the primary cosmic ray model. Before they are fed to the simulation code for the propagation in air, they are tested to determine whether they pass the rigidity cutoff, i.e., the geomagnetic barrier. For a sampled cosmic ray, the 'history' is examined by solving the equation of motion in the negative time direction. When the cosmic ray reaches the escape sphere without touching the injection sphere again in the inverse direction of time, the cosmic ray can pass through the magnetic barrier following its trajectory in the normal direction of time.

Note, we refined the virtual detector correction [2] a little. Using the inside of the circle with radius of θ_d as the virtual detector, the flux Φ_{θ_d} obtained with the virtual detector and the flux Φ_0 at the real target detector are related by

$$\Phi_{\theta_d} \simeq \Phi_0 + \Phi_0' \theta_d^2 \,, \tag{1}$$

The term with Φ_0' may be canceled out using two virtual detectors, with radii of θ_1 and θ_2, as

$$\Phi_0 \simeq \frac{\theta_1^2 \Phi_2 - \theta_2^2 \Phi_1}{\theta_1^2 - \theta_2^2} = \frac{\Phi_2 - r^2 \Phi_1}{1 - r^2}, \tag{2}$$

where we assumed $\theta_1 > \theta_2$.

We study the ratio of estimated statistical errors $F(r) \equiv \Delta\Phi_0/\Delta\Phi_1$ as the function of r, and find that the ratio takes the minimum value $\sqrt{(5)} \simeq 2.236$ at $r = 1/\sqrt{2} \simeq 0.707$, whereas we took $r = 0.5$ in Ref. [2]. However, the ratio $\Delta\Phi_0/\Delta\Phi_1$ is a slowly varying function of r near the minimum, and the ratio at $r = 0.5$ is not too bad (2.517).

We take $r_1 = 1113.6$ km corresponding to the angle from the center of the Earth of 10 degrees and $r_2 = 787.4$ km corresponding to 7.071 degrees. The "virtual detector correction" is applied up to $E_\nu = 10$ GeV, as we find a large difference between before and after the virtual detector and correction for some directions.

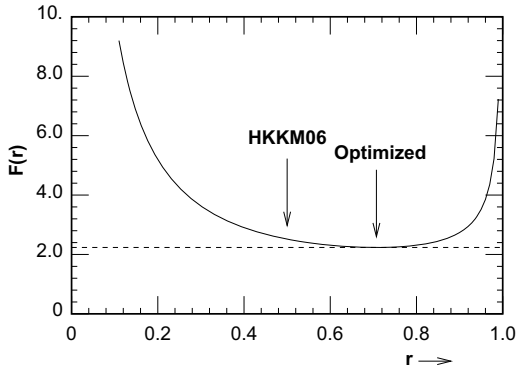

Figure 3: The variation $F(r) \equiv \Delta\Phi_0/\Delta\Phi_1$ as the function of r. It has a minimum value $\sqrt{5} \simeq 2.236$ at $r = 1/\sqrt{2} \simeq 0.707$ indicated by "Optimized". The "HKKM06" indicates the $r = 0.5$ used in Ref. [2], where the F-value is a little larger than the optimized one ($F(0.5) = 2.517$).

We show the estimated statistical error of this work, for near-vertical directions and for near-horizontal directions averaging over all azimuth angles, in Fig. 4. For the horizontal directions, the opening angle of the virtual detector decrease with $\cos\theta$, where θ is the zenith angle. Therefore, the statistical error for near-horizontal directions is larger than that for near-vertical directions. We find the statistical errors are well below 1 % for the average over the azimuth angles. For each azimuth bin, however, the statistical errors reach a few percent for some directions. The largest statistical errors are found at the energy just below 10 GeV, due to the virtual detector correction applied up to this energy.

3 Calculated Atmospheric Neutrino flux

We show the calculated atmospheric neutrino fluxes with the modified-JAM in this section. In the left panel of Fig. 5, the calculated atmospheric neutrino spectra are shown averaged over all directions from 0.1 GeV to 32 GeV for Kamioka, together with the ones calculated in our previous work, and those of the Bartol group [10][11], and the FLUKA group [12]. Above 32 GeV, the 3D calculation is smoothly connected to the 1D calculation carried out in the previous work. As the modified-JAM is used below 32 GeV, any difference above that is due to the difference of the calculation scheme between 3D and 1D. However, the difference between present and previous works [2] is very small in the figure above 1 GeV. On the other hand, the atmospheric neutrino fluxes calculated with the modified-JAM show an increase from the previous one below 1 GeV, as is expected from the increase of atmospheric muon spectra below 1 GeV/c.

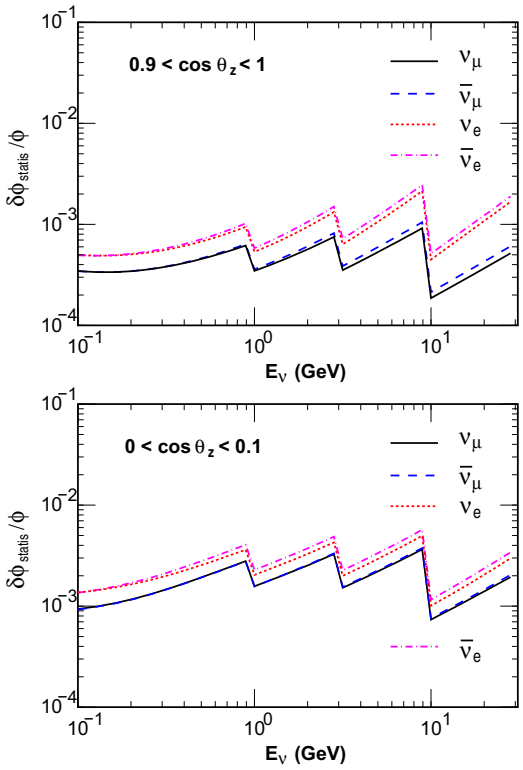

Figure 4: The ratio of statistical errors to the flux value in this work. We show the statistical errors for near-vertical directions ($0.9 < \cos\theta_z < 1$) in the upper panel, and for near-horizontal directions ($0.9 < \cos\theta_z < 1$) in the lower panel, both averaging over all azimuthal directions.

4 Estimation of Error of the atmospheric neutrino flux

We have estimated the error of the calculated atmospheric neutrino flux from the comparison of calculated atmospheric muon flux with the observed one in Ref. [2]. However, atmospheric neutrinos below 1 GeV have little things to do with the muons observed at sea level, and the flux error was not estimated there. We show the weights in the phase space of $p + Air \to \pi$ interaction responsible to the production of low energy (0.32 GeV/c) ν_μ, ν_e, and for μ at balloon altitude, and at the sea level in Fig. 6.

The shape of the weight distribution for muons at balloon altitude is also different from that for atmospheric neutrinos, However, we can scan the weight distribution in the phase space for the low energy atmospheric neutrinos, using that for the low energy muons at the balloon altitude, since we could reproduce the observed muon flux within 10% errors in the momentum rage of 0.5 – 2.5 GeV/c for μ^+, and 0.5 – 5.0 GeV/c for μ^- in Fig. 1.

We assume variations of the pion production in the the phase space of $p + Air \to \pi$, and calculate the ratio $\Delta\phi_\nu(E_\nu)/[\Delta\phi_\mu]_{max}$ for a neutrino energy, where $[\Delta\phi_\mu]_{max}$ is the maximum variation of muon flux in the

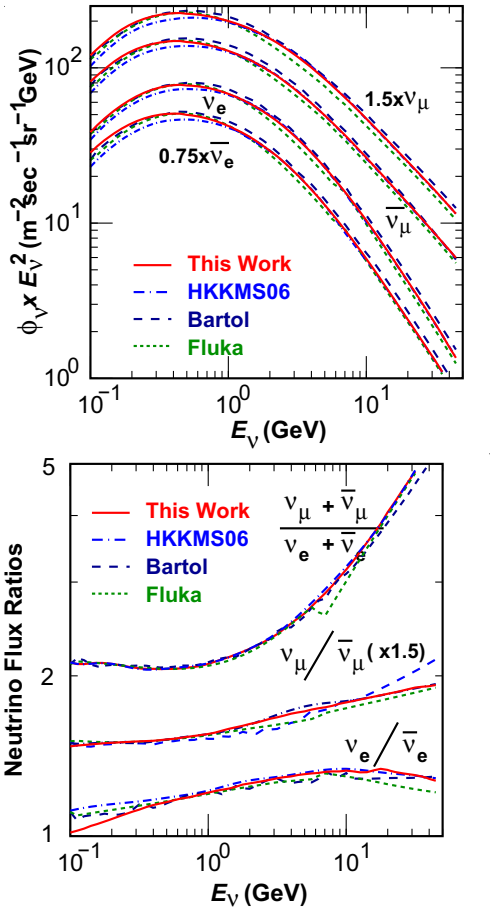

Figure 5: Comparison of atmospheric neutrino fluxes calculated for Kamioka averaged over all directions (left panel), and the flux ratios (right panel), with other calculations. The dashed lines are the calculation by the Bartol group [10][11], dotted lines for the FLUKA group [12], and dash dot for our previous calculation (HKKM06).

above momentum range. Taking 1,000,000 set of such a variation, we summarized the ratios as the accumulation probability shown in Fig. 7, as the function of neutrino energy. Note, we sum all the neutrino flux and carried out this study.

With this study and the residual of the muon flux at the balloon altitude, we estimate the uncertainty of the atmospheric neutrino flux below 1 GeV is around 15% at 0.3 GeV, and 20% at 0.1 GeV.

References

[1] M. Honda, *et al.* , Phys. Rev, 2004, **D70**, 043008.
[2] M. Honda, *et al.* , Phys. Rev., 2007, **D75**, 043006.
[3] S. Roesler, *et al.* , arXive;hep-ph/0012252.
[4] M. Honda, *et al.* , Phys. Rev., 2011, **D83**, 123001.
[5] K. Niita, *et al.* , Radiat. Meas., 2006, **41**, 1080–1090.

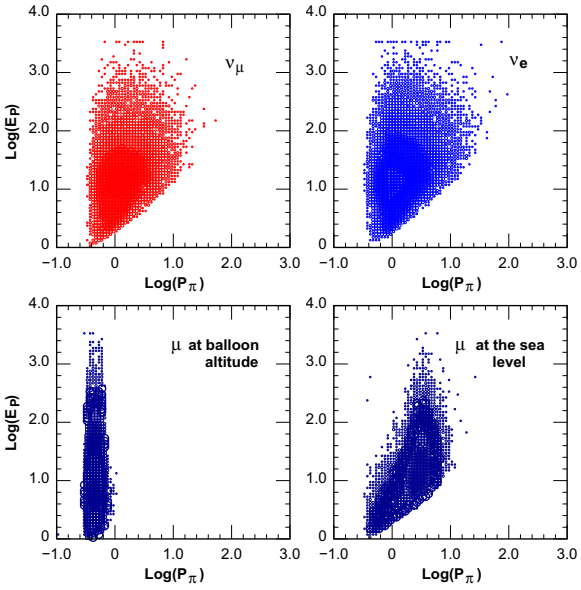

Figure 6: The comparison of the phase space for ν_μ (upper left panel) and ν_e (upper right), and for μ at balloon altitude (lower left). and at the sea level (lower right).

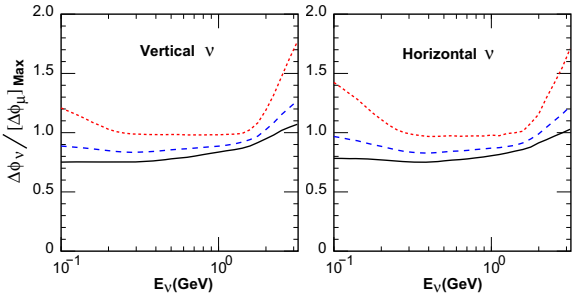

Figure 7: Accumulation probability of neutrino flux variation for 0.9, 0.95, and 0.99 as the function of neutrino energy.

[6] Harp. Collaboration, Astropart. Phys., 2008, **30**, 124–132.
[7] K. Abe, *et al.* , (BESS Collaboration), Phys. Lett., 2003, **B564**, 8–20.
[8] see http://www.ngdc.noaa.gov/IAGA/vmod/igrf.html.
[9] see http://nssdc.gsfc.nasa.gov/space/model/atmos/us_standard.html.
[10] G. D. Barr, *et al.* , Phys. Rev., 2004, **D70**, 023006.
[11] see http://www-pnp.physics.ox.ac.uk/barr/fluxfiles/index.html.
[12] G. Battistoni, *et al.* , Astropart. Phys. 2003, **19**, 269–290.

32ND INTERNATIONAL COSMIC RAY CONFERENCE, BEIJING 2011

The Potential of Spaced-based High-Energy Neutrino Measurements via the Airshower Cherenkov Signal

JOHN F. KRIZMANIC[1,2], JOHN W. MITCHELL[2]
[1]*CRESST/USRA*
[2]*NASA/Goddard Space Flight Center, Greenbelt, Maryland, 20771 USA*
John.F.Krizmanic@nasa.gov
DOI: 10.7529/ICRC2011/V04/1331

Abstract: Future space-based experiments, such as OWL [1] and JEM-EUSO [2], view large atmospheric and terrestrial neutrino targets. With energy thresholds slightly above 10^{19} eV for observing airshowers via air fluorescence, the potential for observing the cosmogenic neutrino flux associated with the GZK effect is limited. However, the forward Cherenkov signal associated with the airshower can be observed at much lower energies. A simulation was developed to determine the Cherenkov signal strength and spatial extent at low-Earth orbit for upward-moving airshowers. A model of tau neutrino interactions in the Earth was employed to determine the event rate of interactions that yielded a tau lepton which would induce an upward-moving airshower observable by a space-based instrument. The effect of neutrino attenuation by the Earth forces the viewing of the Earth's limb to observe the ν_τ-induced Cherenkov airshower signal at above the OWL Cherenkov energy threshold of $\sim 10^{16.5}$ eV for limb-viewed events. Furthermore, the neutrino attenuation limits the effective terrestrial neutrino target area to $\sim 3 \times 10^5 km^2$ at 10^{17} eV, for an orbit of 1000 km and an instrumental full Field-of-View of 45°. This translates into an observable cosmogenic neutrino event rate of $\sim$1/year based upon two different models of the cosmogenic neutrino flux, assuming neutrino oscillations and a 10% duty cycle for observation.

Keywords: Neutrino, Space-based Measurements, UHECRs, Cherenkov, Simulations

1 Introduction

Future space-based air fluorescence experiments employ wide field-of-view optics from a orbiting platform(s) to monitor a vast amount of the atmosphere. For the OWL (Orbiting Wide-angle Light Collectors) mission, the mass of the viewed atmosphere corresponds to more than 10^{13} metric tons (mtons). The design choices for OWL were driven by the goal to measure the UHECR spectrum, via the air fluorescence technique, with high statistics above $\sim 10^{19}$ eV. Studies indicated that the ability to measure neutrino interactions in the atmosphere via the air fluorescence signature exists, but the predicted event rate based upon cosmogenic neutrino flux models [3] is $<$ 1/year (assuming a duty cycle of 10%) due to the paucity of neutrino flux above 10^{19} eV. Furthermore, the neutrino event rate quickly diminishes as the energy threshold becomes further away from the $\sim 3 \times 10^{19}$ eV threshold for full neutrino aperture, which assumes both OWL satellites stereoscopically view each event.

Airshowers also produce an intense, beamed Cherenkov signal. OWL simulation studies indicated that the energy threshold for observing the optical Cherenkov signal form a nadir-viewed, upward-moving vertical airshower initiated by a particle at sea level would be $\sim 10^{15.5} eV$. OWL also views a large terrestrial area: assuming 1000 km orbits and the two OWL satellites are tilted to view a common area, the terrestrial area monitored ranges from 6×10^5 km^2 for a 500 km satellite separation to nearly 2×10^6 km^2 for a 2000 km satellite separation. These vast areas offer a large neutrino target, depending upon the depth that provides a measurable signal. Tau neutrino charged-current (CC) interactions offer a mechanism to exploit this large, terrestrial neutrino target: at high energies, the produced tau lepton has a sufficient Lorentz-boosted length to escape the Earth, decay in the atmosphere, and create an upward moving airshower that could be observed via the Cherenkov signal.

This paper details the calculations used to quantify the sensitivity of measuring the cosmogenic neutrino flux using space-based measurements, assuming the performance defined by the OWL experiment, of the Cherenkov signal created from upward-moving tau neutrino induced airshowers originating in a terrestrial neutrino target.

2 Optical Cherenkov Signal Simulation

In order to determine the optical Cherenkov signal strength and profile at a orbiting instrument, a computer-based simulation was constructed based upon parameterizations described by Hillas [4, 5]. The charged-particle density for an airshower is given by the Greisen parameterization as a function of shower age, with the airshower electron angu-

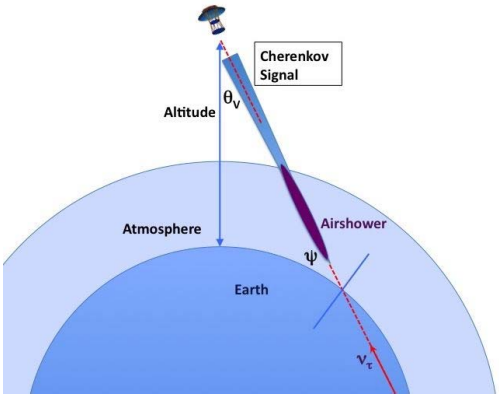

Figure 1: Schematic of the Cherenkov signal generated by an upward-moving airshower induced by a tau neutrino interacting in the Earth.

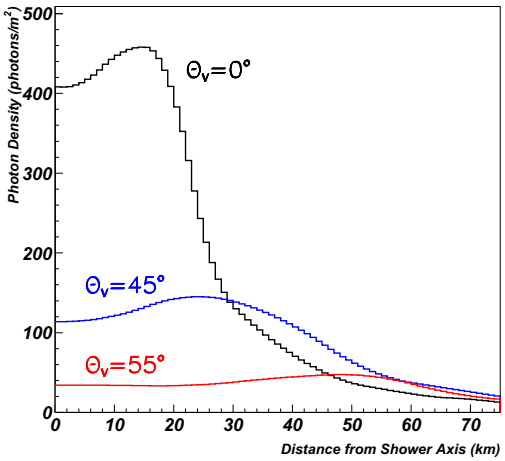

Figure 2: The radial profile of the simulated Cherenkov light density at an altitude of 1000 km for upward-moving 10^{17} eV airshowers viewed at angles of 0°, 45°, and 55°.

lar distribution and the energy-dependent, charged-particle track length fraction defined by well-behaved mathematical functions dependent upon shower age. The index of refraction of air is given as a function of atmospheric grammage, or altitude, which defines the Cherenkov angle and Cherenkov energy threshold. The latter, combined with the charged-particle track length fraction, determines the fraction of the particles in the airshower that contribute to the Cherenkov signal for a given altitude. The atmosphere is described by the Shibata parameterization [6], and the wavelength-dependent attenuation of UV light in the atmosphere is described by a parameterization [7] based upon more detailed models.

The parameterizations are then used to generate the Cherenkov signal at an arbitrary altitude for an upward-moving airshower. The lateral spread of the charged particles in the shower was not considered since this is a small effect for large viewing distances. A 100 m airshower step size was used starting at sea level, and the sampling of the electron angular distribution at each step was $\leq 10^{-3}$ radians. The charged particle track length fractions were sampled in decades of energy for each step, from the Cherenkov energy threshold to a factor of 10 below the total airshower energy. The Cherenkov light was generated at each step from 200 nm to 600 nm in increments of 25 nm, but the effects of ozone absorption, in the atmospheric attenuation model, significantly reduces the signal below ∼300 nm. Two numerical azimuthal integrations were performed: one defined by the Cherenkov angle about the electron angular sampling vector, and the other by angular sampling vector about the shower direction.

The effects of the Earth's curvature were modeled as these become important for viewing angles away from the nadir direction. Figure 1 illustrates the geometry of this effect in relation to an upward moving airshower induced by a tau neutrino interaction in the Earth near the Earth's limb. The Cherenkov airshower simulation accounts for this effect by determined the proper angle, shown as ψ in the figure, at each shower propagation distance step, relative to the viewing angle θ_V. Thus the atmospheric attenuation depth and the distance from the shower and the UV detector in orbit can be accurately determined.

The results of the Cherenkov airshower simulation are shown in Figure 2 for $\theta_V = 0°, 45°$, and $55°$ at an altitude of 1000 km. The curves show the Cherenkov light density (photons/m^2) as a function of radial distance from the projected location of the airshower core in the plane perpendicular to the airshower direction at 1000 km altitude. The form of the curves show that the Cherenkov light cone (illustrated in Figure 1), is approximately uniform in photon density up to a radius which closely corresponds to that defined by the Cherenkov angle at shower maximum and the distance from shower maximum to the measurement. This implies that a good energy resolution can be achieved by sampling the uniform part of the distribution, e.g. by one of the two OWL satellites. The lateral size of the Cherenkov light cone also defines the solid angle: 1.3×10^{-3} steradians for the nadir ($\theta_V = 0°$) case and 1.9×10^{-3} sr for $\theta_V = 55°$, which corresponds to viewing close to the Earth's limb (at an altitude of 1000 km, the Earth's limb is given by $\theta_V \approx 60°$). A comparison of the results presented in Figure 2, after scaling the energy and altitude, are in good agreement (30% difference) with results which employ a full airshower Monte Carlo and more detailed atmospheric attenuation modeling [8].

The factor of ∼10 decrease in the photon density for $\theta_V = 55°$, as compared to the nadir case, is mainly due to the effect of the Earth's curvature. A factor of ∼5 reduction is due to a $1/r^2$ effect (for 0° the distance from 1000 km altitude to shower max is 990 km while it is 2190 km for the 55° case) and a factor of ∼2 reduction is due to atmospheric attenuation of the Cherenkov signal.

The signal strength in an OWL 'eye' is defined by the 3 m optical aperture, the optical transmission, and the quantum efficiency of the focal plane detector. When these are combined, the photo-electron signal strength in an

E_τ (eV)	Depth (km) ($\rho = 1 \frac{g}{cm^3}$)	Depth (km) ($\rho = 2.3 \frac{g}{cm^3}$)	Mass (mtons) for 10^6 km^2
10^{15}	0.05	0.05	1.3×10^{14}
10^{16}	0.5	0.5	1.3×10^{15}
10^{17}	5	5	1.3×10^{16}
10^{18}	29	16	7.6×10^{16}
10^{19}	18	10	4.8×10^{16}

Table 1: The terrestrial neutrino target depth for ν_τ CC interactions, for water and rock targets, and the target mass for 10^6 km^2 for rock as a function of energy.

OWL pixel is approximately the photon density in units of photons/m^2, which unit of the ordinate axis in Figure 2. Thus a Cherenkov signal of 400 photons/m^2 corresponds to a signal in a OWL instrument of $\sim$400 photo-electrons.

3 Cosmogenic Neutrino Rate Determination

For charged-current tau neutrino interactions in the Earth, the target depth is estimated by the propagation distance of the tau lepton: $\gamma c\tau$. At energies above 10^{16} eV, neutrinos and antineutrinos have similar cross-sections for neutrino-quark scattering, and the produced lepton carries $\sim$75% of the incident neutrino energy at 10^{16} eV with the energy fraction increasing to $\sim$80% at 10^{20} eV [9]. $E_\tau = E_\nu$ is assumed for this ICRC paper. At higher energies, catastrophic energy losses (a convenient parameterization is used [10]) limit the effective depth of the neutrino target above $\sim 10^{18}$ eV. Table 1 details the terrestrial neutrino target depth for ν_τ interactions, as a function of E_ν, for both water and rock and calculates the mass for a target area of 10^6 km^2 assuming rock ($\rho = 2.3$ g/cm^3). Note that tau energy losses limit the target depth above $\sim 10^{18}$ eV while the maximum neutrino target mass also occurs at $\sim 10^{18}$ eV.

Assuming a terrestrial neutrino target area of 10^6 km^2, the rate of cosmogenic neutrino interactions that lead to an observable tau-induced, upward-moving airshower via the Cherenkov signal can be calculated by numerically integrating the neutrino flux, cross-section, target mass, ..., with respect to the neutrino energy, and accounting for the solid angle of the Cherenkov signal. Two cosmogenic flux models were used, the Bartol ($\Omega_\Lambda = 0.7$) model [3] and a more recent calculation by Scully&Stecker [11]. The models, both which assume proton dominated UHECRs, provide the electron and muon neutrino and antineutrino fluxes. These were summed for each model and divided by 3 to predict the ν_τ flux, eg assuming neutrino oscillation yields equal flavor fractions at Earth.

Figure 3 shows the results presented as observable events/year per energy decade for the two cosmogenic models, assuming a solid angle of 1.5×10^{-3} sr, a terrestrial neutrino target area of 10^6 km^2 and a 100% duty cycle for the experimental measurement of the Cherenkov signal. The rate prediction based upon the Bartol flux is given by the upper curve while that based upon the Scully&Stecker model is given by the lower curve. An interesting feature is

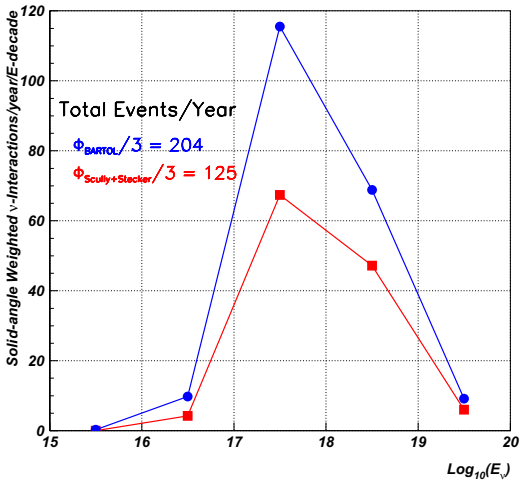

Figure 3: The rate of observable tau neutrino interactions via the airshower Cherenkov signal for two cosmogenic neutrino flux models. The rate is presented in number of events/year per energy decade.

that the event rate does not become appreciable until above 10^{16} eV, indicating that the neutrino target mass, and, to a lesser extent, the neutrino cross-sections, becomes sufficiently large at this energy to yield a significant rate.

While the neutrino rate prediction of > 100 events/year is encouraging, the calculation does not take into account the fact that the duty cycle for observation of the Cherenkov signal is closer to 10% and the Earth is relatively opaque to these energetic neutrinos. This latter point forces the orbiting instrument to view the limb of the Earth to observe airshowers induced by neutrinos with sufficiently short path lengths in the terrestrial target. Figure 4 details the geometry: the orbiting detector must be tilted to view the limb of the Earth, and the effective terrestrial neutrino target is constrained to be no larger than an appropriately short neutrino path length in the Earth.

The problem now effectively becomes one of analytic geometry. The tilt angle of the instrument is defined by its FOV and the angle to the Earth's limb, the calculation of the viewed elliptical area on the Earth's surface is determined by the intersection of the tilted cone defined by the FOV and a sphere of radius 6378 km. The 2-dimensional (eg flat) area of the ellipse can be determined using the conic section relationship between the angle of the plane,

Altitude (km)	Full Area (km^2)	Effective Area (km^2)
500	1.7×10^6	1.6×10^5
1000	3.8×10^6	2.6×10^5
2000	8.9×10^6	3.9×10^5

Table 2: The full and effective viewed surface areas for an 45° FOV instrument, tilted to view the Earth's limb, as a function of altitude. The effective area is constrained by chord equal to the ν interaction length in Earth at 10^{17} eV.

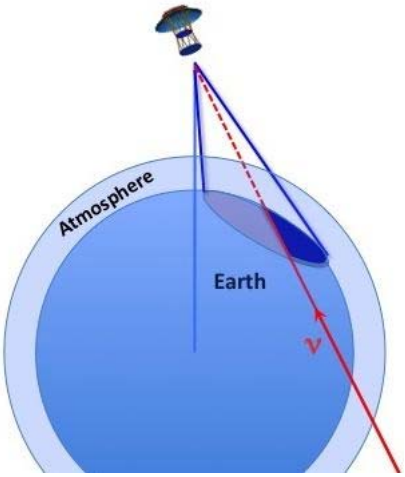

Figure 4: A 2-dimensional schematic of the effective neutrino target area constrained by the ν interaction length. Only those neutrinos with a chord length sufficiently small will be relatively unattenuated by the Earth. While a tilted wide FOV UV imager monitors a large, elliptical area of the Earth, only a small (darkest region) portion samples a significant neutrino flux.

which defines the ellipse in the cone, and the eccentricity of the ellipse [12]. The 2-dimensional area of the viewed ellipse was then increased by 5% to account for the effects of the sphere's (Earth's) curvature. The effective area (darkest area in Figure 4) is defined by the chord whose length is the neutrino attenuation length in Earth, for a particular energy. This describes a truncated ellipse which is inscribed in a rectangle of calculable dimensions. Assuming the truncated ellipse can be approximated by a parabola of similar width, one can use the fact that the area of the parabola is 2/3 that of the bounding rectangle [13] to approximate the area of the truncated ellipse, which is the effective area of the terrestrial neutrino target.

Table 2 presents the total, tilted viewed terrestrial area for an instrument with 45° FOV and the effective neutrino target area at 10^{17} eV, as a function of altitude, determined from the analytic geometrical calculation. While the full area monitored by a tilted instrument is substantial, the effective neutrino target area available near the Earth's limb is reduced by more than a factor of 10, to 2.6×10^5 km^2, assuming a 1000 km altitude.

Combining the energy-dependent effective area results within the numerical integration using the two cosmogenic flux models and assuming 10% duty cycle, the predicted observable tau neutrino event rate is reduced to $\sim$2 event/year using the Bartol model and $\sim$1 event/year using that of Scully&Stecker.

4 Conclusions

Simulation studies of the Cherenkov signal from upward-moving airshowers indicate that an orbiting experiment with a 3 m optical aperture and UV sensitivity of an OWL instrument would have an energy threshold of slightly higher than 10^{16} eV for airshowers generated near the Earth's limb. This is well-matched for tau-induced airshowers generated by cosmogenic neutrino interactions in the Earth. However, the 10% duty cycle inherent for the Cherenkov observation and the Earth's attenuation of the neutrino flux limit the effective terrestrial area, which is estimated to be $\sim 3 \times 10^5$ km^2 for $E_\nu = 10^{17}$ eV, assuming an instrument with a 45° full FOV tilted to observe the Earth's limb. Using two different cosmogenic neutrino flux models, the predicted observable event rate is $\sim$1 event/year. While factor of 2 improvements may be available using different orientations of the two OWL satellites or realizing a gain in the duty cycle, the net effect of these improvements may be balanced by potential decreases caused by more realistic modeling of the energy distribution of the create tau lepton, the airshower generated by the tau decay, and the inherent shower fluctuations.

While the tau-induced airshowers could be observed via the air fluorescence technique, which has a much larger observational solid angle than that inherent to the Cherenkov signal, the higher energy threshold of $\sim 10^{19}$ eV (and a factor of $\sim$10 higher for viewing near the Earth's limb), severely limit the sensitivity to the cosmogenic neutrino flux. This reinforces a similar result from more detailed Monte Carlo studies of the ability of OWL to measure airshowers induced by cosmogenic electron neutrinos in the atmosphere, which predict < 1 event/year. However, if the energy threshold for air fluorescence could be reduced to 10^{18} eV for an OWL-type mission, studies have indicated that the measurable cosmogenic neutrino event rate would be $\sim$50 events/year for the ν_e atmospheric channel, assuming a 10% duty cycle. There could also be a significant observable rate from ν_τ interacting in the Earth observed via air fluorescence, if the energy threshold could be reduced.

References

[1] F.W. Stecker et al., NucPhysB, 2004, **136**: 433-438.
[2] JEM-EUSO Collaboration, M. Bertaina, NucPhysB Proc Sup, **190**: 300-307.
[3] R. Engel, D. Seckel, T. Stanev, PhysRevD, 2001, **64**(9): 093010.
[4] A.M. Hillas, JourPhysG, 1982, **8**(10): 1461-1473.
[5] A.M. Hillas, JourPhysG, 1982, **8**(10): 1475-1492.
[6] T. Gaisser:1990, *Cosmic Rays and Particle Physics*, Cambridge University Press.
[7] J.F. Krizmanic, 26th ICRC (Salt Lake): 1999, 2-388.
[8] D. Kieda, 27th ICRC (Hamburg): 2001, Paper 6407.
[9] Gandhi et al., PhysRevD, 1998, **58**(9): 093009.
[10] S. Palomares-Ruiz, A. Irimia, T. Weiler, PhysRevD, 2006, **73**(8): id 083003.
[11] S.T. Scully, F.W. Stecker, AstropartPhys, 2011, **34**(7): 575-580.
[12] www.mamikon.com/USArticles/CircumSolids.pdf.
[13] Archimedes of Syracuse: 3rd century BC, *Quadrature of the Parabola* ; translation via *The Works of Archimedes*: 1953, ed. Sir Thomas L. Heath, Dover.

HE.2.5: Muon and neutrino tomography

32ND INTERNATIONAL COSMIC RAY CONFERENCE, BEIJING 2011

Density Imaging of Volcanos with Atmospheric Muons

FELIX FEHR[1], for the TOMUVOL Collaboration*
[1] *Clermont Université, Université Blaise Pascal, CNRS/IN2P3, Laboratoire de Physique Corpusculaire, BP 10448, 63000 Clermont-Ferrand, France, *http://www.tomuvol.fr*
fehr@clermont.in2p3.fr
DOI: 10.7529/ICRC2011/V04/0671

Abstract: Their capability to penetrate large depths of material renders high-energy atmospheric muons a unique probe for geophysical explorations. Provided the topography of the target is known, the measurement of the attenuation of the muon flux permits the cartography of matter density distributions revealing spatial and possibly also temporal variations in extended geological structures. A Collaboration between volcanologists, astroparticle- and particle physicists, TOMUVOL, was formed in 2009 to study tomographic muon imaging of volcanos with high-resolution tracking detectors. This contribution presents preparatory work towards muon tomography as well as flux measurements obtained after the first months of data taking at the Puy de Dôme, an inactive lava dome volcano in the Massif Central in south-central France.

Keywords: Volcanos; Atmospheric Muons; Muon Imaging

1 Introduction

Cosmic rays impinging upon Earth interact with atoms in the atmosphere to produce a continuous flux of high-energy, secondary muons. As these muons are, depending on their energy, able to penetrate large depths of material, they can serve as a unique probe for geophysical research.

The idea of using atmospheric muons for probing extended structures is itself not new. In fact, atmospheric muons were used to estimate the snow overburden on a mountain tunnel as early as 1955 [1] and the first archaeological prospection based on muon imaging dates back to the early 1960s, when L.W. Alvarez et al. were searching for hidden chambers in Chepren's pyramid [2].

Today, new particle detectors motivate further studies to exploit the full potential of muon imaging. One of the most exciting applications is the exploration of volcanos [3]; this is pursued by the TOMUVOL Collaboration. Initiated in 2009, TOMUVOL is a common project of particle- and astroparticle physicists and volcanologists who collaborate on the development of a robust, portable system for imaging of volcanos using atmospheric muons. Such a system can complement traditional methods (i.e. gravimetric and electrical resistivity measurements) to improve the understanding of volcanic structures and might also help to reduce volcanic hazards.

The basic idea behind muon imaging of volcanos is that measuring the absorption of the muon flux as function of the direction at a fixed location permits mapping out the average column density in the volcano once the topography is known. By repeating the measurement from different locations, three-dimensional models of the matter density distribution can then be computed. These models will be of great interest to volcanologists, as matter density can readily be interpreted in terms of state and transition.

Presently, the TOMUVOL Collaboration is operating a muon detector at the flank of the Puy de Dôme, an inactive volcanic dome in the *Chaîne des Puys* [4] situated in the Massif Central (south-central France). In the initial phase of the project, muon flux measurements were performed and the data are now analyzed to obtain a first radiographic image. The next phase is dedicated to taking a detailed three-dimensional map of the density distribution in the Puy de Dôme and to validate the results by comparing with gravimetric and electrical resistivity measurements on the same site. In the future, after technical enhancements, the same methodology might be applied to other targets.

In the present paper we report on preparatory work and measurements taken at the Puy de Dôme in the initial phase of the project. In Section 2, the detection site and the experimental setup are described in some detail. Important experimental aspects including detector positioning and track reconstruction are considered. Preliminary results of the first months of data taking are then presented in Section 3. Based on this, we evaluate the prospects of muon imaging in the concluding section.

2 The Experiment at the Puy de Dôme

Detection Site The Puy de Dôme (alt. $1464\,\mathrm{m}$ a.s.l.) is of volcanic origin and was formed some $11,000$ years ago [5].

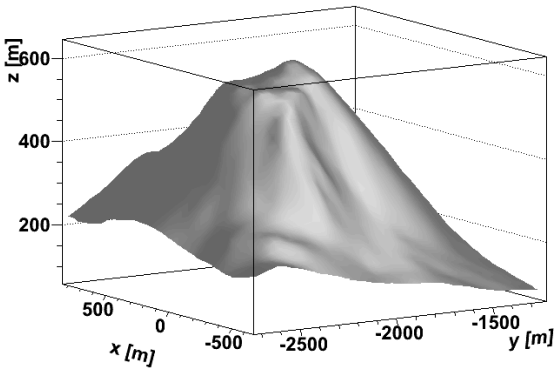

Figure 1: Topography of the Puy de Dôme. The origin indicates the position of the detector during the first months.

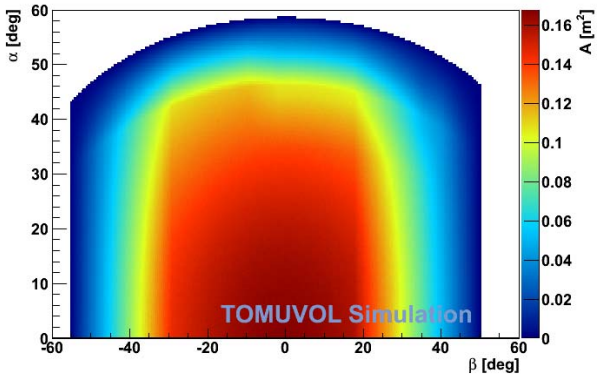

Figure 2: Acceptance of the initial setup ($\mathcal{A} = 0.16\ \mathrm{m}^2$) evaluated with a ray-tracing simulation.

It has a remarkable structure with two domes originating from two subsequent eruptions, which occurred within a short time interval.

For the first radiographic measurements, a muon detector has been installed $600\ \mathrm{m}$ below the summit at a distance of $2\ \mathrm{km}$. The detector has been deployed underground in a basement to reduce the impact of low-energy background. Figure 1 displays the location of the detector and the topography of the surrounding area.

Muon Detector and Data Taking Main requirements on the muon detector are good resolution, low noise, robustness, portability, and scalability at low cost. The TOMUVOL Collaboration has opted for a muon detector based on three parallel planes of Glass Resistive Plate Chambers (GRPCs) [6]. A single chamber consists of two parallel thin glass plates kept at a distance of about $1\ \mathrm{mm}$ using tiny ceramic balls as spacers so that gas can circulate between the plates. The outer sides of the glass plates are coated with a thin layer of highly resistive material on which high voltage, typically $7\ \mathrm{kV}$, is applied. A thin Mylar layer serves as insulation between the anode and a layer of copper cells of $1\ \mathrm{cm}^2$ size assembled on one face of a Printed Circuit Board (PCB) of $50.0 \times 33.3\ \mathrm{cm}^2$. On the other face of the PCB are attached the readout ASICs, named HARDROC2 [7]. In total 48 HARDROC2 ASICs are connected on one PCB, each of them handling 8×8 pads. A full square meter chamber consists then of three slabs, each with two PCBs, having in total 9142 readout channels. The chambers are embedded in steel cassettes and are vertically mounted onto a movable aluminum support framework.

Charged particles, passing through the chambers, ionize the gas and produce charge cascades, which in turn induce charge signals on the copper plates. In its standard configuration, the detector is operated in avalanche mode with high voltage being adapted to environmental pressure and temperature conditions. The gas is a mixture of forane (93%), isobutane (5%) and SF6 (2%) regulated to a total throughput of about $1\ \mathrm{liter/h}$ by a gas distribution system.

For the data readout, Field Programmable Gate Arrays (FPGAs) implemented on the detection slabs are connected via their USB interface to a desktop PC. Three independent comparators in the readout electronics provide amplitude information. In the data-taking mode the ASICs buffer every signal above threshold and send the recorded data upon arrival of a trigger signal generated at $10\ \mathrm{Hz}$ to the PC on which data acquisition and monitoring software are running. Run control and monitoring software have been customized for the experiment based on the cross-platform acquisition framework XDAQ. The whole setup is controlled remotely through a long-range WIFI network. This link is also used to stream the recorded data to a central server. A video camera surveys the installation at all hours.

To protect the electronics against moisture, the detector has been installed under a tent of polyethylene foil. Additionally, a dehumidifier ventilates dry air under the tent. Environmental data (i.e. temperature, pressure and humidity) are recorded every $15\ \mathrm{min}$ and are archived in a data base.

From January to April 2011 data have been taken continuously with two $1\ \mathrm{m}^2$ chambers supplemented by a third chamber of $1/6\ \mathrm{m}^2$ size. The distance between the first and the second chamber was $49\ \mathrm{cm}$, the one between the second and the third, smaller chamber, $9\ \mathrm{cm}$. The geometrical acceptance of this setup, evaluated with a ray-tracing simulation, is shown as function of the altitude α and the azimuth β (measured w.r.t. the direction of the summit) in Fig. 2. During 65.8 days of data taking with the detector pointing towards the Puy de Dôme, 8 million muon tracks from the entire sky have been recorded. (See Fig. 3) The duty cycle in this phase reached almost 90 percent with only a few short interruptions for detector maintenance operations and systematic tests. After April 6th, the detector support framework was upgraded and a third $1\ \mathrm{m}^2$ chamber replaced the small chamber. A framework for a mobile $1\ \mathrm{m}^2$ detector is now under development. In the following, we will focus on the data obtained with the initial detection setup.

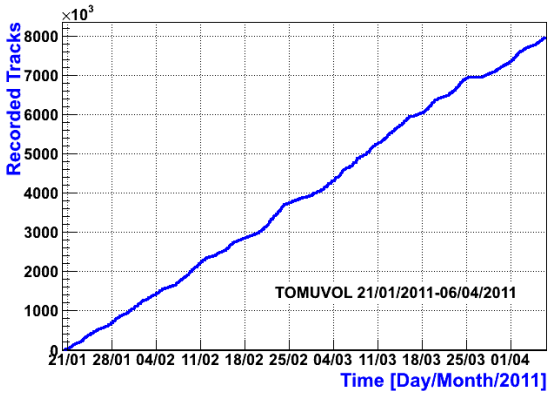

Figure 3: Number of recorded tracks as function of the observation time during the first data-taking phase.

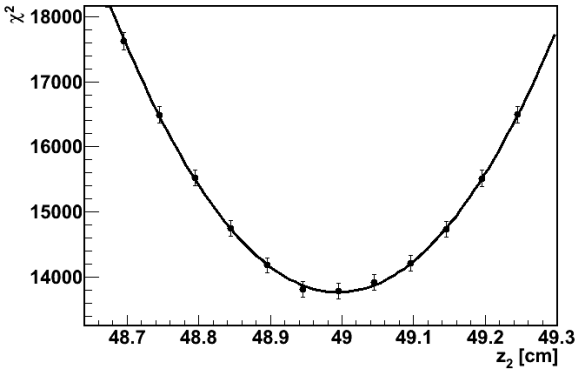

Figure 4: Alignment of the z-position of the second detection plane. The sum of the track χ^2 follows a parabola.

Track Reconstruction The reconstruction algorithm preselects track candidates by considering straight lines between all possible hit combinations in the outermost detection planes in a common time window of $0.4\ \mu$s. These track candidates are then filtered by requiring a matching hit in the central detection plane within a distance of 3 cm to the track candidate. For each selected candidate, hits in a corridor of 3 cm are attributed to the track and merged into hit clusters on each detection plane. The final track is then obtained analytically using the method of least squares. After removal of the selected hits from the time frame, the procedure is iterated to identify and reconstruct possible bundles of charged tracks passing the detector simultaneously. The overall quality of the track reconstruction has been verified by inspecting its χ^2-distribution. The χ^2 is defined by the sum of residuals squared divided by the spatial resolution on a 1 cm^2 cell. Its distribution agrees well with the expected exponential form for a straight line fit on three detection planes with two degrees of freedom. Overall, a position resolution of 0.4 cm and an angular resolution of 0.5 deg in both α and β are achieved.

Terrain Survey and Detector Positioning Accurate topographical data are required to compute density images. In March 2011 the Puy de Dôme and its surroundings were mapped precisely with an airborne LIDAR. In this operation the travel time of the emitted laser beam reflected at the ground has been measured and the altitude was calculated with respect to a GPS antenna aboard the aircraft. Analysis of the recorded data is currently underway and an overall precision of better than 10 cm on a 0.5 m grid is expected to be achieved for the final digital elevation model.

To exploit the potentially available precision, the muon detector has been carefully aligned with respect to the volcano. For this purpose GPS based position measurements of the local surroundings have been made. A reference frame in the basement has been defined by tachymetric measurements through the skylights of the basement. Finally the detection planes were positioned with respect to this frame. Additionally, the alignment of the detection planes has been checked with the help of recorded muon tracks. To this end, the sum of the individual track χ^2s is minimized by varying the alignment parameters. An example of this procedure is given in Fig. 4, where the χ^2 is shown as function of the z-coordinate of the second detection chamber together with a parabolic fit. Even if the procedure is limited as the track χ^2 stays invariant under global rescaling of the coordinate axes, it nevertheless provides an important crosscheck of the detector alignment.

3 First Results

Shadow of the Puy de Dôme With the help of the alignment constants obtained as described above, the arrival directions of the recorded muon tracks are transformed into a global coordinate system whose y-axis ($\beta = 0°$) is pointing towards the summit of the volcano. Figure 5 presents the shadow cast in the flux of atmospheric muons by the Puy de Dôme in this coordinate system. For the flux measurement the measured event rates have been divided by the detector acceptance shown in Fig. 2. This preliminary measurement is based on 65.8 days of data taking with an effective

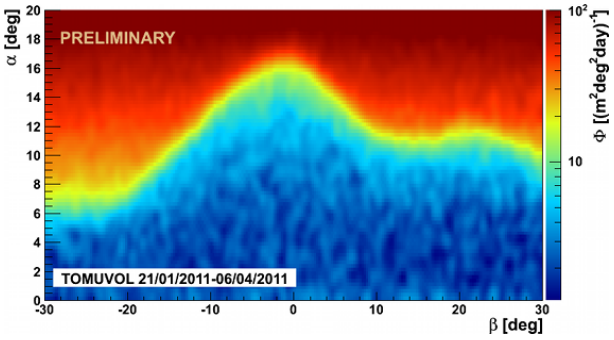

Figure 5: Shadow cast in the atmospheric muon flux by the Puy de Dôme.

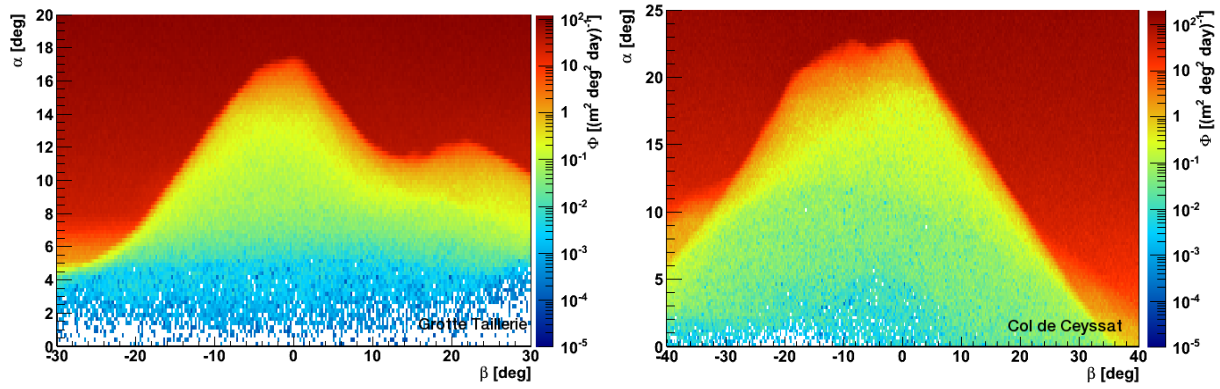

Figure 6: Estimated muon flux through the "Puy de Dôme" assuming an homogeneous rock density of $1.66\ \mathrm{g/cm^3}$ for two different detection sites located at the flank of the volcano. The simulation confirms that the upper part (red, yellow and green regions in the above plots) of the Puy de Dôme will be accessible for muon imaging with an $1\ \mathrm{m}^2$ detector.

detection area of $\mathcal{A} = 0.16\ \mathrm{m}^2$. Note that a smoothing algorithm has been applied to the recorded map in order to reduce artificial bands (Moiré-patterns) typical of digital images. Due to the short exposure time of the data set, the significance of the flux through the volcano is statistically limited to regions close to the surface. The observed shape is in good agreement with the actual outline of the volcano. The full statistics accumulated until July 2011 is currently being analyzed in order to extract the first radiographic density distributions.

Expected Muon Fluxes and Prospects of Muon Imaging
Detailed measurements of the nearly horizontal muon flux as function of the muon energy have been carried out by several experiments (e.g. [8]), so that the atmospheric muon flux spectrum can be considered sufficiently well known. Although systematic effects such as altitude dependence and seasonal variations, which, however, mainly affect the low-energy part of the spectrum, might have to be considered in practice. Thus, by propagating muons according to their physical spectrum through the known topography with dedicated propagation codes (e.g. [9]), reliable estimates of the residual muon flux can be derived.

The resulting estimates of the residual muon flux through the Puy de Dôme at two different detection sites at the flank of the volcano are shown in Fig. 6. Note that those distributions are based on an homogeneous rock density of $1.66\ \mathrm{g/cm^3}$ corresponding to preliminary density measurements on the volcano. As a result, the simulation confirms that the Puy de Dôme will be accessible for muon imaging with an $1\ \mathrm{m}^2$ detector.

Besides flux estimates, the simulation also provides a means to measure density distributions. Indeed, only detailed knowledge of absorption curves as function of the traversed depth derived from the simulation gives access to density distributions. Different approaches to compute the density and the corresponding systematic errors are currently studied and will be subject of subsequent publications.

4 Conclusions and Outlook

The TOMUVOL Collaboration explores tomographic imaging of volcanos with atmospheric muons. For this purpose, a GRPC based detector was installed at the flank of the Puy de Dôme in January 2011. Preparatory work for the computation of a tomographic density map, including a precise topographical LIDAR survey of the volcano, have been performed, and the detector has been carefully positioned w.r.t. the volcano. Algorithms for track reconstruction, detector alignment and image reconstruction have been developed and are now applied to first data.

The detector is now going to be relocated to several more places around the volcano in order to realize a complete, three-dimensional density map. In parallel, comparisons with gravimetric and electrical tomographies will be made. Moreover, technical improvements are on the way to enhance the mobility of the detection setup; this should also facilitate future applications to possibly active volcanos under even more challenging environmental conditions.

From the first data and the performed simulation, we can conclude that muon imaging proves to be a promising technique with interesting applications in the near future.

The TOMUVOL *Collaboration acknowledges support from the University Blaise Pascal of Clermont-Ferrand, CNRS, Région Auvergne, Conseil Général du Puy-de-Dôme. We also thank Mr. Dreher, owner of the Grotte Taillerie du Puy-de-Dôme, who kindly hosted the* TOMUVOL *detector for seven months.*

References

[1] E.P. George, Commonwealth Engineer (July 1955), 455
[2] L.W. Alvarez et al., Science 167, (1970), 832
[3] K. Nagamine et al., Proc. Jpn. Acad., Ser B 80 (2004), 179
[4] P. Boivin et al., Volcanologie de la Chaîne des Puys, 5th ed. (2009)
[5] D. Miallier et al., C.R. Geoscience 342 (2010), 847-854
[6] I. Laktineh, Journal of Physics, Conf. Ser 160 (2009), 012030
[7] N. Seguin-Moreau, Proc. of TWEPP Prague (2007) and IEEE Hawei (2007)
[8] S. Matsuno et al., Phys. Rev. D 29 No. 1, (1984)
[9] D. Chirkin, W. Rhode, arXiv:hep-ph/0407075v2

Searching for cavities in the Teotihuacan Pyramid of the Sun using cosmic muons

S. AGUILAR[1], R. ALFARO[1], E. BELMONT[1], R. CADENA[1], V GRABSKI[1], T. IBARRA[1], V. LEMUS[1], L. MANZANILLA[2], A MARTINEZ-DAVALOS[1], A.MENCHACA-ROCHA[1], M. MORENO[1], AND A. SANDOVAL[1].
[1]*Instituto de Física, Universidad Nacional Autónoma de México México*
[2]*Instituto de Investigaciones Antropológicas, Universidad Nacional Autónoma de México México*

menchaca@fisica.unam.mx, grabski@fisica.unam.mx
DOI: 10.7529/ICRC2011/V04/1117

Abstract: The Pyramid of the Sun, at Teotihuacan, Mexico, is being searched for possible hidden chambers, by means of muon attenuation measurements inside the pyramids volume. The muon tracker is located in a tunnel, running below the base and ending close to the symmetry axis of the monument. This study presents a brief description of the experimental technique and data analysis, as well as a comparison of the first year preliminary experimental results with physics simulations using GEANT4.

Keywords: Cosmic muons, muon radiographi

1 Introduction

The use of cosmic muons to measure inhomogeneities in large volumes is a rapidly growing field. A classical example of this was the experiment carried out by Luis Alvarez et al. [1] who measured the attenuation of cosmic muons in the mass of the Keops Pyramid, in Giza, Egypt, while searching for hidden empty chambers. Although this technique has been applied to other practical problems, few archeological monuments present the necessary conditions to carry out a muon attenuation inspection of its volume. Among those exceptions is in the Mexican Pyramid of the Sun at Teotihuacan, hereafter referred to as Pyramid of the Sun. In a previous presentation [2] in this conference series, we described a project aimed at solving important archaeological questions concerning the Sun at Teotihuacan, using muon attenuation. Here we present an update on this project, which began its data-taking few months ago, including important experimental aspects, and details of the corresponding GEANT 4 Monte Carlo [3] simulations which are compared with our first experimental image.

2 Experimental setup

The instrumental array (Fig. 1) consists of four 1m x 1m scintillator planes ($SC1, SC2, SC3\&SC4$), for muon identification and background-radiation rejection, and six MWPCs (also having a 1m x 1m sensitive area) for muon-tracking purposes. The plastic scintillators used were 1.5 cm-thick BC404 read on two opposite its extremes using 1 m x 1cm x 1cm BC484 wavelength-shifting bars (WLSB),

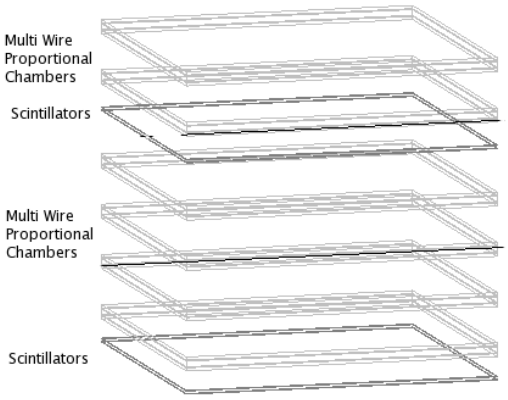

Figure 1: Detector schematic view.

each coupled to photo-multiplier PMT XP2802 tubes on one of its extremes. The other WLSB-extreme was covered with a thin aluminum sheet for light- reflection. Two of the scintillator planes ($SC1\&SC2$), contained in light-tight aluminum boxes, were placed at the bottom of the detection system, while the other two were placed just below the upper-most MWPC, for solid-angle maximization purposes. The registration efficiency is fairly independent on the position of the surface of each plane and is larger than 95%. The usage of 4 scintillator planes allows the estimation of absolute trigger efficiency. The 200-wire MWPC anode was read using the delay-line method with a $4ns$ pitch, using standard copper-layered circuit-board sheets

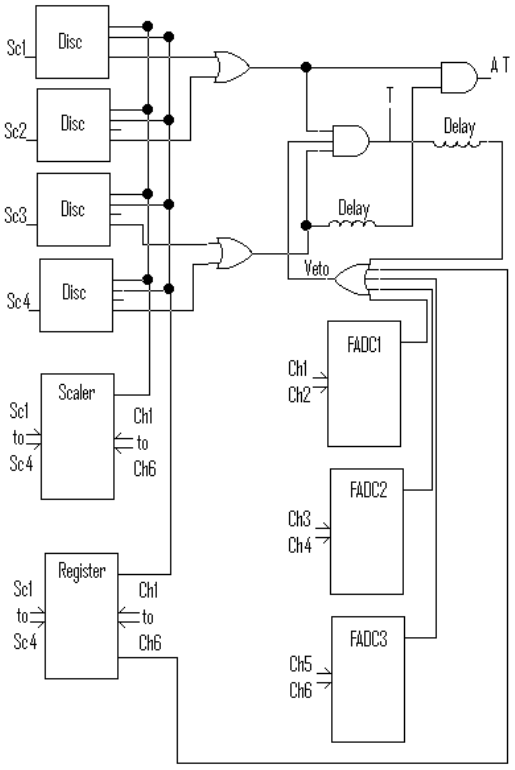

Figure 2: DAQ Block diagram.

as cathodes, mounted on CNC-machined aluminum frame and Lucite spacers, to guarantee a $5mm \pm 0.5mm$ anode-cathode separation. A fast, low-noise and very high gain $A = 2500$ voltage preamplifier was developed [4] by us for this system. The gas used is a 90% $Ar + 10\%CO_2$ mixture, handled through using manual gas flow regulators and exhaust oil bubblers.

3 Signal processing and DAQ

Standard NIM electronics modules are used to process the scintillator and MWPC signals according to the circuit schematically described in Fig. 2. The data acquisition DAQ trigger was obtained by connecting the fast-logic signals from the two upper scintillators to a fast coincidence unit in OR mode, and similarly for the two bottom ones ($SC3\&SC4$), then requiring a coincidental AND signal between the upper and lower scintillator pairs. The preamplified analogic signals from the two extremes of each MWPC were digitized using CAEN v1729-VME 4-channel 12 bit sampling-flash ADC ($FADC$) similar to one described in [5].

For rapid off-line efficiency-monitoring, all 12 $MWPC$ signals are also processed using commercial constant-fraction discrimination modules, the corresponding logic signals are connected to a (VME) 16 channel fast input-output register and a (VME) 16 channel scalar. Both, the DAQ and the PMT & MWPC HV supplies are remotely monitored and controlled using an internet data-line. Gas pressure and flow is also monitored remotely.

The digitized data processing has been carried out using a single board CPU Concurrent Technology. The read out is synchronized with the trigger interruption. For each trigger 12-bit 12 time spectra from $FADC$, counters bit (with an input output register) and scalar information is reading through VME bus. The trigger time is fixed using CPU Unix time, which is saved for each trigger. The busy signal is organized from the hardware and software buses are unified as OR and have been used to veto the coincidence module performing the trigger. The dead time of read-out is of order of $10ms$. For the few Hz trigger rate will not introduce significant trigger lost. The volume of a week information is about $100Gb$.

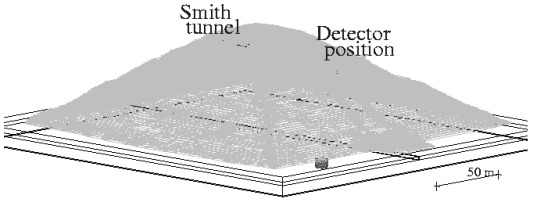

Figure 3: Pyramid volume used in Monte Carlo simulation.

4 Simulation

The muon transport through the body of pyramid is simulated using the GEANT4 Monte Carlo package [3]. The pyramid shape is constructed using an aerial gray-scale photo taken. The contours of equal gray palette in the photo have been digitized and used as the contours of the pyramid shape at a given altitude (see Fig 3). There is also GPS leveling measurements of the gross pyramid structures. Although these measurements are less detailed, so that they and cant be used as a base for the construction of the pyramid shape, nevertheless, they are used to estimate the systematic uncertainties of the used shape. The comparison of these two alternative methodologies shows that for the pyramid gross structures lie within $2m$ of each other. Approximately the same level of error is observed in the estimation of the height of the pyramid. The photographic measurements relative errors depend on the thickness of the lines and are of the order of $1m$. The detector position inside the tunnel is also estimated to be better than $1m$. The orientation of the detector main axis is measured relative to magnetic north pole, and is about 1 degree. Initial muon energy spectrum and angular distribution simulations are performed as in study [6], where the pyramid geometry and other details of the simulations can also be found. The simulation results of the projection angles distribution is presented in Fig 4. This distribution shape is easily correlated to the pyramid gross features. For exam-

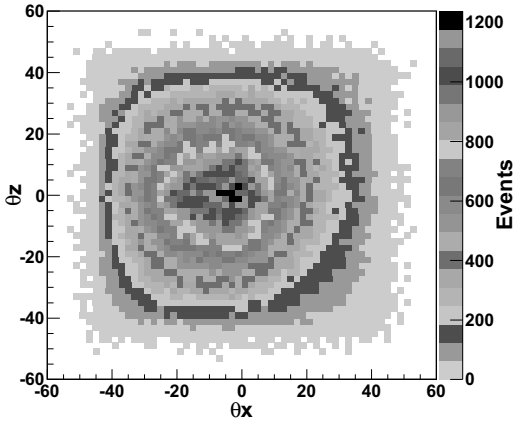

Figure 4: 2D-plot of projection angles from Monte Carlo Simulation.

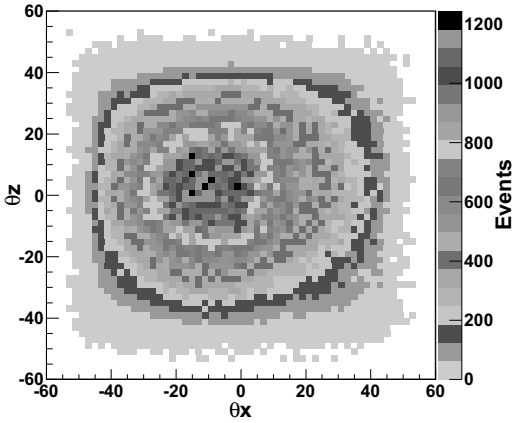

Figure 5: Experimental projection angles 2D-plot.

ple, since the detector location on the z-axes lies close to the pyramids symmetry center, the θ_z-profiles should also show a near-symmetric distribution, reflecting the approximately symmetric shape of the pyramid. The $\theta_x$profile is not symmetric relative to the vertical direction, because the detector is located farther away from the symmetry center in that direction. Another observable which can be used to calibrate the experimental conditions in general is the total trigger rate, which depends on many parameters, such as the pyramid shape and density profile, the detector position, and the muon detection efficiency.

5 Results

The trigger rate was sufficiently stable during the 6-month measurement, being $2.7(\pm 0.05)Hz$, which is close to the Monte-Carlo simulation predictions of 2.62, reflecting that the detector position, pyramid average-thickness and average density, used in the simulations are consistent with the observation. The muon-track coordinate corresponding to each chamber has been estimated by means of the FADC signal shape analysis [4]. For each FADC signal up to 3 timing candidates are considered, and the best pair for each chamber is chosen previously by the total time $(200x4ns = 800ns)$ sum-rule. The tracks have been reconstructed using 2-, and 3-fired chambers conditions for each coordinate. In case of 3-fired chambers, the track is estimated by the linear fit. The shift of the position from the fit for each chamber, have been used to estimate the coordinate resolution as well as the angular resolution. The coordinate resolution is almost the same for all chambers, about $1.0cm$, corresponding to an angular resolution for each projection angle of about 1.1 degree. To be able to compare experimental data with the simulation one should also correct the coordinate dependence of the efficiency of each chamber. The coordinate distributions obtained by the Monte-Carlo simulation have been used for that purpose.

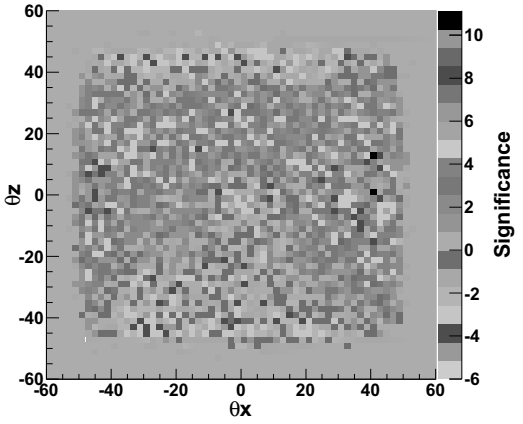

Figure 6: 2D-plot of bin-by-bin difference betweeen simulation and experimental data.

Efficiency-dependent on the zenith angle location corrections need also be included, since the chamber detection process is not included the simulations. This is possible due to the low efficiency of reconstructed tracks $(20 - 30\%)$. Once all those corrections are taken into account for each chamber, the results of two-dimensional plot on projection angles is presented in Fig 5, which is seemingly similar to what is shown in Fig 4, though one can notice a slight difference in the θ_x dependence. Other observables, such as the mean values and the standard deviations are also close to the values in Fig 4. One also can notice a slight difference on the maximum position on the θ_x axes. To make this difference more visible the bin by bin difference of these to distributions is presented in Fig 6, in significance units (defined as bin difference divided on the error of that difference). Probably this large area mass difference on θ_x direction ($\theta_x < -20$ and $\theta_x > 20$) is due to the difference between the assumed pyramid geometry in the simulation and the real one.

6 Conclusions

Progress in the muon attenuation experiment carried out at the Pyramid of the Sun, at Teotihuacan, Mexico, is reported, including experimental and simulation details. After 6 months of data taking, experiment-simulation comparisons show qualitative and quantitative resemblances. Given the limited statistics accumulated so far, it is still early to confirm, or discard, the possibility of a human-size hidden empty cavity within the pyramids volume.

Acknowledgments

Authors acknowledge the partial support from CONACYT grants G39091-E and 131877 as well as PAPIIT-UNAM grant IN115107.

References

[1] L.W. Alvarez et al., Science **167**, (1970) 832.
[2] R. Alfaro et al., Proceedings of the 30th ICRC, Vol. **5** (HE part 2), pages 1265-1268.
[3] S. Agostinelli et al., NIM **A 506**, (2003) 250-303.
[4] J.M. Lpez-Robles et. al. IEEE Tr. Nucl. Sc. **52** (2005)2841-2845.
[5] S. Aguilar et al.,Proc. 1st Intl. Conf. on Intr. and Appl. Sciences, Cancun, Mexico Oct 2010 ID SAI101.
[6] V. Grabski et al, NIM **A 585** (2008) 128–135.

HE.2.6: New experiments and instrumentation

32ND INTERNATIONAL COSMIC RAY CONFERENCE, BEIJING 2011

Fabrication and testing system for plastic scintillator muon counters used in cosmic showers detection

M. PLATINO[1], F. SUAREZ[1], M.R. HAMPEL[1], D.A. ALMELA[1], A. KRIEGER[1], D. GORBEÑA[1], A. KAKAZU[1], F. GALLO[1], A. FERRERO[1], G. DE LA VEGA[1], A. LUCERO[1], M. VIDELA[1], O. WAINBERG[1], A. ETCHEGOYEN[1] AND P. O. MAZUR[2]

[1] *Instituto de Tecnologías en Detección y Astropartículas, (CNEA, CONICET, UNSAM), Av. Gral. Paz 1499 (1650), Buenos Aires, Argentina*

[2] *Fermi National Accelerator Laboratory, Batavia, IL, USA*

manuel.platino@iteda.cnea.gov.ar

DOI: 10.7529/ICRC2011/V04/0008

Abstract: In this paper we present the fabrication, testing and initial calibration system for scintillator modules to be used as muon counters for cosmic ray particle shower detection, developed in the ITeDA facilities. Each muon counter has an area of 30 m^2, divided in three scintillator modules of 10 m^2, and is made of plastic scintillator strips with doped optical fibers glued to them, which guide the light to 64 pixel photomultiplier tubes. Each module is buried to detect only the muon component of the cosmic shower. The scintillator modules are tested with a "scanner" that consists of an $x - y$ positioning system that moves a 5 mCi ^{137}Cs radioactive source over the module taking data at fixed locations. The scanner both tests the module for possible fabrication defects and stores the light-attenuation curve parameters. A complete description and specifications of the fabrication process and materials used for the construction of the scintillator modules is presented. Also, a complete scanning process of a 64 strip scintillator module is performed and results are presented and compared with an initial calibration performed with a muon telescope.

Keywords: Particle detectors, Detector design and construction technologies and materials

1 Introduction

This work presents the fabrication, testing and calibration system of large (30 m^2) muon counters, composed of plastic scintillators used to transform cosmic radiation into light. These detectors are designed to work buried underground to count muons from radiation showers produced in the atmosphere by cosmic rays. Among their many requirements, it is only mentioned here those affecting the mechanical design of the detectors:

- *Number of muon counters:* $\sim$ 85 muon counters are required by the project in which they will be used [1]. Therefore, they must be easy and fast to manufacture, at a production rate of $\sim$ 2 per month.
- *Muon sensitivity:* The muon counters need a shielding of $\sim$ 540 g/cm^2 [1] which means that they must be buried $\sim$ 2.25 m underground (considering local soil density of (2.38 $\pm$ 0.05) g/cm^3 [2]) to provide shielding from the electro-magnetic component of the shower. An access pipe of 1.3 m of diameter used for electronics maintenance will be sealed to the detectors.
- *Detection area:* The optimum design parameter for the determination of the number of muons at 600 m $N_\mu(600)$ (shower muon content estimator) is an area of 30 m^2 divided in 192 segments [3]. Thus, the muon counter is divided in three 10 m^2 scintillator modules of 64 channels each.
- *Lifetime:* Ageing of the components must be seriously considered. Therefore, plastic scintillators were chosen.
- *Modular construction:* The scintillator strips must be assembled into scintillator modules which are easy to handle, relatively rugged to resist the deployment, and provide light-tight and water-tight seals.
- *Cost and transportation:* To minimize cost, PVC (Polyvinyl Chloride) was chosen for the module casing. The mechanical design of the modules must allow the usage of regular trucks for transportation to avoid a sensible impact on the costs, since distances larger than 1000 km must be covered for their deployment.

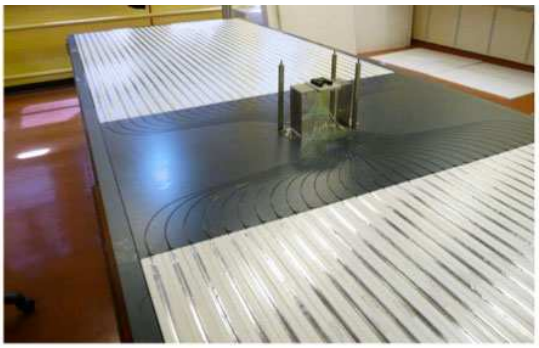

Figure 1: Picture of a module being fabricated. Shown are the 64 scintillators split in two groups of 32, with an optical connector for the PMT in the middle.

2 The scintillator modules

2.1 Scintillation system

The scintillator modules being described in this work are composed of 64 extruded plastic scintillator bars with a 41 mm $\times$ 10 mm rectangular cross section and 4 m length. The bars have a white reflective outer layer of titanium dioxide (TiO_2) and a groove, without the TiO_2 layer, into which a wavelength-shifting fiber is glued with optical cement to match the refraction indexes. The groove is covered with a reflective aluminium tape to seal the reflective properties of the scintillator. The attenuation length of the extruded scintillator bars is ($\sim 55 \pm 5$) mm (with the TiO_2 layer), therefore the light pulses must be transported to a photomultiplier tube (PMT) using an optical fiber.

The fibers chosen for the scintillator modules are 1.2 mm rounded Saint-Gobain BCF-99-29AMC multi-clad fibers. They have the same dopant as the BCF-92 fibers (the standard model catalogued by Saint-Gobain) but at twice the concentration. These fibers have maximum light absorption and emission at 410 nm and 485 nm respectively [4], while the scintillators emit light at $\sim$ 400 nm. Then the light pulses are converted into electronic pulses through a PMT (64 channels Hamamatsu UBA H8804-200MOD) which has a quantum efficiency large enough at $\sim$ 485 nm ($\sim 30\%$, [5]) for this application. An alignment system between the 64 fibers and each of the PMT's 64 pixels is required to minimize the light attenuation and cross talk in the fiber to PMT transition boundary.

2.2 Modules mechanical design and fabrication

Since the scintillator strips are about 4 cm wide and 4 m long each, it was decided to split the module in two sections of 32 channels, with the holding structure for the PMT in the middle (see Figure 1). This design has the advantages of a cheaper transportation, less optical fiber wastage due to a reduced path between the farther scintillator and the PMT in the middle of the module, and easy access to the modules for maintenance after deployment because the module itself can be used as an access platform for the technicians. This is possible because the PMT sits in the middle of the module and not aside of it.

The connection between the optical fibers and the PMT is made through a black Polyoxymethylene (POM) optical connector, which holds the 64 optical fibers. This connector is placed at the center of the module and it is held with a stainless support that gives it a 1 cm freedom of movement for correct coupling with the PMT. The connector is directly attached to the PMT, which is fixed to the modules through a couple of springs to hold the connector to the PMT with a certain pressure. The roughness of the plastic surface on each fiber termination is minimized with a diamond polishing tool mounted on a fly-cutter. Optical grease (BC-630 from Saint-Gobain) is applied to the PMT window to minimize reflections. The module casing is mainly formed by a PVC frame made of 1 cm $\times$ 4 cm section bars, closed with 2 mm thick extruded PVC sheets. All of the module PVC pieces are custom-made (cut and/or soldered) from extruded PVC bars, sheets, and tubes (for the electronics dome in the middle of the scintillator module). PVC was chosen because it is cheap, easy to mechanize and to solder. The manufacturing process of all the pieces that compose the module (see Figure 2) is mainly automated by using a 2 m $\times$ 3.5 m CNC milling machine. The electronics dome (Figure 2, right) is built in two pieces. The lower one is fixed to the PVC casing and provides the exit for the cabling and the protection for the optical connector. The higher piece of the electronics dome is removable and provides access for electronics maintenance or replacement. Both parts of the dome are sealed together with a rubber O-ring to provide water and light tightness.

The assembling of the module casing and the scintillators is mostly performed manually, and all of their components are glued together to conform a big solid plastic piece. Of all the critical manufacturing processes, the fiber handling and the gluing process are the most critical ones. Fiber damage and non-uniformity in the application of the optical cement must be avoided. Also, the gluing of the PVC pieces of the module casing requires extreme care to ensure the water-tightness of the scintillator module, which is verified through a pneumatic testing procedure before the module is delivered.

The modules are handled during transportation and deployment with a steel hanger structure that holds the module in 24 points along its top surface throughout 4 "U" profiles (see Figure 2, left panel). The module is surrounded by polystyrene foam sheets in order improve its resistance to bumps and sunlight exposure during transportation and deployment.

3 Testing

The module testing and calibration requires measuring the mean single photoelectron (SPE) number produced by an

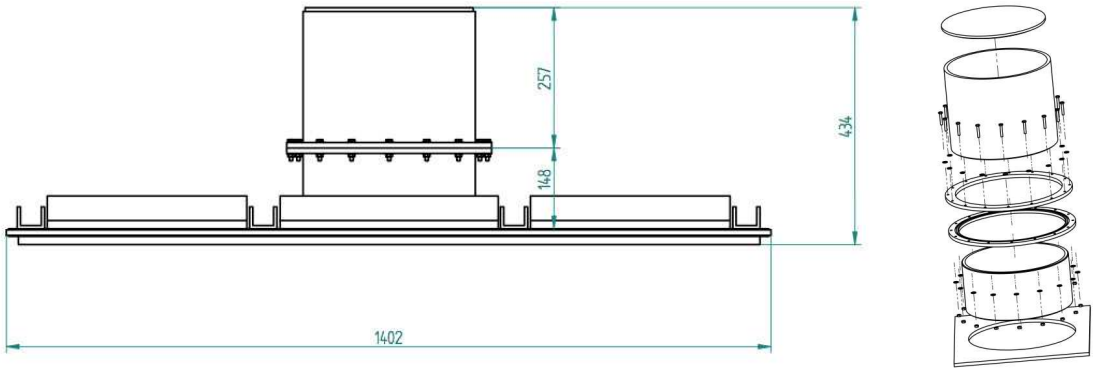

Figure 2: Blueprints of the PVC casing of the scintillator modules. Left: Longitudinal cut. Right: Electronics dome.

impinging particle (in this work, from the background cosmic radiation) on each of the 64 scintillator strips at a given distance from the PMT, i.e. the light-attenuation curve.

3.1 Module testing system: The scanner

The response of each scintillator strip can be characterized with a 5 mCi γ-emitter ^{137}Cs radioactive source contained on a lead cylinder mounted on a $x-y$ positioning system or "scanner". The cylinder acts as a shielding according to safety regulations and provides collimation for the radiation beam. The $x-y$ positioning system has a total effective displacement of 3.75 m in the x axis and 9.5 m in the y axis, motorized with two stepping motors. An electrical current is produced in each PMT channel, as it is generated by the the flow of light coming from the scintillator bars through the fibers, excited by the radioactive source at different points along the scintillator bars. This current is obtained by averaging the total current value of all the SPE pulses, and is transformed to voltage via a circuit that measures the voltage drop on a 220 $k\Omega$ resistor. The testing system has an acquisition board that measures the DC current generated in each of the 64 pixels of the PMT. The current values do not provide an absolute magnitude of the SPE number, but they do provide a much faster measurement of the light-attenuation curve if we complement the current measurement with a SPE coincidence measurement at a single chosen position, in a preliminary calibration of the scanner using a muon telescope. The variations in gain between electrical channels of the PMT [6] and the current to voltage converter hardware [7] must be taken into account.

3.2 Scanner calibration

To calibrate the scanner, an ad-hoc designed muon telescope [7] via a time-coincidence experiment is used. A charge histogram is produced at specific points along the scintillator bar and divided by the corresponding gain measurement for each PMT channel (and by the mean SPE charge) in order to determine the number of SPEs of each

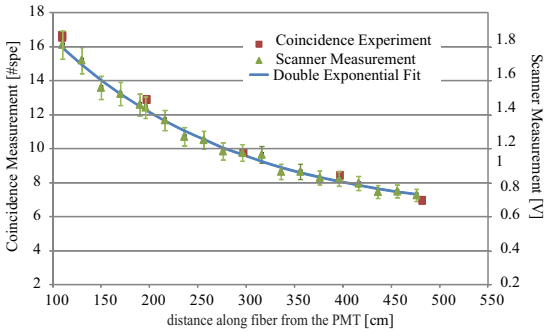

Figure 3: Superposition of the number of SPEs measured with the muon telescope together with scanner measurements on the same scintillator-fiber-PMT set up. The x axis is distance along the fiber from the PMT, the y axes are signal amplitudes measured in SPE for the coincidence measurements and volts for the scanner measurements. Figure adapted from [7].

coincidence event. This number is recorded for each position along the main scintillator bar and a light-attenuation curve is thus obtained which acts as a reference for the measurements to be performed with the radioactive source. The whole setup is assembled separately from the module for one bar, and is placed in a dark box.

To verify that the scanner calibration method as proposed is viable, we need to compare the measurements of the muon telescope with the scanner measurements of current taken on the same scintillator-fiber-PMT set up. The results of these measurements, along with the ones of the muon telescope are shown in Figure 3. This figure shows a clear agreement between scanner and muon telescope measurements. Included in the plot is the double exponential fit performed using the measured data with the muon telescope (see eq. (10) in [8]). The middle point, at distance 295 cm from the PMT was picked arbitrarily and used as a reference to match the tendency curve produced by the muon telescope measurements with the scanner measurements, for a relative calibration. The rest of the data set follows the same tendency of the double exponential fit, either for

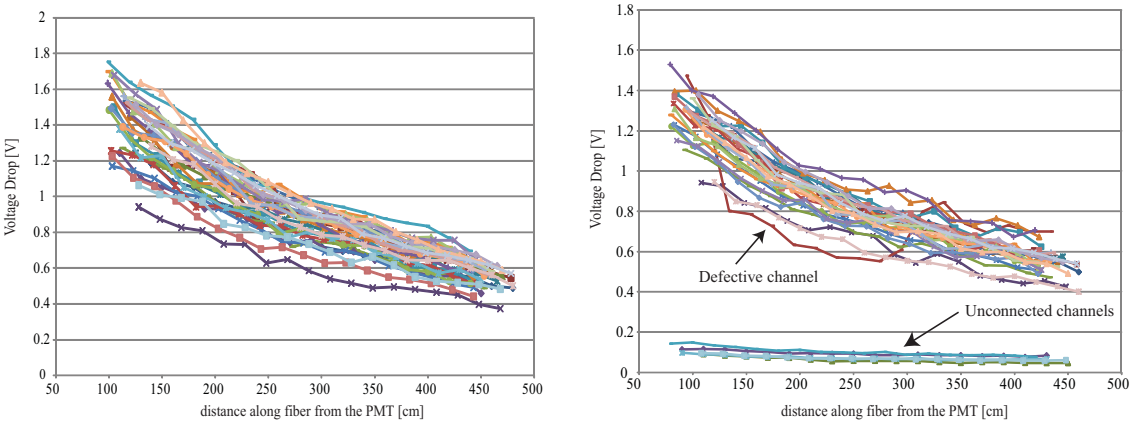

Figure 4: The left panel shows the scanning results for the first 32 channels of the scintillator module tested. The 32 curves are superimposed, one for each channel. The right panel shows the measurement results for the second 32 channels. The y axis is a voltage drop. The x axis is the distance along the fiber from the PMT to the point of radiation. Figure adapted from [7].

the SPE measurements or the voltage measurements validating our scanner method.

3.3 Scanner measurement results

The scanning was performed in the 9 m long by 1.4 m wide scintillator module shown in Figure 1. Results are shown in Figure 4, which reveal significant variations between channels. The main factors that may produce these variations are: i) The fiber, which can produce these discrepancies if one is broken or if there are inhomogeneities in its fabrication. ii) The scintillator, the same argument mentioned for the fibers also applies to the scintillators. iii) The PMTs quantum efficiency. The gain non-uniformity was compensated in the plots of Figure 4, leaving only quantum efficiency variations from one pixel to the other as a possible source of variations from the PMT. iv) Deficiencies in the fabrication of the scintillator module, which can affect the collection of light from the scintillator to the PMT: defects on the fiber-scintillator gluing process, erroneous focalization in the optical connector from the fiber to the PMT due to displacement of the whole set with respect to the pixels, or defectively applied optical grease.

Module manufacturing defects can be studied in greater detail if we look at channel 40 (in the right panel of Figure 4 channel 40 corresponds to the highlighted line), where a significant drop in current in the intermediate points along its corresponding scintillator bar can be clearly seen. This fact points to a possible defect in the application of the optical cement for that particular channel, as mentioned in iv) above. Also, there are 5 channels that show a very low signal (see right panel). These channels are not broken but they were left intentionally unconnected to scintillators in order to debug the muon counters emulating different field conditions that might affect the future module design.

4 Summary

The fabrication process of the plastic scintillator modules, as well as their testing and a laboratory calibration system has been outlined. The materials used for their fabrication, their mounting and mechanical design is provided. A testing system is described that provides a reliable and fast way to detect defects in the fabrication process. The agreement between the light attenuation tendency curves generated by background muons measurements and the scanner measurements validates the testing procedure and improves the knowledge of the module behavior.

References

[1] M. Platino for the Pierre Auger Collaboration, Proc. 31^{st} ICRC (Łódź-Poland), 2009, 5: 14-17.

[2] B. Wundheiler: 2010, Caracterización de un Prototipo de Contador de Muones para AMIGA, bachelor's degree thesis, Universidad de Buenos Aires.

[3] D. Supanitsky *et al.* , Astroparticle Physics, 2008, 29: 461-470, (doi:10.1016/j.astropartphys.2008.05.003).

[4] Saint-Gobain Ceramics and Plastics Inc.: 2005, Scintillation producs, scintillating optical fibers specification datasheet.

[5] Hamamatsu Photonics K.K.: 2008, UBA (Ultra Bialkali) and SBA (Super Bialkali) photomultiplier tube series specification datasheet.

[6] F. Suarez *et al.* , Proc. 32^{nd} ICRC (these proceedings, Beijing-China), 2011, #20.

[7] M. Platino *et al.* , Journal of Instrumentation, 2011, *In print*, (JINST 016P 0311).

[8] F. Sánchez and G. Medina-Tanco, Nuclear Instruments and Methods, 2010, **A**(620): 182-191, (doi:10.1016/j.nima.2010.03.110).

32ND INTERNATIONAL COSMIC RAY CONFERENCE, BEIJING 2011

A Fully Automated Test Facility for Multi Anode Photo Multiplier Tubes

FEDERICO SUAREZ[1], AGUSTÍN LUCERO[1], ALBERTO ETCHEGOYEN[1], ALEJANDRO ALMELA[1], CARLOS REYES[1], DAMIÁN ALONSO[1], EMMANUEL PONSONE[1], FEDERICO BARABAS[1], GONZALO DE LA VEGA[1], MARIELA VIDELA[1], MANUEL PLATINO[1], OSCAR WAINBERG[1]

[1]*ITeDA: Instituto de Tecnologías en Detección y Astropartículas (CNEA-CONICET-UNSAM), Av. Gral Paz 1499 (1650) Buenos Aires, Argentina.*

federico.suarez@iteda.cnea.gov.ar

DOI: 10.7529/ICRC2011/V04/0020

Abstract: Multi-anode photo multiplier tubes (PMT) are commonly used in astroparticle physics observatories as well as in other applications. They need to be automatically tested when they are to be used in large numbers. Such a test facility has been developed to evaluate multi-anode PMTs. The facility, located at ITeDA in Buenos Aires, is capable of fully testing a 64 pixel PMT per day. It automatically measures the following parameters for each pixel: gain, dark pulse rate, single photoelectron distribution, and cross-talk. The test system is able to perform all relevant data analyses both in pulse amplitude and/or charge. It can also make uniformity plots of relevant parameters for all pixels. Using this facility, ultra bi-alkali PMTs have already been tested and evaluated. The test results and the schematics of the test system are presented in this work.

Keywords: test system, multi-anode, photo multiplier tube, PMT, UBA, ultra bi-alkali, cross-talk, spe, darkpulse, gain, 64 pixel, multi-pixel

1 Introduction

The test facility, located at ITeDA (Instituto de Tecnologías en Detección y Astropartículas), Buenos Aires, Argentina, was originally developed in order to automatically test large numbers of different type of photo multiplier tubes (PMTs). However, the test setup is currently tuned to perform multi-anode PMTs testing due to the current scientific projects in which this facility is involved. The system is currently dedicated to characterize and ensure the quality of Hamamatsu H8804-200MOD PMTs for the enhancement project called AMIGA (Auger Muons and Infill for the Ground Array) [1] of the Pierre Auger Observatory. These PMTs have a built-in R7600 64 channels PMT, ultra bi-alkali (200) photocathode, standard polarization chain (like the one for the H7546), and a special casing for alignment purposes (MOD).

The PMTs are generally tested for different reasons depending on the phase of the projects in which they are used. In this case, the aim is: 1) to characterize certain parameters of the PMTs which have incidence on the design and simulation [2] of the particle detectors where they will be used, 2) to have a better idea of the capabilities of such PMTs, and 3) to accomplish the quality assurance plan of the project.

Testing the 64 channels of a PMT automatically is a challenging job since it is like testing 64 PMTs at the time, so it requires novel means to manage the 64 output signals and to perform the automatic control of individual light injection to the 64 pixels. Furthermore, due to the testing requirements of different projects, the knowledge of different parameters of the signals is required such as the signals peak, area, rise-time, fall-time, etc. Thus, the test system must be able to sample the traces with fast digitizers (i.e. very fast ADCs, analog to digital converter boards) instead of just sensing the signal charge by using QDCs (charge to digital converters). The sampling data acquisition system imposes a very delicate treatment of many signals to avoid any external and internal interferences (described in the following sections). This last characteristic makes a big difference in increasing the capabilities of the system in respect to other automated PMTs test facilities, such as the one at the Pierre Auger Observatory [3] which inspired this work.

Finally, testing multi-anode PMTs has an additional difficulty compared to test regular PMTs. It requires to have an alignment system to match the light source to the corresponding pixel, to be able to perform the light-injection to different pixels of the PMT independently. The accuracy of the alignment system must be of hundredths of mm otherwise, very important tests such as cross-talk (described later) cannot be performed.

2 Test Facility

2.1 Setup

As shown in fig. 1, the test system setup is currently tuned to test one 64 pixels PMT at a time. The light-proof facility is performed with "dark-boxes" due to the fact of the reduced size of the H8804 PMTs. The external dark-box provides the required optical shielding and the interlock system to automatically shut down the high voltage for safety reasons.

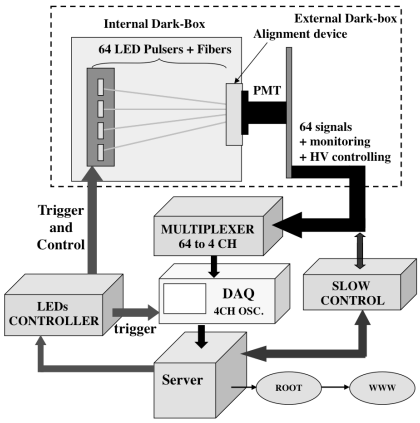

Figure 1: Simplified test system setup for multi-anode PMTs.

The light source is made out of 64 blue LED pulsers with individual intensity controlling. The LED pulsers are suitable due to the lack of timing tests requirements. Nevertheless, in order to fulfill the testing requirements for XT (cross-talk), the light pulses are carried through green WLS (WaveLength Shifter) optical fibers which have an emission wavelength peaked at ∼500 nm. The fibers are provided by Saint-Gobain, like the ones used in the particle detectors where the PMTs are going to be used. The complete light source (the 64 pulsers and optical fibers) are optically shielded with an internal "dark-box" to avoid direct exposure of the PMT to the LED pulsers. Besides, each optical fiber is covered with an optical absorber to avoid any possible optical XT between the fibers.

The DAQ (Data Acquisition) system is based on a 4 channels oscilloscope (a Tektronics DPO7014, 1 GHz and 5 GS/s), because it is very versatile and provides several advantages to perform manual testing in case of need. However, it was needed to introduce a 64 to 4 analog multiplexer since the PMT has 64 output signals and the oscilloscope is a 4 channel digitizer. This multiplexer has been custom designed at ITeDA so any of the 64 inputs can access to any of the 4 outputs, with an analog bandwidth up to 1 GHz. Besides, as part of the facility EMC design (Electromagnetic Compatibility), special care was taken when designing this multiplexer to avoid introducing either XT between the signals or any interference.

Due to the the location of this facility, handling high frequency and low level signals is not trivial because the radio broadcasting is very crowded in the region, and generates a big EMI (electromagnetic interference). Besides, good cabling shielding is needed to avoid any capacitive/inductive interaction between the signals. Thus, following the system EMC design, the cabling for signals carriage is performed with high quality 50 Ω coax-cables with improved shielding and high density polystyrene core to reduce the signals attenuation. Gold plated connectors are used for all the signal cabling connections.

The signals extraction of the H8804 PMT is not trivial either, because the 64 outputs are concentrated in a ∼2 cm × 2 cm array and must feed the 64 coax cables. This operation is performed through a 4 layer custom designed board (called socket board) that also supplies the HV to the PMT, and extracts some monitoring parameters from the system. Again, this board has an special design to provide good EMC.

The complete transmission lines from the PMT output to the oscilloscope input (socket board, cables and connectors, and multiplexer) were characterized with a vector network analyser, and the transmission parameters are used to compensate the signals measured by the oscilloscope. Thus, all the results plotted by the system are equivalent to the results that would be obtained right at the output of the PMT.

2.2 Methodology

First, the PMTs must be aligned to the optical fibers before being able to test the PMTs. This alignment must be very precise because the optical fibers have a diameter of 0.8-1.2 mm (depending on the type of detector being manufactured) and the pixel size of the H8804 PMTs is 2 mm × 2 mm. Any deviation in the alignment may lead to a wrong XT measurement. Thus, the alignment of the PMT to the fibers is performed in the same way than the alignment of these PMTs to the AMIGA detector [4], i.e. by using a floating plastic piece (called "cookie") which holds the optical fibers. The cookie has two fixed holes that match up with two metal pins inserted into the wings of the PMT case (special case that gives the MOD characters to the PMT name). The metal pins are previously fixed in the correct place with respect to the dynode assembly of the PMT through the usage of a high definition camera and a micro-meter 3 axes (x-y-w) positioning system.

Thus, the PMT testing procedure consists of the following steps:

1. Align the PMT to the cookie that holds the optical fibers.
2. Connect the PMT into the testing dark-box.
3. Wait until the PMT cools down and gain stabilizes. Currently, it is decided to wait about 24 hs. for all the PMTs because we know that it is long enough even

for some atypical PMTs, and because the amount of PMTs being tested in not large so far. However, this step can be automatically monitored by the system and the waiting period can be adjusted automatically for each PMT.

4. Run the tests. The testing period depends on which tests are performed, but it generally takes between 12 to 24 hs. for the 64 channels. The testing period requires absolutely no human intervention.

5. An operator analyses the monitoring parameters and the test results, and approves the test or re-runs it if needed. Some of these analyses can be performed automatically but specification limits are being defined to better set the rejection criteria.

6. Complete the database with the test results. Even if the system stores most of the data analysis plots, test system monitoring variables, timestamps, etc., the operator must complete a database with the test results and remarks, as required by the QA (Quality Assurance) plan of the facility.

The stability of the test system during the testing period of one complete PMT (about a day or more) is ensured by the monitoring parameters and the consistency of the test results, defining the re-test of the PMT if any abnormal situation is detected. Reference PMTs are used to check the reproducibility of the measurements by following the test procedure many times consecutively, and these PMTs are also used to monitor the mid and long term stability of system. However, the reference PMTs may vary their parameters with long periods of time so the transmission lines of the system are also checked periodically with a vector network analyser to see if there are changes in the system itself that may lead to a possible misinterpretation of the reference PMTs long-term parameters.

3 Tests Performed and Results

Every test is performed to each of the 64 channels of the H8804 PMTs, giving parameters both in signal charge and peaks. All of the results can be automatically plotted for each channel individually or they can be presented all together in 2D or 3D plots as a function of the pixel number to evaluate the uniformity of the parameters all around the PMT.

Even if there are many different tests that can be performed with such a versatile system, only the main tests performed to the first twelve H8804 tested PMTs are briefly described bellow. It is worth to mention that some of the plots have some particular entries that are known to be a little biassed (at the tails of the distributions) because of the automatic nature of the test system and the fitting failures that it can produce. However, the automatically generated histograms presented below were not used to reject PMTs, they were used to get the general trend of the parameters. Nevertheless, the operator is able to analyse the results individually and manual fitting or PMT re-testing can be performed if needed to reject a PMT.

3.1 SPE distribution

The SPE (Single Photo-Electron) distribution for the signals areas gives the absolute gain of the dynode chain for each PMT channel.

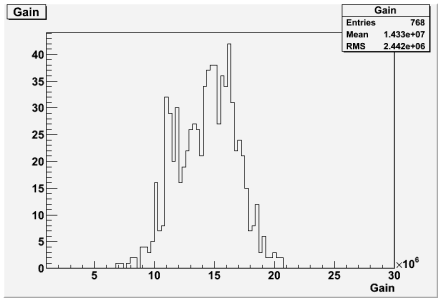

Figure 2: Gain histogram of the all the channels of the first twelve H8804-200MOD PMTs tested.

However, because of the particular usage of these PMTs, it is also important to perform the SPE distribution for signal peaks. This gives a better idea on how the analog front-end of the detectors must be designed, and it also gives an estimation of the threshold level to be set in the discriminators.

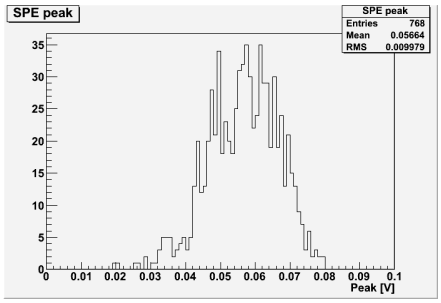

Figure 3: Average signal peak histogram generated by a SPE for all the channels of the first twelve H8804-200MOD PMTs tested. The PMT channels where loaded with 50 Ω.

As shown in fig. 2 and fig. 3, the gain and the average signal peak produced by a SPE of any pixel of these PMTs is assumed to be $(14.3 \pm 2.4) \times 10^6$ and (57 ± 10) mV, respectively.

3.2 Dark-pulse rate

It is the emission rate (in Hz) of pulses at the PMT output that surpasses a determined threshold, with no photocathode excitation. In the case of the H8804, this thresh-

old is set to 1/3 of the average SPE peak since it is the approximate threshold to be used in the discriminators at the analog front-end of the AMIGA detectors. As can be seen in fig. 4, the average dark-pulse rate of any pixel is assumed to be (3.5 ± 2.8) Hz. However, care must be taken when using this value in simulations since the distribution is not symmetric. The average dark-pulse rate is low because the photo-cathode section corresponding to each pixel is very small, even if these PMTs have ultra bi-alkali photo-cathode which seems to be not noisier than regular bi-alkali photo-cathode.

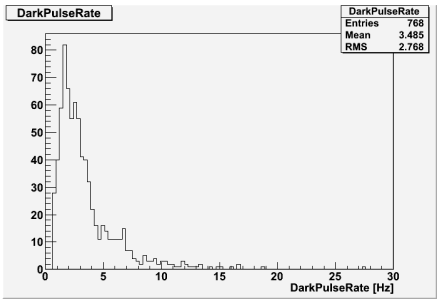

Figure 4: Dark-pulse rate histogram of all the channels of the first twelve H8804-200MOD PMTs tested. The threshold has been set to an amplitude of ∼1/3 average SPE peak.

3.3 Cross-talk (XT)

It is the ratio of the currents measured between two different channel anodes when the photo-cathode region corresponding to only one of the channels is excited. Because each pixel can have up to 8 neighbours, it is defined as total XT to the sum of the XT introduced to any other pixel. Thus, one pixel is illuminated with a pulse of light and then the output signal of this pixel is compared with the signal of all its surrounding pixels. Even if the XT ratio is basically independent of the type (continuous or pulsed) and the level of the excitation, the system is tuned to emulate the behaviour of the AMIGA detector so it generates light pulses so that a few photo-electrons reach the first dynode of the channel under test.

In PMTs, XT is caused by several reasons but mainly because of the numerical aperture of the optical fiber (and its diameter) and the broadening of the electron flow inside of the PMT. Therefore, the test-bench uses the same type of optical fiber and HV (High Voltage) than the ones to be used in the detectors where the PMTs will be working in. It is shown in fig. 5 the total XT of each channel using a Saint-Gobain 0.8 mm optical fiber (69929-MC which is similar to the BCF92 from [5] but more doped). Thus, the total XT of any pixel using this fiber can be assumed as (3.5 ± 0.9) %, to avoid differentiating the pixels with different amount of neighbouring pixels.

Even if it is still not fully analysed, it is believed that the distribution in fig. 5 has two peaks due to the fact that the

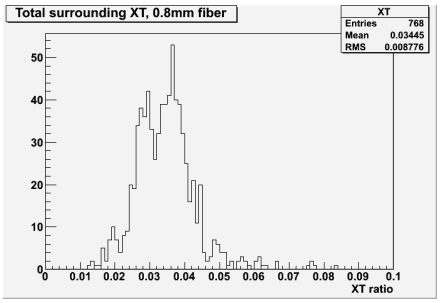

Figure 5: Total cross-talk histogram of all the channels of the first twelve H8804-200MOD PMTs tested, measured with a 0.8 mm multi-clad WLS optical fiber at a voltage of -1000 V.

pixels at the border of the PMT will generate lower XT (left peak) because they have less neighbours than the pixels at the middle of the PMT (right peak).

4 Conclusions and future work

Twelve 64 channels Hamamatsu H8804-200MOD PMTs with ultra bi-alkali were completely tested using this unique and fully automated test facility. All the tested PMTs were fully operational and the main parameters were inside the specifications stated by their datasheets, so there were no rejections. Characterization of their gain, dark-pulse rate, SPE peak, and cross-talk, was performed for each channel of all the PMTs. General trends of these parameters were successfully obtained and used as data input for the particle detectors design, and to accomplish the quality assurance plan of the project in where these PMTs will be used.

Some other tests like after-pulsing and quantum efficiency are currently being developed, although some preliminary non-automatic tests were performed. Specification limits to all of the parameters are also being defined to provide better order requirements to Hamamatsu for the production phase of the project.

References

[1] A. Etchegoyen for The Pierre Auger Collaboration, 30th ICRC, Mérida, México, 2007, **5**:1991.

[2] B. Wundheiler for The Pierre Auger Collaboration, 32nd ICRC, Beijin, China.

[3] D. Barnhill, F. Suarez, et al., NIM-A **591(2008)** 453-466.

[4] A. Ferrero, et al. Modules Laboratory Procedures, 2008, ITeDA.

[5] Sain-Gobain Crystals scintillating optical fibers brochure.

Design and optimization of the electromagnetic particle detector in LHAASO-KM2A

JIA LIU[1], XIANGDONG SHENG[1], JING ZHAO[1] ON BEHALF OF THE LHAASO COLLABORATION
[1]*Key Laboratory of Particle Astrophysics, Institute of High Energy Physics, CAS, Beijing, 100049, P.R. China*
shengxd@ihep.ac.cn
DOI: 10.7529/ICRC2011/V04/0258

Abstract: In LHAASO project, there will be 5137 Electromagnetic particle Detectors (EDs) used to detect the densities and arrival time of secondary charged particles in the extensive air showers (EASs). As one kind of scintillator detector, the design of ED and its optimization have been studied in detail, including the optimized sizes of the tiles based on two kinds of scintillator types and corresponding scintillation light readout modes, etc. In addition, the critical times of scintillator tiles and characteristics of the operating photomultiplier tubes (PMTs) are also presented, as well as the temperature coefficients and ripple indices of the candidate module power supplies. 60 new ED prototypes will be assembled and take data at YBJ in the future.

Keywords: scintillator tile, extensive air showers, electromagnetic particle detector, photomultiplier tube

1 Introduction

In the Large High Altitude Air Shower Observatory (LHAASO) project [1], the whole detector array will be built at Yangbajing (YBJ) valley of Tibet with high altitude of 4300m. As a main detector array, one square Kilometer extensive air showers (EASs) array (KM2A) consists of 5137 electromagnetic particle detectors (EDs, 15m spacing) and 1209 muon detectors (MDs, 30m spacing) distributing within the region with a radius of 560m [2]. Obtaining the highest sensitivity ($1\%I_{Crab}$) at the highest Gamma ray energy, it aims at the following targets, 1) the discovery of the Galactic CR sources; 2) the survey of the northern sky, exploring the origin of galactic cosmic rays; 3) the study of Cosmic ray physics, etc.

Now, as a kind of scintillator detectors and based on the requirements of KM2A sensitivity, each ED will have an efficient detection area with 1m × 1m to measure the densities and arrival time of secondary charged particles (above 5MeV) in the EASs with time resolution less than 2ns and detection efficiency better than 95%. Considering the large dynamic range of the primary cosmic ray particles, as well as the sizes and their lateral distributions of EAS events, it is required each ED should measure the charged particle densities in a large dynamic range from 1particle(25% in resolution) to 4000 particles(<5% in resolution) per meter square. To realize their long-term operation in YBJ environment (4300m, 0.6 atm., -25ºC to 40ºC), the critical time of two kinds of scintillator tiles and gain variation of the **photomultiplier tube** (PMTs) have also been concerned and studied, as well as the appropriate EDs' inner structures and crusts, which should be water-repellent and easy to maintain.

An ED prototype array, consisting of 42 old scintillator detectors (used in L3C+Cosmics experiment), has been taking data smoothly at YBJ for about one year. Compared with the results from ARGO data analysis, the performances of ED array have been validated to achieve good angular resolution and fine stability. More physics results are being studied in detail [3].

New studies in the design of ED and its optimization have been done, mainly concerning the sizes of each scintillator tile and scintillation light readout modes, as well as the characteristics of the operating PMTs and module power supplies, etc.

2 Design of ED and its optimization

Scintillator detectors are applied widely to many present cosmic ray experiments in the world, such as AS γ experiment [4], YAC and L3C ones [5][6], where the scintillation tiles with different sizes are used as detection effective region to convert the deposit energies of the incoming charged particles into scintillation light and the light will be collected and transferred to one PMT's photocathode with some wavelength shifting (WLS) fibers or an air guide. Based on the above detection and readout modes, to obtain new designs of ED, the following factors are focused on, such as the characteristics of scintillator tiles, optimized tiles' sizes, readout modes (WLS fibers or air guide), the requirements of operating PMTs and its power supplies, as well as the crusts of ED,

etc. Here, the contents of electronics and DAQ system aren't presented in detail.

Two kinds of Chinese scintillator products (their sample units are called tiles, light outputs are both about 40% Anthracene), KEDI type and ST-401 one, are chosen as the candidate detection materials, while three types of PMTs, Electron Tubes 9903kB type, HAMAMATSU R11102 type and PHOTONIS XP2012B one, are chosen to be candidate PMTs used in the ED design and its optimization. In addition, WLS fibers (BCF92, Φ 1.5mm) and Tyvek sheet (0.27mm thick) are applied to the whole tests, as well as certain kind of silicon oil and optical cement (BC600), etc.

To study the performance of scintillator tile detectors composed by the above components, a telescope was set up with 2 small scintillator tile detectors (called trigger detectors, 10cm×10cm×5cm each, 2 XP2012B PMTs are equipped in them) to choose the incoming singly charged relativistic particles (minimum ionizing particles (MIPs)). The signals from the PMTs are processed with an electronics readout system, which is based on one 9U VME crate, where one FEE modules with 16 channels are used to measure the charge and time message with the charge resolution of 20%@1pC and time resolution of 0.5ns.

Furthermore, a GEANT4-based simulation package has been developed, with which the corresponding simulation work can be done to deal with those corresponding processes occurring in scintillator detectors, including scintillation light generation, transmission, collection and its conversion into photoelectrons at the PMT's photocathode. Since the simulation results are consistent with the tested ones, it benefits the whole good progress in the ED design and optimization greatly.

2.1 ED's design with air guide

Some tiles with different sizes and scintillator types, such as 50cm×50cm×5cm (ST-401 type, old scintillator), 25cm×25cm×2cm (ST-401 type, new tiles) and 25cm×25cm×1cm (KEDI type, new tiles), are applied to the detector prototypes with the area of a quarter of 1m2 and an infundibular air guide of 60cm high, where the inner surface of air guide is smeared with a layer of Titanium dioxide(TiO2). Here, an XP2012B tybe PMT is operated with the gain of 4.72×10^6 at -1600V in the whole test processes.

To study the uniformity of the whole prototype, an old scintillator tile of 50cm×50cm×5cm are used. Scanning the different positions by moving the telescope on tope of it (see Fig.1), the testing results presents that the average value of photoelectrons obtained by PMT is about 18 and the average time resolution is about 1.5ns, while their ratios of RMSs to the mean values are less than 5% and 8%, respectively. Although there is good uniformity similarly, the average values of obtained photoelectrons are about 7 and 3.8 for two new tiles with size of 25cm ×25cm×2cm and 25cm×25cm×1cm.

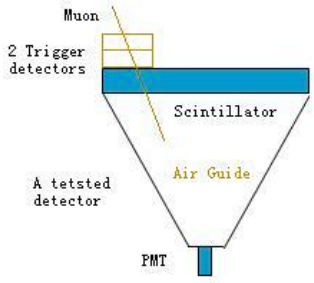

Fig.1 Sketch map of a scintillator detector with air guide readout tested by a telescope

Now, the simulation work are being done to optimize the design of this kind of scintillator detector with 1m× 1m, including the suitable sizes of air guide.

2.2 ED's design with WLS fibers

Here, the ED prototype will consist of 16 scintillator tiles (25cm×25cm each). The optimized design will depend on the following factors, 1) the concrete size of each scintillator tile; 2) the size and quantity of WLS fibers; 3) fiber placement in scintillator tile; 4) optical coupling modes between different components, such as Fiber-scintillator coupling and Fiber-PMT's window coupling, etc.

In the experiments, the tested tiles are produced with different sizes. Concretely, their lengths are fixed, 25cm, for both KEDI type tiles and ST-401 ones. The widths are 5cm, 15cm, 25cm for KEDI type tiles, while it is 25cm for ST-401 type ones. As to the thicknesses of different tiles, they are 1.0cm and 1.5cm for all KEDI type tiles, while it is 2cm for all ST-401 type ones. Another typical difference between KEDI tiles and ST-401 ones is that each KEDI type tiles is with 5 or 8 holes-making (25cm×Φ 1.5mm each) in the middle of it, while each ST-401 type tile is with 8 grooves (25cm× 1.6mm×1.8mm or 25cm×1.6mm×2.5mm each)) at its surface. These holes and grooves are set for the placements of WLS fibers.

With the telescope choosing the single incoming MIPs, the above tiles and others components, the studies of performances of ED with fiber readout mode have been done in further detail (see Fig.2).

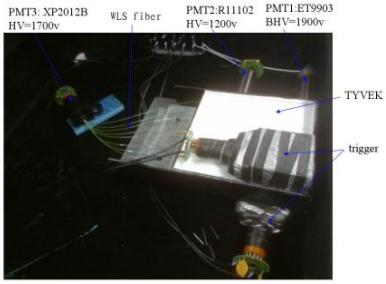

Fig.2 one photo of test system with a telescope

The photoelectrons obtained by the PMTs and the corresponding time resolution are concerned. Here, three kinds of PMTs are used in the tests, while each tile is covered with a layer of Tyvek sheet. The testing results of one KEDI tile are shown at Fig.3.

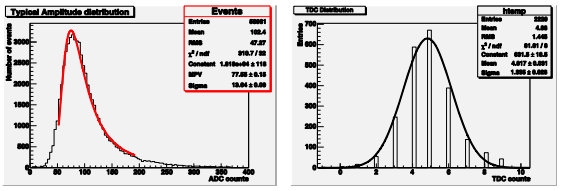

Fig.3 the distribution of amplitudes (left) (Landau distribution) of the tested tile (5cm × 25cm × 1.5cm) and time of flight (right) between one trigger detector and tested one in case of single particle.

The results show that the photoelectrons increase once the width of a tile become larger, but it increases slowly and the time resolution becomes a little worse once the width exceeds 15cm. So it is suitable for the width to choose 25cm in present design. Validated by the simulation results, the optimized depths are 1.5cm for KEDI type tiles and 2cm for ST-401 type ones, respectively. Three kinds of methods to increase the collection efficiency of the trapped scintillation light in WLS fibers (polished ends) are applied in the tests, 1) one end of each WLS fiber coated an aluminium layer; 2) one end of each WLS fiber glued with a piece of enhanced specular reflector (ESR); 3) bending a double long WLS fiber and placing it in the two neighboring grooves or holes. The light collection efficiency increases are obtained to be 35%, 80%, 90% from the operation of the above 3 methods, comparing with the ones with only end polishing WLS fibers. So the method 3) will be chosen to be applied in the ED design.

As to the effects of the coupling between WLS fibers and scintillator tiles with different materials, such as optical cement (BC600) and air, it shows that there is more than 40% increase in the coupling with BC600 operating in either the grooves or the holes. In addition, it seems there is a little superiority in the light collection efficiency to use deeper grooves. In the coupling between WLS fibers and scintillator tiles with air and BC600, respectively, the obtained scintillation light efficiency increases are about 20% and 10% by comparing 2.5mm deep grooves with 1.8mm ones. Furthermore, in the coupling between WLS Fibers and the PMT's window, the scintillation light collection efficiency is 30% bigger with silicon oils than with air.

Based on the above detailed studies, two suitable ED designs are shown in Fig.4. Concretely, for the design of ED with KEDI type scintillator tiles, the tile's size is 25cm×25cm× 1.5cm and 8 holes (25cm×Φ 1.5mm each) in the middle. A total 4 WLS fibers (310cm long and Φ 1.5mm) will be placed in the 8 holes of tiles with air coupling. Here, the average value of photoelectrons obtained in 1st anode of the PMT is about 16 and the time resolution is about 1.8ns. For the design of ED with ST-401 type tiles, each tile size is 25cm×25cm×2cm with 8 grooves (25cm×1.6mm×1.8mm each). A total 4 WLS fibers (310cm long and Φ 1.5mm) will be placed in the grooves with air coupling. According to this design, the average value of photoelectrons obtained in 1st anode of a PMT is about 21 and the time resolution is about 1.8ns for each ED.

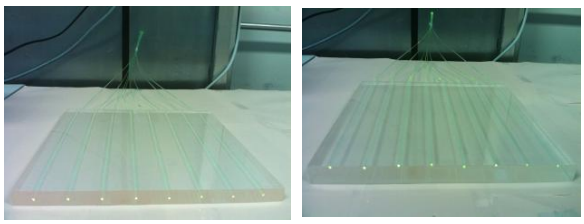

Fig.4 Two designs of scintillator tile with WLS fibers (KEDI type tile (left), ST-401 type tile (right))

A telescope detection system has been designed to scan the scintillator tiles in batch. To keep good uniformity of each ED, every 16 tiles with almost the same amplitude will be picked up and assembled in one ED. A total 128 WLS fibers will guide the scintillation light to the photocathode of one PMT (ET9903kB type or R11102 one). All the above scintillator tiles, one PMT and one module power supply are packed in one aluminium/plastic water-repellent box. On the top of the box, a layer of LEAD convertor with 5mm thickness are used to increase the detection efficiency, which is beneficial to improve angular resolution and position resolution of the KM2A.

3 Critical times of scintillator tiles

Considering the concrete environment at YBJ site and long operation time of open-air LHAASO array, the long term stability of scintillator tiles are concerned seriously. So their lifetime or critical time have been being studied with two accelerated aging experiments [7], dynamic temperature variation aging experiment and thermal aging one [8] at Institute of High Energy Physics (IHEP) recently. Here, the critical time is defined to be the time when its light output has decreased by 20%.

In the dynamic temperature variation aging experiment, two kinds of scintillator tiles (KEDI type and ST-401 one) were put in a simulation environment box, where the temperature varied from -30℃ to 40℃ alternately. The tiles' light outputs are measured every 90 times. There is an accumulative 480 times in total. Assuming the scintillator tiles had undergone two days in one alternation, it shows that the critical times are about 9 and 15 years for ST-401 type tiles and KEDI ones.

In accelerated thermal aging experiment, KEDI type tiles were conducted at three high temperature points, 60, 70, 80℃. For each temperature point, the light outputs of the tested tiles are measured every 50hours. Considering that the logarithm of the critical time is in inversely proportion to the temperature, an Arrhenius plot will be obtained. So the critical time at 20℃ will be extrapolated

from the plot. Here, it is about 9 years for KEDI type tiles, while the critical time of ST-401 ones at 20℃ will be obtained soon.

4 Characteristics of the PMTs

The operating PMTs' characteristics are related to the EDs' capabilities, especially in the detection dynamic range and particle number resolution. The characteristics of XP2012B type PMTs, R11102 type and ET9903kB type ones have been being studied in detail [9].

For required PMT, its pulse linearity must cover 3.6 orders of magnitude to detect the particle density in a large dynamic range from 1 to 4000 per square meter. It is suitable for one ED to obtain about 16 p.e. collected at 1st dynode of the PMT when single incoming particle impinges on it, which is consistent with the expected design of the scintillator tiles. Further, total 64000 p.e. (4000 incoming particles) should be measured linearly by the PMT within 5% deviation. Here, the pulse linearities of three kinds of PMTs, R11102 type, ET9903kB type PMTs and XP2012B type, have been measured and are about 3.1, 3.3 and 3.0 orders, respectively. New efforts are being made to modify their dividers or realize dynode readout modes to obtain 3.6 orders.

A two-dimensional scanning system has been constructed and operated to study the PMTs' uniformities. With a purple LED light source scanning over each tested PMT photocathode millimeter by millimeter, the position response of the photocathode is measured and it shows that the non-uniformities (the ratio of RMS to the mean amplitude) within a radius of 7.0mm of each PMT's center are about 6.9%, 9.4% and 17.0% for R11102, XP2012B and ET9903kB types respectively. Based on them, the possible effects on the pulse amplitudes resolution have been estimated and proved to be eligible. Here, it is emphasized that the position response is mainly caused by the photoelectron collection efficiency due to focus electrode and electric field distribution inside the PMT.

The effect from the electromagnetic field on the gain variation of one PMT without any magnetic field has been studied in one elaborate experiment operated at IHEP. By rotating one XP2012B type PMT around the normal of the horizontal and its axis, the measured results show that the earth's Magnetic fields (～0.5G in Beijing or Tibet) affect the gains of PMTs with a maximum variation less than 10% (see Fig.5).

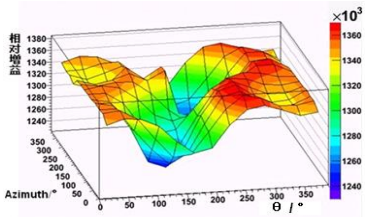

Fig.5 the amplitude distribution of one XP2012B type PMT affected by the geomagnetic fields

The effects from the electromagnetic field of ET9903kB type PMTs and R11102 ones are being studied.

Another important factor to affect the gain of PMT is related to the power supply sources equipped with each PMT. Considering a large annual temperature variation (from -25ºC to 40ºC) and 0.6 atm. at YBJ site, for the operating module power supply, it is required that a temperature coefficient is less than 0.01%/ºC and the ripple index is less than 0.01%. Thus the variation of each PMT Gain can be limited within ±5%. Three kinds of candidate module power supplies, TIANJIN LION type, Dongwen type and Centre type, have been studied in Hebei normal university. All of their parameters meet the present requirements [10].

5 Conclusion and outlook

Some progresses have been made on the design of ED by now. The characteristics of scintillator tiles, operating PMTs and their power supplies have also been studied in detail. But more effort is still needed to realize the pulse linearity of PMT with 3.6 orders, as well as the final design of ED.

60 new ED prototypes will be assembled in half a year. The corresponding quantities of two kinds of scintillator tiles have been ordered, as well as the PMTs and power supplies. The testing systems have been installed and being operated in Shandong University and IHEP, Heibei Normal University, respectively.

New 60 EDs will cover the top of one MD and take data at YBJ. By recording the EAS events, some studies on their performances will be done.

Acknowledgments

The authors would like to express their gratitude to the ARGO Collaboration for the powerful support. This work is partly supported by the Knowledge Innovation Fund (H85451D0U2) of IHEP, Beijing.

[1] Z. Cao et al., LHAASO Collaboration, in: Proceedings of 31st ICRC, 2009.

[2] Huihai He et al., LHAASO Collaboration, in: Proceedings of 31st ICRC, 2009.

[3] Jia Liu et al. LHAASO collaboration, 32nd ICRC, Beijing, 2011

[4] S.W. Cui et al. Proceedings of the 27th International Cosmic Ray Conference, 2001.

[5] Jing Huang et al. AS γ Collaboration, in: Proceedings of 31st ICRC, 2009.

[6] O. Adriani et al., NIMA 488(2002) 209-225

[7] Tianfu Zhou et al. LHAASO collaboration, 32nd ICRC, Beijing, 2011

[8] B.V. Grinyov et al., Radiation Measurements 38 (2004) 825-828

[9] Chao Hou et al. LHAASO collaboration, 32nd ICRC, Beijing, 2011

[10] Shaoru Zhang et al. LHAASO collaboration, 32nd ICRC, Beijing, 2011

Selection of photomultiplier tubes for the LHAASO project

BIN ZHOU[1], CHAO HOU[1] ON BEHALF OF THE LHAASO COLLABORATION
[1]*Institute of High Energy Physics, Beijing, 100049, China*
houchao@ihep.ac.cn

DOI: 10.7529/ICRC2011/V04/0261

Abstract: In order to select the suitable Photomultiplier Tubes (PMTs) for the LHAASO project, specialized test systems are set up to measure the performances of different kinds of PMTs from Hamamatsu and Electron Tubes (ET), such as gain as a function of high voltage, linearity, single photoelectron spectrum, dark noise and cathode uniformity. Several types of PMTs are chosen as the candidates for the projected LHAASO detectors. In this presentation, the PMTs for LHAASO-KM2A and LHAASO-WCDA are reported.

Keywords: LHAASO, PMT, linearity, SPE, uniformity, gain, dark noise.

1 Introduction

The Large High Altitude Air Shower Observatory (LHAASO) is a compound detector array aiming at achieving the accurate observation of gamma ray from 40 GeV to 1 PeV and cosmic ray from 10 TeV to 1 EeV. It distributes in a kilometer square area at Yangbajing (YBJ) International Cosmic Ray Observatory [1-3].

LHAASO consists of 1 km^2 extensive air shower array (KM2A) with 40,000 m^2 muon detectors, 90,000 m^2 water Cherenkov detector array (WCDA), 5,000 m^2 shower core detector array (SCDA) and a wide field of view air Cherenkov / fluorescence telescope array (WFCTA). Thousands of photo-multiplier tubes (PMTs), with diameters of 1 inch, 1.5 inches for LHAASO and 8 inches for WCDA, will act as the photon converter for the above detectors. So PMT selection becomes an important issue of the project.

2 Specification of the LHAASO PMTs

Time measurement with accuracy of 1-2 ns is a key requirement for LHAASO PMTs, for which only PMTs with fast rise-time and narrow transit time spread (TTS) are to be considered, while linearity better than 5% in 3.6 orders of magnitude becomes the most important factor during PMT selection. For the 1 and 1.5-inch PMTs, the required dynamic range is 15-60,000 photo-electrons (PEs), while the 8-inch PMT should reach a dynamic range of 1-4000 PEs. WFCTA requires the 1-inch PMT's linearity is 2% @ 30mA.

Charge of PMT signal varies when the light incidents to different position of the PMT cathode. For LHAASO-KM2A, a photocathode uniformity of better than 20% is required for PMTs. While for WCDA, we don't care this issue very much if the difference between PMTs is less than 10%. Furthermore the geomagnetic effect is also considered for both KM2A and WCDA.

3 Tests of PMTs

Four types of PMTs, Hamamatsu R11102, ET9903kB and Hamamatsu R1924A for KM2A, Hamamatsu R5902 for WCDA, are first chosen as the candidates. A variety of tests are carried out.

3.1 Single photoelectron spectrum

In order to obtain the absolute gain of each candidate PMT, single photoelectron (SPE) spectrum is measured by using an LED as the light source driven by a pulse generator, which provides a trigger signal to the data acquisition system as well. The signal shape is sampled by FADC with the data analyzed in a FPGA providing the charge of the signal. In general, the number of PEs (Npe) generated on the photocathode follows the Poisson distribution

$$P(n) = \frac{e^{-\lambda}\lambda^n}{n!} \qquad (1)$$

The light intensity is controlled thus the probability of seeing signals is about 10%, so P(0)=0.9, P(1)=0.095, and the probability of seeing more than 1 PE is 0.5% [4], i.e., about 0.5% contamination of events caused by 2 or more PEs in SPE spectrum.

Figure 1 shows the SPE spectrum of an 8-inch Hamamastu R5912, from which the corresponding PMT gain is obtained. Then the high voltage response is

measured to calculate the beta value (amplification-voltage coefficient), from which the working high voltage with the required gain is obtained.

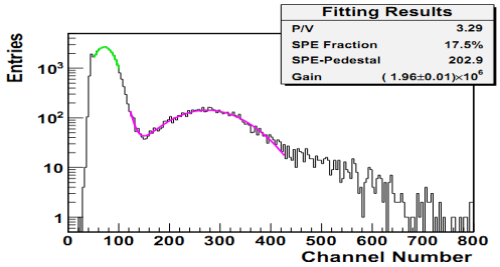

Figure 1. An example of single photoelectron spectrum for the 8-inch PMT.

3.2 Linearity

The non-linearity of PMT is usually caused by space charge effect at the last dynodes when the current is very high. In order to measure the linearity of PMT, two different methods are adopted.

3.2.1 Test for PMTs of KM2A

For KM2A PMTs, the distance between the LED light source and the PMT is varying, equivalent to change the number of photons the PMT accepted. The LED light intensity is maintained stable during the test. Because this is a large range, we use special methods to achieve the goal.

1) Testing system: The light source is a LED light tube with 2 layers of Teflon at the front end. Teflon plays a role in making the light more uniform. The HV of PMT is supplied by high voltage module. An oscilloscope (OSC) is used to take the PMT anode output signal data with 512 moving average. The signal generator provides a TTL trigger signal to OSC and a synchronized LED pulse. In the dark box, there is a sliding rail which is 3 meters long. PMT is fixed on the rail, and the light tube can slide on it. The testing system is shown in figure 2.

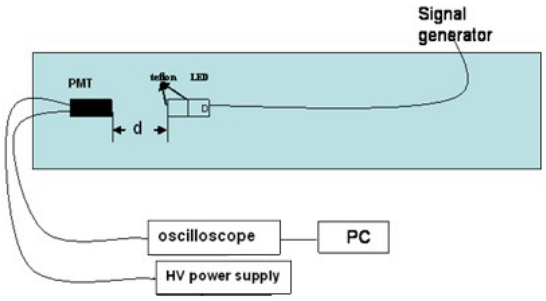

Figure 2. Linearity testing system

2) Measuring method: when the d (distance between light tube and PMT) is longer than 30 cm, the light source can regard as a point. In this way,

$$\left(\frac{I_1}{I_2}\right)=\left(\frac{1/d_1}{1/d_2}\right)^2 \qquad (4)$$

Where I is the light intensity. When d is shorter than 30 cm, the $1/d^2$ model above is not suitable. Since the light source (V, 1W) is not strong enough for us to measure the large signal if d>30cm, short distances measurements should be taken. So we calibrate the light intensity of every position in PMT linearity region.

$$I=\left(A/A_{30}\right)\times I_{30} \qquad (5)$$

Where A is PMT anode output charge. Because the length of the dark box is limited, we cannot measure the signal with the large range of 3.6 magnitudes at only one light intensity. So we choose two different light intensities, and use their ratio (for example 12.5:1) to combine them. The ratio should not be too large to get some points of overlap, and should not be too small to reach the linearity region.

3) Testing results: one of linearity testing results is shown in figure 3. And the results of three 1-1.5-inch PMTs can be seen at Table 1.

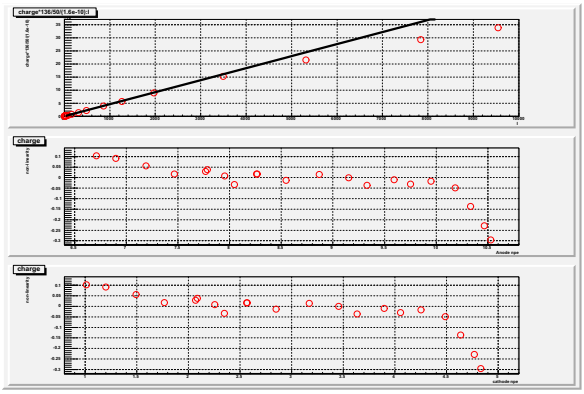

Figure 3. Linearity of R11102. In the top picture, x axis is relative light intensity and y axis is the measuring value. In the middle one, x axis is PMT anode output charge number, y axis is the percentage of nonlinearity. In the bottom picture, x axis is the cathode photoelectron number, y axis is the nonlinearity.

3.2.2 Test for PMTs of WCDA

For WCDA 8-inch PMTs, the so-called AB method is used [5], where an array of two LEDs, L_A and L_B, are deployed, acting as the light sources, shining lights to the PMT in testing. These two LEDs can be lit individually or both together at the same time, while the charge of the PMT pulse is measured, marked with Q_A, Q_B and Q_C for cases of L_A, L_B and both together, respectively. During the test, these two LEDs are pulsed to have almost same intensity. Then, the nonlinearity is defined as the following:

Nonlinearity = $[Q_C - (Q_A + Q_B)] / (Q_A + Q_B)$.

Tests show that the non-linearity of all the 8-inch PMTs exceed 5% when Npe>700, which do not meet the dynamic range requirement. In order to solve this

problem, a way using dynode readout to enlarge the dynamic range is in study.

3.3 Photocathode Uniformity

The non-uniformity of PMT anode output signal when the light incidents to different position of PMT cathode is probably caused by

- The distribution of cathode material is not uniform;
- Focusing electrode structure and electric field in PMT distribution lead to difference of photoelectron collection efficiency;
- Geomagnetic effect;

Experimentally, we measure the anode output signal's uniformity when LED vertically incidents on cathode's different position. LED is controlled by a stepping motor (e.g., figure 4), 1mm each step and cover the area of 4*4 cm^2 [6]. Charge value of anode signal of each step is recorded. The scan results of three types PMT are shown in figure 5. From the picture, different types of PMTs have different uniformity distributing character. It has direct correlation on the electric field distribution between cathode and the first dynode. PMT is rotated to three angles on horizontal direction, and the geomagnetic effect is ruled out. In conclusion, the uniformity distributing character is determined by the inner structure of PMT. In consideration of the characteristic of scintillator detectors, the coupled area of fiber hank and PMT cathode is a roundness area (radius 13mm) in the centre of cathode. Therefore, we pay more attention on the variety of anode output amplitude of different type PMT in this area. The value of uniformity is calculated as mean/RMS which can be obtained from the distribution of the charge of PMT anode output. And the results are shown in Table 1. We can see R11102 has lowest non-uniformity. The maximum difference of signals' mean values at different positions of 8-inch PMT's photocathode is about 32%.

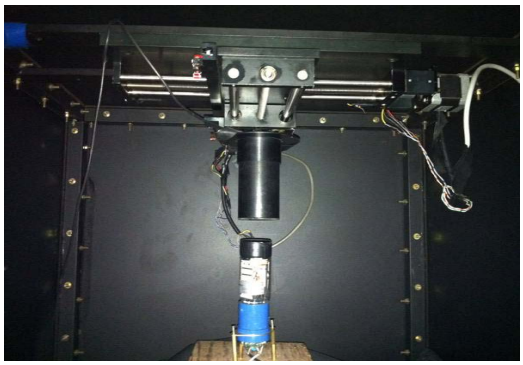

Figure 4. Picture of the testing system. The stepping motor can move in two dimensions. The light tube is on top and perpendicular to the PMT cathode.

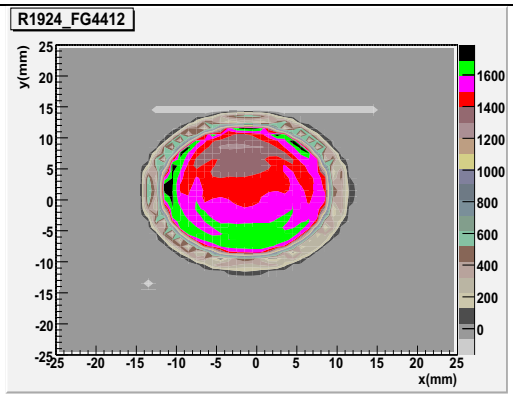

Figure 5. Result of two-dimension scanning of 9903kB, as an example.

Dark noise rate

In the dark noise rate measurement, HV is on, but LED off. The dark noise rates for each PMT at different thresholds can be measured after the signal is amplified and discriminated. The dark noise rate of an 8-inch PMT is shown in figure 6.

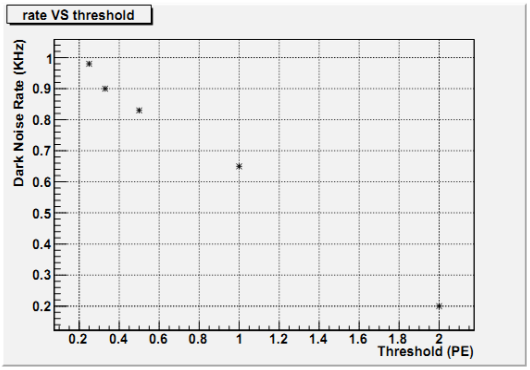

Figure 6. Dark noise rates of different thresholds for a 8-inch PMT.

3.4 The effect of the geomagnetic field of PMT

The test method is as follows: A pulsed and uniformed blue LED is used to shine on the photocathode of the PMT. The PMT is placed with the photocathode facing upward; the PMT and LED are rotated together in 30 degree steps. The LED intensity is kept constant during the whole rotating process. The 0 degree means that a special pin on the PMT (e.g., pin 20 for the PMT R5912) is pointing to the local magnetic north. The PMT is rotated anticlockwise (towards west). The test result for an 8-inch PMT is shown in figure 7. It shows that the maximum variety of photoelectron collection efficiency was up to ~31% at different orientations, with the maximum appeared at the direction of ~110°.

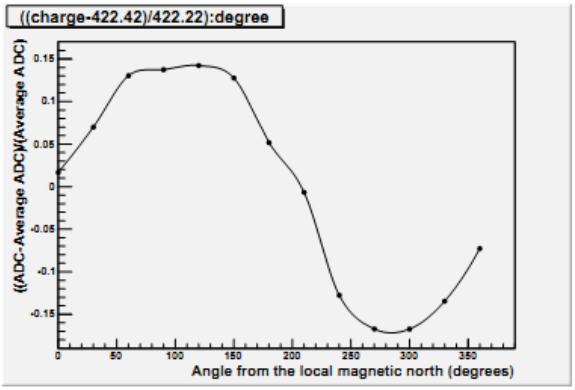

Figure 7. The effect of the geomagnetic field of an 8-inch PMT.

4 Results and discussions

4.1 KM2A PMTs

KM2A electromagnetic particle detectors (EDs) [7] will use about 5137 PMTs. We have performed the tests above on the 3 candidates PMTs to determine their suitability for the EDs. The test results of the three candidates are shown in Table 1. Both candidate R11102 and ET9903kB PMTs have good linearity to satisfy our requirement. The non-uniformity of R11102 and ET9903kB are both less than 20%, but R11102 is better.

4.2 WCDA PMTs

For WCDA, an engineering array has been established at YBJ [8], where nine 8-inch Hamamastu PMTs are deployed. The test results of the nine Hamamastu 8-inch R5912 PMT is shown in Table 2. A new measurement of these nine PMTs located in the pond at YBJ gives similar results. We get the conclusion that all of these nine PMTs satisfy our needs, except the dynamic range. And the test results in the pond are all consistent with the results at the laboratory of Beijing.

5 Acknowledgment

This work is partly supported by the Knowledge Innovation Fund (H85451D0U2) of IHEP, Beijing.

6 Reference

[1] Zhen Cao et. al. (LHAASO collaboration), 31st ICRC, LORZ, (2009).
[2] Huihai He et. al. (LHAASO collaboration), 31st ICRC, LORZ, (2009).
[3] Zhiguo Yao for the LHAASO Collaboration, PROCEEDINGS OF THE 31st ICRC, LORZ(2009)
[4] A.K. Tripathi, S. Akhanjee, K. Arisaka, Nuclear Instruments and Methods in Physics Research A 497 (2003) 331-339
[5] David Barnhill et. al., PROCEEDINGS OF THE 28th ICRC, Tsukuba(2003)
[6] Lihong Chen et. al., Nuclear Electronics and Detection Technology
[7] Xiangdong Sheng et. al. (LHAASO collaboration), 32st ICRC, LORZ, (2011).
[8] Mingjun Chen for the LHAASO Collaboration, PROCEEDINGS OF THE 32nd ICRC, Beijing(2011)

Table 1. The test results for 1 and 1.5-inch PMTs

PMT	HV (V)	β	gain	Uniformity (radius<13 cm)	Max. Anode current (mA) (Nonlinearity<±5%)	Cathode linearity scale (Npe)
R11102	982.3	8.17±0.05	0.50×10^6	6.91%	70.6	$10\sim10^{4.5}$
ET9903kB	1599.1	6.83±0.03	0.44×10^6	17.06%	96.0	$10\sim10^{4.6}$
R1924A	787.5	7.88±0.03	0.73×10^6	>20%	22.8	$2.5\sim6.4\times10^3$

Table 2. The test results for all 8-inch PMTs of engineering array.

PMT SN	HV (V)	beta	P/V	Non-Linearity	Rate (kHz)
SD2585	1266	7.98	2.50	820	1.01
SD2602	1265	8.48	2.39	934	1.92
SD2538	1164	8.05	4.68	745	0.52
SD2514	1213	8.01	3.53	680	0.94
SD2580	1279	8.43	2.76	730	0.65
SD2586	1248	7.83	4.30	730	1.41
SD2559	1132	7.92	5.84	625	0.95
SD2576	1215	7.88	3.30	620	1.01
SD2590	1273	7.77	3.50	764	0.83

The long-term stability of plastic scintillator for electromagnetic particle detectors

ZHOU, TIANFU[1], HE, HUIHAI[2], SHENG, XIANGDONG[2], ON BEHALF OF THE LHAASO COLLABORATION
[1]*Yunnan University Kunming, 650091, China*
[2] *Institute of High Energy Physics, Beijing, 100049, China*

zhoutianfu@ihep.ac.cn

DOI: 10.7529/ICRC2011/V04/0267

Abstract: In order to study the long-term stability of plastic scintillator (PS) for the LHAASO-KM2A, an experiment has been done to simulate the Yangbajing environment, where the temperature around the tested scintillator is in large dynamic variation. The attenuation length of light and the light output are measured to monitor the quality variation of scintillator. In addition, accelerated thermal aging tests of scintillator are also made. Here the PS operational time can be estimated and its lifetime is determined from an Arhenius plot.

Keywords: temperature; thermal aging; lifetime

1 Introduction

The Large High Altitude Air Shower Observatory (LHAASO) project [1] is proposed to study gamma ray astronomy from sub-TeV to 1PeV and cosmic ray physics from 5TeV to 1EeV by using a compound detector array distributed in one kilometer square. The proposed detector consists of KM2A [2], 4 WCDAs, SCDA, WFCA and 2 LIACTs. KM2A is the primary array in LHAASO project, which consists of 5137 Electromagnetic particle Detectors (EDs) [3] and 1209 Muon Detectors (MDs) [4]. EDs (1m×1m×1.5cm each) are used to detect the densities and arrival times of secondary charge particles (>5MeV), which need more than 80,000 plastic scintillator tiles in all project. The operational time of array is more than 10 years. Consequently, it is important to study properties of plastic scintillator, especially long-term stability.

In this work, the properties of tile parameters are experimentally studied for the EDs of KM2A. In order to study the long-term stability of plastic scintillator (PS), an experiment has been done to simulate the Yangbajing environment, where the temperature around the tested scintillator is in large dynamic variation (-30℃~40℃). The light output is measured to monitor the quality variation of scintillator. In addition, accelerated thermal aging tests of scintillator at temperature of 60◦C, 70◦Cand 85◦C are conducted. The light output is measured every 50 h.

To predict the PS operational time, the well-known principle of temperature—time superposition is used [5]. This principle establishes the equivalency of temperature influence and its duration. By using it, accelerated aging is conducted in isothermal conditions under different temperatures that are usually higher than the operational temperatures.

2 Aging mechanisms

Environmental aging is a basic parameter characterizing long time stability even without the effect of radiation. Such aging may be seen as yellowing or clouding or crazing of the surface or cracking in depth. In all cases the light output decreases. It is known that tile surface can craze — develop microcracks — which rapidly destroys the capability of plastic scintillator to transmit light by total internal reflection. It is important to develop a prognostic method for sample stability. In developing an accelerated aging test it is important to achieve the maximum likeness to the natural degradation processes.

We assume that polystyrene aging is due to the following mechanisms:

1. Thermooxidative processes resulting in the creation of peroxides which absorb in the region of the scintillating radiation.

2. Mechanical degradation due to chemical stress crazing which causes surface cracks that disrupt light transmission.
3. Diffusion of low molecular components of the formulation which can cause both surface and internal defects. In this case yellowing, clouding of the interior or the surface, and cracking can arise.
The above mechanisms lead to changes in the scintillation efficiency which in any realistic case is due to one or at most a few parameters. These parameters determine the practical usefulness of any scintillator composition. We have investigated the effect of the following two parameters on the efficiency of polystyrene scintillator:
1. The influence of temperature for long times on the light output.
2. The effect of temperature shock, simulate the Yangbajing temperature variation (-30℃~40℃), stimulate cracking.
Two experimental methods are given below.

3 Test system

3.1 Experimental setup

In this paper, we use a 250mm-square and 15mm-thick plastic scintillator and a 600 mm-long WLS fiber (BCF92, SAINT-GOBAIN) with a diameter of 1.5 mm. We measure the amplitude distribution and time resolution, when a cosmic-ray muon penetrates through the scintillator.
We test a plastic scintillator tile with WLS fibers [6]. We hole the scintillator tile to embed WLS fibers. The wavelength of scintillation light produced in the scintillator tile is converted to a longer wavelength by the WLS fiber embedded in the tile. Converted light is transmitted to a photomultiplier tube (PMT) by the WLS fiber [7]. The WLS fiber is coupled to the PMT with air (Figure. 1).
A signal from the PMT connected to the WLS fiber is digitized using a VME charge ADC module and a TDC module, and readout with a PC.

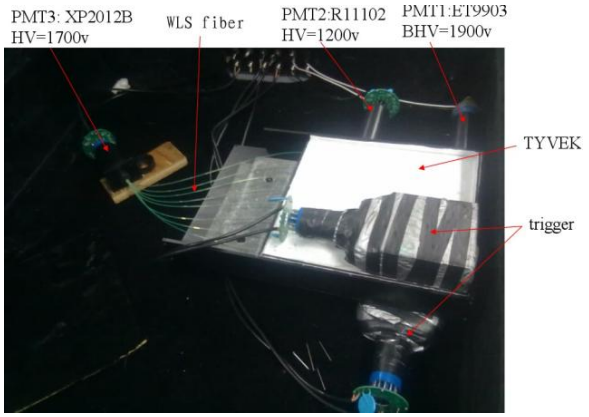

Figure1. Experimental setup: Scintillation tile and the WLS fiber system with PMT

The target scintillator sandwiched with the WLS fiber is placed between two trigger scintillation counters, each of which is 100 mm square and 50 mm thick in size as shown in Figure1. The spacing of two trigger counters is 100 mm.
A trigger signal is generated when both of the two trigger counters are hit. The TDC is started by the signal of the upper trigger counter, and stopped by the signal from the PMT of the target scintillator tile.

3.2 Electronics readout system

The electronics readout system is based on single VME crate, with a FEE module (16 channels) put in one VME crate. In each channel, the PMT signal is sent to a high speed amplifier and then fed to the two branches, i.e., the two range CR-(RC)4 shaping circuits, which integrate the total charge of the PMT signal in parallel. The gains for these two shaping circuits are different. The high gain is about 20 times larger than the low gain. The outputs of the two shapers are continuously sampled at a speed of 40MHz by two FADCs. The sampling data are sent directly to FPGA for further processing such as range selection, data pipelining, peak finding, and data buffering, etc. The signal for time measurement is first sent to a fast discriminator at a given programmable threshold to generate a timing pulse, whose leading edge defines the arrival time of the signal. The over-threshold timing pulse is sent to TDC as the start signal. The trigger signal deriving from trigger system is used as the stop signal. The time difference between the start signal and stop signal are save in TDC. The TDC is built by using internal resources of a high-performance FPGA chip. The major components of the TDC are two ultra high speed gray-code counters. The first counter changes at the rising edge of the 320MHz clock, while the other changes at the falling edge. The time difference between the start signal and stop signal are measured via these two counters with time resolution (RMS) less than 0.5ns.

3.3 Stability of system

In order to ensure accuracy of experimental measurement, repeated measurements were conducted. The measurement error of mean value is 1.76%, and MPV value is 1.16%, as it is shown in Figure2.

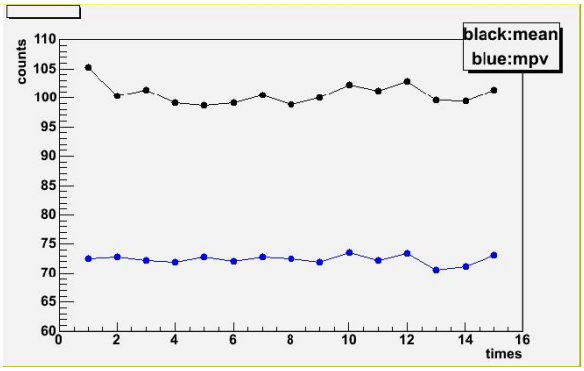

Figure2. Monitoring system by repeated measurements, the measurement error of mean value is 1.76%, and MPV value is 1.16%

We do the calibration error of electronics readout system (VME charge ADC module) using Standard pulse signal produced by signal generator. The systemic error is 1.0%. It is show that the test system is stable.

4 Experiments results

4.1 High and low temperature aging test

High and low temperature aging tests of materials—plastic scintillator A(25cm × 25cm × 2cm), B(25cm × 25cm × 1cm) and WLS fiber (BCF92, SAINT-GOBAIN)—were made.

In this work, thermostat box was used; the temperature around the tested scintillator is in large dynamic variation, varying -30℃ to 40℃. The samples were tested every 90 times. We assume that it is equivalent to 2 days after varying one time. Figure3 shows a typical amplitude distribution. We fit the amplitude distribution with a Landau distribution and take the MPV value, and then translate into number of photoelectrons. The test result is given as Figure4.

We define the critical time to be the time when the light output has decreased by 20%, it can be seen that the operational time scintillator A is 8.7yr, B is 15.3yr; and WLS with B tile is 12.2yr.

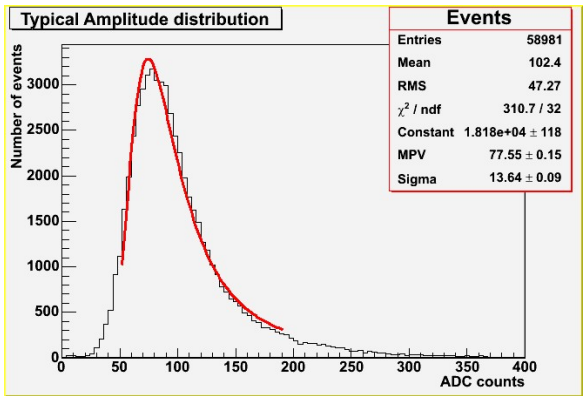

Figure3. Typical Amplitude distribution of one PS tile in case of single Muon, fit the distribution with a Landau distribution and take the MPV value.

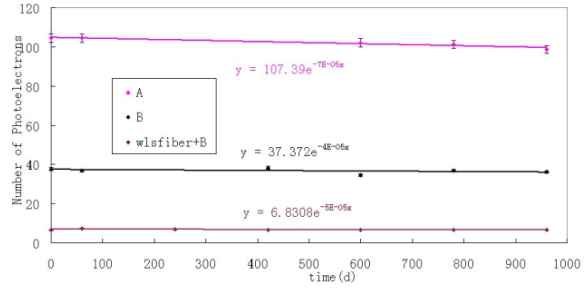

Figure4. The variation curve of Npe (number of photoelectron) after varying 480 times (about 960 days).

4.2 Accelerated thermal aging test

The tiles (scintillator A) are cut from PS obtained by bulk polymerization and finished by polished surface treatment. Tile Unit size is 25cm×25cm×1.5cm, covered with white diffuse Tyvek sheet, and making 8 holes(Φ1.5mm,3cm spacing). Thermal aging of the PS was conducted in air for 200 h at 60◦C, 70◦C and 85◦C. the temperature are below the glass transition temperature of the samples. The samples were tested after every 50 h exposure. There two ways of readout, direct readout (PMT1, PMT2) and fiber readout (PMT3) as shown in Figure1.

We define the critical time to be the time when the light output has decreased by 20% [8]. The lifetime at 20 degrees centigrade is determined from an Arhenius plot, where the logarithm of the critical time is inversely proportional to the temperature.

The influence of heating at 60◦C, 70◦C and 85◦C for 200 h manifests itself in a decrease in the light yield. After 200 h at 85◦C the light yield of WLS fiber readout change is 12–18%. And the light yield of direct readout change is markedly increased, the light yield change is16–25%. The results of measurements of light yield for different tiles are presented in Figure5, Figure6 and Figure7.

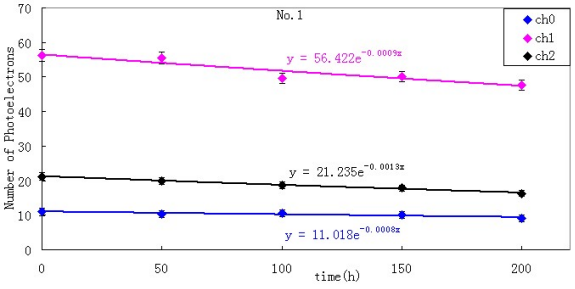

Figure5. Light yield of tiles under accelerated aging (250×250×15 mm^3, T =85◦C).ch0: WLS fiber readout; ch1 and ch2: direct readout.

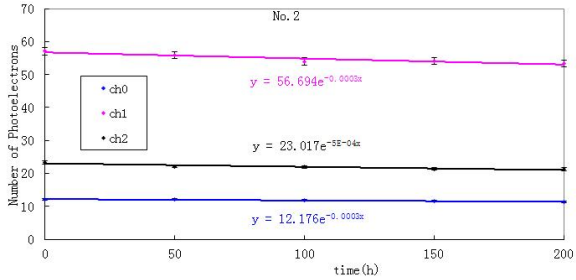

Figure6. Light yield of tiles under accelerated aging (250×250×15 mm^3, T =70◦C).ch0: WLS fiber readout; ch1and ch2: direct readout.

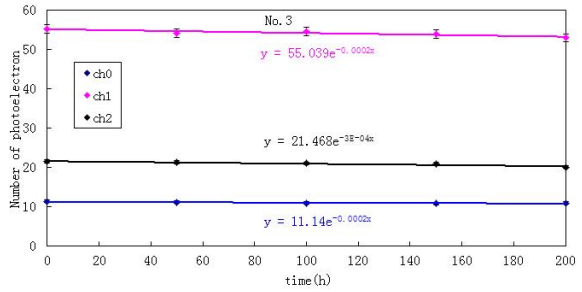

Figure7. Light yield of tiles under accelerated aging (250×250×15 mm^3, T =60◦C).ch0: WLS fiber readout; ch1and ch2: direct readout.

According to the result of accelerated aging at 60◦C, 70◦C and 85◦C, the operation time predictions for a 20% change of light yield can be calculated by using Arhenius plot (Figure8). It can be seen that the operational time scintillator B is 8.9yr, and scintillator B with WLS fiber is 7.8yr.

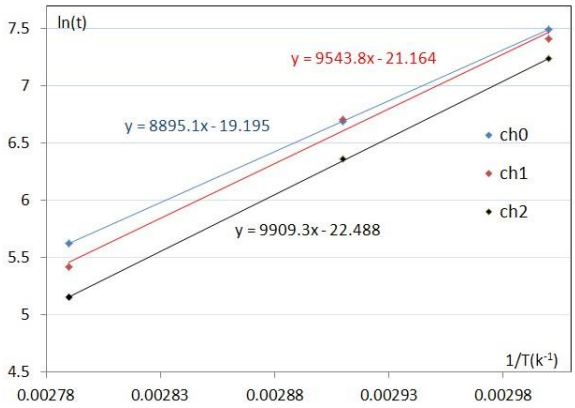

Figure8. Arhenius plot, ch0: WLS fiber readout; ch1and ch2: direct readout.

5 Conclusion

It is important to study long-term stability of plastic scintillator (PS) for the LHAASO-KM2A. According to high and low temperature aging tests simulating the Yangbajing environment, it can be seen that the operational time scintillator A and B PS tiles are 8.7 yr; WLS with B tile is 12.2 yr when the light output has decreased by 20%. According to the result of accelerated thermal aging test, the lifetime scintillator B is 8.9yr, and scintillator B with WLS fiber is 7.8yr.

Acknowledgments

This work is partly supported by the Knowledge Innovation Fund (H85451D0U2) of IHEP, Beijing.

References

[1] Z. Cao et al. (LHAASO Collaboration), 31th ICRC, LORZ, (2009)
[2] Huihai, He et al. (LHAASO Collaboration), 31th ICRC, LORZ, (2009)
[3] Xiangdong, Sheng et al. (LHAASO Collaboration), 32th ICRC, Beijing, (2011)
[4] G. Xiao et al. (LHAASO Collaboration), 32th ICRC, Beijing, (2011)
[5] Karpuchin, O.N., Predicted of long-term stability of polymer materials. Plast. Massy. No 11, pp. 27 – 29, (1978)
[6] T. Asakawa et al., Nuclear Instruments and Methods in Physics Research A 340, 458, (1993)
[7] M. Chikawa et al., Proc. 28th Int. Cosmic Ray Conf. (Tsukuba), 2, 1033 (2003)
[8] V. Senchishin et al., New Radiation Stable and Long-Lived Plastic Scintillator for the SSC. (1993)
[9] B.V. Grinyov et al., Long-term stability scintillation tiles for LHCb detector. Radiation Measurements 38 825 – 828, (2004)

32ND INTERNATIONAL COSMIC RAY CONFERENCE, BEIJING 2011

Design and implementation of the electronics for the Askaryan Radio Array testbed and future plans

PATRICK S. ALLISON[1], FOR THE ARA COLLABORATION
[1]*Ohio State University, Columbus, OH 43210, United States*
allison.122@osu.edu

DOI: 10.7529/ICRC2011/V04/0744

Abstract: A testbed to understand the polar radio environment for the future Askaryan Radio Array (ARA) ultrahigh energy neutrino detector. was deployed during the 2010-2011 polar season, and is currently operating and acquiring data. The testbed consisted of custom digitization and triggering hardware for 8 antennas, and a data acquisition system based on a commercial off-the-shelf single board computer. The design of the testbed electronics will be discussed. For the prototype ARA stations, with a total of 16 wider spaced antennas presents additional challenges due to the large buffer required. The design of the prototype stations, due to be deployed in 2011-2012, will also be presented.

Keywords: ARA, neutrino, South Pole

1 Introduction

The discovery of ultra-high energy cosmic rays (UHECRs) beyond $100\ \mathrm{EeV}$ has led to considerable interest in neutrino detection at these energies, since the propagation of UHECRs through cosmological distances must produce neutrinos due to the Greisen-Zatsepin-Kuzmin (GZK) process [1][2]. The Antarctic polar ice is an excellent detection mechanism for neutrinos above $1\ \mathrm{PeV}$ through the Askaryan mechanism [3], and has been used in several previous pioneering experiments such as RICE [5] and ANITA [4].

The Askaryan Radio Array is a planned $200\,\mathrm{km}^2$ array ("ARA-37") at the South Pole to definitively detect cosmogenic GZK neutrinos, combining experience from the RICE, ANITA, and IceCube projects. In order to determine the RF environment at the South Pole, a testbed station was deployed during the 2010-2011 polar season, based heavily on existing proven ANITA technology based around the LAB3 digitizer [7]. The testbed consists of 14 total in-ice antennas, with 2 horizontal and 2 vertical polarization (Hpol and Vpol) antennas near the surface, and 4 Vpol and 6 Hpol antennas buried approximately $20\,\mathrm{m}$ below the surface. The Vpol antennas have a bandwidth of $150 - 850\,\mathrm{MHz}$, and the Hpol antennas have a bandwidth of $250 - 850\,\mathrm{MHz}$. An additional 2 low-frequency ($30 - 300\,\mathrm{MHz}$) surface antennas were also deployed. The testbed station has a similar in-ice horizontal geometry (around $20\,\mathrm{m}$ diameter) to the planned ARA stations, but the deployed antennas are significantly shallower ($20\,\mathrm{m}$ versus $200\,\mathrm{m}$) and with less vertical spacing between the antennas ($5\,\mathrm{m}$ versus $20\,\mathrm{m}$).

Two additional full ARA-37 level stations are planned for deployment in the 2011-2012 and 2012-2013 polar seasons. The design is based somewhat on the testbed, but with significantly different digitization. Since the ARA stations have antennas significantly deeper in the ice, the index of refraction is much higher ($n \sim 1.8$) than in the testbed ($n \sim 1.3$). For the testbed, a signal transits across the station on the order of $\sim 100\,\mathrm{ns}$ - for the full ARA station, it is closer to $\sim 200\,\mathrm{ns}$, including propagation time differences in the cables. The analog depth of the LAB3 ($260\,\mathrm{samples}$) is insufficient to capture transits across a full ARA station at greater than $2\,\mathrm{GHz}$, and certainly insufficient to capture a multi-station coincidence. Therefore, a deeper, buffered architecture was developed, called the Ice Radio Sampler (IRS2).

2 ARA Testbed Electronics

The testbed electronics consists of a custom digitization board - the Ice Cube Radio Readout (ICRR), shown in Fig. 1, a USB interface board, and a commercial off-the-shelf single board computer, the ADI Engineering Cinnamon Bay A520PT.

The ICRR consists of 16 RF input channels and 16 RF triggering channels, one each for each antenna. Each of the RF channels was passed through a $13\,\mathrm{dB}$ coupler, and the coupled signal was passed through a calibrated MAX4003 power detector to monitor the RF environment. The direct signal was sent to one of 3 LAB3 ASICs onboard the ICRR.

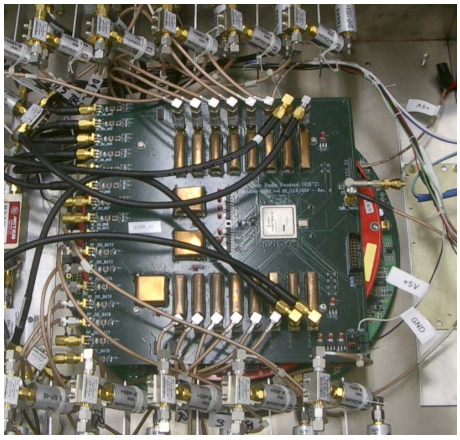

Figure 1: The Ice Cube Radio Readout board. The 16 RF input channels are to the left, and the 16 RF trigger channels are visible on the top and bottom of the board. RF sensitive devices, such as the $20\,\mathrm{dB}$ amplifier used in the trigger input chain and the LAB3 digitizers themselves were enclosed within copper board-level shields. Boards below the ICRR are no longer used.

The LAB3 (Large Analog Bandwidth Recorder and Digitizer with Ordered Readout) is a high-speed RF digitizer developed by the University of Hawaii Instrumentation Development Lab [7]. It is a 9-channel digitizer with a record length of 260 samples. 8 channels are used for RF inputs, and the remaining channel is used for a global clock for synchronization. Due to the large size of the testbed station, the sampling speed for the LAB3 was set to $1\,\mathrm{GHz}$ for sufficient buffer depth, which is very low considering the frequencies of interest reach as high as $850\,\mathrm{MHz}$. To compensate for this, 8 of the channels are sent into an RF splitter, with one output going directly into a LAB3 channel and the other first delayed by 500 ps before going into a second LAB3 channel. This effectively gives a $2\,\mathrm{GHz}$ interleaved sampling for those 8 (high-frequency) channels. The remaining 8 (low-frequency) channels contain the surface and near surface antennas, as well as an additional Hpol and Vpol deep antenna. The interleaved sampling scheme was a compromise due to the limited record length of the LAB3.

The sampling speed of each LAB3 is controlled by a DAC voltage. The sampling speed is monitored by observing the number of system ($40\,\mathrm{MHz}$) clock cycles between 2048 ripple-carry oscillator (RCO) output periods. The RCO output toggles every 256th sample, which means that the RCO period is 512 times the sampling frequency. The FPGA therefore looks for 41,943 clock cycles between the first and 2048th RCO period. If fewer cycles are observed, the DAC value controlling the LAB3 readout speed is increased. If more cycles are observed, the DAC value is decreased.

Before entering the ICRR, the high-frequency channels are split and sent through a $20\,\mathrm{dB}$ amplifier, and then passed through a tunnel diode used as a square-law RF power detector. This signal is then sent into the FPGA as one side of a differential pair, with the other side fixed to a DAC-controlled voltage, effectively using the differential receiver as a high-speed comparator. The low-frequency channels are amplified and sent directly into two separate differential pairs in the FPGA (one positive leg, one negative leg) with DAC-controlled voltages as the other leg on both pairs. This triggering method was not as effective as the high-frequency approach, and will not be used again in the future.

The ICRR also contains 8 individual AD7814 temperature sensors spaced around the board, 7 AD5324 quad-output DACs (for a total of 28 DAC outputs), and 2 LTC1415 12-bit ADC and CD4051B 8-to-1 analog multiplexer for digitizing the MAX4003 power detectors. 24 of the DAC outputs are used for the triggering thresholds (8 for the tunnel diode-based high frequency channels, and 16 for the direct triggering-based low frequency channels), 3 are used for controlling the readout speed of the LAB3, leaving one spare.

The USB interface board for the ICRR contains a Cypress Semiconductor EZ-USB FX2LP USB microcontroller bridge and the flash PROM for the FPGA configuration file. The ICRR/USB interface are then connected to the ADI Engineering Cinnamon Bay A520PT single board computer, which is a low-power ($\sim 5\,\mathrm{W}$) extended temperature Intel Atom-based system operating at $1.33\,\mathrm{GHz}$. The single-board computer is then connected back to the Ice Cube Lab using a Westermo Ethernet extender operating over a standard IceCube quad cable[6], resulting in a bandwidth of a few MB/s.

The Virtex-4 FPGA contains the triggering algorithm which processes the 24 input trigger signals, the readout logic for reading out the LAB3 ASICs, a housekeeping interface for monitoring the temperature, triggering rates, and LAB3 sampling speed, and the software interface. The software interface is based on the USBP project firmware [8], which adapts the EZ-USB slave FIFO interface into a WISHBONE [9] bus interface on the FPGA. This interface is relatively slow due to an effectively half-duplex communication with software, but is sufficiently fast for the testbed goals, and can read out data at approximately $25\,\mathrm{Hz}$. The LAB3 ASICs hold the data until each trigger is fully read out by the software. The single-buffered nature of the testbed design thus implies that in order to obtain low deadtime (less than 10%) the system should trigger on the order of a few Hz. This limitation was driven by time considerations.

Event timing is performed inside the FPGA using a free-running clock cycle counter for intrasecond timing and a pulse-per-second signal provided by a rubidium clock disciplined by a GPS receiver. The Rubidium clock was chosen to provide a stable time reference over long periods

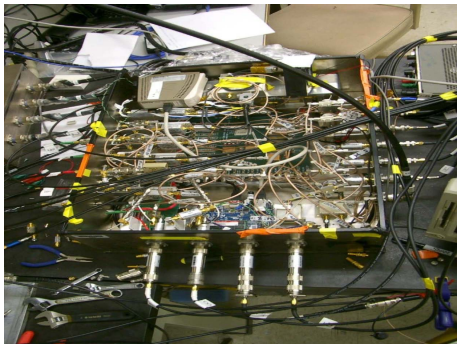

Figure 2: The fully integrated testbed electronics. The ICRR and USB interface board are visible in the middle, the Cinnamon Bay SBC is located near the bottom, and the Westermo ethernet extender is in the top left.

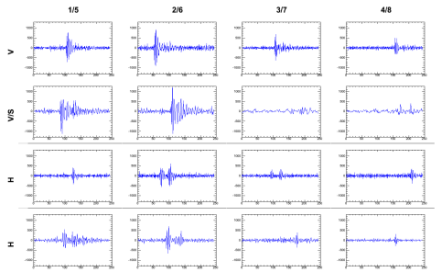

Figure 3: An example calibration pulser event. Because the calibration pulser is very close to the testbed $\sim 30\,\mathrm{m}$, attenuation of the pulse (due to distance from the source) is clearly evident as the pulse propagates across the testbed. The reflection seen in horizontal antennas shortly after the initial pulse is currently believed to be a horizontal piece of metal remaining from the 1950s polar station.

($\sim$ hours) to enable repeated averaging for weak distant calibration pulser signals.

A picture of the fully-integrated testbed electronics is shown in Fig. 2, and an example event originating from a calibration pulser located $\sim 30\,\mathrm{m}$ from the testbed is shown in Fig. 3.

3 ARA Electronics

While the testbed electronics was suitable for RF environment testing at the South Pole, there are several fundamental limitations which prevent the design from being usable for full ARA stations. First, the sampling speed (8 at 2 GHz using interleaved sampling and 8 at 1 GHz) is a clear limitation. Typically, digital sampling is done at least 4 times the highest frequency of interest (so the highest frequency is half of the Nyquist frequency). For the full ARA stations, a sampling speed of 3.2 GHz was chosen. At this sampling speed, the LAB3 architecture is unusable, and thus a new digitizer is required. In addition, the single-buffered nature of the LAB3 design seriously limits the readout speed. Thus, a buffered, very high speed digitizer is required.

To meet these goals, an 8 channel digitizer with an effective analog buffer depth of 32768 samples was developed, termed the Ice Radio Sampler (IRS2). The IRS2 contains 2 64-capacitor sampling cells (termed "blocks") and 512 analog memory blocks. Every 20 ns, one of the two sampling cells is transferred into a block while the other cell samples the RF signal. When a trigger occurs, the desired blocks of analog memory are digitized while the remaining blocks continue sampling. This meets the design goals of a deep, buffered, high-speed design.

To ease development, the equivalent of the ICRR for the full ARA station was split into three separate boards: the ARA Triggering and Readout Interface (ATRI), the Digitizing Daughterboard for ARA (DDA) and the Triggering Daughterboard for ARA (TDA). The ATRI board hosts a Spartan-6 LX150T control FPGA and 4 daughterboard bus connectors. The daughterboard bus is made of two Samtec QSE/QTE connectors - on the DDA/TDA, the connectors are mounted back-to-back to allow the daughterboards to be stacked. Each daughterboard stack will contain a TDA and DDA, and will service 4 antennas located in one borehole (for a total of 16 antennas). The ATRI board also contains connectors to mount an i-Lotus M12M GPS, and the Cinnamon Bay SBC, as well as connectors to interface to external devices via an $\mathrm{I^2C}$ bus. The ATRI board contains 2 interfaces to the SBC - via USB, using an EZ-USB FX2LP microcontroller, and a direct link to the FPGA using a PCI-Express link present on the SBC connector. The FX2LP microcontroller also contains the FPGA programming interface and controls $\mathrm{I^2C}$ devices present on the ATRI board.

The ATRI board also receives a 10 MHz reference clock signal from an external rubidium clock (disciplined by the GPS) which is distributed to the daughterboard busses and multiplied and sent to the FPGA via an ultra-low jitter Si5367 programmable clock multiplier.

The daughterboard bus contains the signals required to control an IRS2, 8 differential trigger signals, 2 sense/power control lines, an $\mathrm{I^2C}$ bus for each daughterboard stack, and a large number of signals reserved for possible future daughterboards. Each individual daughterboard contains an EEPROM for board identification, a temperature sensor, and a hot-swap controller to provide voltage and current monitoring as well as power control.

The DDA (shown in Fig. 4) contains a single IRS2 and has 4 RF input channels. An additional IRS2 channel is used for the reference clock (for synchronization). Two of the remaining channels are routed to test input channels and the last channel is used to isolate the reference clock from the signals of interest. The DDA also contains a 2-channel DAC to provide voltages to control the IRS2 sampling speed and digitization linearity.

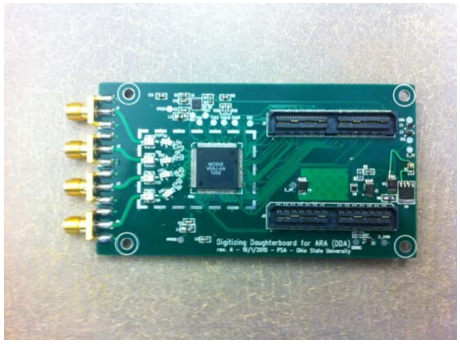

Figure 4: Digitizing Daughterboard for ARA (DDA). The DDA is a daughterboard on the ARA Triggering and Readout Interface (ATRI) board, and hosts a single IRS2 digitizer. 4 of the 8 IRS2 channels are fed by RF inputs (on left), one by a reference clock transmitted over the ATRI bus connectors (on right) and two are test inputs (not visible). The remaining channel is unused.

The DDA sampling speed is monitored by measuring the delay from insertion of the "start sampling" signal (TSA) to its return after propagating through the voltage controlled delay line which starts the sampling at each capacitor (TSAOUT). This delay is measured on the FPGA based on a technique by Quirós-Olozabál *et al.* [10], where the Xilinx Digital Clock Manager (DCM) delay line used for dynamic phase shifting is used to generate a phase-shifted latch for the incoming TSAOUT signal, and a state machine searches through phase shift values to locate the rising edge of TSAOUT. The dynamic phase shift delay line contain 256 total taps, and utilizing a coarse clock 4 times faster than the TSA clock allows for monitoring the TSA to TSAOUT delay to within $40\,\mathrm{ps}$. This technique has several advantages over other FPGA-based TDCs. First, the DCM delay lines are already well-calibrated, and second, the same architecture can be used for all 4 DDA daughterboards hosted by the ATRI since only the signal latch is being shifted, rather than the input signal.

The TDA contains 4 RF triggering channels. The triggering input path is similar to the ICRR, but contains an additional $20\,\mathrm{dB}$ of amplification to move the tunnel diode response to a region with more dynamic range and better response. In addition, the tunnel diode signal is converted into a differential signal using a fully-differential amplifier against a DAC controlled threshold (provided by a 4-channel DAC) before being sent to the FPGA.

The ATRI, DDA, and TDA are all currently in production and a full ARA station is planned for deployment this year, with a second following next year.

4 Conclusion

The Askaryan Radio Array is a planned $200\,\mathrm{km}^2$ scale detector designed to definitively detect GZK neutrinos in quantity. The testbed detector, currently deployed and operating, was based on proven technology from the ANITA experiment. The future ARA-37 station electronics will expand on that technology with deeper buffering and electronics more suitable to a permanent array-level deployment.

References

[1] K. Greisen, Phys. Rev. Lett., 1966, **16**: 748-750.
[2] G. T. Zatsepin, V. A. Kuzmin, Pisma Zh. Eksp. Teor. Fiz., 1966, **4**: 114.
[3] G. A. Askaryan, JETP, 1962, **14**: 441.
[4] P. W. Gorham *et al.* , Phys. Rev. Lett., 2009, **D82**: 022004.
[5] I. Kravchenko *et al.* , Phys. Rev. Lett., 2006, **D73**: 082002.
[6] R. Abbasi *et al.* , Nucl. Instr. Meth. A, 2009, **601**: 294-316.
[7] G. S. Varner *et al.* , Nucl. Instr. Meth. A, 2007, **583**: 447-460.
[8] USBP project. Retrieved from http://www.fpgaz.com/wiki/doku.php?id=fpgaz:usbp.
[9] WISHBONE, Revision B.3 Specification. Retrieved from http://cdn.opencores.org/downloads/wbspec_b3.pdf.
[10] Á. Quirós-Olozábal *et al.* , Int. Conf. on Field Programmable Logic and Applications, 2010: 502-507.

Seasonal variations of the muon flux seen by muon detector BUST

M.BERKOVA[1], V. PETKOV[2], M.KOSTYUK[2], R. NOVOSELTSEVA[2], YU.NOVOSELTSEV[2], P. STRIGANOV[2], M. BOLIEV[2], V.YANKE[1]
[1]*Institute of Terrestrial Magnetism, Ionosphere and Radiowave Propagation RAN of N.V. Pushkov (IZMIRAN), Tritsk, MR, RU-142190, Russia*
[2]*Instutute for Nuclear Research, 60th Oct. Anniversary prospekt 7A, Moscow, RU-117 312, Russia*
yanke@izmiran.ru
DOI: 10.7529/ICRC2011/V04/0751

Abstract: According to the Baksan underground muon telescope (BUST) for the period 2009-2010 it was established a correlation between variations of the muon flux of the energy > 220 GeV at the observation level and variations of the atmosphere temperature profile. The obtained temperature coefficients were compared with the results from other authors. For the analysis, the vertical temperature profile of the atmosphere obtained according to the atmosphere model was used. The temperature effect was excluded from the hourly BUST data for 2009-2010.

Keywords: muons, muon detector, temperature effect, temperature coefficient, effective temperature.

1 Temperature effect

For many decades it was very difficult and sometimes impossible to allow for the temperature effect of the muon cosmic ray component. The main problem was to get the temperature vertical profile of the atmosphere. Until recently aerological sounding was the main source of such data. But there were problems, such as regularity of soundings. And in the case of out-of-the-way detector it was simply impossible to measure the temperature profile. The situation was cardinally changed at the end of the 20th century with the development of global atmospheric models allowing getting the temperature vertical profiles in any place and at any time. These models give us an opportunity to make the most out of the richest data collected by the world network of muon detectors.

It is known that the temperature effect of the muon component is caused by a competition between decay of π/κ and μ and their interaction with the atmospheric nuclei due to the change of geometric atmosphere dimensions. With atmosphere heating and its consequent expansion the number of π/k decays is increasing and this results in positive temperature effect. Simultaneously with the atmosphere expansion the μ path to the detector is increasing what results in the negative temperature effect as μ decay becomes more possible.

The positive temperature effect of cosmic rays measuring by the underground detectors was first observed by M.Forro in 1947 [1]. After the π-meson discovering Miyazima supposed that the positive temperature effect originated due to the competition between decay of new particles and their absorption by nuclear interactions [2]. Later on P.Barret et al. in 1952 wrote about the temperature effect in [3]. In this paper the authors introduced the concept of the "effective temperature" as the temperature of some conventional isothermal atmosphere that the muon intensity in passing through such atmosphere was the same as in passing through the real atmosphere with the temperature distribution T (h). By using the effective temperature the temperature effect was calculated and defined as "a relative change of the muon intensity per 1 degree temperature change".

The goal of this work is to exclude the temperature effect from the data of the BUST muon telescope for 2009-2010 using the model temperature data and to determine temperature coefficients for this period.

2 The methods of accounting the temperature effect

In 1956 L.Dorman and E.Feinberg in [4] brought in a function *W(h)* meaning "a temperature coefficient density" and cosmic ray variations due to the atmospheric temperature effect are determined as:.

$$\left.\frac{\delta N}{N}\right|_T = \int_0^{h_0} W_T^{\mu}(h)\cdot\delta T(h)\cdot dh \qquad (1)$$

where $\delta N/N$ - variations due to the temperature effect, $\delta T(h)$ - temperature variations of the atmosphere determined as a divergence of the running temperature

profile and the temperature profile in the base period *B:* $\delta T(h) = T(h) - T_B(h)$. Densities of the temperature coefficients $W_T^{\mu}(h)$ have a dimension of $\frac{\%}{^{\circ}K \cdot atm}$ and they are calculated for different depths and angles. The integral method (1) makes it possible to calculate the temperature effect with high accuracy determining mostly by a precision of the temperature coefficient densities $W_T^{\mu}(h)$. The full description of this method one can find in [5]. The formula (1) can be written as:

$$\frac{\delta N_{\mu}}{N_{\mu\ Temp}} = \int_0^{h_0} W_T^{\mu}(h)\delta T(h)dh = \int_0^{h_0} W_T^{\mu}(h)dh \cdot \frac{\int_0^{h_0} W_T^{\mu}(h)\delta T(h)dh}{\int_0^{h_0} W_T^{\mu}(h)dh}$$

or $$\frac{\delta N_{\mu}}{N_{\mu\ Temp}} = \alpha_T \cdot \delta T_{Teff} = \hat{\alpha}_T \frac{\delta T_{eff}}{\overline{T}_{eff}} \qquad (2)$$

here $\alpha_T = \int_0^{h_0} W_T^{\mu}(h)dh$ (%/degree) - temperature coefficient, and effective temperature is:

$$T_{eff} = 1/\alpha_T \cdot \int_0^{h_0} W_T^{\mu}(h)T(h)dh \qquad (3)$$

Along with the temperature coefficient α_T the dimensionless temperature coefficient $\hat{\alpha}_T$ is often used and it can be expressed as $\hat{\alpha}_{_T} = \alpha_T \cdot \overline{T}_{eff}$. It is seen from (2) that the dimensionless $\hat{\alpha}_T$ is a regression coefficient between the intensity variations and the temperature variations. The effective temperature doesn't simplify calculations in comparison with the integral method but it allows to determine α_T by experiment. This method was developed by Barrett et al. [3] in 1952 and it is an analog of the integral method (1) as in the both methods the contributions of all atmosphere levels are allowed for with the proper weights. The main contribution to the μ intensity is provided by muons originated from the π decay. But for μ of high energies >100 GeV registering by the underground detectors the full muon intensity depends on both π and κ decay [6]. The κ contribution can exceed 20%, and the more measuring energies the more it is. In this work the calculations have been done on the assumption that muons registering by the BUST are originated from π (80%) and *k* (20%). decay

Together with the classic integral method in order to allow for the muon temperature effect some approximate methods are also used: the method of effective level of generation [7], the method of mass-average temperature [8]. These methods are based on some essential assumptions limiting their application.

So, the method of effective level of generation, as it is seen from its name, is based on the assumption that μ are generally generated at the isobaric level usually taking for 100 mb, and its height is changing with the change of atmosphere temperature: $\delta I_T = \alpha_H \delta H + \alpha_T \delta T$, where α_H (%/km) - is so-called decay factor, negative effect and α_T (%/C)- positive temperature coefficient.

The method of mass-average temperature is based on the assumption that the temperature coefficient density is changed in a small way with the atmosphere depth *h* (just for the ground-based detectors), that allows us to carry out the average $\overline{\alpha}_T$ behind the integral sign and to transform (1) into $\frac{\delta N_{\mu}}{N_{\mu\ Temp}} = \int_0^{h_0} W_T^{\mu}(h)\delta T(h)dh = \overline{\alpha}_T \cdot \delta T_m$, where T_m - mass-average temperature.

3 Temperature data

In this work the data of the Global Forecast System (GFS) temperature model representing by the National Centers for Environmental Prediction — NCEP (USA) has been made use of [9]. GFS model makes it possible to obtain both retrospective and prognostic data. The model output data are temperature at the 17 isobaric levels: observation level, 1000, 925, 850, 700, 500, 400, 300, 250, 200, 150, 100, 70, 50, 30, 20, 10 hPa for four times 00, 06, 12 and 18 hours every day. The data are interpolated on the grid of 1°×1° resolution. To obtain hourly data the interpolation by the cubic spline function [10] on six nodal points (four points for a running day plus at one point left and right) is carried out. The accuracy of this model is about one degree for all isobaric levels and little more for the ground level [11].

4 BUST

Last years for the purpose of neutrino oscillations study and search for dark matter particles the projects with underground detectors registering high energy particles are developed. Seasonal variations observing at the most of underground detectors are studied in many papers, for example [12-16]. In figure 1 from [12] there are experimental points of temperature coefficients (dimensionless) for some underground detectors, and there are also curves obtaining by the Monte-Carlo method for different models of μ generation. The experimental point for the BUST is from [13]. The square in figure 1 is our result.

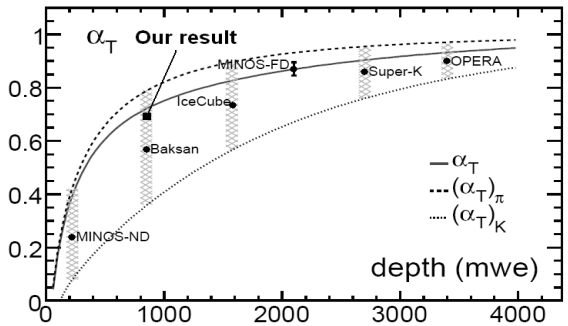

Figure 1. Theretical α_T - solid curve, $\alpha_{T\pi}$ - top curve, α_{TK} – bottom curve. Square – our result.

The Baksan Underground Scintillation Telescope of the Institute for Nuclear Research RAS is located in the Caucasus Mountains (43.28° N and 42.69° E) inside the

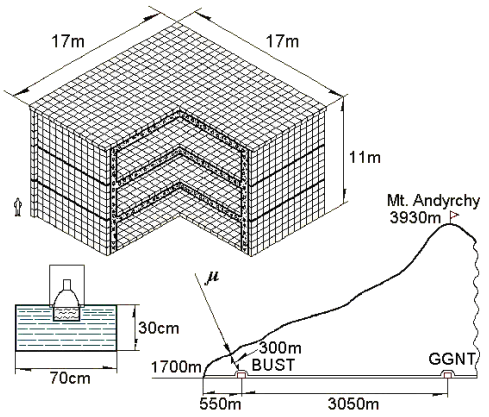

Figure 2. The BUST

mine of 24×24×16 m^3 under the Andyrchy mountain. There is 350 m of rock vertical depth (850 mwe) over the telescope. The BUST is parallelepiped of 16.7×16.7×11.1 m^3 consisting of 8 planes (4 inner and 4 outer) of detectors (each of 70×70×30 c m^3) with liquid scintillator (Fig. 2). The range of measuring energies is 0.5-500 GeV. The μ threshold energy is 220 GeV. The observatory level is 1700 m above sea level, average pressure is 820 mb [17].

5 Data analysis

The original BUST 15-minute data were transformed into hourly data. The barometric effect for the BUST is negligible, so the data weren't corrected for the pressure. It should be noted that the original data have some gaps. Before the data processing small gaps (hours) were filled in by smoothing, and big gaps were left unaltered. The BUST has seasonal variations and it is seen from the series of daily data for 2007-2010 years in figure 3.

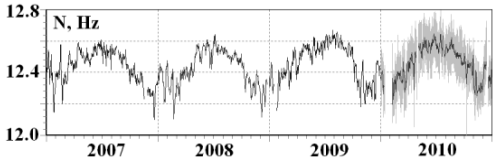

Figure 3. Average daily data for the BUST (2007-2010). There is also hourly data for 2010.

In this paper the temperature effect was determined by the method of the effective temperature. To calculate the effective temperature by (3) the densities of temperature coefficients $W_T^{\mu}(h)$ for the BUST energies (>220 GeV) were used [6]. These W_T for high energies accounting for decay of π (80%) and k (20%) [6] are represented and compared with approximation from [3] in figure 4.

In figure 5 the calculated effective temperature for 2009 is compared with the temperature profile at isobaric levels of 10, 20, 30 and 50 mb. Lower levels aren't represented though in our calculations the whole vertical profile was taken into account.

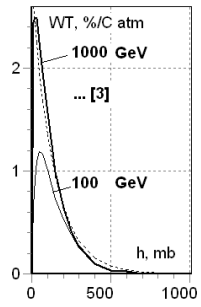

Figure 4. $W_T(h)$ [6]

In figure 6 there are observed by the BUST muon rate (black curve), calculated effective temperature T_{eff} (right scale) and free from temperature effect muon rate (grey curve) for 2009-2010 years. It is clearly seen from figure 6 that the annual wave was removed after excluding the temperature effect.

For the quantitative estimation of calculated effective temperature T_{eff} and experimental temperature coefficient α_T the correlations between observed muon rate variations and effective temperature deviations from the average annual effective temperature were built. The correlation pictures for 2009 (left) and for 2010 (right) are in figure 7. After the correlation analysis we get correlation coefficient ρ and temperature coefficients α_T for 2009 and 2010 years (Table 1). The calculated values (especially for 2009) are in good agreement with the earlier values get for the BUST [13]: ρ = 0.97±0.02 and α_T = 0.372±0.038 % / K

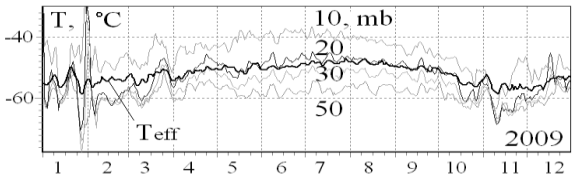

Figure 5. Temperature profile at the standard isobaric levels (10, 20, 30 and 50 mb) and effective temperature for the BUST (2009)

Correlations between observed and calculated BUST temperature variations is in figure 8. Obtained values are close to the line with a regression coefficient equal 1.

It is clear that free from temperature variations muon rate must have a normal distribution. To check the used method a histogram of BUST muon rate was built: before and after the temperature effect excluding (figure 9). After the processing the distribution is close to Gauss and the half-width of the distribution $A_{1/2} = 2\sigma/N$ is about 1 %.

All obtained results for the BUST (2009-2010) are represented in Table 1. There are average muon rates free from temperature effect N, root- mean-square deviations of the normal rate distribution σ , correlation coefficients ρ , temperature coefficients α_T and $\hat{\alpha}_T$ and base effective temperatures T_{eff} .

	N, Hz	***σ, Hz***	**ρ**	**α_T, % / °K**	$\overline{T}_{eff}$ **, °K**	$\hat{\alpha}_T$
2009	12.468	0.070	0.97	0.32±0.02	221.11	0.71±0.04

2010	12.458	0.062	0.91	0.30±0.02	220.07	0.66±0.04

Table 1. Calculated BUST parameters for 2009-2010

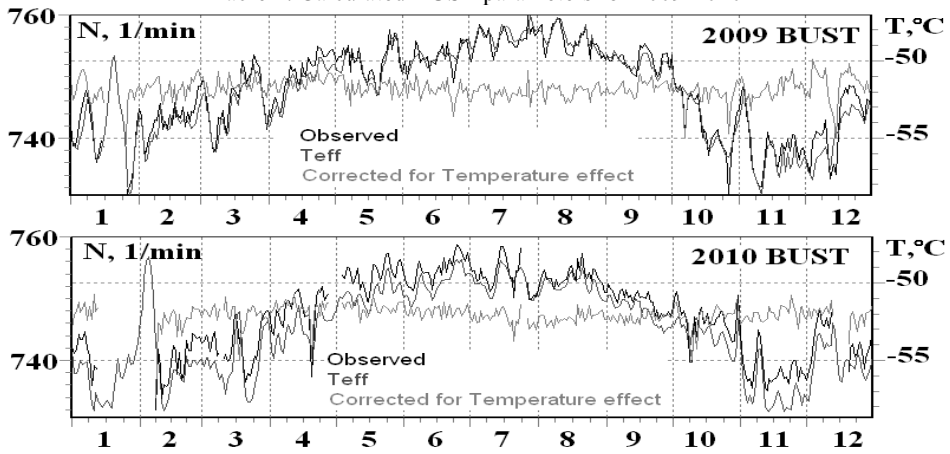

Figure 6. Comparison of stratosphere time series and muon rate for the BUST (2009-2010).

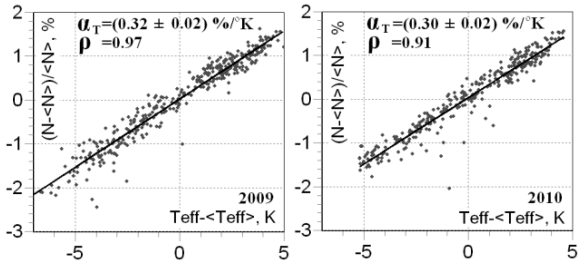

Figure 7. Temperature coefficient for the BUST.

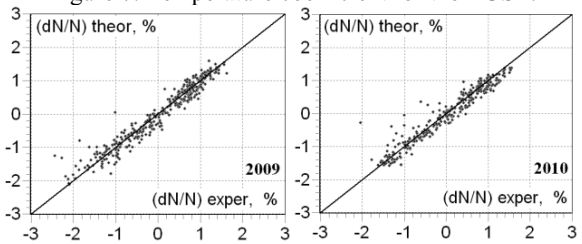

Figure 8. Correlation between observed and calculated temperature variations for the BUST

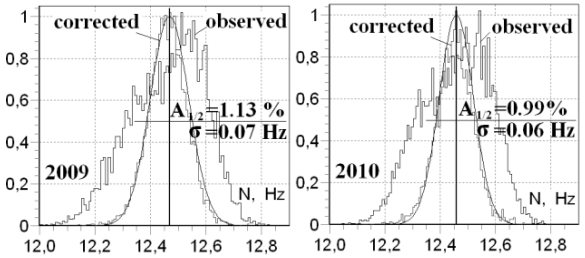

Figure 9. Distribution before (blue) and after (red) excluding the temperature effect and Gauss.

Coefficients $\hat{\alpha}_T$ obtained in this work are in good agreement with experimental and calculated values for the BUST from [12] in figure 1.

6 Conclusions

1) The model data of the vertical temperature profile and used method of the temperature variations determination (the effective temperature method) make it possible to exclude the temperature effect with proper accuracy.

2) There is a good positive correlation between muon rate variations and effective temperature change that makes it possible to obtain the value of the temperature coefficient. The average temperature coefficients for 2009-2010 are α_T=(0.31±0.04) %/ºK and $\hat{\alpha}_T$ =0. 69 ±0,04.

Acknowledgements

This work is partially supported by Russian FBR grants 11-02-01478 and 11-02-13106, Program № 6 BR of the Presidium RAS "Neutrino Physics and Neutrino Astrophysics" and by the Federal Targeted Program of Ministry of Science and Education of RF contract no. 14.740.11.0609 and "Research and Development in Priority Fields for the Development of Russia's Science and Technology Complex for 2007-2013", contract no. 16.518.11.7072.

[1] M. Forro, Phys. Rev., 1947, **72**: 868
[2] T. Miyazima, Prog. Theor. Phys., 1948, **3** (1): 99-100
[3] P.H.Barrett et. al.,. Rev. Mod. Phys., 1952, **24**: 133
[4] L.Dorman, E.Feinberg, UFN, 1956, **59** (6): 189-228
[5] L.Dorman: 1972, Meteorological Effects of Cosmic Rays, Nauka
[6] L.V.Volkova, Nucl. Phys., 1970, **12** (2): 347-359
[7] Duperier A., Proc. Phys. Soc., 1949, A **62**: 684-696
[8] V.M.Dvornikov, Yu.Ya.Krest'yannikov, A.V.Sergeev, Geom. Aeronom, 1976, **16**. (5): 923-925
[9] http://www.nco.ncep.noaa.gov/pmb/products/gfs/ - NCEP
[10] G.E.Forsythe et. al.: 1980, Computer methods for mathematical computations, Mir
[11] M.Berkova et. al.,. Izv. RAS, Ser.Phys., 2011, **75** (6): 887-891
[12] E.W.Grashorn et al., Astropart. Phys., 2010, **33**: 140
[13] Yu.Andreev et al., Proc. 21st ICRC (Adelaide), 1990
[14] S.Tilav, et al., Proc. 31st ICRC (Lodz), 2009
[15] P.Adamson et al., Phys. Rev. D **81**, 012001, 2010
[16] Ambrosio M. et al., Astropart. Phys., 1997, **7**: 109

[17] V.V.Alekseev et al., Izv. AN USSR ser. Phys., 1980, **44** (3): 609

KM3NeT status and plans

PAUL KOOIJMAN[1] (FOR THE KM3NET CONSORTIUM)
[1]*University of Amsterdam, the Netherlands*

H84@nikhef.nl

DOI: 10.7529/ICRC2011/V04/0800

Abstract: The KM3NeT project is aiming to produce the most sensitive neutrino telescope ever built. Its envisaged location in the deep Mediterranean Sea optimizes the sensitivity for neutrino sources near the Galactic centre. During the past year a number of major decisions have been made on technical implementations. We have adopted an optical module (DOM) configuration housing many small photomultipliers rather than earlier traditional designs having a single large PMT. The readout electronics is incorporated into this digital optical module. The site-to-shore communication is provided by an electro-optical cable allowing unique colour point-to-point communication between each DOM and the shore station readout system. Each mechanical supporting structure consists of twenty 6 m long bars with a DOM at each end. The bars have a vertical separation of 40 m giving the full structure a height of around 900 m. The foreseen budget allows for construction of about 300 of such structural units. Together they will create an instrumented volume of between 5 and 8 km^3. The sensitivity to point sources near the Galactic centre surpasses that of any other telescope by two orders of magnitude.

Keywords: Neutrino; deep-sea; Galactic centre;

1 Introduction

Detecting high energy neutrinos from sources in the cosmos indicates the unambiguous presence of charged pion production. This process is necessarily accompanied by production of neutral pions which through their decay generate photons. But whereas high energy photons can also be produced by the energy boosting process of inverse Compton scattering the only process for producing charged pions is that of the interaction of high energy protons with either matter (i.e. other protons) or photons. Neutrinos therefore act as a marker for the presence of high energy protons in astrophysical objects. These objects would then be candidates of the sought-after sites producing the ultra high energy cosmic rays that bombard our atmosphere.

A neutrino telescope works mainly on the principle of detecting particles formed in the interaction of neutrinos with the seawater or the nearby rock of the seabed. The interaction products, most notably the muon formed in the interaction of a muon-neutrino, travel at a velocity exceeding the speed of light in water and therefore emit Cherenkov light along their path length. The excellent transparency of the sea water allows for this light to be detected at distances exceeding 100 m from the muon track. The telescope therefore is in principle a three dimensional array of photo-sensors distributed sparsely over a large volume of sea water. Using the expected time-space correlations of the detected light, the muon track can be reconstructed and its direction determined.

Major backgrounds are expected from the interaction of cosmic rays in our atmosphere, which produce large fluxes of high energy muons traversing the detector from above. Therefore the telescopes are most sensitive to the neutrinos that traverse the Earth and are registered as upward going neutrinos. As a consequence the position on Earth defines, to a large extent, to which part of the sky the telescope is sensitive. Telescopes in the northern hemisphere are predominantly sensitive to the southern sky, which contains the Galactic centre. This area, that contains many sources of high energy photons [1], is therefore a prime objective for the KM3NeT detector, the new telescope network to be built on the bottom of the Mediterranean Sea.

2 Technical design

In designing a detector to be placed at the bottom of an ocean there are several difficulties that must be addressed:

- the ambient hydrostatic pressure;
- the corrosive environment of the seawater;
- the distance from shore for the communication;
- the force on the structure due to the sea currents;
- the backgrounds due to downward going muons;

- the backgrounds due to ^{40}K decay.

For the physical process of detecting neutrinos from sources near the Galactic centre there are additional requirements

- optimal angular resolution of the reconstructed muon; combined with a
- large sensitive area facing the Galactic centre.

This led during the KM3NeT design study[1] to an investigation of many feasible designs, which have been studied in detail. In 2010, during the preparatory phase, this led to a decision on the optimal technical design.

2.1 Optical Modules

The sensors are housed in commonly used deep-sea glass spheres. In order to address the backgrounds from ^{40}K the module must be able to separate multiple photons (most likely signal) from single photons (most likely potassium background) with high efficiency and purity. To provide an efficient measurement of the atmospheric muon background the efficiency of the module is made as uniform in angle as possible. Finally to reduce the number of high pressure feed-throughs as large a photo-sensitive area as possible is put in a single sphere. This led to the design [2] shown in Figure 1. The major optical component is a photomultiplier of 76 mm diameter, surrounded by a 90 mm diameter light concentrator ring [3]. A custom low power (<45 mW) Cockroft-Walton base [4] provides the high voltage for the photomultiplier. It includes an amplifier-discriminator [5] on the output. This allows for the photomultipliers to be run at lower gain (~10^6), to reduce the collected anode charge over the lifetime of the experiment, and implements directly a time-over-threshold readout of the PMTs.

The spheres house 31 of these tubes (19 in the lower hemisphere and 12 in the upper). Following the IceCube example, all digitizing and readout electronics is also housed in this KM3NeT digital optical module (DOM). Finally the DOM also has instrumentation that allows for the reconstruction of the position (acoustic piezo) [6], determination of the orientation (compass and tilt meter) and calibration of the timing ("nano-beacon") [7]

The prototyping of the module was performed with the XP53X2B photomultiplier of Photonis[2]. Unfortunately the manufacture of photomultipliers ceased at Photonis in 2009. In the meantime four manufacturers[3] have expressed interest in the production of the photomultiplier tubes. Some of them have already produced prototypes that are close to or pass specification [8]. The delivery of a sufficient number for assembly of several prototypes is expected by the end of August. These prototypes will be used for lab tests short term in-situ tests on the prototype mechanical structure and in long-term tests in the ANTARES detector.

[1] European Union: FP6 – 011937/FP7 – 21225

[2] Photonis SA, Brive la Gaillarde, France

[3] ET Enterprises Ltd, Riverside Way, Uxbridge, U.K.; Hamamatsu Photonics K.K, Japan;
Zhan Chuang Photonics, Hainan, China;
MELZ-EVP, Zelenograd Moscow, Russia

The electronics necessary for the readout of the DOM is based on an FPGA. At present it is being investigated if the FPGA can incorporate the "time-stamping" of the signal. Alternatively an external timing chip can be used. The FPGA also controls the photomultiplier high voltages and the additional sensors in the DOM.

Figure 1: The KM3NeT DOM showing the photomultipliers with the light concentrator rings, the foam support, the aluminium cooling structure and the blanked cable feed-through.

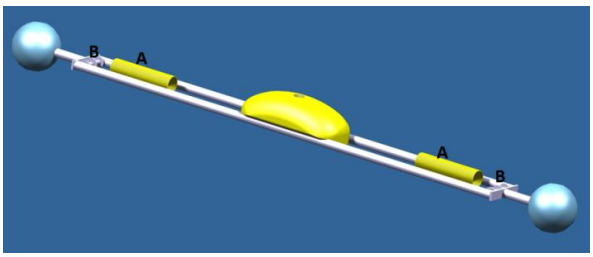

Figure 2: Layout of the horizontal structure. The two DOMs are placed at either end of the 6m structure. The coils of readout cable (A) and rope handling drums (B) are indicated. The exact shape of the central buoy is being optimized.

2.2 Mechanical support structure

The sensors must be distributed over a large volume of seawater and to that end are supported on narrow vertical structures that are weighted down on the seabed by an anchor and held vertical with the aid of a buoy at the top of the structure. For the performance of the detector, it turns out to be advantageous to have a horizontal extension to the structure. This allows for more efficient triggering and an increase of efficiency for low energy neutrinos and a reduction of ambiguities in the tracking. The size of the horizontal extent is of course a compromise in performance and ease of handling of the structure during assembly and deployment on the seabed. These considerations have led to a structure of 6 m length with a DOM positioned at each end (a storey, shown in Figure 2). Twenty of such storeys are then suspended, alternately perpendicular, from four 5 mm Dyneema® ropes with an inter-storey distance of 40 m. The active storeys

start at 100 m from the seabed, so that the total height of the structure (a tower) is 860 m. Two cables, carrying optical fibres for the readout and conductors for the power, run the length of the structure. For the deployment a full tower is brought as a single package to the seabed. The buoy is released and the storeys are drawn from the package one-by-one. During this process the ropes held taut by unwinding them from braked synchronized drums. The readout cables are stored, spiralled around two of the ropes. The strorey includes just sufficient buoyancy to stabilize the structure during unfurling, while still allowing for a controlled release of each storey. Hydrodynamic calculations have shown that the structure can be held vertical within 150 m (top displacement) in sea currents of up to 30 cm per second. At present a full set of prototype structures are being manufactured for test deployments in the coming year.

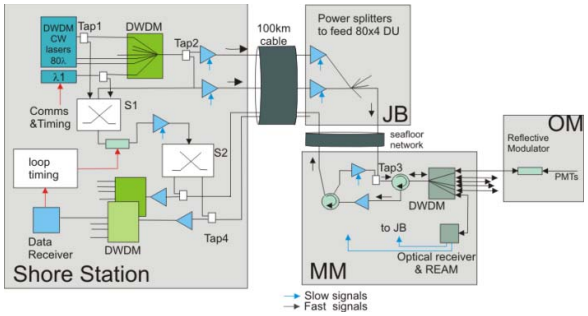

Figure 3: The fibre optic network showing lasers a on the shore, the amplifiers at the end of the main cable, the DWDM systems and the timing circuitry.

2.3 Readout technology

To allow for the data selection to take place in a computer farm on shore, where the data of the full detector are brought together, the connection from the telescope to the shore must have a high bandwidth. Taking into account the counting rate induced by the ^{40}K background and the overall size of the detector, this leads to a transfer rate of several hundred gigabits per second. Therefore the readout technology uses optical fibres. The scheme uses dense wavelength division multiplexing (DWDM) to provide up to 80 readout channels (wavelengths) per optical fibre running from telescope to shore [9]. Each DOM will have its own optical channel directly to shore. All communications lasers will be housed on shore and are of the continuous wave type. These carrier waves are amplified in the deep sea and split such that individual wavelengths are sent, on one downlink fibre, to each tower. There the wavelengths are split into separate fibres that each run to a DOM. At the DOM the carrier wave is modulated with the data from the photomultipliers and reflected back using reflective electro-absorption modulators (REAM)[4]. The data from all DOM fibres are collected and multiplexed then transferred via a downlink fibre to shore. Because of the reflection at the DOM it is possible to incorporate a system to measure the time delay incurred by the signals in the transport to shore. A schematic of the full system is shown in Figure 3. The system has been lab-tested and industry standard bit-error rates have been achieved for transfers over 100 km of fibre. The timing accuracy has been measured to be better than 50 ps.

A system using partial modulation of the downlink carrier signal provides a method for the control of the DOM high voltages and instrumentation.

2.4 Telescope layout

In the KM3NeT technical design report [8] the sensitivity to different physics channels has been investigated. Most notably the sensitivity to the sources of TeV photons, published by the H.E.S.S. collaboration, has been studied. To this end a "standard" telescope layout was introduced consisting of 157 towers arranged in a hexagon. The full telescope would then consist of two such building blocks. More recently it has been noticed that the sensitivity improves slightly when the towers are distributed over a larger number of smaller building blocks. The reason is that the angular resolution does not improve anymore when the tracklength extends beyond about a kilometre, whereas the effective volume of the telescope is merely the product of the range of the produced muon and the surface subtended perpendicular to the direction being investigated. The latter is larger when the same number of towers is distributed over smaller blocks. Presently we are investigating a telescope consisting of the total of 320 towers distributed in a network of five or six smaller blocks each containing around 50 to 60 towers. To enhance the detection of neutrinos with very high energies (>500 TeV) the option is being investigated, where the towers of one of these building blocks are distributed in a sparse configuration with the towers separated by several hundred meters to cover an area of more than ten square kilometers.Technically the separation of the telescope into a network of more, smaller, building blocks is also advantageous as power distribution becomes simpler. The impact of possible failures are reduced and contained within these smaller blocks.

3 Physics sensitivity

The final layout of the detector depends on many parameters. The distance between structures, the size of the building blocks, water absorption and scattering lengths, trigger and tracking strategies to suppress backgrounds, the risks the different layouts imply, while always keeping in mind that deployment should not be compromised and the power distribution can be done with as low power loss as possible. The consortium is performing a systematic simulation study in order to optimize the sensitivity specifically for Galactic sources with realistic energy spectra and to identify the parameters that have the largest impact on the sensitivity. It is already clear that the sensitivity will improve over what was presented in the KM3NeT technical design report. The studies are on-going and the final sensitivity has not yet been fully optimized. Therefore Figure 4 shows the guaranteed

[4] CIP Technologies, Ipswich, U.K.

sensitivity. The sensitivity for point sources is compared to that of IceCube. Several things should be noted. The sensitivity is much more uniform in declination than that of IceCube, which is due to the position on and the rotation of the Earth. KM3NeT outperforms IceCube at the declination of its best sensitivity even though that point is only below the horizon 15% of the time. The KM3NeT sensitivity is conservative as it is estimated using a binned method rather than the unbinned method used by IceCube. The use of an unbinned method requires a careful study of the effects of backgrounds on the point spread function of the tracks, and therefore only makes sense for data. The use of this method typically improves sensitivity by about a factor two. The Galactic centre and the H.E.S.S. sources are all covered with a sensitivity two orders of magnitude better than any other detector. If the high energy gamma rays from these sources are substantially due to the pions then the sensitivity of KM3NeT is sufficient to observe a 3σ signal in a few years of running.

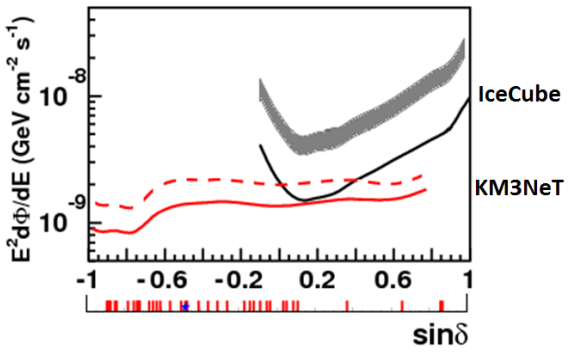

Figure 4: Sensitivity of the KM3NeT to neutrino point sources with an E^{-2} spectrum for one year of observation, as a function of the source declination. The red lines indicate the flux sensitivity (90% CL; full line) and the discovery flux (5σ , 50% probability; dashed line). Both are estimated with the binned analysis method. The black line is the IceCube flux sensitivity for one year, estimated with the unbinned method (full line) [10]. IceCube's discovery flux (5σ , 50% probability) is also indicated (shaded band, spanning a factor 2.5 to 3.5 above the flux sensitivity). The red ticks at the bottom of the horizontal axis show the positions of Galactic gamma ray sources the position of the Galactic Centre is indicated by a blue star.

4 Conclusions

The technical design of the KM3NeT detector has been optimised and prototype construction is beginning in order to validate all elements of the design. The telescope will have a sensitivity sufficient to observe neutrino production in Galactic sources.

[1] H.E.S.S colaboration. H.E.S.S. source catalogue. [Online]. http://www.mpi-hd.mpg.de/hfm/HESS/pages/home/sources/

[2] P. Kooijman, 2011, Nucl. Instrum. and Meth., **A626-627**: S139.

[3] O. Kavatsyuk, Q. Dorosti-Hasankiadeh, H. Löhner , 2011, Nucl.Instrum. and Meth., **A626-627**: S154.

[4] P.Timmer et al., 2010, J. Inst., **5**: C12049.

[5] D. Gajana et al., 2010, J.Inst, **5**: C12040.

[6] K. Graf, 2011, Nucl.Instrum. and Meth., **A626-627**: S217.

[7] F. Salesa-Greus, 2011, Nucl. Instrum. and Meth., **A626-627**: S237.

[8] KM3NeT technical design report, 2010, ISBN 978-90-6488-033-9, http://km3net.org/KM3NeT-TDR.pdf

[9] J. Hoogenbirk, 2011, Nucl. Instrum. and Meth., **A626-627**: S166

[10] R. Abassi et al., 2009, Astrophys.J., **701**: L47.

32ND INTERNATIONAL COSMIC RAY CONFERENCE, BEIJING 2011

Status and Recent Results of the Acoustic Neutrino Detection Test System AMADEUS

ROBERT LAHMANN[1] FOR THE ANTARES COLLABORATION
[1]*Erlangen Centre for Astroparticle Physics (ECAP)*
robert.lahmann@physik.uni-erlangen.de
DOI: 10.7529/ICRC2011/V04/0894

Abstract: The AMADEUS system is an integral part of the ANTARES neutrino telescope in the Mediterranean Sea. The project aims at the investigation of techniques for acoustic neutrino detection in the deep sea. Installed at a depth of more than 2000 m, the acoustic sensors of AMADEUS are based on piezo-ceramics elements for the broad-band recording of signals with frequencies ranging up to 125kHz. AMADEUS was completed in May 2008 and comprises six "acoustic clusters", each one holding six acoustic sensors that are arranged at distances of roughly 1m from each other. The clusters are installed with inter-spacings ranging from 15 m to 340 m. Acoustic data are continuously acquired and processed at a computer cluster where online filter algorithms are applied to select a high-purity sample of neutrino-like signals. In order to assess the background of neutrino-like signals in the deep sea, the characteristics of ambient noise and transient signals have been investigated. In this article, the AMADEUS system will be described and recent results will be presented.

Keywords: AMADEUS, ANTARES, Neutrino telescope, Acoustic neutrino detection, Thermo-acoustic model

1 Introduction

Measuring acoustic pressure pulses in huge underwater acoustic arrays is a promising approach for the detection of cosmic neutrinos with energies exceeding 100 PeV. The pressure signals are produced by the particle showers that evolve when neutrinos interact with nuclei in water. The resulting energy deposition in a cylindrical volume of a few centimetres in radius and several metres in length leads to a local heating of the medium which is instantaneous with respect to the hydrodynamic time scales. This temperature change induces an expansion or contraction of the medium depending on its volume expansion coefficient. According to the thermo-acoustic model [1, 2], the accelerated expansion of the heated volume—a micro-explosion—forms a pressure pulse of bipolar shape which propagates in the surrounding medium. Coherent superposition of the elementary sound waves, produced over the volume of the energy deposition, leads to a propagation within a flat disk-like volume (often referred to as *pancake*) in the direction perpendicular to the axis of the particle shower. After propagating several hundreds of metres in sea water, the pulse has a characteristic frequency spectrum that is expected to peak around 10 kHz [3, 4, 5]. As the attenuation length in sea water in the relevant frequency range is about one to two orders of magnitude larger than that for visible light, a potential acoustic neutrino detector would require a less dense instrumentation of a given volume than an optical neutrino telescope.

The AMADEUS project [6] was conceived to perform a feasibility study for a potential future large-scale acoustic neutrino detector. For this purpose, a dedicated array of acoustic sensors was integrated into the ANTARES neutrino telescope [7]. In the following, the AMADEUS device will be described and recent results will be presented.

2 The ANTARES Detector

The ANTARES neutrino telescope was designed to detect neutrinos by measuring the Cherenkov light emitted along the tracks of relativistic secondary muons generated in neutrino interactions. A sketch of the detector, with the AMADEUS modules highlighted, is shown in Figure 1. The detector is located in the Mediterranean Sea at a water depth of about 2500 m, roughly 40 km south of the town of Toulon at the French coast at the geographic position of 42°48′ N, 6°10′ E. ANTARES was completed in May 2008 and comprises 12 vertical structures, the *detection lines*. Each detection line holds up to 25 *storeys* that are arranged at equal distances of 14.5 m along the line, starting at about 100 m above the sea bed and interlinked by electro-optical cables. A standard storey consists of a titanium support structure, holding three *Optical Modules* (each one consisting of a photomultiplier tube inside a water-tight pressure-resistant glass sphere) and one cylindrical electronics container

A 13th line, called *Instrumentation Line (IL)*, is equipped with instruments for monitoring the environment. It holds six storeys. For two pairs of consecutive storeys in the IL, the vertical distance is increased to 80 m. Each line is fixed on the sea floor by an anchor equipped with electronics and

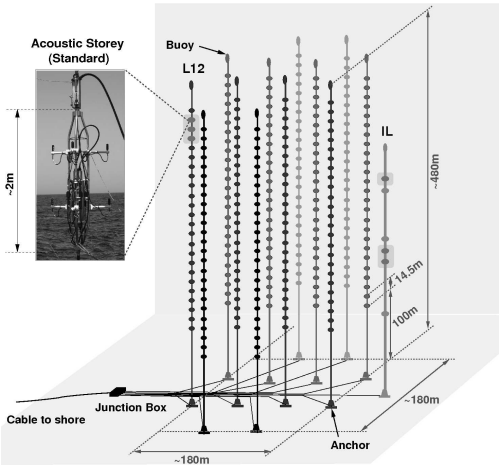

Figure 1: A sketch of the ANTARES detector. The six acoustic storeys are highlighted and a photograph of a storey in standard configuration is shown. L12 and IL denote the 12th detection line and the Instrumentation Line, respectively.

held taut by an immersed buoy. An interlink cable connects each line to the *Junction Box* from where the main electro-optical cable provides the connection to the shore station.

3 The AMADEUS System

Within the AMADEUS system [6], acoustic sensing is integrated in the form of *acoustic storeys* that are modified versions of standard ANTARES storeys, in which the Optical Modules are replaced by custom-designed acoustic sensors. Dedicated electronics is used for the amplification, digitisation and pre-processing of the analogue signals. Figure 2 shows the design of a standard acoustic storey with hydrophones. Six acoustic sensors per storey were implemented, arranged at distances of roughly 1 m from each other. The data are digitised with 16 bit resolution and 250 k samples per second.

The AMADEUS system comprises a total of six acoustic storeys: three on the IL, which started data taking in December 2007, and three on the 12th detection line (Line 12), which was connected to shore in May 2008. AMADEUS is now fully functional and routinely taking data.

Two types of sensing devices are used in AMADEUS: hydrophones and *Acoustic Modules* [6]. The acoustic sensors employ in both cases piezo-electric elements for the broad-band recording of signals with frequencies ranging up to 125 kHz. For the hydrophones, the piezo elements are coated in polyurethane, whereas for the Acoustic Modules they are glued to the inside of standard glass spheres which are normally used for Optical Modules.

The measurements presented in this article were done with the hydrophones. Their calibration will be discussed in Sec. 4.

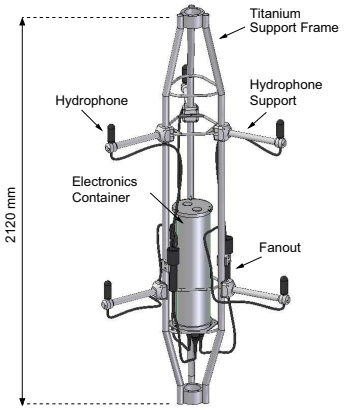

Figure 2: Drawing of a standard acoustic storey, or acoustic cluster, with hydrophones.

The AMADEUS on-shore trigger[1] searches the data by an adjustable software filter; the events thus selected are stored to disk. This way the raw data rate of about 1.5 TB/day is reduced to about 10 GB/day for storage. Currently, three trigger schemes are in operation [6]: A minimum bias trigger which records data continuously for about 10 s every 60 min, a threshold trigger which is activated when the signal exceeds a predefined amplitude, and a pulse shape recognition trigger. For the latter, a cross-correlation of the signal with a predefined bipolar signal, as expected for a neutrino-induced shower, is performed. The trigger condition is met if the output of the cross-correlation operation exceeds a predefined threshold. For the latter two triggers, the thresholds are automatically adjusted to the prevailing ambient noise and the condition must be met in at least four sensors of a storey.

4 Ambient Noise

Ambient noise, which can be described by its characteristic power spectral density (PSD), is caused by environmental processes and determines the minimum pulse height that can be measured, if a given signal-to-noise ratio (SNR) can be achieved with a search algorithm. To measure the ambient background at the ANTARES site, data from one sensor on the IL07 taken from the beginning of 2008 until the end of 2010 were evaluated. After quality cuts, 27905 minimum bias samples (79.9% of the total number recorded in that period) were remaining for evaluation, each sample containing data continuously recorded over a time-span of $\sim$10 s. For each of these samples, the noise PSD (units of V^2/Hz) was integrated in the frequency range $f = 10 - 50$ kHz, yielding the square of the ambient noise for that sample, as quantified by the output voltage of the hydrophone. Preliminary studies using the

1. While this functionality might be more commonly denoted as filtering, it is ANTARES convention to refer to the "on-shore trigger".

shower parametrisation and algorithms from [4] indicate that this range optimises the SNR for the expected neutrino signals.

The frequency of occurrence distribution of the resulting noise values, relative to the mean noise over all samples, is shown in Fig. 3. Also shown is the corresponding cumulative distribution. For 95% of the samples, the noise level is below $2\langle\sigma_{\rm noise}\rangle$, demonstrating that the ambient noise conditions are stable.

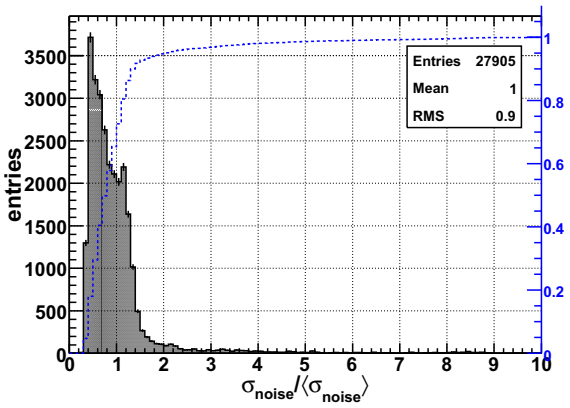

Figure 3: Frequency of occurrence distribution for the ambient noise in the range $10 - 50$ kHz, relative to the mean ambient noise recorded over the complete period of three years that was used for the analysis (left scale, filled histogram). Also shown is the cumulative distribution, normalised to the total number of entries of the distribution (right scale, dotted line).

All sensors have been calibrated in the laboratory prior to deployment. The absolute noise level can be estimated by assuming a constant sensor sensitivity[2] of -145 ± 2 dB re 1V/µPa. With this value, the mean noise level is $\langle\sigma_{\rm noise}\rangle = 10.1^{+3}_{-2}$ mPa with the median of the distribution at 8.1 mPa.

Currently, the detection threshold for bipolar signals corresponds to a SNR of about 2 for an individual hydrophone. For this SNR, the median of the noise distribution corresponds to a signal amplitude of ∼15 mPa, equivalent to a neutrino energy of ∼1.5 EeV at a distance of 200 m [3]. By applying pattern recognition methods that are more closely tuned to the expected neutrino signal, this threshold is expected to be further reduced.

5 Transient Sources

Transient sources, e.g. from sea mammals, may create signals containing the characteristic bipolar pulse shape that is expected from neutrino-induced showers. Furthermore, the pulse shape recognition trigger (see Sec. 3) selects events with a wide range of shapes. Therefore, a classification scheme is being developed that selects neutrino-like events and suppresses background events with high efficiency. After selecting neutrino candidates on the level of a storey, measurements from multiple storeys can be combined to search for patterns that are compatible with the characteristic "pancake" pressure field resulting from a neutrino interaction.

5.1 Source Position Reconstruction

The sensors within a cluster allow for efficient triggering of transient signals and for direction reconstruction. The combination of the direction information from different acoustic storeys yields the position of an acoustic source. Figure 4 shows the reconstructed directions of all sources

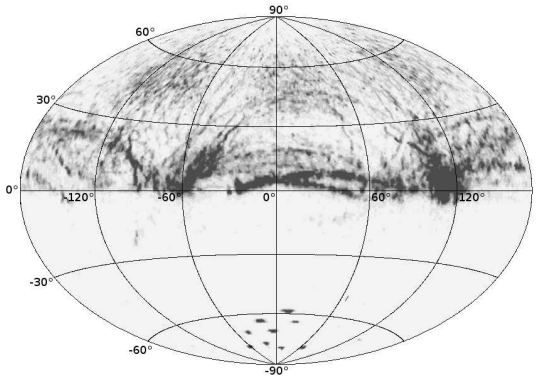

Figure 4: Map of directions of sources as reconstructed with an acoustic storey on Line 12. Zero degrees in azimuth correspond to the north direction, the polar angle of zero corresponds to the horizon of an observer on the acoustic storey. At the bottom, the signals of the emitters of the ANTARES positioning system are visible.

that were triggered during a period of one month. The dark bands of increased acoustic activity can be associated with shipping routes and points of high activity with the directions of local sea ports. It is obvious from Fig. 4 that a fiducial volume for the determination of the background rate of bipolar events must exclude the sea surface.

5.2 Signal Classification

The pulse shape recognition trigger described in Sec. 3 selects a wide range of events each of which can be allocated to one of four classes: Genuine bipolar events that are compatible with signals expected from neutrinos ("neutrino-like events"), multipolar events, reflections of signals from the acoustic emitters of the ANTARES positioning system and random events, where the latter class contains all events that do not fit into any of the other classes. For

2. The ambient noise is originating mainly from the sea surface and hence displays a directivity which has to be folded with the variations of the sensitivity over the polar angle to obtain an effective average sensitivity. For the results presented here, the noise has been assumed to be isotropic.

the classification, simulated signals representing the four classes in equal proportions were produced and a set of features extracted which are highly discriminant between the classes. This feature vector is then fed into a machine learning algorithm [8]. Classification is performed for the signals from individual hydrophones. Subsequently, the results from individual hydrophones are combined to derive a classification for a given acoustic storey. Several algorithms were investigated , the best of which yielded a failure rate (i.e. wrong decision w.r.t. simulation truth) at the 1%-level when applied to the two signal classes "neutrino-like" and "not neutrino-like".

6 Monte Carlo Simulations

Monte Carlo simulations based on [3, 4] are currently being implemented for the AMADEUS detector setup. Figure 5 shows the simulated density of the energy deposition of a 10^{10} GeV hadronic shower, projected into the xz-plane. The z- and x-coordinates denote the directions along the shower axis and a direction orthogonal to the shower axis, respectively. It is mostly the radial energy distribution within the shower which is responsible for the shape and amplitude of the acoustic pulse that is observed in the far field. The resulting pulse is shown in Fig. 6. The corresponding neutrino interaction was generated such that the centre of the hadronic shower for a vertically downgoing neutrino lies within the same horizontal plane as a storey denoted "Storey 2", at a distance of 200 m. This way, the storey lies within the "pancake" of the pressure field. On a storey 14.5 m below that storey, denoted "Storey 1", no signal is observed. This configuration corresponds to two adjacent acoustic storeys on L12 or the two lowermost storeys on the IL07, see Fig. 1. This simulation illustrates the characteristic three-dimensional pattern expected from neutrino-generated pressure waves.

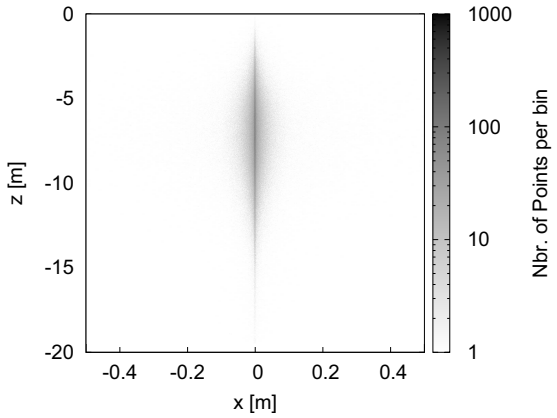

Figure 5: Density of the energy deposition of a 10^{10} GeV hadronic shower resulting from a neutrino interaction, projected from a three-dimensional distribution upon the xz-plane. Bin sizes are 0.01 m in x and 0.1 m in z.

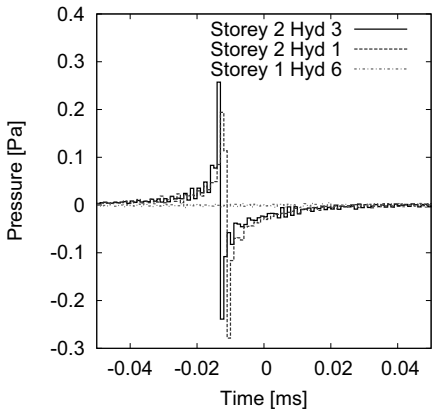

Figure 6: Simulated acoustic signals as recorded with hydrophones in two acoustic storeys with a vertical spacing of 14.5 m. See text for details. For Storey 2, signals from two different hydrophones are shown.

7 Summary and Conclusions

Recent results from the acoustic neutrino detection test system AMADEUS, an integral part of the ANTARES detector in the Mediterranean Sea, have been presented. Measurements of the ambient noise at the ANTARES site show that the noise level is very stable and at the expected level, allowing for measurements of neutrino energies down to $\sim$1 EeV. The current focus of the analysis work is on the classification of transient bipolar events to minimise the irreducible background for neutrino searches. In addition, Monte Carlo Simulations are under development. AMADEUS is excellently suited to assess the background conditions for the measurement of bipolar pulses expected to originate from neutrino interactions.

8 Acknowledgements

This study was supported by the German government through BMBF grants 5CN5WE1/7 and 05A08WE1.

References

[1] G.A. Askariyan *et al.* , Nucl. Instr. and Meth. 164 (1979) 267
[2] J. Learned, Phys. Rev. D 19 (1979) 3293
[3] S. Bevan *et al.* (ACoRNE Collaboration), Astropart. Phys. **28** (3) (2007) 366
[4] S. Bevan *et al.* (ACoRNE Collaboration), Nucl. Instr. and Meth. **A 607** (2009) 389
[5] V. Niess and V. Bertin, Astropart. Phys. **26** (2006) 243
[6] J.A. Aguilar *et al.* (ANTARES Collaboration), Nucl. Instr. and Meth. **A 626-627** (2011) 128
[7] M. Ageron *et al.* (ANTARES Collaboration), arXiv:1104.1607v1 [astro-ph.IM]
[8] M. Neff *et al.* , arXiv:1104.3248v1 [astro-ph.IM]

Prospects of Application of Multi-pixel Avalanche Photo Diodes in Cosmic Ray Experiments

I.M. ZHELEZNYKH[1], Z.YA. SADYGOV[2], B.A. KHRENOV[3], A.F. ZERROUK[4]
[1] *Institute for Nuclear Research, Russian Academy of Sciences, Moscow*
[2] *Joint Institute of Nuclear Research, Dubna, Moscow region*
[3] *D.V. Skobeltsyn Institute of Nuclear Physics, Moscow State University*
[4] *Zecotek Imaging System Pte Ltd, Singapore*

zhelezny@minus.inr.ac.ru

DOI: 10.7529/ICRC2011/V04/1101

Abstract: Possibilities of using in cosmic ray/astrophysical experiments the Multi-pixel Avalanche Photo Diodes – MAPDs which were developed by "Dubna MAPD" collaboration (JINR – INR – IP AZ – "Zecotek Photonics Singapore" Company) are discussed. The achieved basic parameters of the novel deep micro-well MAPDs with sensitive areas of 1-9 mm^2 are as following: spectral range of sensitivity 300-800 nm, gain 5 10^4, operating voltage 65-90 V, threshold of sensitivity - 1 photoelectron, photon detection efficiency (in maximum) ~30%, maximum density of pixels in a MAPD is 40000 pixels/mm^2. The MAPDs have the linear response up to 60000 photons in a light pulse, their filling factor – the ratio of sensitive area to all area – is equal to 100%. The designed photo sensors are planned to be used in orbital imaging detectors in particular observing transient luminous events (TLE) in the atmosphere. New TLE detector will have advantage of high temporal resolution and a possibility to observe events in various "colors" – from UV (300-400 nm) to red (600-800 nm).

Keywords: Silicon Photomultipliers, SiPMs, Multi-pixel Avalanche Photo-Diode; MAPD; orbital imaging detectors

1 Introduction.

1.1. Avalanche Photo-Diodes as solid state analogs of PMTs

In the recent years a few versions of photon counters based on silicon Avalanche Photo-Diodes (APDs) had been discussed at numerous conferences including Cosmic Ray Conferences. Mosaic APD detectors – solid state analogs of multi-channel Photo Multiplier Tubes (PMTs) - can be widely used in the High-Energy Physics, Cosmic Ray Physics, Astrophysics, Medicine etc., (see Proceedings Beaune – 2005 [1-2], [3], ICRC-2007 [4 -5], ICRC-2009 [6]). The interest in the new APDs is driven by their compactness, high quantum efficiency, low operation voltage, insensitivity to magnetic fields and potentially a lower cost in comparison with photomultipliers.
Very good prospects have CCD APDs – CCD with internal gain [7].

In this paper the Multi-pixel APDs with individual micro-wells (MAPDs) [8, 1, 5] which had been developed by "Dubna MAPD" collaboration (Joint Institute of Nuclear Research, Dubna; Institute for Nuclear Research of Russian Ac. Sci., Moscow; Institute of Physics of Azerbaijan Ac. Sci.; "Zecotek Photonics Singapore" Company) are described. The characteristic features of one of the last designs of MAPDs – MAPD-3N [9] are given. A possible application of MAPDs in orbital imaging detectors is discussed. Multi-channel detectors of gamma quanta based on MAPDs and crystal scintillators LFS [10] are also mentioned.

1.2. Early days of Multi-pixel Avalanche Photo-Diodes (MAPDs)

First successful steps in the development of a new type of APD with the local negative feedback had been made in 80th by a collaboration of the Institute for Nuclear Research (Z. Sadygov et al.) and the MELZ Company (V. Golovin et al.). Investigations of avalanche process in various multi-layer silicon structures with resistive layer

to "control" avalanche process in APDs were supported in the framework of the Soviet DUMAND project led by M. Markov in 1981-1991. The MRS (Metal-Resistive layer-Silicon) structures with high resistivity as silicon carbide and amorphous silicon layers had been chosen as a main object of investigation. The first results on planar MRS APDs were published in 1988-1989 [11] (see also [12]).

The next design of APDs with individual vertical resistors – micro-channel MRS APD had good characteristics and became the basic version of MAPDs in 1989-1991 [13].

2 Features and advantages of MAPDs with micro-wells

2.1. Three designs of MAPDs

Three designs of MAPDs developed by INR/JINR between 1991 and 2005 were free of basic design (MRS APD) problems such as a low sensitivity in blue and UV range and a low yield of working devices.

These devices were of following types

- the MAPD with individual surface resistors,
- he MAPD with surface transfer of charge carriers,
- the MAPD with deep buried individual microwells.

Their description was given in [1] (see also [5]).

Characteristics and possible applications of the MAPDs in detectors for the High Energy Physics, in medical researches (PET), etc had been described in a number of papers [14 - 15]

Below some characteristics and the advantages of the third type of MAPD - MAPD-3N produced by "Dubna Detectors Ltd" and "Zecotek Photonics Singapore Pte. Ltd" is presented. MAPD-3N with the active area 3x3 mm^2 has about 3x3x15600~140 thousands pixels (micro-wells). Its structure is shown in Figure 1.

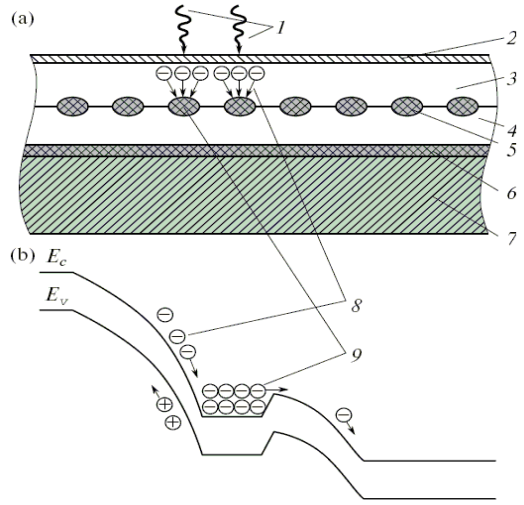

Figure 1. Schematic diagrams showing (a) the cross-section and (b) energy band diagram of MAPD at applied voltage: 1 – incident photons; 2 – high doped p+ layer that provides contact with the p-type epitaxial layer; 3 – second p-type epitaxial layer; 4 – first p-type epitaxial layer; 5 – n+ regions (micropixels); 6 – high doped n+ layer; 7 – n-type silicon substrate; 8 – avalanche region; 9 – charge accumulating microwell of *n*+ type micropixel

2.2. Photon detection efficiency – PDE

In paper [4] photon detection efficiency of SiPM is determined as the product of four factors:

- the light transmission from surface to depletion or drift layers,
- the filling factor of the sensitive area, (sensitive area)/all area),
- the quantum efficiency of silicon,
- Geiger efficiency.

The filling factor of micro-well MAPD is 100% (there are no guard rings, quenching registers, and aluminum conductors around micro-pixels as in SiPM). To increase PDE of MAPDS it is possible to increase their gain. However one has to be careful, if it is necessary, in order not to make worse other parameters, for example the crosstalk.

The PDE of a MAPD-3N is shown in Figure 2.

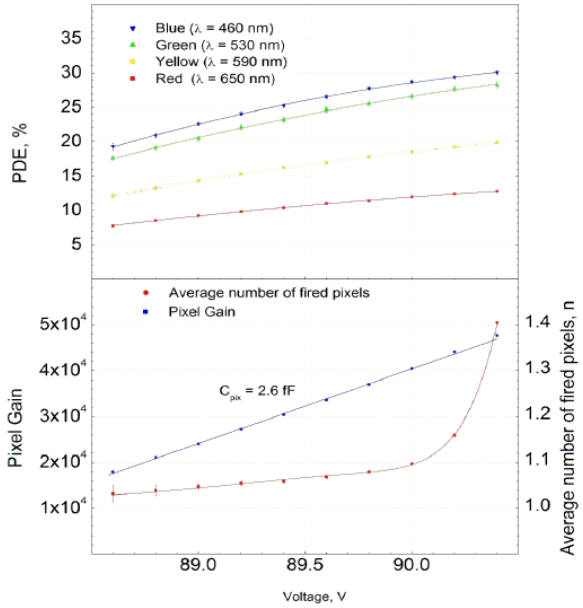

Figure 2. PDE, gain and average number of fired pixels versus bias voltage for the MAPD-3N at T = 15° C.

2.3. PDE, gain, crosstalk and dark current of MAPD-3N

As it is seen in Figure 2 MAPD-3N has a rather high sensitivity to blue light (PDE =~25-30%). The crosstalk (the average number of fired pixels for one detected photon) is low (<5%), if the gain is $2x10^4$ – $4x10^4$.

An optimization of MAPD parameters takes place, if the gain is ~$3x10^4$: then the PDE is ~25% in maximum and the average number of fired pixels is ~5%. And the dark current is ~20 nA (see Figure 3).

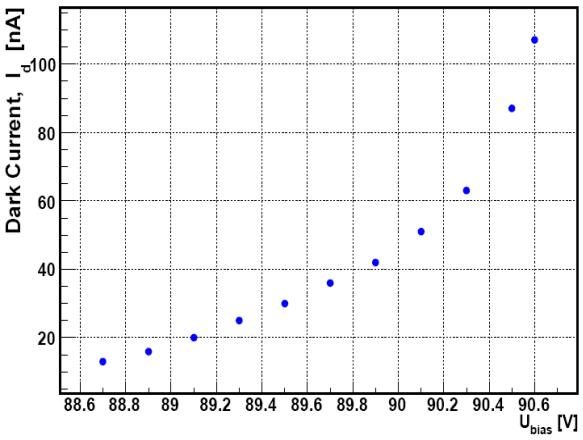

Figure 3. Dark current of MAPD-3N.

2.4. Linear response of MAPD up to 10000 photoelectrons

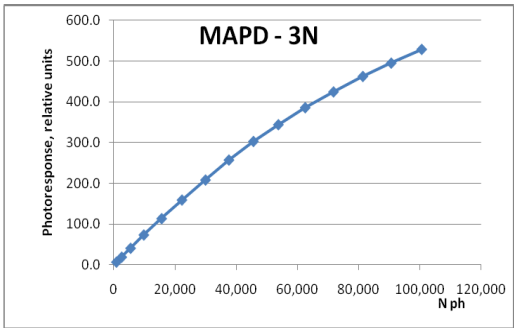

Figure 4. Photo response of MAPD-3N.

Linearity of photo response is a very perspective feature of MAPDs with micro-wells.

2.5. Development of multi-channel modules of gamma detectors based on MAPDs and LFS crystals

4-and 16-channel (mosaic) MAPD-3N modules developed by Dubna MAPD collaboration and the LFS crystal scintillators of 3x3x10 mm^3 developed by Zecotek Innovations [10] were used to construct coordinate-sensitive detectors of gamma quanta.

3 MAPDs and orbital imaging detectors

In many experiments observing various images the high resolution in time and position of photons are needed. Among them the most interesting are images of extreme energy (>50 EeV) fluorescence light tracks of EAS planned in the space experiment JEM-EUSO [16].

Presented above parameters of MAPD (for the MAPD of 3×3 mm^2 size quantum efficiency is ~25% in wavelength range near 400 nm, avalanche dark current 20-30 nA, when gain is $3x10^4$-$5x10^4$ closely suit the needed device parameters in JEM-EUSO – like experiments.
In this case MAPD of 3×3 mm^2 will be the detector pixel in focal plane of the JEM-EUSO lens system with area of 4.5 m^2. Electronics of the detector counts photo electrons in time samples of t=2.5 μs. EAS of energy 100 EeV in maximum of the shower cascade curve produces the count rate of ~100 per time sample. For above mentioned MAPD parameters the internal MAPD noise rate in time sample t is I_d t/(G×1.6 10^{-19}) ~12 counts. Atmospheric noise in the JEM-EUSO MAPD pixel at moonless night expected to be less than 5 counts. Linear response of MAPD to signals with less than 10^4 electrons per 1 mm^2 allows to measure EAS with energies up to 1000 EeV – which is high enough limit as statistics of such very high energy events is negligible due to sharp decrease of EAS event intensity beyond the GZK cut-off. One can see that parameters of MAPD are close to needed in JEM-EUSO – like experiment (although the combination of gain-dark current should be improved for getting lower pixel noise rate).
In experiments devoted to atmosphere transient luminous events (TLE) application of MAPD is even more promising. The TLE signals are six orders of magnitude larger than EAS signals [17]. In study of TLE the imaging detectors with wide field of view (thousands km in the atmosphere) and high space- time resolution (5 km in the atmosphere and 10 μs in time) will be available with MAPD technology.

4 Conclusion.

The current status of MAPDs with deep micro-wells is described. Characterestics of MAPDs produced by the Dubna MAPD collaboration (PDE in blue light ~25-30%, gain ~$5x10^4$, fired pixels ~5%) should be improved and optimized. After that MAPDs might be used in space experiments like the JEM-EUSO project. However the existing MAPDs can be used in space imaging detectors observing transient atmospheric phenomena (luminous events) when global observation of the phenomenon is needed.

Acknowledgements

I. Zheleznykh. and Z. Sadygov are deeply indebted to V. Matveev, A. Olshevski and A. Komar for valuable discussions and support and A. Zagumennyi for given LFS crystals.

References

[1] Z. Sadygov, et al. Nucl. Instr. and Meth. A567, 70 (2006).
[2] D. Renker. Nucl. Instr. and Meth., A567, 48 (2006).

[3] V. Golovin, V. Savelev. Nucl. Instr. and Meth. A518, 560 (2004).
[4] M. Tishima, B. Dolgoshein, R. Mirzoyan, et al. Proc. 30th ICRC, Mexico, 2008. Vol. 5 (HE part 1) 985-988.
[5] I. Zheleznykh, Z. Sadygov, B. Khrenov, et al. Proc. 30th ICRC, Mexico, 2008. Vol. 5 (HE part 2) 1589-1592
[6] H. Miyamoto, M. Tishima, B. Dolgoshein, et al. Proc. 31-st ICRC, Lodz (2009).
[7] Z.Ya. Sadygov, V.N. Jejer, Yu.V. Musienko, et al. Nucl. Instr. and Meth. A504, 301 (2003).
[8] Z. Sadygov. Russian Patent #2316848 of 01.06.2006.
[9] N. Anfimov, et al. Nucl. Instr. and Meth., A617, 78 (2010).
[10] A.I. Zagumennyi, Yu.D. Zavartsev, S.A. Kutovoi. Patent US 7,132,060. PST Filed: Mar.12, 2004.
[11] A. Gasanov, V. Golovin, Z. Sadygov, N. Yusipov. Technical Physics Letters, v.14, No.8, 706 (1988); Microelectronics, v.18, No.1, 88 (1989).
[12] Z. Sadygov et al. IEEE Trans. Nucl. Sci., 43, 3, 1009 (1996).
[13] A.G. Gasanov, Z.Ya. Sadygov, et al. Russian Patent #1702831, priority of 11.10.1989. Z. Sadygov et al. SPIE Proc., v.1621, 158 (1991).
[14] I. Britvitch, E. Lorenz, A. Olshevski, et al. JINST, 1, P088002, 2006. http://www.iop.org/EJ/jinst/
[15] I. Britvitch, E. Lorenz, A. Olshevski, et al. Nucl. Instr. and Meth. A571, 317 (2007).
[16] Takahashi Y. and JEM-EUSO collaboration. The JEM-EUSO mission. New J. Physics. 2009. V.11, doi:10.1088/1367-2630/11/6/06509.
[17] Sadovnichii V.A. et al. Investigation of Space Environment aboard the “Universitetsky-Tatiana” and “Universitetsky-Tatiana-2” satellites. Solar System Research. 2011. V.45, #1, p 3-29.

32ND INTERNATIONAL COSMIC RAY CONFERENCE, BEIJING 2011

The step tracking system of LHAASO-WFCTA

G. XIAO[1],L.L. MA[1], J. XIAO[2] ON BEHALF OF THE LHAASO COLLABORATION
[1] *Particle & Astrophysics Center, Institute of High Energy Physics, CAS*
[2] *Tianjin ship repairing technology institute*
xiaog@ihep.ac.cn
DOI: 10.7529/ICRC2011/V04/1346

Abstract: Based on fully understanding and deeply analyzing the current status of the detecting methods, the step tracking system of Wild Field Cherenkov Telescope (WFCT) has been designed. It is the combination of manufacturing and detecting method to achieve the accurate observation. The telescope rotation precision achieves 0.2°,and through calibration by using stars, the accuracy class is improved to 0.01°.

Keywords: LHAASO, WFCTA, observation accuracy, testing equipment

1 Introduction

Aiming at wide field of view survey for sources of gamma rays at energies above 100 GeV, the search for cosmic ray origins among those gamma ray sources at energies above 30 TeV and energy spectrum measurements for individual cosmic ray species from 30 TeV to 10 PeV, a Large High Altitude Air Shower Observatory (LHAASO) project with a complex array of many types of detectors is proposed. As one of the components of LHAASO project, two wide field of view telescope (WFCT) prototypes were installed at YangBaJing Cosmic Ray Observatory in 2007 and have been successfully running since Aug. 2008. Millions of cosmic ray events have been collected[1].

In order to explore the potential possibilities as imagining cherenkov telescope and deeply understanding detection, analysis method, one of the WFCT telescopes is updated to a step tracking system. The tracking system is used to track the γ ray sources to study the energy spectrum of the sources. In addition, with the large field of view, the telescope can be used to study the extent sources.

In this paper, the details of this tracking system is introduced, on the basis of manufacture precision a further calibration of the point accuracy by using the star light is employed.

2 Step-tracking

A tracking system is designed to track γ ray sources. Due to the large field of view (FOV) ($14^\circ \times 16^\circ$) of the telescope, it takes a point like γ ray source about 50-60 minutes to pass though the FOV of the telescope depending on the declination of the sources, so a step by step tracking mode is chosen.

The interval of the telescope has to change its pointing based on two factors. One is the accuracy of the pointing of the telescope which can be calibrated by bright stars, the other is the uniform observation to the neighborhood of the target, which is used to estimate the background of the target. If the telescope changes its pointing in a short time, the uniformity can be kept very well, however, the calibration of the pointing of the telescope becomes very difficult due to the lack of the use of bright stars.

For example, when the telescope aims to observe the Crab Nebula, the pointing of the telescope is modified every 50 minutes based on requirements of the pointing accuracy and the uniformity of observation. Figure 1 shows the trace of Crab Nebula with the FOV of the telescope in the local coordinates. When Crab is on the positions shown by the red dots, the pointing of the telescope is changed in order to keep the sources always within the FOV of the telescope. And figure 2 shows the uniformity of the observation to the neighborhood of the Crab Nebula. The black area in figure 2 indicates the area with uniform observation. In order to avoid the lost of the uniform area, the pointing accuracy should be high.

3 Mechanical structure

According to the observation requirements, the following three items have to be satisfied with the new step tracking system: (1) a two dimensional rotation system is implemented, and the valid rotation range is [0°-90°] in the vertical direction and [-270°, 270°] in the horizontal direction; (2) the rotation speed of the tracking system can be

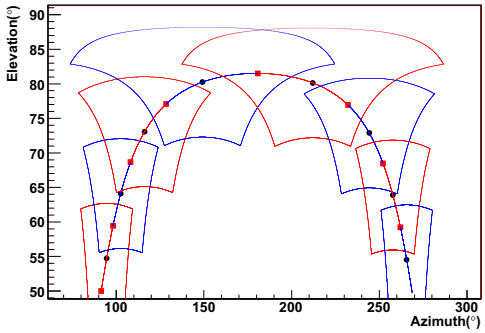

Figure 1: The trace of Crab Nebula in the local coordinates with the FOV of the telescope. The red and blue boxes indicate the FOV of the telescope in the local coordinates. The black dots show the center of the FOV of the telescope (the pointing of the telescope). The red dots indicate the pointing of the telescope is changed.

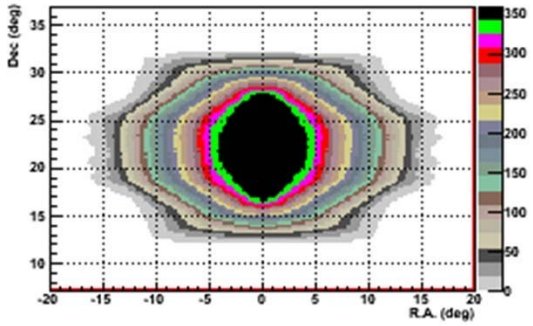

Figure 2: The uniformity of the observation to the neighborhood of the Crab Nebula.

adjusted; (3) in the point of view mechanical system, the rotation precision of the tracking system is less than 0.2°.

The step tracking system is composed of 6 sub-system: base, structure, azimuth-rotation device, zenith-rotation device, hydraulic and electrical system, as shown in figure 3.

The optical device is the most important part of this equipment. It consists of a camera composed of 16×16 PMT arrays, a 4.7 m^2 spherical mirror, hydraulic door and relevant electronics systems. The whole optical device is installed in a shipping container. The weight is around 3 tons.

The optical tube is fixed in the closed frame which is connected by the bolts. Side supports ensure the box rotate reposefully at the zenith, the distortion of all the structures is less than 0.2 mm under the normal operation.

The process of azimuth rotate should be smooth and steady, and the crawl of Hydraulic pressure motor is very serious at low speed, so it would affect the result of testing if we use the motor. The azimuth rotary device is structure with

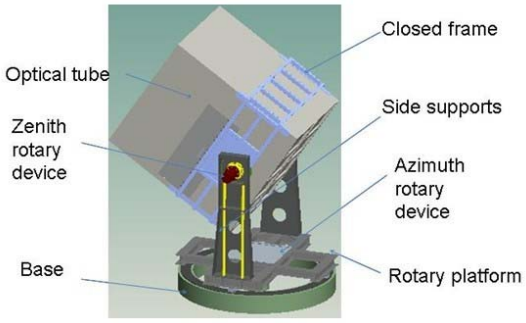

Figure 3: The mechanical structure of detector

Rotary gear reducer and the Turntable Bearing, which suits for the equipment.

Optical tube is set on the rotary platform which is made of profiled bar. The structure cannot be destroyed in Class 12 wind and can normally run in Class 7 wind, so the accuracy of observational data is ensured.

The base is made of reinforced concrete, which contains two parts: the middle support base and the round guide track. The middle support endures all weight of the equipments. The round guide track can keep the equipment from leaning and temporarily bear the force of over loading.

The rotary actuator can rotate the testing box at the zenith, which is composite actuator with gear-wheel and rack. It may modify the hydraulic energy to transmit mechanical energy. The movement of reciprocating piston and rack drives gear output torque and corner.

For Wild Field Cherenkov Telescope, the hydraulic station is the power system and there is overload protection for motor in the electric system. All action are controlled and checked by computer, so it can run automatically in the normal state even without supervision.

As detection system, the minimum angle should be ”arc second”, so the Absolute Encoder is adopted. After debugging and testing the equipment, the rotational errors are less than 0.2° during zenith rotary and azimuth rotary, meeting the design requirements.

4 Pointing calibration by using bright stars

As mentioned in section 2, the pointing accuracy of the tracking system can be achieved within 0.2°. In order to improve the pointing accuracy further, bright UV stars are used to calibrate the pointing of the telescope. In addition, the bight stars can also be used to study the systematics of the tracking system.

4.1 Star light

The telescope is designed to observe the Cherenkov light (300nm-600nm) emitted by the secondary charge particles in the EAS showers. For each air shower event, the signal of Cherenkov light can only lasts a few of nanoseconds, while the trigger window lasts $18\mu s$, thus in most of the trigger window, the telescope records the contribution of night sky background (NSB).

The NSB contains two components, one is the diffuse lamplight from the town of Yangbajing , the other one with well known directions and stable fluxes is from the bright stars appearing in the FOV of the telescopes. The two components are added to the signal of Cherenkov light and is recorded by the telescope. In order to avoid the contribution of the Cherenkov signal, only the average signal in the final 2μs of the trigger window is used to estimate the relative strength of the NSB. In order to reduce the fluctuations of NSB, the value of the recorded NSB is averaged every 10 minutes. The NSB recorded by one PMT in an observation night is shown in figure 4. The peaks in the figure 4 are caused by the bright stars. The peak amplitude of a star light in a PMT depends on its UV magnitude and its projected position on the camera plane. The peaks means a star appeared in the FOV of the telescope again for each change of the telescope. In order to avoid the effect of the diffuse NSB with value around 35 FADC counts, it is subtracted as background.

The positions and fluxes of the bright stars can be obtained from star catalogs. In out analysis, the TD1 catalog is used, which has four different wavelength bands, 1565, 1965, 2365 and 2740 $\mathring{A}$, respectively[2]. The WFCT telescopes are sensitive in the near UV band , so the last wavelength band with flux above $1 \times 10^{-11} erg/cm^2/s$ of TD1 is used.

4.2 Pointing of the telescope

According to the pointing given by the tracking system, the time when the brightest star appears in the FOV of the telescope can be found through the brightest PMT. Although the gain and uniform are calibrated by a led installed on the mirror[1]. ,however, due to the large size of the PMT ($1^\circ \times 1^\circ$), the positions of the PMT can not indicate the positions of the brightest star on the camera accurately. So the weighted center (x_0, y_0) by the FADC counts of the PMT and its neighbors within 2° is considered as the position of the star on the camera. According to the position, the trace of the brightest star on the camera can be obtained shown in figure 5. In figure 5, in order to show the relative positions between the PMTs and the traces of stars obtained by the PMTs, the 256 PMTs are plotted by the red hexagons.

In order to get pointing of the telescope, the trace of the brightest star is fitted by a linear function. When the star is in the middle of the camera in the horizonal direction, it has the same azimuth angle with that of the telescope, while the elevation angle of the star is equal to the elevation of the

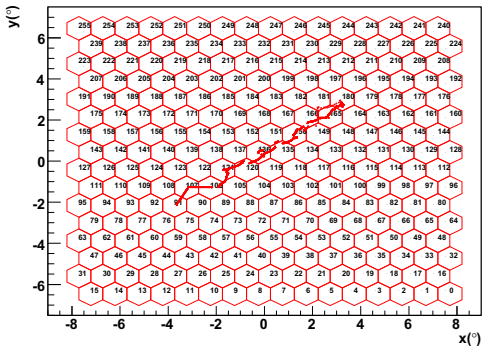

Figure 5: The trace of the brightest star on the camera. The red hexagons indicate the PMTs. The x and y axes indicate the coordinate of the focus plane in degree.

telescope plus the angular distance between the position of the star and the center of the camera.

The spot size formed by the parallel light is from 0.17° to 0.28° from the center of the camera to the edge of it[3]. So in order to get rid of the effects of the nearby stars, the orphan stars which have no surrounding stars within 2° are used to correct the pointing direction of the telescope obtained by the brightest stars, furthermore. In the neighborhood of Crab, there is about eight orphan stars.

The traces of the orphan stars on the camera can be obtained through the pointing of the telescope by the brightest stars. So the positions observed by the telescope of the orphan stars in the horizonal coordinates are obtained. The average differences between observed positions and the real one are reported back to the pointing direction of the telescope and the process is iterated. The difference between the observed one and the one of the star positions in the horizonal coordinates is defined as the accuracy of the pointing direction which are shown in figure 6. The top panel shows the accuracy in the azimuth direction, while the bottom one shows the accuracy in the elevation direction. The RMSs of the distributions are about 0.20° and 0.17°, respectively. Considering the number of the orphan star used, the accuracy of the pointing obtained by the method is better than 0.01°. The pointing of the telescope for each rotation can be calibrated by the method.

With the accuracy of the calibration better than 0.01°, the systematics of the pointing of the tracking system can be studied. For each rotation, the pointings of the telescope are recorded by the tracking system, and the differences between the pointings obtained by the bright stars and the ones from tracking system can be considered as the systematics of the tracking system. One night data is used to study the systematics. The differences for each rotation are shown in figure 7.

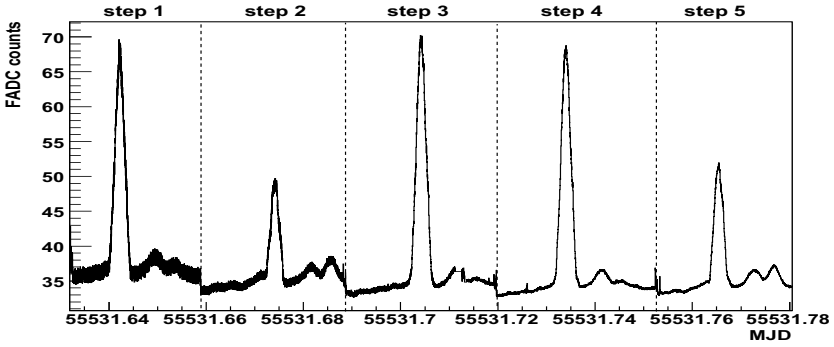

Figure 4: A typical recorded by one PMT in an observation night.

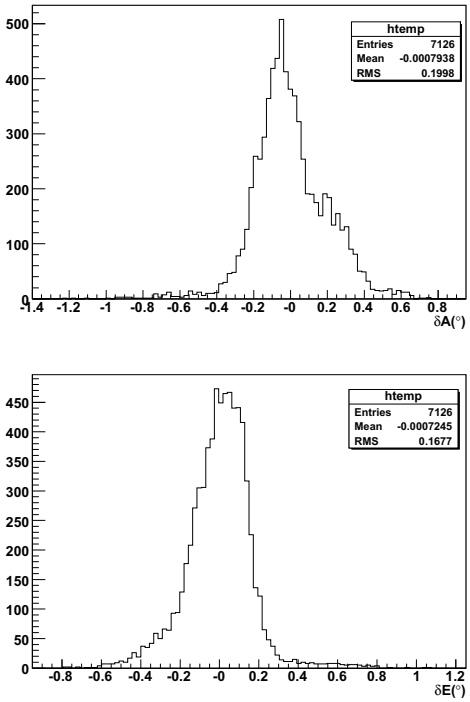

Figure 6: The accuracy of the pointing of the telescope. The upper plot shows the accuracy in the azimuth direction, while the bottom one shows the accuracy in the elevation direction.

5 Conclusion

The two WFCTA telescopes have been running for 4 years smoothly. Recently, the mechanical structure of one of the telescopes has been updated to track the γ ray sources. The accuracy of the pointing of the tracking system is within 0.2°. In order to improve the accuracy of the pointing of the telescope, a method using bright stars to calibrate the pointing of the telescope is used. After calibration, the accuracy of the telescope is better than 0.01° both in azimuth and elevation direction.

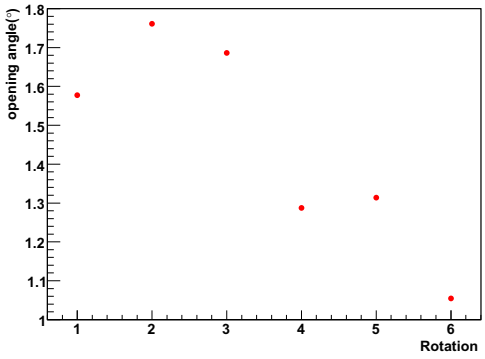

Figure 7: The systematics of the tracking system. The space angle between the pointing of obtained by the stars and the one given by the tracking system.

6 ACKNOWLEDGEMENTS

This work is supported by the Chinese Academy of Sciences (0529110S13) and the Key Laboratory of Particle Astrophysics, Institute of High Energy Physics, CAS. The Knowledge Innovation Fund (H85451D0U2) of IHEP, China. The project 10975145 and 11075170 of NSFC also provide support to this study.

References

[1] S.S. Zhang et al., Nucl. Instr. and Meth. A 629 (2011) 57-C65
[2] G. L. Thompson, et. al. The Science Research Council, 1978, Catalog os Steller Ultraviolet Flux
[3] L. L. Ma, et. al, CPC(HEP & NP), 2011, **35(5)**:483-487